UNIVERSIDAD
DE LA RIOJA

TESIS DOCTORAL

Título

Synthesis, Characterization and Study of Luminescent Au/Ag and Au/Tl Heterometallic Compounds with Mixed Donor Macrocyclic Derivatives

Autor/es

Mattia Nieddu

Director/es

José María López de Luzuriaga Fernández y Vito Lippolis

Facultad

Facultad de Ciencia y Tecnología

Titulación

Departamento

Química

Curso Académico

Synthesis, Characterization and Study of Luminescent Au/Ag and Au/Tl Heterometallic Compounds with Mixed Donor Macrocyclic Derivatives, tesis doctoral de Mattia Nieddu, dirigida por José María López de Luzuriaga Fernández y Vito Lippolis (publicada por la Universidad de La Rioja), se difunde bajo una Licencia Creative Commons Reconocimiento-NoComercial-SinObraDerivada 3.0 Unported.

publicaciones.unirioja.es
E-mail: publicaciones@unirioja.es

SYNTHESIS, CHARACTERIZATION AND STUDY OF LUMINESCENT AU/AG AND AU/TL HETEROMETALLIC COMPOUNDS WITH MIXED DONOR MACROCYCLIC DERIVATIVES

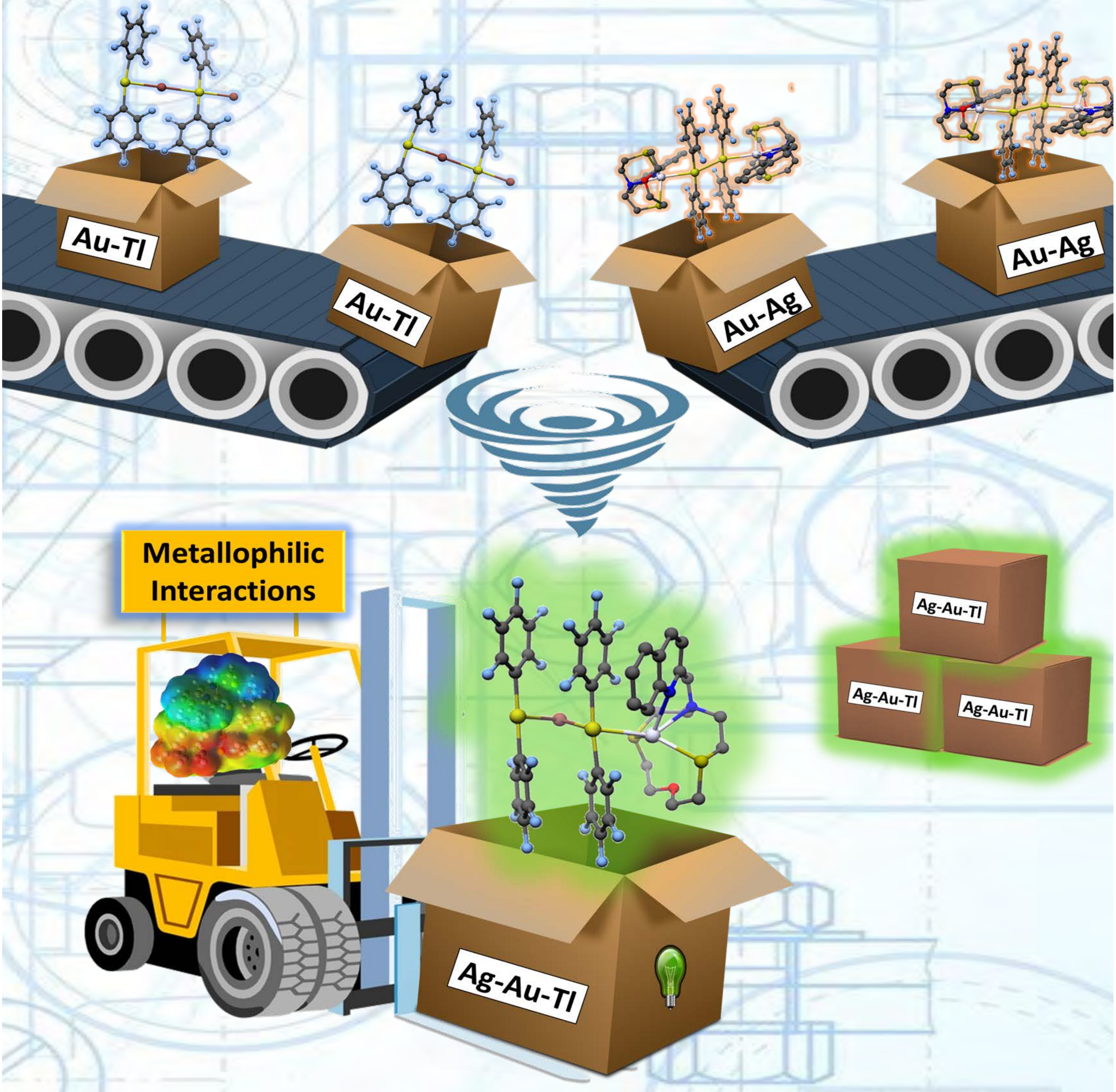

Mattia Nieddu

UNIVERSIDAD DE LA RIOJA
DEPARTAMENTO DE QUÍMICA
ÁREA DE QUÍMICA INORGÁNICA

UNIVERSITÀ DEGLI STUDI DI CAGLIARI
DIPARTIMENTO DI SCIENZE CHIMICHE E GEOLOGICHE
CHIMICA INORGANICA

SYNTHESIS, CHARACTERIZATION AND STUDY OF LUMINESCENT AU/AG AND AU/TL HETEROMETALLIC COMPOUNDS WITH MIXED DONOR MACROCYCLIC DERIVATIVES.

PhD thesis presented in the University of La Rioja and Cagliari

Mattia Nieddu

JOSÉ Mª LÓPEZ DE LUZURIAGA FERNÁNDEZ, Catedrático de Química Inorgánica de la Universidad de La Rioja, y

VITO LIPPOLIS, Professore Ordinario di Chimica Inorganica della Università di Cagliari

CERTIFICAN:

Que la presente memoria, titulada *"Synthesis, characterization and study of luminescent Au/Ag and Au/Tl heterometallic compounds with mixed donor macrocyclic derivatives"*, ha sido realizada entre el Departamento de Química de la Universidad de La Rioja y Scienze chimiche e Biologiche dell'Università di Cagliari, área de Química Inorgánica, bajo nuestra dirección por el Licenciado Mattia Nieddu y autorizamos su presentación para que sea calificada como *Tesis Doctoral*.

Logroño/Cagliari, Febrero de 2018

Prof. Dr. José Mª López de Luzuriaga

Prof. Vito Lippolis

Credere in se stessi è uno dei mattoni più importanti nella costruzione di ogni impresa di successo.

Lydia Maria Child

Realizar la tesis doctoral es un camino muy duro que conlleva un crecimiento no solo desde el punto de vista científico, si no sobre todo desde el punto de vista personal. Son muchas las personas que he encontrado en este camino que han contribuido a la realización de este trabajo y a las cuales estaré eternamente agradecido.
En primer lugar, quería dar las gracias a mis directores de tesis el Prof. Dr. José María López de Luzuriaga y el Prof. Dr. Vito Lippolis sin los que este trabajo no hubiera sido posible. Por trasmitirme la pasión por la investigación que junto a vuestro conocimiento me ha permitido llevar a cabo esto proyecto tan duro pero lleno de satisfacciones. A la Prof. Dra. Elena Olmos y el Dr. Miguel Monge, por soportarme y estar siempre dispuestos a echarme una mano y por supuesto ayudarme con la resolución de estructuras cristalinas y cálculos teóricos.

A todo el grupo de la Universidad de Cagliari y en particular a la Dra. Alessandra Garau, que me ha guiado constantemente en todos los pasos del trabajo en el laboratorio, soportado y apoyado a lo largo de mi camino. El compañero de mil aventuras Giacomo Picci, con quien compartí todo en estos años de Universidad.

A los compañeros de laboratorio, Maria R., Maria G., Rocio, Marta, Daniel, Sonia y Quintana, que me han ayudado a superar momentos duros y complicados y por su infinita disponibilidad y paciencia en la comprensión de mi nuevo idioma el "Itañol".

A los Orgánicos y Platineros por haberme bromeado continuamente sobre mi origen, mi idioma y mi innata capacidad (¡en solo dos años!) de hablar un castellano casi perfecto (merezco la nacionalidad riojana solo por eso). En particular me gustaría dar las gracias a Raúl, David y Nora que han estado particularmente cerca en estos tres años.

A todos los docentes, laborantes, los de conserjería y cafetería para haberme vacilado sobre el número de finales o partidos perdidos de la Juventus contra el Madrid en estos tres años.

Claramente no puedo olvidarme de mis dos hermanos adoptivos David Pascual y July por haberme dado una apoyo fundamental durante estos años y dado la posibilidad de compartir un buen trozo de vida con ellos enseñándome el valor de la verdadera amistad. Mi aventura en Logroño no sería la misma sin vosotros.

Por último, pero no menos importante, un agradecimiento especial va para Alicia, por todas las veces que has estada a mi lado, por haberme soportado, sostenido y ayudado en todo el camino.

Gracias a Todos!!!!!

Il dottorato di ricerca è un camino molto duro che porta alla crescita non solo da un punto di vista scientifico, ma anche dal un punto di vista personale. Ci sono molte persone che hanno contribuito alla realizzazione di questo lavoro e al quale sarò eternamente grato.

Prima di tutto, volevo ringraziare i miei direttori di tesi, il Prof. Dr. José María López de Luzuriaga e il Prof. Dr. Vito Lippolis senza la quale la realizzazione di questo lavoro non sarebbe stato possibile. Per trasmettermi la passione per la ricerca che insieme alla loro conoscenza mi ha permesso di realizzare un progetto così duro ma pieno di soddisfazioni. Alla Prof. Elena Olmos e al Dott. Miguel Monge, per essere sempre stati disponibili e naturalmente per avermi aiutato con la risoluzione delle strutture cristalline e dei calcoli teorici.

All'intero gruppo dell'Università di Cagliari e in particolare la dott.ssa Alessandra Garau, che ha costantemente guidato in tutti i passi del mio lavoro e supportato lungo il mio percorso. Al compagno di mille avventure di Giacomo Picci, con il quale ho condiviso tutto in questi anni di Università.

Ai compagni di laboratorio, Maria R., Maria G., Rocio, Marta, Daniel, Sonia e Quintana, che mi hanno aiutato a superare momenti difficili e per loro infinita disponibilita e la pazienza nel capire la mia nuova lingua "L'Itañol ".

Al gruppo di Organica e del Platino per aver continuamente scherzato sulla mia provenienza e la mia straordinaria capacità (in soli due anni!) di parlare uno spagnolo perfetto (mi merito nazionalità Riojana solo per questo). In particolare vorrei ringraziare Raul, David e Nora per essermi stati vicini in questi tre anni.

A tutti gli insegnanti, i tecnici, i bidelli e la caffetteria per le continue prese in giro sul numero di finali o le partite perse della Juventus contro il Real Madrid in questi tre anni.

Chiaramente non posso dimenticarmi dei miei due fratelli acquisiti David Pasqual y July per il loro appoggio fondamentale in questi tre anni e per avermi insegnato ancora una volta il valore della vera amicizia. La mia avventuro a Logroño non sarebbe la stessa senza di voi.

Ultimo ma non meno importante, un ringraziamento speciale ad Alicia, per tutte le volte in cui è stata al mio fianco, per avermi supportato, sopportato e aiutato per tutto il tempo.

Grazie a tutti!!!!!

CONTENTS

Abbreviations.. 7

Resumen.. 9

INTRODUCTION

1. Gold 13
2. Gold and silver 16
3. Gold and thallium 20
4. PhD thesis aim 24
5. References 26

CHAPTER I. SYNTHESIS OF ORGANIC LIGANDS

1.1 Introduction 31
1.2 Coordination chemistry of L_1-L_7 36
1.3 Synthesis of Organic ligands (L_1-L_7) 46
1.4 Template reactions method 47
1.5 High dilution method 48
1.6 Synthesis of L_1 ([12] aneNS_3) and L_3 ([12]aneNS_2O) 49
1.7 Synthesis of L_2 ([12]aneN_2S_2) 50
1.8 Synthesis of L_4 (5-aza-2,8-dithia[9](2,9)-1,10-phenanthrolinophane) 51
1.9 Synthesis of L_5 ([9]aneN_3) 52
1.10 Synthesis of L_6 (5-(2-quinolinylmethyl)-5-aza-2,8-dithia[9](2,9)-1,10-phenanthrolinophane) and L_7 (1-(2-quinolinylmethyl)-[12]aneNS_2O) 53
1.11 References 54

CHAPTER II. GOLD(I)-THALLIUM(I) HETERONUCLEAR COMPOUNDS

2.1 Gold(I)-thallium(I) heteronuclear compounds 59
2.2 N,S,O-mixed-donor crown ligand ethers (L_1-L_3) 62
    2.2.1 Synthesis and characterization 62
    2.2.2 X-ray structural determinations 64
    2.2.3 Photophysical Properties 72

2.2.4 Computational Study 76
2.2.5 Conclusions 89
2.3 Organic ligands with different rig size cavity and donor atoms (L_4-L_5) 90
2.3.1 Introduction 90
2.3.2 Synthesis and characterization 91
2.3.3 X-ray structural determinations 93
2.3.4 Photophysical Properties 98
2.3.5 Computational Study 103
2.3.6 Conclusions 107
2.4 Functionalized macrocyclic systems (L_6-L_7) 108
2.4.1 Introduction 108
2.4.2 Synthesis and characterization 109
2.4.3 X-ray structural determinations 111
2.4.4 Photophysical Properties 119
2.4.5 Computational Study 123
2.4.6 Conclusions 133
2.5 References 134

CHAPTER III. GOLD(I)-SILVER(I) HETERONUCLEAR COMPOUNDS

3.1 Gold(I)-silver(I) heteronuclear compounds........ 145
3.2 N,S,O-mixed-donor crown ligand ethers (L_1-L_3)........ 147
3.2.1. Synthesis and characterizazion 147
3.2.2 X-ray structural determinations 150
3.2.3 Photophysical Properties 160
3.2.4 Computational Study 168
3.2.5 Conclusions 179
3.3 Organic ligands with different rig size cavity and donor atoms (L_4-L_5) 180
3.3.1 Introduction 180
3.3.2 Synthesis and characterizazion 182
3.3.3 X-ray structural determinations 184
3.3.4 Photophysical Properties 190
3.3.5 Computational Study 195
3.3.6 Conclusions 200
3.4 Functionalized macrocyclic systems (L_6-L_7) 201

3.4.1 Introduction 201
3.4.2 Synthesis and characterization 202
3.4.3 X-ray structural determinations 204
3.4.4 Photophysical Properties 208
3.4.5 Computational Study 211
3.4.6 Conclusions 217
3.5 Heterotrimetallic complexes 218
3.5.1 Synthesis and characterization 218
3.5.2 Computational Study and Conclusions 223
3.6 References 232

EXPERIMENTAL SECTION

A. Instrumental and spectroscopic technique used for the characterization of compounds 241
A.1 Elemental analyses 241
A.2 Infrared spectra (FT-IR) 241
A.3 Nuclear magnetic resonance (NMR) 241
A.4 Mass Spectra 241
A.5 Conductivity measurements 241
A.6 X-ray diffraction 242
A.6.1 X-ray diffraction of single crystal 242
A.7 X ray powder diffraction 242
A.8 UV-Vis spectra 242
A.9 Luminescence spectra. Determination of emission life times 243
B. Synthesis of new compounds 243
B.1 Starting materials 243
B.2 Synthesis of N-butoxycarbonyl-1-aza-4,7,10-trithiacyclododecane (Boc-L_1) 243
B.3 Synthesis of 1-aza-4,7,10-trithiacyclododecane (L_1) 244
B.4 Synthesis of 4,11-Bis(tert-butoxycarbonyl)-1,7-dithia-4,11-diazacyclotetradecane (Boc-L_2) 244
B.5 Synthesis of 1,7-dithia-4,11-diazacyclotetradecane (L_2) 245
B.6 Synthesis of N-butoxycarbonyl-1-aza-4,10-dithia-7-oxacyclododecane (Boc-L_3) 245
B.7 Synthesis of 1-aza-4,10-dithia-7-oxacyclododecane (L_3) 246
B.8 Synthesis of N-Boc-5-aza-2,8-dithia[9](2,9)-1,10-phenanthrolinophane (Boc-L_4) 246

B.9 Synthesis of 5-aza-2,8-dithia[9](2,9)-1,10-phenanthrolinophane (L_4) 247

B.10 Synthesis of N-N’-N’’-Tritosyl-1,4,7-triazacyclononane (Tos-L_5) 247

B.11 Synthesis of 1,4,7-Triazacyclononane (L_5) 248

B.12 Synthesis of 5-(2-quinolinylmethyl)-5-aza-2,8-dithia[9](2,9)-1,10-phenanthrolinophane (L_6) 248

B.13 Synthesis of 1-(2-quinolinylmethyl)-1-aza-4,10-dithia-7-oxacyclododecane (L_7) 249

B.14 Synthesis of $[\{Au(C_6Cl_5)_2\}\{Tl(L_1)\}_2][Au(C_6Cl_5)_2]$ (1) 250

B.15 Synthesis of $[\{Au(C_6Cl_5)_2\}\{L_2)\}_2][Au(C_6Cl_5)_2]$ (2) 250

B.16 Synthesis of $[\{Au(C_6Cl_5)_2\}\{TlL_3)\}]$(3) 250

B.17 Synthesis of $[\{Au(C_6F_5)_2\}Tl(L_1)]_2$ (4) 251

B.18 Synthesis of $[\{Au(C_6F_5)_2\}Tl(L_2)]_n$ (5) 251

B.19 Synthesis of $[\{Au(C_6F_5)_2\}Tl(L_3)]_2$ (6) 251

B.20 Synthesis of $[\{Au(C_6Cl_5)_2\}\{TlL_4\}]$ (7) 252

B.21 Synthesis of $[\{Au(C_6Cl_5)_2\}\{Tl(L_5)\}]_{2n}$ (8) 252

B.22 Synthesis of $[\{Au(C_6F_5)_2\}\{TlL_4\}]_n$ (9) 252

B.23 Synthesis of $[\{Au(C_6F_5)_2\}\{Tl(L_5)\}]$ (10) 253

B.24 Synthesis of $[\{Au(C_6Cl_5)_2\}\{Tl(L_6)\}]$ (11) 253

B.25 Synthesis of $[\{Au(C_6Cl_5)_2\}\{Tl(L_7)\}]$ (12) 253

B.26 Synthesis of $[\{Au(C_6F_5)_2\}\{Tl(L_6)\}]$ (13) 254

B.27 Synthesis of $[\{Au(C_6F_5)_2Tl\}\{Au(C_6F_5)_2Tl(L_6)\}]_2$ (14) 254

B.28 Synthesis of $[\{Au(C_6F_5)_2\}\{Tl(L_7)\}]$ (15) 254

B.29 Synthesis of $[\{Au(C_6F_5)_2Tl\}\{Au(C_6F_5)_2Tl(L_7)\}]_n$ (16) 255

B.30 Synthesis of $[\{Au(C_6Cl_5)_2\}\{Ag(L_1)\}]$ (17) 255

B.31 Synthesis of $[\{Au(C_6Cl_5)_2\}\{Ag(L_2)\}]$ (18) 255

B.32 Synthesis of $[\{Au(C_6Cl_5)_2\}\{Ag(L_3)\}]$ (19) 256

B.33 Synthesis of $[\{Au(C_6Cl_5)_2\}\{Ag(L_3)\}]_2$ (20) 256

B.34 Synthesis of $[\{Au(C_6F_5)_2\}\{AgL_1\}]_2$ (21) 256

B.35 Synthesis of $[\{Au(C_6F_5)_2\}\{AgL_2\}]$ (22) 257

B.36 Synthesis of $[\{Au(C_6F_5)_2\}\{Ag(L_3)\}]$ (23) 257

B.37 Synthesis of $[\{Au(C_6Cl_5)_2\}\{AgL_4\}]$ (24) 257

B.38 Synthesis of $[\{Au(C_6Cl_5)_2\}\{Ag(L_5)\}]$ (25) 258

B.39 Synthesis of $[\{Au(C_6F_5)_2\}\{AgL_4\}_2][Au(C_6F_5)_2]$ (26) 258

B.40 Synthesis of $[\{Au(C_6F_5)_2\}\{Ag(L_5)\}_2Au(C_6F_5)_2]$ (27) 258

B.41 Synthesis of $[\{Au(C_6Cl_5)_2\}\{Ag(L_6)\}]$ (28) 259

B.42 Synthesis of $[\{Au(C_6Cl_5)_2\}\{Ag(L_7)\}]$ (29) 259

B.43 Synthesis of $[\{Au(C_6F_5)_2\}\{AgL_6\}_2][Au(C_6F_5)_2]$ (30) 259

B.44 Synthesis of $[\{Au(C_6F_5)_2\}_2\{Ag_2L_6\}]$ (31) 260

B.45 Synthesis of $[\{Au(C_6F_5)_2\}\{AgL_7\}]_2$ (32) 260

B.46 Synthesis of $[\{Au(C_6F_5)_2\}_2\{Ag_2L_7\}]$ (33) 260

B.47 Synthesis of $[\{Au(C_6F_5)_2Tl\}\{Au(C_6F_5)_2Tl\{Au(C_6F_5)_2AgL_7\}\}_2]_n$ (34) 261

C. Crystallographic data 262

D. Computational details 319

E. References 320

Conclusiones 323

ABBREVIATIONS

General

IR!	Infrared
L!	Ligand
Me!	Methyl
Ph!	Fenyl
X!	Halogen
R!	Aril
THF!	tetrahydrofurane
tht!	Tetrahydrothiophene
M!	Transition metal
NMR!	Nuclear Magnetic Resonance
MS!	Mass spectrometry
UV-Vis!	Ultraviolet-Visible
o-!	Orto-
p-!	Para-
m-!	Meta-

In NMR

t!	Triplet
m!	Multiplets
s!	Singlet
d!	Doublet
J!	Coupling constant
ppm!	Parts per million

In IR

v!	Wave number

In X-Ray

ρe!	Eletronic density
Goof!	Goodness of Fit
Refl.!	Reflexiones

In MS

ESI!	electrospray Ionization
m/z!	Mass/Charge
MALDI!	Matrix Assisted Laser Desorption Ionization.

In Luminescence, UV-Vis

ε!	Absorption molar
λ!	wavelength
λexc!	Excitation wavelength
λem!	Emission wavelength
τ!	Life time
F!	Fluorophore
Q!	Disactivating agent
S-V!	Stern-Volmer

Theorical Calculation

HOMO!	Highest Occupied Molecular Orbital
LUMO!	Lowest Occupied Molecular Orbital
DFT!	Density Functional Theory
TD-DFT	Time Dependent Density Functional Theory
SOMO	Single Occupied Molecular Orbital
MP2	Second-order Moller-Plesset pertubation
HF	Hartree–Fock

Resumen

La presente memoria está dedicada a la síntesis y caracterización de complejos heterometálicos Au(I)/M(I) (M(I)= Ag(I), Tl(I)) con ligandos macrocíclicos y derivados. Asimismo, se ha realizado el estudio experimental de las propiedades ópticas de los nuevos complejos y los cálculos teóricos correspondientes que ayuden a la interpretación del origen de estas propiedades. Además, el empleo de ligandos macrocíclicos con capacidades coordinativas y electrónicas diferentes nos ha permitido sintetizar y caracterizar una gran variedad de compuestos con interacciones metalofílicas por reacción con diversos precursores de oro(I), plata(I) y talio(I). En función de los metales(I) y ligandos empleados, se ha dividido esta memoria en cuatro capítulos: En el primer capítulo se aborda la síntesis de nuevos sistemas macrocíclicos con diferentes cavidades y diferentes propiedades coordinativas. Nuestro principal objetivo será evaluar la influencia que tienen los diferentes ligandos tanto en la disposición estructural de los derivados como en las propiedades ópticas. En el segundo y en el tercer capítulo de este trabajo se lleva a cabo la preparación de complejos heterometálicos Au(I)/Tl(I) y Au(I)/Ag(I) con los diferentes ligandos sintetizados anteriormente. En estos apartados se estudia la influencia que ejercen los ligandos coordinados a los metales en las disposiciones estructurales de los compuestos, así como en sus propiedades fotofísicas y en las interacciones metalofílicas. Además, en algunos casos seleccionados, estos compuestos han sido objeto de un profundo estudio a nivel teórico, que nos ha permitido conocer el origen de la luminiscencia observada experimentalmente.

Para concluir, en el último apartado del tercer capítulo se realizó por primera vez la síntesis de un complejo polimérico heterotrimetálico con interacciones Ag/Au/Tl sin precedentes. Además, el estudio teórico a nivel MP2 y HF nos permite explicar la estabilidad de esta nueva interacción

Introduction

1. Gold

Gold, with the chemical symbol Au and atomic number 79, is undoubtedly the first metal known to early civilizations. The characteristics of gold are ductility and malleability, which means it can be stretched into a wire or pounded into other shapes. Gold is the most ductile and malleable element on our planet. In addition, gold is a good conductor of heat and electricity and is not affected by air, humidity, or most chemical agents. However, despite being a noble metal, it is sensitive to chlorine, mercury and a mixture of nitric and hydrochloric acids called ''acqua regia'' for its ability to dissolve the king of metals[1]. Gold is a little abundant metal in the earth's crust; the largest reserve of accessible gold for humans is found in the sea, where it has been calculated that 13,700 million tons of this metal are present[2]. On the other hand, a possible explanation of the origin of gold from the earth's crust has been presented in a paper published in the prestigious journal Nature[3]. In this article it is explained that during the formation of the Earth the molten iron sank until its centre forming the nucleus, taking with it the great majority of the precious metals of our planet, reason why they propose that all the gold present in the terrestrial crust it is due to the impacts of meteorites with high concentrations of this metal (170 ppb)[2]. On the other hand, because it is relatively inert, it is usually found in nature as native gold, sometimes as large nuggets (see Figure 1), but generally in the form of small inclusions in some minerals such as pyrite, quartz veins, slate and metamorphic rocks.

Figure 1. Gold nugget

In recent decades, the study of gold compounds has aroused a great interest as a result of its enormous possibilities. Gold is an element that has a greater relativistic effect, so it suffers the greatest contraction of the atomic radius compared to the elements of the same period (from group 1 (Cs) to group 18 (Rn))[4] (see Figure 2a, left). In fact, according to Einstein's theory of relativity, the mass of a small object increases when its speed approaches to that of light (see Figure 2b, left). This determines, in the heavier atoms and in particular gold, an increase in the speed of electrons around the nuclei due to the increase in the nuclear charge. This is reflected at the same time as an increase in the mass of the electrons with the consequent contraction of the atomic radius according to the Bohr equation (see Figure 2b, right). This effect causes a decrease in the energy of the orbitals s and an increase in the energy of the orbitals d[5],[6] (see Figure 2a, right).

a)

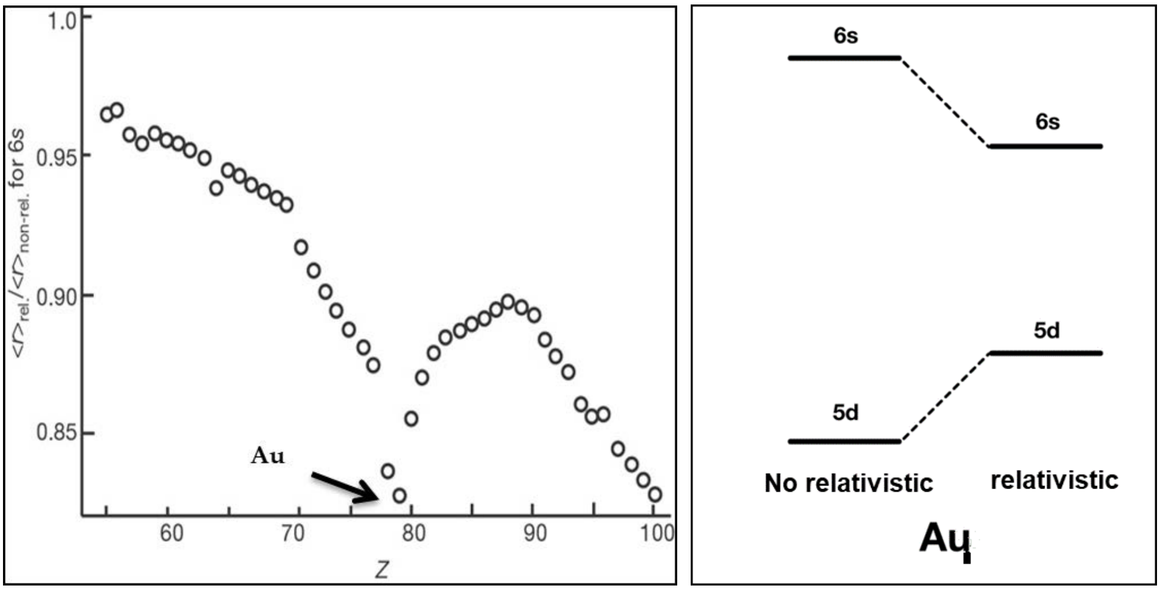

$$M_{(e-rel)} = \frac{m_e}{\sqrt{1 - v_e^2/c^2}} \qquad r = \frac{4\pi\varepsilon_0\hbar^2 n^2}{M_{(e-rel)}e^2}$$

$M_{e\text{-}rev}$= relativistic mass
v_e = elctron speed
r = Bohr radius
h = Plank's costant
n = 1, 2, 3 …….

m_e= mass electron
c = speed light
ε_0= permittivity of free space
e = elementary charge

b)

Figure 2. a) The ratio of relativistic (r_R) and non-relativistic (r_{NR}) radii versus the atomic number for electrons 6s (left). Energy variation of gold orbitals as a consequence of relativistic effects (right). b) influence of the relativistic effect of the electron mass (left) and the Bohr radius (right).

One of the most visible consequences is the typical yellow colour due to the small difference in energy between the orbitals d and the s-p orbitals from which the electrons can be excited by means of blue light, showing the complementary yellow colour characteristic of the gold compared to all the other metals. Furthermore, it has a lower chemical potential than other metals which makes it more resistant to oxidation than silver. Of all the characteristics mentioned so far, the most surprising phenomenon, particularly in the oxidation state one, is the tendency of the gold centers(I) to be located at a smaller distance than the sum of the van der Waals radii, generating dimers, oligomers and polymers with short gold(I)···gold(I)[7],[8] contacts. The existence of the interaction between closed shell metal centers (Au(I): [Xe] $4f^{14}5d^{10}$) is surprising from the point of view of the classical theory, according to which we should expect a Culombian electrostatic repulsion between two positively charged ionic species. For this reason, in 1988 Hubert Schmidbaur coined the term aurophilicity or aurophilic interaction[9] with the aim of defining the new type of interaction capable of explaining the structural phenomenon observed in Au(I) compounds. The theoretical study carried out by Pyykkö and Zhao introduces the effects of electronic correlation which are fundamental to justify and reproduce the phenomenon of aurophilicity[10]. For this same reason, aurophilicity is attributed to the effects of electronic correlation and more concretely to the dispersion forces of van der Waals[11]. The attractive force between the various metal centers is comparable to that of the hydrogen bonds (30-50 kJ/mol)[12],[13], so as to place this interaction in an intermediate position between the covalent/ionic bonds and the van der Waals forces. In reality, gold is not an exception in the periodic table: the original concept of aurophilicity can also be extended to other metals with a closed shell configuration (s^2,d^8 and d^{10})[13]-[21] by developing an evolution to a more general term known as *Metallophilia*. In fact, although they are much less numerous than the compounds containing Au(I)···Au(I) contacts, a considerable interest has aroused about complexes containing Au(I)···M(I) (M(I)= Ag, Tl, Cu) interactions, not only for their photophysical properties[22] and potential applications,[23] but also for theoretical aspects[23].

2. Gold and Silver

Due to the growing interest in the study of Au(I)···M interactions, in recent years numerous complexes have been described that present Au···Ag interactions, observing in many cases how the Au···Ag distance is lower than the gold-gold and silver-silver distances in the homometallic complexes. The synthetic strategy commonly used for the synthesis of Au(I)···Ag(I) heteronuclear compounds is based on the use of polydendate ligands, symmetric or asymmetric, capable of bridging the two metal centers. There are numerous examples where nitrogen-phosphorus mixed-donor ligands or sulfur-phosphorus mixed-donor ligands are used for the synthesis of complexes having Au(I)···Ag(I) interactions. By exploiting the different affinity of donor atoms, it is possible to generate new systems with heterometallic interactions supported by organic binders. One of the first systems synthesized by means of a bidentate ligand was $[AuAg(PPh_2Py)](ClO_4)_2$, where thanks to the selective coordination of the phosphorus atom to the gold center and the nitrogen atom to the silver center, a compound containing a supported Au(I)···Ag(I) interaction was synthesized with a distance of 2.820(1) Å between the metal centers (Figure 3)[25].

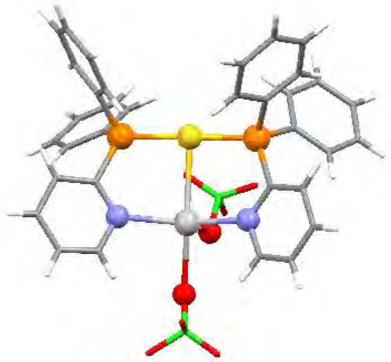

Figure 3. Structure of the compound $[AuAg(PPh_2Py)](ClO_4)_2$. Colour code: (yellow) gold, (grey) silver, (light blue) nitrogen, (red) oxygen, (green) chlorine.

Recently, Catalano and co-workers synthesized different compounds containing M(I)···M(I) interactions exploiting the coordination capacity of 2-(Diphenylphosphino)-1-methylimidazole[26] (dpim).

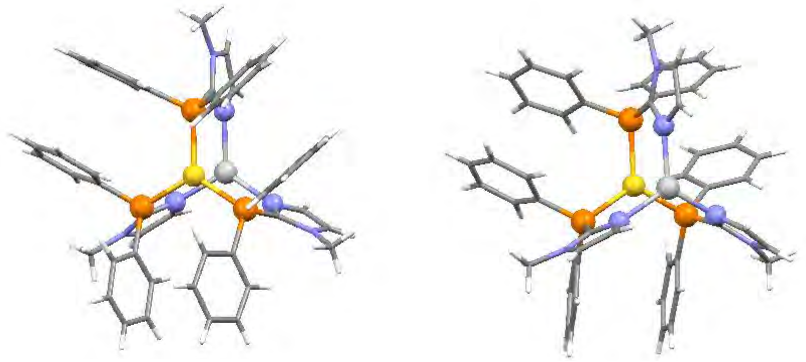

Figure 4. three-coordinate Au(I)···Ag(I) heterobimetallic complex of 2-(Diphenylphosphino)-1-methylimidazole (dpim). Colour code: (yellow) gold, (grey) silver, (light blue) nitrogen, (black orange) phosphor.

Using different synthetic strategies and different derivatives of Ag(I) ($AgBF_4$o $AgClO_4$) and Au(I) (AuCl(tht)) a series of binuclear complexes with metal-metal contacts were synthesized. In this case, the use of the binder dpim favours a three-coordinate Au(I)···Ag(I) heterobimetallic complex that is unprecedented in the literature (Figure 4). Of great interest from a structural point of view is the $AgAu_3$ cluster (see Figure 5) published by Laguna and co-workers in 2004[27] with the diphenylphosphine-2-pyridine ligand (PPh_2py). The central nucleus of the structure consists of a tetrahedron with an oxygen functioning as a μ_3-ligand capping the three gold atoms. Each gold(I)···silver(I) contact is bridged by one PPh_2py ligand with the P atom attached to Au(I) and the pyridyl N atom coordinated to Ag(I). Moreover, by modifying the nature of the μ_3-E capping ligand (E = O, S, Se) the optical properties of the synthesized system are considerably modified: the increase in the size of the donor atom causes a change in the distance Au(I)···Ag(I) generating a red-shift of the emission band.

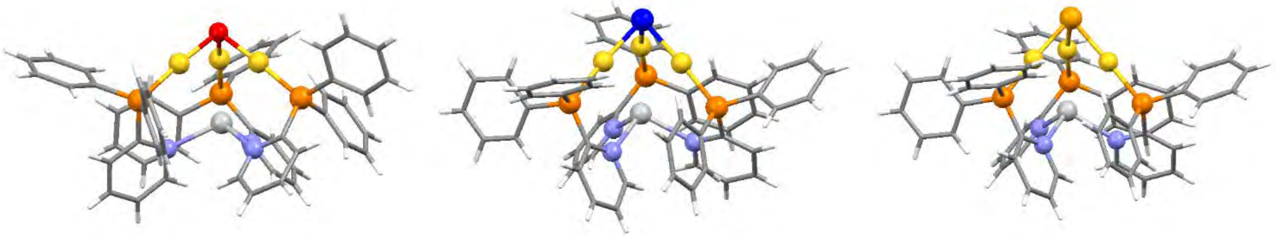

Figure 5. $AgAu_3$ clusters with the diphenylphos-phine-2-pyridine ligand (PPh_2py). Colour code: (yellow) gold, (grey) silver, (light blue) nitrogen, (dark orange) phosphor, (light orange) selenium, (dark blue) sulphur, (red) oxygen.

In recent years, another synthetic strategy for the synthesis of heteropolinuclear systems has found numerous applications. It consists in the acid-base reaction between a negatively or neutrally charged Au(I) derivative, and a salt containing a Lewis-acidic metal (Ag(I), Cu(I) or Tl(I))[28]. In reality, both the structure of the compound obtained and the optical properties depend strongly on the number and type of M(I)···M(I) interactions present. Moreover, the binders that support this type of interactions can play a fundamental role in the coordination of the same metal centers. In this direction, our investigation group has synthesized a large number of compounds thanks to the reaction between the anionic precursor of Au(I) (bis(perhalophenylaryl)aurate(I)) with silver salts that act as Lewis acids[29]-[34]. The first derivative containing Au(I)···Ag(I) interactions obtained according to this synthetic strategy was synthesised from the reaction between the $[NBu_4][Au(C_6F_5)_2]$ and $Ag(ClO_4)$. The synthetic process allows to obtain a polymeric system $[Au_2Ag_2(C_6F_5)_4]_n$ in which the two silver atoms present in the tetranuclear unit are able to react with neutral ligands modifying the photophysical properties of the system as a function of the coordinating ligand[30],[35]-[38] (Figure 6).

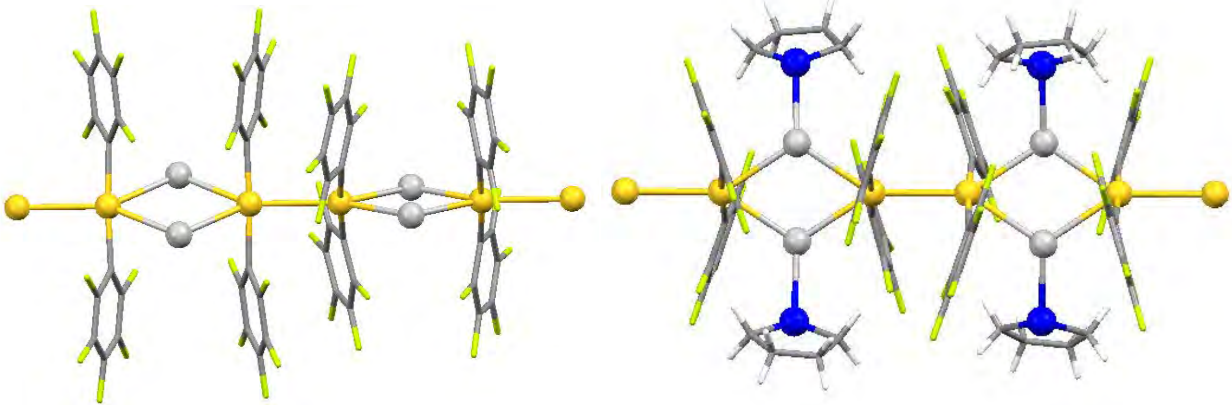

Figure 6. Part of the $[Au_2Ag_2(C_6F_5)_4]_n$ (left) and $[Au_2Ag_2(C_6F_5)_4(tht)_2]_n$ (right) polymeric chains. Colour code: (yellow) gold, (grey) silver, (dark blue) sulfur.

The use of $[Au(C_6X_5)]_2^-$ with different halogen atoms influences the electronegativity of the donor system, and consequently, its basicity and coordination properties. For this same reason the modification of the Au(I) precursor allows to modify the structural and optical properties of the synthesized compounds. For example, our investigation group using different aryl groups linked to the atom Au(I) has synthesized a series of compounds starting from $[Au_2Ag_2(C_6X_5)_4]_n$ (X = Cl, F) and modifying the dimensionality of crown thioethers used during the synthesis as neutral donor ligands (see Figure 7)[39].

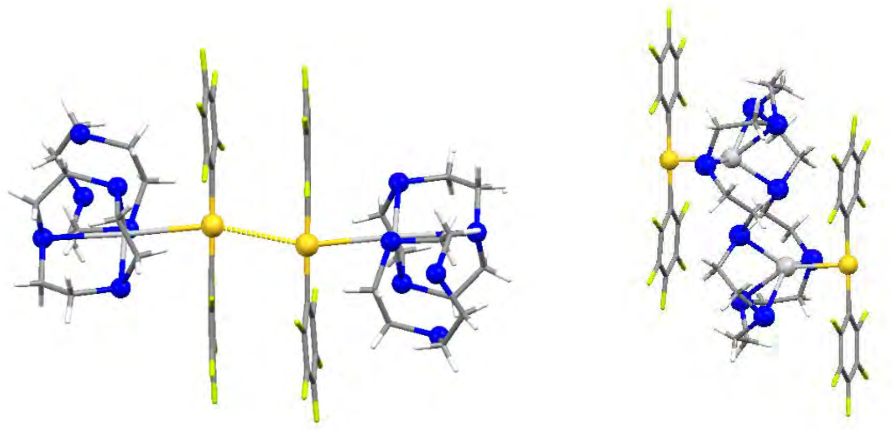

Figure 7. Structure of $[\{Au(C_6F_5)_2\}Ag([9]aneS_3)_2]_2$ (left) and $[\{Au(C_6F_5)2\}_2Ag_2([24]aneS_8)]$ (right). Colour code: (yellow) gold; (grey) silver; (dark blue) sulfur.

From Figure 7, it is clearly seen that by modifying the size and the coordination capacity of the macrocyclic system used, the structural properties of the final system can also be modified, which can affect the photophysical properties of the different compounds.

3. Gold and thallium

As already mentioned above, the growing interest in the study of metallophilic interactions has led many research groups to investigate more on the theoretical aspects that involve the phenomenon. Since the discovery of the phenomenon, there have been numerous efforts to synthesize new complexes containing these weak interactions between metals with different electronic configuration and investigate more on the theoretical aspects involved in this process: whereas the metallophilic attraction between d^{10} metal centers is improved by the relativistic contraction of the s and p orbitals (along with the destabilization of d orbitals)[40],the relativistic contribution to the closed-shell interaction between s^2 metal centers such as Tl(I) actually weakens their dispersive attraction[41]. In this way it was concluded that the attraction between d^{10} metal centers, should be stronger than that between metal centers having d^{10} and s^2 configurations[13],[41]. For this reason, It is not surprising to assume that the presence of Au(I)-Tl(I) interactions strongly depends on the use of organic ligands which, due to structural, electronic or coordination characteristics, may favour this type of interaction. Many of the initially prepared compounds containing Au(I)-Tl(I) interactions were based on the use of charged bridging ligands, so that the structural rigidity of the ligands would stabilize the metal-metal interaction. The first derivative containing an interaction Au(I)-Tl(I) was obtained from the reaction of $[Au(CH_2P(S)Ph_2]^-$ with $Tl^{+.}$ The intermetallic interactions produced a linear polymeric structure where the repeating unit was $[AuTl(CH_2P(S)Ph_2]_n$ (see Figure 8)[42] presenting optical properties that are not observed in any of the starting substrates.

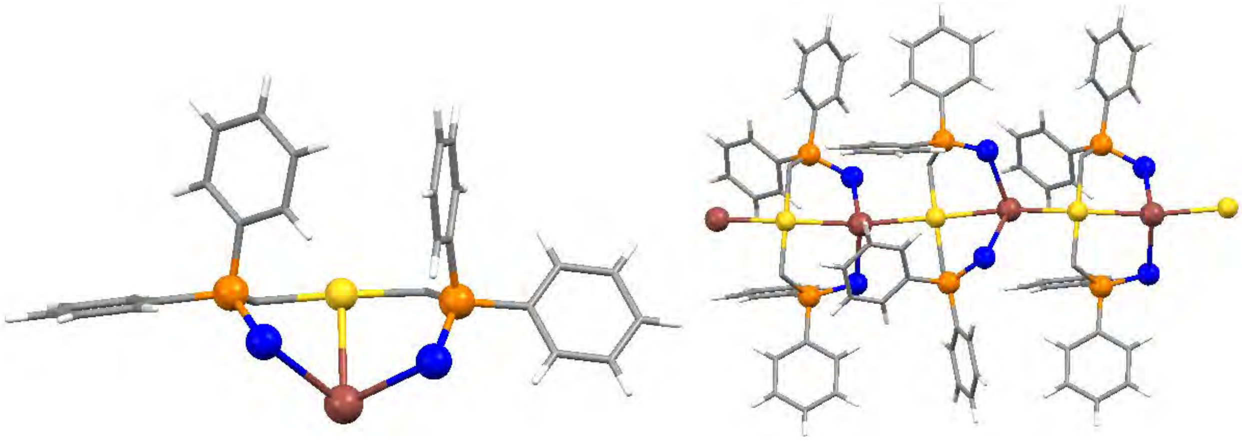

Figure 8. Monomeric unit (left) and polymeric chain (right) of $[AuTl(CH_2P(S)Ph_2]_{n.}$ Colour code: (yellow) gold; (garnet) thallium; (black orange) phosphor; (dark blue) sulfur.

However, in the last few years we have used the acid-base strategy to synthesize compounds containing Au(I)-Tl(I) interactions which consists in a reaction between a rich electron system (as $Au(C_6X_5)_2^-$, $Au(CN)_2^-$, etc.) and a Lewis acid ($TlPF_6$, $TlNO_3$ etc.). In this case, the strong negative charge present on the organometallic compound grants the presence of a strong ionic contribution that can stabilize this type of interaction without the need to use bridging ligands. For example, in 2003 he reaction between $NBu_4[Au(C_6Cl_5)_2]$ and $TlPF_6$ in THF leads to the synthesis of a product of stoichiometry $[AuTl(C_6Cl_5)_2]_n$[23] which can be used as a precursor for the synthesis of complexes with Au(I)-Tl(I) interactions. However, The structural arrangement can also be influenced by the presence of solvents with a coordination capacity: the preparation of the two polymeric systems $[Tl(OPPh_3)_2Au(C_6F_5)_2]_n$ and $[Tl(OPPh_3)(THF)Au(C_6F_5)_2Tl(OPPh_3)]_n$ (Figure 9) in two different solvents show a linear chain with alternating metal centers in a zig-zag disposition with Au(I)–Tl(I) distances of 3.0529(3), 3.14528(3), 3.1630(3) and 3.3205(3)˚A (L: tetrahydrofuran) or 3.2438(3), 3.0937(3), 3.2705(4) and 3.1492(3)˚A (L: acetone). Interestingly, in these cases the environments around the thallium atoms are alternatively pseudotetrahedral and distorted trigonal-bipyramidal (see Figure 9)[43].

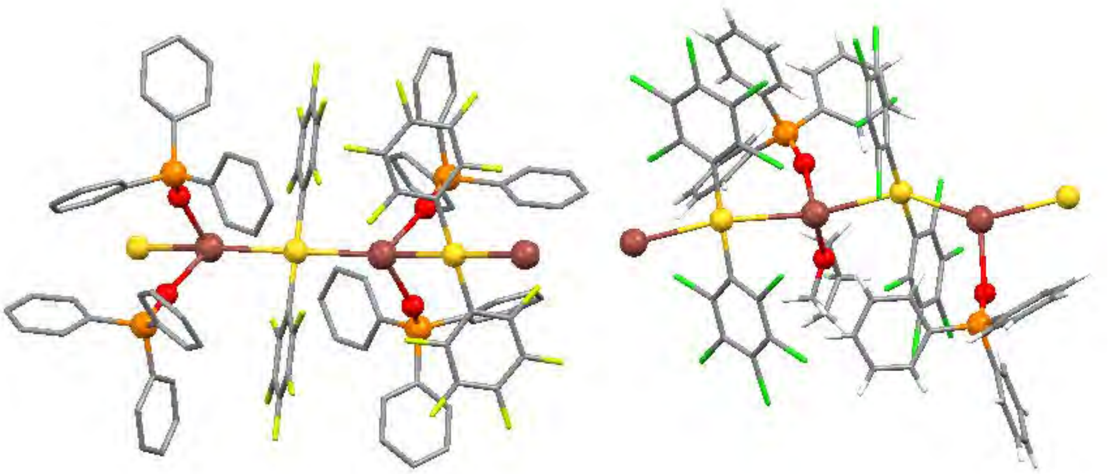

Figure 9. Linear chains showing different environments at the thallium centres. $[Tl(OPPh_3)_2Au(C_6F_5)_2]_n$ (left); $[Tl(OPPh_3)(THF)Au(C_6F_5)_2Tl(OPPh_3)]_n$ (right). Colour code: (yellow) gold; (garnet) thallium; (black orange) phosphor; (red) oxygen.

In the same manner, the only difference in the aryl groups bonded to gold produces important changes in the solid state structures formed in similar acid–base reactions in the presence of 4,4'-bipyridine. Thus, the reaction of the basic $[AuR_2]^-$ (R = C_6F_5,C_6Cl_5) with the salt $TlPF_6$ in the presence of 4,4'-bipyridine in tetrahydrofuran leads to highly luminescent materials of stoichiometry

$[Tl(bipy)]_2[Au(C_6F_5)_2]_2$ or $[Tl(bipy)][Tl(bipy)_{1/2}(thf)][Au(C_6Cl_5)_2]$ (bipy: 4,4'-bipyridine), respectively (see Figure 10)[44].

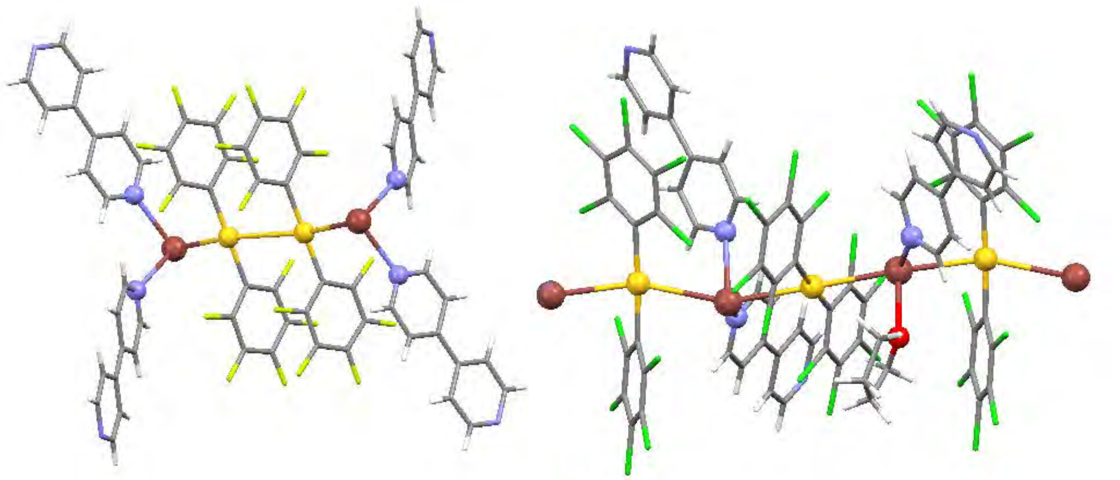

Figure 10. Tl–Au–Au–Tl (left) and Au–Tl–Au–Tl' (right) disposition of metal atoms $[Tl(bipy)]_2[Au(C_6F_5)_2]_2$ and $[Tl(bipy)][Tl(bipy)_{1/2}(thf)][Au(C_6Cl_5)_2]$. Colour code: (yellow) gold; (garnet) thallium; (light blue) nitrogen.

Extremely interesting is not only the different structural arrangement dependence on the coordination of the dissolvent inside the heterometallic complex, but also the arrangement of the metal centers in the two different structures: in the complex $[Tl(bipy)]_2[Au(C_6F_5)_2]_2$ (Figure 10 (right)), the tetramer unit found presents a nonalternating sequence of variance ions [+−−+], which should not be supported by the simple rules of Coulomb forces. An extension of this work is to prepare linear chains using perhalophenyl derivatives in the presence of different solvents that could vary the structure and consequently, the luminescent properties. Thus, for instance, the reaction between $NBu_4[Au(C_6Cl_5)_2]$ and $TlPF_6$ in acetone leads to the synthesis of a product of stoichiometry $[Au_2Tl_2(C_6Cl_5)_4]$·acetone[45]; while if the solvent is tetrahydrofuran the stoichiometry of the product is $[AuTl(C_6Cl_5)_2]_n$. The crystal structure of the complex $[Au_2Tl_2(C_6Cl_5)_4]$·acetone consists of a tetranuclear unit where the metals are held together through four unsupported Au–Tl interactions within the range 3.0331(6)–3.1887(6) ˚A and an additional Tl–Tl interaction of 3.6027(6) ˚A, resulting in a loosely bound butterfly cluster (see Figure 11).

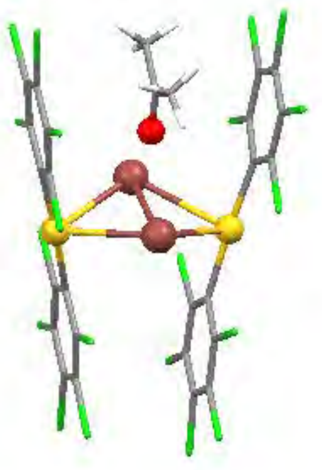

Figure 11. Crystal structure of $[Au_2Tl_2(C_6Cl_5)_4]$·acetone showing the butterfly disposition of the metals.

Recently, also the use of crown thioethers for the synthesis of heterometallic Au(I)-Tl(I) compounds gave good results[46]: compounds of stoichiometries $[\{Au(C_6X_5)_2\}Tl(L)]_2$ or $[\{Au(C_6F_5)_2\}_2Tl_2(L)]$ are obtained depending on the size of the macrocyclic ligand, which can act as a terminal or as a bridging S-donor ligand. The formation of Tl–S bonds and Au(I)···Tl(I) or Au(I)···Tl(I) and Au(I)···Au(I) contacts leads to unusual structures for Au/Tl complexes with polymeric $[–L–Tl–Au–Au–Tl–]_n$ or tetranuclear [L–Tl–Au–Au– Tl–L] or [Au–Tl–L–Tl–Au] dispositions, clearly influenced by the nature of the ligands at the metal centres (see Figure 12).

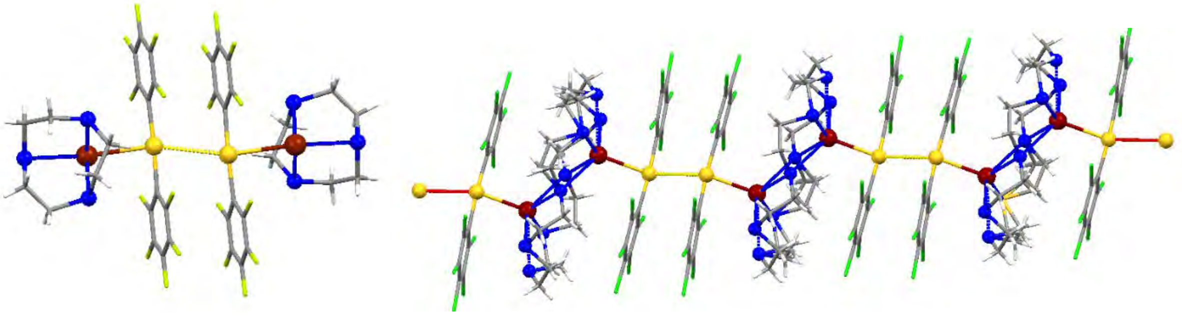

Figure 12. Crystal structure of $[Tl([9]aneS_3)Au(C_6F_5)_2]_2$ (left) and $[\{Tl([24]aneS_8)Au(C_6Cl_5)_2\}_2]_n$ (right).

As it is clear from Figure 12, the different dimensionality and coordinative capacity of the macrocyclic (from $[9]aneS_3$ to $[24]aneS_8$) allows the expansion of the [L-Tl-Au-Au-Tl-L] molecular system in a $[-L-T-Au-Au-Tl-L-]_n$ polymeric system by modifying the number of donor atoms of the organic ligand.

4. PhD thesis aims

Taking into account the obtained results so far, in the work carried out, we propose the synthesis and characterization of new organometallic heteropolinuclear gold(I)-thallium(I) or gold(I)-silver(I) compounds with mixed thia–aza-oxo macrocyclic ligands of various dimensions and macrocyclic systems appropriately functionalized with the 2-methylquinoline unit (see Figure 13). The choice to use this type of ligands lies in the structural, electronic and coordination characteristics of macrocyclic systems: the possibility to play with the size of the organic ligand used, the number and type of donor atoms present allows us to compare different parameters that can influence both the structural nature and the optical properties of the diffused compounds obtained. In particular, the **L_1-L_3** binders will allow us to synthesize different heterometallic compounds evaluating them as macrocycles of the same dimensionality but different donor atoms will be able to influence the structural characteristics and the optical properties of the obtained compounds; **L_4-L_5** ligands will allow us to evaluate how macrocycles of different size and different coordination capacity can influence the metallophilic interactions present in the synthesized systems; Finally, **L_6-L_7** ligands, containing the 2-methylquinoline unit, allow us to modify the stoichiometry of the different reactions made by generating materials with unique structural and electrotonic properties.

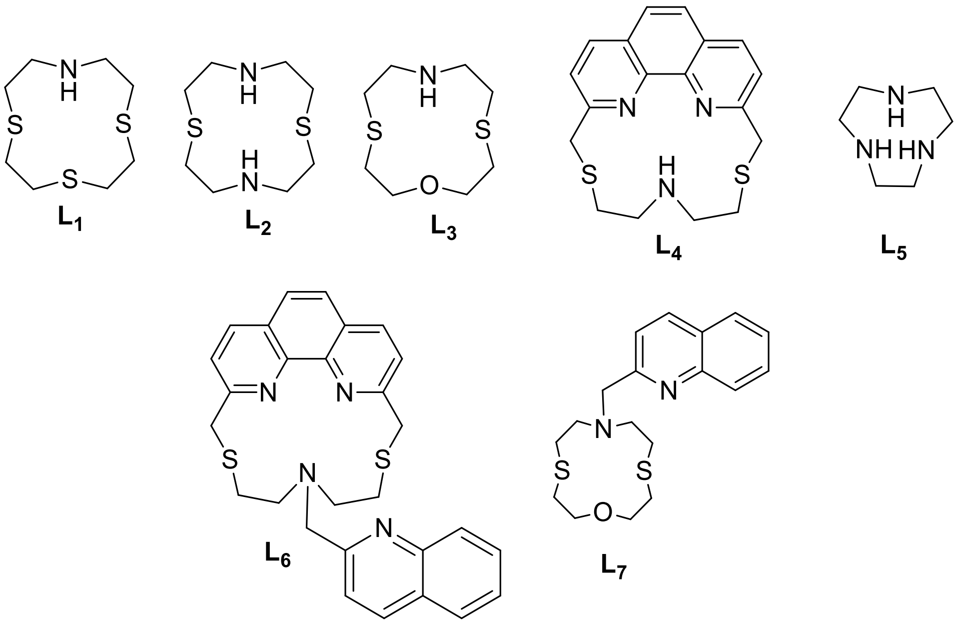

Figure 13. Macrocyclic system **L_1-L_7**.

In chapter one we will describe the different strategies used for the synthesis of the macrocyclic systems designed for supporting the metallophilic interactions in the final new heteropolinuclear systems.

In chapter two, we will study the reactivity of the different ligands synthesized with the $[\{Au(C_6X_5)_2\}Tl]_n$ (X=F,Cl) precursors, describing the synthesis, structural characterization and optical properties of the new heteropolinuclear derivatives obtained. These materials contain metallophilic interactions that will be analyzed by means of a complete computational study.

In chapter three, indeed we will study the reactivity of the different ligands synthesized with the $[\{Au(C_6X_5)_2\}Ag]_n$ (X=F,Cl) precursors, describing the synthesis, structural characterization and optical properties of the new heteropolinuclear derivatives obtained. These materials also contain metallophilic interactions that will be analyzed by means of the theory. In this way, in each chapter it will be possible to evaluate not only the influence of the neutral ligands on the structures and the optical properties of the synthesized systems, but also the different structural and photophysical properties as a function of the halogen atoms in the aryl unit of the $[Au(C_6X_5)_2]^-$ fragment.

5. References

[1] N. N. Greenwood, A. Earnshaw, *Chemistry of the Elements*, **1997**.

[2] Webelements.com.

[3] M. Willbold, T. Elliott, S. Moorbath, *Nature,* **2011**, 477, 195-198.

[4] P. Pyykkö, *Angew. Chem.,* **2002**, 41, 3573-3578.

[5] P. Pyykko, J. P. Desclaux, *Acc. Chem. Res.,* **1979**, 12, 276-281.

[6] N. Bartlett, *Gold Bull.,* **1998**, 31, 22-25.

[7] H. Schmidbaur, *Gold Bull.,* **2000**, *33*, 3-10.

[8] H. Schmidbaur, A. Schier, *Chem. Soc. Rev.,* **2008**, 37, 1931-1951.

[9] F. Scherbaum, A. Grohmann, C. Krüger, H. Schmidbaur, *Angew. Chem.,* **1988**, 27, 1542-1544.

[10] P. Pyykkö, Y. Zhao, *Inorg. Chem.,* **1991**, *30*, 3787-3788.

[11] P. Pyykkö, *Angew. Chem.* **2004**, 43, 4412-4456.

[12] A. Codina, E. J. Fernandez, P. G. Jones, A. Laguna, J. M. López De Luzuriaga, M. Monge, M. E. Olmos, J. Pérez, M. A. Rodríguez, *J. Am. Chem. Soc.,* **2002**, 124, 6781-6786.

[13] L. H. Gade, *Angew. Chem.,* **2001**, 40, 3573-3575.

[14] H. Schmidbaur, *Chem. Soc. Rev.,* **1995**, 24, 391-400.

[15] H. Schmidbaur, *Gold Bull.,* **1990**, 23, 11-21.

[16] W. E. Lindsell, *Comprehensive Organometallic Chemistry II*, **1995**.

[17] P. Pyykkö, Y. Zhao, *Angew. Chem.,* **1991**, 30, 604-605.

[18] P. Pyykkö, *Chem. Rev.,* **1997**, 97, 597-636.

[19] P. Pyykkö, N. Runeberg, *J. Chem. Soc. Chem. Commun.,* **1993**, 0, 1812-1813.

[20] P. Pyykkö, M. Straka, *Phys. Chem. Chem. Phys.,* **2000**, 2, 2489-2493.

[21] O. Crespo, A. Laguna, E. J. Fernández, J. M. López De Luzuriaga, P. G. Jones, M. Teichert, M. Monge, P. Pyykkö, N. Runeberg, M. Schütz et al., *Inorg. Chem.,* **2000**, 39, 4786-4792.

[22] D. M. Roundhill, J. P. Fackler, *Optoelectronic Properties of Inorganic Compounds*, Springer US, **1999**.

[23] E. J. Fernández, J. M. López De Luzuriaga, M. Monge, M. E. Olmos, J. Peréz, A. Laguna, A. A. Mohamed, J. P. Fackler, *J. Am. Chem. Soc.,* **2003**, 125, 2022-2023.

[24] P. Pyykkö, *Chem. Rev.,* **1997**, 97, 597-636.

[25] M. Olmos, A. Schier, H. Schmidbaur, *Z. Naturforsch.,* **1997**, 52b, 203-208.

[26] V. J. Catalano, S. J. Horner, *Inorg. Chem.,* **2003**, 42, 8430-8438.

[27] Q. M. Wang, Y. A. Lee, O. Crespo, J. Deaton, C. Tang, H. J. Gysling, M. C. Gimeno, C. Larraz, M. D. Villacampa, A. Laguna, et al., *J. Am. Chem. Soc.,* **2004**, 126, 9488-9489.

[28] E. J. Fernández, A. Laguna, J. M. López De Luzuriaga, *Dalt. Trans.,* **2007**, 1969-1981.

[29] O. Crespo, E. J. Fernández, M. Gil, M. Concepción Gimeno, P. G. Jones, A. Laguna, J. M. López De Luzuriaga, M. E. Olmos, *Dalt. Trans.,* **2002**, 0, 1319-1326.

[30] E. J. Fernández, M. C. Gimeno, A. Laguna, J. M. López De Luzuriaga, M. Monge, P. Pyykkö, D. Sundholm, *J. Am. Chem. Soc.,* **2000**, 122, 7287-7293.

[31] E. J. Fernández, P. G. Jones, A. Laguna, J. M. López De Luzuriaga, M. Monge, M. E. Olmos, R. C. Puelles, *Organometallics,* **2007**, 26, 5931-5939.

[32] A. Laguna, M. Lo, E. J. Ferna, M. Monge, P. Pyykkö, N. Runeberg, E. J. Fernández, A. Laguna, J. M. López De Luzuriaga, M. Monge, et al., *Eur. J. Inorg. Chem.,* **2002**, *55,* 750-753.

[33] E. J. Fernández, A. Laguna, J. M. López De Luzuriaga, M. Monge, M. Elena Olmos, R. C. Puelles, *J. Phys. Chem. B,* **2005**, 109, 0, 20652-20656.

[34] E. J. Fernández, J. M. López De Luzuriaga, M. Monge, M. E. Olmos, R. C. Puelles, A. Laguna, A. a Mohamed, J. P. Fackler, *Inorg. Chem.,* **2008**, 47, 0, 8069-8076.

[35] E. J. Fernández, A. Laguna, J. M. López De Luzuriaga, M. Monge, M. Montiel, M. E. Olmos, M. Rodríguez-Castillo, *Organometallics,* **2006**, 25, 3639-3646.

[36] R. Uson, A. Laguna, M. Laguna, B. R. Manzano, P. G. Jones, G. M. Sheldrick, *J. Chem. Soc. Dalt. Trans.,* **1984**, 0, 285-292.

[37] R. Usón, A. Laguna, M. Laguna, P. G. Jones, G. M. Sheldrick, *J. Chem. Soc. Chem. Commun.* **1981**, 1, 1097-1098.

[38] E. J. Fernández, A. Laguna, J. M. López De Luzuriaga, M. Monge, M. Montiel, M. E. Olmos, J. Perez, R. C. Puelles, J. C. Saenz, *Dalt. Trans.,* **2005**, 0, 1162-1164.

[39] A. J. Blake, R. Donamaria, V. Lippolis, J. M. López De Luzuriaga, E. Manso, M. Monge, M. E. Olmos, *Inorg. Chem.,* **2014**, 53, 10471-10484.

[40] P. Pyykkö, N. Runeberg, F. Mendizabal, *Chem. - A Eur. J.,* **1997**, 3, 1451-1457

[41] P. Pyykkö, M. Straka, T. Tamm, *Phys. Chem. Chem. Phys.,* **1999**, 1, 3441-3444.

[42] S. Wang, G. Garzón, C. King, J. chun Wang, J. P. Fackler, *Inorg. Chem.,* **1989**, 28, 4623-4629.

[43] E. J. Fernández, A. Laguna, J. M. López De Luzuriaga, F. Mendizabal, M. Monge, M. E. Olmos, J. Pérez, *Chem. - A Eur. J.,* **2003**, 9, 456-465.

[44] E. J. Fernández, P. G. Jones, A. Laguna, J. M. López De Luzuriaga, M. Monge, J. Pérez, M. E. Olmos, *Inorg. Chem.,* **2002**, 41, 1056-1063.

[45] E. J. Fernández, J. M. López De Luzuriaga, M. Monge, M. E. Olmos, J. Pérez, A. Laguna, *J. Am. Chem. Soc.,* **2002**, 124, 5942-5943.

[46] A. J. Blake, R. Donamaría, E. J. Fernández, T. Lasanta, V. Lippolis, J. M. López De Luzuriaga, E. Manso, M. Monge, M. E. Olmos, *Dalt. Trans.,* **2013**, 42, 11559-11568.

Chapter 1

Synthesis of organic ligands

1.1 Introduction

A macrocycle ligand is a cyclic molecule consisting of a minimum of nine atoms (including heteroatoms) having a ring structure characterized or not by the presence of unsaturations[1]. This definition includes a range of practically unlimited compounds of synthesizable macrocycles since varying the number or the nature of the donor atoms, and therefore the size of the macrocyclic cavity, it is possible to vary the affinity of the ligand for a given substrate. Indeed, for many years the synthesis of macrocyclic systems of different nature has played a fundamental role in all aspects of modern chemistry, allowing chemists to open new frontiers in the synthesis of supramolecular systems. These compounds are identified as receptors of many chemical species, such as metal ions[2]-[8] or organic/inorganic anions[9],[10], thanks to their structural variability. In fact, the synthesis and study of macrocycles have suffered a tremendous growth and their complexation chemistry with a wide variety of metal ions has been extensively studied[11]. Macrocycles are important and powerful ligands in transition metal coordination chemistry for the thermodynamic and kinetic stabilities of their metal complexes due to their conformational stability. For example, in 2004 Martin Schröder and co-workers published a study on conformational and stereochemical flexibility in cadmium(II) complexes of aza-thioether macrocycles [12] (see Figure 1).

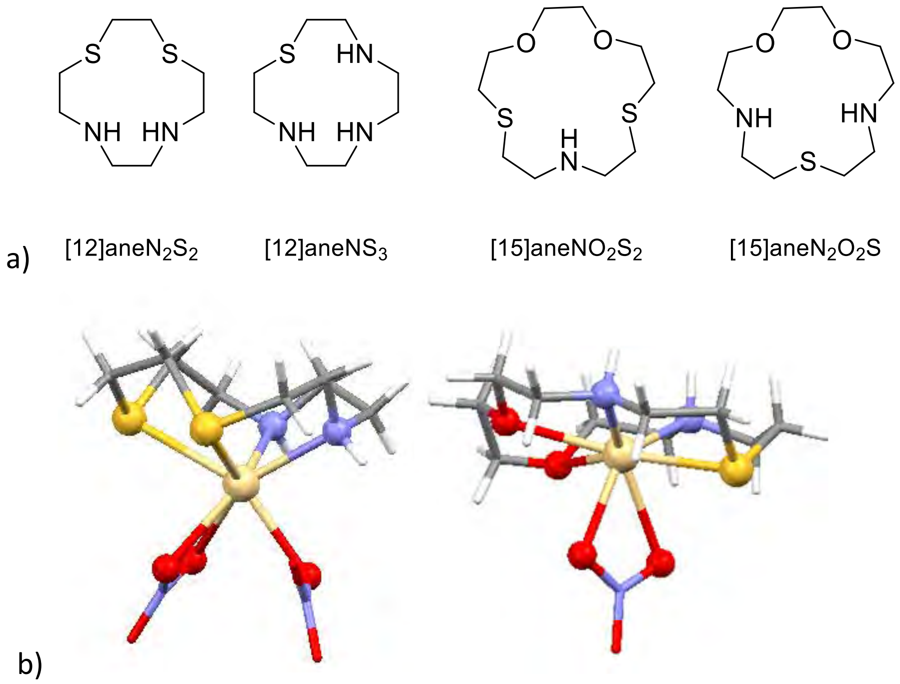

Figure 1. a) Example of aza-thioether macrocycles; b) Single-crystal X-ray structures of $[Cd(NO_3)_2([12]aneN_2S_2)]$ (left), $[Cd(NO_3)([15]aneNO_2S_2)^+]$ (right). Colour code: (off-white) cadmium, (blue) nitrogen, (yellow) sulfur, (red) oxygen.

From the structural analysis it was clearly observed that the flexible nature of the coordination sphere of the metal centre significantly influences the conformational arrangement of the coordinated macrocyclic units. In addition, there seems to be a strong correlation between the Cd-O bond distance and the nitrate ion position, in which the presence of a macrocyclic bond nearby determines the elongation of the bond. However, the size of the macrocycle influences the possible sphere of coordination of the metal centre too: with the smaller macrocycles, the metal is positioned outside the macrocyclic cavity, suffering from a greater exposure to the possible coordination of further ligands. Furthermore, the development of synthetic strategies to generate the multitude of existing macrocycles has allowed chemists to use these materials as possible molecular sensors, metal sequestering agents, mimetics of enzymes, and carriers for transport through membranes[13]-[16]. They are able to form stable and selective complexes with a variety of inorganic and organic cations, and by reaction with some anionic and neutral organic and biological substrates give supramolecular compounds with specific properties and applications[17]. For instance, in 2006 Rita Delgado and co-workers demonstrated the thermodynamic stability of the complex $\{Cd[17](DBF)N_2O_2\}(NO_3)_2$ (DBF= dibenzofuran). The size of the Cd^{+2} is optimal for the $[17](DBF)N_2O_2$ macrocycle and the resulting complex shows a strong thermodynamic stability compared to that of other metal ions (see Figure 2) and for this reason it can be used as metal sequestering agents at different pH value [18].

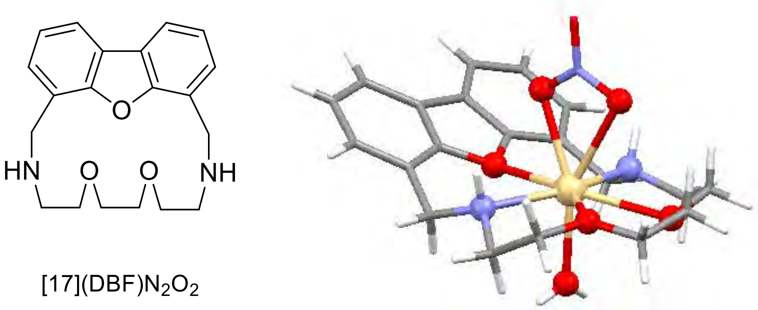

Figure 2. Single-crystal X-ray structure of $\{Cd[17](DBF)N_2O_2\}(NO_3)_2\}^+$ (DBF=dibenzofuran). Colour code: (off-white) cadmium, (blue) nitrogen, (red) oxygen.

The search for systems with peculiar properties has led to the development of macrocyclic systems functionalized with appropriate donor groups that confer unique characteristics to the system synthesized [19]. These ligands have been synthesized in large number because they have proved to be useful for a great variety of different chemical applications. In 2014 Vito Lippolis and co-workers, starting from the known macrocyclic ligands 1-aza-4,7,10-trithiacyclododecane ($[12]aneNS_3$), 1,7-

diaza-4,10-dithiacyclododecane ([12]aneN_2S_2), and 2,8-dithia-5-aza-2,6-pyridinophane ([12]anePyNS_2), synthesized molecular fluorescence sensors for metal ions bearing a coumarin moiety as fluorogenic unit[20] (see Figure 3).

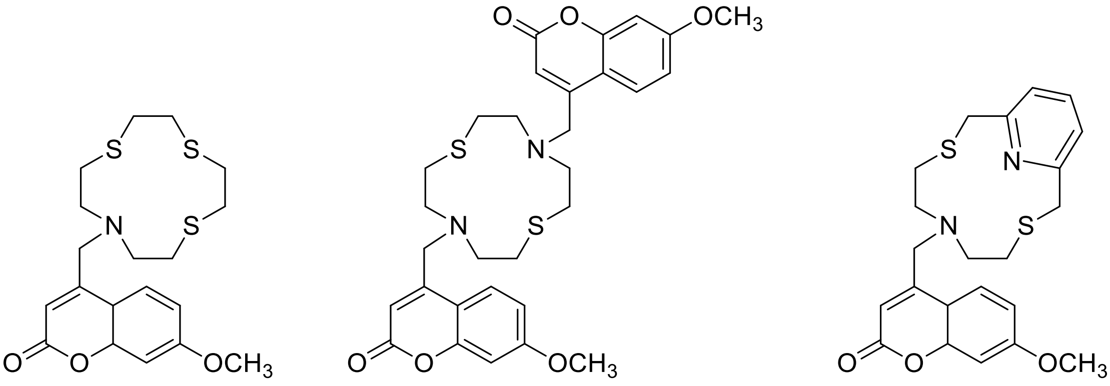

Figure 3. Molecular fluorescence sensors for metal ions with coumarin units.

The selectivity of macrocycles accompanied by the photophysical properties of coumarin allow to synthesize highly selective systems for the Hg^{+2} ion for the development of optical sensors for the same heavy metal in natural water and for intracellular mercury imaging in cells in vitro (see Figure 5). Probably the presence of N-S donor atoms plays a significant role in the functioning mechanism of the synthesized system. In some cases, however, the active unit responsible for the optical properties of the system is integrated into the structure of the macrocycle. This is the case of the mixed donor crowns containing the 1,10-phenanthroline unit as an integral part of the macrocyclic structure which show selectivity for heavy metals such as lead(II), cadmium(II) or mercury(II)[21](see Figure 4).

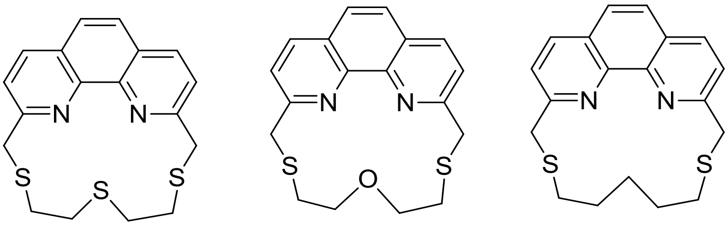

Figure 4. Mixed donor macrocycles containing a phenanthroline unit.

In addition, macrocyclic ligands are used as carriers to study the transport through membranes of anions. An example was reported by Bradley D. Smith and co-workers who study the ability to transport the chloride anion through the vesicular membrane[15]: they demonstrated the effectiveness of the macrocyclic system **A** (as compared to systems **B** and **C**, Figure 5) to transport the chloride ion through the vesicle membrane via the formation of hydrogen bonds. They also studied the influence of different cations on the efficiency of the process.

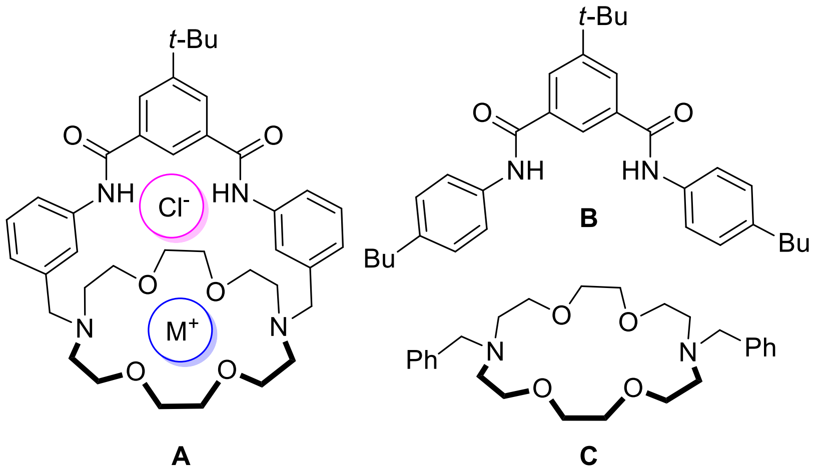

Figure 5. Structures of **A** M^+ Cl^- complex and partial ion receptors **B** and **C**.

In recent years, the high coordination capacity of the thio-crown ethers macrocyclic systems has also been exploited to support metal-metal interactions between closed-shell transition metal cations giving excellent results (see Introduction). For instance, in 2013 and 2014, studies were published concerning the Au-Ag or Au-Tl heterometallic interactions using macrocyclic systems of different dimensions[22],[23]. In these cases, it is explained in detail how the cavity size of the macrocyclic system, the number of donor atoms and the rigidity of the structure of the system play a decisive role in the formation of these weak interactions. The arrangement of the compound has consequences on the optical properties of the system, since the strength of the present metallophilic interactions plays a fundamental role on the photophysical properties of the synthesized complexes. Moreover, computational calculations allowed to explain the origin of the photophysical proprieties responsible for the fluorescent or phosphorescent emission processes observed in the synthesized compounds. However, there are no cases published in the literature in which mixed N-S-O donor macrocyclic are used to support these weak interactions; In this chapter we describe the synthesis and the characterisations of organics ligands used to support this type of interactions (see Figure **6**); these include mixed N-S/N-S-O/N macrocyclic ligands (**L_1-L_5**) and mixed N-S/N-S-O macrocyclic systems functionalized with quinoline unit (**L_6-L_7**).

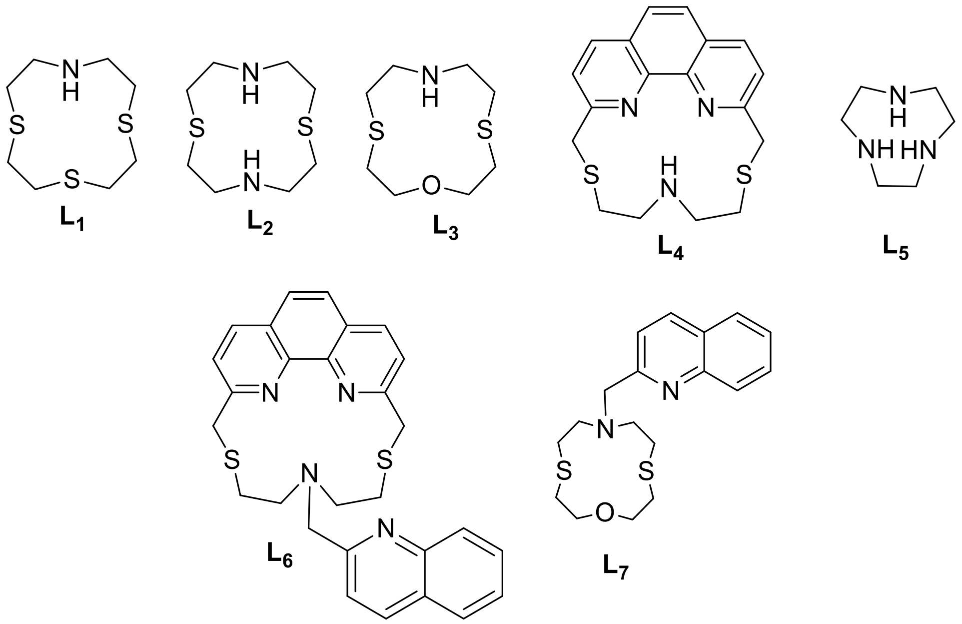

Figure 6. Macrocyclic ligands.

1.2 Coordination chemistry of L_1-L_7

As discussed previously, the study of macrocyclic chemistry represents a major area of activity which impinges on a range of other areas in both chemistry and biochemistry. In particular, the synthesis as well as the study of the coordinative properties of macrocyclic systems containing different donor atoms represent a very interesting challenge. For this reason, in this paragraph, I am going to focus in more detail on the chemistry of macrocyclic systems used by observing with an enlargement lens the coordination characteristics of these systems.

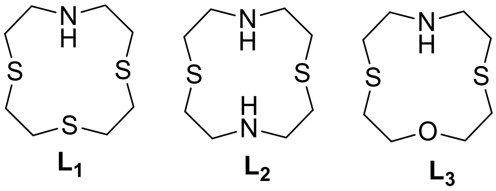

Figure 7. **L_1-L_3** Macrocyclic ligands.

The possible application in the medical-biological field of systems with a high coordination ability such as those shown in Figure 7, has aroused considerable interest in all aspects of modern chemistry. For example, the coordinating capacity of **L_1** was exploited for the synthesis and characterization of ^{68}Cu radioactive complex used to detect hydrogen sulfide within the human body (see Figure 8)[24]. Recent studies show that gas as hydrogen sulfide, nitric oxide and carbon monoxide are to be involved in various phenomena giving information on physiological changes in the body.

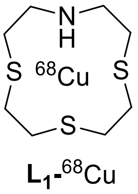

Figure 8. Radiative complex **L_1**-^{68}Cu.

For this reason, the possibility of observing in real time the presence of these compounds through optical imaging of their complexes is essential to diagnose and localize diseases that produce the formation of gaseous molecules as a secondary effect.

However, also the kinetics of the formation of metal complexes aroused considerable interest. For instance, in 2005 Liselotte Siegfried and Thomas A. Kaden published a study of **L_2** on the kinetics of formation of copper(II)-nickel(II) complexes under different conditions (see Figure 9). From the results obtained it is evident that the formation of possible hydrogen bonds with the solvent or protonation of the amine group present in the macrocyclic system makes the formation of the complexes much more difficult due to modification of the macrocyclic system conformation and making it less suitable for coordination with the target metallic centre [25].

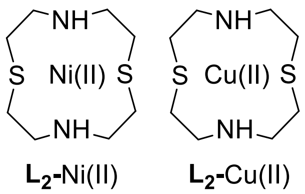

Figure 9. radiative complexes **L_2**-Ni(II) (left), **L_2**-Cu(II) (right).

The macrocyclic **L_1**-**L_3** (see Figure 7) systems over the years have been widely used not only for the synthesis of metal complexes but also as a starting product for the formation of functionalized macrocyclic systems featuring unique characteristics. For example, in 2007 Yoichi Habata and co-workers[26] used the **L_1** binder as a starting product for the formation of compounds with very different electronic characteristics. By changing the electronic characteristics of the aromatic moiety with which the macrocycle has been functionalized, it is possible to hypothesize a self-assembling mechanism that leads to the formation of different systems. In particular, the use of electron withdrawing groups eliminates the possibility of formation of C-H···π interactions between the macrocycle system and the phenyl fragment causing a modification of the structural features of the system. This behaviour is evident from the diagram shown in Figure 10 where the different structural arrangements of the silver complexes can be observed. In this case the weak interaction between the methylene group of the macrocycle and the aromatic moiety play a fundamental role in the formation silver(I) complexes both in solution and in solid state (see Figure 10).

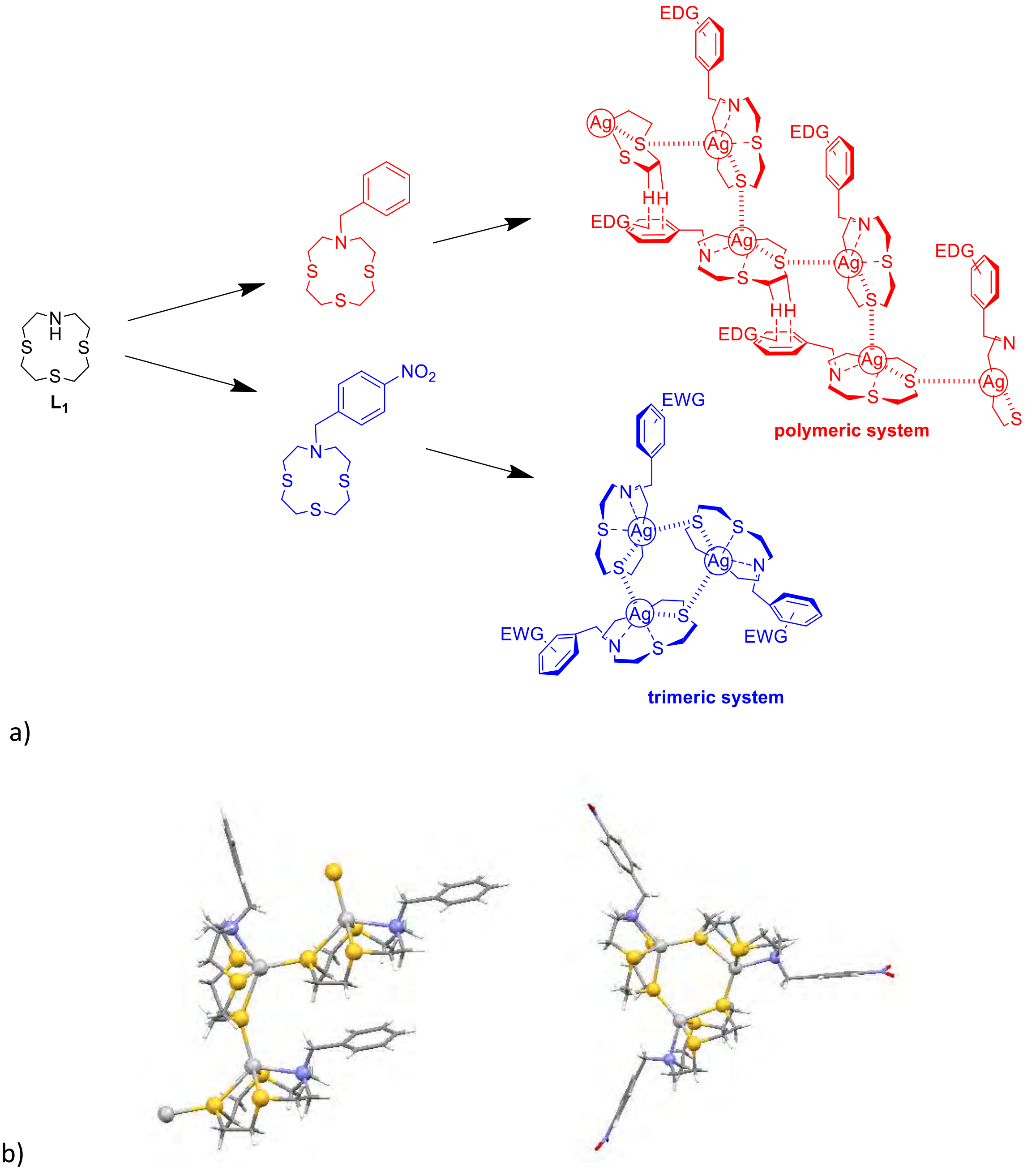

Figure 10. a) Schematic representation of the polymeric ([(Ag)N-Benzyl-1,4,7-trithia-10-azacyclododecane)][OCF_3SO_3]) and trimeric ([(Ag)N-(4′-Nitrobenzyl)-1,4,7-trithia-10-azacyclododecane][OCF_3SO_3] systems ; structure of the polymeric ([(Ag)N-Benzyl-1,4,7-trithia-10-azacyclododecane]$^+$) (left) and trimer ([(Ag)N-(4′-Nitrobenzyl)-1,4,7-trithia-10-azacyclododecane]$^+$) system (right). Colour code: (grey) silver, (yellow) sulfur, (blue) nitrogen.

In the same way, the use of functionalized macrocyclic systems allows us not only to study how the effect of the various substituents can influence the intrinsic properties of the macrocycle, but also allows us to develop new devices with unlimited applications. For example, in electrochemistry macrocyclic systems are widely used to evaluate the stability of the different oxidation states of a metal center. Through the study of the cyclic voltammetry of the different complexes it is possible to evaluate the stability and the reversibility of the observed red-ox process. In particular, **L_2** was used to study the stability of complexes formed with zinc, copper, cadmium and mercury[18] centers. However, the potential of these systems is not limited to the study of the stability of the complexes but it is possible to appropriately functionalize the macrocycles to generate devices known as chemosensors. In 2003, a study was published where **L_2-L_3** macrocyclic ligands were functionalized with one active ferrocene unit[27]. This system allowed to develop red-ox molecular sensors to detect metals such as Cu(II), Zn(II), Cd(II), Hg(II), and Pb(II) as a function of the observed redox potential variation (see Figure 11).

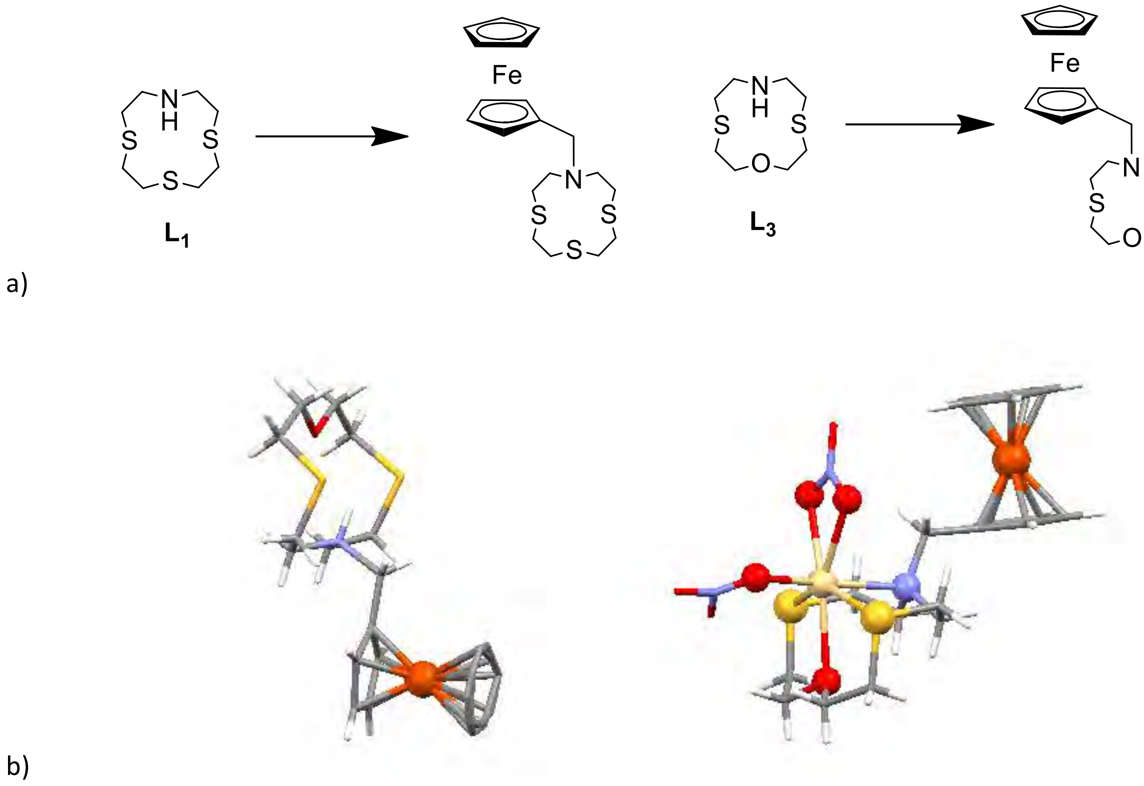

Figure 11. a) Ferrocene derivatives of **L_1,L_3**; b) view of the cation N-ferrocenylmethyl-1-aza-4,10-dithia-7-oxacyclododecane and of the complex [Cd(N-ferrocenylmethyl-1-aza-4,10-dithia-7-oxacyclododecane)$(NO_3)_2$]. Colour code: (off-white) cadmium, (yellow) sulfur, (blue) nitrogen, (red) oxygen.

Also, **L_4-L_5** (see Figure 12) have been used over the years for a variety of applications. For example, the recovery of heavy metals with high toxicity or precious metals from residual water is an operation that requires the use of specific binders that are able to guarantee a high selectivity for the desired species.

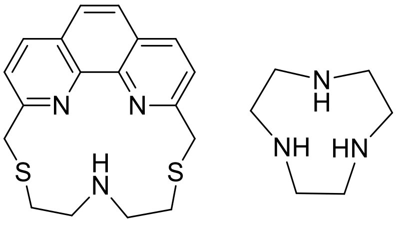

$\mathbf{L_4}$ $\mathbf{L_5}$

Figure 12. L$_4$-L$_5$ macrocyclic ligands.

In this regard, **L$_4$** was tested together with other macrocyclic systems (see Figure 13) with different metals (Ag (I), Hg (II), Cu(II)) showing a marked selectivity towards silver and mercury allowing the almost total recovery of the metal centers passing as complexed species from the phase aqueous to the organic phase[28].

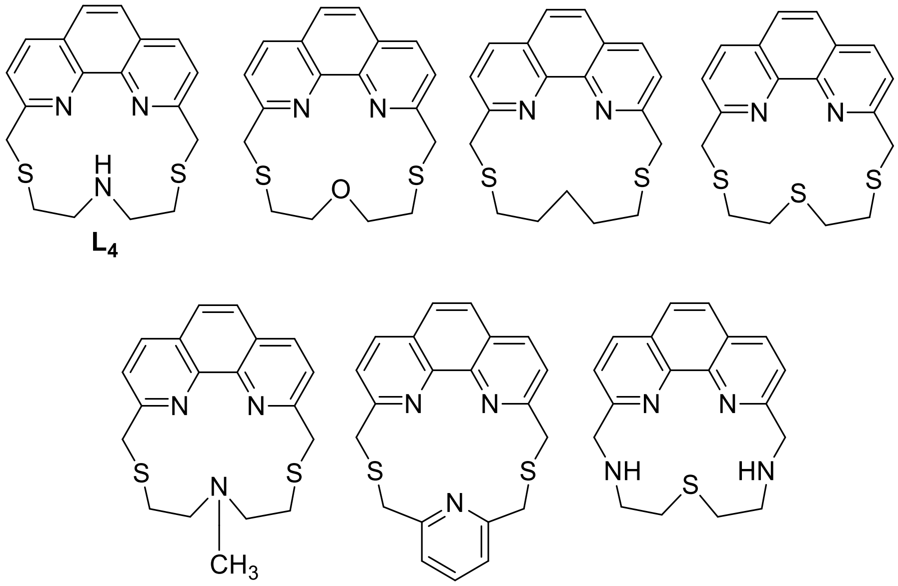

$\mathbf{L_4}$

Figure 13. Mixed-donor macrocycles containing the 1,10-phenanthroline subunit considered for the extraction of metal cations from water solutions.

In addition, macrocyclic systems similar to those shown in Figure 13 have been successfully used as biomimetic model of the coordination environment in blue copper proteins (see Figure 14). This has allowed to investigate more on the redox process that occurs in biological systems, as it was also in this case, it was observed the almost total reversibility of the equilibrium copper(II)-copper(I)[21].

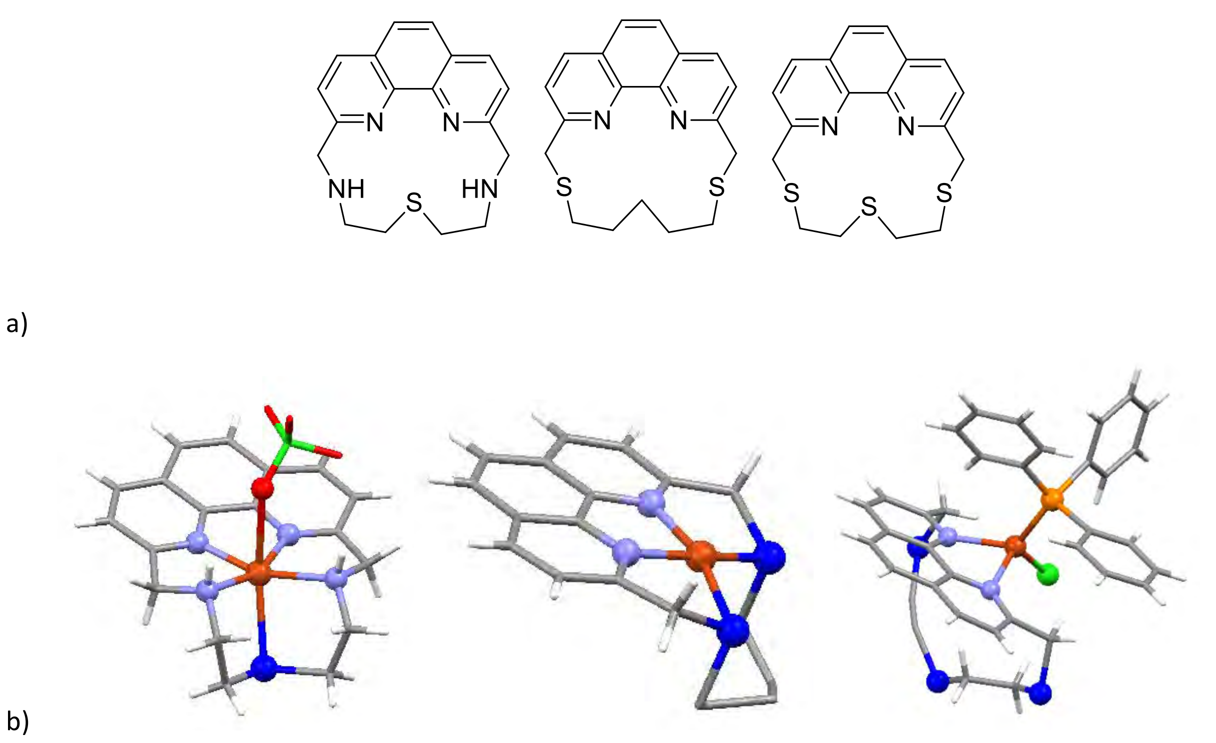

Figure 14. a) Mixed-donor macrocycles containing the 1,10-phenanthroline subunit considered for the biomimetic model and corresponding structures with Cu(II). Colour code: (dark orange) copper (weak blue) nitrogen, (dark blue) sulfur, (red) oxygen, (weak orange) phosphorus, (green) chlorine.

In comparison with the other organic systems, **L_5** is one of the most used macrocyclic as well as a simple coordination system for different metal centers (Cu, Zn, Cd, W, Au, Re, Os) and as a starting material for the synthesis of more complex systems. For example, in 2006 Zijian Guo published a biological study performed with the L_5-Au(III) [29] (see Figure 15) complex to evaluate the cytotoxicity of this system with cells of two different tumours.

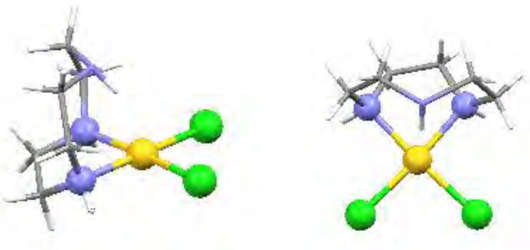

Figure 15. Molecular structure of $[Au(TACN)Cl_2]^+$ (TACN= triazacyclononane) Colour code: (yellow) gold, (blue) nitrogen, (green) chlorine.

Not only applications in the biological field, even the synthesis of materials with unique magnetic properties can be generated through the use of macrocyclic systems that act as a support for the different metal centres. V. Marvaud and co-workers published a study on the synthesis and characterization of the magnetic portions of a Mo_6Cu_{14} cluster where the TACN (triazacyclononane) ligand supports the whole system[30]. The study carried out clearly shows that the magnetic properties of this system increase considerably after irradiating the system with a red light. The use of the **L_5** binder as a support is essential to guarantee the correct structural arrangement of the system that guarantees the formation of the metallic cluster (See Figure 16).

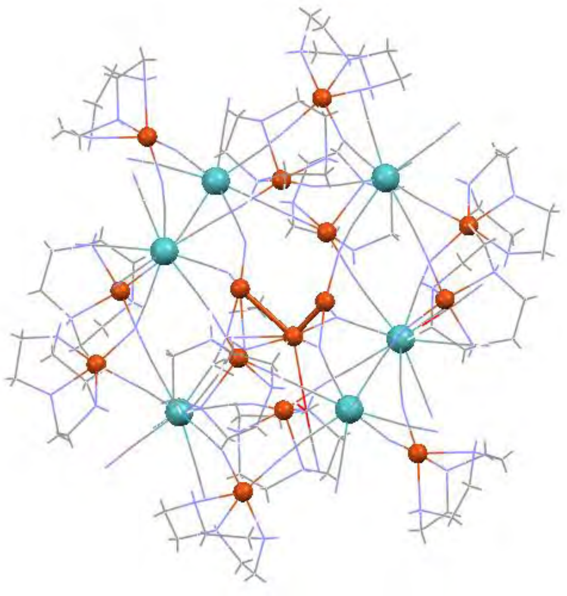

Figure 16. Crystal structure of $[Mo_6Cu_{14}]$. Colour code: (blue) cobalt, (red) copper.

The **L_6**-**L_7** (see Figure 17) are synthetized for the first time by us. However, the presence of the 2-methylquinoline unit allows us to investigate in more detail the photophysical properties of these systems. Quinolines and their derivatives are important constituents of several pharmacologically active synthetic compounds[31]-[33]. They show biological activities such as DNA binding capability[34], antitumor[35], and DNA intercalating carrier[36].

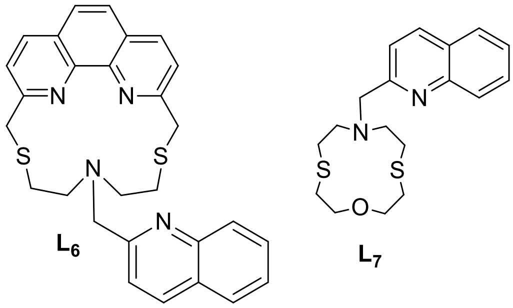

Figure 17. **L_6-L_7** macrocyclic ligands.

The quinoline based receptors are used for various metal ion detections. Especially the zinc ion sensing by quinoline based receptors is of great value[37]-[40]. For example, in 2009 the synthesis and characterization of a series of molecular sensors able to detect the presence of zinc in aqueous solution by the variation of the fluorescent emission of the system, was reported[41]. The synthetized molecular sensors are constituted by a unit of **L$_5$** or similar systems functionalized with the quinoline active unit. The marked selectivity of the system allows to determine the presence of this metal ion in solution by the changes in the fluorescent emission intensity of the system (see Figure 18).

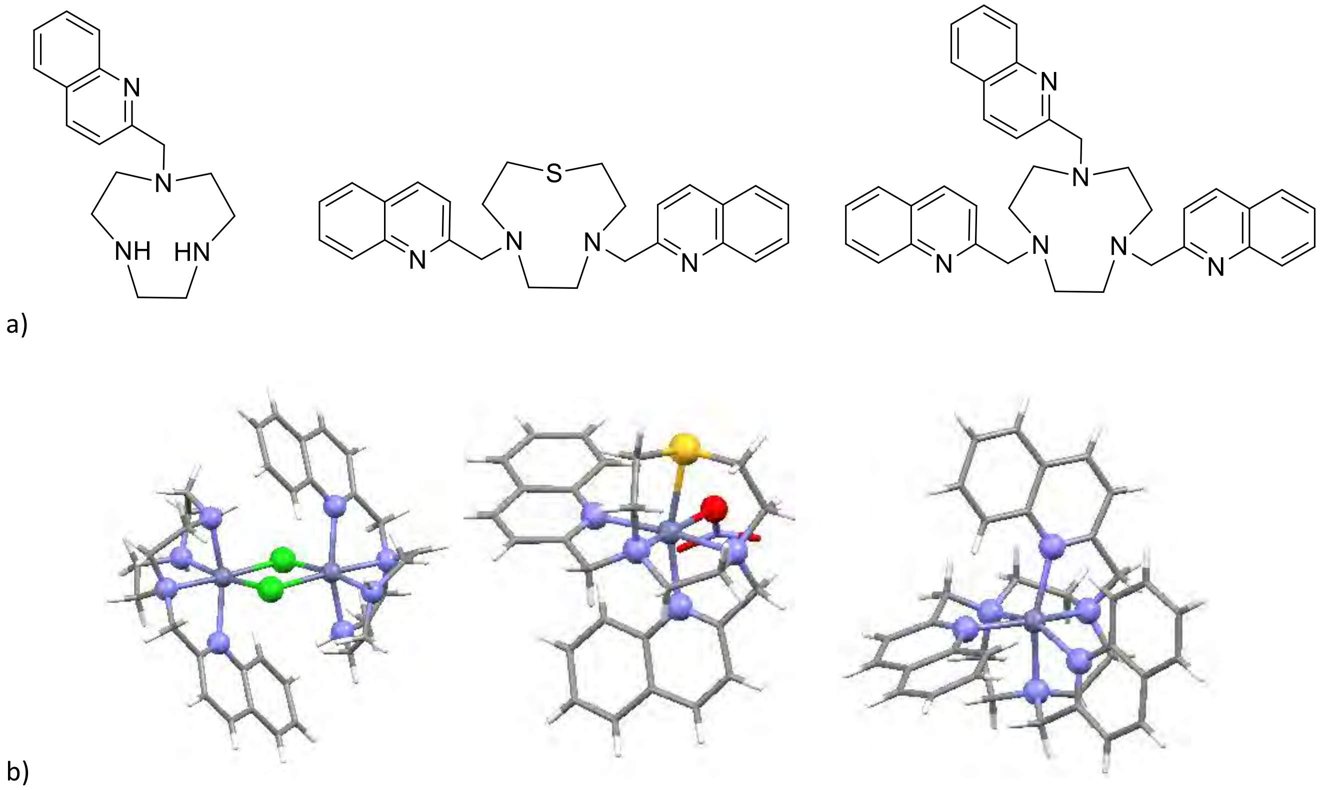

Figure 18. a) Fluorescent molecular sensors (N-methylquinoline-1,4,7-triazacyclononane (left); bis-(N-methylquinoline)-1,4-diaza-7-thiacyclononane (middle); tris-(N-methylquinoline)-1,4,7-triazacyclononane (right)); b) crystal structures with Zn^{2+} [(Zn)(N-methylquinoline-1,4,7-triazacyclononane)(Cl)]$_2^{2+}$ (left); ([(Zn)bis-(N-methylquinoline)-1,4-diaza-7-thiacyclononane(NO$_3$)]$^+$ (middle); [(Zn)tris-(N-methylquinoline)-1,4,7-triazacyclononane]$^{2+}$ (right) . Colour code: (dark grey) zinc, (blue) nitrogen, (yellow) sulfur, (red) oxygen, (green) chlorine.

Furthermore, in some cases it is possible to hypothesize a cellular application of this type of study. For instance, in in 2010 it was published a study related to the possible application of a molecular fluorescence sensor which can be used for qualitative/quantitative determinations of Cd^{2+} by fluorescence microscopy because of the selectivity of this system for this metal ion[42]. Its fluorescence signal is directly correlated with Cd^{2+} content in cells (see Figure 19).

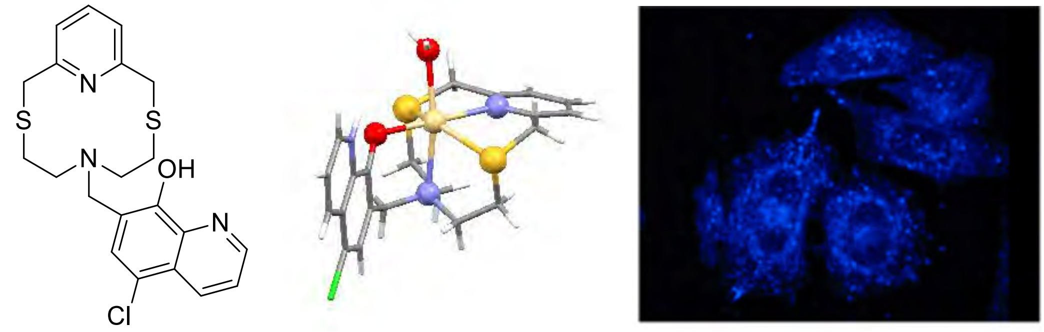

Figure 19. Fluorescencent molecular sensor (N-(5-clhoro-8-hydroxyquinoline)-2,8-dithia-5-aza-2,6-pyridinophane) (left), crystal structure ([(Cd)N-(5-clhoro-8-hydroxyquinoline)-2,8-dithia-5-aza-2,6-pyridinophane]$^+$) (middle) and confocal fluorescence images of Cd^{2+} in Saos-2 cells (right). Colour code: (off-white) cadmium, (blue) nitrogen, (yellow) sulfur, (red) oxygen, (green) chlorine.

Recently, promising anion recognition[43],[44] and amino acid binding[45] properties have been shown. In fact, a recent study has shown the possibility of using macrocyclic systems containing quinoline as an active unit to detect the presence of oxy pyrophosphate in aqueous solution[46]. This possibility is due to a metal cation (zinc) complex, which through the coordinative system present in the compound interacts with the anion present in aqueous solution (pyrophosphate anion) modifying the photophysical properties of the synthesized molecular sensor (see Figure 20).

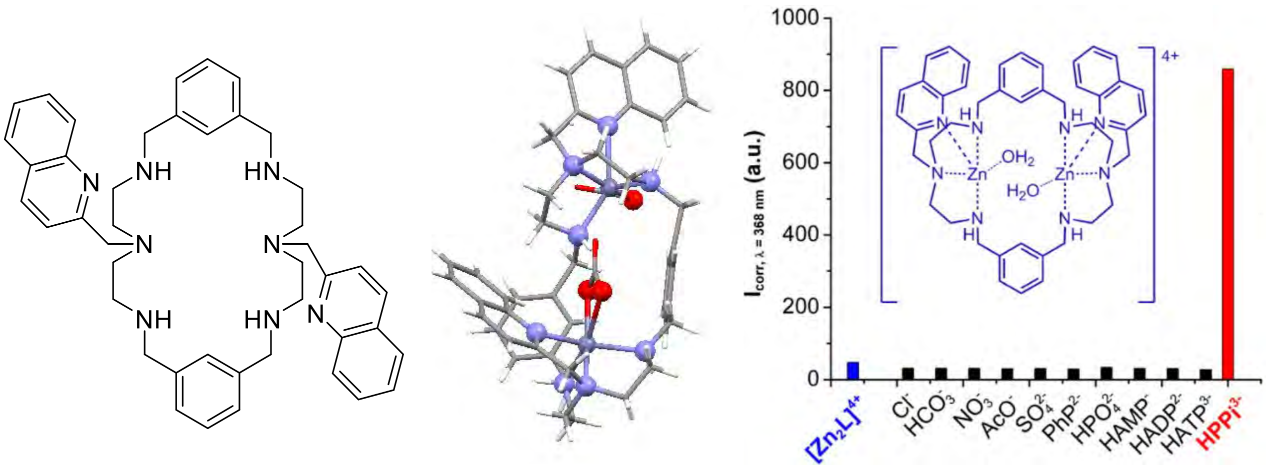

Figure 20. Fluorescent molecular sensor of (3-(2-Quinolinylmethyl)-1,5-diphthalimido-3-azapentane) (left), crystal structure ($[(Zn)_2$(3-(2-Quinolinylmethyl)-1,5-diphthalimido-3-azapentane)$(NO_3)_2]^{2+}$) (middle) and fluorescence intensity change of $[Zn_2$(3-(2-Quinolinylmethyl)-1,5-diphthalimido-3-azapentane)$]^{4+}$ (blue) upon addition of each anion and upon addition of $HPPi^{3-}$ (pyrophosphate ion) (red bar) (right). Colour code: (dark grey) zinc, (blue) nitrogen, (red) oxygen.

The coordinating properties of these organic ligands and the different applications that related to them have made these devices extremely attractive for the synthesis of heterometallic systems containing metallophilic interactions.

1.3 Synthesis of Organic Ligands (L^1-L^7)

The properties of macrocycles strongly depend on the presence in their structure of different donor atoms such as nitrogen, sulfur and oxygen, and on their ring size. For this reason, over the years there have been countless efforts in the development of synthetic techniques used for the synthesis of this series of compounds. During the synthesis of macrocycles, the most delicate phase is definitely the cyclization. In general, this phase of synthesis can take place according to two different mechanisms (see Figure 21): cyclization of an open chain precursor (a); 1:1 (or 2:2) condensation of two (or four) components (b).

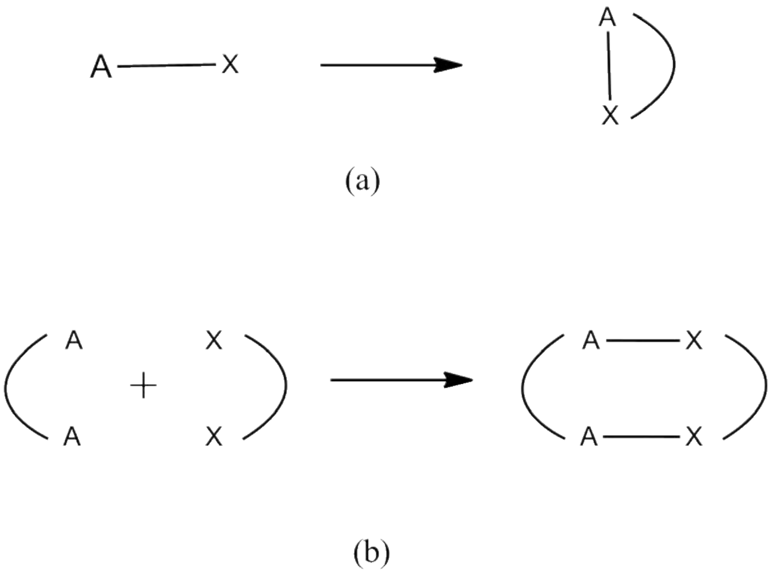

(a)

(b)

Figure 21. General mechanisms of a cyclization reaction

Generally, the synthetic procedures consist of typical nucleophilic substitution reactions to carbon atoms bound to good outgoing groups such as alkyl or acyl halides (chlorinated, brominated, iodinated)[47]. On the other hand, nucleophiles, are generally alcoholic and thiolic functions or their sodium salts. The difficulties encountered in the synthesis of a macrocyclic ligand are related to the cyclization reaction can lead to the formation of secondary products (side reactions) such as oligomers given by the union of the fragments used for the macrocycle formation. This can considerably reduce the yield of the desired product.

There are two methods that allow to minimize the side reactions; the template reaction method[48] and the high dilution method[48].

1.4 Template reaction method

The template method is based on the assumption that an appropriate metal ion can influence the progress of a chemical reaction towards the formation of a given product by controlling the orientation of the active sites present; in our particular case the metal, once coordinated, imposes a particular stereochemistry to the binding sites that can therefore be the subject of a series of multistage reactions. These reactions are impossible to implement in the absence of the metal, which address the whole process towards the formation of the macrocycle. For the choice of the metal ion, one should take into account the principle of Pearson for which a soft metal preferably binds soft donor atoms, while one hard one adapts to donor ones of the same type. For example, alkaline metals have been successfully used in the preparation of crown ethers (see Figure 22), while transition metals are better suited for the synthesis of macrocycles that possess donor atoms such as sulfur and selenium.

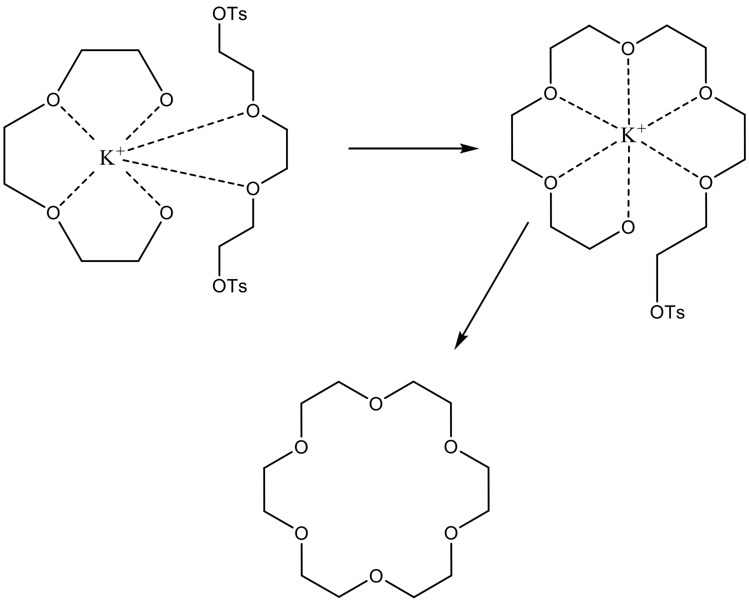

Figure 22. Template effect.

The choice of the metal plays a fundamental role, not only avoiding the formation of by-products, but also controlling kinetically the reaction, which influences the ring size of the macrocycle synthesized during the whole process. The only disadvantage of this method is the difficulty in obtaining the free ligand since the complexes with the macrocycles are naturally stable and inert.

1.5 High dilution method

This method consists of slowly adding the reagents (over several hours) under high dilution conditions (high amounts of solvent). In this way, intramolecular reactions are favoured with respect to the intermolecular reactions that would lead to the formation of oligomers; the disadvantage is that this method requires very long reaction times.

The synthesis of most sulfur macrocycles consists of the reaction catalysed by Cs_2CO_3 in DMF at high dilutions, between a dithiol and the appropriate dialogenide. With regard to mixed macrocycles containing e.g. nitrogen atoms, these must be protected with appropriate groups (BOC [tert-butoxycarbonyl], Ts [tosyl]), which can be removed easily after synthesizing the desired macrocycle. An example is shown in Scheme 1:

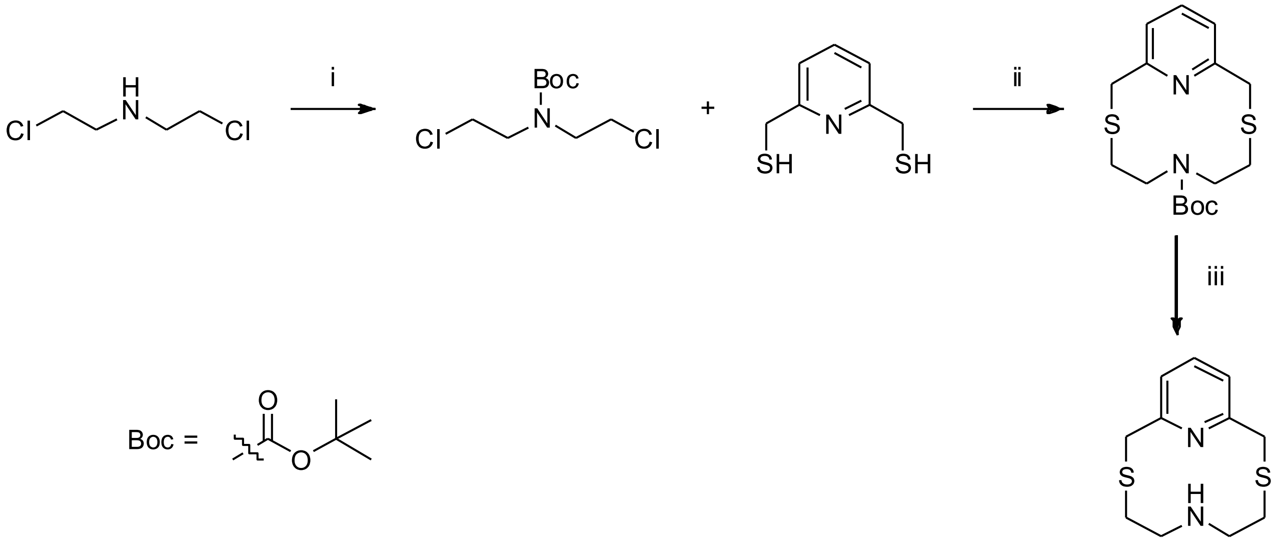

Scheme 1. Reaction conducted with the high dilution method. (i) Boc_2O, NaOH, 0°, 24 h; (ii) Cs_2CO_3, DMF, 55°C, 48 h; (iii) CH_2Cl_2/TFA, r.t.

Once the macrocycle has been synthesized, the protecting group Boc is removed in acidic conditions through the use of trifluoroacetic acid (TFA) in dichloromethane (DCM), in a 1: 1 ratio. The characteristic that makes it easily removable in such conditions depends on the fact that there are two excellent outgoing groups: CO_2, which is eliminated from the equilibrium as gas, and the tert-butyl cation which is relatively stable in an acidic environment. This later, can give through a mechanism of elimination E_1 (monomolecular), 2-methylpropene, or it can give, through substitution SN_1 (monomolecular) with the trifluoroacetic acid, terz-butil trifluoroacetate.

1.6 Synthesis of L_1 ([12] aneNS$_3$), L_3 ([12]aneNS$_2$O).

The synthesis of most of sulphur-containing macrocycles is based on the cyclisation of a dithiol and an appropriate di-halogen derivative in the presence of Cs_2CO_3 in DMF in high diluition conditions as shown in Scheme 2 for **$L_{1,3}$**. Once the secondary amino nitrogen has been protected by the introduction of the Boc, the condensation reaction of the N-Boc-bis (2-chloroethyl) amine with bis(2-mercaptoethyl)sulphide (**L_1**) or bis(2-mercaptoethyl)ether (**L_3**) leads to the formation of the macrocycle Boc-**$L_{1,3}$**; the protective group is subsequently removed by reaction with a mixture of trifluoroacetic acid/dichloromethane (TFA/DCM) in a 1:1 ratio for about two hours; the product thus obtained is 1,4,7-tritia-10-azacyclododecane (**L_1**) or 1-aza-4,10-dithia-7-oxacyclododecane (**L_3**) (see Scheme 2).

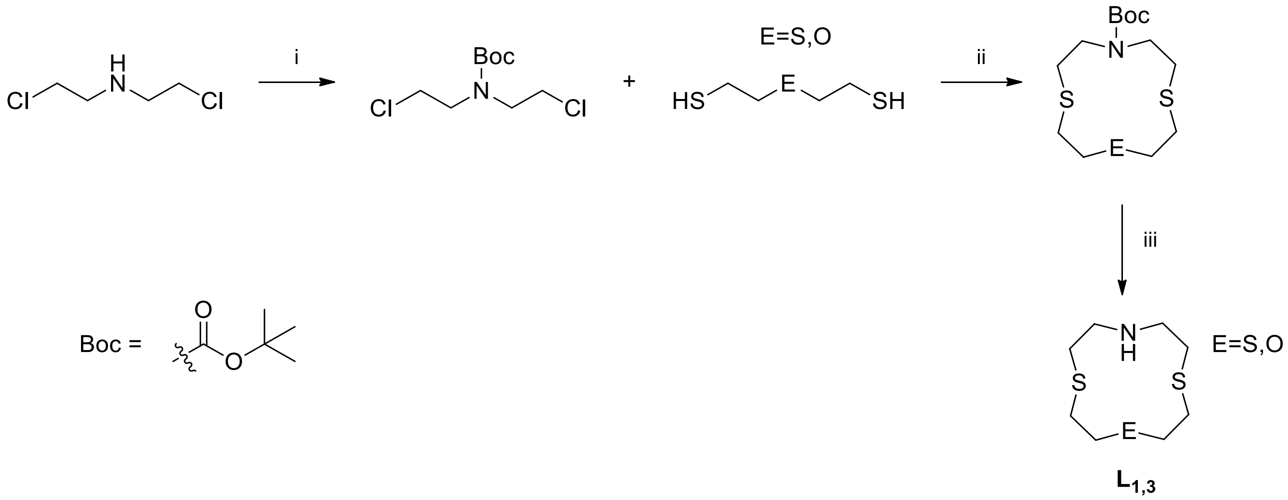

Scheme 2. Synthesis of **$L_{1,3}$**. (i): Boc_2O, NaOH, 0°, 24 h; (ii) Cs_2CO_3, DMF, 55°C, 48 h; (iii) CH_2Cl_2/TFA, r.t.

1.7 Synthesis of L_2 ([12]aneN_2S_2).

L_2 known as 1,7-dithia-4,11-diazacyclotetradecane is synthesized according to the scheme shown in Scheme 3 and 4. Once the amino-group has been protected by the introduction of the Boc, the protected amine reacted with potassium thioacetate to give N-tert-Butoxycarbonyl(2-thioacetoxyethyl)amine (see Scheme 3). Subsequently the thioacetate group is reacted at room temperature with sodium methoxide releasing the -SH groups. As previously explained for the synthesis of **L_2**, the condensation reaction of the N-Boc-bis(2-chloroethyl)amine with N-Boc-bis(2-mercaptoethyl)amine leads to the formation of the macrocycle Boc-**L_2** (see Scheme 4); The last step is the deprotection of the amine group through a mixture of trifluoro acetic acid / dichloromethane for about two hours. The product thus obtained is 1,7-dithia-4,11-diazacyclotetradecane (**L_2**)[49].

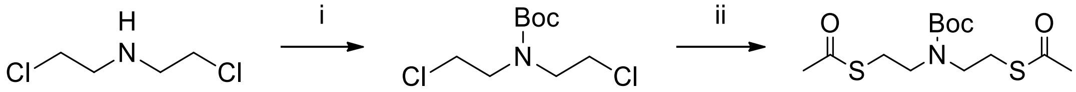

Scheme 3. Synthesis of N-tert-Butoxycarbonyl(2-thioacetoxyethyl)amine. (i): Boc_2O, NaOH, 0°, 24 h; (ii) CH_3COSK, DMF, 48 h, r.t.

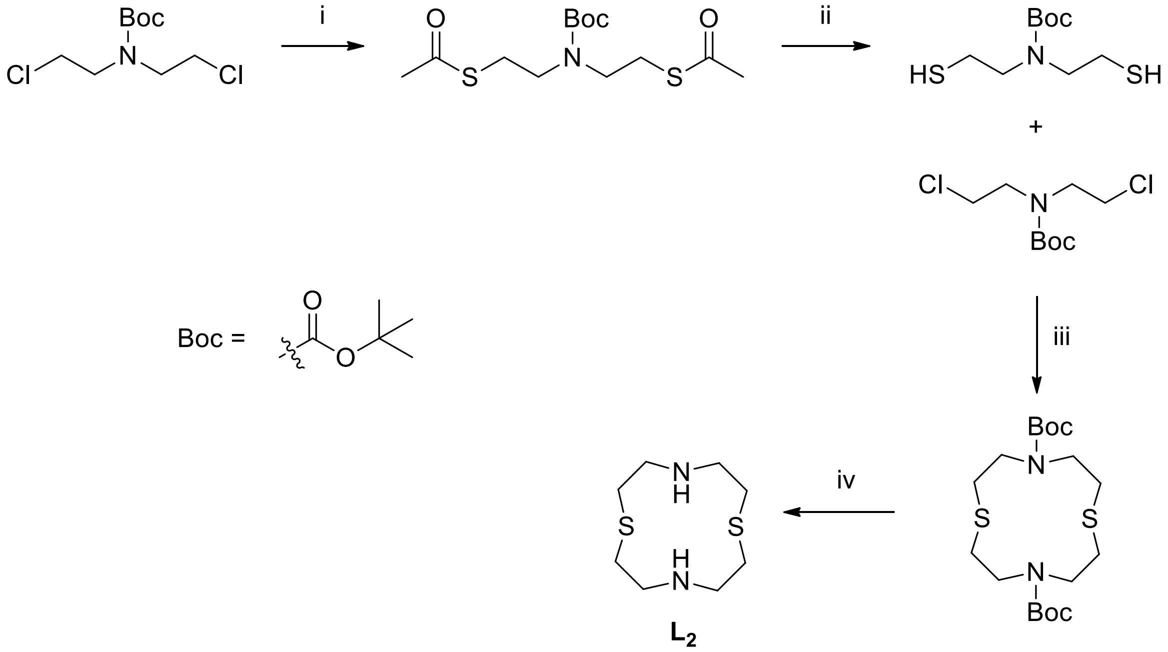

Scheme 4. Synthesis of **L_2**. (i) CH_3COSK, DMF, 48 h, t.r.; (ii) MeONa, MeOH, r.t. 10 min; (iii) Cs_2CO_3**,** DMF, 55°C, 48 h; (iv) CH_2Cl_2/TFA, 2 h, r.t.

1.8 Synthesis of L_4 (5-aza-2,8-dithia[9](2,9)-1,10-phenanthrolinophane).

The synthesis of the $\mathbf{L_4}$ has been described in the experimental part and is summarized in Scheme 5. Briefly, it consists of the oxidation of the 2,9-dimethyl-1,10-phenanthroline to the corresponding dialdehyde with SeO_2, then it is reducted to 2,9-bis (hydroxymethy1) -1,10-phenantholine. Subsequently a chlorination phase with thionyl chloride was carried out. Finally, the cyclization reaction of the 2,9-bis(chloromethyl)-1,10-phenanthroline with N-Boc-bis(2-mercaptoethyl)ammine and subsequent deprotection leads to the formation of the macrocycle $\mathbf{L_4}$;

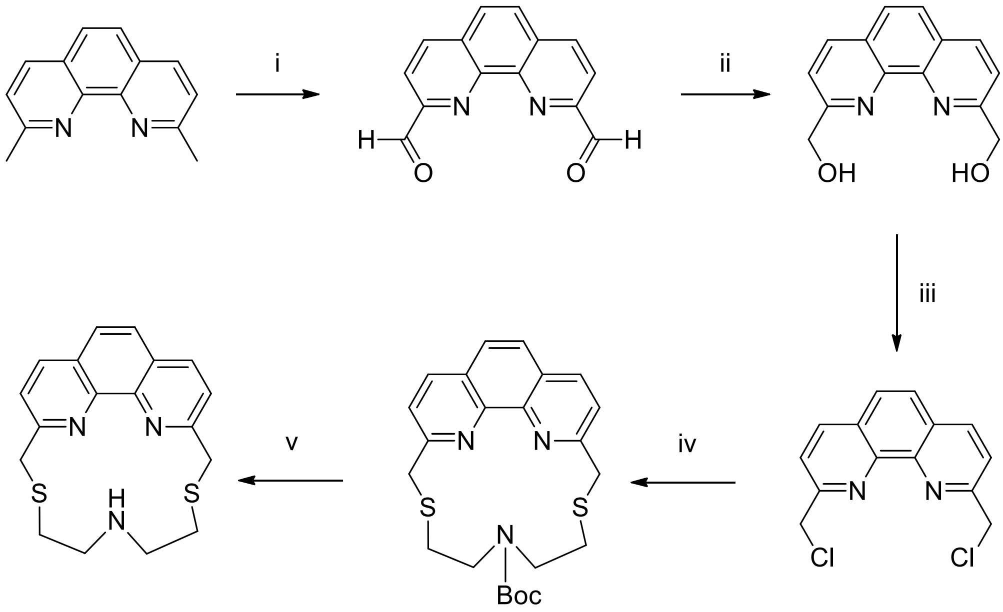

Scheme 5. Description of the synthesis of ligands $\mathbf{L_5}$. (i): SeO_2, dioxane, reflux; 4 h; (ii) $NaBH_4$, ethanol, reflux 2 h; (iii) $SOCl_2$, r.t., 8 h; (iv) $(HSCH_2CH_2)_2N$-Boc, Cs_2CO_3, dimethylformamide (DMF), 55 °C; (v) CH_2Cl_2/TFA, r.t.

1.9 Synthesis of L_5 ([9]aneN_3).

As seen previously, the cyclization of a dithiol and an appropriate dihalogen derivative allows to synthesize a variety of sulfur-containing macrocycles. On the contrary, for the synthesis of macrocyclic ligands containing only N-donors in the aliphatic portion of the ring, appropriate ditosilated salts are used as nucleophilic precursors (see Scheme 6). This procedure is characterised by a troublesome deprotection step of the nitrogen atom(s) after the cyclisation reaction, which is normally performed in concentrate H_2SO_4 at 90°C.

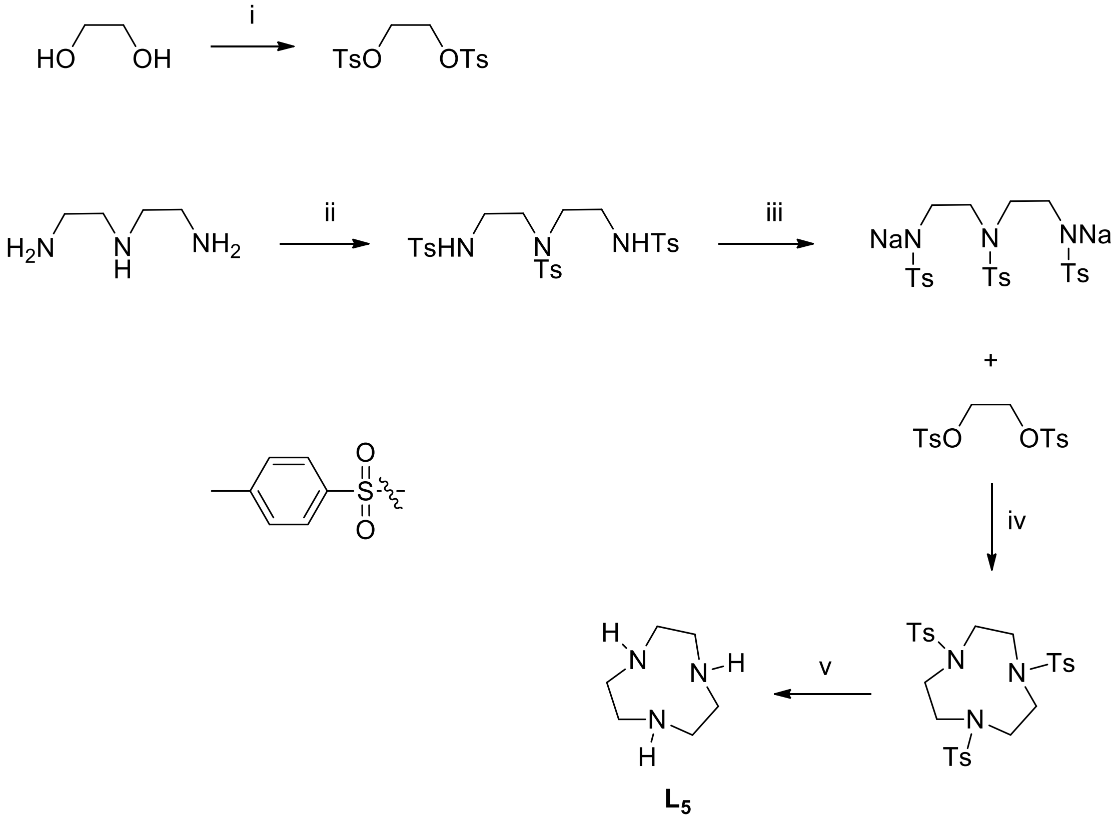

Scheme 6. Synthesis of **L_5**. (i): TsCl, Et_3N, DCM, r.t., 24 h (ii) TsCl, Et_3N, DCM, r.t., 24 h; (iii) Na, abs. EtOH, 2 h; (iv) DMF, 100°C, 24 h; (v) H_2SO_4, 90 °C, 24 h.

The synthesis of **L_5** ([9]aneN_3) follows this methodology: the first step consists in the protection of the amine-groups with the tosyl-group and subsequently the formation of the sodium salt by treatment with metallic sodium. At the same time, the hydroxylic groups of ethylene glycol with the tosyl-group are protected: this step allows to transform the alcohol-groups (bad leaving groups) into excellent leaving groups, ensuring the successful outcome of the cyclization reaction. After cyclization, the tosyl group is removed by sulfuric acid at a temperature of 90 ° C.

1.10 Synthesis of L_6 (5-(2-quinolinylmethyl)-5-aza-2,8-dithia[9](2,9)-1,10-phenanthrolinophane) and L_7 (1-(2-quinolinylmethyl)-[12]aneNS_2O).

The most common synthetic route for the functionalization of macrocyclic nitrogen atoms consists in the nucleophilic attack of suitable alkyl or aryl halides[50]-[54] to the amino groups.

The $\mathbf{L_{6,7}}$ ligands were synthesized starting from $\mathbf{L_{3,4}}$ ([12]aneNS_2O, 5-aza-2,8-dithia[9](2,9)-1,10-phenanthrolinophane) and one equivalent of 2-methylquinoline in dichloromethane (see Scheme 7). The reaction is based on a simple nucleophilic substitution of the chlorine atom by the macrocycle nitrogen atom. K_2CO_3 has the purpose of neutralizing the hydrochloric acid formed during the reaction.

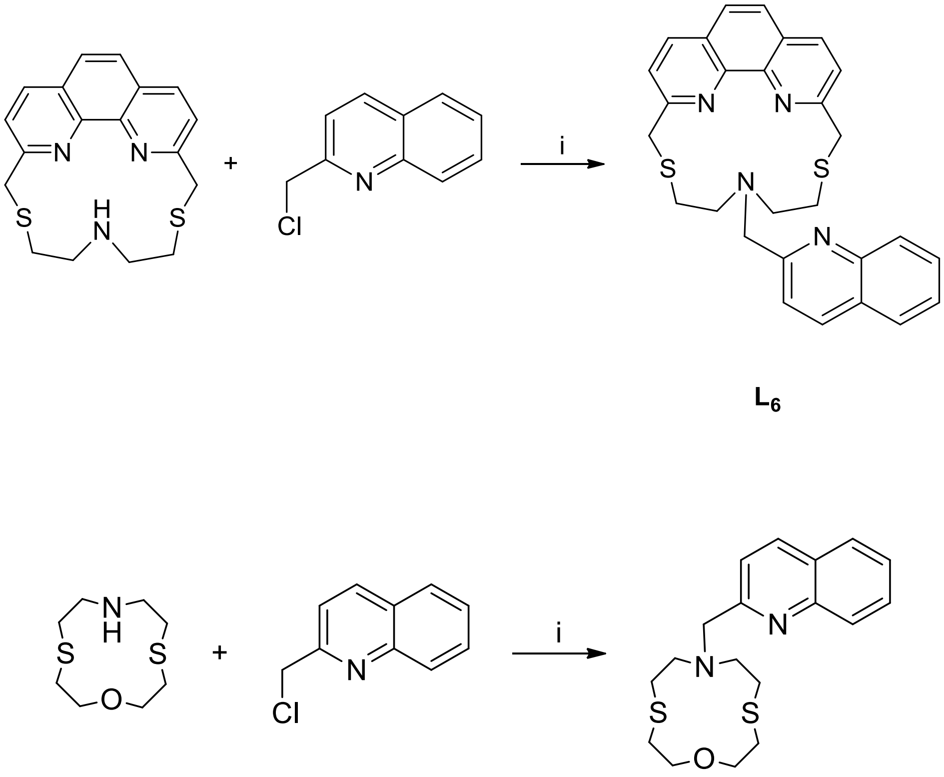

$\mathbf{L_6}$

$\mathbf{L_7}$

Scheme 7. Synthesis of $\mathbf{L_{6,7}}$. (i) K_2CO_3, CH_3CN, 80°C, 24 h.

1.11 References

[1] L. F. Lindoy, *The Chemistry of Macrocyclic Ligand Complexes*, Cambridge University Press, Cambridge, **1989**.

[2] M. A. Masood, R. Jagannathan, P. S. Zacharias, *J. Chem. Soc. Dalt. Trans.,* **1991**, *0*, 2553-2557.

[3] K. J. Takeuchi, M. S. Thompson, D. W. Pipes, T. J. Meyer, *Inorg. Chem.,* **1984**, *23*, 1845-1851.

[4] P. Antunes, P. M. Campello, R. Delgado, M. G. B. Drew, V. Félix, I. Santos, *Dalt. Trans.,* **2003**, 0, 1852-1860**.**

[5] E. C. Constable, J. Lewis, M. C. Liptrot, P. R. Raithby, M. Schröder, *Polyhedron,* **1983**, *2*, 301-302.

[6] C. W. G. Ansell, J. Lewis, P. R. Raithby, J. N. Ramsden, M. Schröder, *J. Chem. Soc. Chem. Commun.,* **1982**, *0*, 546-547.

[7] M. Ghosh, T. Weyhermüller, K. Wieghardt, *Dalt. Trans.,* **2010**, *39*, 1996.

[8] A. J. Blake, J. Casabò, F. A. Devillanova, L. Escriche, A. Garau, F. Isaia, V. Lippolis, R. Kivekas, V. Muns, M. Schröder, et al., *J. Chem. Soc. Dalt. Trans.,* **1999**, *0*, 1085-1092.

[9] P. B. Savage, S. K. Holmgren, S. H. Gellman, *J. Am. Chem. Soc.,* **1994**, *116*, 4069-4070.

[10] V. Havel, J. Svec, M. Wimmerova, M. Dusek, M. Pojarova, V. Sindelar, *Org. Lett.,* **2011**, *13*, 4000-4003.

[11] I. Galván, A. Jorge, F. Solano, K. Wakamatsu, *Spectrochim. Acta Part A Mol. Biomol. Spectrosc.* **2013**, *110*, 55-59.

[12] M. W. Glenny, L. G. A. Van De Water, W. L. Driessen, J. Reedijk, A. J. Blake, M. Schröder, *Dalt. Trans.,* **2004**, 1953-1959.

[13] T. E. S. Ali, S. A. A. Abdel-Ghaffar, K. M. El-Mahdy, S. M. Abdel-Karim, *Turkish J. Chem.* **2013**, *37*, 160-169.

[14] R. W. Hay, T. Clifford, D. T. Richens, P. Lightfoot, *Polyhedron,* **2000**, *19*, 1485-1492.

[15] A. V. Koulov, J. M. Mahoney, B. D. Smith, *Org. Biomol. Chem.,* **2003**, *1*, 27-29.

[16] H. Adams, M. Elsegood, D. Fenton, S. Heath, *J. Chem. Soc., Dalt. Trans.,* **1999**, 2031-2037.

[17] P. M. Reddy, K. Shanker, R. Rohini, V. Ravinder, *Int. J. ChemTech Res.,* **2009**, *1*, 367-372.

[18] F. Li, R. Delgado, M. G. B. Drew, V. Félix, *Dalt. Trans.* **2006**, 0, 5396-5403.

[19] K. P. Wainwright, *Coord. Chem. Rev.*, **1997**, 166, 35-90.

[20] C. Bazzicalupi, C. Caltagirone, Z. Cao, Q. Chen, C. Dinatale, A. Garau, V. Lippolis, L. Lvova, H. Liu, I. Lundström, et al., *Chem. - A Eur. J.,* **2013**, *19*, 14639-14653.

[21] M. C. Aragoni, M. Arca, F. Demartin, F. A. Devillanova, F. Isaia, A.Garau, V. Lippolis *Inorg. Chem.*, **2002**, *41*, 6623-6632.

[22] A. J. Blake, R. Donamaría, E. J. Fernández, T. Lasanta, V. Lippolis, J. M. López De Luzuriaga, E. Manso, M. Monge, M. E. Olmos, *Dalt. Trans.,* **2013**, *42*, 11559-11570.

[23] A. J. Blake, R. Donamaria, V. Lippolis, J. M. López De Luzuriaga, E. Manso, M. Monge, M. E. Olmos, *Inorg. Chem.,* **2014**, *53*, 10471-10484.

[24] Y. Jeong Soo, S. Swarbhanu et all., Patent WO/2016/163727, **2016**.

[25] L. Siegfried, T. A. Kaden, *Dalt. Trans.,* **2005**, 0, 1136-1140.

[26] Y. Habata, K. Noto, F. Osaka, *Inorg. Chem.,* **2007**, *46*, 6529-6534.

[27] C. Caltagirone, A. Bencini, F. Demartin, F. A. Devillanova, A. Garau, F. Isaia, V. Lippolis, P. Mariani, U. Papke, L. Tei, et al., *Dalt. Trans.,* **2003**, 0, 901-909.

[28] M. C. Aragoni, M. Arca, A. Bencini, S. Biagini, A. J. Blake, C. Caltagirone, F. Demartin, G. De Filippo, F. A. Devillanova, A. Garau, et al., *Inorg. Chem.,* **2008**, *47*, 8391-8404.

[29] P. Shi, Q. Jiang, J. Lin, Y. Zhao, L. Lin, Z. Guo, *J. Inorg. Biochem.,* **2006**, *100*, 939-945.

[30] N. Bridonneau, L. M. Chamoreau, G. Gontard, J. L. Cantin, J. Von Bardeleben, V. Marvaud, *Dalt. Trans.,* **2016**, *45*, 9412-9418.

[31] H. I. El-Subbagh, S. M. Abu-Zaid, M. A. Mahran, F. A. Badria, A. M. Al-Obaid, *J. Med. Chem.,* **2000**, *43*, 2915-2921.

[32] A. A. Watson, G. W. J. Fleet, N. Asano, R. J. Molyneux, R. J. Nash, *Phytochemistry,* **2001**, *56*, 265-295.

[33] Jerom and K.H. Spencer, *Eur. Pat. Appl.* EP 277794, **1988.**

[34] G. J. Atwell, B. C. Baguley, W. A. Denny, *J. Med. Chem.,* **1989**, 2, 396-401.

[35] L. Hu, Z. R. Li, Y. Li, J. Qu, Y. H. Ling, J. D. Jiang, D. W. Boykin, *J. Med. Chem.,* **2006**, 46, 6273-6282.

[36] Y. L. Chen, I. L. Chen, C. C. Tzeng, T. C. Wang, *Helv. Chim. Acta,* **2000**, 83, 989-994.

[37] S. Banthia, A. Samanta, *J. Phys. Chem. B,* **2006**, 110, 6437-6440.

[38] C. C. Woodroofe, S. J. Lippard, *J. Am. Chem. Soc.,* **2003**, 125, 11458-11459.

[39] X. Y. Chen, J. Shi, Y. M. Li, F. L. Wang, X. Wu, Q. X. Guo, L. Liu, *Org. Lett.,* **2009**, 11, 4426-4429.

[40] S. Aoki, K. Sakurama, N. Matsuo, Y. Yamada, R. Takasawa, S. Tanuma, M. Shiro, K. Takeda, E. Kimura, *Chem. - A Eur. J.,* **2006**, 12, 9066-9080.

[41] M. Mameli, M. C. Aragoni, M. Arca, M. Atzori, A. Bencini, C. Bazzicalupi, A. J. Blake, C. Caltagirone, F. A. Devillanova, A. Garau, et al., *Inorg. Chem.,* **2009**, *48*, 9236-9249.

[42] M. Mameli, M. C. Aragoni, M. Arca, C. Caltagirone, F. Demartin, G. Farruggia, G. De Filippo, F. A. Devillanova, A. Garau, F. Isaia, et al., *Chem. - A Eur. J.,* **2010**, *16*, 919-930.

[43] C. R. Bondy, P. A. Gale, S. J. Loeb, *J. Am. Chem. Soc.,* **2004**, 126, 5030-5031.

[44] F. Y. Wu, X. F. Tan, Y. M. Wu, Y. Q. Zhao, *Spectrochim. Acta - Part A Mol. Biomol. Spectrosc.,* **2006**, 65, 925-929.

[45] D. Kalita, H. Deka, S. S. Samanta, S. Guchait, J. B. Baruah, *J. Mol. Struct.,* **2011**, *990*, 183-196.

[46] L. M. Mesquita, V. André, C. V. Esteves, T. Palmeira, M. N. Berberan-Santos, P. Mateus, R. Delgado, *Inorg. Chem.,* **2016**, *55*, 2212-2219.

[47] A. IUriĭ, Y. A. Zolotov, *Macrocyclic Compounds in Analytical Chemistry*, Wiley, **1997**.

[48] E. C. Constable, *Metal Ligand Reactivity*, Wiley-VCH Verlag GmbH & Co. KGaA, Weinheim, FRG, **2005**.

[49] J. D. Chartres, A. M. Groth, L. F. Lindoy, M. P. Lowe, G. V. Meehan, *J. Chem. Soc., Perkin Trans., 1,* **2000**, 3444-3450.

[50] B. Dey, J. H. Coates, P. A. Duckworth, S. F. Lincoln, K. P. Wainwright, *Inorganica Chim. Acta,* **1993**, *214*, 77-84.

[51] L. J. Farrugia, N. M. Macdonald, R. D. Peacock, *J. Robb.*, **1995**, 0, *5387*.

[52] K. P. Wainwright, *Adv. Inorg. Chem.,* **2001**, *52*, 293-334.

[53] P. V. Bernhardt, G. A. Lawrance, *Coord. Chem. Rev.,* **1990**, *104*, 297-343.

[54] K. Wieghardt, *Angew. Chem.*, **1988**, *60*, 509-516.

Chapter 2

Gold(I)-Thallium(I) Heteronuclear compounds

2.1 Gold(I)-thallium(I) heteronuclear compounds

As reported in the introduction, there is a strong tendency of heavy metal atoms to form molecular or polymeric systems with metal-metal distances shorter than the sum of van der Waals radius. In particular, in the case of gold(I) the number of complexes formed and featuring dimers, oligomers or polymers based on the interactions between the different metal centers[1] with a force comparable to that of hydrogen bonds[2]-[5] is particularly abundant.

In fact, thanks to the development of instrumental techniques and to the development of new synthetic strategies, the study of these interactions is more detailed, showing that gold is not an exception in the periodic table, but that metal centers with similar configuration present the same behaviour. In time, many examples of heterometallic systems featuring interacting metal centres with different configurations have been synthesised: d^{10}-d^{10} (Ag(I)-Ag(I))[6]-[21], Cu(I)-Cu(I)[22]-[34], Hg(II)-Hg(II)[35], Cd(II)-Cd(II)[36]-[41], Pt(0)-Pt(0)[42]-[44], Pd(0)-Pd(0))[42][43], d^8-d^8 (Pt(II)-Pt(II)[45]-[52], Pd(II)-Pd(II)[52]-[66]), s^2-s^2 (Tl(I)-Tl(I)[67]-[73], Pb(II)-Pb(II)[74]-[78]), s^2-d^8 (Tl(I)-Pt(II)[79]-[81], Tl(I)-Ir(I)[82]-[83]), s^2-d^{10} (Tl(I)-Au(I)[84]-[88], Tl(I)-Pt(0)[41], Pb(II)-Au(I)[84]), d^8-d^{10} (Pt(II)-Au(I)[89]-[96], Pt(II)-Ag(I) [97]-[99], Pt(II)-Cd(II)[100], Pt(II)-Hg(II)[101]-[102], Pd(II)-Au(I)[103]-[105]). These compounds have been subjected to numerous theorical studies[106] due to their peculiar spectroscopic properties deriving from the metallophilic interactions. In particular, computational studies have shown that Au(I)-Tl(I) heteronuclear systems show little tendency to form this type of weak interactions; while the relativistic effects seem to cause an increase of this tendency with different metal centers, the same effect causes a weakening of this tendency with s^2-metals[107]. Despite the difficult tendency of these metal centers to form this type of interactions, numerous examples are known containing metallophilic interactions s^2-d^{10} due to additional electrostatic forces, effects of crystalline packing or due to the architecture of the organic ligand used. For example, the metallophilicity between Au (I) and Tl (I) centers with an equilibrium distance of about 3 Å, includes an ionic contribution of about 80% respected to the total energy of the system[86]. Consequently, the rationalization of these systems is a challenge both from the synthetic and theorical point of view and from the theoretical point of view.

According to the strong ionic contribution necessary for the stabilization of these interactions, the most used synthetic strategy for the synthesis of gold-thallium heteropolinuclear systems is the basic-acid synthetic strategy developed at the beginning of the 80's by Laguna and co-workers for the preparation of gold-silver complexes and later used by others as H. Patterson for the preparation of gold-thallium heteronuclear ones; this strategy consists of the reaction between a rich electron system ($Au(C_6X_5)_2^-$, $Au(CN)_2^-$, etc.) and a Lewis acid ($TlPF_6$, $TlNO_3$ etc.). In particular, this methodology allowed the synthesis and characterization of the compound $Tl[Au(CN)_2]$[108], prepared by the reaction of $TlNO_3$ and $K[Au(CN)_2]$[109]; the Au-Tl interactions present in this compound influence the energy, intensity and deactivation process of the transition responsible for the photophysical properties of the system. In the same way, the groups of Prof. Fackler and Burini described a series of systems containing the unit $[Au_3TlAu_3]$[110] obtained by reaction of a 1-benzylimidazolate (bzim) trinuclear derivatives of Au(I) with the acid cation Tl^+ (see Figure 1).

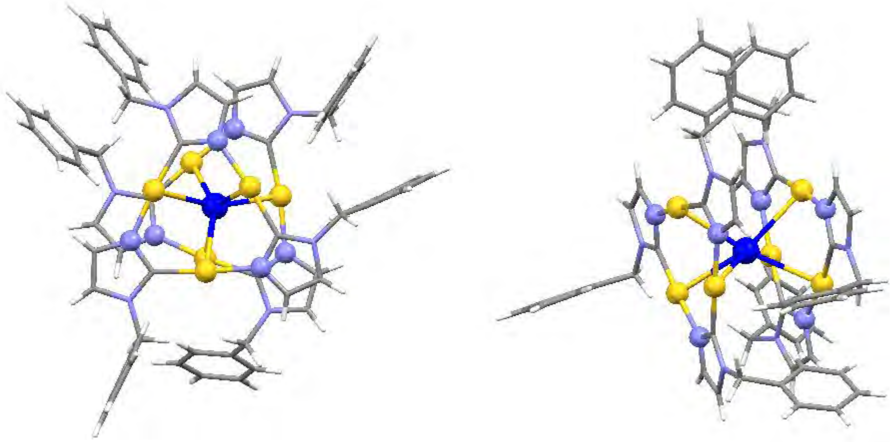

Figure 1. Structure of $[Tl\{[Au(\mu\text{-}N^3,C^2\text{-bzim}]_3\}_2]^+$

Polyhalogenphenyl derivatives of different metal ions have been frequently used to prepare polymetallic systems containing Pd[54], Pt[111], Cu[112], Ag[113] or Au[1]. These electron withdrawing groups ($C_6F_5^-$, $C_6F_3H_2^-$, $C_6(CF_3)_3H_2^-$), are capable of stabilizing anionic metal species allowing the preparation of precursors with different electronic characteristics for their use in basic acid reactions.

In particular, the use of bis (polyhalophenyl) aurate complexes as Lewis bases for the preparation of polymeric derivatives with different metal centers dates back more than 20 years. In spite of this, our group of investigations has been responsible for the preparation of an important polymeric heteronuclear Au-Tl compound by reaction of the $Au(C_6X_5)_2^-$ (X=Cl, F)[114],[115] aurate species and $TlPF_6$ (Equation 1).

$$[NBu_4][Au(C_6X_5)_2] + TlPF_6 \xrightarrow[\text{2) } CH_2Cl_2]{\text{1) THF}} [Au(C_6X_5)_2Tl]_n + [NBu_4]PF_{6(s)}$$

Equation 1.

As shown in equation 1, the synthesis of these systems takes place in two phases: reactions of the precursors, volume reduction and precipitation of the compounds in dichloromethane. In addition, the indicated compounds are capable of reacting with different N-, O- or S-donor ligands, forming derivatives in which the ligands are coordinated at the centre of thallium(I). The steric characteristics of the ligands as well as the presence of different donor atoms can play a fundamental role in the modification of the structural arrangement as in the photophysical properties of the resulting systems. For example, the use of N-donor ligands such as bipyridine[116], triethylenetetramine (trien) [119], tetramethylenediamine (TMDA)[117] or 1,10-phenantroline[118], affords polymeric compounds that show an emission wavelength above 600 nm. On the other hand, the use of ketones as ligands affords butterfly Au_2Tl_2 clusters whose emission wavelength is more energetic than those corresponding to the polymeric compounds mentioned previously [119]. Furthermore, the use of crown thioether ligands such as [9]aneS_3 (1,4,7-trithiacyclononane) or [14]aneS_4 (1,4,8,11-tetrathiacyclotetradecane) affords tetranuclear discrete molecules with a L-Tl-Au-Au-Tl-L disposition in which the crown thioether acts as a terminal ligand, thus preventing polymerization. By contrast, if a bulkier larger macrocycle such as [24]aneS_8 (1,4,7,10,13,16,19,22-octathiacyclotetraeicosane) is employed, its behaviour as bridging ligand gives rise to an Au-Tl-L-Tl-Au disposition, and affords the formation of polymeric chains as a result of unsupported aurophilic contacts between the Au(I) centres[120]. Additionally, in previous works we have established that the variations on the basic properties of the gold(I) precursor by changing the halogens presents in the aryl group, directly affects the characteristics of the final complexes obtained in the reactions. This is mainly due to the different electronegativity and steric demand of the aryl groups, and hence, different structural and photophysical properties are observed in the final products[121]-[123]. Taking all the above into account, in the first part of this thesis we decided to study the reactivity of the heterometallic polymeric compound $[\{Au(C_6X_5)_2\}Tl]_n$ (X = F, Cl) with the N,S,O-mixed-donor crown ethers **L_1**-**L_3** to synthesize a new class of compounds containing Au(I)-Tl(I) metallophilic interactions (see Figure 2).

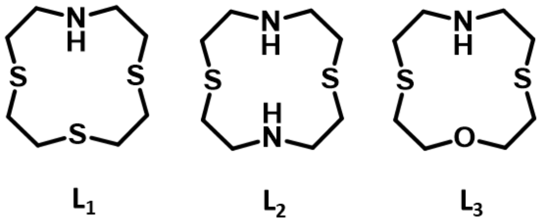

Figure 2. N,S,O-mixed-donor crown ethers used in the reactivity with $[\{Au(C_6X_5)_2\}Tl]_n$ (X = F, Cl).

In this case, we wanted to evaluate how the three macrocycle systems with the same dimensionality but different type of donor atoms (O, S, N) can influence both the structural properties and the optical properties of the synthetized heterometallic systems featuring Au(I)-Tl(I) interactions.

2.2 N,S,O-mixed-donor crown ligand ethers (L_1-L_3)

2.2.1 Synthesis and characterization of complexes featuring Au(I)-Tl(I) interactions

The heterometallic complexes **1**-**6** were obtained by reaction of the polymeric compound $[\{Au(C_6X_5)_2\}Tl]_n$ (X=F,Cl) with equimolar amount of the different N,S,O-mixed-donor crown ethers **L_1**-**L_3** in tetrahydrofuran and precipitated with hexane (see Scheme 1). The substitution of the chlorine atoms presents in the aryl moieties bound to the gold(I) atom with the fluorine atoms does not seem to affect the stoichiometry of the different reactions, but it influences the structural dispositions and spectroscopic properties of the final products. All the obtained compounds are insoluble in dichloromethane, acetonitrile and diethyl ether although they appear to be soluble in O-donor solvents. However, the solubility of the chlorinated compounds is lower than the solubility of the fluorinated complexes.

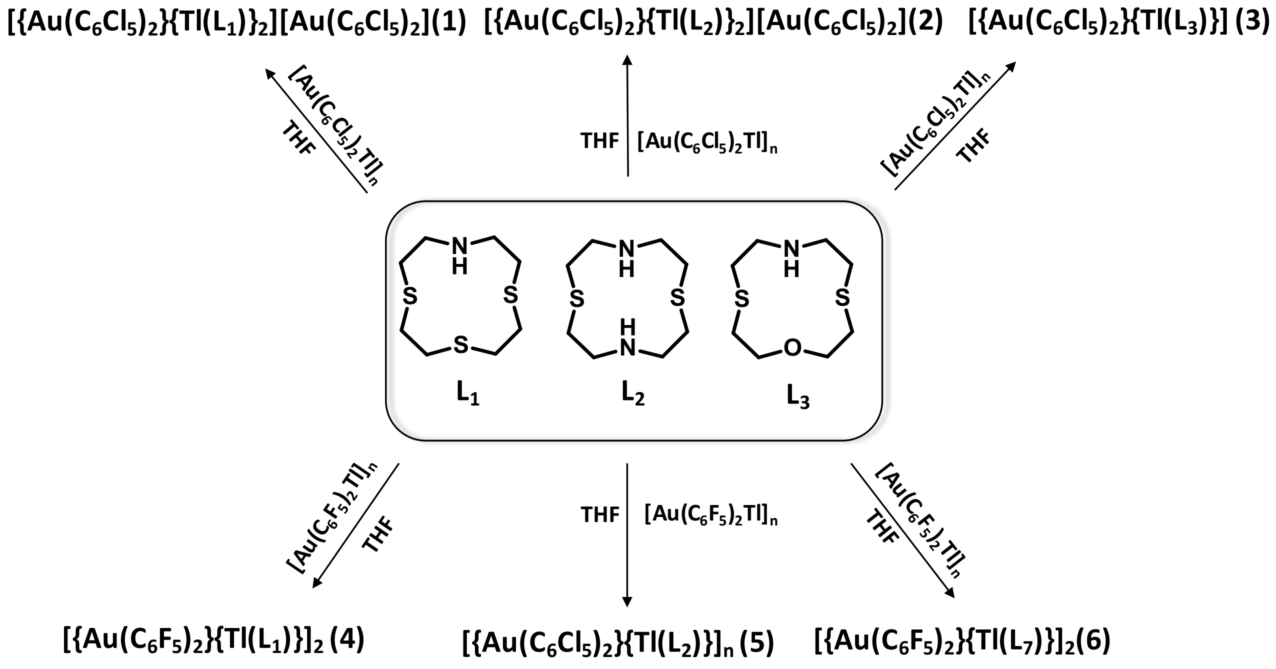

Scheme 1.

The elemental analyses and spectroscopic data of the obtained complexes are in accordance with the proposed stoichiometries (see Experimental Section). Their IR spectra show, among others, absorptions arising from the $C_6F_5^-$[124] and $C_6Cl_5^-$[125] groups bonded to gold(I) at approximately 1500, 950 and 780 cm^{-1}, or about 834 and 614 cm^{-1}, respectively. The presence of the $[Au(C_6F_5)_2]^-$ fragment in **4-6** is evident in their ^{19}F NMR spectra, which resemble that of the precursor complex $NBu_4[Au(C_6F_5)_2]$, and seem to indicate that a dissociative process giving rise to aurate(I) anions and thallium(I) cations takes place in solution. Regarding the NMR spectrum of all the complexes, they show proton resonances very similar to the chemical shifts observed for the free ligands. Therefore, the coordination of the macrocyclic ligands to thallium does not significantly affect the position of the resonances observed in their ^1H NMR spectra, nor does the dissociative process affect the N,S-donor molecules. Thus, the ^1H NMR spectra of **1** and **4** display two multiplets at 2.72 and 2.91 ppm (**1**) or at 2.77 and 2.98 ppm (**4**), with 1:3 relative integrations, and corresponding to the hydrogen atoms of the methylene groups adjacent to nitrogen or to sulphur, respectively. The ^1H NMR spectra of **2** and **5** show two multiplets at 2.81 and 2.98 ppm (**2**) or at 2.89 and 3.05 ppm (**5**), due to the protons of the methylene groups bonded to the N or S atoms of the ring, respectively, and with 1:1 relative integrations. Finally, in the ^1H NMR spectra of the other two products (complexes **3** and **6**), we can see two multiplets at 2.68-2.79 and 3.51 ppm (**3**) or at 2.69 and 3.49 ppm (**6**), due to the protons of the methylene groups bonded to the N,S or O atoms of the ring, respectively, and with 1:3 relative integrations.

Regarding their mass spectra (MALDI$^-$), the compound synthesised display a peak due to the unit $[\{Au(C_6X_5)_2\}_2Tl]^-$ at m/z = 1594 (**1**-**3**) or 1267 (**4-6**) or a signal corresponding to $[Au(C_6X_5)_2]^-$ at m/z = 695 (**1**-**3**) or 531 (**4**-**6**), the latter appearing as parent peak in all the cases. In their MALDI$^+$ mass spectra, peaks due to the fragment $[Tl(L)]^+$ appears at m/z = 428 (**1**, **4**) or 411 (**2**-**3**, **5**-**6**), showing experimental isotopic distributions in agreement with the theoretical ones.

Finally, the molar conductivity measurements of the six complexes in acetone agree with a dissociative process in solution, showing values corresponding to uni-univalent electrolytes (see Experimental section).

2.2.2 X-ray structural determinations

In the case of **1**-**3**, single crystals suitable for X-Ray diffraction analyses were grown. Although the six crystal structures contain similar structural moieties, $[Au(C_6X_5)_2]^-$ and $[Tl(L)]^+$ units, there are significant differences among them. The crystal structures of **1** and **2**·2THF, with pentachlorophenyl ligands bonded to gold(I), show the same ionic structure, which consists of a trinuclear $[\{Au(C_6Cl_5)_2\}\{Tl(L)\}_2]^+$ cation featuring a novel L-Tl-Au-Tl-L trinuclear disposition and a $[Au(C_6Cl_5)_2]^-$ fragment as counter-ion (see Figure 3 and Table 1-2).

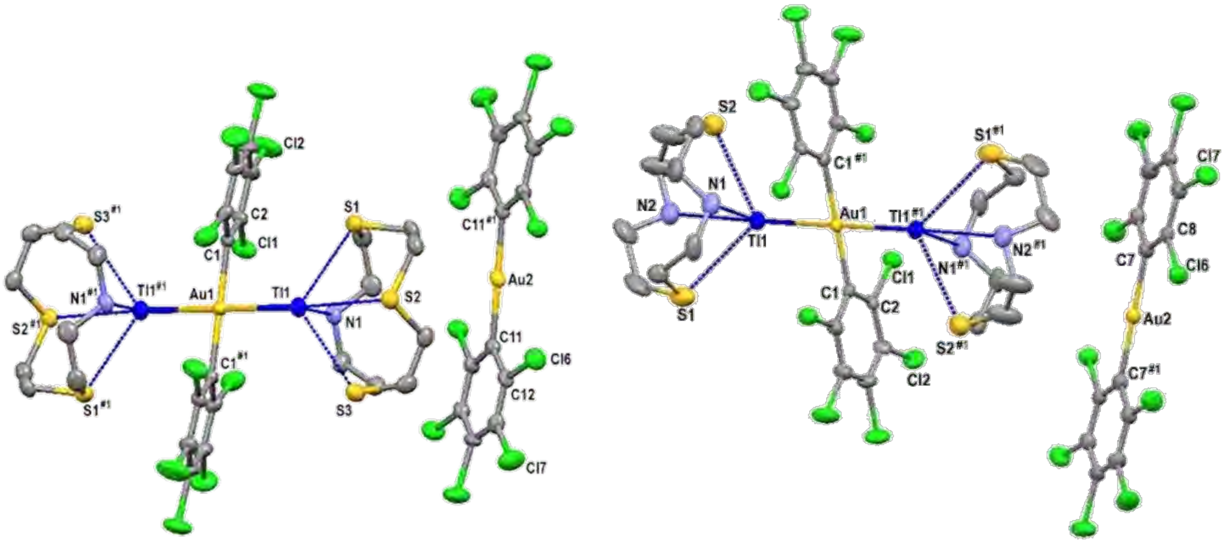

Figure 3. Crystal structures of **1** (left) and **2**·2THF (right) with the labeling scheme adopted for the atom positions. Hydrogen atoms and THF molecules in the case of **2**·2THF are omitted for clarity, and ellipsoids are drawn at the 30% level. #1 −x + 1, −y + 1, −z; #2 −x + 1, −y + 1, −z +1(1). #1 −x, −y, −z + 1; #2 −x, −y, −z (2·2THF).

The intermetallic distances within the cations are different depending on the macrocyclic ligand employed, showing a Au-Tl distance of 3.2411(2) Å in the [12]aneNS$_3$ (**L$_1$**) derivative **1**, shorter than that of 3.3853(5) Å observed in the [12]aneN$_2$S$_2$ (**L$_2$**) complex **2**·2THF. Nevertheless, both of them lie within the range of the Au-Tl distances described till date, which varies from 2.804(6) Å, observed in $[AuPdTl(P_2phenantroline)_3](BF_4)_2\cdot 2.5CH_2Cl_2$[88] , to 3.4899(6) Å, found in [Tl(2,2'-bipy))]$[Au(C_6F_5)_2]$[118], and they both are longer than the average Au-Tl distance of 3.064 Å. Each gold atom is linearly coordinated to two pentachlorophenyl groups, displaying normal Au-C bond lengths of 2.058(5) and 2.046(5) Å in **1**, and of 2.056(10) and 2.041(12) Å in **2**·2THF. Totally different is the structural arrangement observed for the complex **3**, which consists of a binuclear system

[{Au(C_6Cl_5)$_2$}{Tl(L_3)}] held by an Au(I)-Tl(I) interaction (see Figure 4 and Table 3). The intermetallic distance between the metal centres is quite different from the previously illustrated system (3.0221 (4)) probably due to the greater electronic availability of gold, given the presence of a single heterometallic interaction. Again, the gold(I) atom is linearly coordinated to two pentachlorophenyl groups, displaying normal Au-C bond lengths of 2.056 (7) and 2.058 (7) Å.

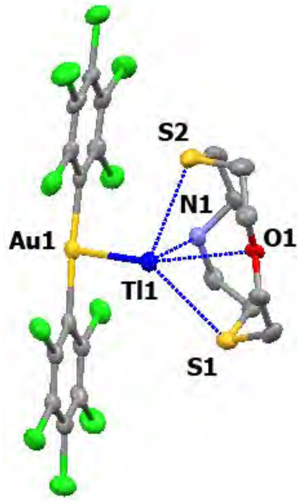

Figure 4. Crystal structures of **3** with the labeling scheme adopted for the atom positions. Hydrogen atoms are omitted for clarity, and ellipsoids are drawn at the 30% level.

Table 1. Selected bond lengths [Å] and angles [°] for **1**.

Au(1)-Tl(1)	3.2410(2)	Tl(1)-S(1)	3.0984(13)
Au(1)-C(1)	2.058(5)	Tl(1)-S(2)	3.2018(14)
Au(2)-C(11)	2.045(5)	Tl(1)-S(3)	3.0808(14)
Tl(1)-N(1)	2.724(4)		
C(1)-Au(1)-C(1)#1	180.0	Au(1)-Tl(1)-S(2)	167.17(2)
Tl(1)#1-Au(1)-Tl(1)	180.0	S(1)-Tl(1)-S(3)	109.70(3)
C(11)-Au(2)-C(11)#2	180.0		

Symmetry transformations used to generate equivalent atoms:

#1 -x+1,-y+1,-z;#2 -x+1,-y+1,-z+1

Table 2. Selected bond lengths [Å] and angles [°] for **2** 2THF.

Au(1)-Tl(1)	3.3853(5)	Tl(1)-N(2)	2.710(12)
Au(1)-C(1)	2.057(10)	Tl(1)-S(1)	3.110(5)
Au(2)-C(7)	2.041(12)	Tl(1)-S(2)	3.089(5)
Tl(1)-N(1)	2.709(11)		
C(1)#1-Au(1)-C(1)	180.0	Au(1)-Tl(1)-N(2)	158.6(3)
Tl(1)#1-Au(1)-Tl(1)	180.0	S(1)-Tl(1)-S(2)	114.11(12)
C(7)#2-Au(2)-C(7)	180.0		

Symmetry transformations used to generate equivalent atoms:

#1 -x+2,-y+2,-z+1 #2 -x,-y,-z

Table 3 Selected bond lengths [Å] and angles [°] for **3**.

Au(1)-Tl(1)	3.0221(4)	Tl(1)-N(1)	2.653(6)
Au(1)-C(1)	2.056(7)	Tl(1)-S(1)	3.2128(1)
Au(1)-C(7)	2.058(7)	Tl(1)-S(2)	3.1321(19)
Tl(1)-O(1)	3.1280(1)		
C(1)-Au(1)-C(7)	176.4(3)	N(1)-Tl(1)-Au(1)	76.43(12)
C(1)-Au(1)-Tl(1)	88.79(17)	N(1)-Tl(1)-S(2)	68.44(13)
C(7)-Au(1)-Tl(1)	88.75(17)	Au(1)-Tl(1)-S(2)	102.42(4)

The Tl-N bond distances are similar in the crystal structures of **1** and **2**·2THF, with values of 2.724(4) Å in **1** and 2.709(11) and 2.710(12) Å in **2**·2THF, and are intermediate between those described for the thallium(I) derivatives with cyclic N- or N,S-donor ligands [Tl(Me$_3$[9]aneN$_3$)]PF$_6$ (2.59(2)-2.63(1) Å) [126] or [Tl([9]aneN$_2$S)][ClO$_4$] (2.26(2)-2.68(2) Å)[127] and [Tl([18]aneN$_2$S$_4$)]PF$_6$ (2.834(4) and 2.992(4) Å)[128]. However, the Tl-N bond distance in **3** is smaller than those described for **1** and **2**·2THF.

Regarding the Tl-S bonds, in **1** there are two shorter (3.0807(14) and 3.0987(13) Å) and one longer (3.2018(14) Å) distances, the former two nearly equal to those found in **2**·2THF and **3** (3.089(5) and 3.110(5) Å for **2**·2THF; 3.1321(19) and 3.2128(1) for (**3**)), and to those reported for [Tl([9]aneS$_3$)]PF$_6$ (3.092(3)-3.114(3) Å)[129].These distances are in general shorter than in the related Au/Tl compounds with crown thioethers [{Au(C$_6$Cl$_5$)$_2$}$_2$Tl$_2$([24]aneS$_8$)]$_n$ (3.256(7)-3.587(7) Å), [{Au(C_6F_5)$_2$}$_2$Tl$_2$([24]aneS$_8$)] (3.201(2)-3.418(3) Å) and [{Au(C_6F_5)$_2$}Tl([9]aneS$_3$)]$_2$ (3.0246(17)-3.1154(19) Å)[120], as well as in the thallium derivatives [Tl([18]aneN$_2$S$_4$)]PF$_6$ (3.1299(13)-3.4778(15) Å)[128], [Tl([18]aneS$_6$)]PF$_6$ (3.164(5)-3.370(5) Å)[128]and [Tl([24]aneS$_8$)]PF$_6$ (3.2413(11)-3.4734(14) Å)[130]. Only in the case of [Tl([9]aneN$_2$S)][ClO$_4$], which also shows stronger Tl-N bonds, the Tl-S distances are shorter than in these three new complexes, showing values of 2.920(8) and 2.955(7) Å)[130].

Finally, an extended polymeric (**1**,**2**·2THF) or dimeric structures (**3**) are formed in the crystal lattices via weak intermolecular Tl···Cl contacts of 3.6998(13) Å in **1**, 3.6597(32) Å in **2**·2THF and of 3.6601(12) in **3** (see Figure 5). The main difference between both unidimensional polymers in the cases of **1** and **2**·2THF, and dimers in the case of **3**, is the relative position of the chlorine atoms of the aryl groups involved in these interactions: *ortho* in the structure of **1**, *para* in that of **2**·2THF and *meta* in the structure **3** (see Figure 5). Additionally, complex **1** also displays a couple of intramolecular Tl···Cl contacts of 3.4903(14) and 3.6257(14) Å.

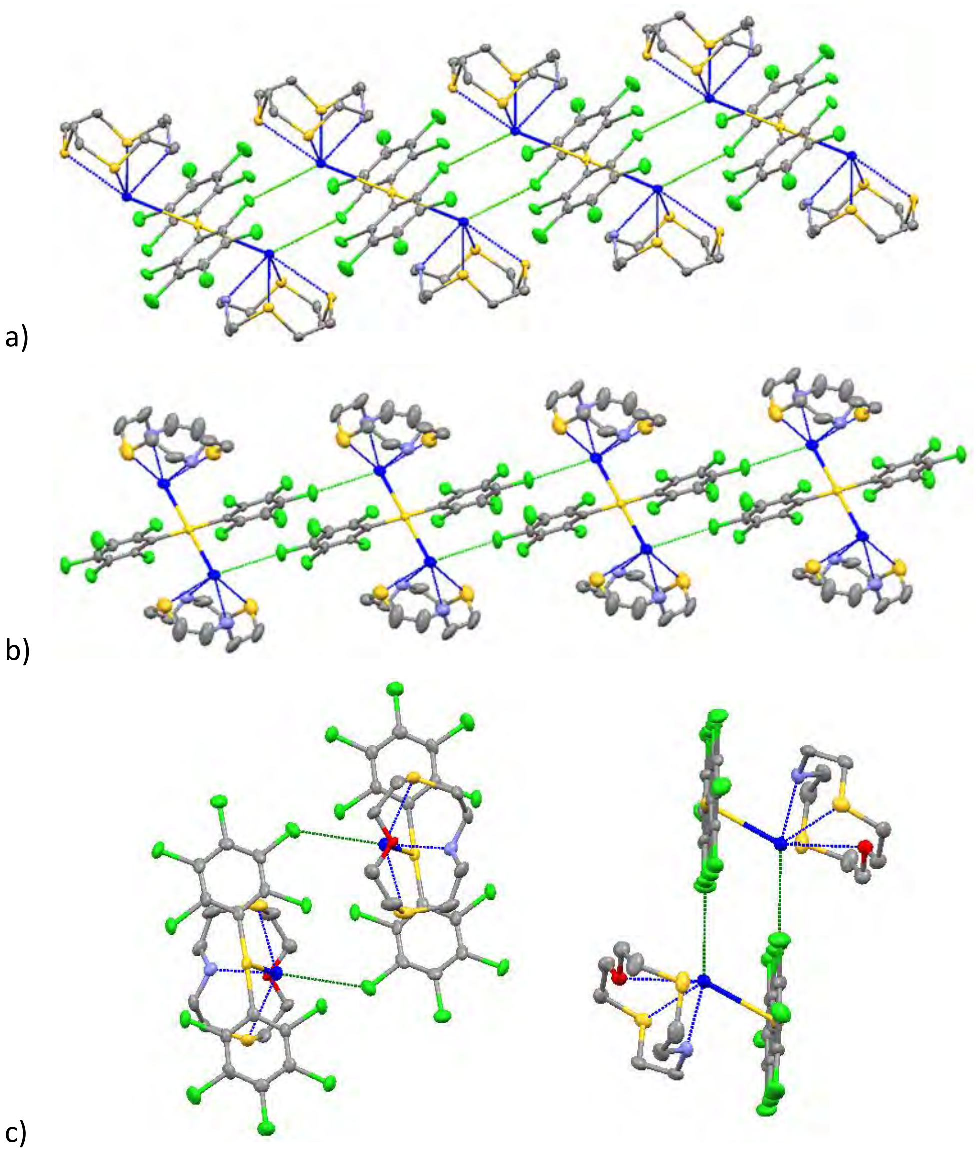

Figure 5. 1D polymeric structures of **1** (a), **2**·2THF (b) and **3** (c) formed via Tl···Cl interactions.

The substitution of the chlorine by fluorine atoms in the aryl groups bonded to gold(I) leads to significant differences in the crystal structures of the resulting complexes **4**-**6**. Thus, the structure of **4** and **6** consists of a tetranuclear neutral molecule with a central Au_2Tl_2 core (see Figure 6 and Tables 4 and 5), similar to the loosely bound butterfly clusters previously described by our research group for some Au(I)/Tl(I) complexes containing O-donor ligands [119],[131]. However, in complexes **4** and **6** the Au_2Tl_2 unit is planar and no Tl···Tl interaction is observed (Tl-Tl distance of 5.289 Å and 4.545 in **4** and **6** respectively), while the previously reported structures display a folded core with Tl···Tl contacts between 3.6027(6) Å in $[Au_2Tl_2(C_6Cl_5)_4]\cdot(Me_2CO)$[131] and 3.7152(4) Å in $[Au_2Tl_2(C_6Cl_5)_4]\cdot(acacH)$[119]. This disposition of the metals, together with the presence of bulkier ligands at the thallium(I) center, is probably the reason why the Au-Tl distances in the crystal structures of **4** and **6** (3.3171(4)-3.3816(4) Å;3.2576(6)) are also longer than in the cited compounds, in which the Au-Tl distances lie within the 3.0167(4)-3.2414(3) Å range. Furthermore, neither intra- nor inter-molecular aurophilic interactions are observed in **4** and **6**, where the minimum Au-Au distance is 4.111 Å(**4**)/4.668(**6**). The only difference found between the two structures is the disorder present at the oxygen atom and the nitrogen atom given the similar electronic density associated with the two respective atoms.

Table 4. Selected bond lengths [Å] and angles [°] for **4**.

Au(1)-Tl(1)	3.3170(4)	Tl(1)-N(1)	2.767(5)
Au(1)-Tl(1)#1	3.3815(4)	Tl(1)-S(1)	3.1644(15)
Au(1)-C(1)	2.061(5)	Tl(1)-S(2)	3.1569(16)
Au(1)-C(11)	2.055(5)	Tl(1)-S(3)	3.1686(15)
C(11)-Au(1)-C(1)	177.4(2)	S(1)-Tl(1)-S(3)	106.65(4)
Tl(1)-Au(1)-Tl(1)#1	104.27(2)	S(2)-Tl(1)-Au(1)	159.85(3)
Au(1)-Tl(1)-Au(1)#1	75.71(1)	N(1)-Tl(1)-Au(1)#1	171.25(10)

Symmetry transformations used to generate equivalent atoms:
#1 -x+1,y,-z+1/2

Table 5. Selected bond lengths [Å] and angles [°] for **6**.

Tl(1)-Au(1)	3.2576(6)	Tl(1)-O(1)	3.1388(4)
Tl(1)-Au(1)#2	3.2576(6)	Tl(1)-N(1)	2.780(17)
Au(1)-C(1)#3	2.077(10)	Tl(1)-N(1)#1	2.780(17)
Au(1)-C(1)	2.077(10)	Tl(1)-S(1)	3.3026(1)
C(1)#3-Au(1)-C(1)	176.8(6)	N(1)-Tl(1)-Au(1)	88.8(3)
N(1)-Tl(1)-Au(1)#2	168.5(2)	N(1)#1-Tl(1)-Au(1)	168.5(2)
N(1)#1-Tl(1)-Au(1)#2	88.8(3)		

Symmetry transformations used to generate equivalent atoms:

#1 -x+1,y,-z+1/2 #2 -x+1,-y+3/2,z #3 x,-y+3/2,-z+1/2

The gold atoms in the structures of **4** and **6** are again linearly coordinated to two aryl groups (C-Au-C = 177.3(2)° and 176.8(6)° in **4** and **6**, respectively), with typical Au-C bond lengths of 2.063(5) in **4**, 2.055(5) Å and 2.077(10) in **6**.

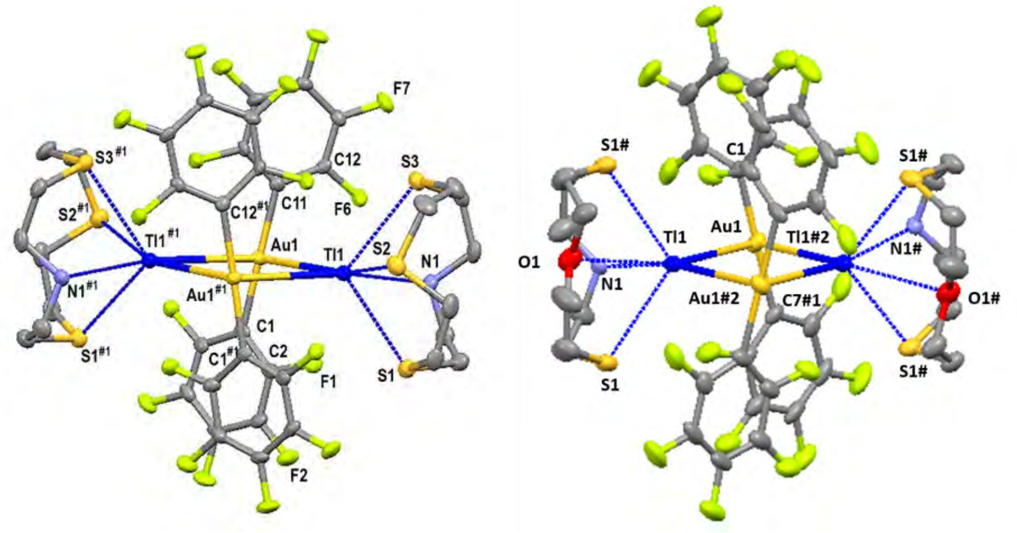

Figure 6. Molecular structure of compounds **4** (left) and **6** (right) with the labelling scheme adopted for the atom positions. Hydrogen atoms are omitted for clarity and ellipsoids are drawn at the 30% level. #1 –x+1,y,–z+1/2.

As observed in Figure 6, the thallium atoms are coordinated by the four donor atoms of the [12]aneNS_3 (**4**) or [12]aneNS_2O (**6**) crown ligand and also interact with both gold centres, which results in a distorted octahedral environment for each thallium(I), and makes the lone pair of thallium stereochemically non active. The Tl-N distances of 2.767(5)-2.780(17) Å are shorter than in **1** and **2**·2THF, and are also intermediate between those found in [Tl(Me_3[9]aneN_3)]PF_6 (2.59(2)-2.63(1) Å)[126] or [Tl([9]aneN_2S)][ClO_4] (2.26(2)-2.68(2) Å)[127] and [Tl([18]aneN_2S_4)]PF_6 (2.834(4) and 2.992(4) Å)[128]. The Tl-S distances in **4** and **6** (between 3.1569(16) and 3.1686(15) Å in **4;** 3.2026(1) in **6**) are also in general longer than in **1** (3.0808(14)-3.2018(14) Å), **2**·2THF (3.089(5) and 3.110(5) Å) and [{Au(C_6F_5)$_2$}Tl([9]aneS_3)]$_2$ (3.0246(17)-3.1154(19) Å)[120], but shorter than in the related Au(I)/Tl(I) complexes [{Au(C_6Cl_5)$_2$}$_2$Tl$_2$([24]aneS_8)]$_n$ (3.256(7)-3.587(7) Å) and [{Au(C_6F_5)$_2$}$_2$Tl$_2$([24]aneS_8)] (3.201(2)-3.418(3) Å)[120].

Finally, we were also able to grow single crystals for **5**, but the low quality of these crystals, as well as the high degree of disorder found in the ligand [12]aneN_2S_2 (**L₂**), did not allow us to determine bond lengths and angles with the adequate accuracy, although a rough description of the structure can be done, and the absence of intermetallic interactions in this case can be definitively confirmed. The crystal structure of **5** can be described as a polymeric chain of alternating [Au(C_6F_5)$_2$]$^-$ and

$[Tl([12]aneN_2S_2)]^+$ units, in which the sulphur atoms of the N,S-mixed-donor crown ether $\mathbf{L_2}$ as well as the fluorine atoms in the ortho position of the pentafluoriphenyl rings act as bridges (Figure 7 and Table 6). This disposition avoids the formation of Au···Tl interactions (Au-Tl = 4.080 Å), which are present in the crystal structures of **1**, **2**·2THF, **3**, **4** and **6**.

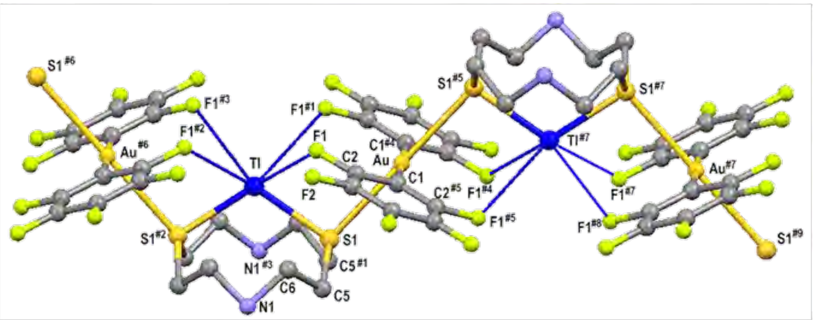

Figure 7. Schematic representation of the 1D polymeric structure of **5.**

Table 6. Selected bond lengths [Å] and angles [°] for **5**.

Au(1)-C(1)#1	2.02(5)	Tl(1)-N(1)	2.74(5)
Au(1)-C(1)	2.02(5)	Tl(1)-N(2)	2.76(6)
Au(2)-C(7)#2	2.02(4)	Tl(1)-S(1)	3.09(2)
Au(2)-C(7)	2.02(4)	Tl(1)-S(2)	3.11(2)
C(1)#1-Au(1)-C(1)	180(2)	N(1)-Tl(1)-N(2)	85.8(17)
C(7)#2-Au(2)-C(7)	180.000(5)	N(1)-Tl(1)-S(1)	65.8(11)
N(2)-Tl(1)-S(1)	66.2(12)	N(1)-Tl(1)-S(2)	66.9(12)
S(1)-Tl(1)-S(2)	113.4(5)	N(2)-Tl(1)-S(2)	66.1(12)

Symmetry transformations used to generate equivalent atoms:

#1 -x,-y,-z #2 -x,-y,-z+1

2.2.3 Photophysical Properties

The absorption spectra of complexes **1**-**3** show similar features to those described for other related gold(I)–thallium(I) derivatives previously reported[120]. All complexes display two intense absorptions bands at about 230 and 350 nm in THF solutions; these bands are also present in the spectra of the heterometallic precursor $[\{Au(C_6Cl_5)_2\}Tl]_n$ and in the gold(I) complex $NBu_4[Au(C_6Cl_5)_2]$ (see Figure 8). Therefore, it is likely that the band at high energy arises from transitions between π orbitals of the perhalophenyl groups, while the transitions in the low energy region probably involve orbitals of the gold centres. Thus, these absorptions could be assigned to π→π* and Au→π* transitions in the $[Au(C_6Cl_5)_2]^-$ fragments, respectively. At this regard, similar assignments have been done for related gold(I) complexes with aromatic substituents [132],[133]; nevertheless, in the case of the high-energy absorption the possibility of an n→σ* transition in the N,S,O-mixed-donor ligands cannot be ruled out, since these ligands show an absorption at 234 nm of less intensity at similar concentrations.

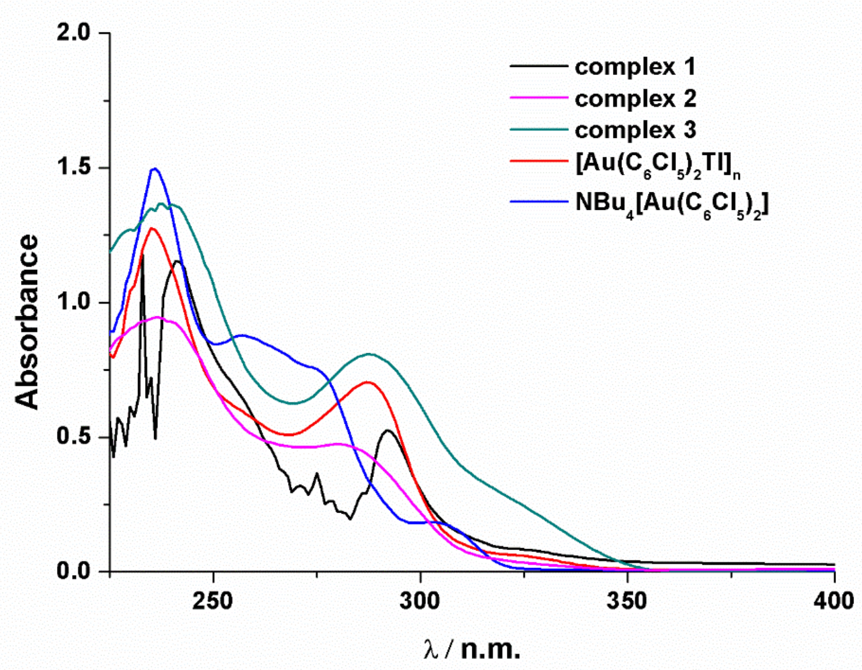

Figure 8. Absorption spectra of complex **1**-**3** and the gold precursors $NBu_4[Au(C_6Cl_5)_2]$ and $[\{Au(C_6Cl_5)_2\}Tl]_n$ in THF solution ($C \approx 2.5x10^{-5}$ M).

In the case of the pentafluorophenyl derivatives **4**-**6**, the spectra show different profiles as they also display differences in their structures (see X-ray structures discussion). In all cases, the absorptions observed for the precursors $[Au(C_6F_5)_2Tl]_n$ and $NBu_4[Au(C_6F_5)_2]$ appear in the spectra, and the assignations can be the same as those reported for the compounds **1**-**3**. In addition, a well-defined absorption at 278 nm for complex **4** or a lower energy tail in complex **6** are likely to be due to transitions in which orbitals of the metal centres are important (see Figure 9).

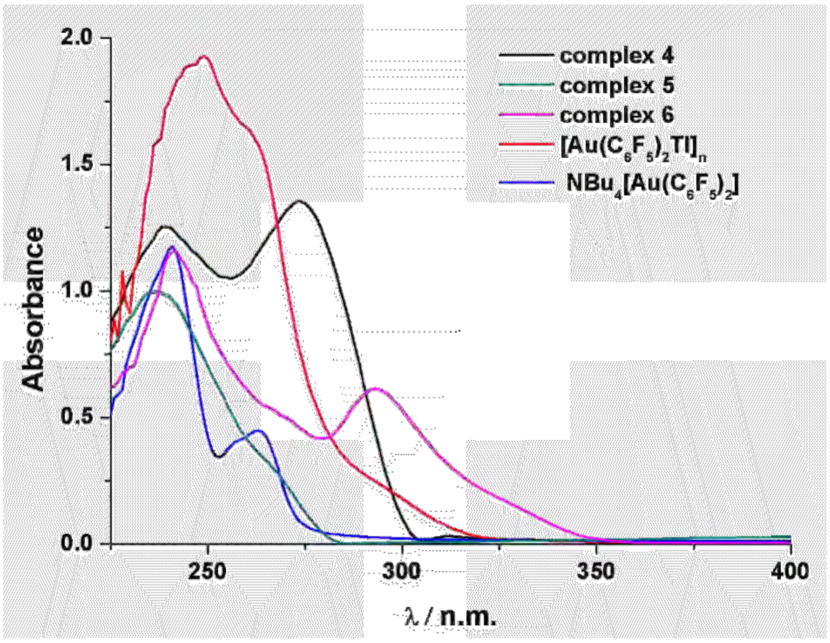

Figure 9. Absorption spectra of complex **4**-**6** and the gold precursors $NBu_4[Au(C_6F_5)_2]$ and $[\{Au(C_6F_5)_2\}Tl]_n$ in THF solution ($C \approx 2.5x10^{-5}$ M).

Analogously to other compounds featuring heterometallic interactions, also complexes **1-4** and **6** are strongly luminescent in the solid state; nevertheless, complex **5** in which the intermetallic interactions are absent does not show any emission, confirming the importance of these interactions in the optical behaviours of this type of compounds. Thus, they display emissions in solid state between 495 and 512 nm at room temperature, and between 475 and 500 nm when the measurements are carried out at the liquid nitrogen temperature (77 K) (see Figure 10 and Table 7). The different energies seem to be related to the different structures of the complexes in the solid state, which depend, among other factors, on the N,S,O-mixed-donor ligand and the perhalophenyl groups bonded to the gold centre, and no sign of a unique dependence on the Au-Tl distances results evident. While complex **2**, with the longest Au-Tl distance (3.3853(5) Å), displays the emission at the lowest energy, complex **1**, with the shortest intermetallic distance (3.2411(2) Å), shows the highest emission energy; the same behaviour can be observed for the complexes **4** and **6**: complex **4**, with two different Au-Tl distances (3.3171(4) and 3.3816(4) Å), displays the emission at energy lower than that of complex **6** featuring a shorter Au-Tl distance (3.2576(6) Å). Totally different is the behaviour observed for the complex **3** where, despite the distance thallium(I)-gold(I) is extremely short (3.0221(4) Å) an emission value comparable to that of the complexes **1**-**2** and **4** is observed.

At this regard, in complexes featuring gold(I)-thallium(I) interactions whose emissions are metal centred, it is generally expected that the shorter the intermetallic interactions the longer the wavelength of the luminescent emission[134].

It is also curious that in the case of complex **3** the emission at 77 K leads to a lower energy emission, but no bathochromic shift is observed in the case of complex **2**. The absence of the expected bathochromic shift, usually observed in complexes whose emissions arise mostly from metal-centred transitions, can been related to a rigidochromic effect arising from the rigidity of their structures [84],[121],[135],[136]. Nevertheless, the contribution from orbitals of the interacting metal centres in the transitions responsible for the optical behaviour results evident, since none of the complexes show luminescence in solution. This result is likely to be related to the rupture of the metal–metal interactions promoted by the solvent (see molar conductivity values in the Experimental section).

Thus, taking into account the previous comments, we can propose that the presence of intermetallic interactions in the solid state, as well as their number and strength, seem to be the key to explain the luminescence of these complexes. Nevertheless, another factor that should be considered is the disposition of these metal centres in the crystal structures, which is determined by the electronic characteristics and the number and type of the donor centres of the thioether-crown ligands.

Table 7. Photophysical properties of complexes **1**-**6**

	UV-vis in THF (nm)	Solid (RT) em(exc)	Solid (77K) em (exc)	τ (ns)	Φ (%)
Complex 1	241 (ε = 38333) 292 (ε = 17000)	495 (395)	513 (395)	434 ± 3	2.5
Complex 2	236 (ε = 33333) 284 (ε = 14851)	500 (368)	500 (358)	273 ± 8	5.2
Complex 3	240 (ε = 30333) 287 (ε = 13851)	501(389)	513 (365)	482 ± 21	7
Complex 4	240 (ε = 64545) 278 (ε = 60454)	493 (340)	472 (340)	633 ± 13	5.8
Complex 5	241 (ε = 31004) 260 (ε = 11790)	---	---	---	---
Complex 6	243 (ε = 62545) 290 (ε = 30454)	467 (371)	474 (371)	490 ± 22	6.2

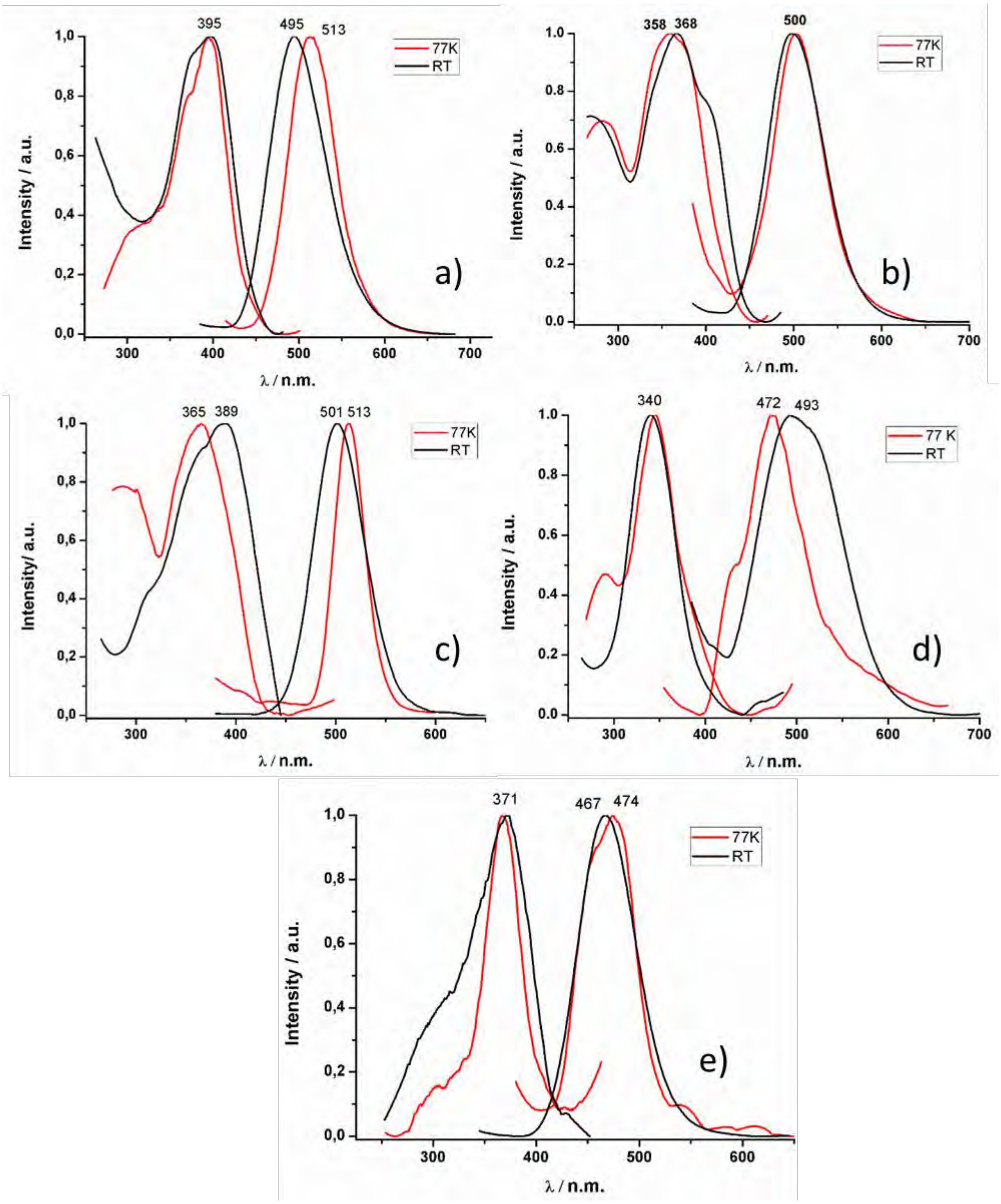

Fig. 10. Excitation and emission spectra for complexes **1**(a), **2**(b), **3**(c)**, 4**(d) and **6**(e) in the solid state at RT and 77 K.

2.2.4 Computational Study

The assignment of the origin of the luminescence and the justification of the similar emission energies, despite the different structural arrangements found in solid state, is not straightforward. Consequently, additional tools are needed and, for this reason, we carried out Density Functional Theory (DFT) and Time-Dependent Density Functional Theory (TD-DFT) calculations on model systems **1a**, **3a** and **4a** of complexes **1**, **3** and **4**, respectively (see Figure 11). These model systems permit to compare several parameters that can influence the photophysical properties, such as the different $C_6Cl_5^-$ or $C_6F_5^-$ perhalophenyl groups bonded to gold(I), the different nuclearity (binuclear, trinuclear or tetranuclear complexes), the different metallic arrangements or the different ligands (see Figure 11).

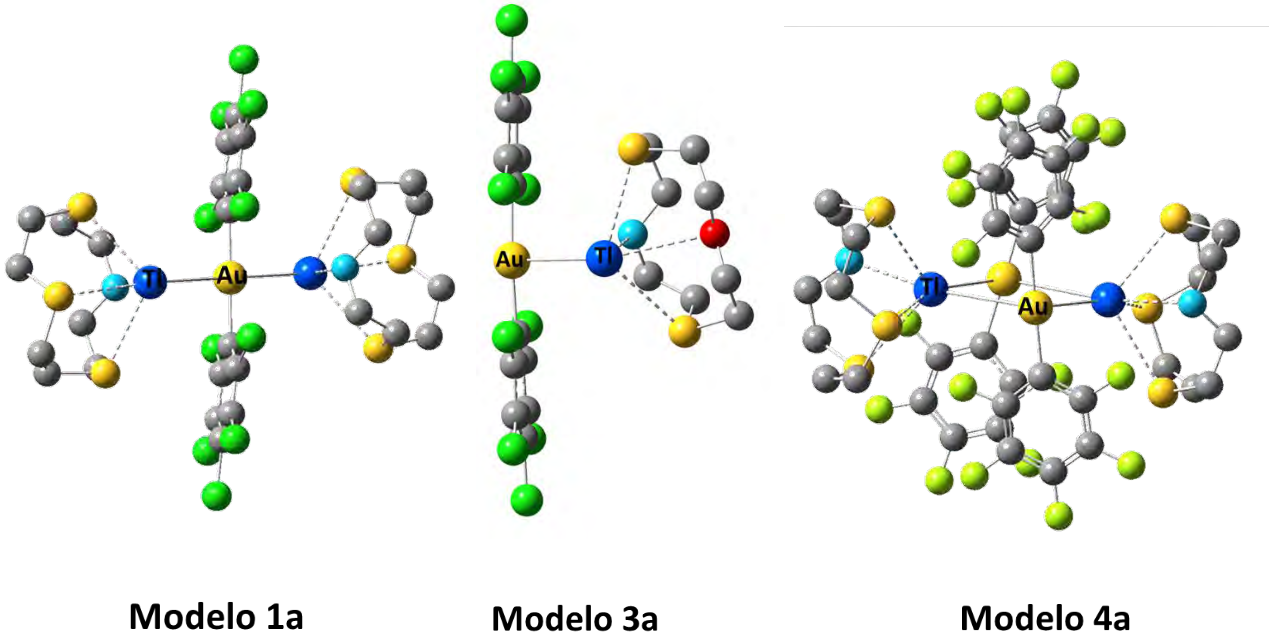

Figure 11. Theoretical model systems $[\{Au(C_6Cl_5)_2\}\{Tl([12]aneNS_3)\}_2]^+$ (**1a**), $[\{Au(C_6Cl_5)_2\}\{Tl([12]aneNS_2O)\}]$(**3a**) and $[\{Au(C_6F_5)\}Tl([12]aneNS_3)]_2$(**4a**).

Thus, model **1a** corresponds to the trinuclear cation found for complex **1**, representing the Au(I)···Tl(I) interactions between one $[Au(C_6Cl_5)_2]^-$ anionic fragment and two cationic $[Tl([12]aneNS_3)]^+$ ones. At the same time, model **3a** corresponds to the binuclear neutral system found for complex **3** which represents the Au(I)···Tl(I) interactions between one $[Au(C_6Cl_5)_2]^-$ anionic fragment and one $[Tl([12]aneNS_2O)]^+$ complex cation.

Finally, model **4a** corresponds to the Au(I)···Tl(I) interaction between two $[Au(C_6F_5)_2]^-$ anionic fragments and two $[Tl([12]aneNS_3)]^+$ complex cations, leading to a square-like tetranuclear arrangement of the metals. We first computed the electronic structures for models **1a**, **3a** and **4a** at DFT level of theory. Figure 12 and Table 8-10 display the most important frontier molecular orbitals (MOs) and the population analysis of those MOs, respectively. From these data we can anticipate the contribution of each part of the molecule to the frontier molecular orbitals.

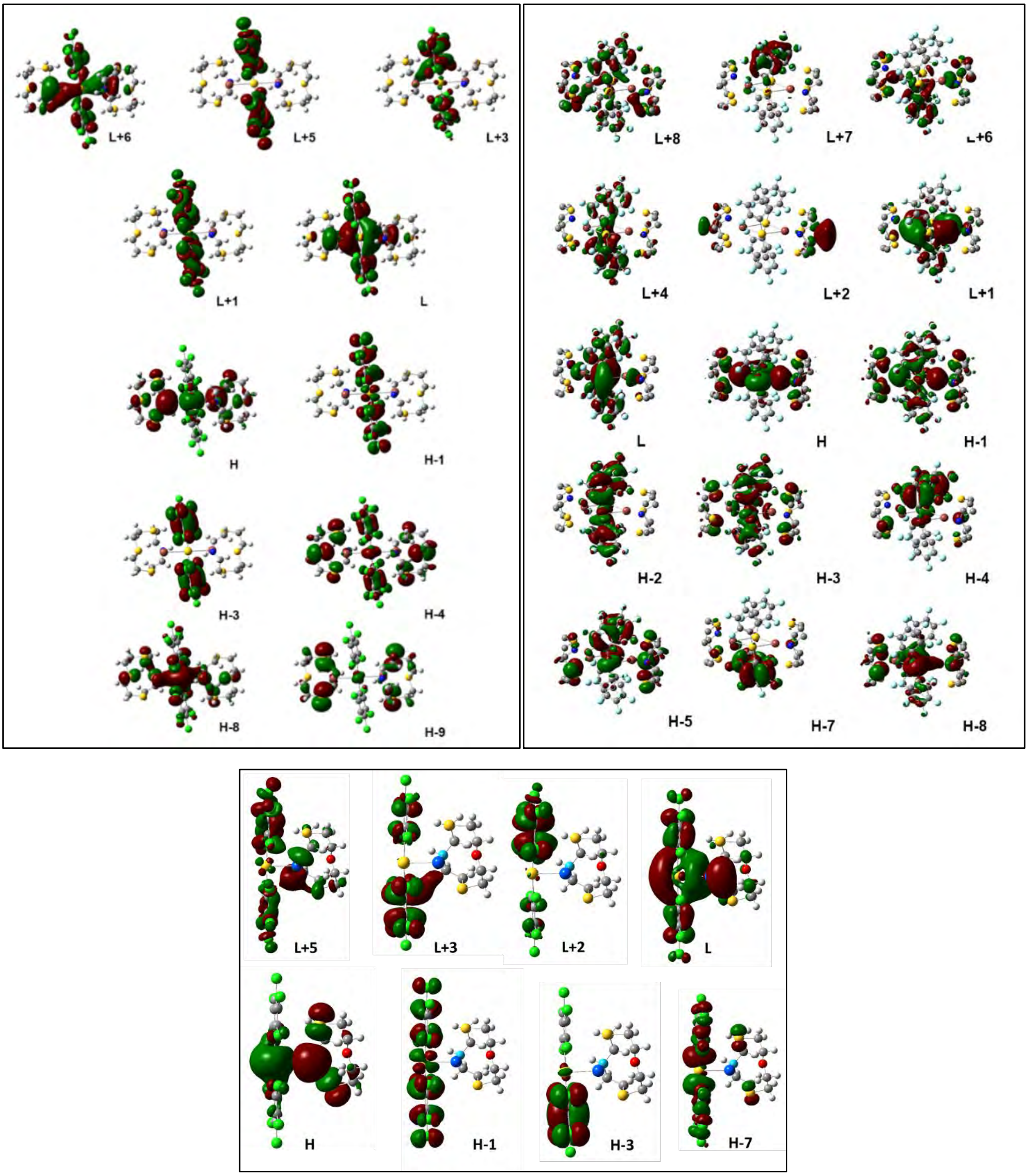

Figure 12. Frontier molecular orbitals (isovalue = 0.02) for model systems **1a** (left), **4a** (right) and **3a**(below). (L=LUMO; H=HOMO)

In the case of the trinuclear or binuclear cationic complexes $[\{Au(C_6Cl_5)_2\}\{Tl([12]aneNS_3)\}_2]^+$ **1a** and $[\{Au(C_6Cl_5)_2\}\{Tl([12]aneNS_2O)\}]$ **3a** the highest occupied molecular orbital (HOMO) and the lowest empty molecular orbital (LUMO) are mainly localized at the metal centres Au(I) and Tl(I). For complex **1a**, the rest of occupied and empty frontier molecular orbitals from HOMO-1 to HOMO-9 and from LUMO+1 to LUMO+6 are mostly located at the $[12]aneNS_3$ and $C_6Cl_5^-$ ligands, being the contribution of the pentachlorophenyl groups important in the lower empty orbitals from LUMO+1 to LUMO+6. A similar behaviour can be observed for complex **3a**: also in this case the full orbitals as well as the empty orbitals are mainly localized on the $C_6Cl_5^-$ aryl fraction and on the organic ligand (from HOMO-1 to HOMO-7; from LUMO+1 to LUMO+5) with the exception of some orbitals where the metal centers give an important contribution (LUMO+4, LUMO+5). Model $[\{Au(C_6F_5)\}\{Tl([12]aneNS_3)\}]_2$ **4a** shows common features with the previous model but also some differences. Both the HOMO and LUMO orbitals are, again, mainly located at the metal centres. Lower energy occupied orbitals display a mixed metal/ligand character with a higher contribution from both $[12]aneNS_3$ and C_6F_5- ligands. In contrast to model **1a** and **3a**, the higher empty MOs from LUMO+1 to LUMO+8 display a predominant Au-Tl character for model system **4a**.

Table 8. Population analysis (%) for model system **1a**.

Model	**Orbital**	**L**	**Au**	**Tl**	**C_6X_5**
1a	L+6	8	31	41	19
	L+5	1.2	21	9	68
	L+4	6	18	14	61
	L+3	2	9	10	78
	L+2	2	5	8	84
	L+1	1	17	18	64
	LUMO	6	22	51	21
	HOMO	30	20	42	7
	H-1	2	14	2	81
	H-2	60	1	35	3
	H-3	1	2	7	90
	H-4	58	9	19	14
	H-5	28	7	4	60
	H-6	55	5	32	7
	H-7	15	5	13	67
	H-8	27	38	9	25
	H-9	89	5	4	3

Table 9. Population analysis (%) for model system **3a.**

Model	**Orbital**	**L**	**Au**	**Tl**	**C_6X_5**
3a	L+5	5	19	56	20
	L+4	5	36	48	11
	L+3	3	3	8	87
	L+2	4	5	10	81
	L+1	2	29	14	55
	LUMO	7	22	44	26
	HOMO	27	33	29	11
	H-1	1	18	1	80
	H-2	0	6	2	92
	H-3	2	2	1	94
	H-4	30	24	9	37
	H-5	16	22	7	55
	H-6	86	2	6	6
	H-7	8	17	1	74

Table 10. Population analysis (%) for model system **4a.**

Model	**Orbital**	**L**	**Au**	**Tl**	**C_6X_5**
4a	L+8	3	60	34	3
	L+7	5	39	47	8
	L+6	4	68	24	4
	L+5	4	50	42	5
	L+4	15	35	35	15
	L+3	6	16	77	0
	L+2	4	4	92	0
	L+1	15	27	34	23
	LUMO	7	47	28	17
	HOMO	25	24	46	5
	H-1	18	13	37	32
	H-2	18	16	25	40
	H-3	41	11	21	26
	H-4	5	6	6	83
	H-5	30	24	8	37
	H-6	43	7	9	41
	H-7	50	30	10	10
	H-8	2	11	1	86

The first 20 singlet−singlet excitations were computed for all model systems at the TD-DFT level of theory as described in the Computational Details section and compared with the experimental excitation spectra for complexes **1**, **3** and **4**. Since the lifetimes for these complexes lie in the microseconds range and they display large Stokes shifts, suggesting phosphorescent processes, we also computed the lowest singlet−triplet excitation at TD-DFT level for model systems **1a**, **3a** and **4a**. The results including the most important excitations are depicted in Table 11 and Figure 13.

Table 11. TD-DFT first Singlet-Singlet Excitation Calculations and Lowest Singlet-Triplet Excitations for Model Systems **1a**, **3a** and **4a**.

Model	exc.	λ_{calc} (nm)	f (s)	contributions
1a	$S_0 \rightarrow S_1$:	321	0.4016	HOMO → LUMO (98)
	$S_0 \rightarrow S_2$:	286	0.2550	HOMO-1 → LUMO (96)
	$S_0 \rightarrow S_3$:	277	0.0189	HOMO-5 → LUMO (50) HOMO-4 → LUMO (25)
	$S_0 \rightarrow S_4$:	268	0.0164	HOMO-8 → LUMO (17) HOMO-5 → LUMO (24) HOMO-4 → LUMO (53)
	$S_0 \rightarrow S_5$:	257	0.0546	HOMO-8 → LUMO (68)
	$S_0 \rightarrow S_6$:	255	0.0109	HOMO-3 → LUMO+1 (60)
	$S_0 \rightarrow S_7$:	246	0.0800	HOMO → LUMO+5 (22) HOMO → LUMO+6 (47)
	$S_0 \rightarrow S_8$:	243	0.0270	HOMO(-9) → LUMO (23) HOMO-2 → LUMO+1 (37)
	$S_0 \rightarrow T_1$:	413		HOMO-3 → LUMO+3 (15) HOMO-1 → LUMO (34)
3a	$S_0 \rightarrow S_1$:	310	0.1441	HOMO →LUMO (48)
	$S_0 \rightarrow S_2$:	292	0.2667	HOMO-1 →LUMO (48)
	$S_0 \rightarrow S_3$:	265	0.0113	HOMO →LUMO+2 (34)
	$S_0 \rightarrow S_8$:	264	0.0132	HOMO-1 →LUMO+1 (27)
	$S_0 \rightarrow S_{12}$:	254	0.0208	HOMO →LUMO+5 (12)
	$S_0 \rightarrow S_{16}$:	248	0.0140	HOMO-1 →LUMO+3 (12)
	$S_0 \rightarrow S_{18}$:	244	0.0144	HOMO-7 →LUMO (19)
	$S_0 \rightarrow T_1$	363	0.0000	HOMO-2→LUMO+3 (15) HOMO-1→LUMO (13)
4a	$S_0 \rightarrow S_1$	271	0.0363	HOMO → LUMO+2 (93)
	$S_0 \rightarrow S_2$	268	0.1132	HOMO-1 → LUMO (23) HOMO → LUMO+4 (54)
	$S_0 \rightarrow S_3$	265	0.0331	HOMO-1 → LUMO (71) HOMO → LUMO+4 (15)
	$S_0 \rightarrow S_4$	259	0.1272	HOMO → LUMO+6 (43) HOMO → LUMO+8 (40)
	$S_0 \rightarrow S_5$	257	0.0892	HOMO-2 → LUMO (68) HOMO → LUMO+7 (13)
	$S_0 \rightarrow S_6$	255	0.0142	HOMO-3 → LUMO (29) HOMO-1 → LUMO+1 (35) HOMO → LUMO+8 (14)
	$S_0 \rightarrow S_7$	254	0.0796	HOMO-3 → LUMO (17) HOMO-1 → LUMO+1 (16) HOMO → LUMO+7 (36)
	$S_0 \rightarrow S_8$	251	0.0341	HOMO-4 → LUMO (56) HOMO-3 → LUMO (12)
	$S_0 \rightarrow S_9$	250	0.0615	HOMO-8 → LUMO (15) HOMO-5 → LUMO (51)
	$S_0 \rightarrow S_{10}$	248	0.0112	HOMO-2 → LUMO+1 (86)
	$S_0 \rightarrow S_{11}$	245	0.0111	HOMO-7 → LUMO (51)
	$S_0 \rightarrow T_1$	363	0,0000	HOMO-2 → LUMO (17)

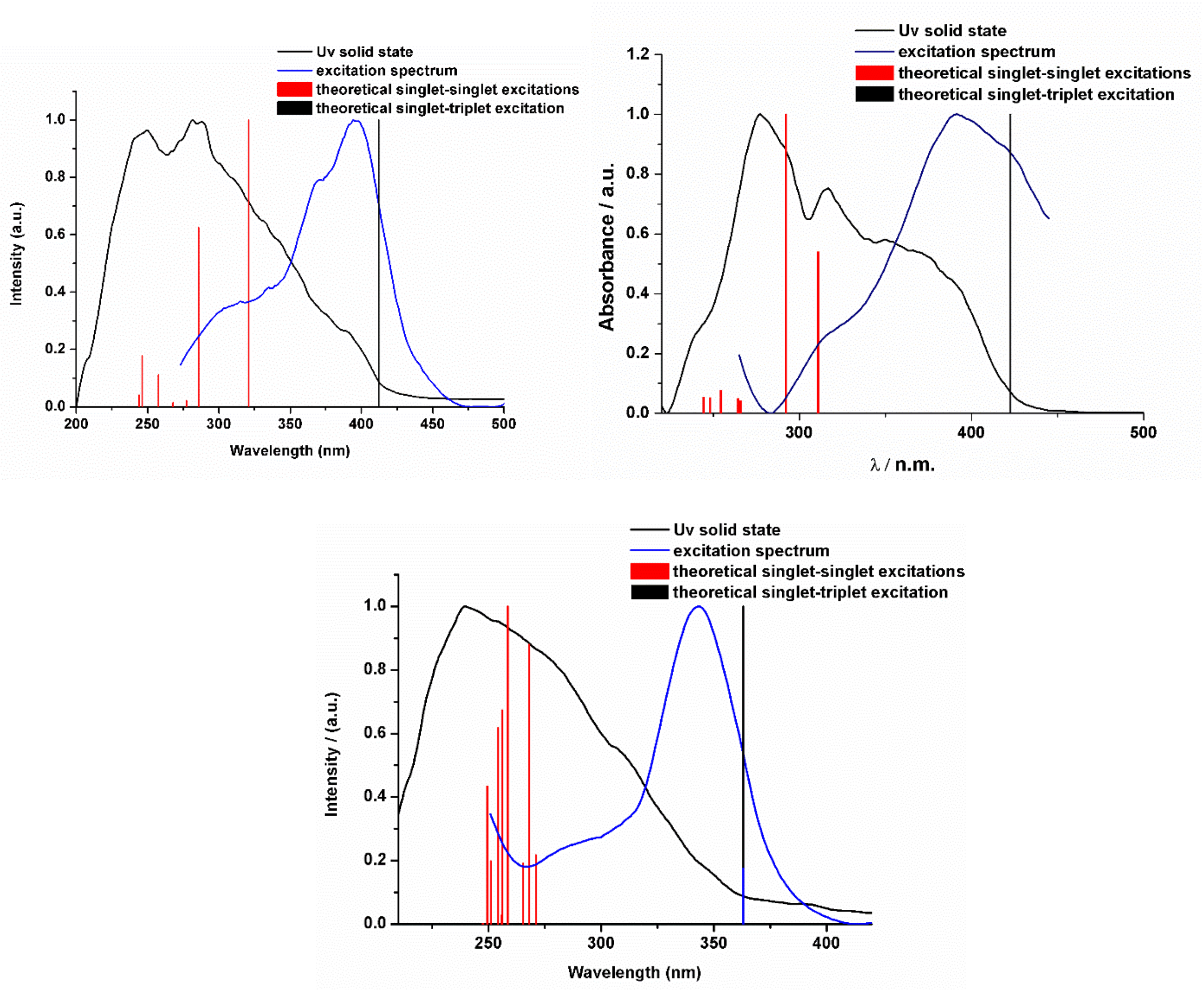

Figure 13. Experimental UV-Vis solid state absorption spectrum (black line), Experimental excitation solid stat (blue line) and TD-DFT singlet–singlet (red bars) and singlet triplet excitation/s (blue bar) for model systems **1a** (left),**3a** (right) and **4a** (below).

The most intense TD-DFT singlet–singlet excitations for model [Au(C_6Cl_5)$_2$Tl([12]aneNS$_3$)] (**1a**) appear between 243 and 320 nm, whereas the lowest singlet–triplet excitation appears at 413 nm. These values are in agreement with the experimental excitation spectrum for complex **1** for the singlet-triplet transition, which shows a maximum at 400 nm and with the UV-Vis absorption spectrum in solid state for the allowed singlet-singlet transitions. If we analyse the TD-DFT results for model **1a** we can observe that the main contribution of the most intense computed singlet-singlet electronic transition at 321 nm arises from a HOMO-LUMO transition. From the population analysis results (Table 8), this excitation can be attributed to a metal-centred transition between the interacting Au-Tl centres with a small charge transfer contribution from the [12]aneNS$_3$ ligand to the $C_6Cl_5^-$ one. Other intense singlet-singlet excitations at higher energy (between 286 to 257 nm) consist of transitions between ligand-based orbitals (HOMO-1, HOMO-4, HOMO-5 and HOMO-8) to the metal-based LUMO orbital. The highest energy singlet-singlet transitions (between 255 to 243 nm) display a mixed character with predominant ligand contributions. The lowest computed singlet-triplet excitation is mainly due to a HOMO-1-LUMO transition, which can be related to the phosphorescent process found experimentally and attributed to a charge transfer from the $[Au(C_6Cl_5)_2]^-$ unit to the interacting Au-Tl metal centres.

The most intense TD-DFT singlet–singlet excitations for model $[Au(C_6Cl_5)_2Tl([12]aneNS_2O)]$ **3a** appear between 244 and 310 nm, whereas the lowest singlet–triplet excitation appears at 422 nm. These values are in agreement with the experimental excitation spectrum for complex **3** for the singlet-triplet transition, which shows a maximum at 389 nm and with the UV-Vis absorption spectrum in solid state for the allowed singlet-singlet transitions. The analyse of TD-DFT results for model **3a** show that the main contribution of the most intense computed singlet-singlet electronic transition at 292 nm arises from a HOMO-1-LUMO transition. From the population analysis results (see Table 11), this excitation can be attributed to a transition between the aromatic fraction and the metal centers. Other intense singlet-singlet excitations at lower energy (310 nm) can be attributed to a metal-centred transition between the interacting Au-Tl centres with a small charge transfer contribution from the $[12]aneN_2SO$ ligand to the C_6Cl_5- one. The highest energy singlet-singlet transitions (between 265 to 244 nm) display a mixed character between different part of the molecule. In spite of the low contribution of the involucrate molecular orbitals, also in this case the triplet singlet transition seems to be due to an electronic transfer process which mainly involves the metal centers (HOMO-1-LUMO).

Model $[\{Au(C_6F_5)\}Tl([12]aneNS_3)]_2$ (**4a**) displays the most intense TD-DFT computed singlet–singlet excitations between 245 and 271 nm, whereas the lowest singlet–triplet excitation appears at 363 nm. These values are in fairly good agreement with the experimental absorption spectrum in solid state, which shows a maximum at 240 nm and a low-energy shoulder at ca. 326 nm for the singlet-singlet transitions and with the excitation spectrum that shows a maximum at 345 nm. The main contribution of the most intense singlet-singlet electronic excitation computed at 259 nm is due to two transitions between HOMO-LUMO+6 and HOMO-LUMO+8. Taking into account the character of these orbitals, this transition can be attributed to a metal-centred transition between the interacting Au-Tl centres with a small charge transfer contribution from the $[12]aneNS_3$ ligand to the metals. Other intense singlet-singlet excitations at lower energy (between 271 to 265 nm) take place between metal-based orbital (HOMO) or mixed orbital (HOMO-1) to the metal-based LUMO and LUMO+4 orbitals. The highest energy singlet-singlet excitations (between 256 to 245 nm) can be mainly attributed to arise from charge transfer transitions between mixed ligand-metal or ligand based orbitals (HOMO-1 to HOMO-7) and metal-based orbitals (LUMO and LUMO+7). Finally, the computed lowest singlet-triplet excitation, which is responsible for the phosphorescent character of the emission for complex **4**, is mainly due to a HOMO-2-LUMO transition. Taking into account the character of these orbitals this transition can be attributed to a metal-centred transition between the interacting Au-Tl centres with a minor charge transfer contribution from the [12]aneNS$_3$ and C$_6$F$_5$- ligands to the metals. Figure 14 shows the electronic density of the molecular orbitals in the triplet-singlet transitions for all models.

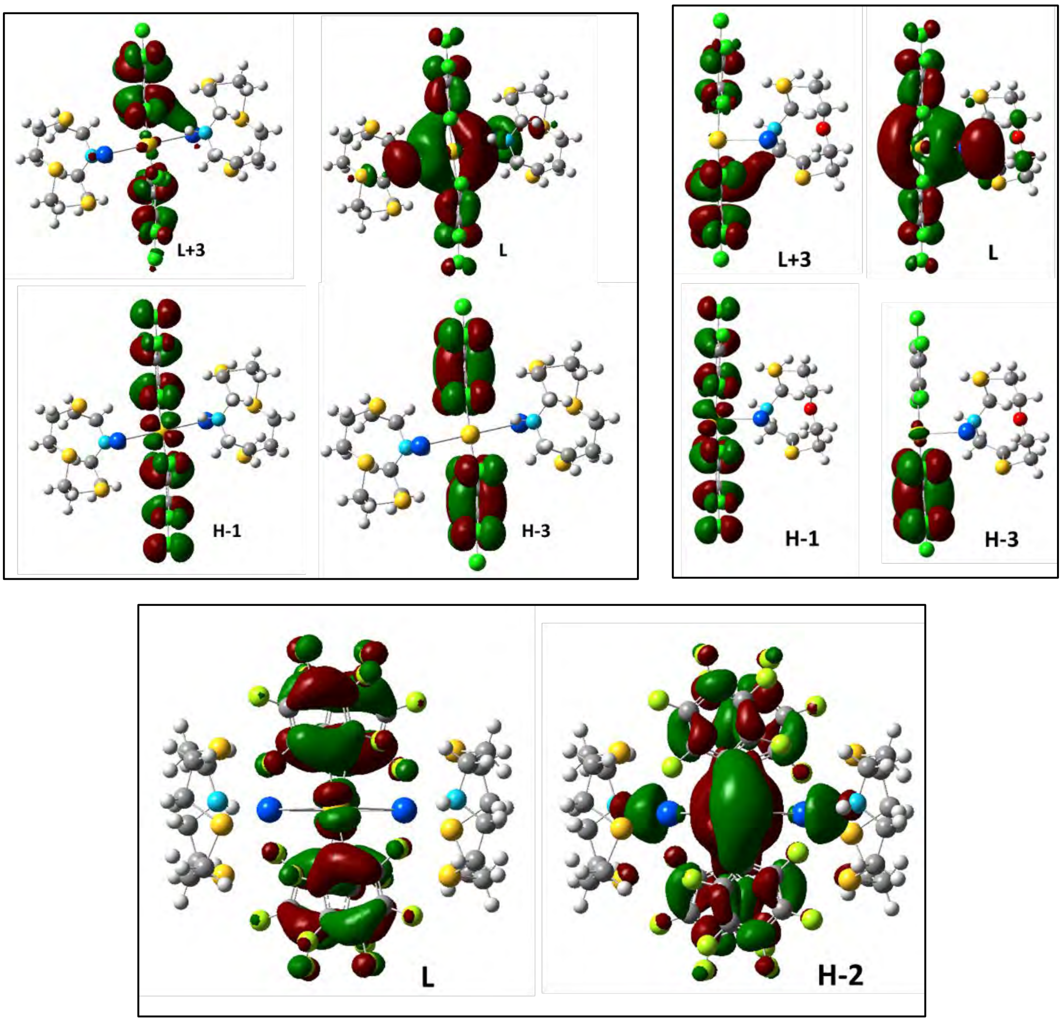

Figure 14. Most important frontier molecular orbitals (isovalue = 0.02) for model system **1a**, **3a** and **4a** involved in the singlet-triplet transitions. (L=LUMO; H=HOMO).

In order to assign the origin of the emission found experimentally for complexes **1**, **3** and **4,** we computed the optimization of the ground state (S_0) and the lowest triplet excited state (T_1) from which the phosphorescent emission takes place, for model systems **1a**, **3a** and **4a**

This type of theoretical approach allows us to analyse the most important molecular distortions of the models when changing from the ground to the lowest triplet excited state, that can be related to the part of the molecules involved in the phosphorescent properties. In a second step, we can also analyse the shape of the frontier orbitals for the S_0 and T_1 structures, that would confirm the parts of the molecule involved in the electronic transition (SOMO-SOMO-1) responsible for the phosphorescent behaviour of these systems.

Regarding the structural distortions, Figure 15-16 and Table 12 display the most important optimized distances for models **1b**, **3b** and **4b** in the ground state S_0 and T_1 excited state. First of all, it is worth mentioning that the optimized structures in the S_0 state for models **1b** and **3b** agree well with the experimental X-ray diffraction data as it can be observed from the intermetallic Au-Tl distances, metal-ligand bonds and internal C-C, N-C and S-C distances. If we analyse the main distortion of model systems **1b** and **3b** in the T_1 excited state, there is a clear shortening of the intermetallic Au(I)-Tl(I) distances ranging from 3.189-3.202 Å (S_0) to 2.832 Å (T_1) for model **1b**; from 2.994 Å (S_0) to 2.704 Å (T_1) for the model system **3b**; and, finally, from 3.249-3.407 Å (S_0) to 2.891-3.016 Å (T_1) in the case of model **4b**, leading to intermetallic distance contractions of ca. 11% for all model systems. These intermetallic distance shortenings suggest a main role of the closed shell Au···Tl interaction in the phosphorescent properties of the complexes. A secondary distortion found for both model systems when going from the S_0 to the T_1 excited state is a slight decrease of the Tl-N and Tl-S distances, which suggests a minor role of the ligand in the emissive behaviour of complexes **1**, **3** and **4**.

Table 12. Selected structural parameters for complexes **1**, **3** and **4** and the corresponding model in the ground (S_0) and the lowest triplet excited state (T_1), at DFT level of theory. Distances are in angstroms (Å); angles and dihedral angles in deg (º).

	Au-Tl	Au-C	Tl-E[a]	C-Au-C	Tl-Au-Tl	C-E[a]
1	3.241	2.058 2.046	2.725 3.081-3.202	180.0	180.0	1.475-1.482 1.810-1.821
1 S_0	3.189-3.202	2.067-2.069	2.819 3.174-3.204	179.5	178.4	1.460-1.464 1.830-1.841
1 T_1	2.832	2.061	2.750 3.049-3.169	180.0	180.0	1.459-1.461 1.830-1.842
3	3.022	2.051 2.073	2.638 3.135-3.221 3.1385	176.26	-	1.473-1.489 1.786-1.839 1.430-1.440
3 S_0	2.994	2.055 2.063	2.783 3.207-3.247 3.122	176.26	-	1.451-1.449 1.825-1.836 1.407-1.408
3 T_1	2.703	2.056 2.063	2.685 2.861-2.892 3.133	176.26	-	1.448-1.444 1.826-1.841 1.408-1.504
4	3.317-3.382	2.063 2.055	2.772 3.156-3.169	177.3	104.3	1.493-1.496 1.814-1.842
4 S_0	3.249-3.407	2.064-2.068	2.945 3.192-3.300	178.8	75.4	1.457-1.460 1.829-1.841
4 T_1	2.891-3.016	2.065-2.075	2.951-2.953 3.104-3.270	171.4	89.6	1.450-1.452 1.829-1.840

[a] E = N or S atoms. [b] C atoms of the C_6F_5 ligands

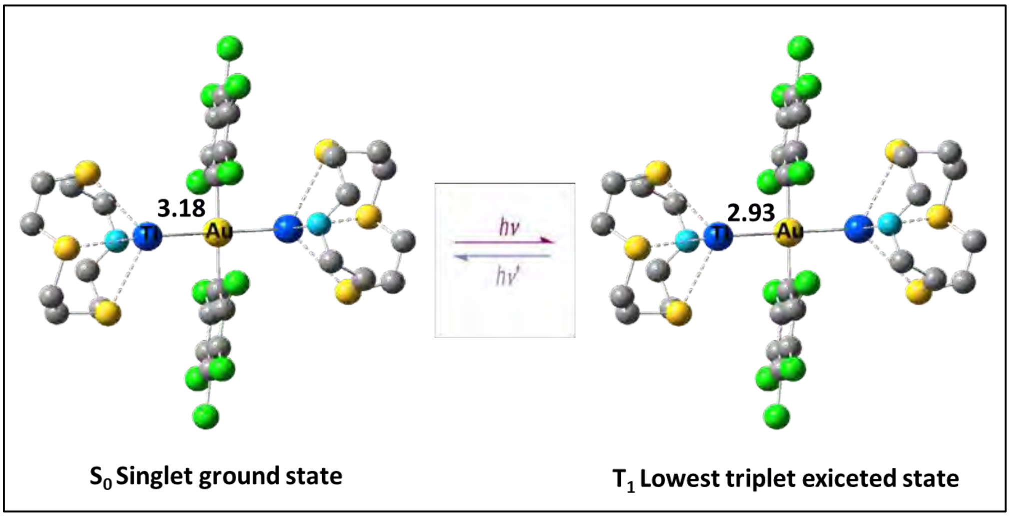

Figure 15. Optimized structures of the ground and lowest triplet excited states for model **1b.**

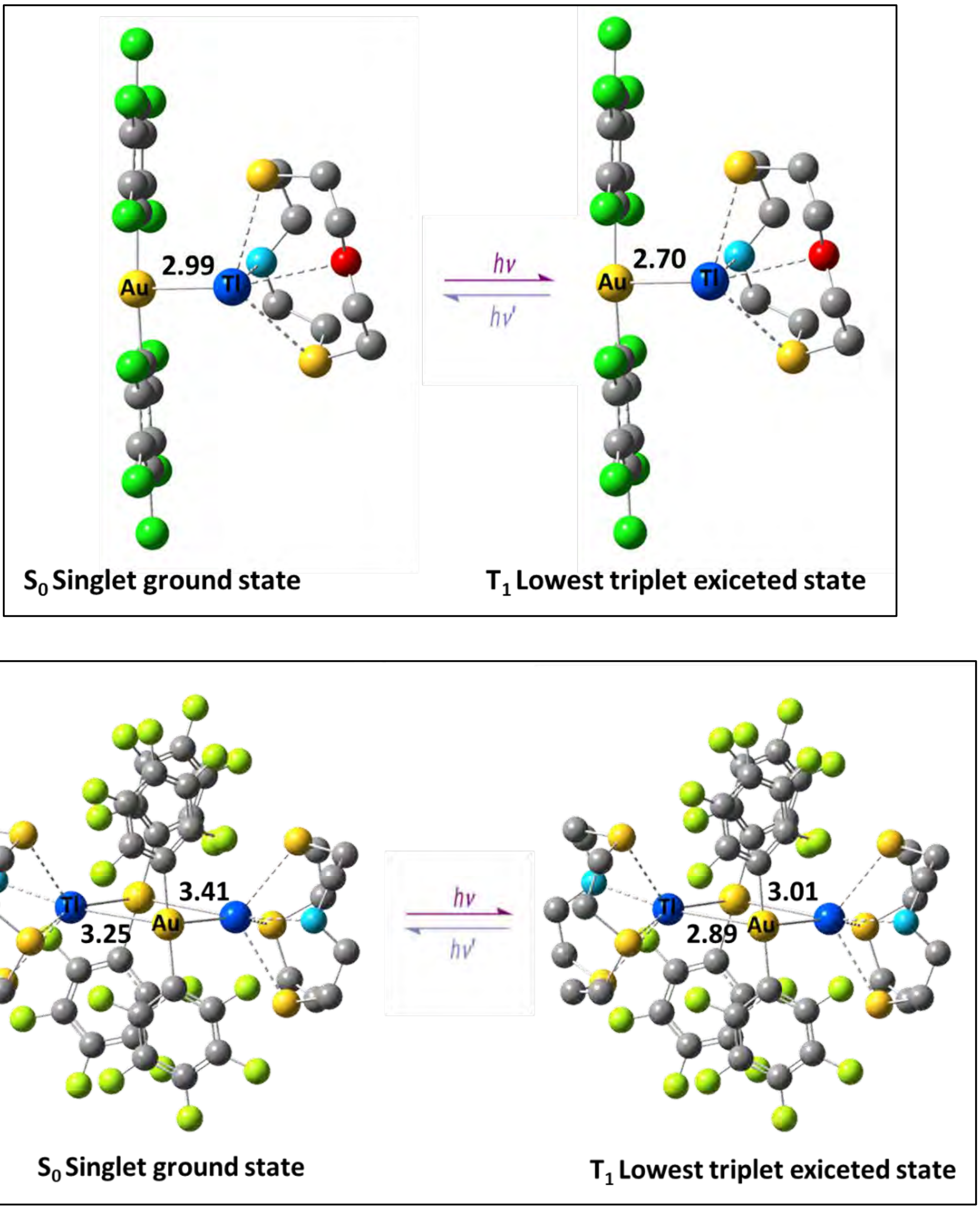

Figure 15. Optimized structures of the ground and lowest triplet excited states for models **3b** (up) and **4b** (down).

The analysis of the shape of the frontier molecular orbitals (Figure 16) of the lowest triplet excited state T_1 (SOMO and SOMO-1), shows up for both models, that the Au-Tl interacting metals are mainly involved in the phosphorescent emission from the T_1 state (SOMO-SOMO-1 transition), with some contribution from the ligands. If we compare the shape of SOMO and SOMO-1 orbitals for models **1b, 3b** and **4b** we can also confirm a small charge transfer contribution from the metals to the organic ligands. Therefore, in view of the analysis of the molecular distortions and the electronic structure of the frontier orbitals of the T_1 state for models **1b**, **3b** and **4b** we can conclude that the phosphorescent emission process can be ascribed to a forbidden metal centred (Au-Tl) transition with a small metal (Au-Tl) to ligand ([12]aneNS$_3$ or [12]aneNS$_2$O) charge transfer contribution.

Finally, in order to confirm the accuracy of our computational approach we have computed the emission energies for models **1b**, **3b** and **4b** as the difference between the energy of the T_1 optimized structures and the same structure in the S_0 ground state (Figure 17). The computed emissions clearly match the experimental ones for the complexes **1b**, **4b**, while there is an error of about 60 nm regarding model **3a**. The deviation from the emission theoretically encountered may be due to packing phenomena which give rise to weak contacts that can influence the emission energy encountered experimentally (495 nm at RT and 512 nm at 77K exp *vs.* 512 nm theor. (**1b**); 501 nm at RT and 512 at 77K vs 442 nm theor. (**3b**); 495 nm at RT and 475 nm at 77K exp *vs.* 475 nm theor. (**4b**)).

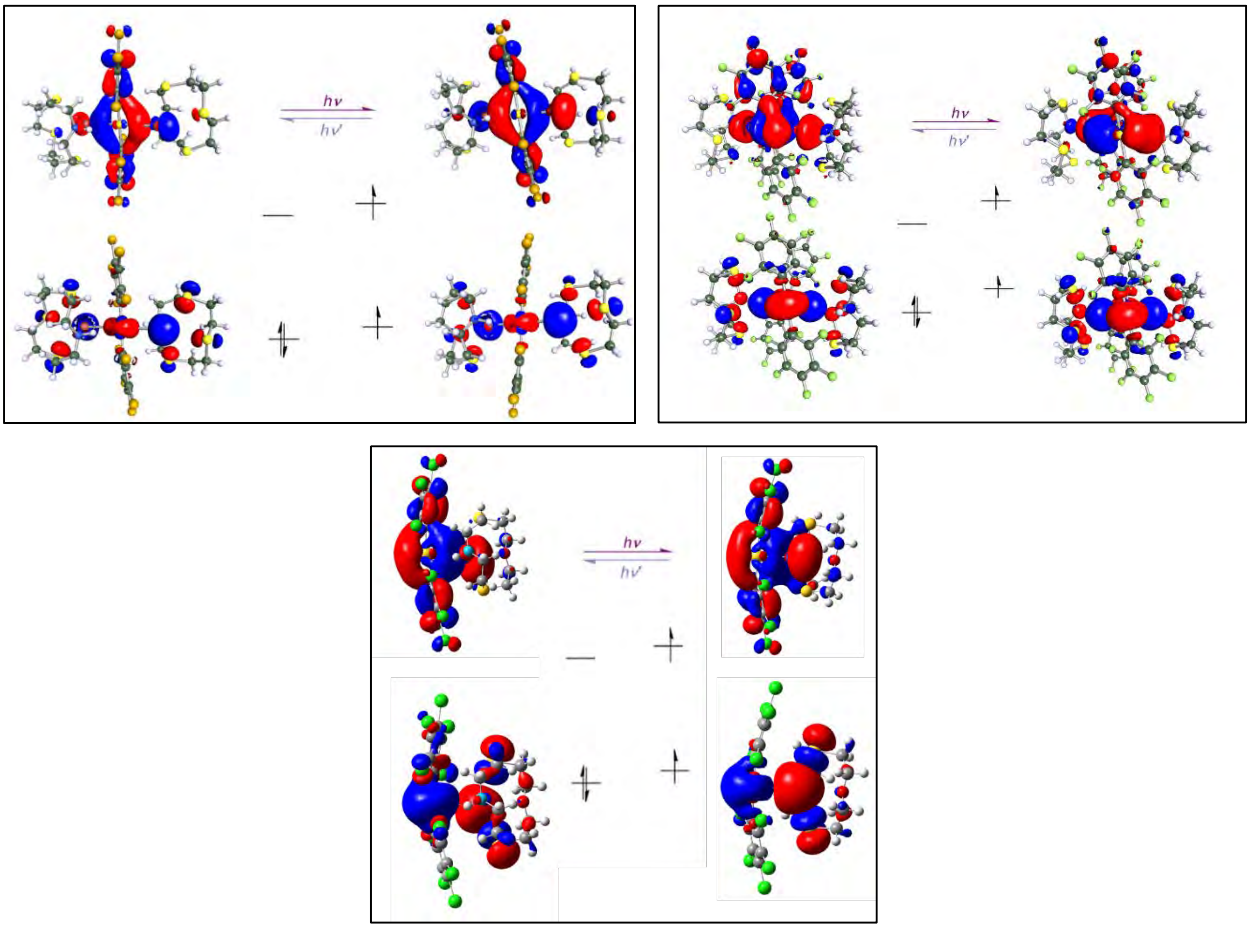

Figure 16. Frontier molecular orbitals HOMO-LUMO and SOMO-SOMO-1 diagrams for models **1a** (left), **4a** (right) and **3a**(below).

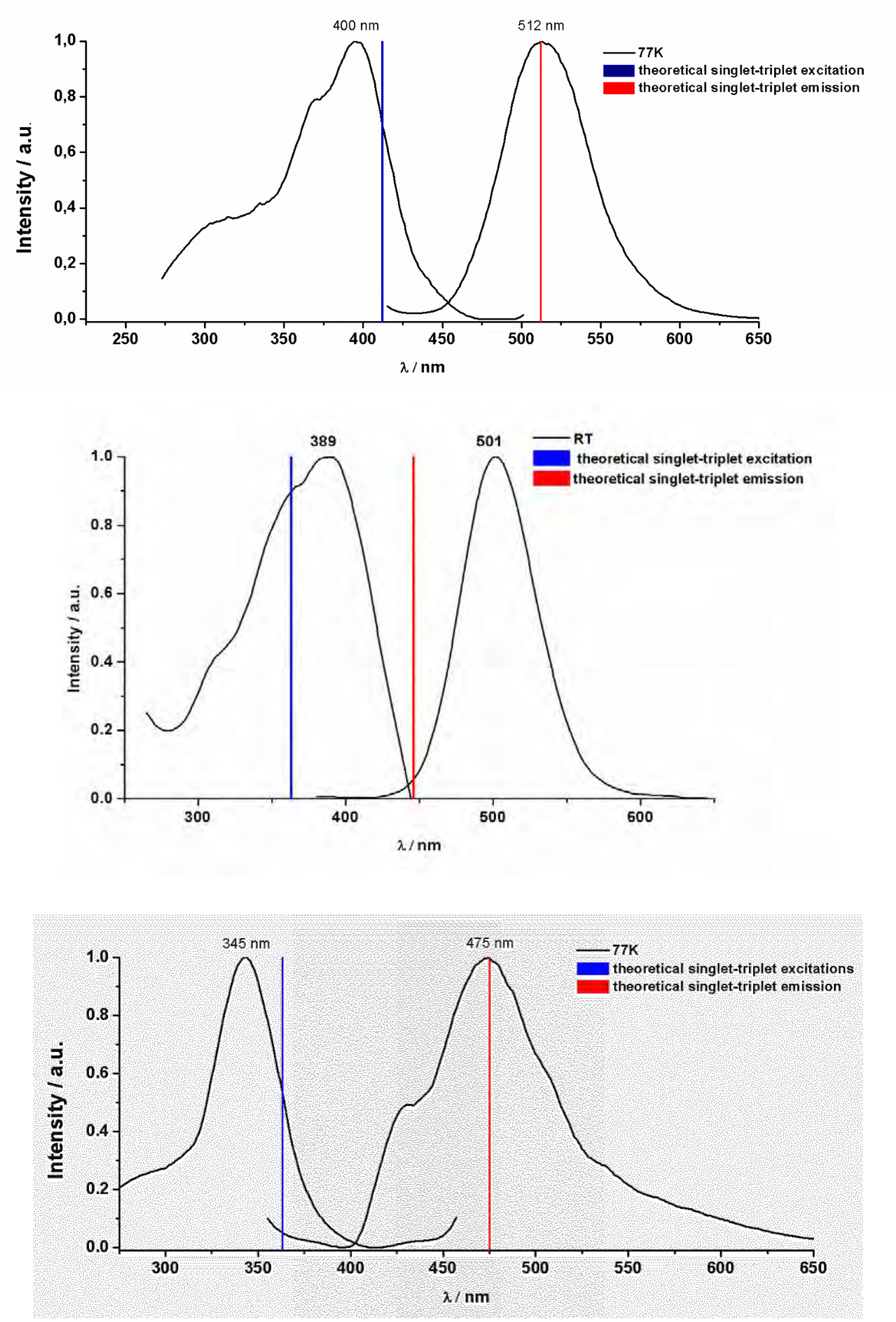

Figure 17. Excitation and emission spectra at 77 K (black profile) and TD-DFT predicted singlet-triplet excitation (blue bar) and triplet-singlet emission (red bar) for model systems **1a** (top), **3a** (middle) and **4a** (bottom).

2.2.5 Conclusions

The use of the macrocyclic ligands **L_1-L_3** in the reaction with $[\{Au(C_6X_5)_2\}Tl]_n$ (X = F, Cl) polymeric compounds allows generation of luminescent systems containing different metallophilic interactions displaying unprecedented structural arrangements, such as the $[Tl(I)\cdots Au(I)\cdots Tl(I)]^+$ trinuclear disposition observed for complexes **1** and **2** and the Au_2Tl_2 square arrangement for complex **4**. Luminescent properties are directly correlated to the Au(I)–Tl(I) arrangements more than the distances found in the complexes. The computational studies show that the luminescent properties mainly arise from the metals, whereas the macrocyclic ligands serve as a support for the whole structural system, tuning the luminescence as a consequence of the types of Au(I)···Tl(I) interactions. These results are confirmed by the calculated theoretical emissions that perfectly match the experimental data for the model systems **1a** and **4a**. For the model systems **3a** there is a relevant variation between theoretical emission and emission observed experimentally which can be due to the Au···Au weak contacts present in the crystal packing of the complex which can influence the emission energy (see Figure 18). In fact, the presence of the gold(I)-gold(I) interaction (although the distance is slightly higher than the sum of the van der walls radii and cannot be considered a strong interaction) causes a lowering of the calculated theoretical emission energy. Unfortunately, the distance too long does not allow us to meet convergence parameters that can give a good result during the optimization process. In addition, the change in the functional used (pbe) would not allow us to compare the calculation made for this model with respect to those obtained by the calculation made for the models used for the other complexes (**1a**,**4a**).

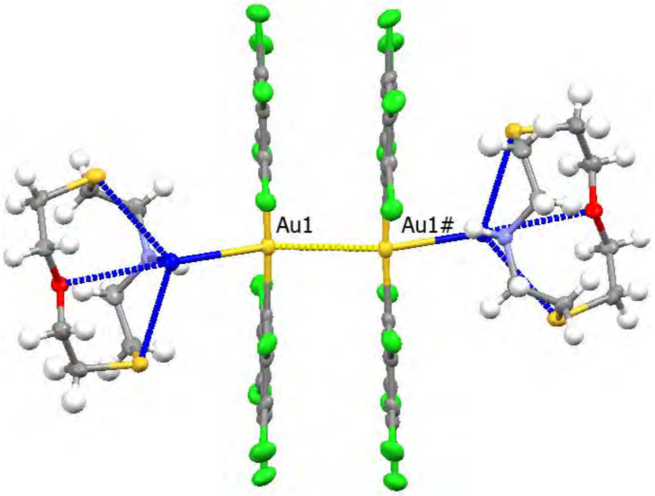

Figure 18. Au(I)···Au(I) interaction in the complex **3.**

2.3 Ligands with different ring size cavity and donor atoms (L$_4$-L$_5$)

2.3.1 Introduction

As reflected in the results obtained through the use of macrocyclic systems **L$_1$**-**L$_3$**, it is obvious that the different nature of the ligands as well as the different electronic properties of the systems $[Au(C_6X_5)]^-$ can influence in a determined way both the structural characteristics and the photophysical properties of the synthesized compounds. Taking into account all of this, we have decided to follow this same line of investigation by modifying the ring size cavity, the nature of the donor atoms and the coordination capacity to evaluate the significant variations, both in the structural dispositions and in the optical properties, in the synthesized complexes (see Figure 19). In particular, we decided to study the reactivity of the ligands **L$_4$** and **L$_5$** with heterometallic compounds $[\{Au(C_6X_5)_2\}Tl]_n$ to see the possibility to obtain new materials with different structural arrangements (from discrete units of different nature to polymeric systems) and different luminescent properties.

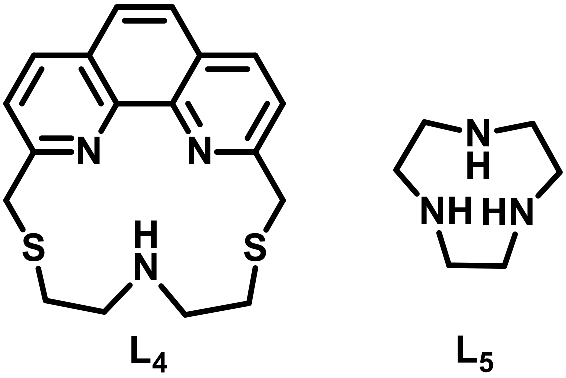

Figure 19. N,S,O-mixed-donor macrocyclic ligand.

The macrocyclic derivatives **L$_4$** contains inside the structure the unit 1,10-phenanthroline. The 1,10-phenanthroline unit is a classic chelating bidentate ligand for transition metal ions that has played an important role in the development of coordination chemistry [137]–[139] and still continues to be of considerable interest as versatile starting material for organic, inorganic and supramolecular chemistry. In fact, its electronic characteristics and the presence of nitrogen atoms makes this system ideal for the coordination of the majority of metal centers. Moreover, its photophysical properties already exploited in the past for various applications, make it an extremely interesting starting material to synthesize new systems containing metallophilic interactions between different metal centers. Furthermore, the possibility of combining the photophysical properties of this unit with the coordination capabilities of a macrocyclic system can play a key role in the formation and strength of new intra or intermolecular interactions. In the same way the macrocyclic system 1,4,7-triazacyclononane (**L_5**) has been widely used in the past both for its coordinating properties and for the possibility of functionalizing this ligand through the secondary amine groups with organic systems with unique characteristics. For these reasons both macrocycles represent attractive starting products for the synthesis and characterization of complexes containing gold-thallium heterometallic interactions and for the study of their photophysical properties. Taking into account the obtained results so far, we decided to study the reactivity of the heterometallic compounds $[\{Au(C_6X_5)_2\}Tl]$ with **L_4** and **L_5**. Through the use of this type of ligands, it was possible to obtain new materials with different structural arrangements (from discrete units of different nature to polymeric systems). In fact, the size of the macrocycle, the number and variety of donor atoms or the variation of halogen atoms in the aryl fraction can play a determining role both in the structural arrangement and in the optical properties of the obtained heterometallic complexes.

2.3.2 Synthesis and characterization

The heterometallic complexes **7**-**10** were obtained through the reaction between the polymeric starting compounds $[\{Au(C_6X_5)_2\}Tl]_n$ (X = F, Cl) with equimolar amounts of the respective macrocyclic ligands (**L_4**-**L_5**) that contain different donor atoms (N, O, S) in THF and precipitating them with hexane (scheme 2). The substitution of chlorine atoms with fluorine atoms in the aryl groups does not affect the stoichiometry of the reaction although it modifies the structural arrangement of the resulting complexes. Scheme 2 shows the stoichiometries of the compounds obtained from the reactions between the ligands and the Au(I)/Tl(I) precursors. Despite the structural variety of the complexes obtained and the presence of metallophilic interactions, only the complexes with **L_5** are luminescent in the solid state. All the compounds are insoluble in dichloromethane, acetonitrile and diethyl ether although they appear to be soluble in O-donor solvents. However, the solubility of the chlorinated compounds is lower than the solubility of the fluorinated complexes. Their elemental analyses and spectroscopic data are in accordance with the proposed stoichiometries (see Experimental Section). Their IR spectra show, among others, absorptions arising from the C_6F_5[124] and C_6Cl_5[125] groups bonded to gold(I) at approximately 1500, 950 and 780 cm^{-1}, or about 834 and 614 cm^{-1}, respectively.

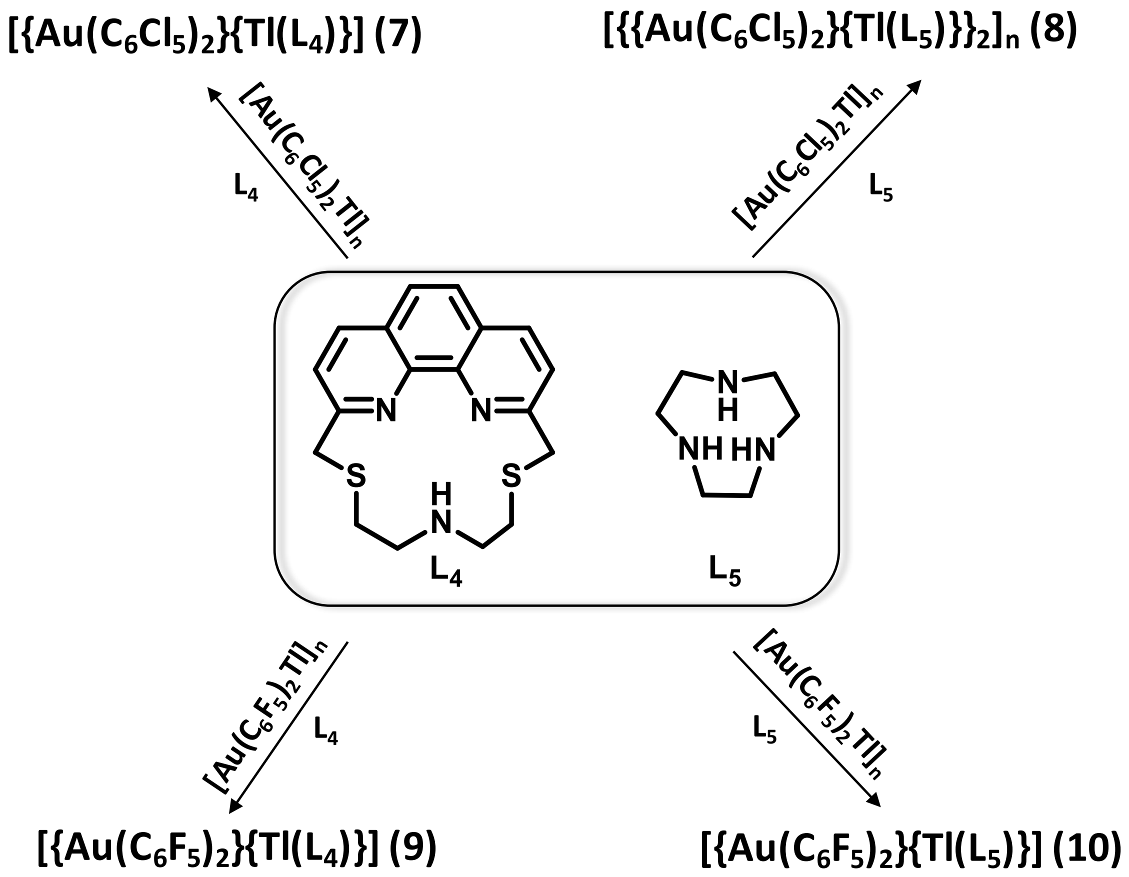

Scheme 2.

The presence of the $[Au(C_6F_5)_2]^-$ fragment in **9,10** is evident from their ^{19}F NMR spectra, which resemble that of the precursor complex $NBu_4[Au(C_6F_5)_2]$, and seem to indicate that a dissociative process giving rise to aurate(I) anions and thallium(I) cations takes place in solution. The NMR spectrum of all the complexes show a significant modification in the chemical shifts as compared to those of the free ligands. This fact means that the coordination of the macrocyclic ligands to thallium significantly affect the position of the resonances observed in their ^1H NMR spectra. Thus, the ^1H-NMR spectra of **7** and **9** display a multiplet signal at 2.43-2.74 and an singlet at 4.44-4.64 with 1:2 relative integrations, and corresponding to the hydrogen atoms of the methylene groups adjacent to nitrogen or to sulphur. Furthermore, three groups of aromatic signals can be observed due to the presence of the 1,10-phenanthroline unit which show a chemical shift at 7.73, 7.87, 8.38 and 7.73,7.89,8.43 for the complexes **7** and **9** respectively. In the ^1H-NMR spectra of **8** and **10** a strong broadening of the signals due to the coordination of the macrocyclic system to the metal centre is observed. Both complexes show a signal between 2.80-3.03 or 2.78-3.01 for **8** and **10**, respectively. Regarding their mass spectra (MALDI(−)), they display either a peak due to the unit $[\{Au(C_6X_5)_2\}_2Tl]^-$ at $m/z = 1594$ (**7**,**8**) and 1267 (**9**,**10**) or a signal corresponding to $[Au(C_6X_5)_2]^-$ at $m/z = 695$ (**7**,**8**) and

531 (**9**,**10**), the latter appearing as parent peak in all the cases. In their MALDI(+) mass spectra, peaks due to the fragment $[Tl(L)]^+$ appears at *m/z* = 546 (**7**,**9**) or 332 (**8**,**10**), showing experimental isotopic distributions in agreement with the theoretical ones.

Finally, the molar conductivity measurements of the four complexes in acetone agree with a dissociative process in solution, showing values corresponding to univalent electrolytes (see Experimental).

2.3.3 X-ray structural determinations

Single crystals suitable for X-ray diffraction studies were obtained by slow diffusion of n-hexane into a saturated solution of the complexes in toluene (complexes **7**, **9**) or dichloromethane (complex **8**). Despite the numerous attempts, for the complex **10** it was not possible to obtain a single crystal suitable for determining the crystalline structure; the formula in this case represents the stoichiometry of the synthesized complex.

Although the crystal structures of complexes **7** and **9** contain similar structural motifs, $[Au(C_6X_5)_2]^-$ and $[Tl(L)]^+$ units, there are some slight differences among them. The crystal structures of **7** and **9**, with pentachlorophenyl or pentafluorophenyl ligands bonded to gold(I), show the same neutral asymmetric unit, which consists of a binuclear $[\{Au(C_6X_5)_2\}\{Tl(L)\}_2]$ system with a Au(I)-Tl(I) interactions (see Figure 20 and Tables 13 and 14).

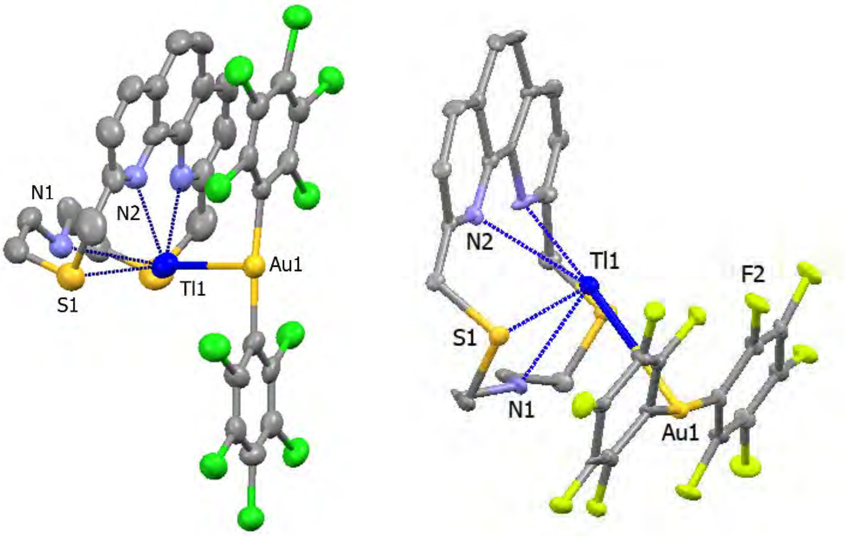

Figure 20. Crystal structures of **7** and **9** with the labeling scheme for the atom positions. Hydrogen atoms are omitted for clarity, and ellipsoids are drawn at the 30% level.

The intermetallic distances within the cations are different depending on the perhalophenyl group employed, showing a Au-Tl distance of 3.2534(6) Å in the perchlorophenyl derivative **7**, shorter than that of 3.3621(4) Å observed in the perfluorphenyl complex **9**. As shown for the macrocyclic systems described earlier, both Au(I)-Tl(I) distances lie within the range of Au-Tl distances described till date, which varies from 2.804(6) Å, observed in $[AuPdTl(P_2phen)_3](BF_4)_2{\cdot}2.5CH_2Cl_2$[88], to 3.4899(6) Å, found in $[Tl(2,2'\text{-bipy}))][Au(C_6F_5)_2]$[118], and they both are longer than the average Au-Tl distance of 3.064 Å. Each gold atom is linearly coordinated to two pentahalophenyl groups, displaying normal Au-C bond lengths of 2.027(13) and 2.030(11) Å in **7**, and of 2.050(5) for both distances in **9**.

The Tl-N bond distances from the 1,10-phenantroline unit are quite different in **7** and **9** crystal structures, with values of 2.696(10) Å in **7** and 2.9726(1) Å in **9.** While the distances Tl-N in the 1,10-phenatroline unit in the derivative **7** are very similar to those reported in thallium complexes containing this aromatic system[118],[140]-[142], the derivative **9** shows a Tl-N distance greater than those reported previously in the literature described for the thallium(I) derivative as $Tl(1,10\text{-phenantroline})][Au(C_6F_5)_2]$[118] or similar complexes[143]-[145]. The distances Tl-N of the aliphatic fraction of the macrocyclic system (2.703(10) in **7**; 2.775(6) in **9**) are intermediate between those described for the thallium(I) derivatives with cyclic N- or N,S-donor ligands $[Tl(Me_3[9]aneN_3)]PF_6$ (2.59(2)-2.63(1) Å)[126] or $[Tl([9]aneN_2S)]ClO_4$ (2.26(2)-2.68(2) Å)[127] and $[Tl([18]aneN_2S_4)]PF_6$ (2.834(4) and 2.992(4) Å)[128].

Regarding the Tl-S bonds, in **7** the distances are smaller than those observed for the complex **9** (3.093(3) and 3.146(3) in **7**; both distances 3.2308(1) in **9**) and very similar to those reported for $[Tl([9]aneS_3)]PF_6$ (3.092(3)-3.114(3) Å)[129]. In addition, they all are in general shorter or similar to those observed in the related Au/Tl compounds with crown thioethers $[\{Au(C_6Cl_5)_2\}_2Tl_2([24]aneS_8)]_n$ (3.256(7)-3.587(7) Å), $[\{Au(C_6F_5)_2\}_2Tl_2([24]aneS_8)]$ (3.201(2)-3.418(3) Å) and $[\{Au(C_6F_5)_2\}Tl([9]aneS_3)]_2$ (3.0246(17)-3.1154(19) Å)[120], as well as in the thallium derivatives $[Tl([18]aneN_2S_4)]PF_6$ (3.1299(13)-3.4778(15) Å)[128], $[Tl([18]aneS_6)]PF_6$ (3.164(5)-3.370(5) Å)[128]and $[Tl([24]aneS_8)]PF_6$ (3.2413(11)-3.4734(14) Å))[130]. Probably the distances Tl-N or Tl-S in the complex **9** are longer due to the position of the thallium with respect to the whole macrocyclic system.

Table 13. Selected bond lengths [Å] and angles [°] for **7**.

Tl(1)-Au(1)	3.2534(6)	Tl(1)-N(1)	2.703(10)
Au(1)-C(1)	2.030(11)	Tl(1)-N(2)	2.696(10)
Au(1)-C(7)	2.027(13)	Tl(1)-S(2)	3.093(3)
		Tl(1)-S(1)	3.146(3)
C(7)-Au(1)-C(1)	175.1(4)	N(2)-Tl(1)-N(1)	62.2(3)
N(1)-Tl(1)-S(2)	120.8(2)	N(2)-Tl(1)-S(2)	66.1(2)
N(1)-Tl(1)-S(1)	64.6(2)	N(2)-Tl(1)-S(1)	117.7(2)
N(1)-Tl(1)-Au(1)	104.0(2)	N(2)-Tl(1)-Au(1)	85.5(2)
S(2)-Tl(1)-S(1)	122.32(11)	S(1)-Tl(1)-Au(1)	137.83(8)
S(2)-Tl(1)-Au(1)	98.80(7)		

Table 14. Selected bond lengths [Å] and angles [°] for **9**.

Tl(1)-Au(1)	3.3621(4)	Tl(1) -S(1)	3.2308(1)
Au-C(1)	2.050(5)	Tl(1)-N(1)	2.775(6)
Au-C(1)#1	2.050(5)	Tl(1)-N(2)	2.9726(1)
C(1)-Au-C(1)#1	171.8(3)	N(1)-Tl-Au	75.52(14)
C(1)-Au-Tl	88.78(14)	C(1)#1-Au-Tl	88.78(14)

Symmetry transformations used to generate equivalent atoms:

#1 x,y,-z+1/2

Finally, The main difference between two structures is an extended polymeric packing observed only for the complex **9** which is formed via weak intermolecular Tl···F contacts of 3.2017(3) Å (see Figure 21). While, in the complex **7** intramolecular π-stacking contacts can be observed between the aromatic fractions of $Au(C_6Cl_5)^-$ and the phenanthroline unit (Figure 21).

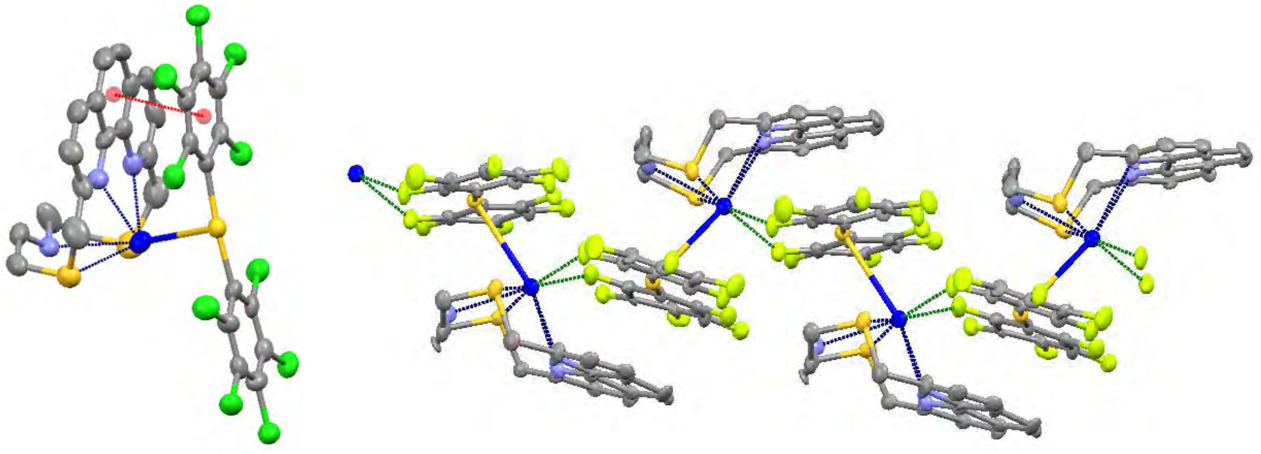

Figure 21. π-stacking (red line) contact of complex **7** (left) and 1D polymeric structures of complex **9** (right).

The substitution of $\mathbf{L_4}$ by $\mathbf{L_5}$ leads to significant differences in the crystal structures of complex **8**. Thus, the structure of the **8** consists of a polymeric system in which the monomeric unit is constituted by a tetranuclear system $[L_4\text{-Tl-Au-Tl-}L_4\text{-Au}]_n$ (see Figure 22 and Table 15). The structural arrangement of this system we can observe some similarities with the crystalline structures shown previously. Despite the smaller size and the different nature of the donor atoms of the macrocyclic system used for the synthesis of complex **8**, we can observe within the monomeric unit a trinuclear arrangement L_5-Tl(1)-Au(1)-Tl(1)#2-L_5 (Au(1)-Tl(1) 3.3377(6)) very similar to that observed in complexes **1** and **2**. The different position of $\mathbf{L_5}$, probably due to the presence of the inert thallium electronic lone pair, makes a weaker interaction possible with an adjacent $[Au(C_6Cl_5)]^-$ unit (Tl(1)-Au(2) 3.5478(6)), allowing the formation of the polymer chain. The Tl-N distances of 2.621(9)-2.671(9) Å are very similar to those found in $[Tl(Me_3[9]aneN_3)]PF_6$ (2.59(2)-2.63(1) Å)[126] or [Tl(3,5-di-tert-butyl-2-hydroxybenzyl)$Me_2[9]aneN_3$] (2,675(4)-2.811(7))[126].

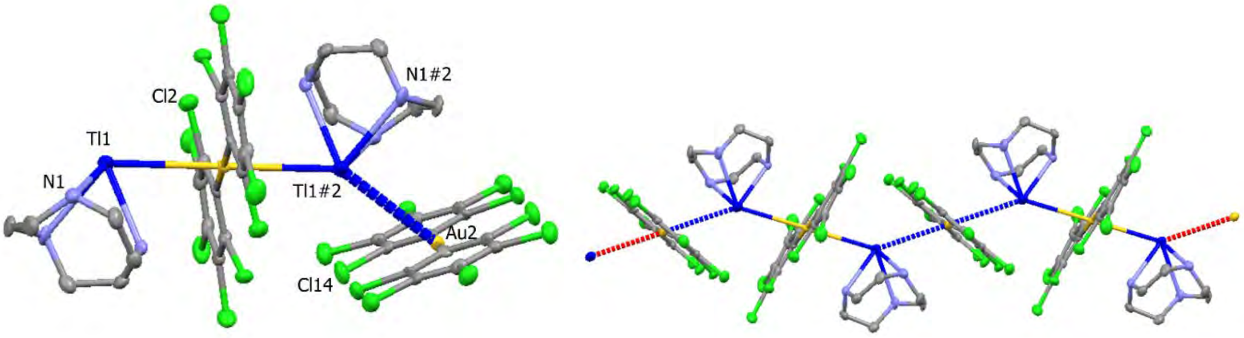

Figure 22. monomeric unit (left) and polymeric structure complex **8** (right).

Table 15. Selected bond lengths [Å] and angles [°] for **8**.

Tl(1)-Au(1)	3.3377(6)	Tl(1)-Au(2)	3.5478(6)
Au(1)-C(1)#2	2.056(9)	Tl(1)-N(1)	2.664(8)
Au(1)-C(1)	2.056(9)	Tl(1)-N(2)	2.621(9)
Au(2)-C(7)	2.039(9)	Tl(1)-N(3)	2.671(9)
Au(2)-C(7)#2	2.039(9)		
Au(1)-Tl(1)-Au(2)	144.289(14)	N(1)-Tl(1)-Au(1)	69.97(16)
Tl(1)-Au(2)-Tl(1)#2	180	N(2)-Tl(1)-Au(1)	118.67(19)
C(7)-Au(2)-C(7)#2	180.0	N(2)-Tl(1)-Au(2)	72.49(18)
Tl(1)-Au(1)-Tl(1)#1	180.0	N(2)-Tl(1)-N(1)	65.6(2)
C(1)-Au(1)-C(1)#1	180.0	N(2)-Tl(1)-N(3)	66.5(3)
N(1)-Tl(1)-Au(1)	69.97(16)	N(3)-Tl(1)-Au(1)	126.63(17)
N(1)-Tl(1)-Au(2)	136.90(16)	N(3)-Tl(1)-Au(2)	89.08(17)
N(1)-Tl(1)-N(3)	65.7(2)		

Symmetry transformations used to generate equivalent atoms:

#1 1-X,1-Y,1-Z; #2 1-X,1-Y,2-Z

Finally, also in this case we can observe Tl-Cl intermolecular contacts of 3.692(5) between the different polymeric chains that determine an expansion of the whole structure in two dimensions (see Figure 23).

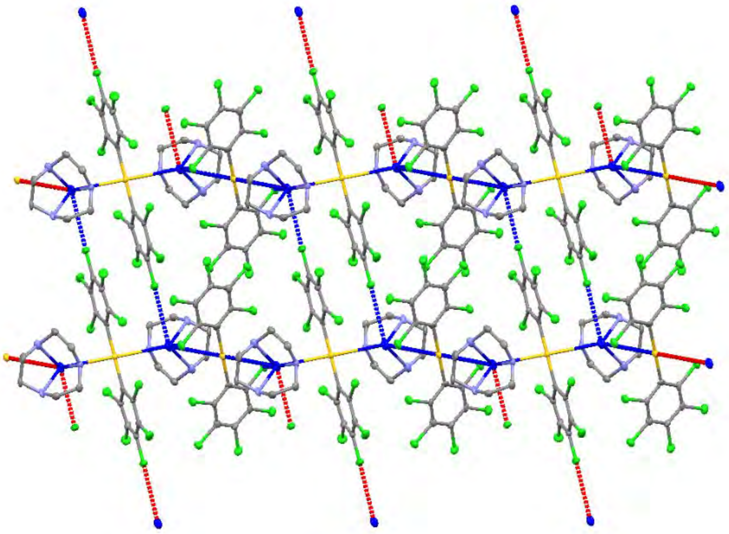

Figure 23. 2D polymeric structures of complex **8**.

2.3.4 Photophysical Properties

Despite the presence of metallophilic interactions inDespite the presence of metallophilic interactions in complexes **7** and **9,** they do not show solid-state luminescence not. However, it is shown in the literature that macrocyclic systems similar to **L$_4$** exhibit an emission band in solution at about 336 nm and they are used as ON-OFF sensors for different metal ions [146]. For this reason, we have investigated the reason for the absence of luminescence in the solid state for the synthesized complexes by studying the behavior of **L$_4$** in solution in the presence of Tl^+. The absorption and fluorescence spectra of **L$_4$** show an absorption band at about 270 nm and a fluorescence band at about 456 nm, respectively (see Figure 24).

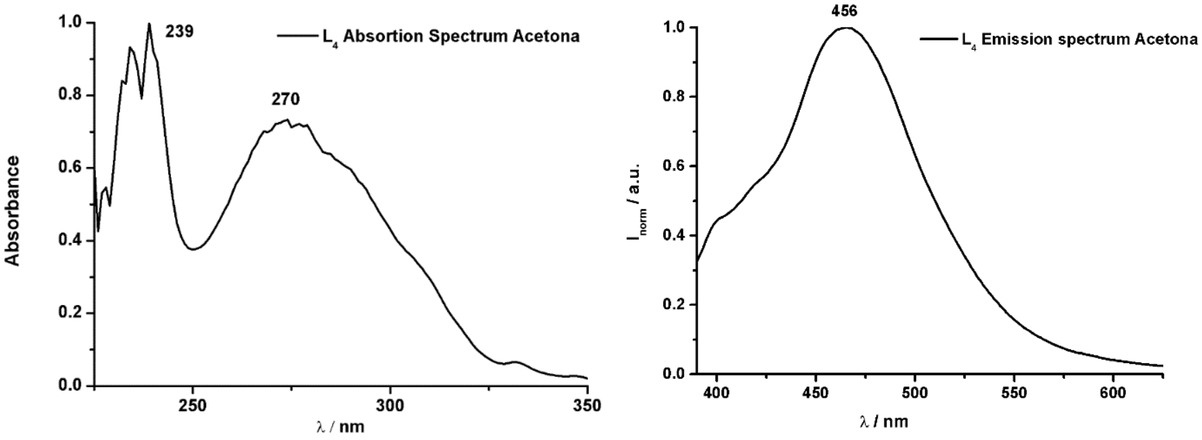

Figure 24. Absorption spectra (left) and emission spectra (right) of **L$_4$** (**L$_4$** = 2,72 x 10^{-4} M in acetone, $\lambda_{ex.}$ 270 nm)

To study the behavior of **L$_4$** in the presence of Tl^+, the variations in the fluorescence spectrum of the ligand were recorded as a result of the addition of increasing amounts of the metal ion. The fluorescence spectrum variation for **L$_4$** in the presence of increasing amounts of Tl^+ is shown in Figure 25. Taking into account the study carried out, a strong decrease of the fluorescent emission was observed for **L$_4$**. In addition, representing the emission intensity as a function of the ratio [Tl^+]/[**L$_4$**] (see Figure 25) it is obvious that the quenching of the system is due to the formation in the solutions of specie [Tl(**L$_4$**)]$^+$.

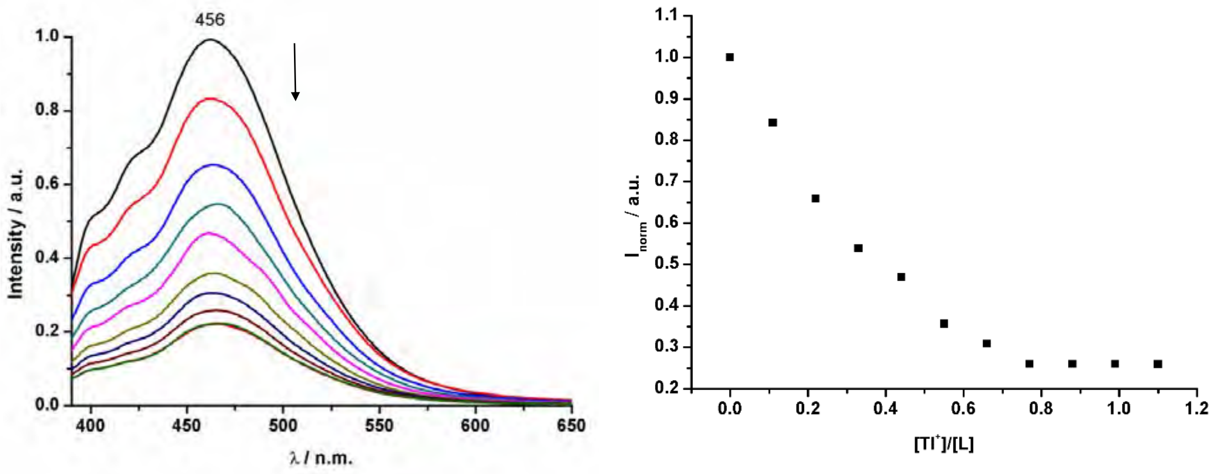

Figure 25. Fluorescence emission spectrum of **L_4** in the presence of increasing amounts of Tl^+ (left); Fluorescence intensity of **L_4** at 456 nm vs. molar concentration of Tl^+ (right).

The next step consists of the study of the quenching mechanism that involves **L_4** considering that the relationship between the concentration of the deactivating agent [Q] and the ratio between the initial intensity of the ligand I_0, and the intensity at different concentrations of the deactivating agent I, is described by the equation of Stern-Volmer[147]-[148]:

$$ {}^{I_0}/_{I} = 1 + K_{sv}[Q]\ (1) $$

By examining the pattern (see Figure 26) for the titration of **L_4** with Tl^+ it is clearly seen that there is a linear correlation between I/I_0 and $[Tl^+]$.

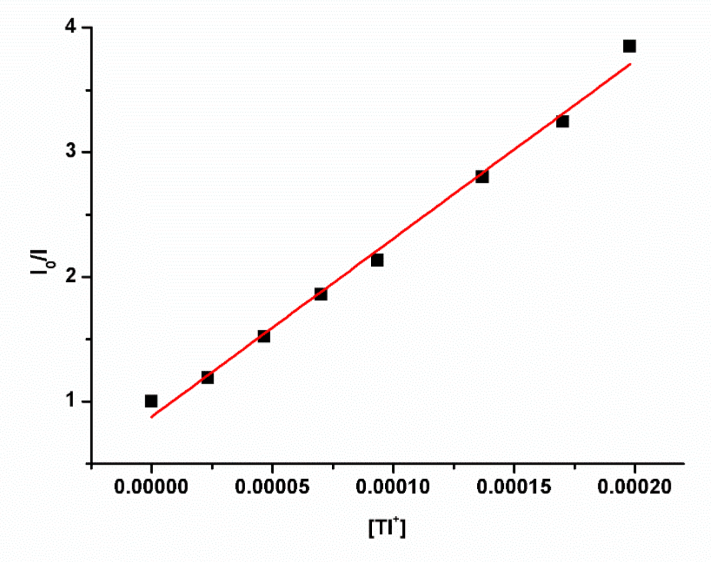

Figure 26: Representation of the ratio I_0 / I (of **L_4** versus $[Tl^+]$ (λex. 270 nm, λem. 456 nm).

From the slope of the straight line, it was possible to determine the K_{sv} value (14302 M^{-1}). Thus, it was possible to suggest that probably the absence of luminescence in the synthesized compounds is mainly due to the coordination of the Tl^+ metal ion to **L_4**.

By lifetime measurements, It is also possible to detect whether it is static or dynamic quenching. (see Figure 27).

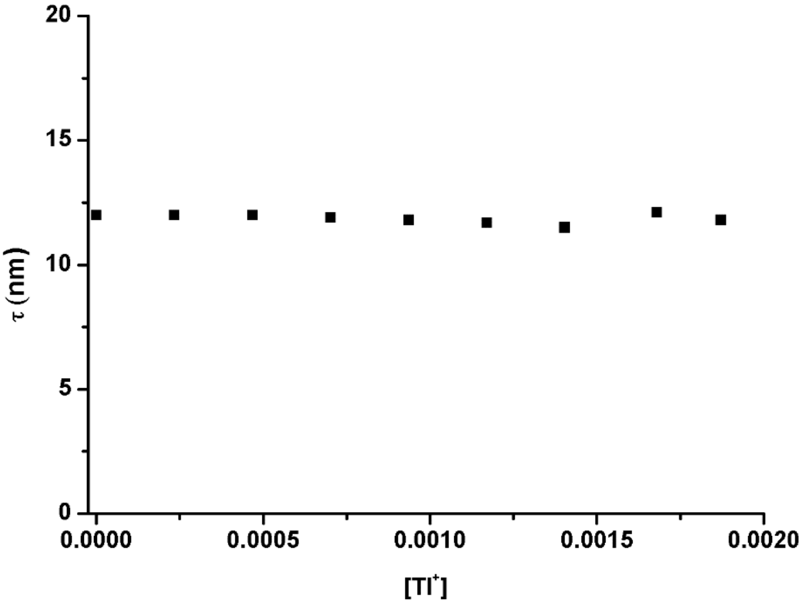

Figure 27. Representation of the relation τ vs [Tl^+] for L_4.

Considering previous reports [149], the constant lifetime with increasing concentrations of $[Tl]^+$, can be concluded that this is a static quenching for the studied system. This behavior is normally observed when quenching is due to the formation of a ground state complex in solution.

On the other hand, the absorption spectra of complexes **8** and **10** show similar features to those described for other related gold(I)–thallium(I) derivatives reported previously by some of us [120]. Thus, both complexes display two intense absorptions at about 230 and 350 nm in THF solutions; these bands are also present in the spectra of the heterometallic precursor $[\{Au(C_6X_5)_2\}Tl]_n$ and in the gold(I) complex $NBu_4[Au(C_6X_5)_2]$ (X=F, Cl) (see Figure 28). Therefore, it is likely that the band at high energy arises from transitions between π orbitals of the perhalophenyl groups, while the transitions in the low energy region probably involve orbitals of the gold centres. Thus, these absorptions could be assigned to $\pi \rightarrow \pi^*$ and $Au \rightarrow \pi^*$ transitions in the $[Au(C_6X_5)_2]^-$ fragments, respectively. At this regard, similar assignments have been done for related gold(I) complexes with aromatic substituents [132],[133]; nevertheless, in the case of the high-energy absorption the possibility of an n→σ* transition in the N-donor ligands cannot be ruled out, since these ligands show an absorption at 240 nm of less intensity at similar concentrations.

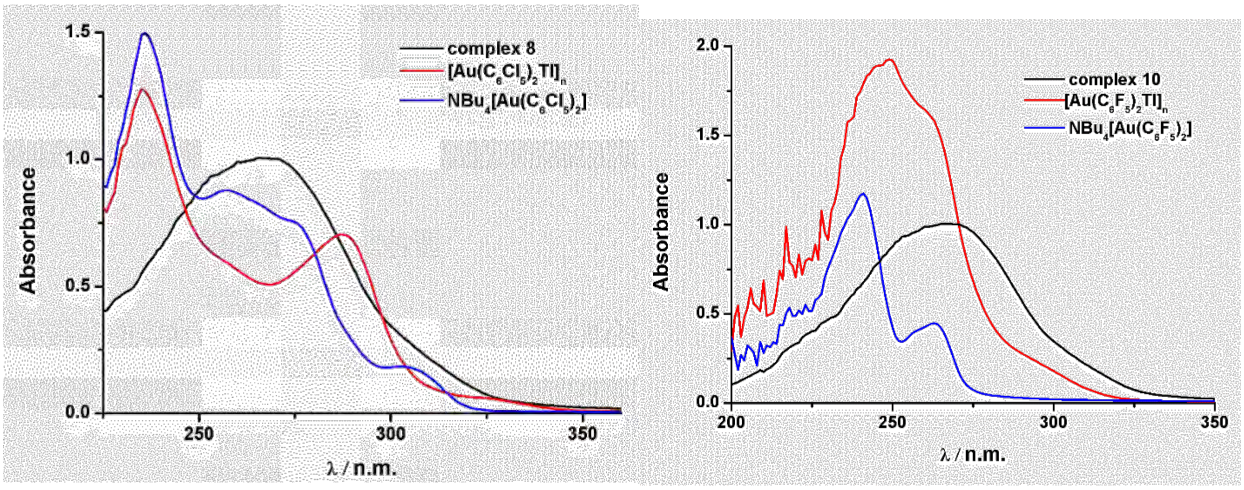

Figure 28. Absorption spectra of complex **8** (left) and **10** (right) and the gold precursors $NBu_4[Au(C_6X_5)_2]$ and $[\{Au(C_6X_5)_2\}Tl]_n$ (X=F,Cl) in THF solution (C ≈ 2,5 x 10^{-5} M).

Unlike the metal complexes synthesized with **L_4**, complexes **8** and **10** are strongly luminescent in the solid state; thus, they display emissions in the solid state between 495 and 512 nm at room temperature, and between 474 and 503 nm when the measurements are carried out at liquid nitrogen temperature (77 K) (Figure 29 and Table 16).

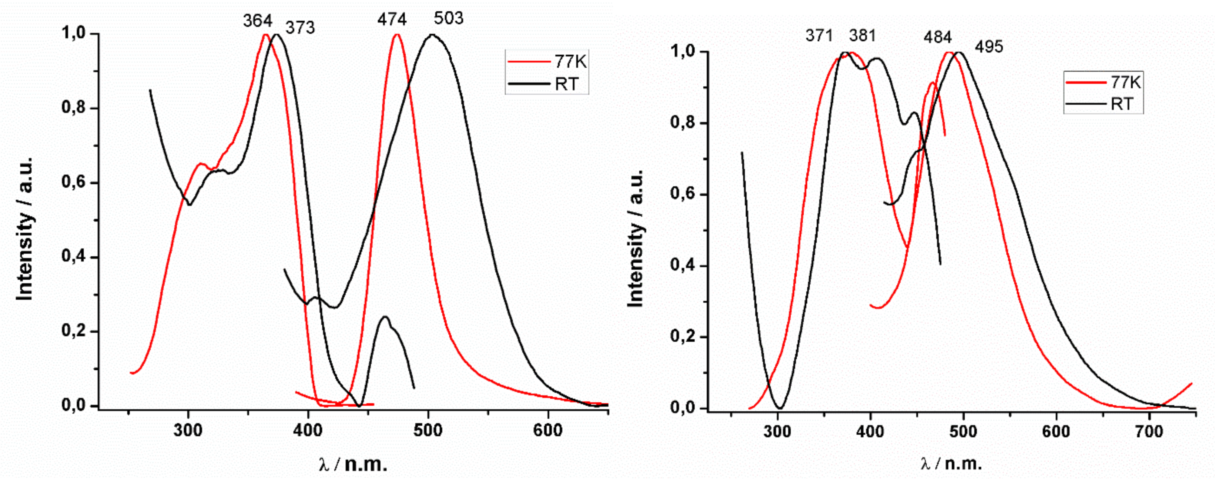

Figure 29. Excitation and emission spectra for complexes **8**(left) and **10**(right) in the solid state at RT and 77 K.

Table 16. Photophysical properties of complexes **8** and **10**.

	UV-vis in THF (nm)	Solid (RT) em(exc)	Solid (77K) em (exc)	τ (ns)	Φ (%)
Complex 8	266 (ε = 40000)	503 (373)	474 (364)	839 ± 3	30.5
Complex 10	267 (ε = 39899)	495 (381)	484 (371)	814 ± 8	20.2

In this case, it is not possible to make a direct comparison between the Au(I)-Tl(I) distances and the luminescence of the compounds given the impossibility of having structural data for the complex **10**. However, both for the structural arrangement and for the aliphatic nature of the macrocyclic systems used it is possible to make a comparison between the optical properties of the complex **8** and those of the complexes **1** and **2**·2THF. Also in the case of **8**, the solid-state luminescence is probably mainly due to the gold-thallium heterometallic interactions present in the synthesized complex. In fact, the complex **8** shows a luminescent emission at about 500 nm which is completely comparable with that observed for compounds **1** and **2**·2THF previously commented previously. In addition, the distance Au (I)-Tl (I) is quite similar (3.3377 (6) in the complex **8**; 3.2410 (2) and 3.3853 (5) in the complexes **1** and **2**·2THF , respectively). For this reason, we can assume that, probably, the interaction between metal centers may be the key to explain the optical properties of **8**. Of course, the weakest interaction between Tl(1)-Au(2) (3.5478(6)) that allows the formation of the polymeric system can influence the optical properties of **8**, and this cannot be neglected to explain the origin of the luminescence of this compound.

Thus, taking into account the previous comments, we can propose that the presence of intermetallic interactions in the solid state, as well as their number and strength, seem to be the key to explain the luminescence of **8**. Nevertheless, another factor that should be considered is the disposition of these metal centres in the crystal structures, in which the coordinative characteristics of **L_5** is determinant.

2.3.5 Computational Study

In order to explain the spectroscopic properties of the complex **8** in relation with the metallophilic interactions present in its crystal structure, we carried out Density Functional Theory (DFT) and Time-Dependent Density Functional Theory (TD-DFT) calculations on a model system **8a** obtained from complex **8**. Compared to the calculations carried out for the complexes **1**,**3**-**4** (discrete molecules), in this case it is necessary to take into account all the metallophilic interactions present in the structure given the polymeric nature of the compound. For the reason of the high computational cost of representing a polymeric molecule, we have chosen a model that take into account the different interactions present in the system as it is that represented in Figure 30.

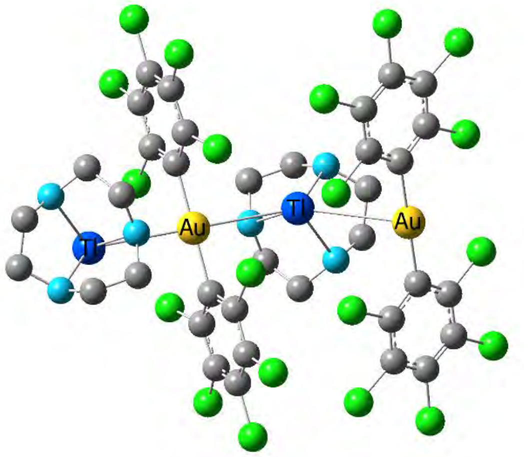

Model 8a

Figure 30. Theoretical model systems [{Au(C_6Cl_5)$_2$}{Tl([9]aneN$_3$)}]$_2$ (**8a**).

Thus, model **8a** corresponds to the tetranuclear neutral unit as the base of the polymeric structure of complex **8**, and representing the Au(I)···Tl(I) interactions between two $[Au(C_6Cl_5)_2]^-$ anionic fragments and two $[Tl([12]aneN_3)]^+$ cationic complexes. We first computed the electronic structures for models **8a** at DFT level of theory. Figure 31 and Table 17 display the most important frontier molecular orbitals (MOs) and the population analysis of those MOs, respectively. From these data we can anticipate the contribution of each part of the molecule to the frontier orbitals.

In this case, the highest occupied molecular orbital (HOMO) and the lowest unoccupied molecular orbital (LUMO) are mainly localized at the metal centres Au(I) and Tl(I). In addition, while the rest of occupied frontier molecular orbitals from HOMO-1 to HOMO-8 are mostly located at the C_6Cl_5

aromatic fractions with some exceptions (HOMO-1, HOMO-4, HOMO-8), the rest of empty frontier molecular orbitals are manly located at the C_6Cl_5, Tl(I) and Au(I) units (from LUMO+1 to LUMO+6).

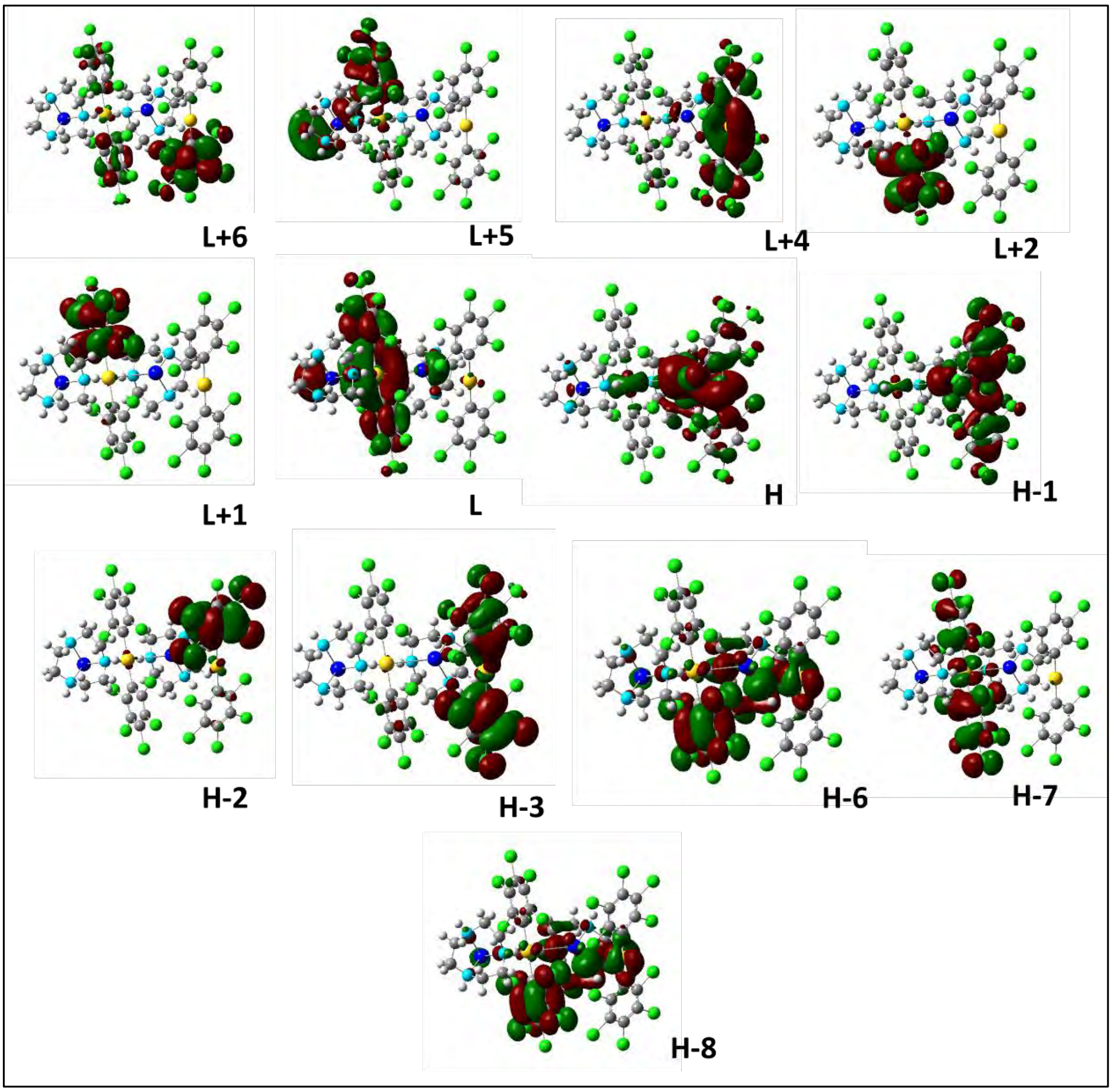

Figure 31. Frontier molecular orbitals (isovalue = 0.02) for model systems **8a** (H=HOMO; L=LUMO).

Table 17. Population analysis (%) for model systems **8a**.

8a	**Tl**	**Au**	**L_5**	**C_6Cl_5**
LUMO+6	10,2	3,84	2,31	83,44
LUMO+5	36,8	25,15	5,47	30,22
LUMO+4	33,16	18,83	1,51	46,26
LUMO+3	42,47	12,62	14,6	29,67
LUMO+2	10,7	20,59	0,79	67,7
LUMO+1	11,66	23,66	0,65	59,35
LUMO	37,35	26	4,18	32,08
HOMO	30,58	47,96	10,56	10,85
HOMO-1	23,15	40,79	13,93	22
HOMO-2	10,61	27,08	5,16	57,08
HOMO-3	1,22	2,28	0,56	95,75
HOMO-4	25,22	31,05	23,21	19,61
HOMO-5	6,37	5,89	6,88	80,64
HOMO-6	3,68	5,22	1,63	89,41
HOMO-7	1,52	19,73	1,66	74,93
HOMO-8	9,53	20,88	32,44	36,83

The first 20 singlet−singlet excitations were computed for the model system **8a** at the TD-DFT level of theory as described in the computational details section (see experimental section) and compared with the experimental excitation spectra for complex **8**. Since the lifetime for this complex is between the nanoseconds and microseconds range, suggesting a fluorescent process, we also computed the lowest singlet−singlet excitation at TD-DFT level for model system **8a**. The results including the most important excitations are reported in Table 18 and depicted in Figure 32.

Table 18. TD-DFT first Singlet-Singlet Excitations calculations for model systems **8a**.

Model	**exc.**[a]	**λ_{calc} (nm)**	**f (s)**[b]	**contributions**[c]
8a	$S_0 \rightarrow S_1$:	363	0.2748	HOMO → LUMO (47)
	$S_0 \rightarrow S_2$:	332	0.0218	HOMO-1 → LUMO(48)
	$S_0 \rightarrow S_4$:	320	0.1297	HOMO-3 → LUMO (27) HOMO-2 → LUMO (16)
	$S_0 \rightarrow S_6$:	310	0.0106	HOMO-3 → LUMO (16) HOMO-2 → LUMO (31)
	$S_0 \rightarrow S_8$:	303	0.0281	HOMO → LUMO+6 (33))
	$S_0 \rightarrow S_{14}$:	286	0.0244	HOMO-7 → LUMO (25)
	$S_0 \rightarrow S_{15}$:	284	0.0754	HOMO-6 → LUMO (25)
	$S_0 \rightarrow S_{16}$:	283	0.0189	HOMO → LUMO(+4) (19) HOMO → LUMO+5 (20)
	$S_0 \rightarrow S_{17}$:	282	0.0172	HOMO-3 → LUMO+2 (13)
	$S_0 \rightarrow S_{18}$:	281	0.0159	HOMO-2 → LUMO+1 (23)
	$S_0 \rightarrow S_{19}$:	280	0.0204	HOMO-8 → LUMO (15)

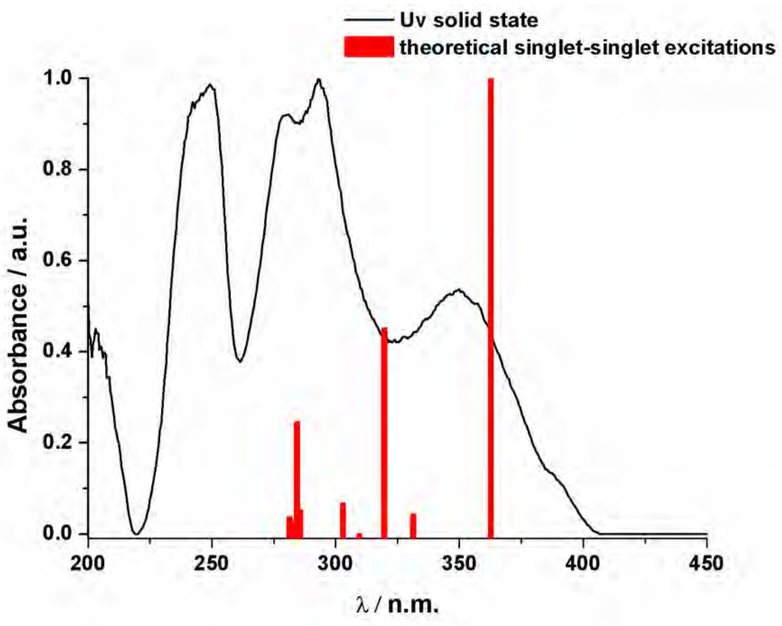

Figure 32. Top: Experimental UV-Vis solid state absorption spectrum (black line) and TD-DFT singlet–singlet excitations (red bars) for model systems **8a**.

The most intense TD-DFT singlet–singlet excitations for model $[Au(C_6Cl_5)_2Tl([9]aneN_3)]_2$ **8a** appear between 280 and 363 nm. These values are in agreement with the experimental excitation spectrum for complex **8** for the singlet-singlet transition, which shows a maximum at 249 and 293 nm in the UV-Vis absorption spectrum in solid state. If we analyse the TD-DFT results for model **8a** we can observe that the main contribution of the most intense computed singlet-singlet electronic transition at 363 nm arises from a HOMO-LUMO transition. From the population analysis results (Table 18), this excitation can be attributed to a metal-centred transition between the two fraction of interacting $Au(C_6Cl_5)_2$-Tl units with a small charge transfer involving the $[9]aneN_3$ ligand (see Figure 33). In addition, also the less intense electronic transition at 331 nm is due to a charge transfer centred mainly on the metal centers (HOMO(-1)-LUMO). Instead, other intense singlet-singlet excitations at higher energy (between 320 to 280 nm) consist of transitions between perchlorophenyl-based orbitals (HOMO-2, HOMO-3, HOMO-6 and HOMO-7) and the metal-based LUMO orbital with some exceptions; while the highest energy electronic transition (282 nm) is due to a $\mathbf{L_5}$-thallium charge transfer, and those at 303, 284ì3 and 281 can be attributed to metal-perchlorophenyl or perchlorophenyl-perchlorophenyl electronic transitions.

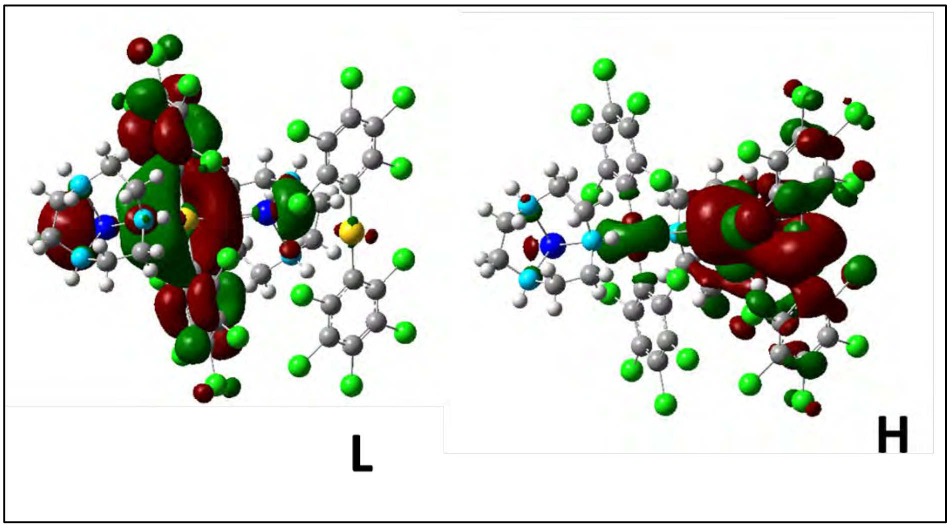

Figure 33. Most important frontier molecular orbitals (isovalue = 0.02) for model system **8a** involved in the singlet- singlet transition at 362 nm (H=HOMO; L=LUMO).

2.3.6 Conclusions

The use of the **L_4** ligand allows the generation of new heterometallic systems containing gold-thallium metallophilic interactions with different structural arrangements. Despite the known photophysical properties of the 1,10-phenanthroline unit contained in the macrocyclic system, all the synthesized systems do not show luminescent emissions in solid state, probably due to the quenching generated by the formation of a ligand-thallium complex in solution. On the other hand, the luminescent properties of **8** is directly correlated to the Au(I)−Tl(I) arrangement more than the Au(I)-Tl(I) distances found in the complex. In this case, the different dimensionality of the macrocyclic system as well as the different donor atoms seem to influence the structural arrangement and the photophysical properties as it can be compared with complexes **1**-**6**. However, despite the fluorescent nature of the transition responsible for the emission of **8**, also in this case the computational studies show that the luminescent emission mainly arise from the interacting metals. In this case, the macrocyclic ligand acts as a spectator that condition the disposition of these metal centres, therefore tuning the luminescence as a consequence of the types of Au(I)···Tl(I) interactions formed.

2.4 Functionalized macrocyclic systems

2.4.1 Introduction

Thanks to the results obtained in the synthesis of the heterometallic compounds previously shown, it can be established that the metallophilic interactions, as well as the nature of ligands used play an important role in determining the optical properties of the resulting compounds showing Au(I)-Tl(I) interactions. In particular, the presence of metallophilic interactions can be strongly influenced by the coordination capacity of the ligands used to support these weak interactions. The number and nature of donor atoms as well as the structural rigidity of the ligand play a determining role both for the number of metallophilic interactions and for their strength, proportional to the metal···metal distance.

The synthesis of transition metal complexes with tuneable photochemical properties is one of the most important challenges in this issue, and the rational design of ligands that can control the self-assembly process in the formation of these complexes is a key factor in these studies. In particular, mixed thia-aza donor macrocyclic ligands are ideal candidates for this goal because their sizes can largely control their coordination chemistry, furthermore their donor properties can be modified by adding pendant substituents that increase the coordination ability of the starting macrocyclic ligands.

Taking all the above into account, we decided to study the reactivity of the quinoline pendant arm derivatives of **L_3** and **L_4** N-quinolinylmethyl-5-aza-2,8-dithia[9](2,9)-1,10-phenanthrolinophane (**L_6**) and N-quinolinylmethyl-1-oxo-7-aza-4,10-dithiacyclododecane (**L_7**), respectively (see Figure 34) with the hetero-dimetallic complex $[AuTl(C_6X_5)_2]_n$ (X=F,Cl) in different molar ratios. Our goal was to study the influence of the number of donor atoms present in the ligand both on the nuclearity and on the photophysical properties of the complexes obtained. Furthermore, we were also interested in analysing the relationship between the number of metal-metal interactions present in the complexes with their emission wavelengths.

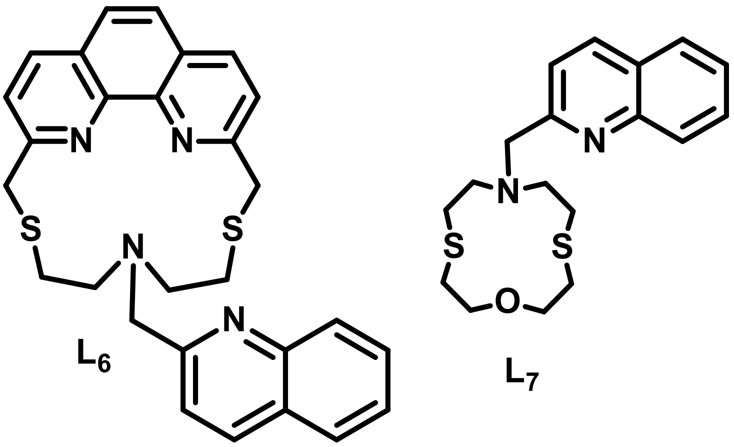

Figure 34. Quinoline pendant arm derivatives of **L$_3$** and **L$_4$** studied.

2.4.2 Synthesis and characterization

We have studied the reactivity of the hetero-dimetallic gold(I)/thallium(I) complex [AuTl(C_6X_5)$_2$]$_n$ (X=F,Cl) against the macrocyclic ligands **L$_6$** and **L$_7$** in different metal-to-ligand molar ratios. The coordination proprieties of the ligands, as well as the molar ratios employed, can influence the dimensionality/nuclearity of the complexes obtained and, hence, the number of intermetallic interactions present in them (Scheme 3). Consequently, compounds with different solid-state structures and optical properties can be obtained.

By reaction of the polymeric gold(I)/thallium(I) compound with equimolecular amounts of the macrocyclic ligands in THF, compounds of different nature are obtained depending on the ligand employed. Thus, the incorporation of methylquinoline pendant-arms in **L$_{6,7}$** leads to dinuclear complexes [{Au(C_6F_5)$_2$}{Tl(**L$_{6,7}$**)}] (**13, 15**) with a L-Tl-Au similar disposition of metals. Unfortunately, the complexes **11**, **12** obtained from the reaction of the respective macrocyclic derivatives (**L$_6$**, **L$_7$**) with the precursor [Au(C_6Cl_5)$_2$Tl]$_n$, we cannot confirm the presence of metallophilic interactions given the impossibility of obtaining single crystals with sufficient quality for X-ray diffraction analysis. Taking into account the higher number of donor atoms present in **L$_6$** and **L$_7$**, we thought to the possibility for them to act also as bridging ligands. Therefore, we decided to carry out the reactions of these two ligands with higher amounts of thallium. Treatment of **L$_6$** with [Au(C_6F_5)$_2$Tl]$_n$ in a Tl/**L** 2:1 molar ratio led to the formation of the new octanuclear compound [{Au(C_6F_5)$_2$Tl}{Au(C_6F_5)$_2$}{Tl(**L$_6$**)}]$_2$ (**14**). This is a discrete macromolecule in which the mixed-donor ligand **L$_6$** bridges two thallium(I) centers through the sulphur-nitrogen atoms of macrocyclic derivative, and that displays Tl···Au···Tl···Au interactions. In contrast, when the same reaction is carried out with **L$_7$** instead of **L$_6$**, the polymeric compound $[\{Au(C_6F_5)_2Tl\}\{Au(C_6F_5)_2\}\{Tl(\mathbf{L_7})\}]_n$ (**16**), featuring a Tl/**L** ratio of 2:1, is obtained; This is a polymeric system in which the mixed-donor ligand $\mathbf{L_7}$ bridges only one thallium(I) center through the sulphur-nitrogen-oxygen atoms of the macrocyclic derivative, given the reduced coordinating capacity of the macrocyclic unit of $\mathbf{L_7}$ compared to that of the $\mathbf{L_6}$. This main difference highlights the importance of the number of donor atoms and the dimensionality of macrocyclic system present in the ligand, a key factor in determining the dimensionality and nuclearity of the compounds obtained.

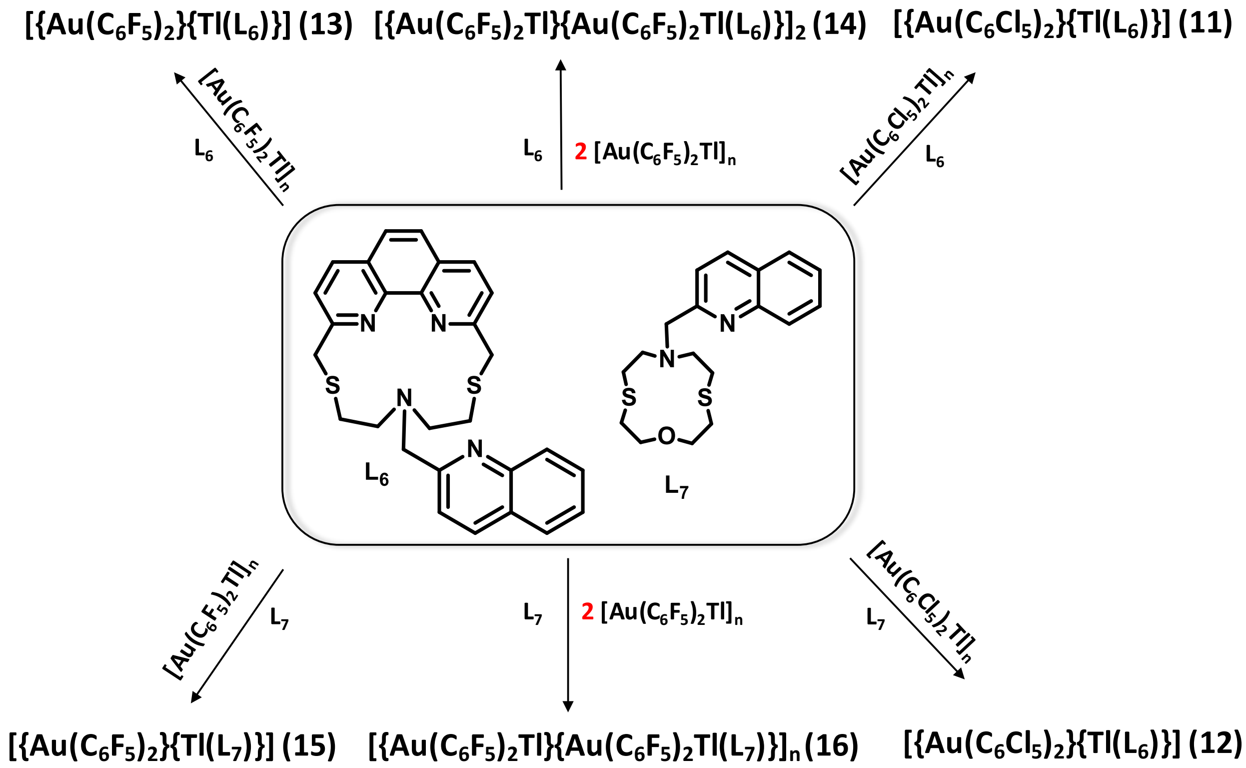

Schema 3

All the complexes are stable in air and moisture for long periods at room temperature, and they are soluble in O-donor solvents such as tetrahydrofuran or acetone, partially soluble in dichloromethane or diethyl ether, and insoluble in hexane. Their elemental analyses and spectroscopic data are in according with the proposed stoichiometry (see Experimental section).

The IR spectra of compounds **11-16** display, among others, absorption bands arising from the pentahalophenyl groups bonded to gold(I) at about 1500, 950 and 780 cm^{-1} (C_6F_5) and at about 834 and 614 cm^{-1} (C_6Cl_5). Complexes **11-16** also display the absorption bands corresponding to quinoline ligands between 1590 and 1770 cm^{-1}.

The conductivity measurements of **11-16** in acetone solution are in according with a dissociation process into $[Au(C_6F_5)_2]^-$ and $[Tl(L)]^+$ ions when dissolved, since they behave as 1:1 electrolytes.

On the other hand, their ^{19}F NMR spectra in [D_8]-tetrahydrofuran resembles that of the gold(I) precursor $NBu_4[Au(C_6F_5)_2]$, showing signals at about -116, -164 and -166 ppm with the characteristic pattern of pentafluorophenylgold(I) derivatives (see Experimental Section). The ^1H-NMR spectra of complexes **11, 13** and **14** show a broadening and slightly shifted signals if compared to those observed in the spectra of the free ligands, so we can conclude that the thallium centre remains coordinated to the ligand in solution. A singlet at around 4.0 (2H) ppm is observed corresponding to the protons of the methylene group bridging the quinoline moiety to the macrocyclic framework. The signals of the aliphatic protons of the macrocyclic ligand appear as multiplets centred between 2.78-3.16 (8H) and 3.93-4.48(4H) ppm, while the signals due to the aromatic protons of the quinoline groups arise as well defined resonances between 7.52 and 8.47 (12H) ppm.

A similar spectrum is observed for the complexes **12**, **15** and **16**. Thus, in these cases it is present a singlet at around 4.02-4.19 (2H) ppm corresponding to the protons of the methylene group bridging the quinoline moiety to the macrocyclic framework. The signals of the aliphatic protons appear as multiplets at about 2.78-3.54 (12H) and 3.8 (4H), while the signals due to the aromatic protons of the quinoline groups arise as well defined resonances between 7.54 and 8.39 (6H) ppm.

Finally, the MALDI(-) mass spectra of the new products show the peak corresponding to the $[\{Au(C_6X_5)_2\}_2Tl]^-$ anion at *m/z* = 1594 (**11**, **12**) or 1267 (**14-16**), or as well as a signal corresponding to $[Au(C_6X_5)_2]^-$ at *m/z* = 695 (**11**, **12**) or 531 (**14**-**16**) are observed, the latter appearing as parent peak in all the cases. In their MALDI(+) mass spectra, peaks due to the fragment $[Tl(L)]^+$ appears at *m/z* = 687 (**11, 13, 14**) or 553 (**12**, **15, 16**). In all of them, the experimental isotopic distributions are in agreement with the calculated ones.

2.4.3 Crystal structures

The crystal structures of complexes **13**-**16** were established by X-ray diffraction studies from single crystals grown by slow diffusion of n-hexane (**13**-**16**) into a saturated solution of the complex in toluene **(13**, **14**) or dichloromethane (**15**, **16**). Unfortunately, despite the numerous efforts made, it was not possible to obtain suitable crystals for determining the crystalline structure of the complexes **11** and **12** given their poor solubilities.

Despite the different size and coordination ability of the macrocytic unit present in the ligands used for the synthesis of the complexes, the hetero-metallic compounds **13** and **15** show a very similar structural arrangement: both can be described as molecular systems containing only one gold(I)-thallium(I) metallophilic interaction supported by the coordination of the respective ligands (see

Figure 35 and Tables 19 and 20). The intermetallic distances within the cations are different depending on the macrocyclic ligand employed, showing a Au-Tl distance of 3.0597(4) Å in the 5-aza-2,8-dithia[9](2,9)-1,10-phenanthrolinophane derivative **13**, shorter than that of 3.2339(4) Å observed in the [12]aneNS_2O derivative complex **15**.

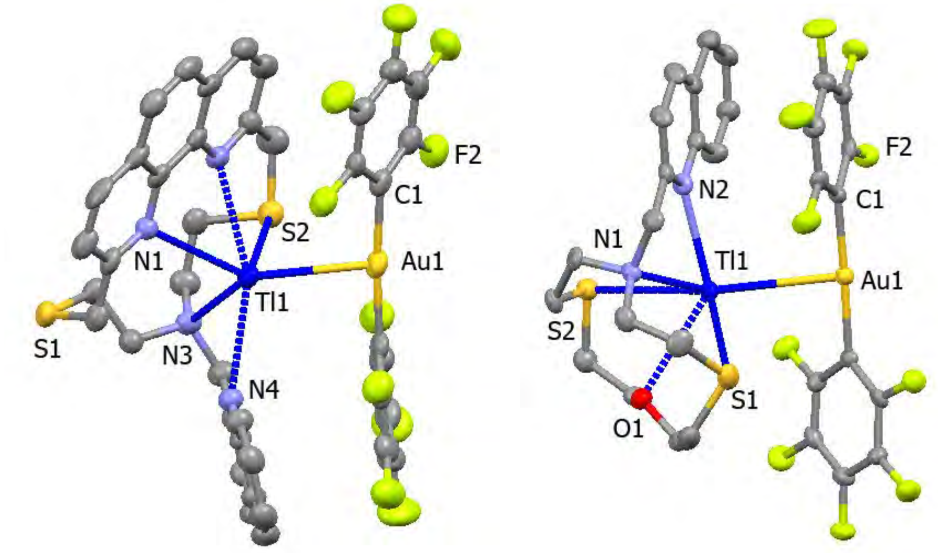

Figure 35. Molecular structure of compound **13** (left) and **15** (right) with the labelling scheme for the atom positions. Hydrogen atoms and solvent molecule are omitted for clarity and ellipsoids are drawn at the 30% level.

Table 19. Selected bond lengths [Å] and angles [°] for **13**.

Tl(1)-Au(1)	3.0597(4)	Tl(1)-N(1)	2.9162(58)
Au(1)-C(1)	2.043(7)	Tl(1)-N(2)	2.9019(54)
Au(1)-C(7)	2.034(7)	Tl(1)-N(3)	2.9634(53)
Tl(1)-S(2)	3.1358(17)	Tl(1)-N(4)	2.9443(55)
Au(1)-Tl(1)-S(2)	71.08(3)	C(7)-Au(1)-C(1)	175.6(3)

Table 20. Selected bond lengths [Å] and angles [°] for **15**.

Au(1)-Tl(1)	3.2339(4)	Tl(1)-N(1)	2.778(6)
Au(1) -C(1)	2.046(7)	Tl(1)-N(2)	2.664(7)
Au(1)-C(7)	2.042(7)	Tl(1)-S(1)	3.1835(2)
Tl(1)-O(1)	3.0339(1)	Tl(1)-S(2)	3.128(2)
C(7)-Au(1)-C(1)	177.2(3)	N(2)-Tl(1)-N(1)	62.7(2)
N(1)-Tl(1)-S(2)	69.42(14)	N(2)-Tl(1)-S(2)	81.25(14)
N(2)-Tl(1)-Au(1)	97.52(14)	S(2)-Tl(1)-Au(1)	157.72(4)

Both of them are longer than the sum of Au(I) and Tl(I) ionic radii (2.96 Å)[150] but similar to those observed in related systems ([Tl(2,2'-bipy)[Au(C_6F_5)$_2$] (3.0120(6))[118] or Tl(1,10-Phen)][Au(C_6F_5)$_2$][118] (3.0825(4)) similar to the complex **13**; [Au_2Tl_2(C_6Cl_5)$_4$](PhMeCO)] (3.2133(3))[70] similar to the complex **15**). In addition, they are also longer than those found in the metallocryptate (TlAu$_2$(P_2-phen)$_3$](PF$_6$)$_3$ ((P_2-phen =2,9-bis(diphenylphosphino)-1,10-phenantroline)[88] (2.9171(5) and 2.9109(5) Å).

The Tl-N bond distances are quite different in **13** and **15** crystal structures, with values between 2.9019(54)-2.9634(5) Å in **13** and between 2.664(7)-2.778(6) Å in **15**. While the Tl-N distances from the 1,10-phenatroline and quinoline framework in the derivative **13** are longer to those reported in thallium complexes containing these aromatic system[143],[151]-[153], the derivative **15** shows a Tl-N distance from the quinoline unit more similar to those reported previously in the literature and described for the thallium(I) derivative [Tl(1,10-phenantroline)][Au(C_6F_5][118]. Finally, the aliphatic Tl-N distances from the macrocyclic frameworks (2.9634(53) in **13**; 2.778(6) in **15**) are quite similar to those described for the thallium(I) complex with cyclic N- or N,S-donor ligands ([Tl(Me$_3$[9]aneN$_3$)]PF$_6$ (2.59(2)-2.63(1) Å, similar to the complex **15**[126]; [Tl([18]aneN$_2$S$_4$)]PF$_6$ (2.834(4) and 2.992(4) Å),[128] similar to the complex **13**).

Regarding the Tl-S bonds, the distances are similar in both compounds (3.1358(17) for **13**; 3.128(2)-3.1835(2) for **15**); the main difference between the two structures lies in the lack of coordination of the sulfur atom S(1) towards the thallium atom in **13**. This can be justified by observing the conformation of the macrocyclic unit which prevents the coordination of the heteroatom, giving preference to the coordination of the three nitrogen atoms and the remaining sulfur (S(2)) atom.

Nevertheless, both complexes show Tl-S distances very similar to those reported for [Tl([9]aneS$_3$)]PF$_6$ (3.092(3)-3.114(3) Å)[129]. In addition, they are shorter than in the related Au/Tl compounds with crown thioethers $[\{Au(C_6Cl_5)_2\}_2Tl_2([24]aneS_8)]_n$ and (3.256(7)-3.587(7) Å), $[\{Au(C_6F_5)_2\}_2Tl_2([24]aneS_8)]$ (3.201(2)-3.418(3) Å), as well as in the thallium derivatives $[Tl([24]aneS_8)]PF_6$ (3.2413(11)-3.4734(14) Å))[130].

As commented above, the increase of the Tl/**L** reaction molar ratio from 1:1 to 2:1 leads to drastic modifications in the dimensionality/nuclearity of the complexes obtained. In the case of complex **14**, it crystallizes as an octanuclear discrete complex where the functionalized macrocyclic system acts as a bridge, simultaneously complexing two atoms of thallium thanks to the high number of donor atoms (see Figure 36 left and Table 21). The central core of this crystal structure is a tetranuclear L-Tl-Au-Tl-L unit (see Figure 36 right and Table 21) that is connected to another analogous tetranuclear fragment through bridging Tl-S bonds. The Au-Tl distances (3.1996(9)-3.4517(8) Å), are considerably longer than in **13** (3.0597(4) Å) or to those observed in related systems containing the 1,10-phenantroline fragment $(TlAu_2(P_2\text{-phen})_3](PF_6)_3$ ((P_2-phen =2,9-bis(diphenylphosphino)-1,10-phenantroline)[88] 2.9171(5) and 2.9109(5) Å; [Tl(1,10-Phen)][$Au(C_6F_5)_2$][118] 3.0825(4)).

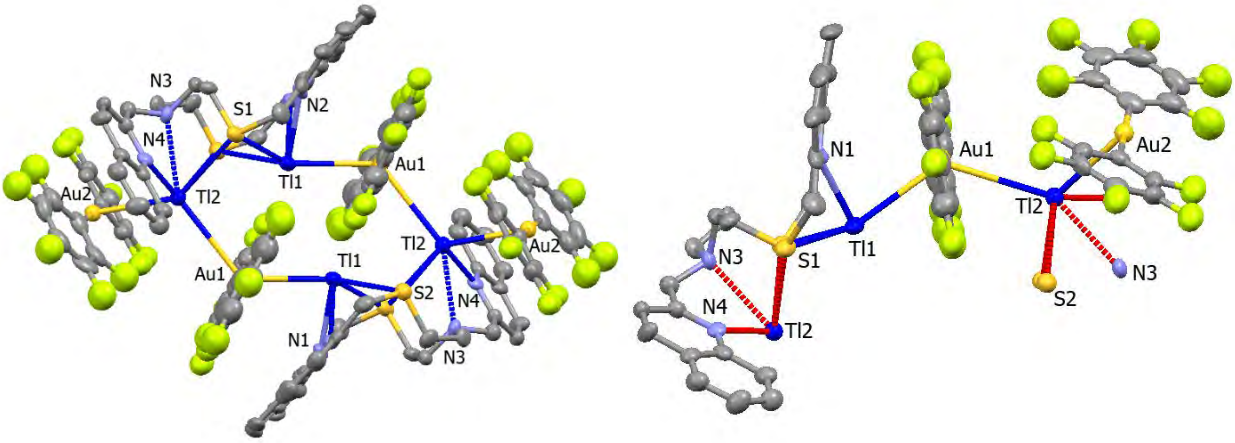

Figure **36.** Molecular structure of compound **14** (left and right) with the labelling scheme for the atom positions. Hydrogen atoms are omitted for clarity and ellipsoids are drawn at the 30% level.

Table 21. Selected bond lengths [Å] and angles [°] for **14**.

Au(1)-Tl(1)	3.1996(9)	Au(2)-Tl(2)	3.0419(7)
Au(1)-Tl(2)	3.4517(8)	Au(2)-C(20)	2.052(15)
Au(1)-C(1)	2.121(9)	Au(2)-C(26)	2.034(13)
Au(1)-C(7)	2.081(9)	Tl(2)-N(3)	2.824(10)
Tl(1)-N(1)	2.667(12)	Tl(2)-N(4)	2.712(10)
Tl(1)-N(2)	2.689(11)	Tl(2)-S(1)	3.5139(29)
Tl(1)-S(1)	3.2551(36)	Tl(2)-S(2)	3.4644(34)
Tl(1)-S(2)	3.2831(30)		
Tl(1)-Au(1)Tl(2)	126.91(3)	C(20)-Au(2)-Tl(2)	87.9(4)
C(1)-Au(1)-Tl(1)	103.6(4)	C(26)-Au(2)-Tl(2)	97.0(3)
C(1)-Au(1)-Tl(2)	91.5(4)	C(26)-Au(2)-C(20)	174.9(5)
C(7)-Au(1)-Tl(1)	80.6(3)	N(1)-Tl(1)-Au(1)	86.9(2)
C(7)-Au(1)-Tl(2)	92.0(3)	N(1)-Tl(1)-N(2)	60.8(4)
C(7)-Au(1)-C(1)	171.2(5)	N(2)-Tl(1)-Au(1)	79.4(2)
N(3)-Tl(2)-Au(1)	149.57(19)	Au(2)-Tl(2)-Au(1)	116.43(2)
N(3)-Tl(2)-Au(2)	90.68(19)	N(4)-Tl(2)-N(3)	63.5(3)
N(4)-Tl(2)-Au(1)	128.3(2)		
N(4)-Tl(2)-Au(2)	85.6(2)		

The Tl-N distances are shorter than those described for complex **13** and observing carefully the structural arrangement of this system, we can clearly see that the shortening of these distances is mainly due to the proximity of the thallium metal centres either to the 1,10-phentantroline unit incorporated in the macrocyclic system or to the N-Me-quinoline moiety, which support the system by coordination of the nitrogen atoms. In fact, the Tl-N distances are very similar to those reported in systems containing 1,10-phenantroline or quinoline framework where the position of the aromatic system is not forced by the presence of a macrocyclic system, which limits their conformational and coordination freedom[118],[140],[151]-[154].

Finally, unlike the Tl-N distances, the Tl-S distances are longer than those previously reported for the complex **13**; observing the structural arrangement, this fact can be justified by the simultaneous coordination of these heteroatoms towards two thallium atoms decreasing the strength and length of these interactions. However, at the same time, thanks to this double interaction an adequate coordination index is established, that guarantees the stabilization of the entire structure thanks to the support of ligands.

Finally, as in the case of the complex **14**, a variation in the structural arrangement is also observed for complex **16** by increasing the Tl/**L** ratio. In fact, this complex display polymeric chains of $[Tl(L)]$-$[Au(C_6F_5)_2]$-Tl-)]-$[Au(C_6F_5)_2]$ units linked via Au-Tl interactions. the Au-Tl bonds in this structure vary from 3.0808(8) to 3.3124(8) Å (see Table 22) and are similar to those observed in other related polynuclear Au/Tl systems with unsupported metal-metal interactions (2.9078(3)- 3.3205(3) Å) [155]-[164]. In addition, looking more closely at the crystalline packaging, we can observe that the entire polymeric system can be described as a linear Au(2)-Tl(2) chain where each thallium atom has a further Au(1)-Tl(1)-$\mathbf{L_7}$ ramification. However, while the metallophilic interactions observed in the polymeric system show relatively shorter distances than those encountered in the complex **14**, the Tl-N, Tl-O and Tl-S distances are quite similar to those described previously for the molecular unit. In addition, as shown in the complex **13**, also in this case it is observed that one of the sulfur atoms of the macrocytic unit [12]aneNS_2O acts as a bridge simultaneously coordinating the two thallium atoms present in the crystalline structure (Tl(1)-S(1) 3.1940(2); Tl(2)-Tl(1) 3.4339(3)).

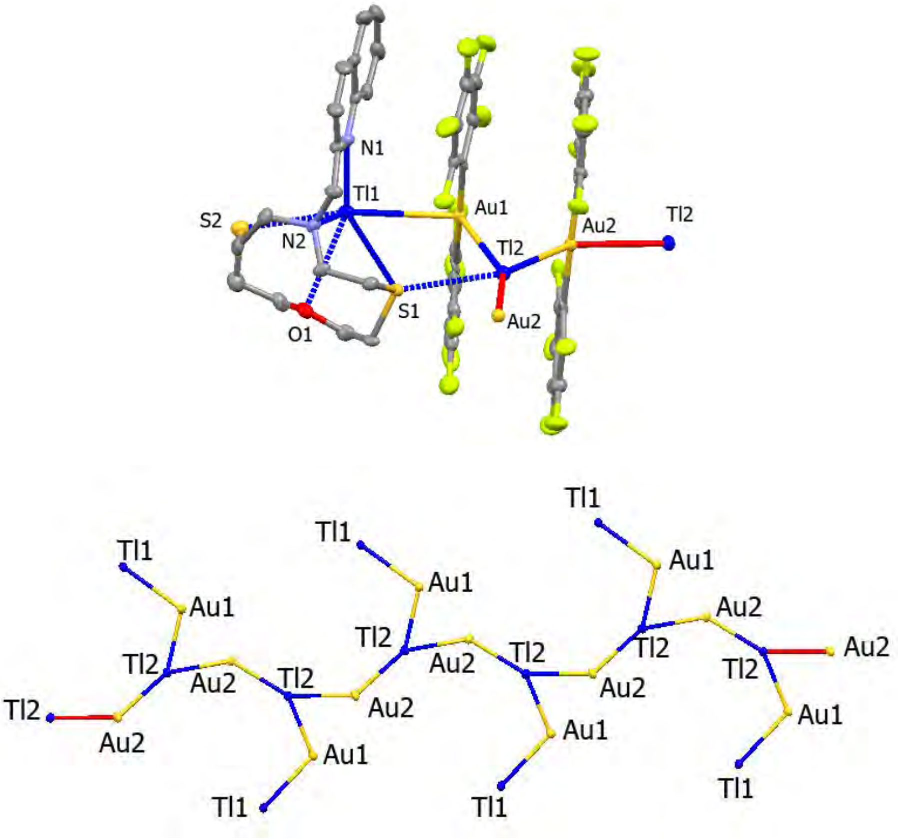

Figure **37.** Monomeric unit (up) and polymeric structure(down) of compound **16** with the labelling scheme for the atom positions. Hydrogen atoms are omitted for clarity and ellipsoids are drawn at the 30% level.

Table 22. Selected bond lengths [Å] and angles [°] for **16**.

Tl(1)-Au(1)	3.3124(8)	Tl(2)-S(1)	3.4339(3)
Tl(2)-Au(1)	3.0216(8)	Tl(1)-N(1)#2	2.684(11)
Tl(2)-Au(2)	3.0852(8)	Tl(1)-N(2)#2	2.733(10)
Tl(2)-Au(2)#1	3.0808(8)	Tl(1)-S(1)	3.1940(2)
Au(1)-C(1)	2.036(15)	Tl(1)-S(2)#2	3.152(3)
Au(1)-C(7)	2.046(16)	Tl(1)-O(2)	3.0128(2)
Au(2)-C(13)	2.019(14)		
Au(2)-C(19)	2.034(15)		
Au(2)#1-Tl(2)-Au(2)	146.72(2)	N(2)#2-Tl(1)-Au(1)	118.3(2)
Au(1)-Tl(2)-Au(2)	144.38(2)	N(2)#2-Tl(1)-S(2)#2	67.4(2)
Au(1)-Tl(2)-Au(2)#1	68.593(18)	Tl(2)#3-Au(2)-Tl(2)	138.13(2)
S(2)#2-Tl(1)-Au(1)	66.37(6)	C(13)-Au(2)-C(19)	174.0(5)
N(1)#2-Tl(1)-Au(1)	98.5(3)	Tl(2)-Au(1)-Tl(1)	113.08(2)
N(1)#2 Tl(1)-S(2)#2	109.2(2)	C(1)-Au(1)-C(7)	172.8(6)
N(1)#2-Tl(1)-N(2)#2	61.9(3)		

Symmetry transformations used to generate equivalent atoms:

#1 -X,1/2+Y,1/2-Z; #2 +X,-1/2-Y,1/2+Z #3 1-X,-1/2+Y,1/2-Z.

Furthermore, in all the complexes π-stacking contacts can be observed between either the aromatic fractions of **$L_{6,7}$** and the perfluorophenyl unit or between pentafluorophenyl rings (3.742 Å for complex **13**; 3.891 and 4.014 Å for complex **14**; 3.625 for complex **15;** 3.626 and 3.798 Å for complex **16**) (see Figure 38).

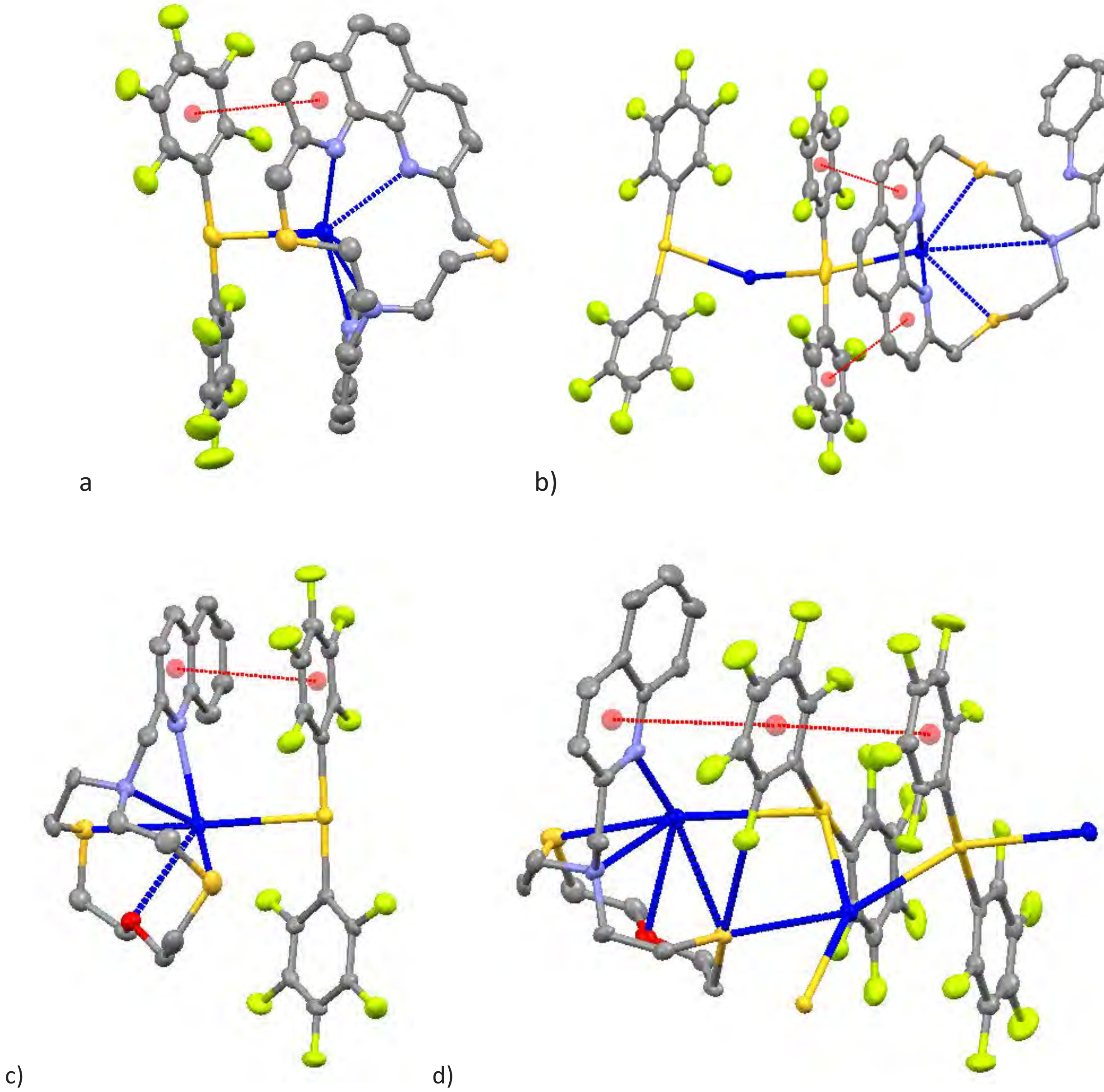

Figure 38. π-stacking (red line) contact of complex a) **13**, b) **14**, c) **15**, d) **16.**

2.4.4 Photophysical Properties

The absorption spectra of all the complexes were recorded in THF solutions (ca. 5 x 10^{-4} M). Complexes **11**-**16** show a broad band at high energy that contains the high energy bands present in the spectra of the heterometallic precursors $NBu_4[Au(C_6X_5)_2]$ and $[Au(C_6X_5)_2Tl]_n$ (X=F, Cl), which have been previously assigned to π→π* and Au→π* transitions in the bis(pentahalophenyl)gold(I) units[132]-[133]. Similarly, the 1,10-phenantroline and quinoline framework show a absorption band at 270 nm and 310 nm respectively, in the same energetic zone, assigned to a π→π* or n→π* transition, which can overlap to the intense bands due to the heterometallic precursors. On the other hand, by looking more closely at the spectrum of the complexes **13**, **14** and **15**, **16**, it can be deduced that the change in stoichiometry does not affect the absorption spectrum. This indicates a dissociative process that involves the breaking of the metallophilic interactions due to the solvation of the different ionic species by the solvent. For this reason, these systems are generally extremely soluble in coordinating solvents and almost totally insoluble in non-coordinating ones. The same conclusion can be made by observing the absorption spectrum of the complexes **11** and **12**.

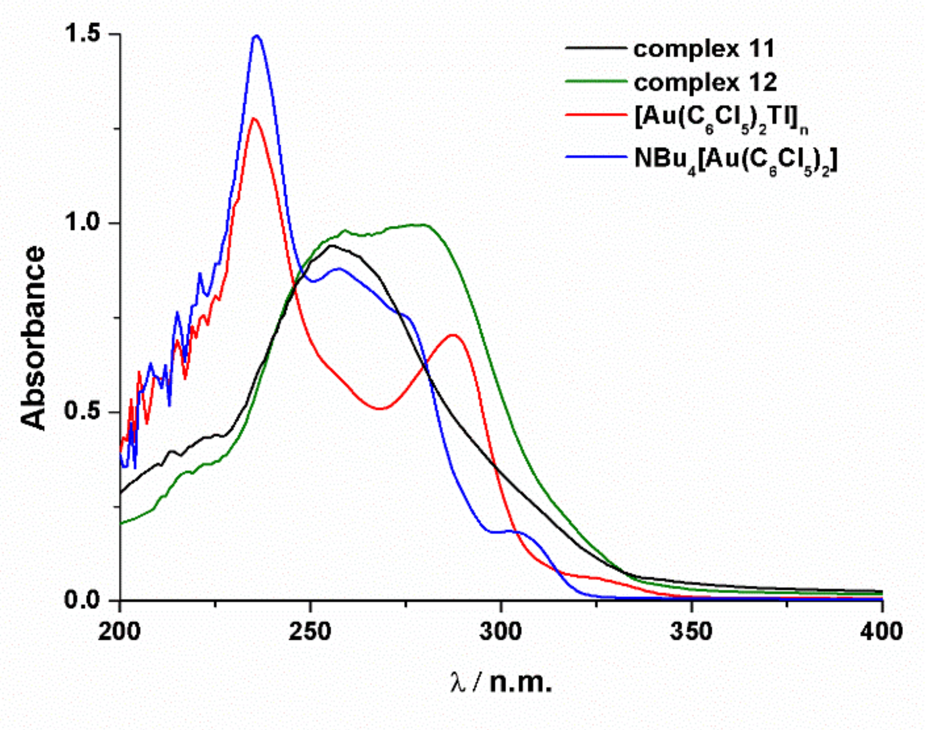

Figure 39. Absorption spectra of complexes **11** and **12** and the gold precursors $NBu_4[Au(C_6Cl_5)_2]$ and $[\{Au(C_6Cl_5)_2\}Tl]_n$ in THF solution (C ≈ 2.5x10^{-5} M).

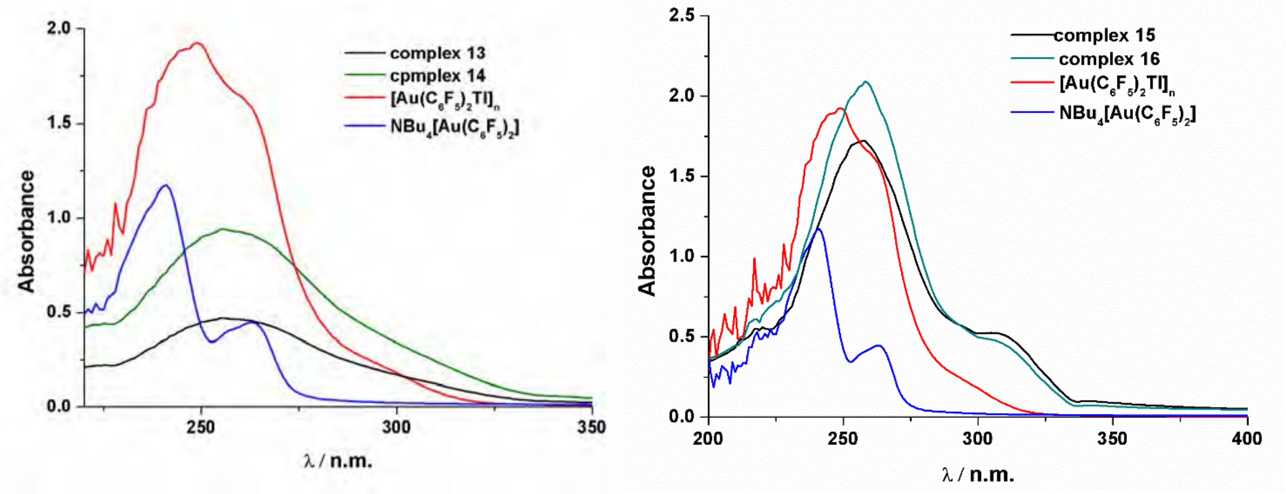

Figure 39. Absorption spectra of complexes **13** and **14** (left), **15** and **16** (right) and the gold precursors $NBu_4[Au(C_6F_5)_2]$ and $[\{Au(C_6F_5)_2\}Tl]_n$ in THF solution (C ≈ 2.5x10^{-5} M).

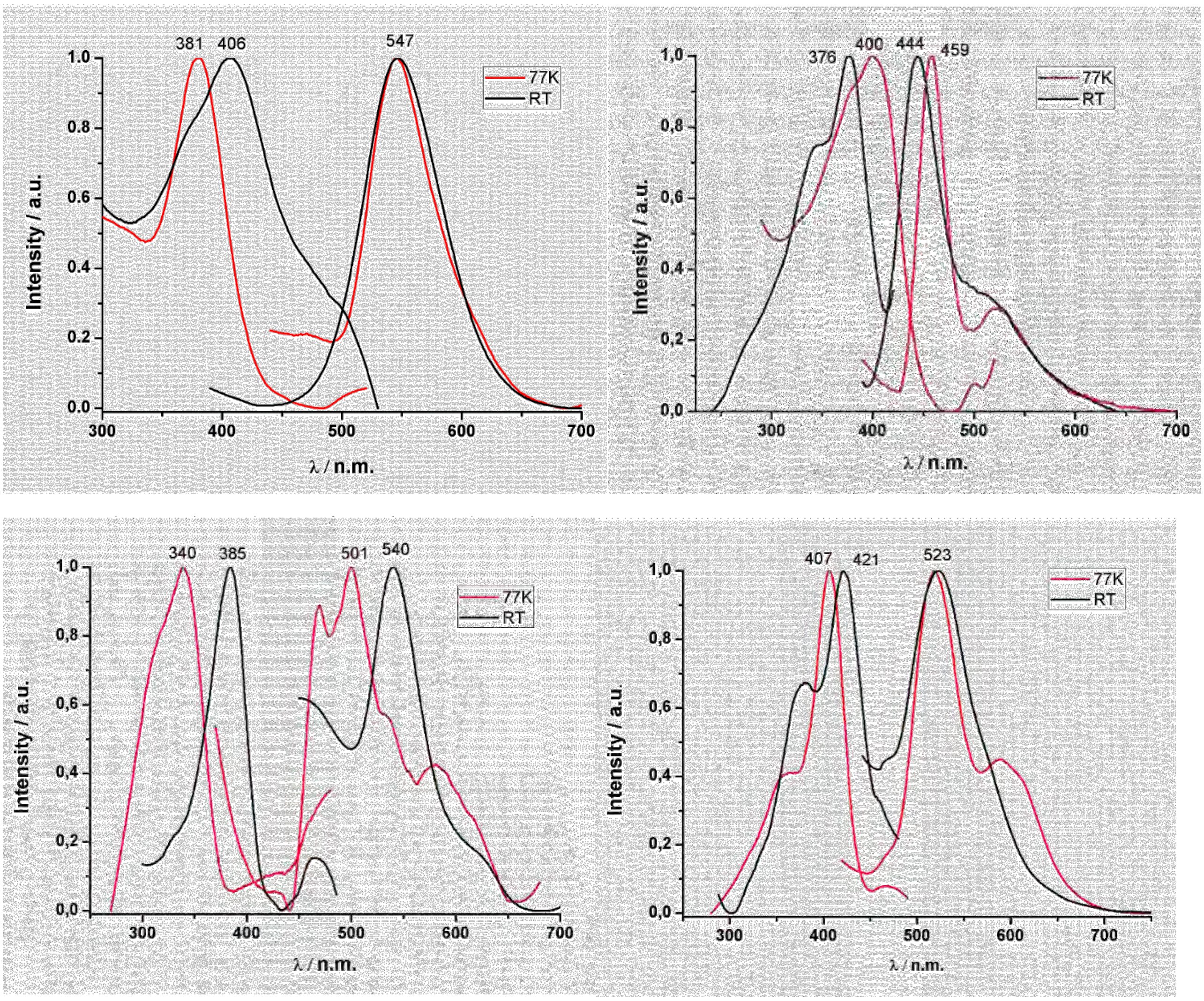

Figure 40. Excitation and emission spectra for complex **12** (up, left), **14** (up, right), **15** (down, left) **16** (down, right) in the solid state at RT and 77 K.

Table 23. Photophysical properties of complexes **11**-**16**

	UV-vis in THF (nm)	Solid (RT) em(exc)	Solid (77K) em (exc)	τ (ns)	Φ (%)
Complex 11	253 (ε = 42333)	-	-	-	-
Complex 12	279 (ε = 63333)	547 (381)	547 (406)	432 ± 8	30.0
Complex 13	256 (ε = 41600)	-	-	-	-
Complex 14	257 (ε = 40789)	444 (376)	459 (400)	280 ± 2	5.0
Complex 15	256 (ε = 60326) 306 (ε = 20800)	523(421)	523(407)	789 ± 20	10.0
Complex 16	257 (ε = 62545) 307 (ε = 20454)	540 (385)	501 (340)	1025 ± 22	11.0

Due to the great structural diversity displayed by the complexes here reported, which, as we have commented, is related to the binding properties of the ligand considered, we found very different optical behaviours in solid state. Thus, all the complexes are luminescent in solid state at room temperature and at 77 K, except complexes **11** and **13** which are not luminescent in solid state. Such behaviour is probably due to the formation of the species $[Tl(\mathbf{L_6})]^+$ which determines the quenching of the luminescent emission; This is an analogous behaviour observed for $\mathbf{L_4}$ containing the 1,10-fentrolin unit in the macrocyclic system. Moreover, all complexes do not display luminescence in solution, which is related to the absence or the rupture of metal-metal interactions promoted by the coordinating solvent (THF).

Thus, complexes **12** and **14**-**16** display emissions in solid state between 444 and 547 nm at room temperature, and between 459 and 547 nm when the measurements are carried out at the liquid nitrogen temperature (77 K) (see Figure 40 and Table 23). Taking the structural data into account, we can establish a relationship between the metal-metal distances and the emission energies for both complexes. For example, considering the number of metallophilic interactions present in the complexes **13** and **14**, it is clear that the increase in the number of Au-Tl contacts (from a single metallophilic interaction in the complex **13** to a Tl-Au-Tl-Au tetranuclear system in the complex **14**) limits the quenching mechanism caused by the coordination of phenanthroline macrocyclic system, allowing to obtain a luminescent system that has an emission at about 444 nm (459 nm at 77K). In addition, the luminescence of complex **14** is temperature dependent, and thus, measurements carried out in solid state at 77 K produce a red shift of the luminescent emissions (from 444 to 459 nm) similar to the behaviour found in other homo- and hetero-polynuclear gold complexes which could be related to the thermal contraction that leads to a reduction in the metal-metal distances reducing the band gap energy[85],[86],[88],[160],[167],[178]. Likewise, similar behaviour can be observed by comparing the photophysical properties of the complexes **15** and **16**: the formation of the Au-Tl polymer chain (complex **16**) leads to an decrease of the emission energy of the polyetheronuclear system with respect to the molecular system (complex **15**) thanks to the increase in the number of Au-Tl contacts.

Nevertheless, it is extremely interesting to note that, in the case of the complexes **12** and **16** the emission energy does not depend on the temperature. This phenomenon, which is described as luminescence rigidochromism [163], is not fully understood and is assigned to a substantial dependence of the emission maxima on the environmental rigidity; it has been described in other luminescent gold-heteropolinuclear systems [164].

Finally, In the case of complex **15**, its emission spectrum shows a broad band at 540 nm at room temperature and two bands at 77 K, one of high intensity placed at 501 nm and another one blue shifted (at 581 nm) of lower intensity (see Figure 41).

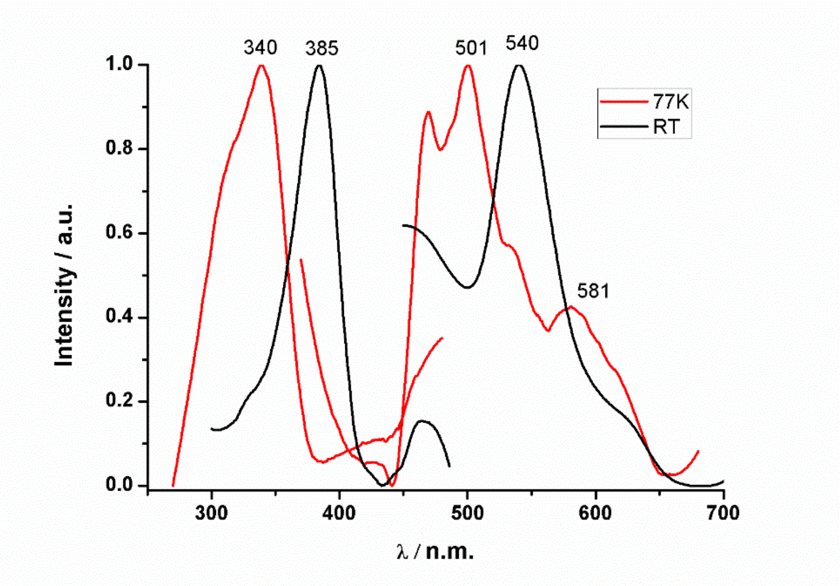

Figure 41. Excitation and emission spectra for complex **15** in the solid state at RT and 77 K.

2.4.5 Computational Study

In view of the results obtained by photophysical measurements and X-ray structural analysis, we performed single-point DFT calculations on simplified model systems of compounds **14**-**16**. Owing to the presence of different Au-Tl distances and arrangements in complexes **14**-**16** we built different dinuclear or tetranuclear model to represent the different coordination environments for each Tl(I) centres (see Figure 42).

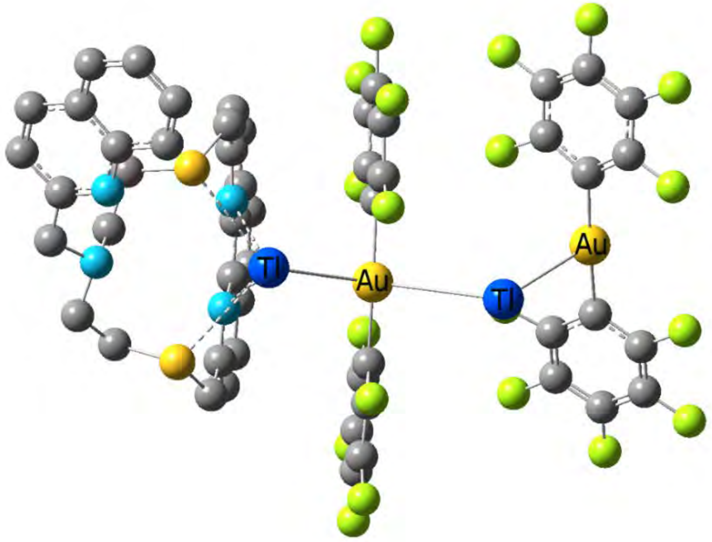

Model 14a

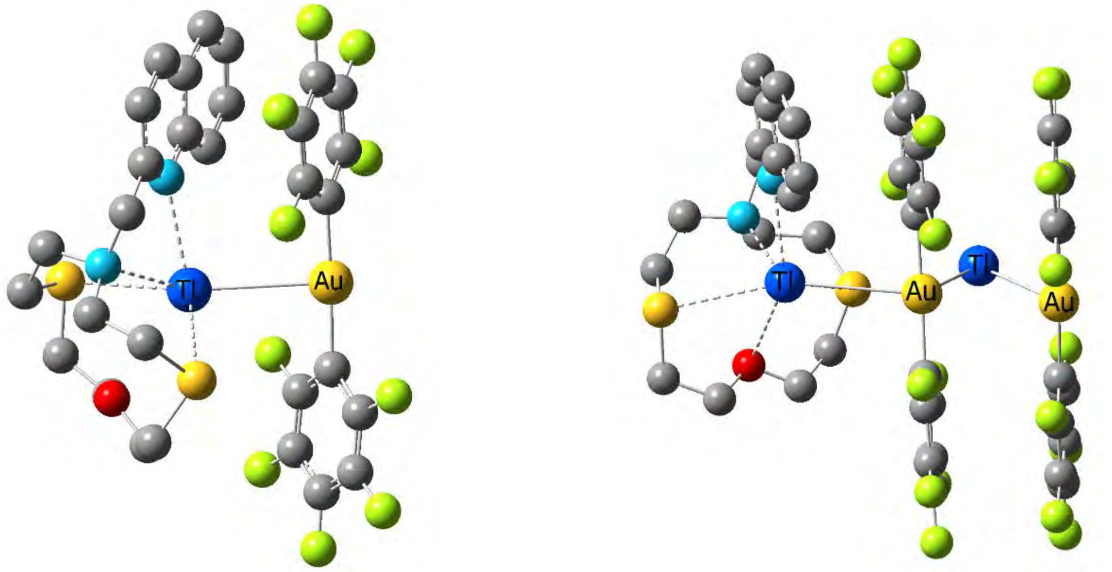

Model 15a

Model 16a

Figure 42. Theoretical model systems [{Au(C_6Cl_5)$_2$}{Tl($\mathbf{L_6}$)}{Au(C_6F_5)$_2$Tl}] (**14a**) (up), [{Au(C_6F_5)}Tl($\mathbf{L_7}$)] (**15a**) (left), [{Au(C_6F_5)$_2$}{Tl($\mathbf{L_7}$)}{Au(C_6F_5)$_2$Tl}] (**16a**) (right).

Given the large number of metal centers contained in complex **14** and the polymeric nature of the complex **16**, in both cases we have constructed tetranuclear models that adequately represent the different metallophilic interactions present in each structure.

Thus, model **14a** corresponds to the tetranuclear molecular found for complex **14**, representing the L···Tl(I)···Au(I)···Tl(I)···Au(I) interactions between two $[Au(C_6F_5)_2]^-$ anionic fragments and $[L(Tl)]^+$, Tl(I) cationic ones. At the same time, model **16a** corresponds to tetranuclear framework founds for complex **16** which represents two different Au(I)···Tl(I) interactions observed in the polymeric chain. Only model **15a,** corresponding to the dinuclear unit found for complex **15**, unequivocally represent the L···Tl(I)-Au(I) interaction between the $[Au(C_6F_5)_2]^-$ anionic fragment and the $[L(Tl)]^+$ cationic unit. It is important to underline that the construction of the models used to perform DFT and TD-DFT calculations of **14** and **16** is due to an adequate compromise between the number of considered metallophilic interactions and computational cost to more adequately describe the origin of the luminescence in the two complexes.

On one hand, for complexes **15** and **16** the lifetime measurements determined by the photon-counting technique in the solid state at room temperature could indicate that the emission probably originates from an excited state of triplet parentage and, consequently, it is tentatively assigned as phosphorescence. On the other hand, for complex **14**, given the smaller life time compared to the other two complexes, we hypothesize a fluorescent emission process responsible for the photophysical properties of the system.

A study of the molecular orbitals (MOs) along with a population analysis was used to check the contribution of each atom to each occupied/lowest orbital for all models. Figures 43-45 and Tables 24-26 display the most important frontier molecular orbitals (MOs) and the population analysis of those MOs, respectively. From these data we can anticipate the contribution of each part of the molecule to the frontier molecular orbitals.

In the case of the tetranuclear molecular model $[\{Au(C_6Cl_5)_2\}\{Tl(\mathbf{L_6})\}\{Au(C_6F_5)_2Tl\}]$ **14a** the population analysis of the highest occupied MOs shows that the HOMO orbital is mainly located on the ligand unit (49%) and the metal centers (Au/Tl 45%), while from HOMO−1 to HOMO−4 a clear main contribution from the C_6F_5 ligands is found with the exception of the HOMO-3 orbital whose electronic density is mainly localized on the organic lignad (93%). On the other hand, while the population analysis of the lowest empty orbital (LUMO) shows a main contribution from the ligand fragment (68 %) with a small contribution from gold atoms (23 %), the LUMO+2, LUMO+3 and

LUMO+5 orbitals are mainly located in the metallic fraction. Finally, the LUMO+1 and LUMO+4 are mainly located on the ligand unit.

Table 24. Population analysis (%) for model systems **14a**.

Model		**L_6**	**Au**	**Tl**	**C_6F_5**
14a	LUMO+5	17	19	47	17
	LUMO+4	86	3	8	3
	LUMO+3	0	17	74	9
	LUMO+2	7	28	48	17
	LUMO+1	92	3	4	2
	LUMO	68	23	8	1
	HOMO	49	16	29	6
	HOMO-1	3	17	3	77
	HOMO-2	0	5	1	93
	HOMO-3	96	1	3	0
	HOMO-4	2	20	3	75

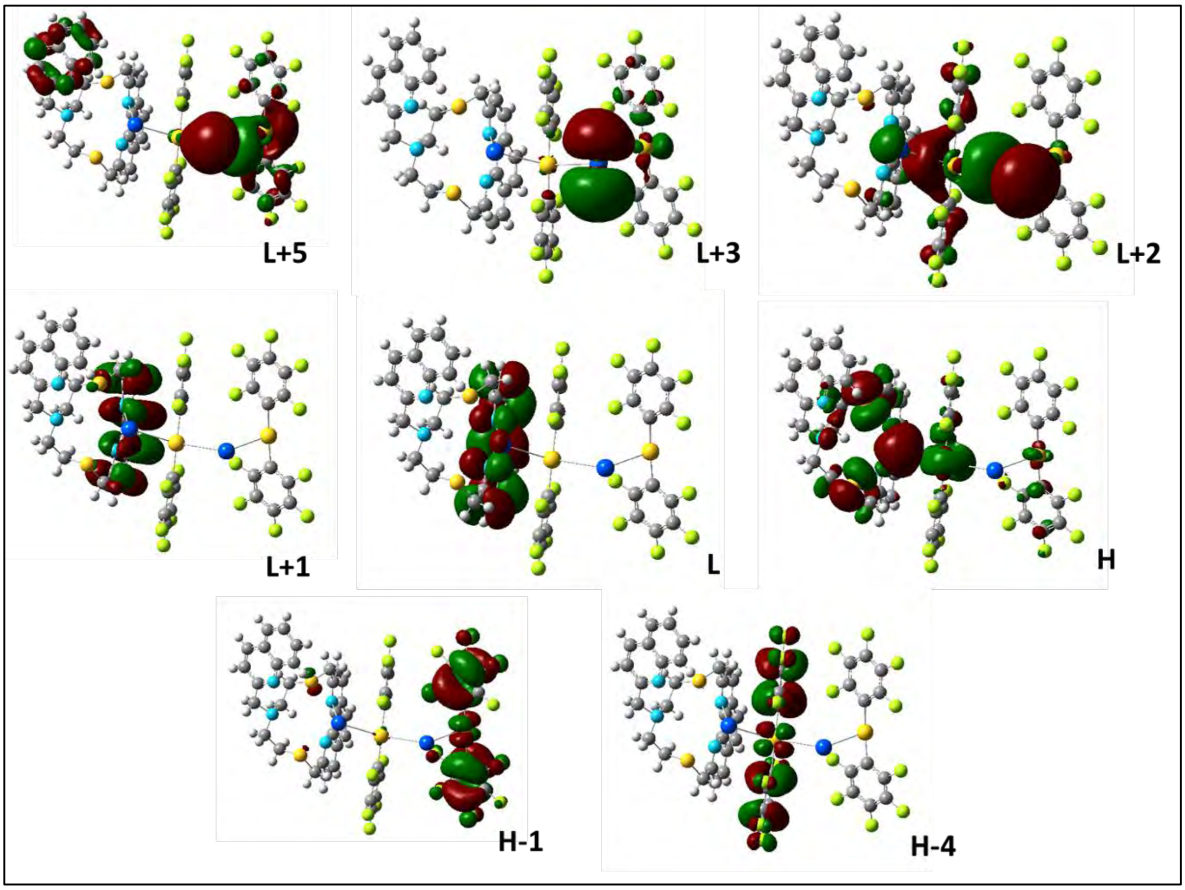

Figure 43. Most important frontier molecular orbitals (isovalue = 0.02) for model system **14a** (L=LUMO; H=HOMO).

A different behaviour can be observed for complex **15a** in which, while the highest occupied molecular orbital (HOMO) is mainly localized on the metal centres Au(I) and Tl(I) (67 %) with a small contribution from the ligand (28 %), the lowest empty molecular orbital (LUMO) is mainly localized on the ligand unit. Furthermore, while occupied frontier molecular orbitals from HOMO-1 to HOMO-4 are mostly located on $C_6F_5^-$ with a small contribution of Au(I), those from HOMO-5 to HOMO-10 show a mixed Au/$C_6F_6^-$/ligand character with a higher contribution of the **L₇** fragment. Finally, with the exception of the LUMO+ 1 where the electronic density is totally localized on ligand unit, from LUMO+2 to LUMO+4 show a mixed Au/Tl character.

Table 25. Population analysis (%) for model systems **15a**.

Model	Orbitals	Au	Tl	NS_2O-Q	C_6F_5
15a	L+4	8	44	30	18
	L+3	18	76	5	1
	L+2	18	50	20	13
	L+1	12	13	74	1
	L	5	8	86	1
	H	29	38	28	5
	H-1	24	1	1	74
	H-2	13	2	5	81
	H-3	2	1	3	95
	H-4	15	3	5	77
	H-5	31	9	49	11
	H-6	1	1	92	6
	H-7	12	3	84	1
	H-8	22	9	47	23
	H-9	19	2	19	59
	H-10	11	3	85	2

Model **16a** shows common features with the previous model but also some differences. While the HOMO orbital is mainly located on the $Au(C_6F_5)_2^-$ moiety, the LUMO orbital, as in model **15a**, displays predominantly a ligand character. The rest of occupied molecular orbitals from HOMO-1 to HOMO-14 show a strong contribution of the C_6F_5 unit with a smaller contribution from each metal although some exceptions are observed (HOMO-5 and HOMO-6 show a strong contribution from metal centers; HOMO-13 and HOMO-14 are prevailingly located on the ligand). Finally, the rest of empty molecular orbitals from LUMO+1 to LUMO+4 show a strong contribution of Au/Tl metals with the only exception of LUMO+2 that present a greater contribution of quinoline derivative **L₇**.

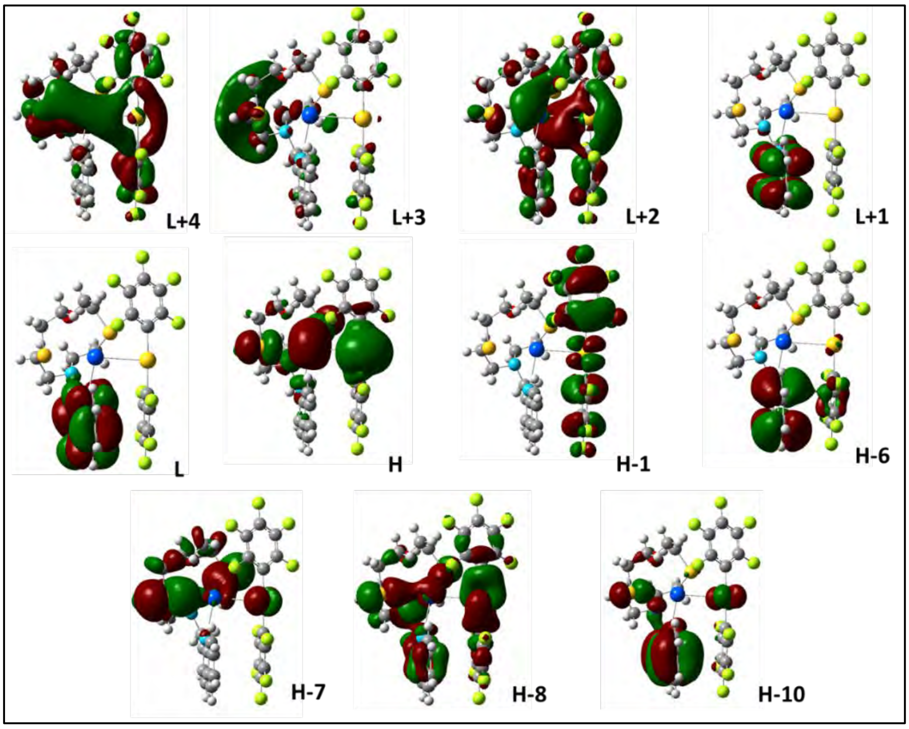

Figure 44. Most important frontier molecular orbitals (isovalue = 0.02) for model system **15a** (L=LUMO; H=HOMO).

Table 26. Population analysis (%) for model systems **16a**.

Model	Orbitals	Au	Tl	NS_2O-Q	C_6F_5
16a	L+4	22	45	17	16
	L+3	22	46	21	10
	L+2	17	20	61	1
	L+1	27	43	7	23
	L	7	13	79	1
	H	21	4	0	75
	H-1	61	16	9	14
	H-2	4	6	0	89
	H-3	3	1	1	95
	H-4	17	5	4	74
	H-5	24	17	4	55
	H-6	24	34	22	20
	H-7	8	8	15	69
	H-8	7	2	9	83
	H-9	20	22	43	15
	H-10	9	11	38	42
	H-11	12	3	27	59
	H-12	12	6	10	72
	H-13	14	7	77	2
	H-14	11	2	84	2

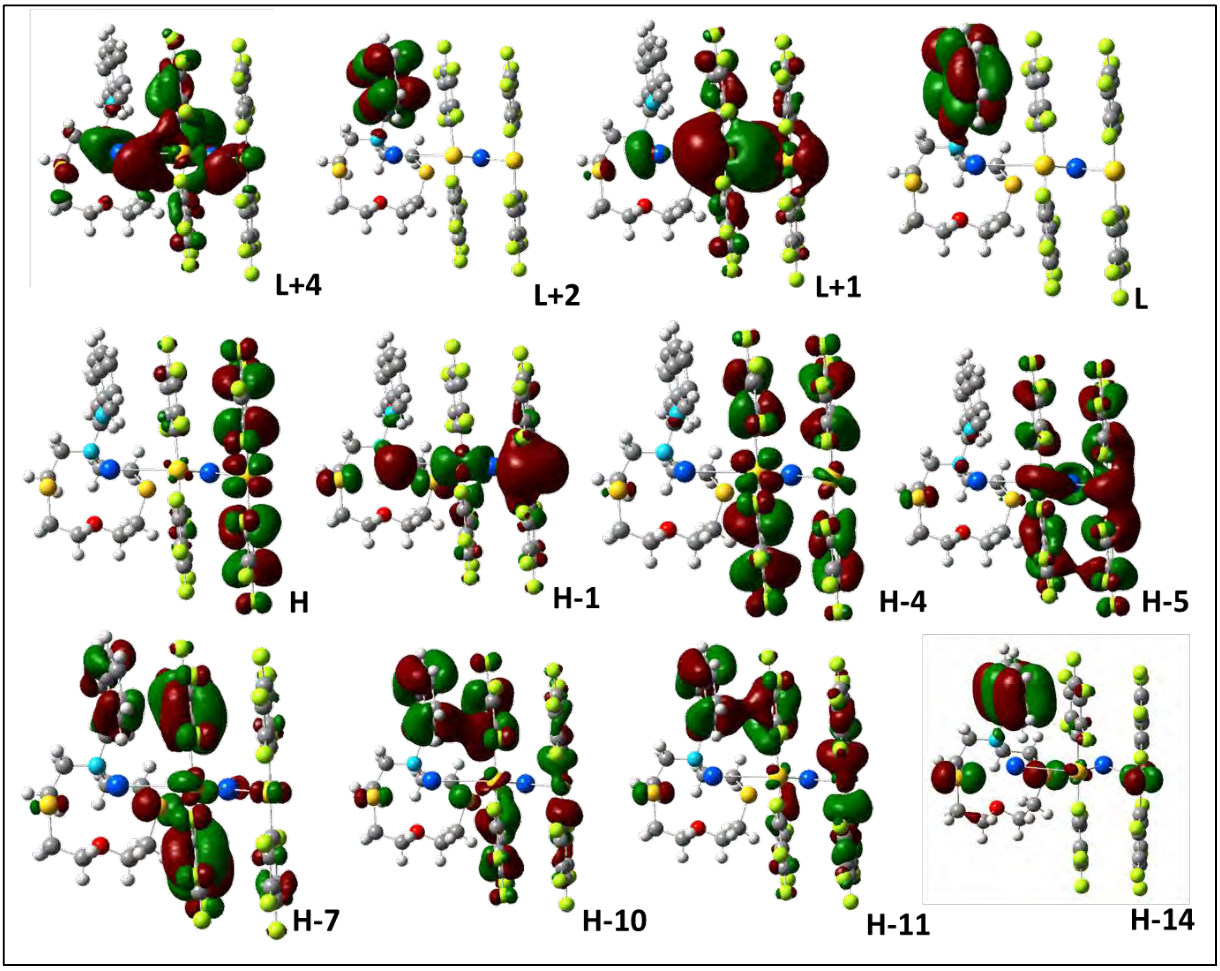

Figure 45. Most important frontier molecular orbitals (isovalue = 0.02) for model system **16a** (L=LUMO; H=HOMO).

The firsts singlet−singlet excitation energies were computed for all model systems at the TD-DFT level of theory as described in the computational details. Since the lifetime for complexes **15** and **16** are near the microseconds range, we also computed the lowest singlet−triplet excitation at TD-DFT level for model systems **15a** and **16a**. We carried out the analysis of the excitation wavelengths, oscillator strengths, and orbitals involved in these electronic excitations, which can be related to the origin of the luminescent behaviour observed experimentally. The results including the most important excitations are depicted in Tables 27-29.

The TD-DFT analysis of the most important single-singlet transitions calculated for model **14a** shows that they appear between 402 and 312 nm, being the most intense singlet-singlet excitations at 332, 330 and 312 nm. The first two transitions consist of a mixture of contributions, HOMO-1→LUMO+2 and a HOMO→LUMO+2, the third singlet-singlet excitation consists of a single contribution, in which the electron arises from HOMO−1 and arrives to LUMO+5. Taking into account that the orbitals involved in these transitions, we could assign the first two important electronic excitations (332 nm and 330 nm) to transitions between the C_6F_5 or ligand unit and the Au/Tl centers; while the third important singlet-singlet excitation is due to a pure transition between the C_6F_5 unit and the metal centers. The results agree well with the experimental excitation spectrum in solid state for complex **14** (See Figure 46 and Table 27).

Table 27. TD-DFT first Singlet-Singlet Excitation Calculations and Lowest Singlet-Triplet Excitations for Model system **14a**.

Model	**exc.**	**λ_{calc} (nm)**	**ƒ (s)**	**contributions**
14a	$S_0 \rightarrow S_1$:	402	0.0105	HOMO→LUMO (47.5)
	$S_0 \rightarrow S_9$:	332	0.1130	HOMO(-1)→LUMO+2 (23.9) HOMO→LUMO+2 (22.2)
	$S_0 \rightarrow S_{10}$:	330	0.2016	HOMO(-1)→LUMO+2 (22.9) HOMO→LUMO+2 (23.4)
	$S_0 \rightarrow S_{14}$:	321	0.0192	HOMO(-1)→LUMO+3 (39.5)
	$S_0 \rightarrow S_{17}$:	317	0.0501	HOMO(-4)→LUMO+2 (40.8)
	$S_0 \rightarrow S_{20}$:	312	0.1018	HOMO(-1)→LUMO+5 (32.4)

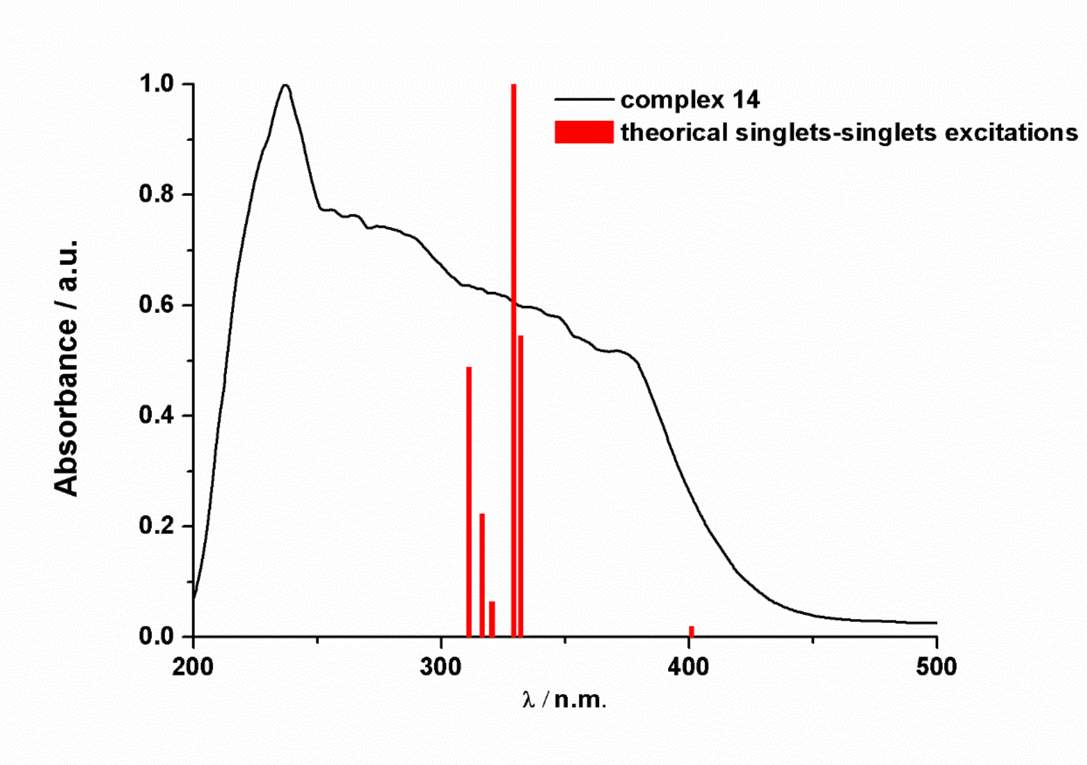

Figure 46. Top: Experimental UV-Vis solid state absorption spectrum (black line) and TD-DFT singlet–singlet excitations (red bars) for model systems **14a**.

In the case of models **15a** and **16a** which represent the complexes with the higher lifetime and a larger Stokes' shift (7445 and 4631 for **15** and **16** respectively) suggesting a phosphorescent process, the first 20 singlet-singlet and the lowest singlet−triplet excitation energies were computed at the TD-DFT level of theory. Thus, in model **15a** the most intense singlet−singlet excitations appear between 290 and 252 nm, whereas the lowest singlet−triplet excitation appears at 497 nm. Again, these values are in agreement with the experimental absorption spectrum that shows a maximum at 228 nm (see Figure 47). The main contributions to the most intense theoretical electronic singlet−singlet excitation at 281 nm arise from the HOMO→LUMO+2 transition and it is due to a charge transfer involving the whole molecule which mainly causes an increase in the electronic density on the thallium atom. The main contribution to the singlet-triplet excitation at 497 nm (from HOMO-6 to LUMO) is due to an intra-ligand transition involving the quinoline framework with a small contribution of C_6F_5 unit. The other two less important singlet-singlet electronic transitions (264 nm, from HOMO to LUMO+4; 252 nm, from HOMO-6 to LUMO) are due a charge transfer transitions from the gold atom to the C_6F_5 unit and from the C_6F_5 fragment to the metal, respectively. The results agree well with the experimental excitation spectrum in solid state for complex **15** (See Figure 47 and Table 28).

Table 28. TD-DFT first Singlet-Singlet Excitation Calculations and Lowest Singlet-Triplet Excitations for Model system **15a**.

Model	exc.	λ_{calc} (nm)	f (s)	contributions
15a	$S_0 \rightarrow S_7$:	290	0.0323	HOMO-6 → LUMO (92)
	$S_0 \rightarrow S_9$:	281	0.1417	HOMO → LUMO+2 (84)
	$S_0 \rightarrow S_{10}$:	271	0.0240	HOMO-10 → LUMO (38) HOMO-8 → LUMO (19) HOMO-6 → LUMO+1 (22)
	$S_0 \rightarrow S_{11}$:	268	0.0100	HOMO-7 → LUMO (78)
	$S_0 \rightarrow S_{12}$:	264	0.0866	HOMO → LUMO+4 (81)
	$S_0 \rightarrow S_{13}$:	261	0.0258	HOMO → L UMO+3 (83)
	$S_0 \rightarrow S_{15}$:	257	0.0105	HOMO-1 → LUMO+1 (73)
	$S_0 \rightarrow S_{18}$:	252	0.1026	HOMO-1 → LUMO+2 (82)
	$S_0 \rightarrow T_1$:	497	0.0000	HOMO-6 → LUMO (74)

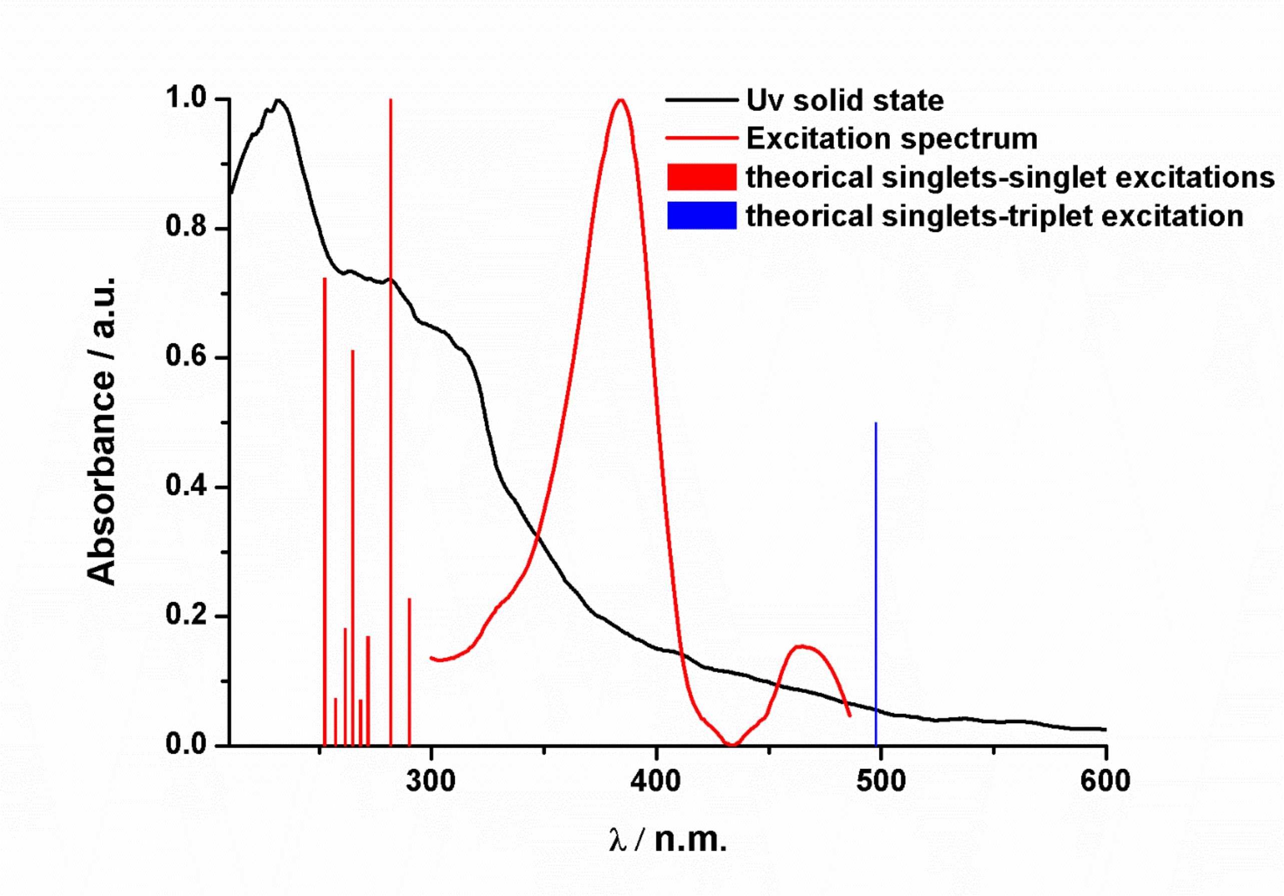

Figure 47. Experimental UV-Vis solid state absorption spectrum (black line) and TD-DFT singlet–singlet and singlet- triplet excitation/s (red bars and blue bar) for model systems **15a.**

Finally, the TD-DFT analysis of the most important single-singlet transitions calculated for model **16a** shows that they appear between 321 and 271 nm, being the most intense singlet-singlet excitations at 320, 319, 283 and 279 nm. While, the first two most intense transitions consist of a mixture of contributions, HOMO-1→LUMO+1 and a HOMO→LUMO+1, the third and the fourth singlet-singlet excitations consist of a single contribution, in which the electron arises from HOMO−4 or HOMO-5 and arrives to LUMO+1. Taking into account the orbitals involved in these transitions, we could assign the first two most important electronic excitations (320 an 319 nm) to transitions between the C_6F_5 unit or gold atoms and the Tl centers; while the third and fourth important singlet-singlet excitation (283 and 279) is due to a pure transition between C_6F_5 and the metal centers. the main contribution to the singlet-triplet excitation at 493 nm (from HOMO-6 to LUMO) is due to a mixed transition (from HOMO-10 or HOMO-11 to LUMO) between C_6F_5 unit and the ligand framework. The results agree quite well with the experimental absorption spectrum in solid state for complex **16** (See Figure 48 and Table 29).

Table 29. TD-DFT first Singlet-Singlet Excitation Calculations and Lowest Singlet-Triplet Excitations for Model system **16a**.

Model	**exc.**	**λ_{calc} (nm)**	**f (s)**	**contributions**
16a	$S_0 \rightarrow S_5$:	321	0.0268	HOMO-7 -> LUMO (27)
				HOMO-4 → LUMO (41)
	$S_0 \rightarrow S_6$:	320	0.1385	HOMO-1 → LUMO+1 (51)
				HOMO → LUMO+1 (43)
	$S_0 \rightarrow S_7$:	319	0.0780	HOMO-1 → LUMO+1 (40)
				HOMO → LUMO+1 (54)
	$S_0 \rightarrow S_{15}$:	284	0.0168	HOMO-11 → LUMO (33)
				HOMO-10 → LUMO (55)
	$S_0 \rightarrow S_{16}$:	283	0.0768	HOMO-4 → LUMO+1 (86)
	$S_0 \rightarrow S_{17}$:	279	0.0657	HOMO-5 → LUMO+1 (78)
	$S_0 \rightarrow S_{18}$:	274	0.0261	HOMO-14 → LUMO (45)
	$S_0 \rightarrow S_{19}$:	272	0.0634	HOMO-1 → LUMO+2 (44)
				HOMO-1 → LUMO+4 (28)
	$S_0 \rightarrow S_{20}$:	271	0.0240	HOMO-1 → LUMO+4 (39)
	$S_0 \rightarrow T_1$:	493	0.0000	HOMO-11 → LUMO (17)
				HOMO-10 → LUMO (28)

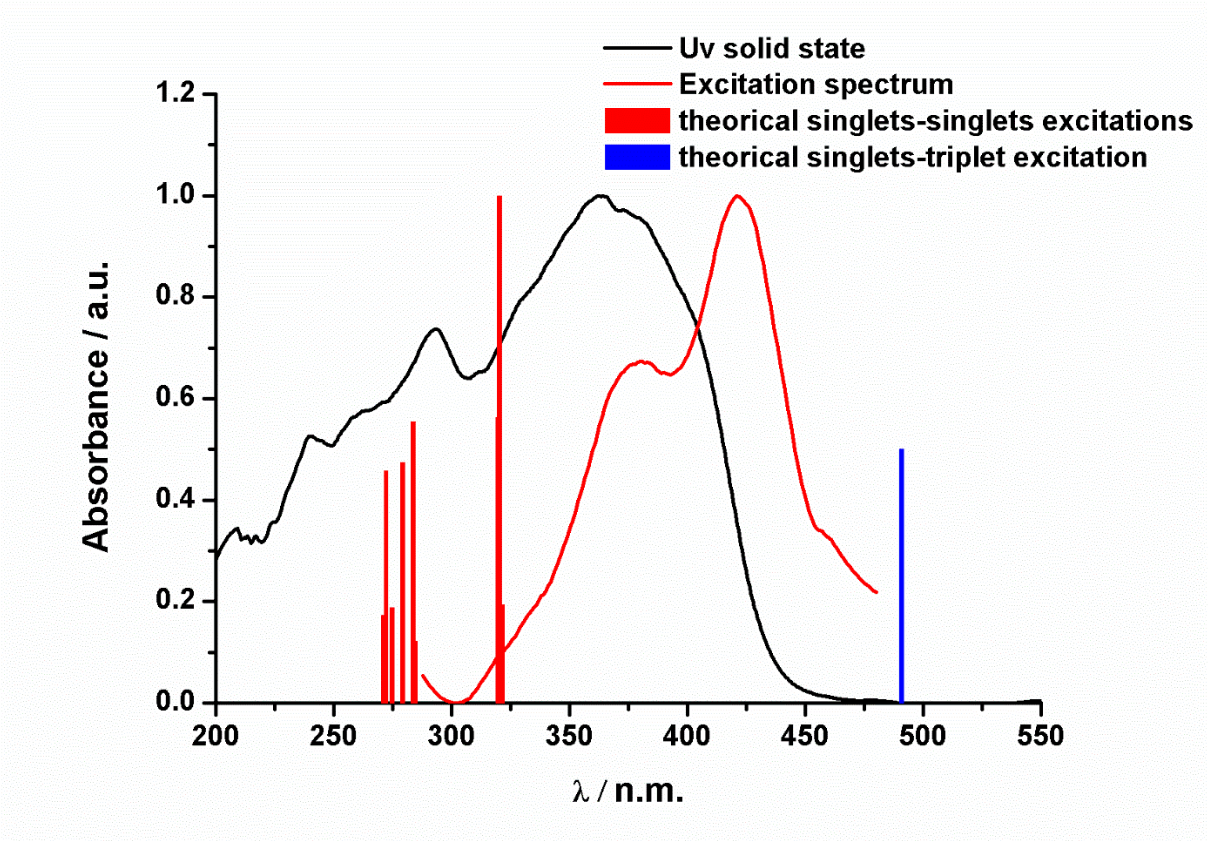

Figure 48. Experimental UV-Vis solid state absorption spectrum (black line) and TD-DFT singlet–singlet and singlet- triplet excitation/s (red bars and blue bar) for model systems **16a**.

2.4.6 Conclusions

In this part of PhD thesis, we have reported the synthesis and study of new six heteronuclear Au/Tl complexes, four of them containing Au···Tl interactions, prepared by reaction of $[Au(C_6F_5)_2Tl]_n$ with mixed-donor macrocyclic ligands (**L_6**, **L_7**). The modification of the coordination properties of the ligands by changing the donor atoms in the macrocycle or by adding methylquinoline pendant-arms, as well as the employment of different Tl/L molar ratios, lead to complexes with an increasing nuclearity and number and/or nature of weak Au···Tl interactions as the number of donor atoms in the ligands increases. The optical properties of these new compounds are closely related to their structures. Thus, while the absence of luminescence of the complex **13** in the solid state is probably due to the quenching of the 1,10-phenanthroline unit following the formation of the $[Tl(\mathbf{L_6})]^+$ complex cation, the luminescent properties of complex **14** have their origin in transitions between orbitals involving the macrocyclic ligands or the pentafluorophenyl unit and the Au/Tl metals.

In contrast, In the case of complexes **15** and **16a** which show the higher lifetime and a larger Stokes' shift, phosphorescent processes are suggested. Thus, while in the model **15a** the phosphorescent emission is due to an electronic transition between the pentafluorophenyl unit and the thallium atom, in the model **16a** is due a charge transfer between the pentafluorophenyl unit and the quinoline framework.

The justification of the photophysical properties of the complexes with a high number of metal centers is an extremely complicated matter: the election of the suitable model that contains all the interactions present in the molecule and at the same time is representative of the real situation of the system synthesized system it is an interesting challenge for all computational chemists.

For this reason, the calculations related to the complex **14** and **16** (polynuclear complexes with more than four heavy atoms) represent a possible interpretation of the fluorescent or phosphorescent process of the synthesized molecule. In fact, if we look carefully the calculation for the model **16a** we can clearly see that the excitation falls slightly outside the real absorption spectrum of the complex **16**; this may be due both to the non-representative model of all the interactions.

2.5 References

[1] E. J. Fernández, A. Laguna, M. E. Olmos, *Advances in Organometallic Chemistry*, **2005**, 52, 77-141.

[2] H. Schmidbaur, *Nature*, **2001**, 413, 31-33.

[3] H. Schmidbaur, *Gold Bull.*, **1990**, 23, 11-13.

[4] H. Schmidbaur, *Gold Bull.*, **2000**, 33, 3-10.

[5] H. Schmidbaur, *Gold: Progress in Chemistry, Biochemistry and Technology,* John Wiley & Sons, Chichester, **1999**.

[6] A. O. Larsen, W. Leu, C. N. Oberhuber, J. E. Campbell, A. H. Hoveyda, *J. Am. Chem. Soc.,* **2004**, 126, 11130-11131.

[7] B. S. Lim, A. Rahtu, J. S. Park, R. G. Gordon, *Inorg. Chem.*, **2003**, 42, 7951-7958.

[8] V. Niel, A. L. Thompson, M. C. Muñoz, A. Galet, A. E. Goeta, J. A. Real, *Angew. Chem.*, **2003**, 42, 3760-3763.

[9] Y. Yamamoto, Y. Kosaka, Y. Tsutsumi, Y. Kaburagi, K. Kuge, Y. Sunada y K. Tatsumi, *Eur. J. Inorg. Chem.,* **2004**, 22, 134-142.

[10] K. Tang, X. Xie, L. Zhao, Y. Zhang, X. Jin., *Eur. J. Inorg. Chem.*, **2004**, 22, 78-85.

[11] D. Sun, R. Cao, W. Bi, J. Weng, M. Hong, Y. Liang, *Inorg. Chim. Acta,* **2004**, 357, 991-1001.

[12] E. Fournier, F. Lebrun, M. Drouin, A. Decken, P. D. Harvey, *Inorg. Chem.,* **2004**, 43, 3127-3135.

[13] X. H. Bu, Y.-B. Xie, J.-R. Li, R.-H. Zhang, *Inorg. Chem.,* **2003**, 42, 7422-7430.

[14] P. Vaqueiro, A. M. Chippindale, A. R. Cowley, A. V. Powell, *Inorg. Chem.*, **2003**, 42, 7846-7851.

[15] P. C. Zachariadis, S. K. Hadjikakou, N. Hadjiliadis, S. Skoulika, A. Michaelides, J. Balzarini, E. De Clercq, *Eur. J. Inorg. Chem.,* **2004**, 1420-1426.

[16] X.-L. Lu, W.-K. Leong, L. Y. Goh, A. T. S. Hor, *Eur. J. Inorg. Chem.,* **2004**, 22, 2504-2513.

[17] Y. A. Wanniarachchi, M. A. Khan, L. M. Slaughter, *Organometallics*, **2004**, 23, 5881-5884.

[18] P. Lin, R. A. Henderson, R. W. Harrington, W. Clegg, C.-D. Wu, X.-T. Wu, *Inorg. Chem.*, **2004**, 43, 181-188.

[19] I. Beloso, J. Castro, J. A. García-Vázquez, P. Pérez -Lourido, J. Romero, A. Sousa, *Inorg. Chem.,* **2005**, 44, 336-351.

[20] N. Schultheiss, D. R. Powell, E. Bosch, *Inorg. Chem.,* **2003**, 42, 5304-5310.

[21] W. J. Evans, D. G. Giarikos, D. Josell, J. W. Ziller, *Inorg. Chem.*, **2003**, 42, 8255-8261.

[22] T. S. Lobana, R. Sharma, S. Mehra, A. Castineiras, P. Turner, *Inorg. Chem.,* **2005**, 44, 1914-1921.

[23] S. Masaoka, D. Tanaka, Y. Nakanishi, S. Kitagawa, *Angew. Chem.*, **2004**, 43, 2530-2534.

[24] C. Näther, I. Jess, *Eur. J. Inorg. Chem.,* **2004**, 14, 2868-2876.

[25] S. L. Jain, P. Bhattacharyya, H. L. Milton, A. M. Z. Slawin, J. A. Crayston, J. D. Woollins, *Dalt. Trans.,* **2004**, 0, 862-871.

[26] R. Kanehama, M. Umemiya, F. Iwahori, H. Miyasaka, K. Sugiura, T. Yamashita, Y. Yokochi, H. Ito, S. Kuroda, H. Kishida, H. Okamoto, *Inorg. Chem.*, **2003**, 42, 7173-7181.

[27] K. K. Kamar, L. R. Falvello, P. E. Fanwick, J. Kim, S. Goswami, *Dalt. Trans.*, **2004**, 0, 1827-1832.

[28] M. Bera, W. T. Wong, G. Aromi, J. Ribas, D. Ray, *Inorg. Chem.,* **2004**, 43, 4787-4789.

[29] E. V. Dikarev, K. W. Andreini, M. A. Petrukhina, *Inorg. Chem.*, **2004,** 43, 3219-3224.

[30] J. Schneider, M. Kockerling, R. Kopitzky, G. Henkel, Eur. J. *Inorg. Chem.*, **2003**, 0, 1727-1734.

[31] H. Hanika-Heidl, S. E. H. Etaiw, M. S. Ibrahim, A. S. B. El-Din, R. D. Fischer, *J. Organomet. Chem.*, **2003**, 684, 329-337.

[32] H. Huang, S.-Y. Yu, H.-B. Liu, M. Shi, *Polyhedron*, **2004,** 23, 55-58.

[33] I. Ara, J. R. Berenguer, E. Eguizábal, J. Forniés, J. Gómez, E. Lalinde, *J. Organomet. Chem.,* **2003**, 670, 221-234.

[34] M. Barquín, M. J. G. Garmendia, S. Pacheco, E. Pinilla, S. Quintela, J. M. Seco, M. R. Torres, *Inorg. Chim. Acta*, **2004**, 357, 3230-3236.

[35] M. L. Cole, G. B. Deacon, P. C. Junk, K. Konstas, P. W. Roesky, *Eur. J. Inorg. Chem.,* **2005**, 6, 1090-1098.

[36] M. Veith, S. Mathur, V. Huch, *Chem. Ber.*, **1993**, 126, 2383-2388.

[37] W. Cen, K. J. Haller, T. P. Fehlner, *Organometallics*, **1992**, 11, 3499-3501.

[38] M. Veith, S. Mathur, V. Huch, *J. Am. Chem. Soc.*, **1996**, 118, 903-904.

[39] R. Wang, M. Hong, D. Yuan, Y. Sun, L. Xu, J. Luo, R. Cao, A. S. C. Chan, *Eur. J. Inorg. Chem.*, **2004**, 1, 37-43.

[40] R. Wang, L. Han, F. Jiang, Y. Zhou, D. Yuan, M. Hong, *Cryst. Growth Des.*, **2005**, 5, 129-135.

[41] M. Veith, S. Mathur, V. Huch, *Inorg. Chem.*, **1996**, 35, 7295-7303.

[42] E. G. Mednikov, L. F. Dahl, *Dalt. Trans.,* **2003**, 0, 3117-3125.

[43] Y. Yamamoto, T. Ohno, K. Itoh, *Organometallics,* **2003**, 22, 2267-2272.

[44] Z. Beni, R. Scopelliti, R. Roulet, *Inorg. Chem. Commun*., **2004**, 7, 935-937.

[45] I. Ara, J. Forniés, L. Gabilondo, M. A. Usón, *Inorg. Chim. Acta,* **2003**, 347, 155-160.

[46] J. R. Berenguer, M. Bernechea, J. Forniés, A. García, E. Lalinde, M. T. Moreno, *Inorg. Chem.,* **2004**, 43, 8185-8198.

[47] J. Ruiz, V. Rodríguez, A. Pérez, G. López, D. Bautista, *J. Organomet. Chem.*, **2004**, 689, 2080-2086.

[48] S. Yamazaki, Z. Taira, T. Yonemura, A. J. Deeming, *Organometallics,* **2005**, 24, 20-27.

[49] J. S. L. Yeo, J. J. Vittal, A. T. S. Hor, *Eur. J. Inorg. Chem.,* **2003**, 2, 277-280.

[50] W. Lu, M. C. W. Chan, N. Zhu, C. M. Che, C. Li Z. Hui, *J. Am. Chem. Soc*, **2004**, 126, 7639-7651.

[51] D. Herebian, E. Bothe, F. Neese, T. Weyhermuller, K. Wieghardt, *J. Am. Chem. Soc.*, **2003**, 125, 9116-9128.

[52] J. Forniés, J. Gómez, E. Lalinde, M. T. Moreno, *Chem. Eur. J.*, **2004**, 10, 888-898.

[53] U. Christmann, R. Vilar, A. J. P. White, D. J. Williams, *Chem. Commun*., **2004**, 0, 1294-1295.

[54] A. C. Albéniz, P. Espinet, R. Manrique, A. Pérez-Mateo, *Chem. Eur. J.,* **2005**, 11, 1565-1573.

[55] P. Espinet, C. Hernández, J. M. Martín-Álvarez, J. A. Miguel, *Inorg. Chem.,* **2004**, 43, 843-845.

[56] M. Gorlov, A. Fischer, L. Kloo, *J. Organomet. Chem.,* **2004**, 689, 489-492.

[57] M. Kim, F. P. Gabbaï, *Dalt. Trans.,* **2004**, 0, 3403-3407.

[58] J. K.-P. Ng, G.-K. Tan, J. J. Vittal, P. H. Leung, *Inorg. Chem.,* **2003**, 42, 7674-7682.

[59] Y. Tatsumi, T. Naga, H. Nakashima, T. Murahashi, H. Kurosawa, *Chem. Commun*., **2004**, 0, 1430-1431 .

[60] B. C. Tzeng, G.-H. Lee, S.-M. Peng, *Inorg. Chem. Commun*., **2004**, 7, 151-154.

[61] J. Vicente, J. A. Abad, R. Clemente, J. López-Serrano, M. C. Ramírez de Arellano, P. G. Jones, D. Bautista, *Organometallics,* **2003**, 22, 4248-4259.

[62] J. M. Vila, G. Alberdi, M. T. Pereira, M. Marino, A. Fernandez, M. López-Torres, R. Ares, *Polyhedron*, **2003**, 22, 241-246.

[63] W.-K. Wong, H. Liang, M.-Y. Yung, J.-P. Guo, K.-F. Yung, W.-T. Wong, P. G. Edwards, *Inorg. Chem. Commun*., **2004**, 7, 737-740.

[64] J. H. K. Yip, J. Wu, K.-Y. Wong, K. P. Ho, L. L. Koh, J. J. Vittal, *Eur. J. Inorg. Chem.,* **2004**, 5, 1056-1062.

[65] K. Umakoshi, Y. Yamauchi, K. Nakamiya, T. Kojima, M. Yamasaki, H. Kawano, M. Onishi, *Inorg. Chem.,* **2003**, 42, 3907-3916.

[66] A. D. Burrows, M. F. Mahon, S. P. Nolan, M. Varrone, *Inorg. Chem.,* **2003**, 42, 7227-7238.

[67] F. Wiesbrock, H. Schmidbaur, *J. Am. Chem. Soc*., **2003**, 125, 3622-3630.

[68] R. J. Wright, A. D. Phillips, S. Hino, P. P. Power, *J. Am. Chem. Soc*., **2005**, 127, 4794-4799.

[69] R. P. Sharma, R. Bala, R. Sharma, J. Raczynska, U. Rychlewska, *J. Mol. Struct.*, **2005**, 738, 247-252.

[70] E. J. Fernández, J. M. López de Luzuriaga, M. E. Olmos, J. Pérez, A. Laguna, M. C. Lagunas, *Inorg. Chem.,* **2005**, 44, 6012-6018.

[71] E. J. Fernández, A. Laguna, J. M. López De Luzuriaga, M. Monge, M. Montiel, M. E. Olmos, J. Pérez, *Organometallics*, **2004**, 23, 774-782.

[72] E. J. Fernández, A. Laguna, J. M. López De Luzuriaga, M. Montiel, M. E. Olmos, J. Pérez, *Inorg. Chim., Acta*, **2005**, 358, 4293-4300.

[73] E. J. Fernández, J. M. López De Luzuriaga, M. Monge, M. E. Olmos, J. Pérez, A. Laguna, J. Am. Chem. Soc., **2002**, 124, 5942-5943.

[74] S. Hino, M. M. Olmstead, A. D. Phillips, R. J. Wright, P. P. Power, *Inorg. Chem.*, **2004**, 43, 7346-7352.

[75] V. Lozan, B. Kersting, *Eur. J. Inorg. Chem.,* **2005**, 3, 504-512.

[76] F. Stabenow, W. Saak, H. Marsmann, M. Weidenbruch, *J. Am. Chem. Soc*., **2003**, 125, 10172-10173

[77] W. P. Leung, Q. W. Y. Ip, S.-Y. Wong, T. C. W. Mak, *Organometallics*, **2003**, 22, 4604-4609.

[78] B.-P. Yang, J. G. Mao, Y.-Q. Sun, H.-H. Zhao, A. Clearfield, Eur. J. *Inorg. Chem.*, **2003**, 23, 4211-4217.

[79] J. R. Berenguer, J. Forniés, B. Gil, E. Lalinde, *Chem. - A Eur. J.* **2005,** 12, 785-795.

[80] L. R. Falvello, J. Forniés, R. Garde, A. García, E. Lalinde, M. T. Moreno, A. Steiner, M. Tomás, I. Usón, *Inorg. Chem.,* **2006**, 45, 2543-2552.

[81] J. P. H. Charmant, J. Forniés, J. Gómez, E. Lalinde, R. I. Merino, M. T. Moreno, A. G. Orpen, *Organometallics,* **2003**, 22, 652-656.

[82] M. C. Comstock, T. Prussak-Wieckowska, S. R. Wilson, J. R. Shapley, *Organometallics*, **1997**, 16, 4033-4040.

[83] A. L. Balch, J. K. Nagle, M. M. Olmstead, P. E. Reedy Jr., *J. Am. Chem. Soc.*, **1987**, 109, 4123-4124.

[84] S. Wang, G. Garzón, C. King, J. C. Wang, J. P. Fackler Jr., *Inorg. Chem.*, **1989**, 28, 4623-4629.

[85] S. Wang, J. P. Fackler Jr., C. King, J. C. Wang, *J. Am. Chem. Soc.*, **1988**, 110, 3308-3311.

[86] E. J. Fernández, A. Laguna, J. M. López De Luzuriaga, F. Mendizábal, M. Monge, M. E. Olmos, J. Pérez, *Chem. Eur. J.,* **2003**, 9, 456-465.

[87] O. Crespo, E. J. Fernández, P. G. Jones, A. Laguna, J. M. López de Luzuriaga, A. Mendía, M. Monge, M. E. Olmos, *Chem. Commun*., **1998**, 0, 2233-2234.

[88] V. J. Catalano, M. A. Malwitz, *J. Am. Chem. Soc.*, **2004**, 126, 6560-6561.

[89] M. Crespo, J. Sales, X. Solans, *J. Chem. Soc. Dalt. Trans.*, **1989**, 0, 1089-1092.

[90] C. E. Briant, D. I. Gilmour, D. M. P. Mingos, *J. Chem. Soc. Dalt. Trans.*, **1986**, 4, 835-841.

[91] M. F. Hallam, M. A. Luke, D. M. P. Mingos, I. D. Williams, *J. Organomet. Chem.*, **1987**, 325, 271-283.

[92] T. Zhang, M. Drouin, P. D. Harvey, *Inorg. Chem.*, **1999**, 38, 4928-4936.

[93] L. Manojlovic-Muir, A. N. Henderson, I. Treurnicht, R. J. Puddephatt, *Organometallics,* **1989**, 8, 2055-2061.

[94] H. H. Murray, D. A. Briggs, G. Garzón, R. G. Raptis, L. C. Porter, J. P. Fackler Jr., *Organometallics*, **1987**, 6, 1992-1995.

[95] C. E. Briant, D. I. Gilmour, D. M. P. Mingos, *J. Organomet. Chem.*, **1984**, 267, C52-C55.

[96] G. A. Carriedo, J. A. K. Howard, F. G. A. Stone, M. J. Went, *J. Chem. Soc. Dalt. Trans.,* **1984**, 11, 2545-2551.

[97] Q. H. Wei, G. Q. Yin, Z. Ma, L. X. Shi, Z. N. Chen, *Chem. Commun*., **2003,** 17, 2188-2189.

[98] E. Alonso, J. Forniés, C. Fortuño, A. Martín, A. G. Orpen, *Organometallics*, **2003**, 22, 5011-5019.

[99] V. W. W. Yam, C. K. Hui, S. Y. Yu, N. Zhu, *Inorg. Chem.*, **2004**, 43, 812-821.

[100] J. Fernández, J. Forniés, B. Gil, J. Gómez, E. Lalinde, M. T. Moreno, *Organometallics*, **2006**, 25, 274-2283.

[101] I. Ara, J. Forniés, L. Gabilondo, M. A. Usón, *Inorg. Chim. Acta*, **2003**, 347, 155-160.

[102] T. Tanase, E. Goto, H. Takenaka, T. Horiuchi, Y. Yamamoto, J. Kuwabara, K. Osakada, *Organometallics*, **2005**, 24, 234-244.

[103] O. Crespo, A. Laguna, E. J. Fernández, J. M. López De Luzuriaga, P. G. Jones, M. Teichert, M. Monge, P. Pyykkö, N. Runeberg, M. Schütz, H. J. Werner, *Inorg. Chem.*, **2000**, 39, 4786-4792.

[104] B.-H. Xia, H.-X. Zhang, C.-M. Che, K.-H. Leung, D. L. Phillips, N. Zhu, Z.-Y. Zhou, J. Am. Chem. Soc., **2003**, 125, 10362-10374.

[105] P. D. Harvey, A. Eichhofer, D. Fenske, *J. Chem. Soc. Dalt. Trans.*, 1998, 0, 3901-3904.

[106] P. Pyykkö, *Chem. Rev.*, **1997**, 97, 597-636.

[107] P. Pyykkö, M. Straka, T. Tamm, *Phys. Chem. Chem. Phys.*, **1999**, 1, 3441-3444.

[108] Z. Asseffa, F. DeStefano, M. A. Garepapaghi, J. H. LaCasce Jr., S. Oulette, M. R. Corson, J. K. Nagle, H. H. Patterson, *Inorg. Chem.*, **1991**, 30, 2868-2876

[109] P. Fischer, A. Ludi, H. H. Patterson, A. Hewat, *Inorg. Chem.*, **1994**, 33, 62-66

[110] A. Burini, R. Bravi, J. P. Fackler Jr., R. Galassi, T. A. Grant, M. A. Omary, B. R. Pietroni, R. J. Staples, *Inorg. Chem.*, **2000**, 39, 3158-3165

[111] J. R. Berenguer, M. Bernechea, J. Forniés, E. Lalinde, J. Torroba, *Organometallics*, **2005**, 24, 431-438.

[112] A. Sundararaman, R. A. Lalancette, L. N. Zakharov, A. L. Rheingold, F. Jäkle, *Organometallics*, **2003**, 22, 3526-3532.

[113] W. Tyrra, M. S. Wickleder. Z. Anorg, *Allg. Chem.*, **2002**, 628, 1841-1847.

[114] E. J. Fernández, J. M. López de Luzuriaga, M. Monge, M. E. Olmos, J. Pérez, A. Laguna, A. A. Mohammed, J. P. Fackler, *J. Am. Chem. Soc.*, **2003**, 125, 2022-2023.

[115] E. J. Fernández, A. Laguna, J. M. López de Luzuriaga, M. Monge, M. Montiel, M. E. Olmos, J. Pérez, *Organometallics*, **2004**, 23, 774-782.

[116] E. J. Fernández, A. Laguna, J. M. López de Luzuriaga, M. E. Olmos, J. Pérez., *Dalt. Trans.*, **2004**, 0, 1801-1806.

[117] E. J. Fernández, A. Grau, A. Laguna, T. Lasanta, V. Lippolis, J. M. López De Luzuriaga, M. Montiel, M. E. Olmos, *Organometallics*, **2010**, 29, 2951-2958.

[118] E. J. Fernández, P. G. Jones, A. Laguna, J. M. López De Luzuriaga, M. Monge, M. E. Olmos, J. Pérez, *Z. Naturforsch.*, **2004**, 59b, 1379-1386.

[119] E. J. Fernández, J. M. López De Luzuriaga, M. E. Olmos, J. Pérez, *Inorg. Chem*., **2005**, 44, 6012-6018.

[120] A. J. Blake, R. Donamaría, E. J. Fernández, T. Lasanta, V. Lippolis, J. M. López De Luzuriaga, E. Manso, M. Monge, M. E. Olmos., *Dalt. Trans.*, **2013**, 42, 11559-11570.

[121] E. J. Fernández, P. G. Jones, A. Laguna, J. M. López De Luzuriaga, M. Monge, J. Pérez, M. E. Olmos, *Inorg. Chem.*, **2002**, 41, 1056-1063.

[122] E. J. Fernández, A. Laguna, J. M. López De Luzuriaga, M. Monge, M. Montiel, M. E. Olmos, J. Pérez, *Organometallics*, **2004**, 23, 774-782.

[123] E. J. Fernández, A. Laguna, T. Lasanta, J. M. López De Luzuriaga, M. Montiel, M. E. Olmos, *Organometallics*, **2008,** 27, 2971-2979.

[124] R. Usón, A. Laguna, M. Laguna, B. R. Manzano, P. G. Jones and G. M. Sheldrick, *J. Chem. Soc. Dalt. Trans.*, **1984**, 0, 285-292.

[125] R. Usón, A. Laguna, M. Laguna, B. R. Manzano and A. Tapia, *Inorg. Chim. Acta*, **1985**, 101, 151-153.

[126] K. Wieghardt, M. Kleine-Boymann, B. Nuber, J. Weiss, *Inorg. Chem.*, **1986**, 25, 1309-1313.

[127] U. Heinzel, A. Henke, R. Mattes, *J. Chem. Soc. Dalt. Trans.*, **1997**, 4, 501-508.

[128] A. J. Blake, G. Reid, M. Schroder, *J. Chem. Soc. Dalt. Trans.*, **1992**, 0, 2987-2992.

[129] A. J. Blake, J. A. Greig, M. Schroder, *J. Chem. Soc. Dalt. Trans.*, **1991**, 1, 529-532.

[130] A. J. Blake, D. Fenske, W.-S. Li, V. Lippolis, M. Schroder, *J. Chem. Soc. Dalt. Trans*., **1998**, 0, 3961-3968.

[131] E. J. Fernández, J. M. López De Luzuriaga, M. Monge, M. E. Olmos, J. Pérez, *J. Am. Chem. Soc.*, **2002**, 124, 5942-5943.

[132] L. J. Larson, E. M. McMacauley, B. Weissbart, D. J. Tinti, *J. Phys. Chem*., **1995**, 99, 7218-7226.

[133] E. J. Fernández, J. M. López de Luzuriaga, M. Monge, M. Montiel, M. E. Olmos, J. Pérez, A. Laguna, F. Mendizábal, A. A. Mohamed, J. P. Fackler, *Inorg. Chem.*, **2004**, 43, 3573-3581.

[134] J. M. López de Luzuriaga, *Modern Supramolecular Gold Chemistry*, Wiley-VCH, Weinheim, **2008**.

[135] R. Donamaría, M. C. Gimeno, V. Lippolis, J. M. López De Luzuriaga, M. Monge, M. E. Olmos, *Inorg. Chem.*, **2016**, 55, 11299-11310.

[136] M. Wrighton, D. L. Morse, *J. Am. Chem. Soc*., **1974**, 96, 998-1003.

[137] L. A. Summers, *Adv. Heterocycl. Chem*., **1978,** 22, 1-69.

[138] Sammes P.G.; Yahioglu G., Chem. Soc. Rev., **1994,** 23, 327-334.

[139] C. R. Luman, F. N. Castellano, *Comprehensive Coordination Chemistry*, vol. 1, Elsevier, Oxford, UK, **2004**.

[140] S. H. Tarulli, O. V. Quinzani, O. E. Piro, E. E. Castellano, E. J. Baran, *Z. Anorg. Allg. Chem*., **2003**, 629, 1975-1979.

[141] M. Ghadermazi, Zh. Strukt. Khim, *J. Struct. Chem.*, **2016** , 57, 1020-1023.

[142] V. V. Skopenko, V. V. Ponomareva, K. V. Domasevich, J. Sieler, R. Kempe, E. B. Rusanov, *J. Gen. Chem.*, **1997**, 67, 893-895.

[143] I. Ahmadian, A. Abedi, V. Amani, N. Safari, *Res. Chem. Intermed*., **2015**, 41, 2971-2978.

[144] Guibin Ma, A. Fischer, J. Glaser, Eur. *J. Inorg. Chem.*, **2002**, 22, 1307-1314.

[145] T.L. Blundell, H. M. Powell, *Proc. R. Soc. London, Ser. A*, **1972**, 331, 161-165.

[146] Aragoni, M. C., Arca, M., Demartin, F., Devillanova, F. A., Isaia, F., Garau, A. et al., *Inorg. Chem.*, **2002**, 41, 6623-6632.

[147] J. R. Lakowicz, *Principles of Fluorescence Spectroscopy*, Springer London, Limited, **1986**.

[148] B. Valeur, *Molecular Fluorescence: Principles and Applications*, Wiley Online Library, **2001**.

[149] T Lasanta, J. M. López-de-Luzuriaga, M. Monge, M. E. Olmos, D. Pascual, *Chem. Eur. J.,* **2013,** 19, 4754-4766.

[150] L. Pauling, *The Chemical Bond*, Cornell University Press: Ithaca, New York, **1967**.

[151] V. J. Catalano, B. L. Bennett, H. M. Kar, B. C. Noll, *J. Am. Chem. Soc*., **1999,** 121, 10235-10236.

[152] L. Pech, Yu. Bankovsky, A. Kemme, V. Belsky, E. Silina, Y. Ashaks, *Chem. Heterocycl. Compd.*, **2002,** 38, 789-792.

[153] J. C. Peters, S. B. Harkins, S. D. Brown, M. W. Day, *Inorg. Chem.*, **2001**, 40, 5083-5091.

[154] W. J. Baxter, G. Gafner, *Inorg. Chem.*, **1972**, 11, 176-178.

[155] E. J. Fernández, J. M. López de Luzuriaga, M. Monge, M. E. Olmos, J. Perez, A. Laguna, A. A. Mohamed, J. P. Jr. Fackler, *J. Am. Chem. Soc*., **2003**, 125, 2022-2023.

[156] E. J. Fernández, J. M. López de Luzuriaga, M. Monge, M. Montiel, M. E. Olmos, J. Perez, A. Laguna, F. Mendizabal, A. A. Mohamed, Jr. J. P. Fackler, *Inorg. Chem.,* **2004**, 43, 3573-3581.

[157] E. J. Fernández, A. Laguna, J. M. López de Luzuriaga, M. Monge, M. Montiel, M. E. Olmos, J. Perez, *Organometallics*, **2004**, 23, 774-782.

[158] E. J. Fernández, A. Laguna, J. M. López de Luzuriaga, M. Montiel, M. E. Olmos, J. Perez, *Inorg. Chim. Acta*, **2005**, 358, 4293-4300.

[159] E. J. Fernández, A. Laguna, J. M. López de Luzuriaga, F. Mendizabal, M. Monge, M. E. Olmos, J. Perez, *Chem. Eur. J.* **2003**, 9, 456-465.

[160] E. J. Fernández, A. Laguna, J. M. López de Luzuriaga, M. Montiel, M. E. Olmos, J. Perez, *Organometallics,* **2005**, 24, 1631-1637.

[161] E. J. Fernández, A. Laguna, J. M. López de Luzuriaga, M. E. Olmos, J. Perez, *Dalt. Trans*., **2004**, 0, 1801-1806.

[162] E. J. Fernández, P. G. Jones, A. Laguna, J. M. López de Luzuriaga, M. Monge, M. Montiel, M. E. Olmos, J. Perez, *Z. Naturforsch.,* **2004**, 59b, 1379-1386.

[163] E. J. Fernández, P. G. Jones, A. Laguna, J. M. López de Luzuriaga, M. E. Monge, M. Olmos, J. Perez, *Inorg. Chem.,* **2002**, 41, 1056-1063.

[164] E. J. Fernández, A. Laguna, T. Lasanta, J. M. López de Luzuriaga, M. Montiel, M. E. Olmos, *Organometallics*, **2008**, 27, 2971-2979.

Chapter 3

Gold(I)-Silver(I) Heteronuclear compounds

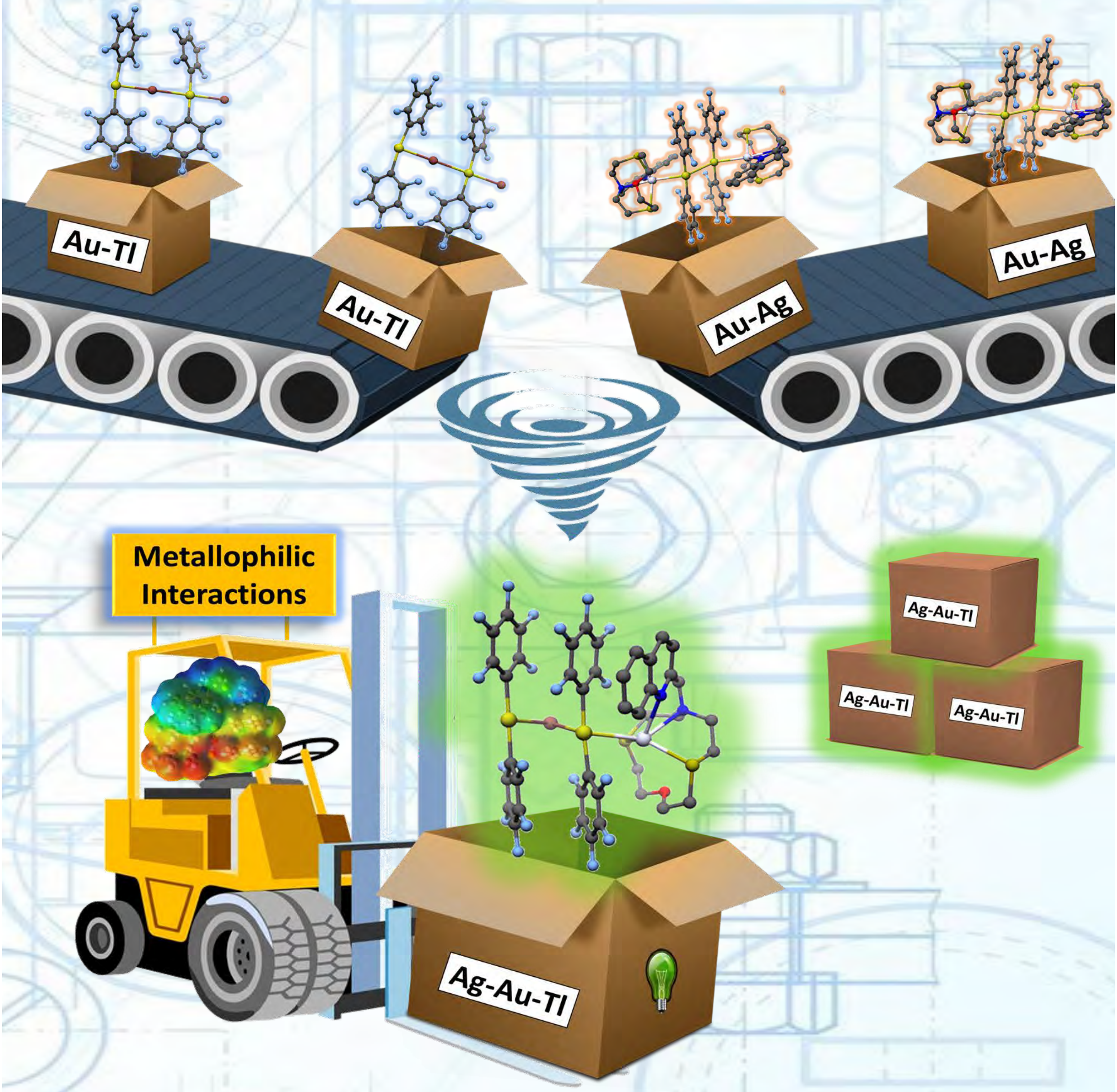

3.1 Gold(I)-silver(I) heteronuclear compounds

Given the theoretical and experimental interest generated in recent years around the existence of the aurophilic interaction[1]-[6] and, more generally, around the interactions between gold(I) and different metals with a closed shell electronic configuration[7]-[10], in particular silver(I)[11]-[15], our group of research has developed over the years, through the use of the acid-base strategy, the synthesis of heteropolinuclear compounds featuring unsupported interactions between gold(I) and silver(I) by using organometallic gold compounds, such as bis(perhalophenyl)aurate (I), and silver acid salts[16]-[18].

The chemistry of gold aryl derivatives is one of the topics of greatest interest in organometallic chemistry and has given rise to the publication of several articles starting from the development of the first synthesis [19]-[24]. In fact, over the years, it has been observed that the number of synthesized aryl derivatives has increased considerably thanks to the use of perhalophenyl groups, which considerably increase the thermodynamic stability as well as the kinetic stability of the synthesized compounds. Moreover, the influence of the nature of the basic gold(I) precursor used on the structures, metallophilic interactions and optical properties of the synthesized complexes has been widely demonstrated [25]. In particular, over the years our research group has been responsible for the synthesis of important gold(I)-silver(I) heterometallic systems through the reaction of the $Au(C_6X_5)^{2-}$ (X = Cl, F)[26], [27] aurate species and $AgClO_4$[28]-[29] (equation 1).

$$[NBu_4][Au(C_6X_5)_2] + AgClO_4 \xrightarrow[2)\ CH_2Cl_2]{1)\ Et_2O} [Au(C_6X_5)_2Ag]_{n(s)} + [NBu_4]ClO_4$$

Equation 1.

As shown in equation 1, the synthesis of these systems takes place in two phases: solubilization of silver perchlorate in diethyl ether, addition of tetrabutylammonium bis(perhalophenyl)aurate and addition of dichloromethane. The low solubility of the polymeric system synthetized in this solvent mixture allows direct filtration of the final product with a high degree of purity. Their solid-state structures, consisting of tetranuclear Ag_2Au_2 units linked via unsupported Au···Au contacts, make them very interesting from a photophysical point of view since their optical properties are strongly affected by the presence of small organic molecules and can even act as volatile organic compounds sensors[30].

In addition, the indicated compounds are able to react with different N-, O- or S-donor ligands, forming derivatives in which the ligands are coordinated at the silver(I) centres. As already seen in the previous chapter for gold(I)-thallium(I) heterometallic systems, also in this case, the steric characteristics of the ligands, as well as the presence of different donor atoms can play a fundamental role in the modification of the structural arrangements as well as in the photophysical properties of the resulting systems. For example, crown thioethers with a variety of numbers of S-donor atoms have been useful in the synthesis of many coordination compounds featuring a diversity of metal centres [31]-[37]. Such ligands can form stable and inert compounds with a great variety of transition metal ions, in which the metal centre is sometimes forced to adopt uncommon coordination geometries and/or oxidation states[38]. A detailed inspection of the coordination chemistry of p-block [39]-[47] and d^{10} transition metal ions [48]-[54] with crown thioethers is still an open area of research and include some silver(I) complexes with crown thioethers that have been structurally characterized, such as $[Ag([9]aneS_3)2]I_5$ [55] and $[Ag_2([24]aneS_8)(CF_3SO_3)_2(MeCN)_2]_\infty$ [56]-[57]. In the crystal structure of the cation $[Ag([9]aneS_3)_2]^+$ two $[9]aneS_3$ molecules are facially bound to the silver(I) centre imposing an octahedral coordination environment to the metal. In addition, the unusual trinuclear silver(I) complex cation $[Ag_3([9]aneS_3)_3]^{3+}$ incorporates bridging thioether ligands, and the metal ions exhibit a highly distorted tetrahedral coordination environment provided by four S donors[58]. Taking all the above into account, in 2014, our research group published a paper where the effect of the different dimensionality of crown thioethers on both, the structural properties and on the spectroscopic properties of complexes containing heterometallic Au(I)-Ag(I) interactions,[59] was studied. Thanks to the development of this project, the following steps have been laid: to evaluate not only how the cavity size of macrocycles can influence the properties of synthesized systems, but also to evaluate how the possible change of donor atoms can play a decisive role in the synthesis of the different heterometallic complexes. Taking into account the study previously performed in the first part of this Thesis we decided to study the reactivity of the heterometallic polymeric compound $[\{Au(C_6X_5)_2\}Ag]_n$ (X = F, Cl) with N,S,O-mixed-donor crown ethers in order to synthesize a new class of compounds containing Au(I)-Ag(I) metallophilic interactions (see Figure 1).

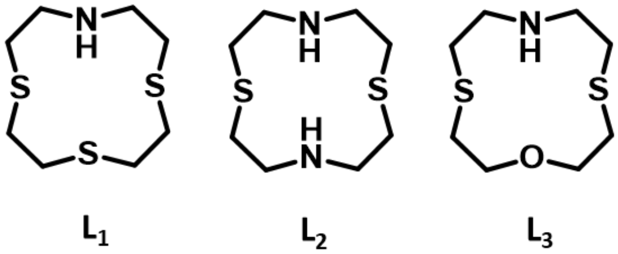

Figure 1. N,S,O-mixed-donor crown ethers used.

In this case, we wanted to evaluate how the three macrocycle systems with the same cavity size but different type of donor atoms (O, S, N) can influence both the structural properties and the optical properties of the synthetized heterometallic systems featuring Au(I)-Ag(I) interactions.

3.2 N,S,O-mixed-donor crown ligand ethers (L_1-L_3)

3.2.1 Synthesis and characterization

We have studied the reactivity of basic gold(I) species of the type $[Au(C_6X_5)_2]^-$ (X = Cl, F) with silver(I) perchlorate in the presence of N,S,O-mixed-donor, such as [12]aneNS_3 (L_1), [12]aneN_2S_2 (L_2), or [12]aneNS_2O (L_3). The modifications in the aryl group and/or in the N,S,O-donor ligand influence both, the number of intermetallic interactions and their strength and, consequently, compounds with different solid state structures and optical properties are obtained. By reaction of the polymetallic chain compound $[\{Au(C_6Cl_5)_2\}Ag]_n$ in the appropriate molar ratio with the N,S,O-mixed-donor crown ethers $\mathbf{L_1}$ or $\mathbf{L_2}$ in tetrahydrofuran (THF), the heteronuclear gold/silver complexes $[\{Au(C_6Cl_5)_2\}\{Ag(\mathbf{L_1})\}]$ (**17**) or $[\{Au(C_6Cl_5)_2\}\{Ag(\mathbf{L_2})\}]$ (**18**) are obtained in good yields as white solids (see Scheme 1). Moreover, by reaction of the polymetallic chain compound $[\{Au(C_6Cl_5)_2\}Ag]_n$ with $\mathbf{L_3}$ by modifying the reaction conditions (reaction time) two structure isomers ($[\{Au(C_6Cl_5)_2\}\{Ag(L_3)\}]$ (**19**) or $[\{Au(C_6Cl_5)_2\}\{Ag(\mathbf{L_3})\}]_2$ (**20**)) were obtained (see Scheme 2). They feature the same **L**/Ag stoichiometry but different metallophilic interactions, which strongly influence also the photophysical properties of the synthesized devices.

The substitution of the chlorine atoms of the aryl groups by fluorine does not affect the stoichiometry of the resulting compounds and so, when $[\{Au(C_6F_5)_2\}Ag]_n$ is treated with the corresponding macrocyclic ligand in tetrahydrofuran (THF), regardless of the molar ratio of the starting reagents, the species $[\{Au(C_6F_5)_2\}\{Ag(\mathbf{L_1})\}]_2$ **(21)**, $[\{Au(C_6F_5)_2\}\{Ag(\mathbf{L_2}\}]$ (**22**) or $[\{Au(C_6F_5)_2\}\{Ag(\mathbf{L_3})\}]$ (**23**) (Schemes 1 and 2) are obtained as white/yellow solids. All the complexes are stable to air and moisture for long periods of time at room temperature (see Schemes 1,2).

Complexes **19**-**23** are soluble in O-donor solvents such as THF or acetone, partially soluble in dichloromethane or acetonitrile, and insoluble in hexane or diethyl ether, while **17** and **18** are nearly insoluble in all the solvents we tested. Moreover, the elemental analyses and spectroscopic data of the obtained complexes are in accordance with the proposed stoichiometries (see Experimental Section).

The presence of the $[Au(C_6F_5)_2]^-$ fragment in **21-23** is evident in their ^{19}F NMR spectra, which resemble that of the precursor complex $NBu_4[Au(C_6F_5)_2]$, and seem to indicate that a dissociative process giving rise to aurate(I) anions and silver(I) cations takes place in solution.

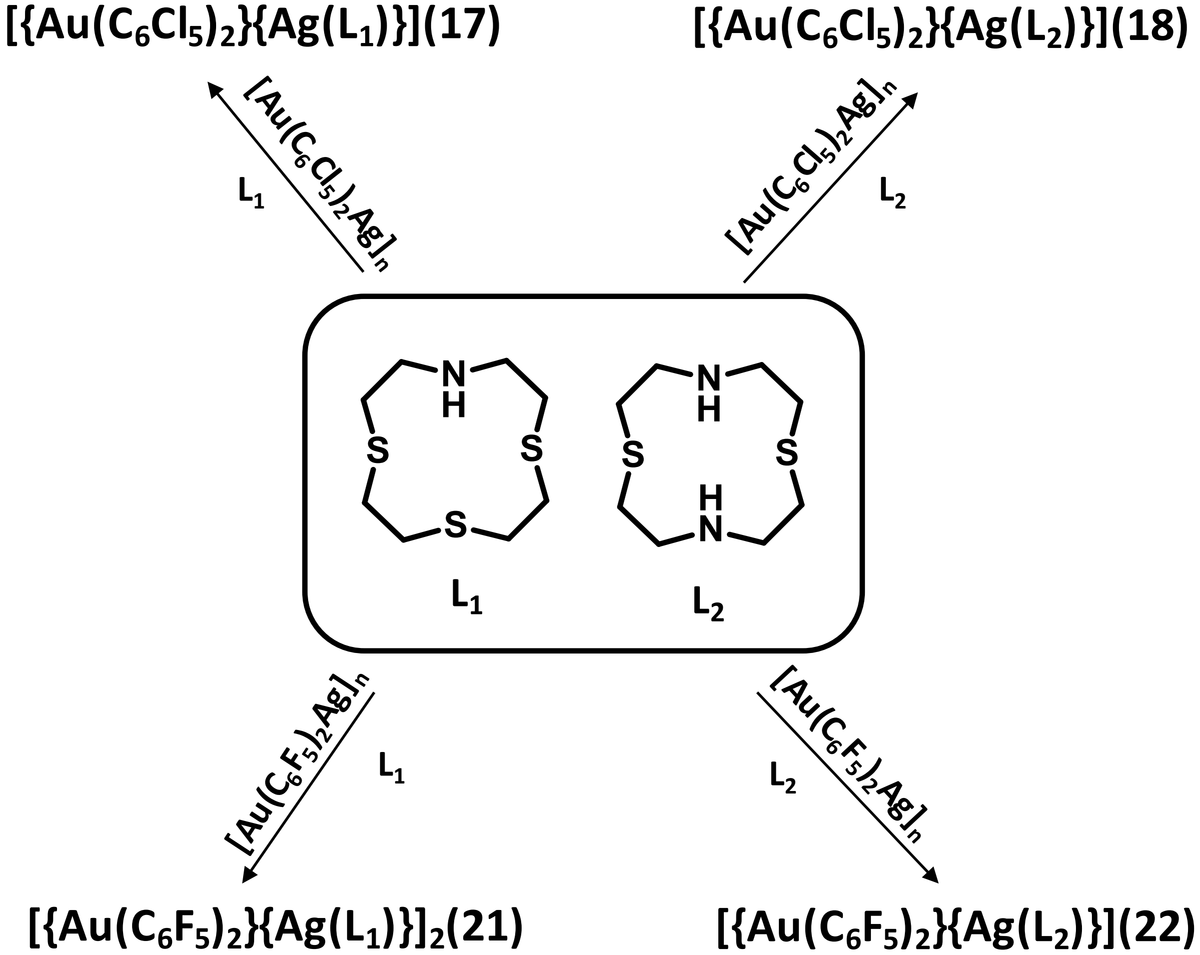

Scheme 1.

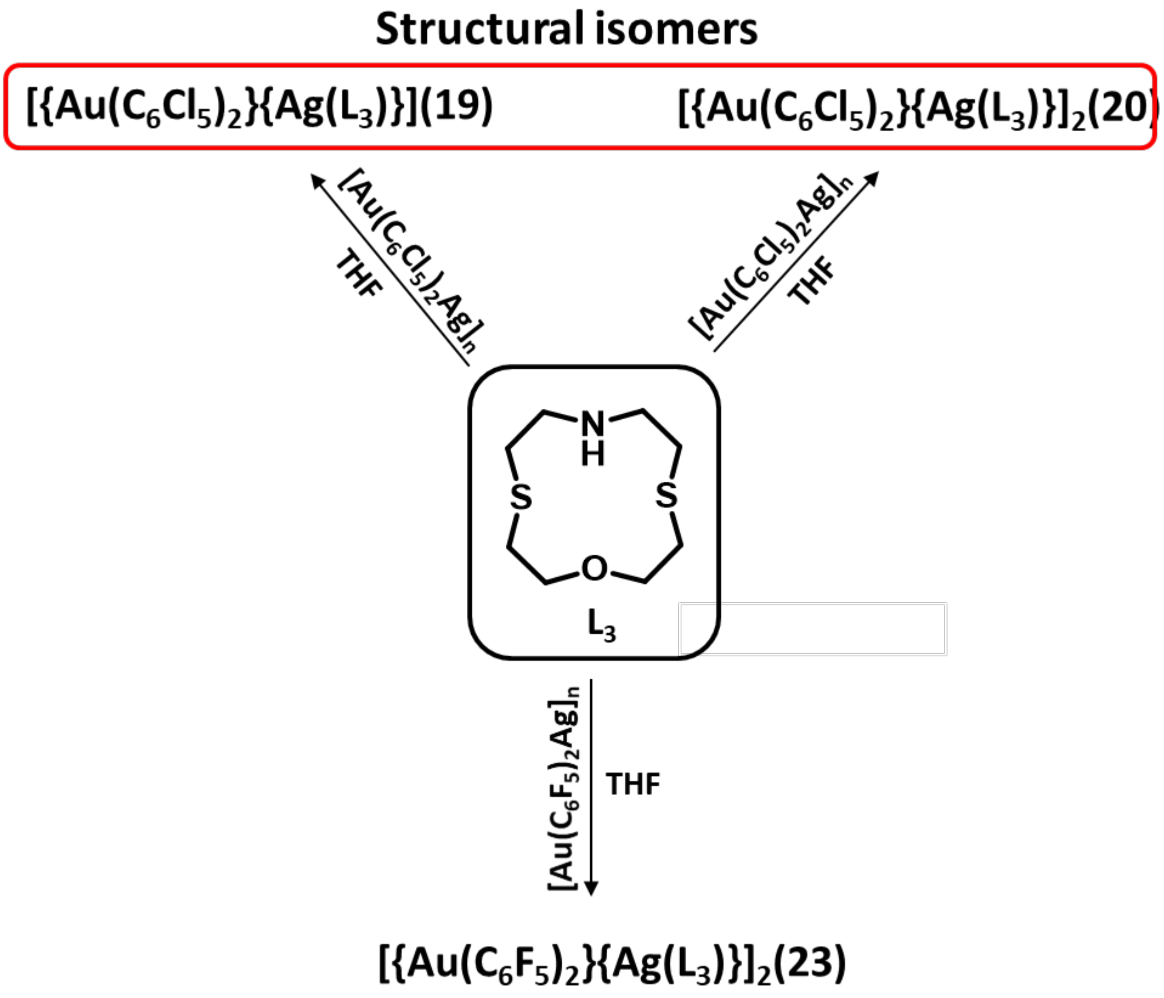

Scheme 2.

Regarding the NMR spectrum of all the complexes, they all show proton resonances very similar to the chemical shifts observed for the free ligands. Therefore, the coordination of the macrocyclic ligands to silver(I) does not significantly affect the position of the resonances observed in their ^{1}H NMR spectra, nor does the dissociative process affect the N,S-donor molecules. Thus, the ^{1}H NMR spectra of **17** and **21** display two multiplets at 2.66-2.73 and 2.80 ppm (**17**), or at 2.69-2.73 and at 2.75-2.78 ppm (**21**), with 1:3 relative integrations, corresponding to the hydrogen atoms of the methylene groups adjacent to nitrogen or to sulphur donors, respectively. In the ^{1}H NMR spectra of **18** and **22,** two multiplets, at 2.62-2.65 and 2.68-2.70 ppm (**18**, **22**), respectively, with 1:1 relative integrations, due to the protons of the methylene groups bonded to the N or S atoms of the ring, appear. Finally, in the ^{1}H NMR spectra of the other three products (**19**, **20**, **23**), we can see two multiplets at 2.75-2.92 and 3.58 ppm (**19**), 2.73-2.98 and 3.58 ppm (**20**) and at 2.72-2.90 and 3.58 ppm (**23**), with 1:3 relative integrations, due to the protons of the methylene groups bonded to the N,S or O atoms of the ring, respectively.

About their mass spectra (MALDI(-)), the compound synthesised display a peak due to the unit $[\{Au(C_6X_5)_2\}_2Tl]^-$ at *m/z* = 1497 (**17**-**20**) or 1168 (**21-21**), or a signal corresponding to $[Au(C_6X_5)_2]^-$ at *m/z* = 695 (**17**-**20**) or 531 (**21**-**23**), the latter appearing as parent peak in all cases. In their MALDI(+) mass spectra, peaks due to the fragment [Ag(**L**)]$^+$ peaks appears at *m/z* = 331 (**17**, **21**) or 312-313 (**18-20**, **22** and **23**), showing experimental isotopic distributions in agreement with the theoretical ones. Their IR spectra show, among others, absorptions arising from the C_6F_5-[60] and C_6Cl_5-[61] groups bonded to gold(I) at approximately 1500, 950 and 780 cm^{-1}, or about 834 and 614 cm^{-1}, respectively. Finally, the molar conductivity measurements of the six complexes in acetone agree with a dissociative process in solution, showing values corresponding to uni-univalent electrolytes (see Experimental).

3.2.2 X-ray structural determinations

Single crystals suitable for X-ray diffraction studies were obtained by slow diffusion of n-hexane Into a saturated solution of the complexes in tetrahydrofurane (complexes **17**, **18**, **20**-**23**) or toluene (complex **19**). Unfortunately, the low quality of some crystals has made it difficult to determine the crystalline structure, even if there is no doubt about the structural arrangement of all the synthesized systems. Tables 1-7 show the most important distances and angles present in the crystal structures. The structures obtained for all complexes recall those obtained for the Au/Tl or Au/Ag systems supported by crown ethers [59],[62]; probably the coordinative abilities of the macrocycles used are similar to the systems considered in previous works. In particular, the three dinuclear complexes **17**-**19** contain $[Au(C_6Cl_5)_2]^-$ units connected to the silver(I) atom of the cationic [Ag(**L**)]$^+$ fragments via unsupported Au(I)···Ag(I) interactions (see Figure 2). In addition, the silver(I) center participates in a weak Ag···C interaction with the ipso carbon atom of one of the perchlorophenyl rings bonded to gold(I). Thus, in all of them, the gold(I) centers of the bis(aryl)aurate(I) units are almost linearly coordinated. In fact, the maximum deviation from linearity for the C−Au−C angle of 6.1° occurs in (**18**), showing typical Au−C distances that range from 2.01(3) to 2.152(13) Å. Nevertheless, there are little differences between them, due to the nature of the macrocyclic ligand bonded to silver, which influence the distance of Ag···C$_{ipso}$ interactions, as well as the Au−Ag distances. In fact, a lengthening of the Au-Ag distance, as well as of the Ag-C$_{ipso}$ distance is observed from the $\mathbf{L_1}$ to the $\mathbf{L_3}$ macrocyclic system (see Tables 1-3). This may be due to the ability of the different macrocycles to interact with the metal centre, which affects the distance of the weak interactions.

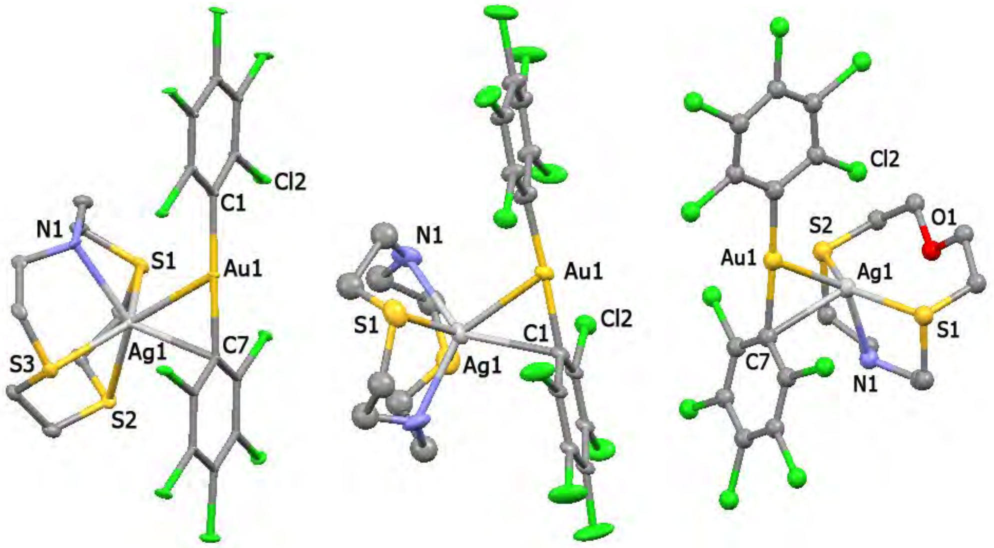

Figure 2. Crystal structures of **17** (left), **18** (middle) and **19** (right) with the labelling scheme adopted for the atom positions. Hydrogen atoms and any solvent molecules are omitted for clarity, and ellipsoids (**17**, **18**) are drawn at the 30% level. For the complex **19** the disorder present in the molecule prevents the anisotropization of the system.

Table 1. Selected bond lengths [Å] and angles [°] for **17**.

Au(1)-Ag(1)	2.789(2)	Ag(1)-N(1)	2.45(2)
Ag(1)-C(7)	2.530(19)	Ag(1)-S(1)	2.659(8)
Au(1)-C(1)	2.04(2)	Ag(1)-S(2)	2.632(8)
Au(1)-C(7)	2.098(11)	Ag(1)-S(3)	2.654(8)
C(1)-Au(1)-C(7)	178.4(10)	N(1)-Ag(1)-S(3)	79.4(6)
S(2)-Ag(1)-S(1)	82.5(3)	N(1)-Ag(1)-S(1)	80.1(6)
S(3)-Ag(1)-S(1)	137.3(3)	N(1)-Ag(1)-S(2)	129.1(6)
S(2)-Ag(1)-S(3)	82.0(3)	S(1)-Ag(1)-Au(1)	97.27(18)
N(1)-Ag(1)-Au(1)	86.8(6)	S(2)-Ag(1)-Au(1)	142.94(19)
		S(3)-Ag(1)-Au(1)	118.46(19)

Table 2. Selected bond lengths [Å] and angles [°] for **18**.

Au(1)-Ag(1)	2.806(3)	Ag(1)-N(1)	2.45(4)
Ag(1)-C(1)	2.67(3)	Ag(1)-N(2)	2.45(4)
Au(1)-C(1)	2.05(3)	Ag(1)-S(1)	2.649(13)
Au(1)-C(7)	2.03(4)	Ag(1)-S(2)	2.644(12)
C(7)-Au(1)-C(1)	173.9(15)	N(1)-Ag(1)-C(1)	138.7(12)
C(1)-Au(1)-Ag(1)	64.4(7)	S(2)-Ag(1)-C(1)	110.7(8)
N(2)-Ag(1)-N(1)	118.9(12)	S(1)-Ag(1)-C(1)	110.6(8)
N(2)-Ag(1)-S(2)	78.2(9)	N(2)-Ag(1)-Au(1)	140.5(9)
N(1)-Ag(1)-S(2)	78.2(8)	N(1)-Ag(1)-Au(1)	97.6(9)
N(2)-Ag(1)-S(1)	81.1(8)	S(2)-Ag(1)-Au(1)	127.0(3)
N(1)-Ag(1)-S(1)	79.3(9)	S(1)-Ag(1)-Au(1)	92.2(3)
S(2)-Ag(1)-S(1)	136.8(4)	C(1)-Ag(1)-Au(1)	43.9(7)
N(2)-Ag(1)-C(1)	102.4(10)		

Table 3. Selected bond lengths [Å] and angles [°] for **19**

Au(1)-Ag(1)	2.806(3)	Ag(1)-N(1)	2.35(2)
Ag(1)-C(7)	2.691(18)	Ag(1)-S(1)	2.566(8)
Au(1)-C(1)	2.01(3)	Ag(1)-S(2)	2.587(8)
Au(1)-C(7)	2.152(13)		
C(1)-Au(1)-Ag(1)	119.6(8)	S(1)-Ag(1)-C(7)	108.1(4)
C(1)-Au(1)-C(7)	176.2(9)	S(2)-Ag(1)-Au(1)	109.14(19)
C(1)-Au(1)-O(2)	104.9(12)	S(2)-Ag(1)-C(7)	109.2(4)
C(7)-Au(1)-Ag(1)	64.2(5)	N(1)-Ag(1)-Au(1)	138.9(5)
O(2)-Au(1)-Ag(1)	135.5(9)	N(1)-Ag(1)-S(1)	81.3(5)
O(2)-Au(1)-C(7)	71.3(11)	N(1)-Ag(1)-S(2)	81.5(5)
S(1)-Ag(1)-Au(1)	107.97(19)	N(1)-Ag(1)-C(7)	92.9(6)
S(1)-Ag(1)-S(2)	139.4(2)		

The intermetallic distances within the cations are different depending on the macrocyclic ligand employed (see Tables 1-3), showing a Au-Ag distances of 2.789(2) Å in the [12]aneNS_3 (**L_1**) derivative **17**, shorter than those observed in the [12]aneN_2S_2 (**L_2**) complex **18** (2.806(3) Å), or [12]aneNS_2O (L_3) complex **19** (2.806(3) Å)**.** These distances are intermediate among those found in the related complexes of crown thioethers (Au-Ag: 3.0763(4), 2.7501(2) and 2.6772(3) Å) [59]. Furthermore, the Ag···C*ipso* contacts in **17**-**19** are intermediate compared to those found in other complexes in which the $[Au(C_6X_5)_2]^-$ units interacts with the silver(I) centers through both Au···Ag and Ag···C$_{ipso}$ contacts (Ag···C distances vary from 2.422(4) in $[Au_2Ag_2(C_6Cl_2F_3)_4(THF)_2]_n$[68] to 2.707(18) Å in $[Au_2Ag_2(4\text{-}C_6F_4I)_4(THF)_2]_n$]).[69]

The Ag-N and Ag-S bond lengths in complexes **17**-**19** lie within the ranges 2.35(2)-2.45(4) and 2.566(8)-2.659(8) Å, respectively, found for Ag-S and Ag-N distances in other silver complexes containing similar systems as ([9-oxo-[12]aneNS_3)(Ag)]$_2$[CF_3SO_3]$_2$[63] [(9-oxo-[12]aneNS_3)Ag]$_n$[CF_3SO_3]$_n$ [(N-acylurea-[12]aneNS_3])Ag][NO_3][64], [(N-(Benzyloxycarbonyl)-[12]aneNS_3)Ag][NO_3][65], [(N-(pyridylmethyl)-[12]aneNS_3)Ag][PF_6][66], [(N-(pyridylmethyl)-[12]aneNS_2O)Ag][PF_6][66] and [(N-CH_2CONH-tBu)-[12]aneNS_3)Ag][NO_3][67]). In complex **19,** as well as in all other complexes containing **L_3**, the conformation of the macrocycle and the Ag-O distance excludes the coordination of this heteroatom to the metallic centre.

The reaction between the macrocyclic system **L_3** and the $[Au(C_6Cl_5)_2Ag]_n$ polymeric complex leads to the formation of two structural isomers: the complex **19**, whose structural arrangement has been described previously, and the complex **20**. The latter can be described as a tetranuclear system, which shows a linear or pseudolinear Ag-Au-Au-Ag arrangement (see Figure 3); the different structural arrangement with respect to the isomer **19** is due to the lack of the Ag-C$_{ipso}$ interaction and to the formation of a new Au-Au interaction. Moreover, during the X-ray structural resolution process a disorder of the metal centres was observed due to the different possible structural positions of the macrocycle, which determines the presence of two asymmetric units within the same system (part A and part B) crystal, which differ mainly in the Au-Ag, Au-S and Au-N distances. Despite the difficulties due to the resolution of the disorder within the system, it can be clearly observed that the Au-Ag distances in the complex **20** (2.664(11) and 2.790(4) Å) are smaller than those found in the structural isomer **19.** Moreover, in this case we can observe an Au-Au distance much shorter than those described in the literature for $[\{Au(C_6F_5)_2\}Ag([14]aneS_4)]_2$ [59]. Finally, the distances Ag-N and Ag-S are very similar to those previously described in the three binuclear complexes **17**-**19** and in this case there is no coordination for the oxygen atom to the silver metal centre.

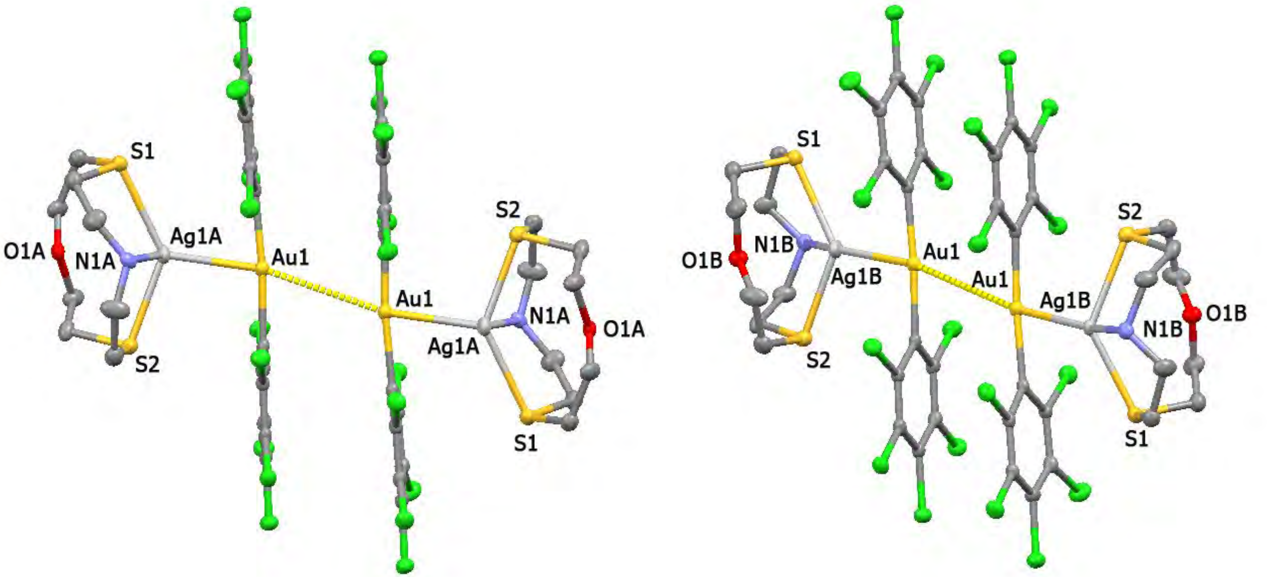

Figure 3. Asymmetric units A (left) and B (right) of crystal structures of **20**. Hydrogen atoms molecules and any solvent molecule are omitted for clarity, and ellipsoids are drawn at the 30% level.

Table 4. Selected bond lengths [Å] and angles [°] for **20**

C(1)-Au(1)	2.041(5)	S(1)-Ag(1)A	2.531(8)
C(7)-Au(1)	2.046(5)	S(2)-Ag(1)B	2.580(5)
Au(1)-Ag(1)B	2.790(4)	S(2)-Ag(1)A	2.612(8)
Au(1)-Ag(1)A	2.664(11)	Ag(1)-N(1)B	2.425(7)
S(1)-Ag(1)B	2.627(5)	N(1)A-Ag(1)A	2.57(3)
Au(1)-Au(1)	3.3852(2)		
C(1)-Au(1)-C(7)	175.32(17)	N(1)B-Ag(1)-Au(1)	156.8(3)
S(1)-Ag(1)-Au(1)	97.01(14)	N(1)B-Ag(1)-S(1)	81.07(18)
S(2)-Ag(1)-Au(1)	116.52(16)	N(1)B-Ag(1)-S(2)	80.24(18)
S(2)-Ag(1)-S(1)	131.0(2)	S(1)-Ag(1)A-S(2)	134.2(3)
S2-Ag(1)A-Au(1)	120.0(3)	S(1)-Ag(1)A-N(1)A	84.1(7)
N(1)A-Ag1A-Au1	94.8(9)	N(1)A-Ag(1)A-S(2)	77.0(6)

The substitution of chlorine by fluorine atoms in the aryl groups bonded to gold(I) leads to small differences in the crystal structures of the resulting complexes **21**-**23**.

In complex **21**, the crystal structure can be described as a tetranuclear system with an almost linear Ag-Au-Au-Ag arrangement very similar to those encountered for the complex **20** (see Figure 4); while the Au-Au distance (3.2633(4) Å) is smaller than that previously discussed. The Au-Ag distance (2.7459(5) Å) is intermediate between those found in the two asymmetric units of the complex **20**. The main difference observed in this structure is the presence of Ag-C_{ipso} contacts, which stabilize the entire system. Furthermore, the Ag···C_{ipso} contact in **21** is longer than that found in all complexes described above (see Table 5).

Complex **21** shows Ag-S distances of 2.652(2), 2.666(2) and 2.714(2) Å that lie within the range of Ag-S distances [2.503(2)-2.9605(7) Å] found for other silver complexes containing **L_1**.[63]-[67] The Ag-N bond length of 2.476(6) Å found in **21** is shorter than those in related complexes [2.485(4)-2.709(9)Å] as ([9-oxo-[12]aneNS$_3$)(Ag)]$_2$[CF$_3$SO$_3$]$_2$[63] [(9-oxo-[12]aneNS$_3$)Ag]$_n$[CF$_3$SO$_3$]$_n$ [(N-acylurea-[12]aneNS$_3$])Ag][NO$_3$][64], [(N-(Benzyloxycarbonyl)-[12]aneNS$_3$)Ag][NO$_3$][65], [(N-(pyridylmethyl)-[12]aneNS$_3$)Ag][PF$_6$][66], [(N-(pyridylmethyl)-[12]aneNS$_2$O)Ag][PF$_6$][66] and [(N-CH$_2$CONH-tBu)-[12]aneNS$_3$)Ag][NO$_3$][67]).

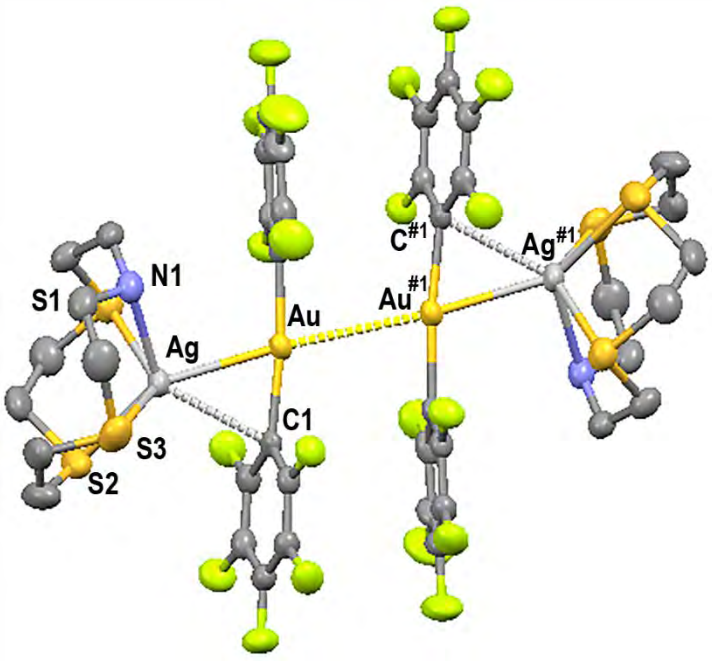

Figure 4. Crystal structures of **21**. Hydrogen atoms molecules and any solvent molecule are omitted for clarity, and ellipsoids are drawn at the 30% level.

Table 5. Selected bond lengths [Å] and angles [°] for **21**.

Au(1)-Ag(1)	2.7459(5)	Ag(1)-N(1)	2.476(6)
Au(1)-Au(1)#1	3.2633(4)	Ag(1)-S(1)	2.714(2)
Ag(1)-C(1)	2.7498(58)	Ag(1)-S(2)	2.666(2)
Au-C(1)	2.057(6)	Ag(1)-S(3)	2.652(2)
Au-C(7)	2.044(6)		
Ag(1)-Au(1)-Au(1)#1	170.135(17)	S(1)-Ag(1)-S(3)	134.81(6)
C(7)-Au-C(1)	173.8(2)	S(2)-Ag-S(3)	82.75(8)
N(1)-Ag-S(1)	77.17(14)	N(1)-Ag(1)-Au(1)	95.61(13)
N(1)-Ag-S(2)	125.47(14)	S(1)-Ag(1)-Au(1)	93.51(4)
N(1)-Ag-S(3)	79.10(15)	S(2)-Ag(1)-Au(1)	135.11(5)
S(1)-Ag(1)-S(2)	80.61(7)	S(3)-Ag(1)-Au(1)	126.76(5)

Symmetry transformations used to generate equivalent atoms:

#1 -x+1,-y+1,-z+1

As previously mentioned, attempts to solve the disorder of some structures prevented the correct evaluation of various interactions, despite the unequivocal nature of the structure obtained. In fact, attempts to determine with accuracy the crystal structure of complex **22** were unsuccessful, although there is no doubt about the overall molecular structure, which shows a dinuclear Au/Ag discrete molecule with a $[Au(C_6F_5)_2]^-$ unit connected to a $[Ag(\mathbf{L_1})]^+$ cation through an Au···Ag interaction reinforced by a Ag···C_{ipso} contact (see Figure 6 and Table 6). In this structure, the macrocyclic ligand $\mathbf{L_2}$ binds the silver(I) atom through all its donor atoms and no Au(I)···Au(I) interaction is detected, thus displaying the same unusual disposition previously observed in $[\{Au(C_6Cl_5)_2\}Ag([14]aneS_4)]$.[59]

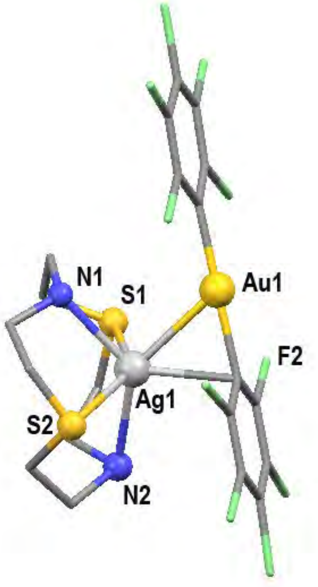

Figure 5. Representative scheme of complex **22**.

Table 6. Selected bond lengths [Å] and angles [°] for **22**.

Au(1)-Ag(1)	2.763(5)	Ag(1)-N(1)	2.49(4)
Ag(1)-C(1)	2.673(19)	Ag(1)-N(2)	2.46(4)
Au(1)-C(1)	2.068(7)	Ag(1)-S(1)	2.592(16)
Au(1)-C(7)	2.30(3)	Ag(1)-S(2)	2.622(16)
C(1)-Au(1)-C(7)	129.7(11)	N(2)-Ag(1)-S(1)	77.7(9)
C(1)-Au(1)-Ag(1)	65.4(5)	N(2)-Ag(1)-S(2)	79.8(9)
N(1)-Ag(1)-S(1)	85.8(9)	N(1)-Ag(1)-Au(1)	138.0(7)
N(1)-Ag(1)-N(2)	118.5(12)	N(2)-Ag(1)-Au(1)	92.5(9)
S(1)-Ag(1)-S(2)	136.0(5)	S(1)-Ag(1)-Au(1)	130.8(5)
N(1)-Ag(1)-S(2)	72.6(10)	S(2)-Ag(1)-Au(1)	87.3(4)

Despite the unequivocal nature of the structural arrangement, the restriction parameters used for the structural resolution of the system do not allow us to make a comparison with the bond distances of the previous complexes obtained.

Finally, exactly as observed in the synthesis of complex **19**, the reaction between **L$_3$** and the $[Au(C_6F_5)_2Ag]_n$ polymeric chain leads to the formation of the heteronuclear complex **23** where Au-Ag and Ag-C$_{ipso}$ interactions can be observed (see Figure 6 and Table 7) . The main difference was found during the structural resolution, since in the unit cell there are two binuclear units with slightly different Au-Ag and Au-C*ipso* distances. Thus, while in both units, the Au-Ag distances are shorter than those encountered in the complex **19**, the Ag-C*ipso* distances are longer than those observed previously. The distances Ag-N (2.405 (12) -2.430 (15) Å) and Ag-S (2.492(4)-2.589(5) Å) are very similar to those described in the previously commented systems, and to some related systems $[Ag(L)]^+$ as ([9-oxo-[12]aneNS$_3$)(Ag)]$_2$[CF$_3$SO$_3$]$_2$[63], [(9-oxo-[12]aneNS$_3$)Ag]$_n$[CF$_3$SO$_3$]$_n$ [(N-acylurea-[12]aneNS$_3$])Ag][NO$_3$][64], [(N-(Benzyloxycarbonyl)-[12]aneNS$_3$)Ag][NO$_3$][65], [(N-(pyridylmethyl)-[12]aneNS$_3$)Ag][PF$_6$][66], [(N-(pyridylmethyl)-[12]aneNS$_2$O)Ag][PF$_6$][66], and [(N-CH$_2$CONH-tBu)-[12]aneNS$_3$)Ag][NO$_3$][67]), previously published.

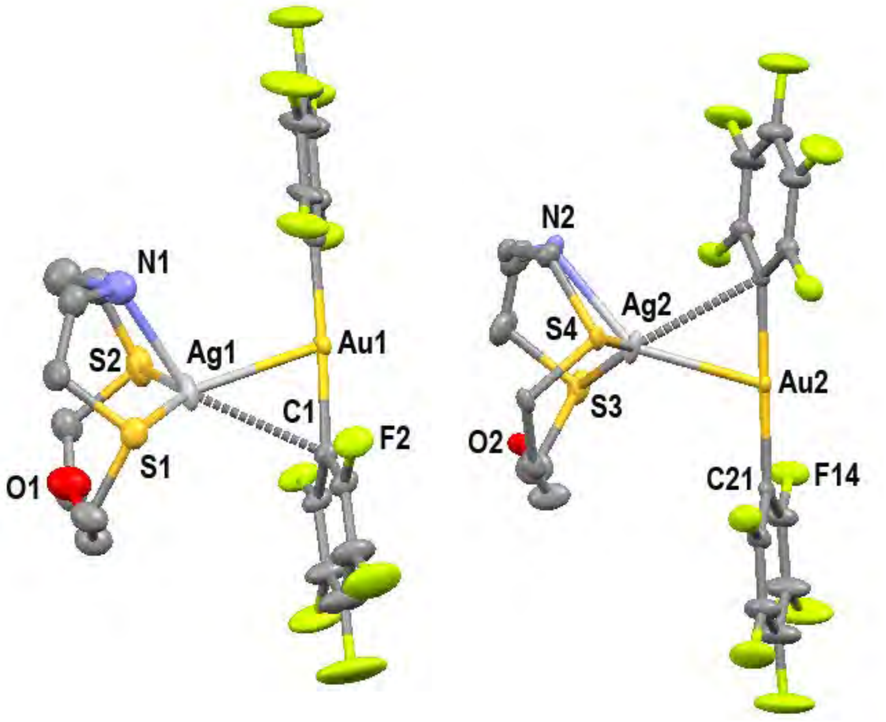

Figure 6. Crystal structures of **23**. Hydrogen atoms molecules and any solvent molecule are omitted for clarity, and ellipsoids are drawn at the 30% level.

Table 7. Selected bond lengths [Å] and angles [°] for **23**.

Au(1)-Ag(1)	2.7069(11)	Au(2)-Ag(2)	2.7247(13)
Au(1)-C(1)	2.029(12)	Au(2)-C(21)	2.052(15)
Au(1)-C(7)	2.063(13)	Au(2)-C(27)	2.033(15)
Ag(1)-S(1)	2.573(4)	Ag(2)-N(2)	2.430(15)
Ag(1)-S(2)	2.501(3)	Ag(2)-S(3)	2.589(5)
Ag(1)-N(1)	2.405(12)	Ag(2)-S(4)	2.492(4)
C(1)-Au(1)-C(7)	178.6(5)	C(27)-Au(2)-C(21)	177.1(6)
S(1)-Ag(1)-Au(1)	93.79(9)	N(2)-Ag(2)-Au(2)	106.9(4)
S(2)-Ag(1)-Au(1)	121.69(8)	S(3)-Ag(2)-Au(2)	95.24(11)
S(2)-Ag(1)-S(1)	137.87(12)	S(4)-Ag(2)-Au(2)	130.34(11)
N(1)-Ag(1)-Au(1)	139.4(3)	N(2)-Ag(2)-S(3)	82.6(4)
N(1)-Ag(1)-S(1)	82.1(3)	N(2)-Ag(2)-S(4)	80.0(4)
N(1)-Ag(1)-S(2)	83.8(3)	S(4)-Ag(2)-S(3)	134.18(15)

Furthermore, in the tetranuclear complexes **20** and **21,** π-stacking contacts can be observed between the aromatic moieties of the perfluorophenyl aurate units, which give further stability to the structures (3.661 and 3.648 Å for complex **20** and **21,** respectively) (see Figure 7).

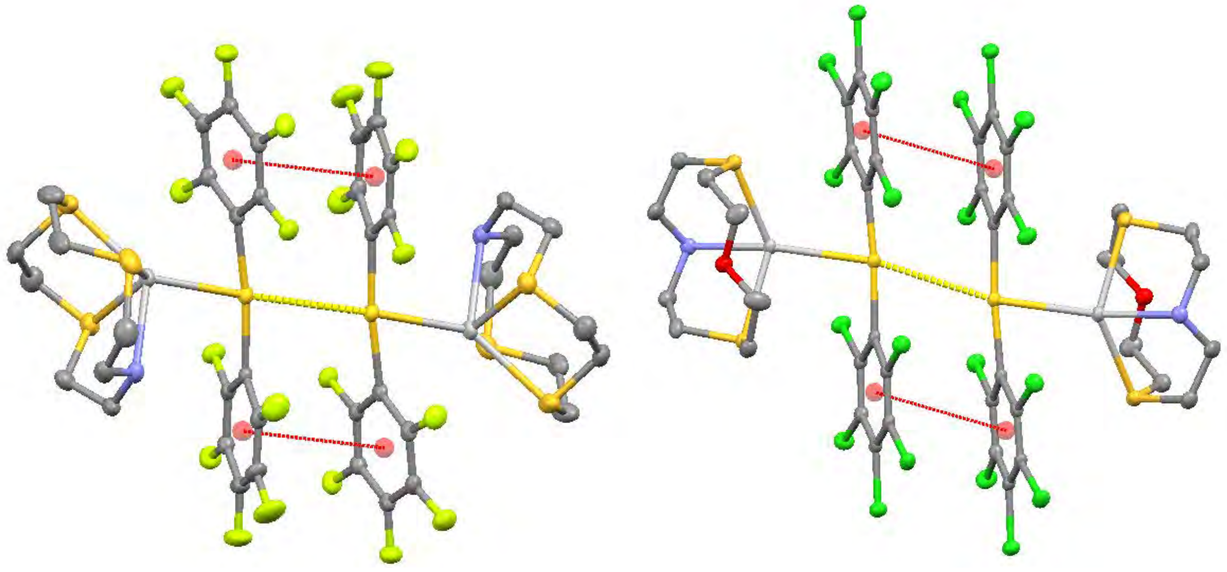

Figure 7. π-stacking (red line) contact in complex **20** (left) and **21** (right).

3.2.3 Spectroscopic properties

According to the high energy of the absorptions as well as to the similarity of the spectra registered for complexes **17**-**20** and the precursors $NBu_4[Au(C_6Cl_5)_2]$ (which displays bands at 242 and 298 nm), $[Au(C_6Cl_5)_2Ag]_n$ (which displays bands at 235,256 and 303 nm) (Figure 8), it is tentatively possible to assign the band observed to ππ* or Au→π* transitions involving the pentachlorophenyl rings. These assignments have been also described in other polymeric complexes built by acid/basic reactions (metal salts/bisperhalophenylgold(I)).[16],[70],[71] Nevertheless, in the case of the high-energy absorptions the possibility of a n→σ* transition in the N,S,O-mixed-donor ligands cannot be ruled out, since these ligands show an absorption at 234 nm of less intensity at similar concentrations.

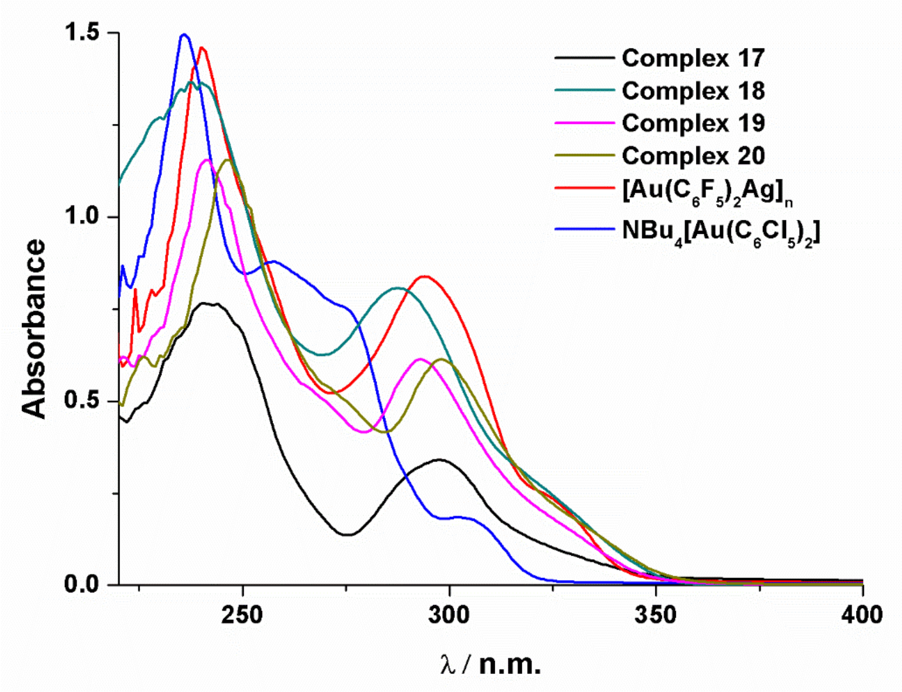

Figure 8. Absorption spectra of complex **17**-**20** and the gold precursors $NBu_4[Au(C_6Cl_5)_2]$ and $[\{Au(C_6Cl_5)_2\}Ag]_n$ in THF solution (C=2.5 x 10^{-5} M).

In contrast to this behaviour, in the case of the pentafluorophenyl derivatives **21**-**23**, the spectra show some differences with respect to those of the precursors $NBu_4[Au(C_6F_5)_2]$ or $[\{Au(C_6F_5)_2\}Ag]_n$ (Figure 9). While complexes **21** and **22** display a band at 246 and 253 nm, respectively, complex **23** shows a band at 269 nm; the latter is slightly red shifted compared to those of the two precursors. In all cases, the rest of the absorptions observed for the two precursors appear in the spectra, and the assignations can be the same as those made for the compounds **17**-**20**.

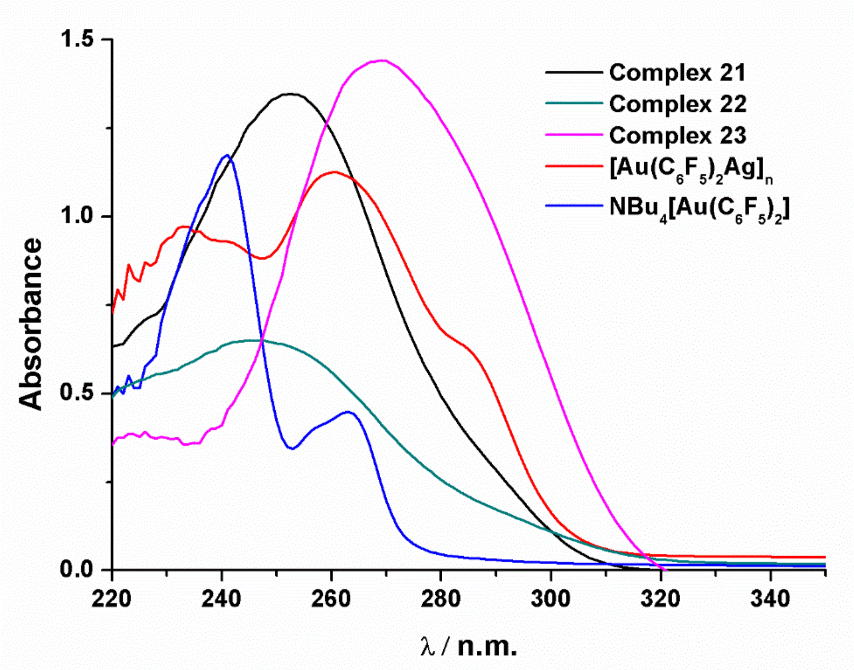

Figure 9. Absorption spectra of complex **21**-**23** and the gold precursors $NBu_4[Au(C_6F_5)_2]$ and $[\{Au(C_6F_5)_2\}Ag]_n$ in THF solution (C=2.5 x 10^{-5} M).

Despite the numerous reactions carried out, the little structural variety observed in the seven complexes obtained (**17**-**23**) is reflected in the optical responses when the complexes are irradiated with UV light in the solid state. All complexes display a strong blue luminescence (between 442 and 472 nm) with the exception of complex **20** which shows an emission at about 500 nm (green), both at room temperature and at 77K (see Table 8-9 and Figures 10-11). None of them is emissive when they are irradiated in solution, probably due to the dissociation of the counterparts in solution, as suggested by the mass spectra and the conductivity measurements.

Thus, complexes **17**-**19** show a decrease in emission energy (from 463 to 442 nm) as a function of the increase in the Au-Ag distances (from 2.789(2) in complex **17** to 2.806(3) Å in complexes **18**,**19**) and, consequently, in the Ag-C_{ipso} distances (from 2,530(19) in complex **17** to 2.67(3) Å in complex **18** and 2,691(18) Å in complex **19**). It can be observed a red shift of the emission energy in the complex **20**, probably due to the presence of the aurophilic interaction, which causes a greater stabilization of the system.

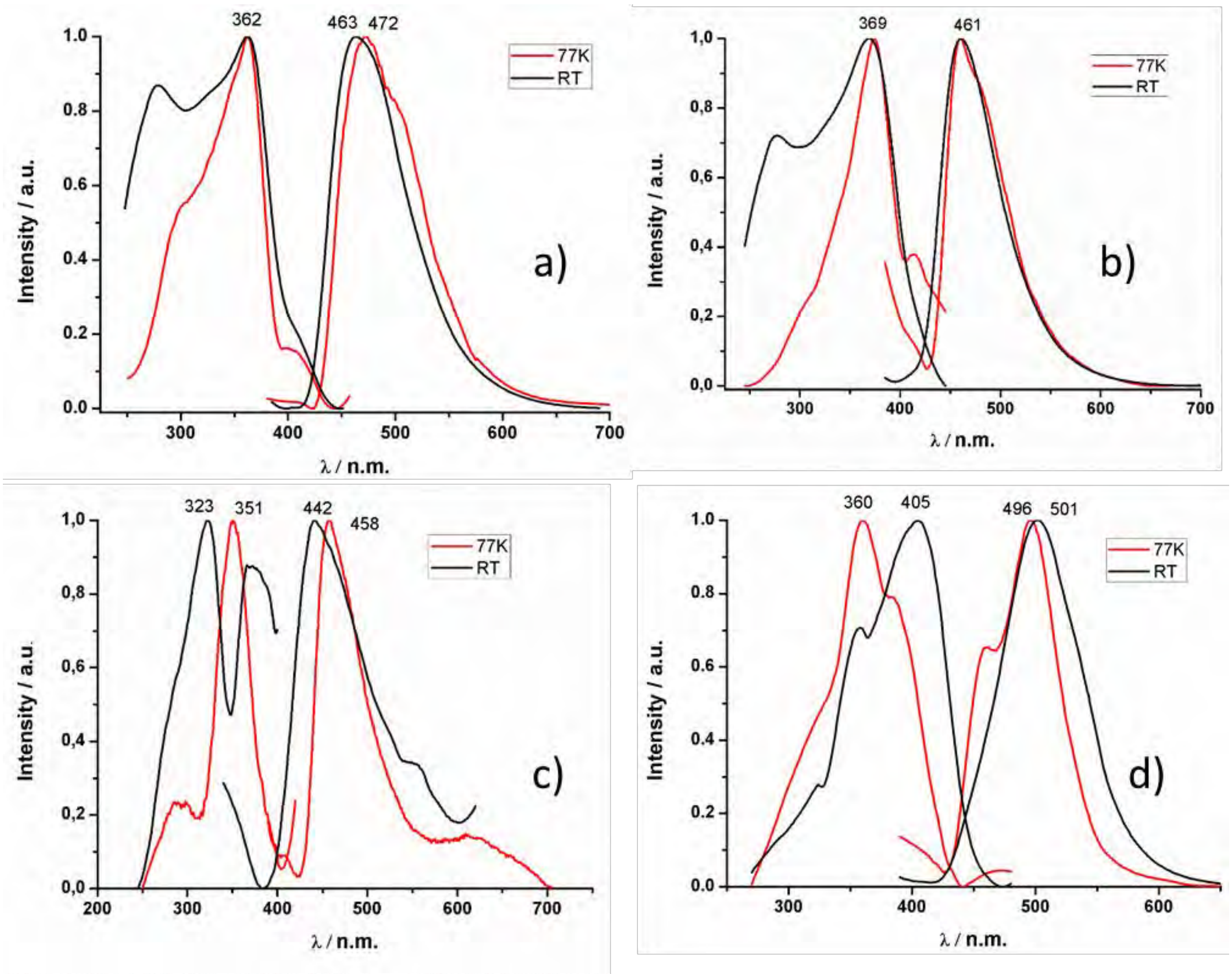

Fig. 10. Excitation and emission spectra for complexes **17**(a), **18**(b), **19**(c) and **20**(d) in the solid state at RT and 77 K.

Table 8. Photophysical properties of complexes **17**-**20.**

	UV-vis in THF (nm)	Solid (RT) em(exc)	Solid (77K) em (exc)	τ (ns)	Φ (%)
Complex 17	241 (ε = 30400) 297 (ε = 13200)	463 (362)	472 (363)	2082 ± 11	7.5
Complex 18	241 (ε = 34400) 288 (ε = 12000)	461 (369)	461 (369)	1942 ± 78	5.2
Complex 19	242 (ε = 36000) 292 (ε = 12200)	442 (323)	458 (351)	892 ± 21	7
Complex 20	247 (ε = 36000) 297 (ε = 14454)	501 (405)	496 (360)	1020 ± 13	5.8

On the other hand, in the fluorinated derivatives (complexes **21**-**23**) it is difficult to make a correlation between the metal-metal distances and the increase or decrease of the emission energies for the different systems. The different nuclearity of complex **21,** the disorder encountered in the crystal structure of the complex **22,** and the two structurally similar units but with different Au/Ag distances found in the complex **23** make difficult to correctly interpret the behaviour of these systems.

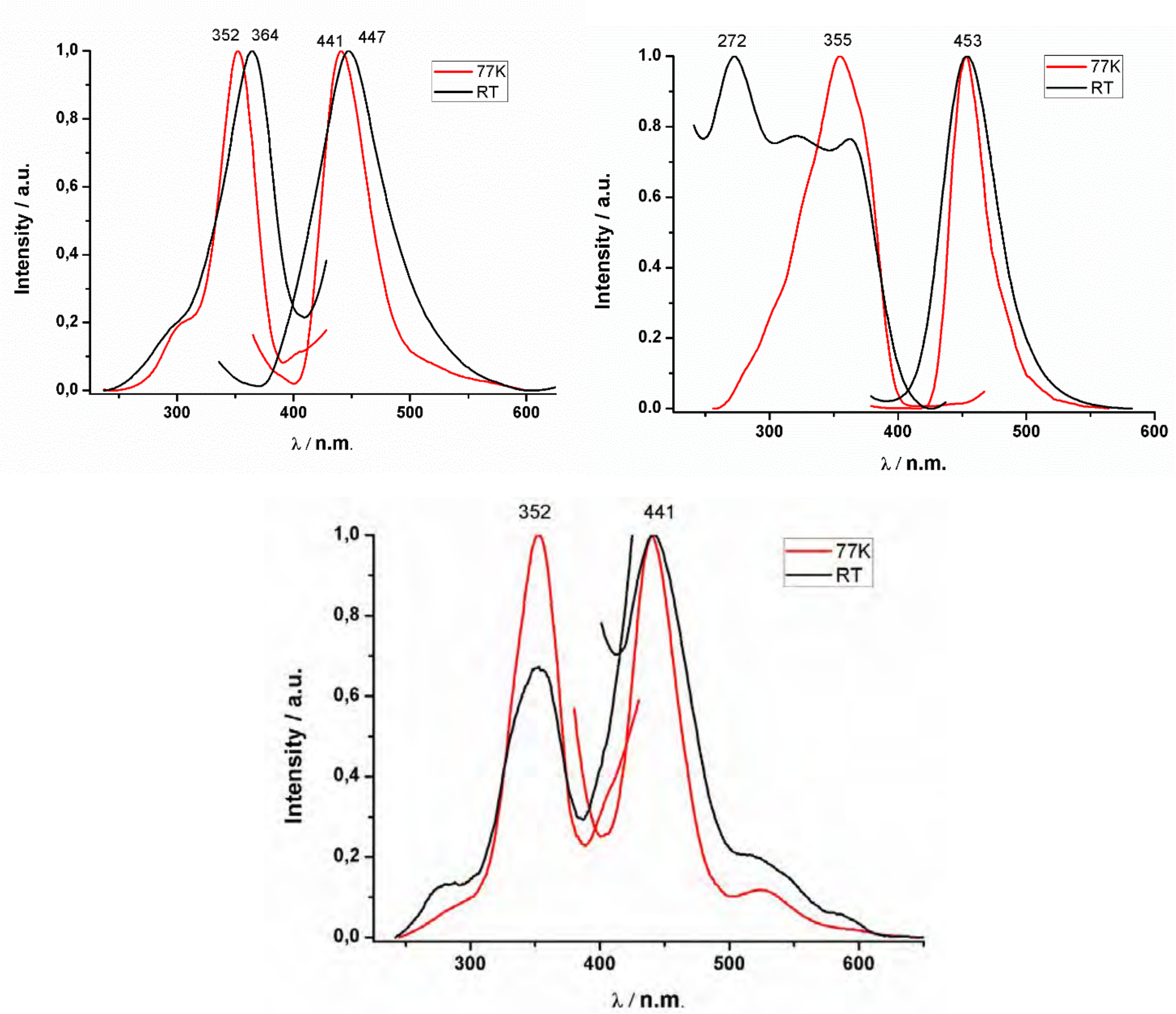

Fig. 11. Excitation and emission spectra for complexes **21**(left), **22**(right) and **23**(down) in the solid state at RT and 77 K.

Table 9. Photophysical properties of complexes **21**-**23.**

	UV-vis in THF (nm)	Solid (RT) em(exc)	Solid (77K) em (exc)	τ (ns)	Φ (%)
Complex 21	250 (ε = 21790)	447 (364)	441 (352)	670 ± 10	4
Complex 22	248 (ε = 22545)	453 (272)	453 (355)	350 ± 32	24
Complex 23	267 (ε = 22545)	441 (352)	441 (352)	720 ± 1	5

Finally, while in some compounds the lowering of the temperature causes a very slight increase of the emission energy (complexes **20** and **21**), in others (complexes **17** and **19**) a red-shift of the emission band is observed. The bathochromic effect is commonly due to a contraction of the crystalline system, which causes a decrease in the energy difference between the frontier orbitals. Moreover, in the complexes **18**, **21** and **22** it is observed that the temperature variation does not influence the emission energy of the compounds (rigidochromism). It is curious that the systems containing **L₂** show this behaviour both in the Au/Ag complexes as well as in the Au/Tl complexes (see Chapter 2). Probably the symmetry of this ligand and the interactions with the metallic center have a strong influence on the structural rigidity of the system.

In addition to all said previously, in the case of compound **19** a peculiar behaviour is observed since when it is subjected to a slight pressure with a spatula in a mortar, a change in the colour of its luminescence occurs. This phenomenon is called Mechanochromism and is defined as a change in luminescence in response to a mechanical stimulus such as grinding or crushing that can induce either phase transitions in solid state or chemical transformations. This phenomenon is better known in organic compounds such as dyes, liquid crystals and polymers[16],[72]-[74]. However, in recent years, the study of this phenomenon in organometallic compounds has increased, having been described in complexes that present metals such as Zn(II), Pt(II), Ag(I), Cu(I), Al(III) and Ir(III)[75], as well as in mono- and bi-nuclear gold complexes[76], in which this behaviour is normally related to the formation or rupture of intermolecular metallic contacts, π-π interactions between rings, or changes in molecular conformation.

In this way, when the crystalline compound **19** is ground in a mortar, a strong change in its emission can be observed, from white to green. As shown in Figure 12, the broadband emission at 442 nm (black line) corresponding to the crystalline species disappears completely, and a narrower band appears centered at 517 nm (grey line). This mechanical stimulus causes a displacement of the emission band of 75 nm (3281.6 cm^{-1}).

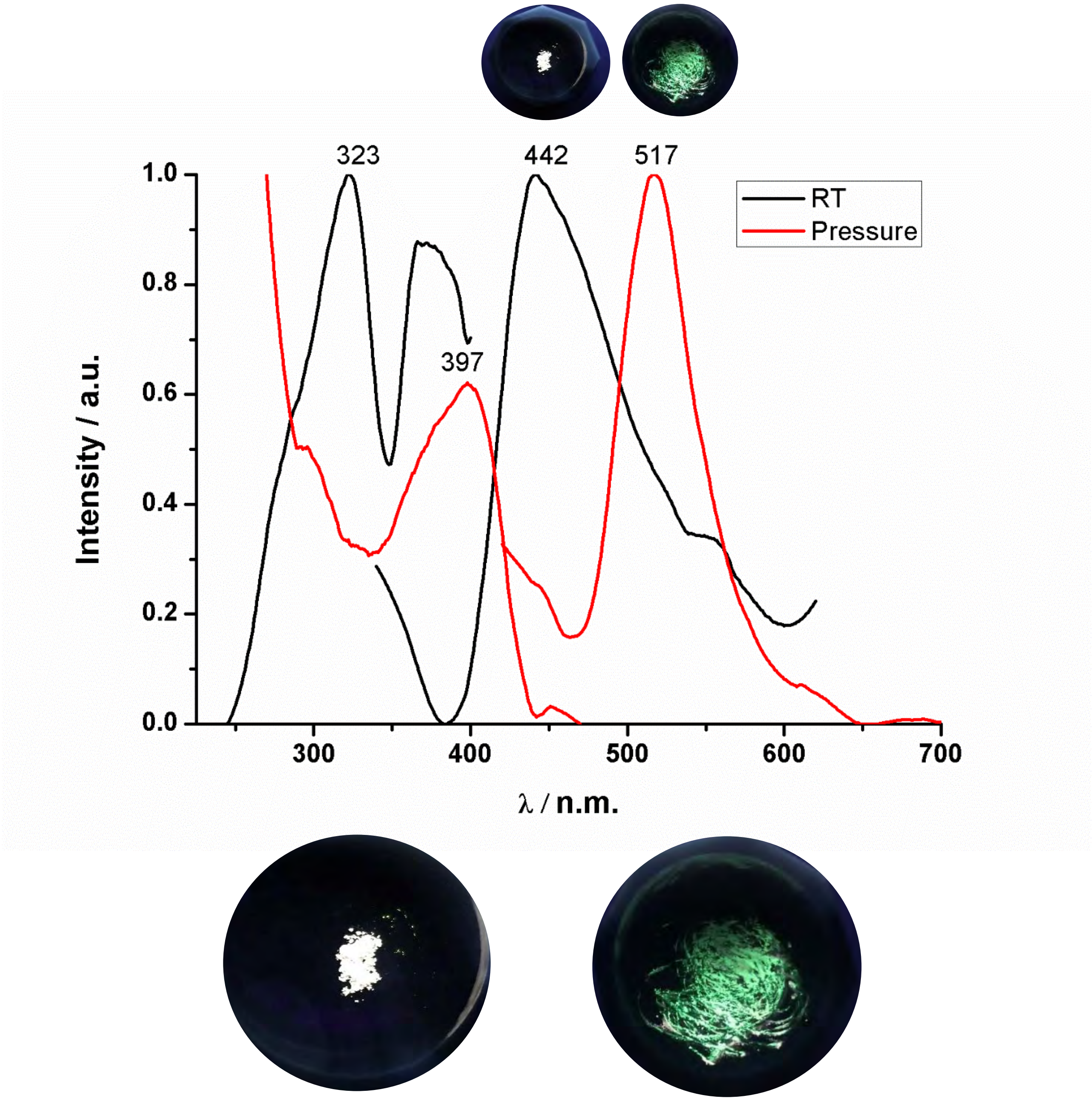

Figure 12. Emission spectra of compound **19** at room temperature, before (black) and after (red) grinding of complex 19. Images show the luminescence before (right) and after (right) grinding of complex **19**.

In order to give an explanation to this fact, a powder X-ray diffraction spectroscopy study was carried out on this system(see Figure 13). From these diffractograms it can be observed that before and after the grinding of the samples, the patterns are identical, which allows us to rule out processes of phase changes. The appreciable widening of the bands in the spectrum of the derivatives subjected to pressure is consistent with a certain degree of partial amorphization. Therefore, we propose that the change in observed luminescence is due to a partial interconversion between the crystalline phase and an amorphous phase.

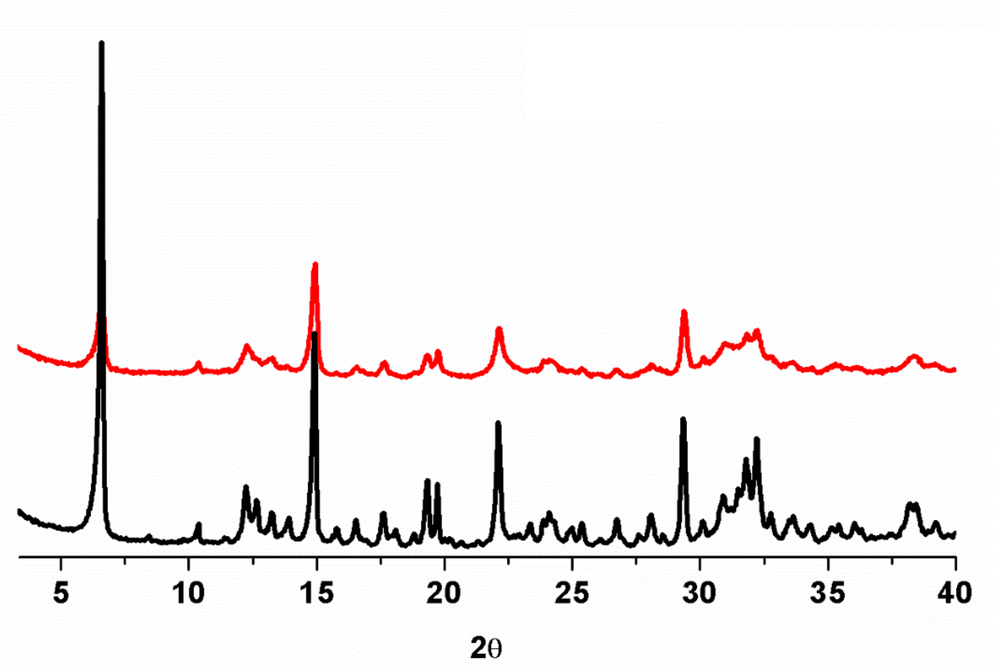

Figure 13. X-ray powder diffraction patterns of compound **19** before pressing (black) and then (red).

However, despite the similar structural characteristics, the complexes **17** and **18** did not show the same mechanochromic properties observed for the complex **19** (see Figure 14). In these cases the application of a pressure to the microcrystalline systems causes a simple enlargement of the band following the structural deformations that the system undergoes, but without changing the maximum emission band. If we look more closely at the structures of the three complexes analysed, it can be found that the greatest difference, in addition to the larger distances Ag-Au and Ag-C_{ipso}, resides in the relative position of the perchlorophenyl rings; in complexes **17** and **18** the aromatic rings turn out to be parallel to each other, while in complex **20** are perpendicular. This fact probably influences the rigidity of the structural system, which together with the amorphization of the system under pressure, causes a drastic reduction in the emission energy.

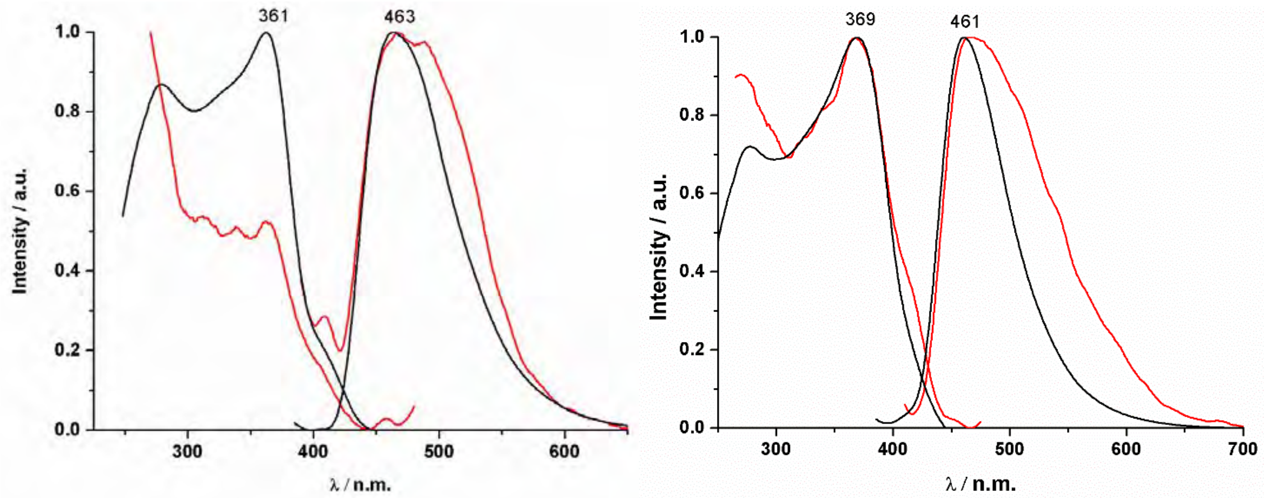

Figure 14. Emission spectra of compounds **17** (left) and **18** (right) at room temperature, before (black) and after (red) grinding of complexes.

3.2.4 Computational Study

In order to give an explanation to the observed optical behaviour, a theoretical study has been carried out, which allows qualitatively to interpret the luminescent properties, comparing the results with those obtained experimentally. In order to try to establish the contribution of the different orbitals and atoms in to the electronic transitions, we carried out Density Functional Theory (DFT) and Time-Dependent Density Functional Theory (TD-DFT) calculations on some of the crystalline structures obtained experimentally (Figure 15).

Given the problems related to the structural disorder present in the complexes **17**-**19**, which represent relatively similar structures, we decided to perform the calculations based on the system with better structural parameters that allow us more accurately to describe the reality of the system. For this reason, the $[\{Au(C_6Cl_5)_2\}\{L_1(Ag)\}$ binuclear model **17a** featuring a Au(I)···Ag(I) interaction and representative of the complex **17**, was chosen to explain the luminescent properties of complexes **17**-**19.**

As commented above, the crystalline structure of complex **20** shows disorder in both the ligand and the silver centre. For this reason, according to the position of the unit $[Ag(L_3)]^+$, model **20a** was constructed to interpret the photophysical properties of the complex. Thus, model **20a** corresponds to the tetranuclear neutral system found in complex **20**, which represents the Au(I)···Ag(I) and Au(I)···Au(I) interactions between one $[Au(C_6Cl_5)_2]^-$ anionic fragment and one $[Ag(L_3)]^+$ complex cation, or between two $[Au(C_6Cl_5)_2]^-$ anionic fragments. However, despite the attempts made to interpret the properties of this tetranuclear system, it was impossible to obtain results that adequately interpret the photophysical properties of the system. Probably this is due to the high disorder present in the crystalline structure.

Finally, models **21a**, **22a** and **23a** represent the different crystalline structures of the fluorinated derivatives **21**-**23**. In the three models we can observe the different Au(I)···Ag(I) and Au(I)···Au(I) interactions present in the respective complexes. A study of the molecular orbitals (MOs) along with a population analysis was used to check the contribution of each atom to each occupied orbital for all the models (see Tables 10-14 and Figure 16-19). From these data, we can anticipate the contribution of each part of the molecule to the orbitals involved in the transitions responsible for the photophysical properties.

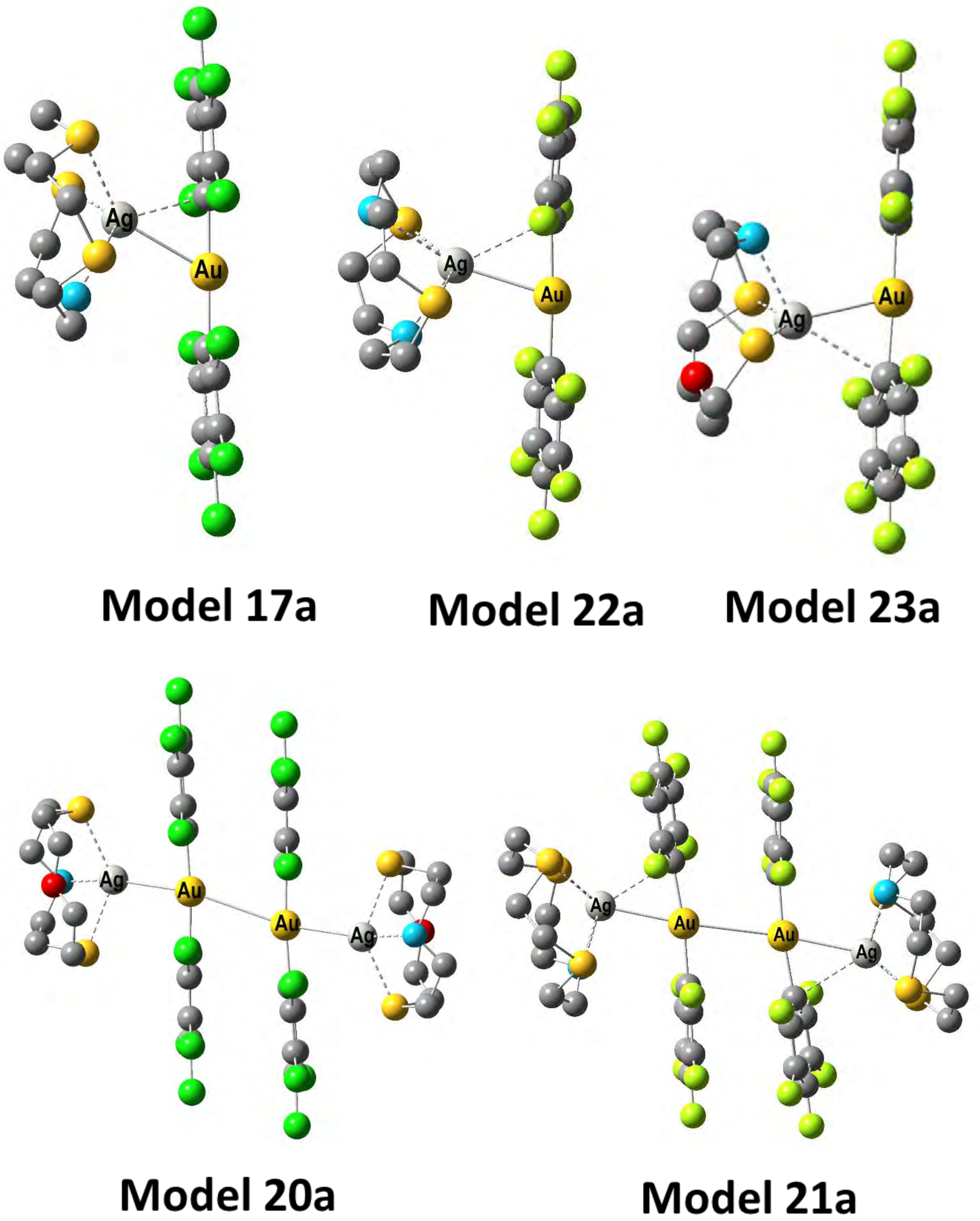

Figure 15. Theoretical model systems [{Au(C_6Cl_5)$_2$}{Ag(L_1)}] (**17a**), [{Au(C_6Cl_5)}Tl(L_3)]$_2$ (**20a**), [{Au(C_6F_5)}Ag(L_1)]$_2$ (**21a**), [{Au(C_6F_5)$_2$}{Ag(L_2)}] (**22a**) and [{Au(C_6F_5)}{Ag(L_3)}](**23a**).

In the case of the binuclear neutral model [{Au(C_6Cl_5)$_2$}{Ag(L_1)}] **17a,** while the highest occupied molecular orbital (HOMO) displays a mixed character with predominant Au/Ag contributions, the lowest empty molecular orbital is mainly localized on the perchlorophenyl unit (59 %). The rest of occupied frontier molecular orbitals are mostly located on the perchlorophenyl rings (>60 %) with the exception of the orbital HOMO-3 that presents a mixed metals/ligand contribution. In contrast, the rest of lower frontier molecular orbitals are mainly localized on the gold/silver framework (see Table 10 and Figure 16).

Table 10. Population analysis (%) for model system **17a.**

Model	Orbital	L	Au	Ag	C_6Cl_5
17a	L+2	1	40	37	22
	L+1	2	28	68	2
	L	7	12	22	59
	H	19	43	13	26
	H-1	6	29	4	61
	H-2	1	2	1	97
	H -3	52	18	22	8
	H -4	3	3	5	89
	H -5	12	3	8	77

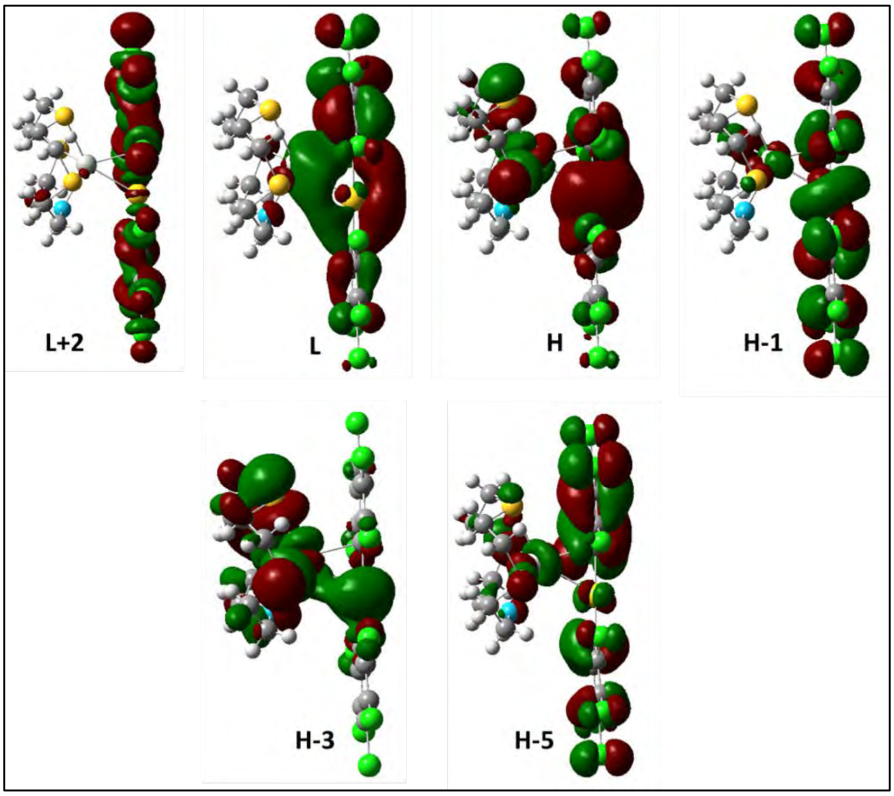

Figure 16. Most important frontier molecular orbitals (isovalue = 0.02) for model system **17a** (L=LUMO; H=HOMO).

Regarding the fluorinated derivatives, the dinuclear model $[\{Au(C_6F_5)_2\}\{Ag(L_1)\}]_2$ (**21a**) shows a high degree of mixing in the contributions from each part of the molecule to the frontier molecular orbitals HOMO and LUMO, which are mostly located on the $[Au(C_6F_5)_2]^-$ unit (69 and 67% respectively), but with an important contribution from the $[Ag(\mathbf{L_2})]^+$ fragment (see Table 11 and Figure 17).

Table 11. Population analysis (%) for model system **21a.**

Model	**Orbital**	**Au**	**Ag**	**C_6F_5**	**L**
21a	L+4	52	30	2	9
	L+3	38	16	4	25
	L	34	23	33	6
	H	51	19	18	10
	H-2	6	27	3	43
	H-3	7	26	3	39
	H-4	33	4	61	1
	H-8	3	3	91	1
	H-10	25	13	55	3

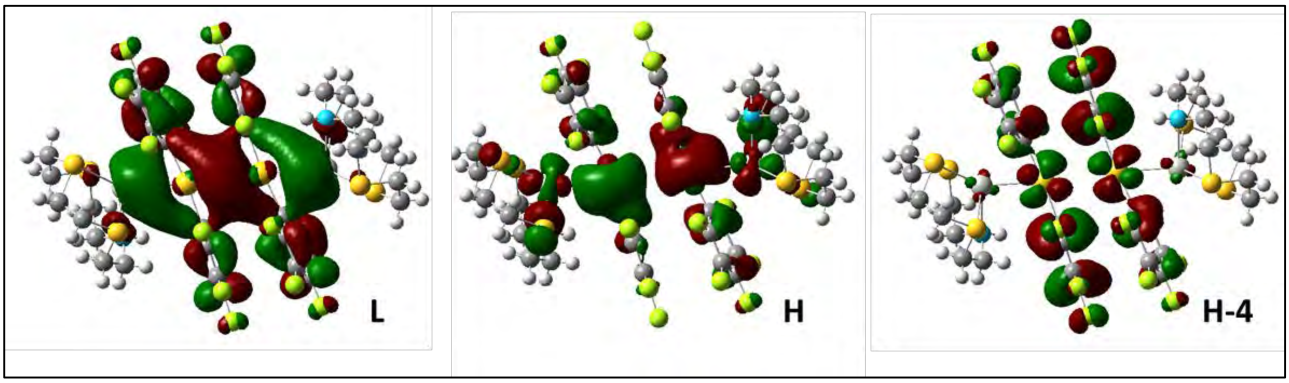

Figure 17. Most important frontier molecular orbitals (isovalue = 0.02) for model system **21a** (L=LUMO; H=HOMO).

In the case of the dinuclear model $[\{Au(C_6F_5)_2\}\{Ag(L_2)\}]$ (**22a**), the lowest unoccupied molecular orbitals LUMO, LUMO+1 and LUMO+2 are delocalized along the whole molecule. The highest occupied molecular orbital HOMO it is mostly located on the $[Ag(\mathbf{L_1})]^+$ fragment, meanwhile HOMO-1 and HOMO-2 are delocalized on the whole molecule with a main contribution from the ligands (see Table 12 and Figure 18).

Table 12. Population analysis (%) for model system **22a.**

Model	Orbital	Au	Ag	C_6F_5	L
22a	L+5	13	35	30	22
	L+4	31	37	20	13
	L+3	12	70	2	16
	L+2	30	35	27	8
	L+1	1	41	19	38
	L	5	28	32	35
	H	8	20	2	70
	H-1	16	14	31	39
	H-2	23	7	44	26
	H-3	11	5	18	67
	H-4	16	17	40	27

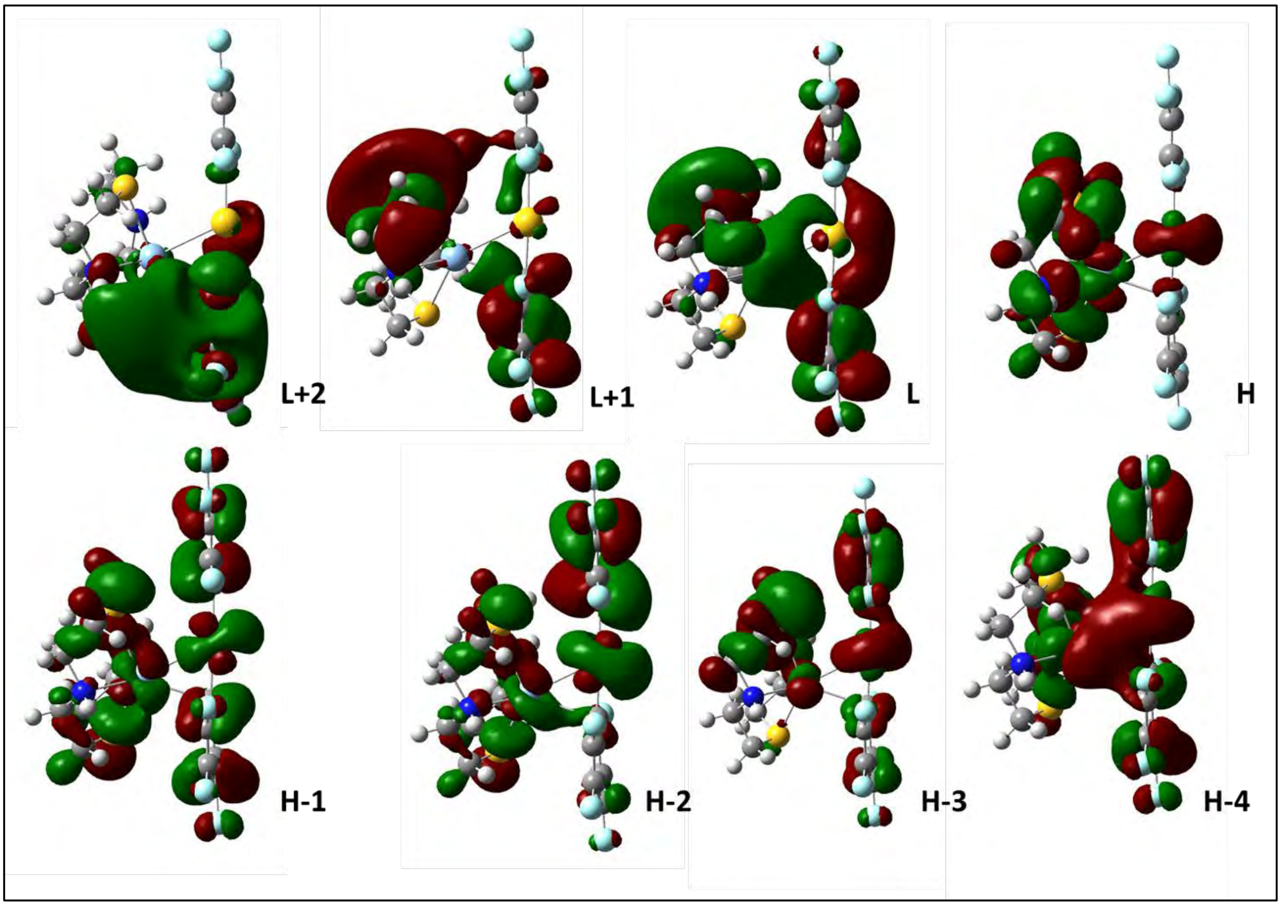

Figure 18. Most important frontier molecular orbitals (isovalue = 0.02) for model system **22a** (L=LUMO; H=HOMO).

A similar situation can also be observed for the dinuclear model $[\{Au(C_6F_5)_2\}\{Ag(L_3)\}]$ (**23a**), where the frontier molecular orbitals HOMO and LUMO present a mixed contribution from the $[Ag(L_3)]^+/C_6F_5$ moieties with a lower contribution from gold. Furthermore, the lowest unoccupied molecular orbitals (LUMOs) as well as the highest occupied molecular orbitals (HOMOs) shows a high degree of mixing in the contributions from each part of the molecule with some exceptions (HOMO-6, HOMO-3 and LUMO+1) (see Table 13 and Figure 19).

Table 13. Population analysis (%) for model system **23a**

model		**Au**	**Ag**	**L**	**C_6F_5**
23a	L+2	17	36	40	8
	L+1	1	86	12	1
	L	12	39	14	35
	H	15	20	25	40
	H-1	27	23	44	5
	H-2	24	17	24	35
	H-3	1	1	1	97
	H-4	14	13	35	37
	H-5	12	10	28	50
	H-6	8	8	13	71
	H-7	56	18	16	10

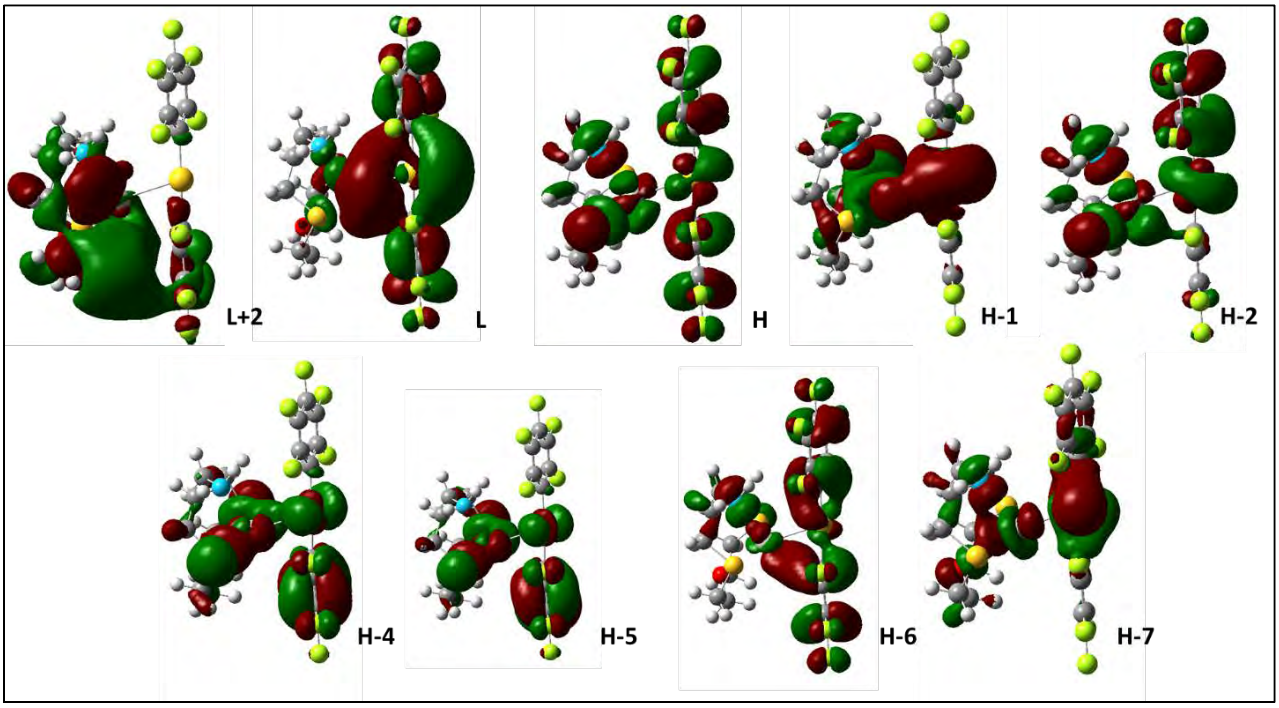

Figure 19. Most important frontier molecular orbitals (isovalue = 0.02) for model system **23a** (L=LUMO; H=HOMO).

The first 20 singlet−singlet excitation energies were computed for all model systems at the TD-DFT level of theory as described in the computational details. Since the lifetime for complexes **17**, **21** and **23** is near the microseconds range, we also computed the lowest singlet−triplet excitation at TD-DFT level for model systems **17a**, **21a** and **23a**. We carried out the analysis of the excitation wavelengths, oscillator strengths, and orbitals involved in these electronic excitations, which can be related to the origin of the luminescent behaviour observed experimentally. The results including the most important excitations are depicted in Tables 14-17 and Figures 20-23.

The TD-DFT analysis of the most important single-singlet transitions calculated for model **17a** shows that they appear between 330 and 259 nm, being the most intense singlet-singlet excitations at 330, 297 and 291 nm, whereas the lowest singlet−triplet excitation appears at 451 nm. The two most intense singlet-single excitations consist of a mixture of contributions, HOMO-3→LUMO and a HOMO-1→LUMO; taking into account the orbitals involved in these transitions, we could assign these electronic excitations to internal transitions between the [Ag(L$_1$)] unit and the C_6Cl_5 framework or between the metals centers. Finally, the singlet-singlet electronic transition at 330 nm as well as the lowest singlet-triplet excitation at 451 nm are due to a pure transition HOMO→LUMO which leads to a transfer of the L/Au electronic density towards the C_6Cl_5 units. These values are in agreement with the experimental excitation spectrum that shows a maximum at 250 nm (see Figure 20).

Table 14. TD-DFT first Singlet-Singlet Excitation Calculations and Lowest Singlet-Triplet Excitations for the Model system **17a**.

Model	**exc.**	**λ_{calc} (nm)**	**f (s)**	**contributions**
17a	$S_0 \rightarrow S_1$	330	0.0705	HOMO →LUMO(45)
	$S_0 \rightarrow S_2$	297	0.1853	HOMO-3 →LUMO(17)
				HOMO-1 →LUMO(26)
	$S_0 \rightarrow S_3$	291	0.1257	HOMO-3 →LUMO(31)
				HOMO-1 →LUMO(16)
	$S_0 \rightarrow S_3$	265	0.0101	HOMO-1 →LUMO+2(19)
	$S_0 \rightarrow S_{10}$	259	0.0158	HOMO-5 →LUMO(18)
	$S_0 \rightarrow T_1$	451	0.0000	HOMO →LUMO(15)

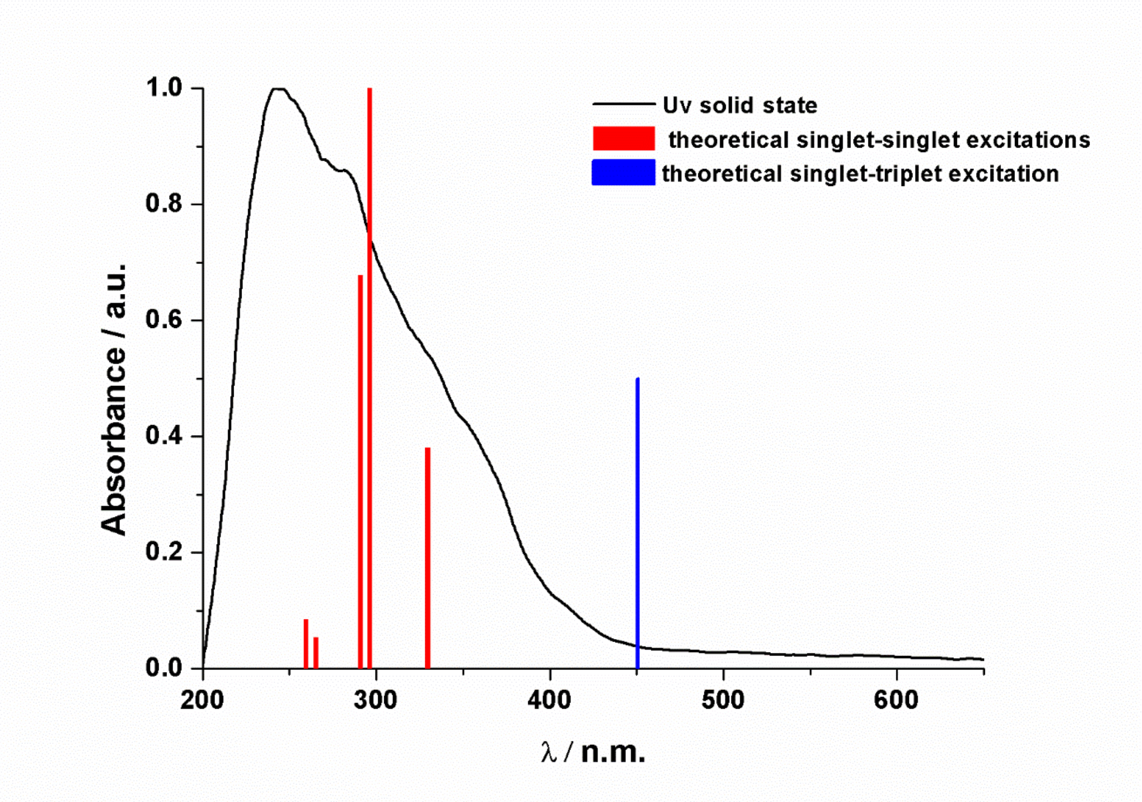

Figure 20. Experimental UV-Vis solid state absorption spectrum (black line) TD-DFT singlet–singlet (red bars) and singlet-triplet excitations (blue bar) for model systems **17a**.

In the case of model **21a**, which show the highest lifetime and the largest Stokes' shift, suggesting a phosphorescent process, the first 20 singlet-singlet and the lowest singlet–triplet excitation energies were computed at the TD-DFT level of theory. Thus, the most intense singlet–singlet excitations appear between 333 and 251 nm, whereas the lowest singlet–triplet excitation appears at 392 nm. Again, these values are in agreement with the experimental excitation spectrum that shows a maximum at 257 nm and a low-energy shoulder at ca. 325 nm (see Figure 21). The main contributions to the most intense theoretical electronic singlet–singlet excitation at 333 nm and the main contribution to the singlet-triplet excitation at 392 nm arise from the HOMO→LUMO transition in both cases. In view of the character of the MOs involved in these contributions, we could assign the origin of the emissive behavior for complex **21** to an internal transition within the $[Au(C_6F_5)_2]^-$ units, with a small contribution of a charge transfer from the $[Au(C_6F_5)_2]^-$ fragment to the [Ag(**L**$_2$)]$^+$ one, due to the presence of the Au(I)···Ag(I) metallophilic interaction (see Table 15). This is in accordance with the results obtained in previous studies in which the computed TD-DFT results for the tetranuclear model $[\{Au(C_6F_5)_2\}Ag([9]aneS_3)_2]_2$ displayed a similar assignment for the electronic excitations responsible for the optical behaviour observed experimentally[59].

Table 15. TD-DFT first Singlet-Singlet Excitation Calculations and Lowest Singlet-Triplet Excitations for Model system **21a**.

Model	exc.	λ_{calc} (nm)	f (s)	contributions
21a	$S_0 \rightarrow S_1$	333	0.5308	HOMO→LUMO(98)
	$S_0 \rightarrow S_2$	282	0.2658	HOMO(-4)→LUMO (97)
	$S_0 \rightarrow S_3$	257	0.0241	HOMO(-8)→LUMO (86)
	$S_0 \rightarrow S_4$	253	0.0351	HOMO(-10)→ LUMO (46)
	$S_0 \rightarrow S_5$	251	0.0118	HOMO(-10)→LUMO (30) HOMO(-3)→LUMO+3 (16) HOMO(-2)→LUMO+4 (15)
	$S_0 \rightarrow T_1$	392	0.0000	HOMO→LUMO (63)

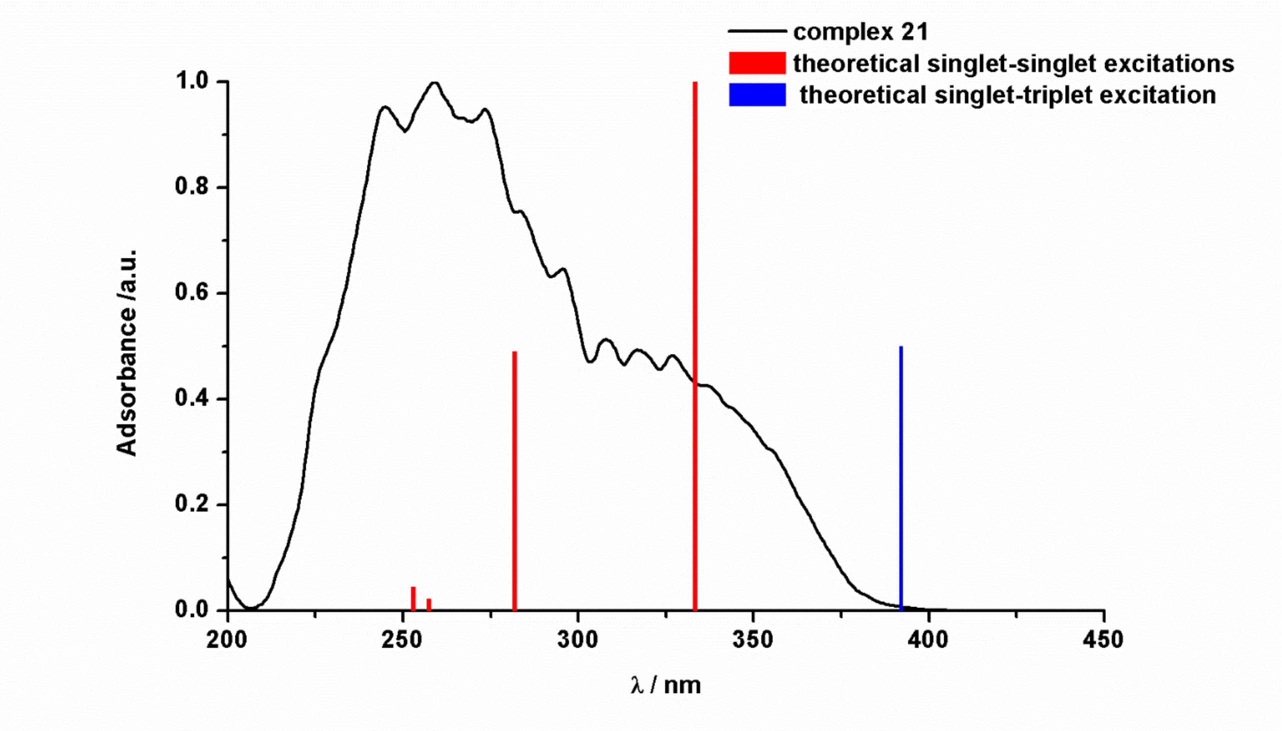

Figure 21. Experimental UV-Vis solid state absorption spectrum (black line) TD-DFT singlet–singlet (red bars) and singlet-triplet excitations (blue bar) for model systems **21a**.

The TD-DFT analysis of the most important single-singlet transitions calculated for model **22a** shows that they appear between 345 and 248 nm, being the most intense singlet-singlet excitations at 301, 284 and 272 nm. The first one consists of a mixture of contributions, HOMO-1→LUMO and a HOMO-1→LUMO+1, the second singlet-singlet excitation is also a mixture of contributions, in which the electron arises from HOMO−2, HOMO−1, and HOMO and arrives to LUMO+2 or LUMO; and the third one is an excitation between HOMO-2 and LUMO+1 orbitals. Taking into account that the orbitals involved in these transitions are distributed along the whole molecular arrangement and that the contribution from the $[Ag(\mathbf{L_1})]^+$ unit is the highest in all cases except in HOMO-2 (33%), we could assign these electronic excitations to internal transitions within the [Ag(**L$_1$**)]$^+$ unit with a small contribution of a charge transfer between the aurate(I) fragment and the [Ag(**L$_1$**)]$^+$ one, due to the presence of the Au(I)···Ag(I) metallophilic interaction. These results agree well with the experimental excitation spectrum in solid state for complex **22** (See Figure 22 and Table 16).

Table 16. TD-DFT first Singlet-Singlet Excitation Calculations and Lowest Singlet-Triplet Excitations for Model system **22a**.

Model	exc.	λ_{calc} (nm)	f (s)	contributions
22a	$S_0 \rightarrow S_1$	345	0.0186	HOMO→LUMO (61) HOMO→LUMO+1 (34)
	$S_0 \rightarrow S_2$	321	0.0220	HOMO→LUMO (31) HOMO→LUMO+1 (55)
	$S_0 \rightarrow S_3$	316	0.0115	HOMO-1→LUMO (57)
	$S_0 \rightarrow S_4$	301	0.0673	HOMO-1→LUMO (17) HOMO-1→LUMO+1 (63)
	$S_0 \rightarrow S_5$	285	0.0415	HOMO-3→LUMO (18) HOMO-2→LUMO (25)
	$S_0 \rightarrow S_6$	284	0.0604	HOMO-2→LUMO (36) HOMO-1→LUMO+2 (20) HOMO→LUMO+2 (31)
	$S_0 \rightarrow S_7$	283	0.0171	HOMO-3→LUMO (20) HOMO-2→LUMO (15) HOMO→LUMO+2 (39)
	$S_0 \rightarrow S_8$	278	0.0147	HOMO-1→LUMO+2 (48)
	$S_0 \rightarrow S_9$	272	0.0634	HOMO-2→LUMO+1 (66)
	$S_0 \rightarrow S_{10}$	265	0.0350	HOMO-4→LUMO (37)
	$S_0 \rightarrow S_{11}$	262	0.0110	HOMO-4→LUMO (17) HOMO-3→LUMO+1 (32)
	$S_0 \rightarrow S_{12}$	261	0.0173	HOMO→LUMO+3 (61)
	$S_0 \rightarrow S_{13}$	251	0.0227	HOMO→LUMO+4 (18)
	$S_0 \rightarrow S_{14}$	248	0.0258	HOMO→LUMO+5 (80)

Finally, the TD-DFT analysis of model **23a** shows that the most important singlet-singlet excitations are between 276 and 227 nm, being the most intense singlet-singlet excitations at 275, 270 and 261 nm, whereas the lowest singlet–triplet excitation appears at 363.5 nm. The most intense singlet-singlet excitation at 261 nm consists of pure contributions from HOMO-2→LUMO excitation; these electronic excitations can be proposed as charge transfer transitions between the metal centers (from gold to silver). The other two more intense singlet-singlet transitions (276 and 270 nm) are due to electronic transitions, which involve an increase in the electronic density on silver; the same behaviour is shown by the lowest singlet–triplet excitation (from HOMO to LUMO) which is due to a transition involving the whole molecule (see Table 17 and Figure 23).

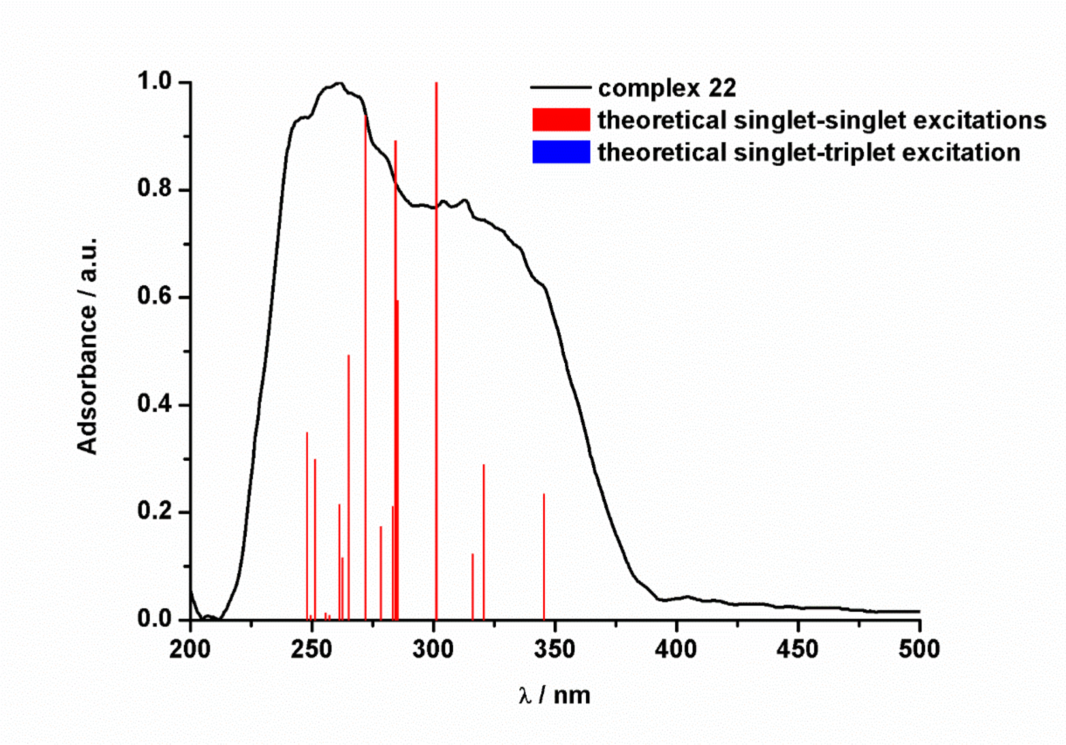

Figure 22. Experimental UV-Vis solid state absorption spectrum (black line) and TD-DFT singlet–singlet (red bars) for model systems **22a**.

Table 17. TD-DFT first Singlet-Singlet Excitation Calculations and Lowest Singlet-Triplet Excitations for Model system **23a**.

Model	**exc.**	**λ_{calc} (nm)**	**f (s)**
$S_0 \rightarrow S_1$	276	0.1222	HOMO→LUMO (43)
$S_0 \rightarrow S_2$	270	0.1743	HOMO-1→LUMO (46)
$S_0 \rightarrow S_3$	261	0.1874	HOMO-2→LUMO (42)
$S_0 \rightarrow S_4$	249	0.0445	HOMO-4→LUMO (30)
$S_0 \rightarrow S_5$	248	0.0197	HOMO → LUMO+2 (34)
$S_0 \rightarrow S_6$	245	0.0138	HOMO-5 → LUMO (27)
$S_0 \rightarrow S_{12}$	231	0.0240	HOMO-7 → LUMO (35)
$S_0 \rightarrow S_{14}$	227	0.0314	HOMO-6 → LUMO (39)
$S_0 \rightarrow T_1$	363	0.0000	HOMO → LUMO (23)

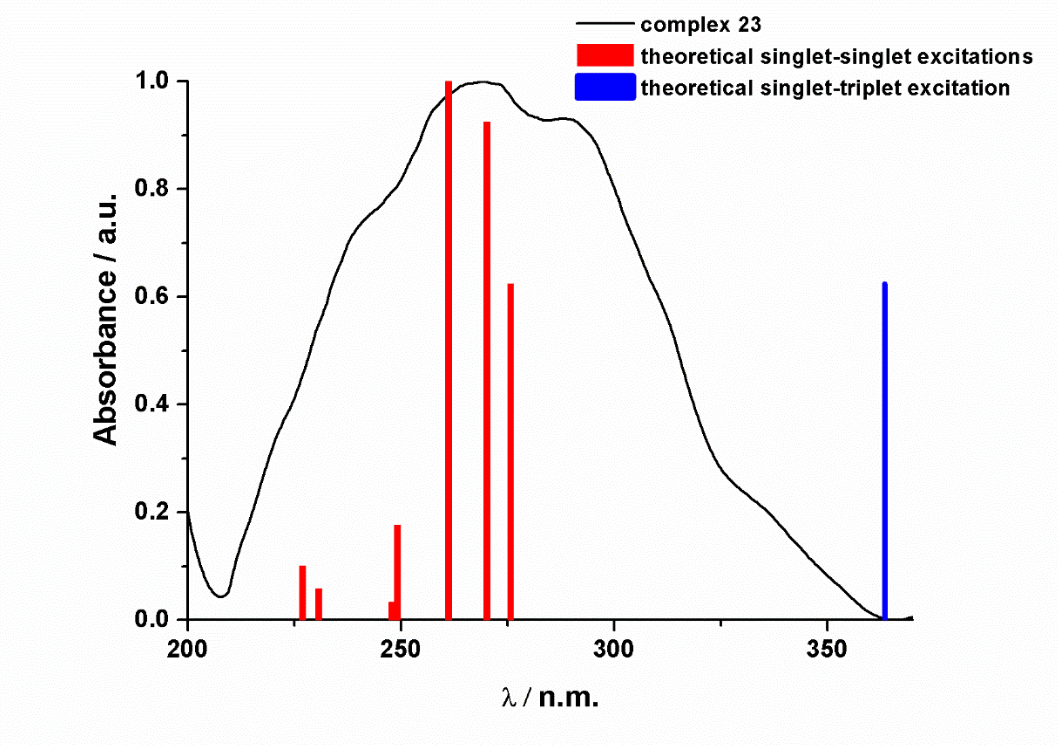

Figure 23. Experimental UV-Vis solid state absorption spectrum (black line), TD-DFT singlet–singlet (red bars) and singlet-triplet excitations (blue bar) for model systems **23a**.

3.2.5 Conclusions

The use of the macrocyclic ligands **L_1-L_3** in the reaction with the [{Au(C_6X_5)$_2$}Ag]$_n$ (X = F, Cl) polymeric compounds allows the generation of luminescent systems containing different metallophilic interactions, which display different structural arrangements, such as the [Ag(I)···Au(I)] binuclear disposition observed for complexes **17-19**, **22**, **23** and the [Ag(I)···Au(I)···Au(I)···Ag(I)] tetranuclear disposition for complexes **20** and **21**. Furthermore, unlike the compounds synthesized with the Au/Tl interactions (complex **1**-**6**) for which the photophysical proprieties are directly correlated to the Au(I)–Tl(I) arrangements, the computational studies of binuclear systems (complexes **17**-**19**, **22**, **23**) show that the luminescent properties mainly arise from the whole molecule, whereas in the tetranuclear systems **21**, the macrocyclic ligands serve as a support for the whole structural system arising the luminescence from the metals. Finally, particularly interesting is the fact that complex **19** is the only system that presents mechanochromic properties; in spite of the structural similarity with complexes **17** and **18**, this is the only system that presents a variation of the luminescent emission on changing the pressure. This allows us to evaluate how even small differences in the ligands can generate large variations in the photophysical properties of the obtained heteronuclear systems.

3.3 Organic ligands with different ring size cavity and donor atoms (L_4-L_5)

3.3.1 Introduction

Following the research line commented in the previous paragraph, we continue analysing the ligand influence on the structural properties and the spectral properties of complexes featuring Au-Ag interactions.

As reflected in the results obtained through the use of macrocyclic systems **L_1-L_3**, it is obvious that the different nature of the organic ligand plays a key role. In fact, from the synthesis of the complexes **17**-**19**, we observed that, despite the structural similarities among the three complex systems, only the complex **19** has mechanochromic properties; this shows how small differences in the organic ligand (exchange of a donor atom) can generate substantial differences in the photophysical properties of the synthesized heteronuclear systems.

Taking into account these general considerations, exactly as we shown in the previous chapter, we have decided to synthesize new complexes containing heterometallic Au/Ag interactions exploiting the different coordination ability of different macrocyclic derivatives. In particular, we decided to study the reactivity of the ligands **L_4** and **L_5** (see Figure 24) with the heterometallic compounds $[\{Au(C_6X_5)_2\}Ag]_n$ to consider the possibility to obtain new materials with different structural arrangements (from discrete units of different nature to polymeric systems) and different luminescent proprieties.

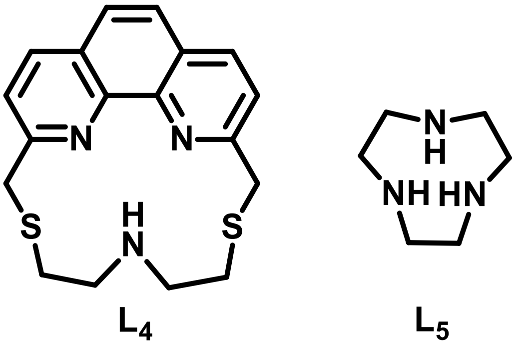

Figure 24. N,S-mixed-donor macrocyclic ligand.

The 1,10-phenanthroline unit contained in the macrocyclic system **L_4** is a classic chelating bidentate ligand for transition metal ions that has played an important role in the development of coordination chemistry [77]–[79]. In particular, the functionalization of this unit, or its introduction into more complicated systems has been used by many investigative groups for different purposes. For example, the coordination chemistry of the 1,10-phenanthroline (phen) derivatives has been examined in several studies[80],[81]. In particular, some O/N coordinating systems form stable complexes with a variety of metal ions. The solution chemistry of its transition-metal complexes has been extensively studied[82]. In addition, the silver(I) ion is regarded as an extremely soft acid that favours coordinating to soft bases such as ligands containing N donor centers. Silver(I) complexes with these soft ligands give rise to an interesting array of stereochemistry and geometric configurations with one-dimensional (1D) chains and two- (2D) and three-dimensional (3D) networks[83],[84]. The final structures and frameworks of these complexes may well depend on a variety of factors such as the ligand structure and the nature of the anions[85]-[88].

Moreover, due to its superb ability to coordinate many metal ions, phen and its derivatives are frequently used in many processes involving metal complexes in which they can be featured in many roles; for example, as ligands for catalysis,[89] or as stabilizing agents for nanoparticle synthesis.[90] 1,10-Phenanthroline derivatives have been used as important heterocyclic ligands for a large number of metal complexes that play an important role in a variety of important technological and medicinal applications; for example, promising applications in the field of electroluminescent materials[91]-[94], organic light-emitting devices (OLED),[95] organic semiconductors,[96] or as chemical nucleases and therapeutic agents, due to their ability to bind or interact with the DNA biomacromolecule.[97]-[100].

In the same way as already mentioned in chapter 1, the macrocyclic system 1,4,7-triazacyclononane (**L_5**) has been widely used for its coordinating proprieties as for its potential applications[101],[102]. Taking into account the obtained results so far, we decided to study the reactivity of the heterometallic compounds $[\{Au(C_6X_5)_2\}Ag]_n$ with **L_4** and **L_5**. Using this type of ligands, it was possible to obtain new materials with different structural arrangements (from discrete units of different nature to polymeric systems) and photophysical proprieties. In fact, the size of the macrocyclic system, the number and variety of donor atoms or the variation of halogen atoms in the aryl moiety of the aurate donor can play a determining role both in the structural arrangement and in the optical properties of the obtained heterometallic complexes.

3.3.2 Synthesis and characterization

Continuing with the synthetic scheme followed in chapter 1 for the compounds that present Au-Tl interactions, and in order to check if the change of thallium with silver can influence the properties of the resulting complexes, we proposed the synthesis of compounds **24**-**27** with a metal/ligand reaction molar ratio of 1:1. Initially, **L_4** and **L_5** were added to a solution of $[\{Au(C_6X_5)_2\}Ag]_n$ in THF, at room temperature. Subsequently, the solvent was partially removed under reduced pressure and the addition of n-hexane led to the precipitation of the compounds **24**-**27** (scheme 3). The substitution of chlorine with fluorine atoms in the aryl groups does not affect the stoichiometry of the resulting compounds, although it modifies their structural features. Scheme 3 shows the stoichiometries of the compounds obtained from the reactions between the ligands and the Au(I)/Ag(I) precursors. Only complexes **25** and **27** (synthesized with **L_5**) are luminescent in the solid state, while the compounds synthetized with **L_4** do not show any emission at room temperature or at low temperature. All the compounds are insoluble in dichloromethane, acetonitrile and diethyl ether, although they appear to be soluble in O-donor solvents. However, the solubility of the chlorinated compounds is lower than the solubility of the fluorinated complexes.

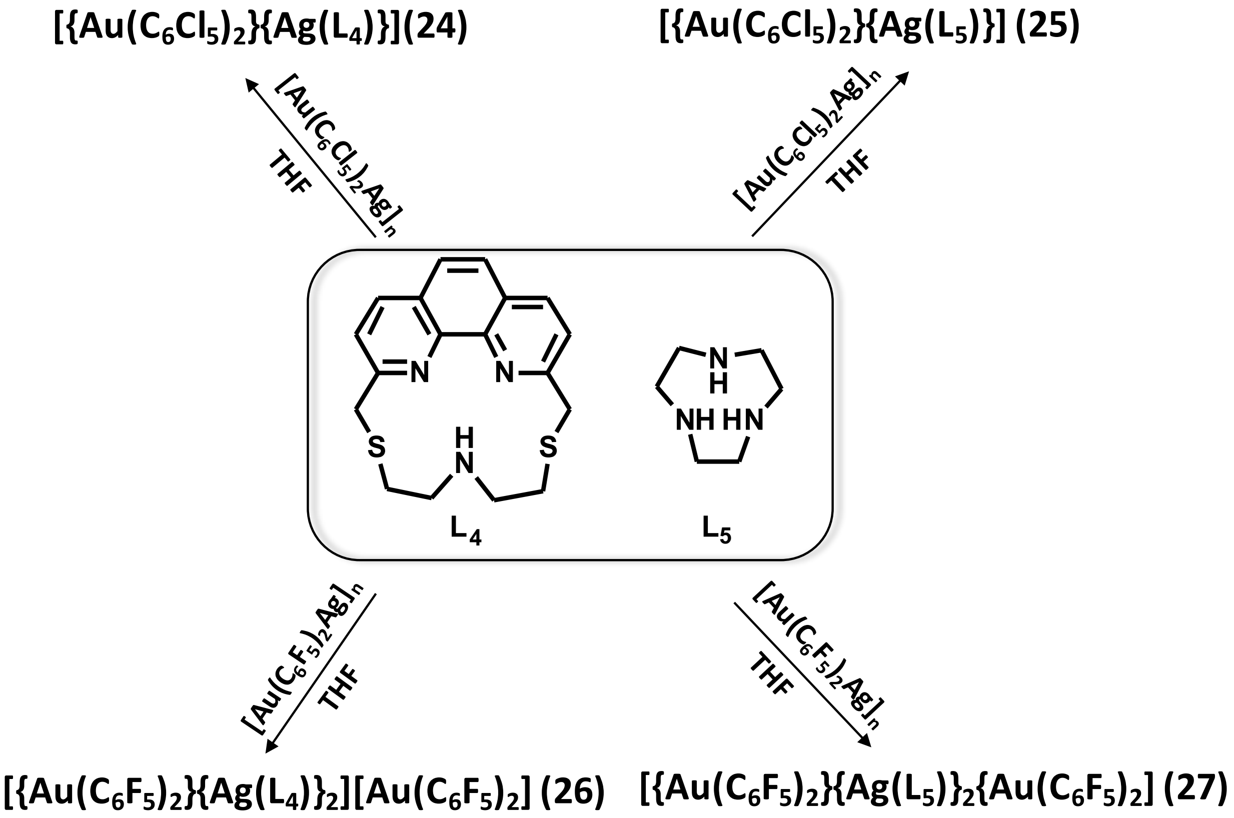

Scheme 3.

The ^{19}F-NMR spectra of the complexes **26** and **27** show the presence of the $[Au(C_6F_5)_2]^-$ fragment, which resembles that of the precursor complex $NBu_4[Au(C_6F_5)_2]$. This seems to indicate that a dissociative process giving rise to aurate(I) anions and thallium(I) cations takes place in solution. Thus, in derivatives **26** and **27,** the flourine atoms in *meta* and *para* positions are located at 167.3(**26**), 164.5(**27**) and 166.0(**26**), 159.6(**27**), respectively, while those in *orto* positions at 117.1(**26**), 113.7(27).

As observed for the thallium(I) complexes, the ^{1}H-NMR spectrum of **24**-**27** show a significant modification in the chemical shifts as compared to those of the free ligands. This fact means that the coordination of the macrocyclic ligands to silver significantly affect the position of the resonances observed in their ^{1}H NMR spectra. Thus, the ^{1}H-NMR spectra of **24** and **26** display a multiple signal at 2.51-2.64 ppm and a singlet at 4.48, 4.44 ppm, respectively, with 1:2 relative integrations, corresponding to the hydrogen atoms of the methylene groups adjacent to nitrogen or to sulphur atoms. Furthermore, three groups of aromatic signals can be observed due to the presence of the 1,10-phenanthroline unit, which shows chemical shifts at 7.64, 7.90, 8.36 and 7.71, 7.93, 8.42 for the complexes **24** and **26**, respectively. In the ^{1}H-NMR spectra of **25** and **27** a strong broadening of the signals due to the coordination of the macrocyclic system to the metal centre is observed. Both complexes show signals between 2.67-2.91 or 2.67-2.80 for **25** and **27**, respectively. Their elemental analyses and spectroscopic data are in accordance with the proposed stoichiometries (see Experimental Section). Their IR spectra show, among others, absorptions arising from the C_6F_5[60] and C_6Cl_5[61] groups bonded to gold(I) at approximately 1500, 950 and 780 cm^{-1}, or about 834 and 614 cm^{-1}, respectively.

Considering the mass spectra MALDI(−), the compound synthesised display a peak due to the unit $[\{Au(C_6X_5)_2\}_2Tl]^-$ at *m/z* = 1498 (**24**, **25**) or 1168 (**26, 27**, or a signal corresponding to $[Au(C_6X_5)_2]^-$ at *m/z* = 695 (**24**, **25**) or 531 (**26**, **27**), the latter appearing as parent peak in all cases. In their MALDI(+) mass spectra, peaks due to the fragment [Ag(**L**)]$^+$ appear at *m/z* = 448 (**24**, **26**) or 242 (**25**, **27**), showing experimental isotopic distributions in agreement with the theoretical ones. Finally, the molar conductivity measurements of the four complexes in acetone agree with a dissociative process in solution, showing values corresponding to uni-univalent electrolytes (see Experimental).

3.3.3 X-ray crystal structure determinations

In the process of crystallization by diffusion of n-hexane in saturated solutions of **24**-**27** in THF, single crystals suitable for the X-ray diffraction analysis were obtained. The crystal structures of **24** and **26,** with the same macrocyclic ligand bonded to silver(I), show different structural arrangements; while complex **24** consists of a binuclear [{Au(C_6Cl_5)$_2$}{Ag(L_4)}] neutral molecule with an unsupported Au/Ag interaction (see Figure 25 (left) and Table 18). The crystalline structure of complex **26** shows a structural disposition that consists of a trinuclear [{Au(C_6F_5)$_2$}{Ag(L_4)}$_2$]$^+$ cation having a L-Ag-Au-Ag-L trinuclear disposition and a [Au(C_6F_5)$_2$]$^-$ fragment as counter-ion (see Figure 25 (right) and Table 19).

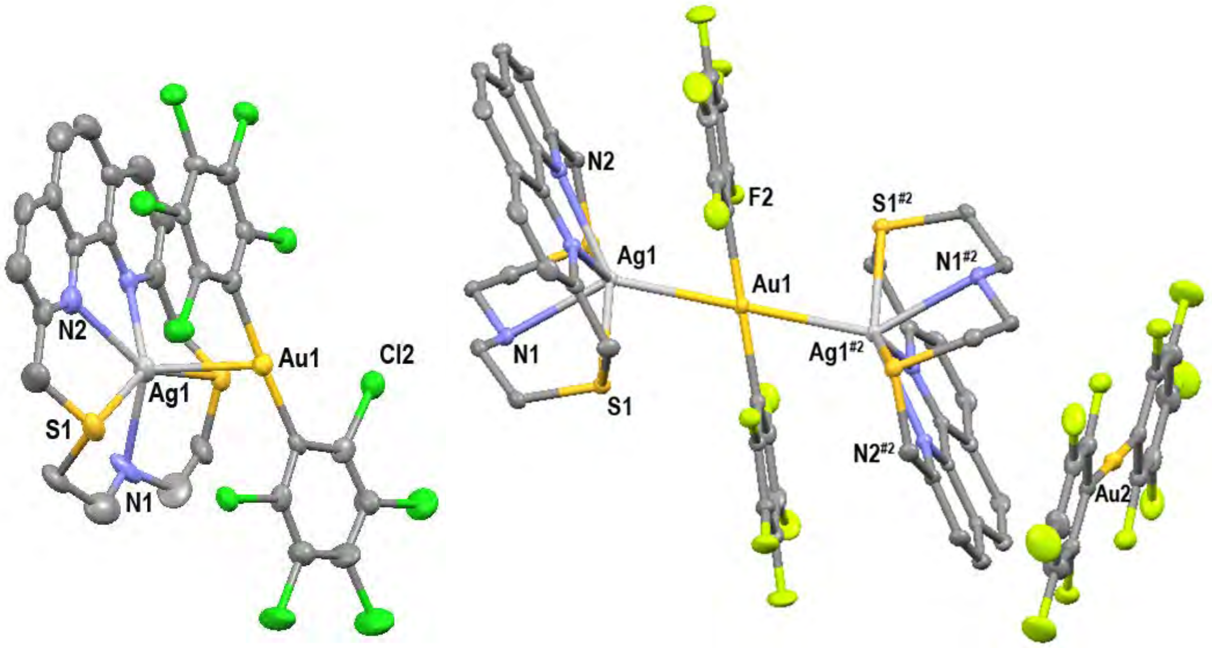

Figure 25. Crystal structures of **24** (left) and **25** (right) with the labelling scheme adopted for the atom positions. Hydrogen atoms and any solvent molecules are omitted for clarity and ellipsoids are drawn at the 30% level.

The intermetallic distances in the compounds are different depending on the perhalophenyl groups in the aurate moiety and on the structural arrangements. In fact, the compounds containing the macrocyclic system **L$_4$** (complexes **24** and **26**) show a Au-Ag distance of 2.8432(4) Å, slightly shorter than that of 2.9597(12) Å observed in the perchlorophenyl complex. Moreover, both Au(I)-Ag(I) distances are very similar to those observed in the related Au/Ag compounds with crown thioethers as ([{Au(C_6Cl_5)$_2$}$_2$Ag$_2$([24]aneS$_8$)][59], [{Au(C_6F_5)$_2$}$_2$Ag$_2$([24]aneS$_8$)][59] or [{Au(C_6F_5)$_2$}Ag([9]aneS$_3$)$_2$]$_2$)[59]).

Each gold atom appears linearly coordinated to two pentahalophenyl groups, displaying normal Au-C bond lengths of 2.051(12) and 2.008(13) Å in **24**, and of 2.049(5) for both distances in **26**.

The aliphatic Ag-N bond distances are quite similar in the crystal structures **of 24** and **26**, with values of 2.474(12), 2.420(11) Å in **24** and 2.512(4) Å in **26**. Furthermore, the Ag-N distances involving the 1,10-phenatroline unit in compounds **24** and **26** fall within the range of distances reported in the literature for related systems (from 2.238(32)[103] to 2.560(22) Å[104]) in ({[Ag(L1)$_{0.5}$(phen)](BF$_4$)·(H$_2$O)$_{0.5}$}$_2$ [104], [Ag$_2$(phen)$_2$(CH$_3$CN)$_2$](ClO$_4$)$_2$[105], [Ag$_2$(phen)$_2$(CH$_3$CN)$_2$](BF$_4$)$_2$[105]), and similar to those of the complex [(N-methyl-2,8-dithia[9],(2,9)-1,10-phenanthrolinophane)Ag(I)][BF$_4$][106].

Finally, while the Ag-N distances involving the aliphatic portion of the macrocyclic system in **24** and **26** (2.499(14) Å (**24**); 2.577(4) Å (**26**)) are intermediate to those described for the silver(I) derivatives with cyclic N- or N,S-donor ligands [2.485(4)-2.709(9) Å][64]-[67]. The Ag-S bonds (2.682(4), 2.709(4) Å for **24**; 2.6576(13), 2.7155(13) Å for **26**) are very similar to those found for the silver complexes such as [Ag(N-acylurea-[12]aneNS$_3$)][NO$_3$][64], [Ag(N-(Benzyloxycarbonyl)-[12]aneNS$_3$)][NO$_3$][65], [Ag(N-(pyridylmethyl)-[12]aneNS$_3$)][PF$_6$][66], [Ag(N-(pyridylmethyl)-[12]aneNS$_2$O)][PF$_6$][66] and [Ag(N-CH$_2$CONH-tBu)-[12]aneNS$_3$)][NO$_3$][67].

Table 18. Selected bond lengths [Å] and angles [°] for **24**·C$_4$H$_8$O.

Au(1)-Ag(1)	2.9597(12)	Ag(1)-N(1)	2.499(14)
Au(1)-C(1)	2.051(12)	Ag(1)-N(2)	2.474(12)
Au(1)-C(7)	2.008(13)	Ag(1)-N(3)	2.420(11)
Ag(1)-S(1)	2.709(4)		
Ag(1)-S(2)	2.682(4)		
C(7)-Au(1)-C(1)	176.8(5)	N(2)-Ag(1)-S(2)	73.0(3)
N(1)-Ag(1)-N(3)	118.0(4)	N(3)-Ag(1)-S(2)	138.9(3)
N(1)-Ag(1)-N(2)	127.5(5)	S(2)-Ag(1)-S(1)	146.24(14)
N(2)-Ag(1)-N(3)	67.2(4)	N(1)-Ag(1)-Au(1)	112.0(3)
N(1)-Ag(1)-S(1)	74.3(4)	N(2)-Ag(1)-Au(1)	113.3(3)
N(2)-Ag(1)-S(1)	140.4(3)	N(3)-Ag(1)-Au(1)	110.9(2)
N(3)-Ag(1)-S(1)	73.3(3)	S(1)-Ag(1)-Au(1)	77.99(8)
N(1)-Ag(1)-S(2)	79.0(3)	S(2)-Ag(1)-Au(1)	93.44(9)

Table 19. Selected bond lengths [Å] and angles [°] for **26**.

Au(1)-Ag(1)	2.8432(4)	Ag(1)-N(1)	2.512(4)
Au(1)-Ag(1)#2	2.8432(4)	Ag(1)-N(2)	2.512(4)
Au(1)-C(1)	2.049(5)	Ag(1)-N(3)	2.577(4)
Au(1)-C(11)	2.049(5)	Ag(1)-S(2)	2.6576(13)
Au(2)-C(1)#1	2.049(5)	Ag(1)-S(1)	2.7155(13)
Au(2)-C(11)#2	2.049(5)		
C(1)#1-Au(1)-C(1)	180.000(1)	N(2)-Ag(1)-S(2)	73.09(10)
C(11)#2-Au(2)-C(11)	180.0(2)	N(3)-Ag(1)-S(2)	76.12(10)
C(11)#2-Au(2)-Ag(1)#2	110.52(13)	N(1)-Ag(1)-S(1)	72.45(10)
C(11)-Au(2)-Ag(1)#2	69.48(13)	N(2)-Ag(1)-S(1)	134.76(9)
C(11)#2-Au(2)-Ag(1)	69.48(13)	N(3)-Ag(1)-S(1)	72.73(10)
C(11)-Au(2)-Ag(1)	110.52(13)	S(2)-Ag(1)-S(1)	138.86(4)
Ag(1)#2-Au(2)-Ag(1)	180.0	N(1)-Ag(1)-Au(2)	107.28(9)
N(1)-Ag(1)-N(2)	65.76(13)	N(2)-Ag(1)-Au(2)	126.28(9)
N(1)-Ag(1)-N(3)	95.22(13)	N(3)-Ag(1)-Au(2)	138.86(9)
N(2)-Ag(1)-N(3)	94.15(13)	S(2)-Ag(1)-Au(2)	106.06(3)
N(1)-Ag(1)-S(2)	137.22(10)	S(1)-Ag(1)-Au(2)	81.70(3)

Symmetry transformations used to generate equivalent atoms:

#1 -x+1,-y,-z+2 #2 -x+1,-y,-z+1

Although the four crystal structures contain similar, $[Au(C_6X_5)_2]^-$ and $[Ag(L)]^+$ units, the substitution of the ligands determines significant differences in the fluoride derivatives. Thus, while the crystalline structure of the complex **25** shows a structural disposition similar to complex **24** (see Figure 26 and Table 20) (which consist in a binuclear $[\{Au(C_6Cl_5)_2\}\{Ag(L_5)\}]$ neutral molecule with an unsupported Au/Ag interaction), complex **27** consist of a novel not linear trinuclear arrangement in which two $[Ag(L_5)]^+$ units interact with a $[Au(C_6F_5)_2]^-$ unit by Ag···Au and Ag···C_{ipso} interactions. A $[Au(C_6F_5)_2]^-$ fragment which interact by an Au···Au interaction balances the charge (see Figures 27 and Table 21). The peculiarity of this structure lies in the unprecedented double Ag···C_{ipso} interaction from the same $[Au(C_6F_5)_2]^-$ fragment and the silver atoms of the two $[Ag(L_5)]^+$ units.

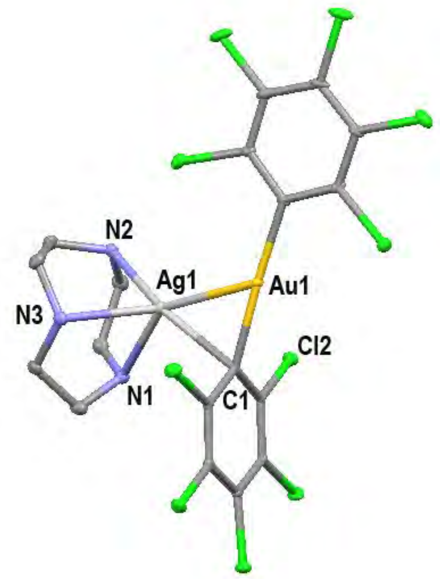

Figure 26. Crystal structures of **26** with the labelling scheme adopted for the atom positions. Hydrogen atoms and any solvent molecules are omitted for clarity and ellipsoids are drawn at the 30% level. #1 -x+1,-y,-z+2 #2 -x+1,-y,-z+1.

Table 20. Selected bond lengths [Å] and angles [°] for **25**.

Au(1)-Ag(1)	2.6915(4)	Ag(1)-N(1)	2.429(4)
Ag(1)-C(1)	2.398(4)	Ag(1)-N(2)	2.365(4)
Au(1)-C(1)	2.081(4)	Ag(1)-N(3)	2.386(4)
Au(1)-C(7)	2.035(4)		
C(1)-Au(1)-C(7)	176.62(17)	N(1)-Ag(1)-N(2)	74.40(14)
C(1)-Au(1)-Ag(1)	58.68(12)	N(2)-Ag(1)-N(3)	76.05(14)
C(7)-Au(1)-Ag(1)	124.70(13)	N(3)-Ag(1)-Au(1)	133.09(10)
N(1)-Ag(1)-Au(1)	142.92(10)	N(3)-Ag(1)-N(1)	74.99(14)
N(2)-Ag(1)-Au(1)	129.07(10)		

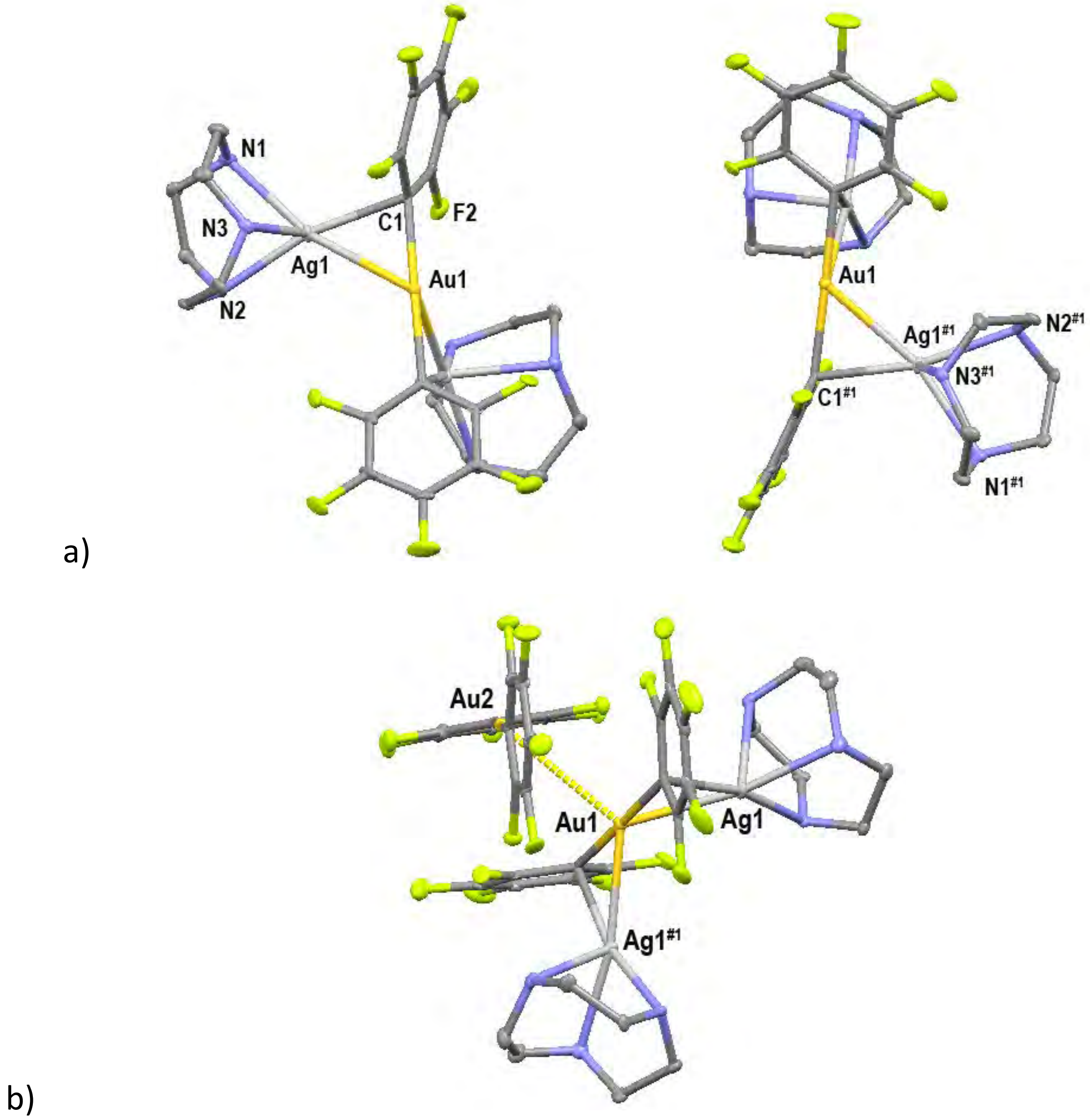

Figure 27. a) Trinuclear $[\{Au(C_6F_5)_2\}\{Ag(L_5)\}_2]^+$ and b) tetranuclear $[\{Au(C_6F_5)_2\}\{Ag(L_5)\}_2][Au(C_6F_5)_2]$ fragment of crystal structure **27** with the labelling scheme adopted for the atom positions. Hydrogen atoms and any solvent molecules are omitted for clarity and ellipsoids are drawn at the 30% level. 1# 1-x,+y,1/2-z.

Table 21. Selected bond lengths [Å] and angles [°] for **27**.

Au(1)-Ag(1)	2.7331(9)	Ag(1)-N(1)	2.324(8)
Au(1)-Au(2)	3.4023(3)	Ag(1)-N(2)	2.411(8)
Au(1)-Ag(1)#1	2.7330(9)	Ag(1)-N(3)	2.464(8)
Au(1)-C(1)#1	2.087(10)	Ag(1)-C(1)#1	2.359(9)
Au(1)-C(1)	2.087(10)		
Ag(1)#1-Au(1)-Ag(1)	110.33(4)	N(1)-Ag(1)-N(2)	75.5(3)
C(1)-Au(1)-Ag(1)#1	56.7(3)	N(1)-Ag(1)-N(3)	74.8(3)
C(1)#1-Au(1)-Ag(1)	56.7(3)	N(1)-Ag(1)-C(1)#1	166.1(3)
C(1)-Au(1)-Ag(1)	124.3(3)	N(2)-Ag(1)-Au(1)	164.79(19)
C(1)#1-Au(1)-Ag(1)#1	124.3(3)	N(2)-Ag(1)-N(3)	73.2(3)
C(1)#1-Au(1)-C(1)	178.6(5)	N(3)-Ag(1)-Au(1)	106.93(19)
N(1)-Ag(1)-Au(1)	119.49(19)		

Symmetry transformations used to generate equivalent atoms:1# 1-X,+Y,1/2-Z

In contrast to the intermetallic distances observed within the phenanthroline complexes (**24** and **26**), the Au(I)-Ag(I) distance observed in complexes **25** and **27** are shorter in the perchlorophenyl derivative (2.6915(4) Å in **25**) than in the perfluorophenyl derivative (2.7331(9) Å in **27**). Furthermore, while complex **25** shows a structural arrangement similar to that observed for the complexes **17**-**19** (binuclear Au/Ag system with Ag-C_{ipso} interaction (2.398 (4) Å), complex **27** shows an unprecedented structural arrangement. In it, each silver(I) center participates in a weak Ag···C interaction with a *ipso* carbon atoms from the same $[Au(C_6F_5)_2]^-$ unit (see Figure 26) which is shorter (2.359(9) Å) than those found in other complexes in which $[Au(C_6X_5)_2]^-$ units interacts with silver(I) centers through both Au···Ag and Ag···C_{ipso} contacts (Ag···C distances vary from 2.422(4) Å in $[Au_2Ag_2(C_6Cl_2F_3)_4(THF)_2]_n$[68] to 2.707(18) Å in $[Au_2Ag_2(4\text{-}C_6F_4I)_4(THF)_2]_n]$.[69] Finally, the Ag-N distances in both complexes **25** and **27** (from 2.324(8) to 2.464(8) Å) are similar to those observed in other complexes containing $[Ag(L_5)]^+$ fragment or related systems as [Ag(tris-(N-methylciano)-[9]aneN_3)][NO_3][107], [Ag_2(tris-(N-methylciano)-[9]aneN_3)][PF_6]$_2$[108] [Ag(tris-(N-methyl)-[9]aneN_3)][NO_3] [109].

3.3.4 Photophysical Properties

As already noted for the 1,10-phenantroline macrocyclic complexes **7** and **9** containing Au-Tl metallophilic interactions, the presence of Au-Ag metallophilic interactions in complexes **24** and **26** does not affect the photophysical properties of the synthesized complexes; despite the presence of metallophilic interactions the complexes do not show solid-state luminescence. However, it is shown in the literature that macrocyclic systems similar to **L_4** exhibit an emission band in solution at about 336 nm and they are used as ON-OFF sensors for different metal ions [110]. For this reason, as for the thallium complexes (see chapter 2), we have investigated the reason for the absence of luminescence in the solid state and the possible quenching mechanism for the synthesized complexes by studying the behavior of **L_4** in solution in the presence of Ag^+. The absorption and fluorescence spectra of **L_4** ligand show an absorption band at about 270 nm and a fluorescence band at about 456 nm (see Figure 28).

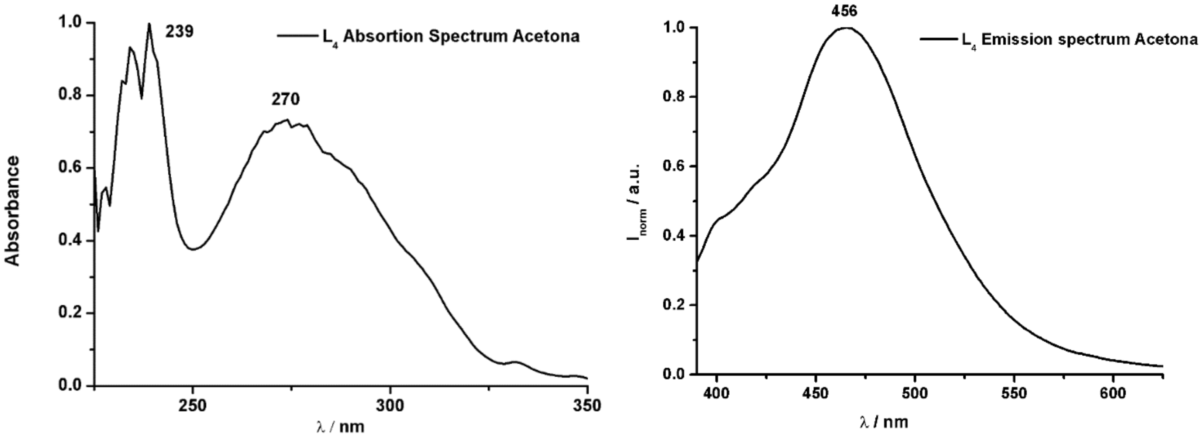

Figure 28. Absorption spectra (left) and emission spectra (right) of **L_4** (**L_4** = 2,72 x 10^{-4} M in acetone, λ_{ex} 270 nm)

To study the behavior of **L_4** in the presence of Ag^+, the variations in the fluorescence spectrum of the ligand were recorded after the addition of increasing amounts of the metal ion in acetone. The fluorescence spectrum variation for **L_4** is shown in Figure 28. Taking into account the study carried out, a strong decrease of the fluorescent emission was observed for **L_4**. In addition, reporting the emission intensity as a function of the ratio $[Ag^+]/[$**L_4**$]$ (see Figure 29) it is obvious that the quenching of the system is due to the formation of solutions of the species $[Ag($**L_4**$)]^+$.

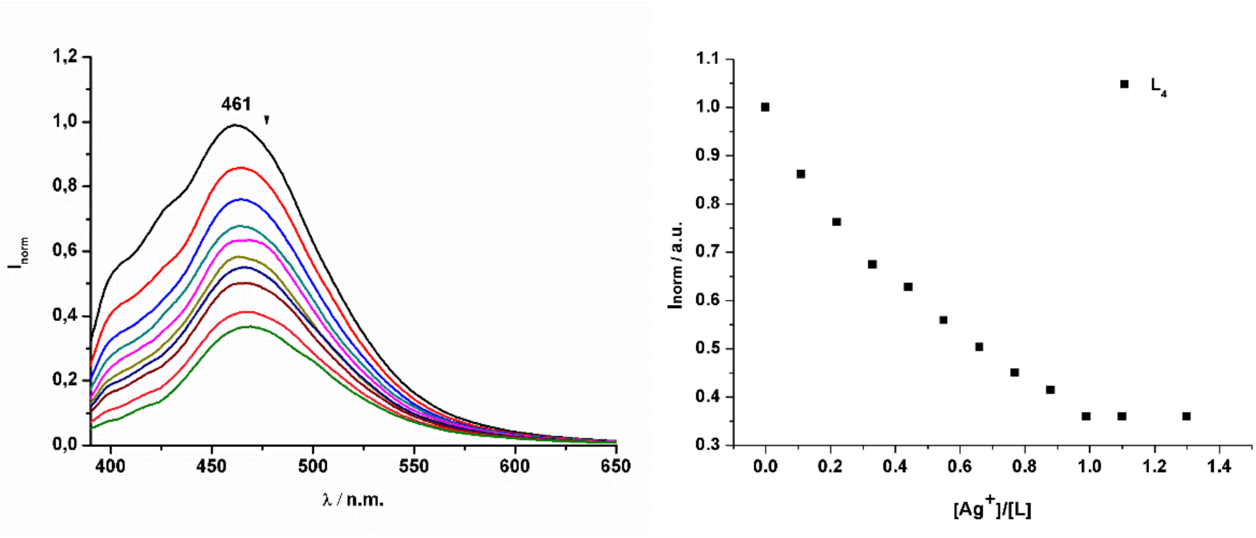

Figure 29. Fluorescence emission spectrum of $\mathbf{L_4}$ in the presence of increasing amounts Ag^+ (left); Fluorescence intensity at 456 nm vs. molar ratio plots for $\mathbf{L_4}$ in presence of Ag^+ (right).

The next step consists in the study of the quenching mechanism that involves $\mathbf{L_4}$, considering that the relationship between the concentration of the deactivating agent [Q] and the ratio between the initial intensity of the ligand $I_{0,}$ and the intensity at different concentrations of the deactivating agent I, described by the equation of Stern-Volmer[111]-[112]:

$$ {}^{I_0}/_{I} = 1 + K_{sv}[Q] \; (1) $$

By examining the pattern (see Figure 30) for the titration of $\mathbf{L_4}$ with Ag^+ it is clearly seen that there is a good linear correlation between I/I_0 and $[Ag^+]$.

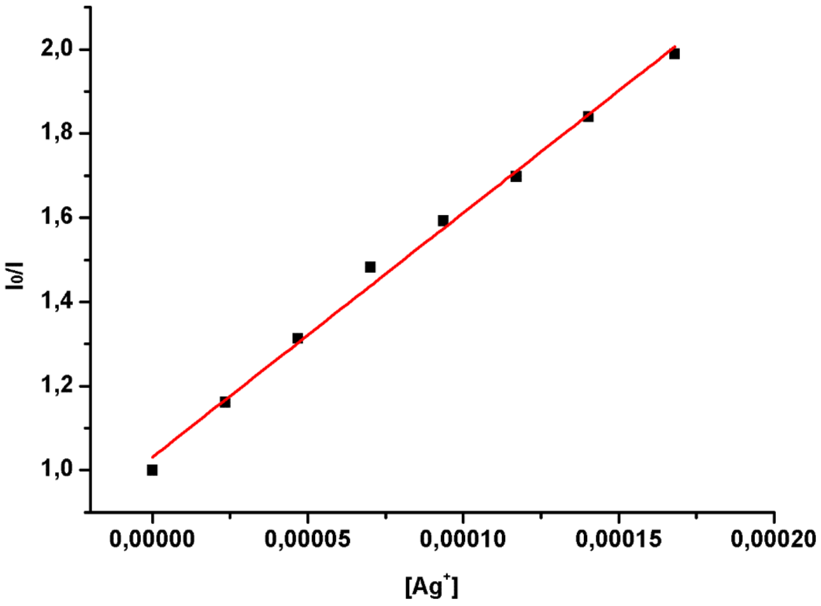

Figure 30. Representation of the ratio I_0 / I (of $\mathbf{L_4}$ versus $[Ag^+]$ (λ_{ex} 270 nm, λ_{em} 461 nm) in acetone.

From the slope of the straight line, it was possible to determine the K_{sv} value (5860 M^{-1}). Thus, it was possible to explain that probably the absence of luminescence in the synthesized compounds is mainly due to the coordination of the Ag^+ metal ion to $\mathbf{L_4}$ accompanied by structural modifications which may occur in the solid state.

It is also possible to detect whether it is static or dynamic quenching, by measuring the lifetime τ as a function of the deactivation concentration of the metal ion $[Ag^+]$ (see Figure 31).

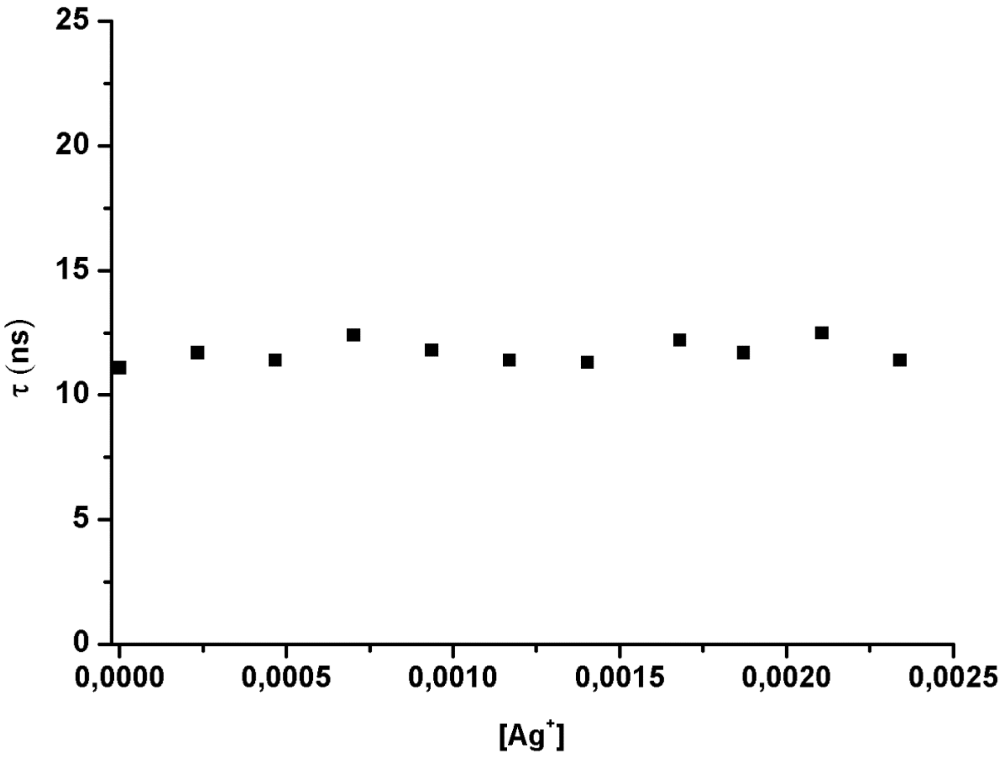

Figure 31. Representation of the relation τ vs $[Ag^+]$ for L_4.

Considering previous measurements reported in the literature [113], it can be concluded that this is a static quenching for the studied system (the lifetime does not vary depending on the concentration). This behavior is normally observed when quenching is due to the formation of complexes in solution in the ground state.

Regarding the optical proprieties of complexes **25** and **27,** the ultraviolet absorption spectra (UV-Vis) in THF solution were analysed at concentrations of about 5.5 x 10^{-5} M. It is observed that both complexes show an intense band at higher energy (250 (**25**) and 257(**27**) nm), the complex **25** showing two other bands at 285 and 329 nm, respectively; while complex **27** shows just another band with lower energy at about 294 nm. Some of these bands are also present in the spectra of the heterometallic precursors $[\{Au(C_6X_5)_2\}Ag]_n$ and in the gold(I) complexes $NBu_4[Au(C_6X_5)_2]$ (X=F, Cl) (see Figure 32). Therefore, it is likely that the band at high energy arises from transitions between π orbitals of the perhalophenyl groups, while the transitions in the low energy region probably involve orbitals of the gold centres. At this regard, similar assignments have been done for related gold(I) complexes with aromatic substituents (Ph_3PAuX (X=Cl) [114], $\{Tl[Au(C_6Cl_5)_2]\}_n$[115]).

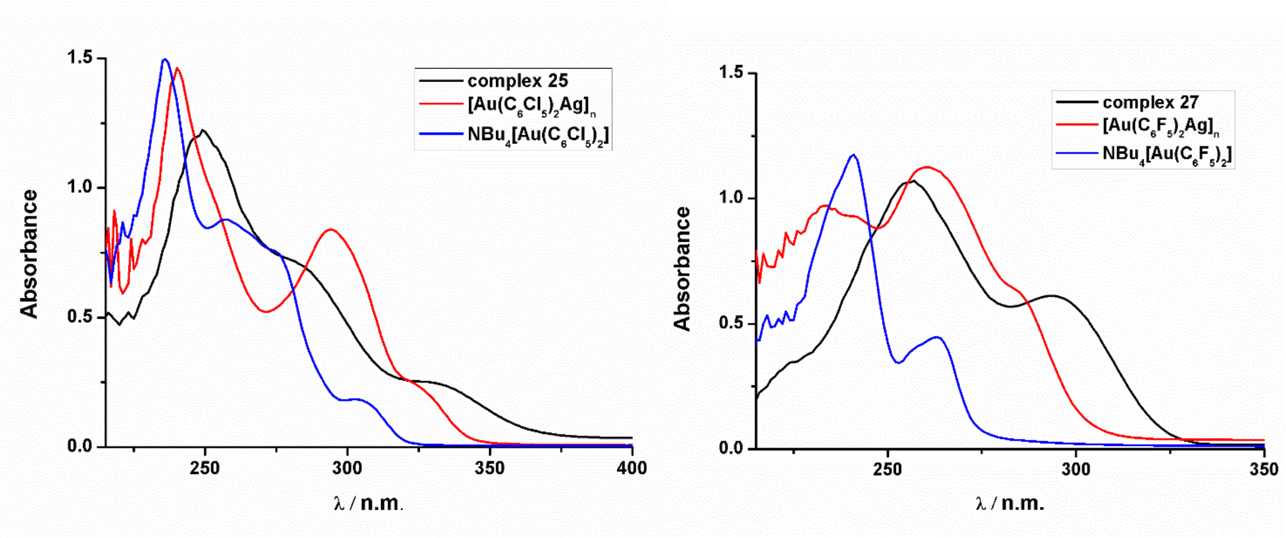

Figure 32. Absorption spectra of complexes **25** and **27** and the gold precursors $NBu_4[Au(C_6X_5)_2]$ and $[\{Au(C_6X_5)_2\}Ag]_n$ in THF solutions (C=2.5 x 10^{-5} M).

Regarding the luminescent properties in the solid state, as already mentioned, only complexes containing $\mathbf{L_5}$ present luminescence in solid state (see Table 22). Thus, while derivative **25** shows one broad emission bands at 541 nm, both at room temperature and at 77K, the derivative **27** shows a strong shift of the low energy luminescent emission when the temperature drops to 77 K (from 534 to 452nm) (Figure 33). This behaviour may be due to the rigidity of the structure, which causes a large increase in the emission energy. Moreover, despite the structural differences, we can observe that as the Au-Ag distance increases (from 2.6915 (4) Å (**25**) to 2.8432 (4) Å (**27**)) an increase in the emission energy is observed. Naturally, also the different nuclearity, the different perhalophenyl groups and the different metal-metal interactions can influence the optical properties of the synthesized compounds.

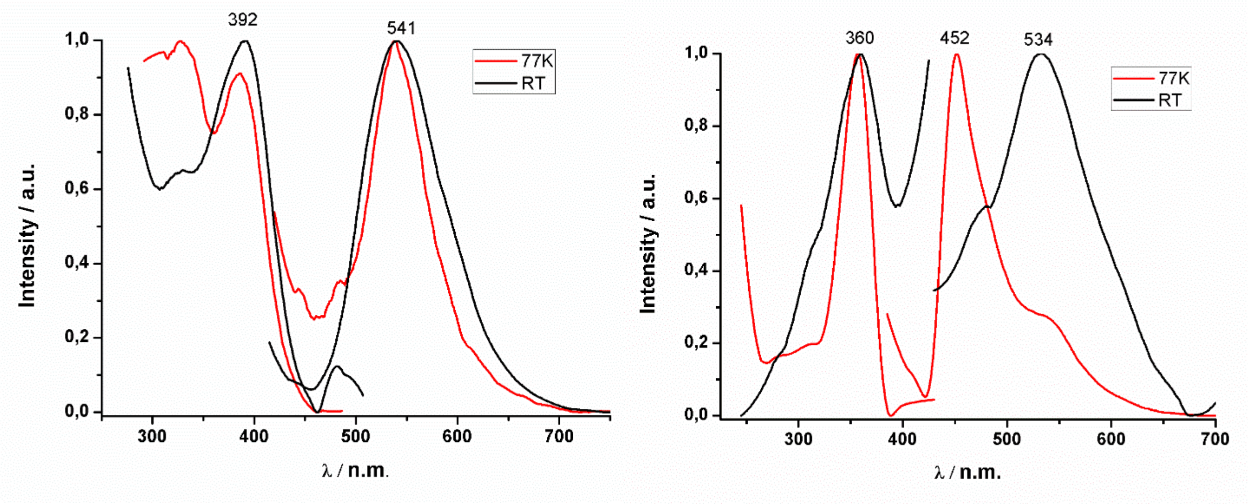

Figure 33. Excitation and emission spectra for complexes **25**(left) and **27**(right) in the solid state at RT and 77 K.

Table 22. Photophysical properties of complexes **21**-**23.**

	UV-vis in THF (nm)	Solid (RT) em (exc)	Solid (77K) em (exc)	τ (ns)	Φ (%)
Complex 25	249 (ε = 48800) 287 (ε = 26800) 332 (ε = 9800)	541 (392)	541 (392)	821 ± 11	10.5
Complex 27	255 (ε = 39230) 294 (ε = 24400)	534 (360)	452 (360)	828 ± 18	7.2

3.3.5 Computational Study

As we have already commented in the previous section, as contrary to what observed in the emission measurements at the solid state for compound **25**, in the case of **27** a displacement of the low energy emission band from 532 to 452 nm is observed on going from room temperature to 77 K. Thus, with the aim to understand the origin of the fluorescent emission of the two compounds, DFT and TD-DFT calculations were carried out on the models **25a** and **27a.**

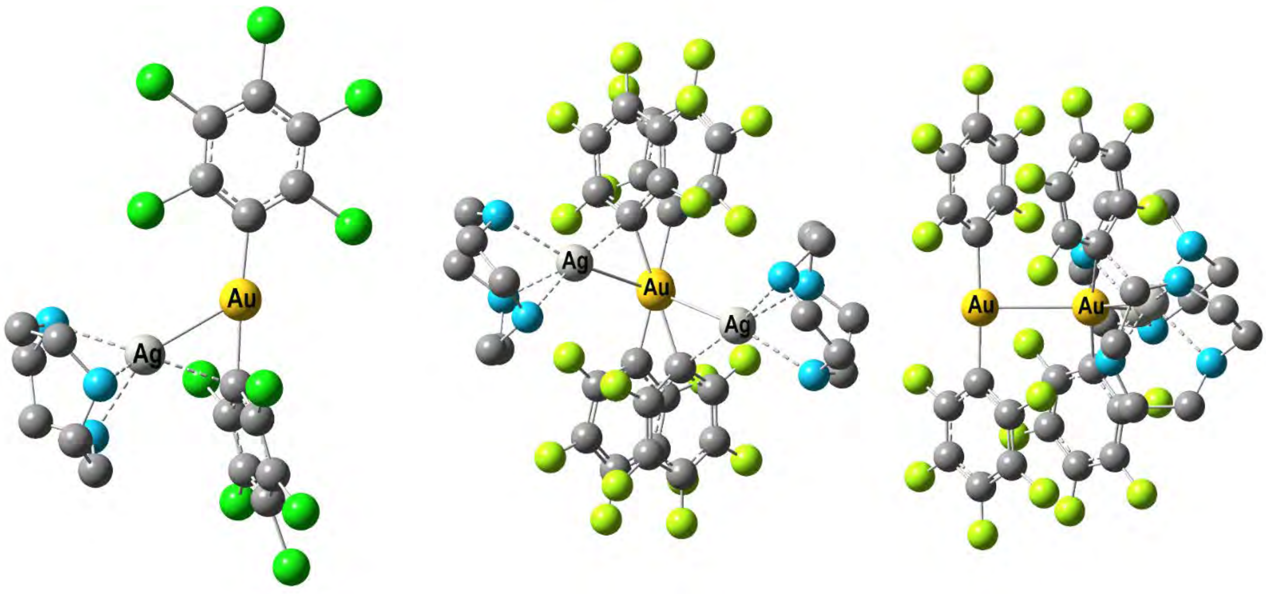

Model 25a **Model 27a (A)** **Model 27a (B)**

Figure 34. Theoretical model systems [{Au(C_6Cl_5)$_2$}{Ag(L_5)}] (**25a**), [{Au(C_6F_5)$_2$}{Ag(L_2)}$_2${Au(C_6F_5)$_2$}] (**27a**).

The model **25a** represents the binuclear [{Au(C_6Cl_5)$_2$}{(L_5)Ag}] system in **25** that shows the presence of one Au(I)···Ag(I) and one Ag(I)···C*ipso* interaction (see Figure 34). In the case of model **27a it** corresponds to the tetranuclear neutral system found in complex **27** and shows the Au(I)···Ag(I) interactions between two [Ag(L_5)]$^+$ complex cations and one [Au(C_6Cl_5)$_2$]$^-$ anionic fragment (see Figure 34 model 27a (A)) and the Au(I)···Au(I) interaction between the two anionic [Au(C_6Cl_5)$_2$]$^-$ fragments (see Figure 34 model 27a (B)). Therefore, the analysis of the population of the most important molecular orbitals was performed to obtain the contributions of the different parts of the molecule involved in the electronic transitions responsible for the photophysical properties of the two compounds (see Figures 35-36 and Tables 23-24).

In the case of the binuclear neutral model [{Au(C_6Cl_5)$_2$}{Ag(L_1)}] **25a,** while the highest occupied molecular orbital (HOMO) displays a mixed contribution from the whole molecule (about 20 % for each fragment), the lowest empty molecular orbital (LUMO) is mainly localized on the [Au(C_6Cl_5)]$_2^-$ anion (80 %). The other empty or occupied molecular orbitals (HOMOs and LUMOs) are mainly localized on the C_6Cl_5 or [Au(C_6Cl_5)]$_2^-$ unit with some exceptions for those MOs where both metals play an important role (see Table 23).

Table 23. Population analysis (%) for model system **25a**

	Au	**Ag**	**L_5**	**C_6Cl_5**
LUMO+3	24	58	1	17
LUMO+2	6	13	1	81
LUMO+1	9	12	1	78
LUMO	18	17	3	62
HOMO	19	33	22	26
HOMO-1	13	5	5	77
HOMO-2	1	1	0	98
HOMO-3	24	27	27	21
HOMO-4	42	20	19	19
HOMO-5	1	2	1	97
HOMO-6	17	20	12	51

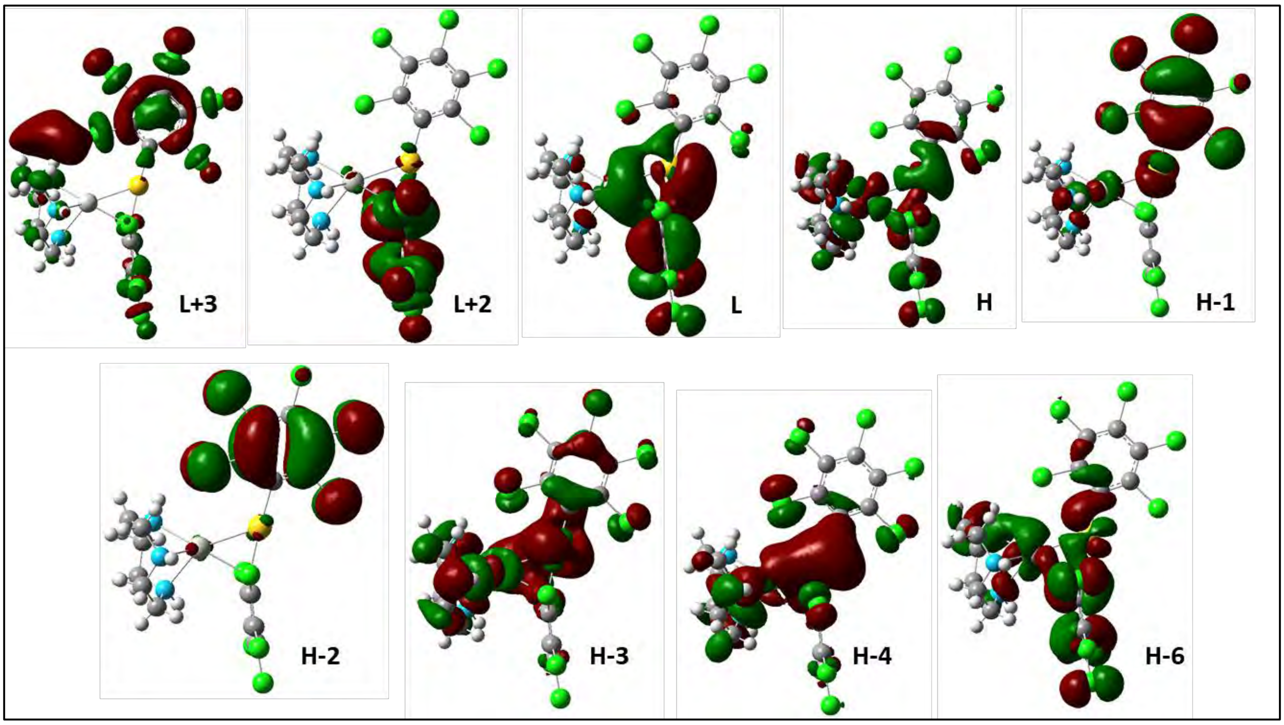

Figure 35. Most important frontier molecular orbitals (isovalue = 0.02) for model system **25a** (L=LUMO; H=HOMO).

Instead, for model **27a,** we have carried out the population analysis and we have collected the data showing the distinct contribution to each molecular orbital of the two $[Au(C_6F_5)_2]^-$ anions (see Table 24). While the Au_A and C_6F_{5A} represent the bis(pentafluorophenyl)aurate fragment interacting with the $[L(Ag)]^+$ units (see Figure 34, model 27a (A)), the Au_B and C_6F_{5B} represent the fragments of bis(pentafluorophenyl)aurate interacting exclusively with the other bis(pentafluorophenyl)aurate anion via Au-Au contact (see Figure 34, model 27a (B)). In this case, unlike what is seen for model **25a,** the highest occupied molecular orbital (HOMO) and the lowest empty molecular orbital (LUMO) are mainly localized on the metal centres Au(I) and Ag(I). Finally, while the rest of occupied molecular orbitals (HOMOs) are mainly localized on the C_6F_{5B} unit with an important contribution of metal centers (see HOMO-3 and HOMO-1), the rest of empty molecular orbitals (LUMOs) show a contribution mainly from the metal centers with some exceptions (see LUMO+1).

Table 24. Population analysis (%) for model system **27a**

	Au_A	**Ag**	**L_5**	**C_6F_{5A}**	**Au_B**	**C_6F_{5B}**
LUMO+2	1	43	1	1	54	0
LUMO+1	1	20	9	49	21	1
LUMO	3	32	4	14	45	2
HOMO	26	20	5	13	28	9
HOMO-1	9	21	12	14	6	38
HOMO-2	28	5	3	9	2	53
HOMO-3	4	26	17	9	8	36
HOMO-4	6	3	1	4	6	80

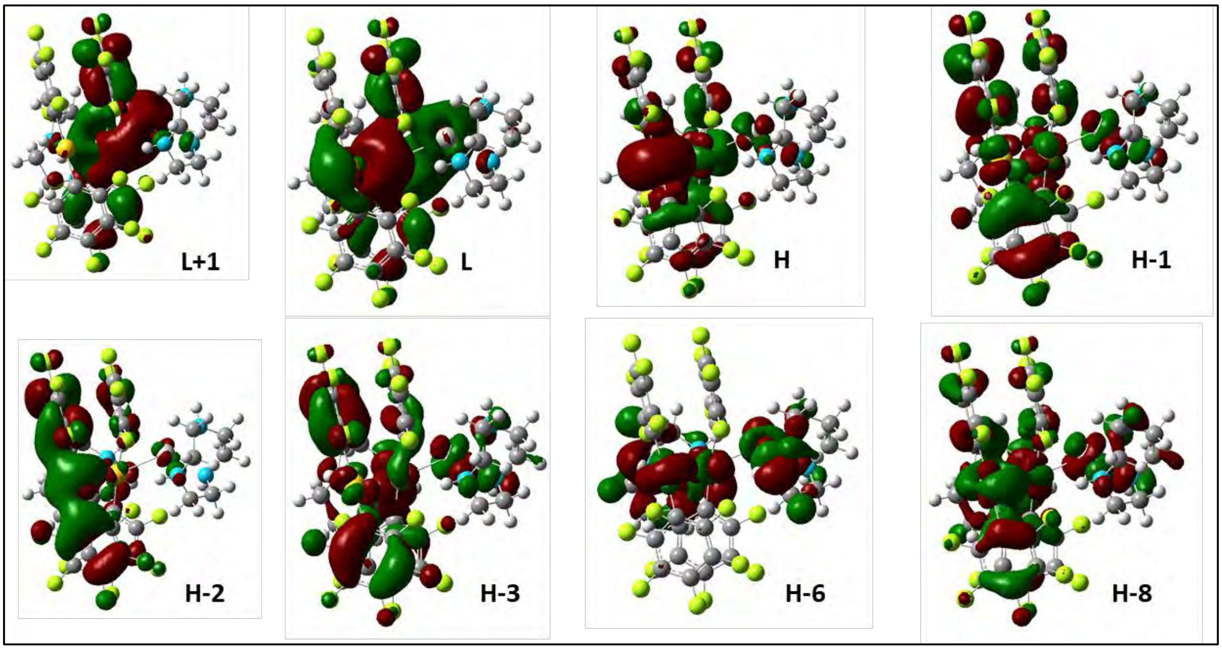

Figure 36. Most important frontier molecular orbitals (isovalue = 0.02) for model system **27a** (L=LUMO; H=HOMO).

The first twenty singlet–singlet excitation energies were computed for all model systems at the TD-DFT level of theory as it was described in the computational details. We carried out the analysis of the excitation wavelengths, oscillator strengths, and orbitals involved in these electronic excitations, which can be related to the origin of the luminescent behaviour observed experimentally. The results including the most important excitations are depicted in Tables 25-26.

Thus, the TD-DFT analysis of the most important single-singlet transitions calculated for model **25a** shows that they appear between 319 and 250 nm, being the most intense singlet-singlet excitations at 319 and 259 nm. Both the first two most intense transitions consist of a single contribution in which the electron arises from HOMO (319 nm) or HOMO-6 (250 nm) and arrives to LUMO, respectively. Taking into account the orbitals involved in these transitions, we could assign the first most important electronic excitations (319 nm) to transitions between the [Ag (L)] fragment and the C_6Cl_5 unit; while the second important singlet-singlet excitation (258 nm) is due to a pure transition between the ligand and the C_6Cl_5 ring. The results agree quite well with the experimental excitation spectrum in solid state for complex **25** (See Figure 37 and Table 26).

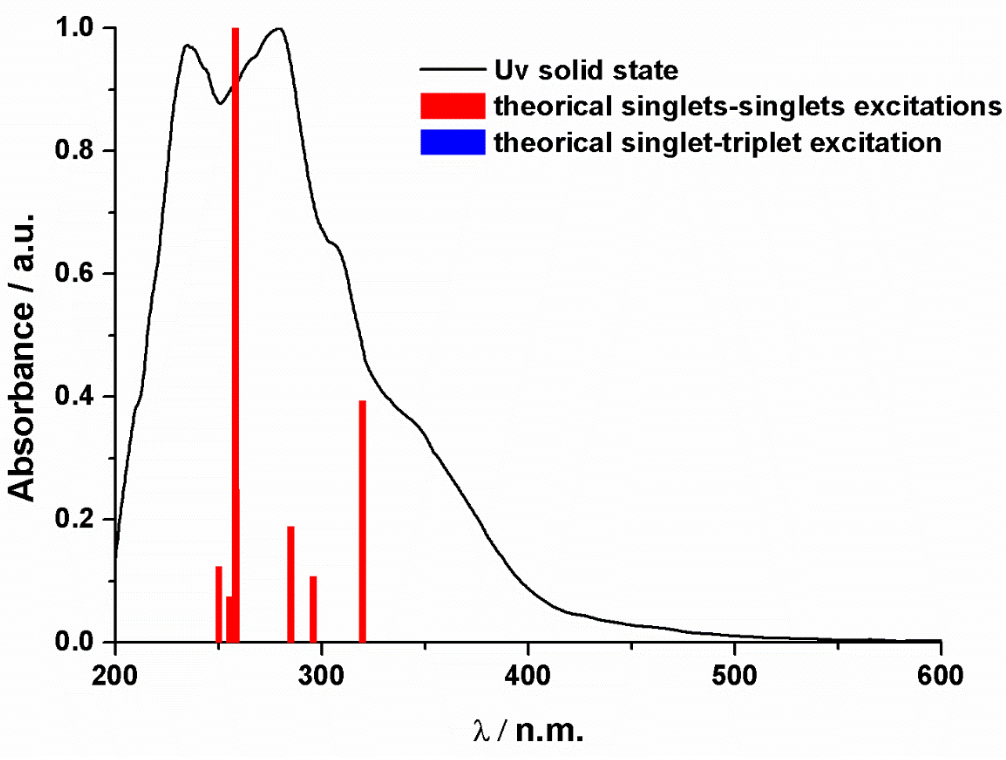

Figure 37. Experimental UV-Vis solid state absorption spectrum (black line) and TD-DFT singlet–singlet excitations (red bars) for model systems **25a**.

Table 26. TD-DFT first Singlet-Singlet Excitation Calculations for Model system **25a**.

Model	exc.	λ_{calc} (nm)	f (s)	contributions
25a	$S_0 \rightarrow S_1$	319	0.0667	HOMO →LUMO (47)
	$S_0 \rightarrow S_2$	295	0.0182	HOMO-3 →LUMO(16) HOMO-1 →LUMO (29)
	$S_0 \rightarrow S_5$	284	0.0321	HOMO-4 →LUMO (16)
	$S_0 \rightarrow S_{12}$	259	0.0423	HOMO-6 →LUMO (13)
	$S_0 \rightarrow S_{13}$	258	0.1696	HOMO-6 →LUMO (24)
	$S_0 \rightarrow S_{14}$	257	0.0126	HOMO-2 →109 (15)
	$S_0 \rightarrow S_{16}$	255	0.0127	HOMO-4 →LUMO+2 (21)
	$S_0 \rightarrow S_{19}$	250	0.0210	HOMO-4 →LUMO+2 (15)

The most intense TD-DFT singlet−singlet excitations for model **27a** appear between 357 and 274 nm. These values are in agreement with the experimental excitation spectrum for complex **27** for the singlet-singlet transition, which shows a maximum at 276 nm, and with the UV-Vis absorption spectrum in solid state for the allowed singlet-singlet transitions (see Figure 38). If we analyse the TD-DFT results for model **27a** we can observe that the main contribution of the most intense computed singlet-singlet electronic transition at 357 nm arises from a HOMO-LUMO transition. From the population analysis results (Table 27), this excitation can be attributed to a transition between the metal centers. Other intense singlet-singlet excitations at lower energy (338 nm) can be attributed to HOMO-LUMO+1 transition between the interacting Au_A-CF_{5A}. The two most intense singlet-singlet excitations have an energy similar to that shown by the solid-state excitation spectrum for the complex **27**. These two different transitions may be responsible for the two different emissions shown by this complex at 77K and at room temperature.

Table 27. TD-DFT first Singlet-Singlet Excitation Calculations for Model system **27a**.

Model	exc.	λ_{calc} (nm)	f (s)	contributions
	$S_0 \rightarrow S_1$	357	0.0806	HOMO → LUMO (48)
	$S_0 \rightarrow S_2$	338	0.0841	HOMO → LUMO+1 (48)
	$S_0 \rightarrow S_4$	302	0.039	HOMO-2 → LUMO (22) HOMO-1 → LUMO+1 (19)
	$S_0 \rightarrow S_5$	300	0.0278	HOMO-3 → LUMO(37)
	$S_0 \rightarrow S_6$	296	0.0147	HOMO-2 → LUMO (24)
	$S_0 \rightarrow S_9$	290	0.0106	HOMO-6 → LUMO (18)
	$S_0 \rightarrow S_{13}$	282	0.0147	HOMO-2 → LUMO+1 (39)
	$S_0 \rightarrow S_{15}$	276	0.0185	HOMO-8 → LUMO (18) HOMO-3 → LUMO+1 (19)
	$S_0 \rightarrow S_{16}$	274	0.0272	HOMO-6 → LUMO+1 (29)

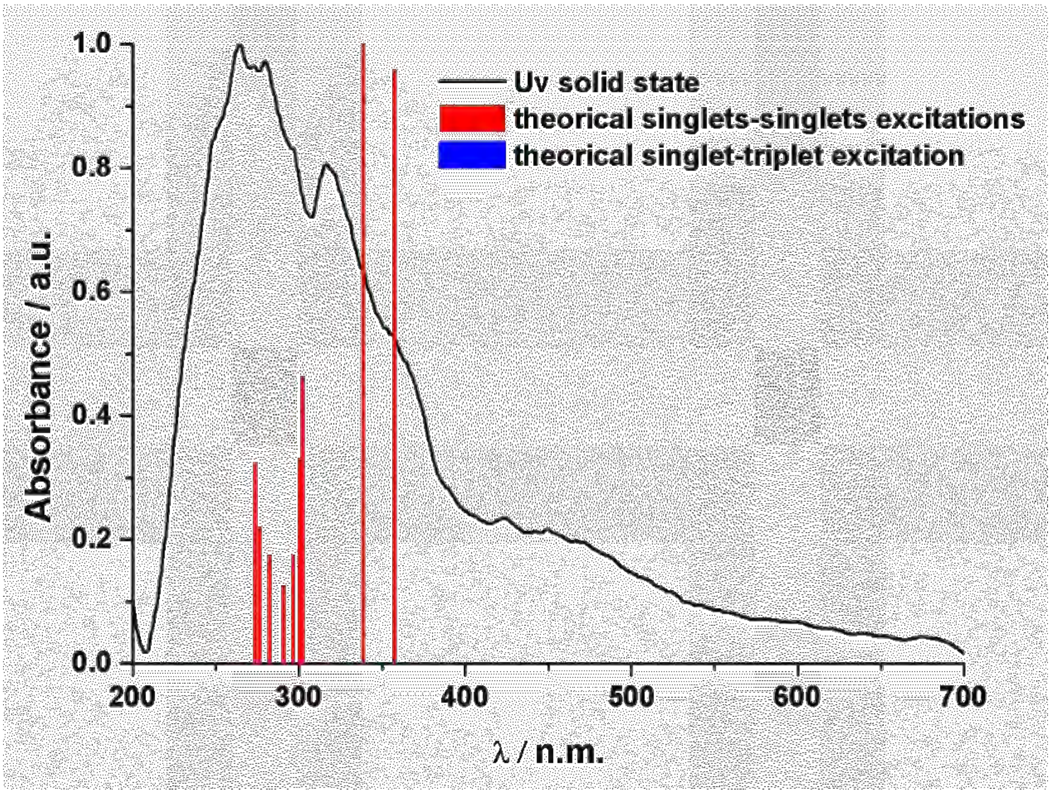

Figure 38. Experimental UV-Vis solid state absorption spectrum (black line) and TD-DFT singlet–singlet excitations (red bars) for model systems **27a**.

3.3.6 Conclusions

The use of ligand **L_4** allows the generation of new heterometallic systems containing gold-silver metallophilic interactions with different structural arrangements and optical proprieties. While the 1,10-phenanthroline derivatives (complex **24** and**26**) do not show any luminescent emission in solid state, probably due to the quenching generated by the formation of [Ag(**L_4**)] unit, 1,4,7-triazaciclononane (**L_5**) derivatives (complexes **25** and **27**) show luminescent properties directly correlated to the different structure of the systems. On one hand, the binuclear complex $[\{Au(C_6Cl_5)_2\}\{Ag(L_5)\}]$ (**25**) show a green emission (541 nm) due a HOMO→LUMO electronic transition between the [(Ag(L)] fragment and the C_6Cl_5 unit. On the other hand, the tetranuclear complex $[\{Au(C_6F_5)_2\}\{Ag(L_2)\}_2\{Au(C_6F_5)_2\}]$ (**27**) shows two emissions at about 452 (77K) and 534 nm (RT). Through TD-DFT calculations, it is possible to explain this different behaviour of **25** and **27** by analysing the contribution of the orbitals to the two most intense electronic transitions (338 and 357 nm); in fact, while the first one can be attributed to HOMO-LUMO+1 transition between gold and the pentafluorophenyl unit, the second one is assigned to a charge transfer between the metal centers. Lastly, it is important to emphasize the unprecedented dual Ag-C_{ipso} interaction present in the complex **27** having the smallest distance of 2.359(9) Å recorded so far.

3.4 Functionalized macrocyclic systems

3.4.1 Introduction

Thanks to the efforts made for the synthesis of the Au/Tl and Au/Ag heterometallic compounds previously shown, it can be established that the metallophilic interactions as well as the nature of ligands used play an important role in determining the optical properties of the resulting compounds featuring Au(I)-Tl(I) and Au(I)-Ag(I) interactions. Specifically, thanks to the efforts made by a number of research groups, it has been established that these factors play an important role in determining the luminescent properties of these compounds[116]-[130]]. Nevertheless, due to the great number of factors that can affect the luminescence, it has not been possible to stablish a relationship between the number of intermetallic contacts in the compounds and their optical properties. For instance, the presence of metallophilic interactions can be strongly influenced by the coordination capacity of the ligands used to support these weak interactions. The number and nature of donor atoms as well as the structural rigidity of the ligand play a determining role both for the number of metallophilic interactions and for their strength, proportional to the metal···metal distance.

In particular, mixed N/S/O-donor macrocyclic ligands are ideal candidates to study structural/properties relationships because of their coordinating properties and size of the ring cavity that can play a key role in the binding features towards different metal ions. Furthermore their donor properties can be modified by adding pendant substituents that increase the coordination ability of the starting macrocyclic ligands.

Taking all the above into account, we decided to study the reactivity of the quinoline pendant arm derivatives of **L_3** and **L_4**, namely N-quinolinylmethyl-5-aza-2,8-dithia[9](2,9)-1,10-phenanthrolinophane (**L_6**) and N-quinolinylmethyl-1-oxo-7-aza-4,10-dithiacyclododecane (**L_7**), respectively (see Figure 39) with the hetero-dimetallic complexes $[AuAg(C_6X_5)_2]_n$ (X = F, Cl) in different molar ratios. Our goal was to study the influence of the number of donor atoms present in the ligand both on the nuclearity and on the photophysical properties of the complexes obtained. Furthermore, we were also interested in analysing the relationship between the number of metal-metal interactions present in the complexes with their emission wavelengths.

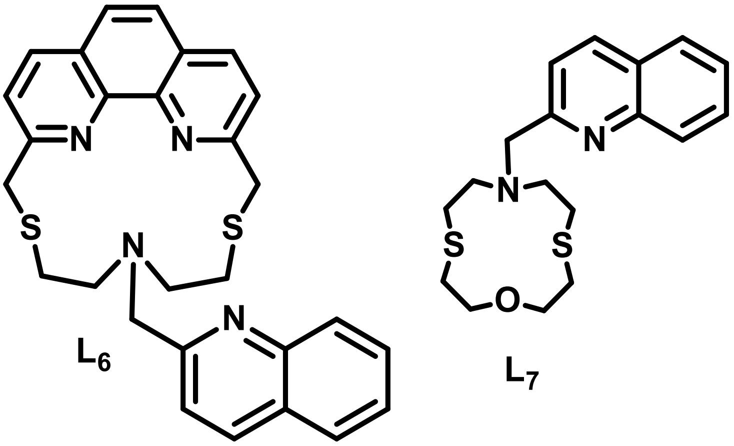

Figure 39. Quinoline pendant arm derivatives of $\mathbf{L_6}$ and $\mathbf{L_7}$ studied.

3.4.2 Synthesis and characterization

The $[Au(C_6X_5)_2Ag]_n$ precursors react with the ligands $\mathbf{L_6}$ and $\mathbf{L_7}$ in THF to afford complexes **28**-**33** (see Scheme 4). Unfortunately, despite numerous attempts to obtain single crystals of complexes **28**, **31** and **33** suitable for X-ray resolution, it was impossible to obtain them for these compounds. In fact, the formulations reported in the scheme 4 simply represent the stoichiometry of the reaction without giving any information on the structural disposition or on the nuclearity of these three compounds. Thus, despite the elemental analysis is in agreement with the molar ratio of the complexes **28** (metal/ligand ratio 1:1) and **31** and **33** (metal/ligand 2:1 ratio), we cannot explain the variation of the photophysical properties as a function of the crystalline structure as we did for the analogous Au/ Tl complexes **(13**-**16**).

All the obtained compounds are insoluble in dichloromethane, acetonitrile and diethyl ether although they are soluble in O-donor solvents. However, the solubility of the chlorinated compounds is lower than the solubility of the fluorinated complexes. The elemental analyses and spectroscopic data of the obtained complexes are in accordance with the proposed stoichiometries (see Experimental Section). Their IR spectra show, among others, absorptions arising from the $C_6F_5^-$[60] and $C_6Cl_5^-$[61] groups bonded to gold(I) at approximately 1500, 950 and 780 cm^{-1} or about 834 and 614 cm^{-1}, respectively.

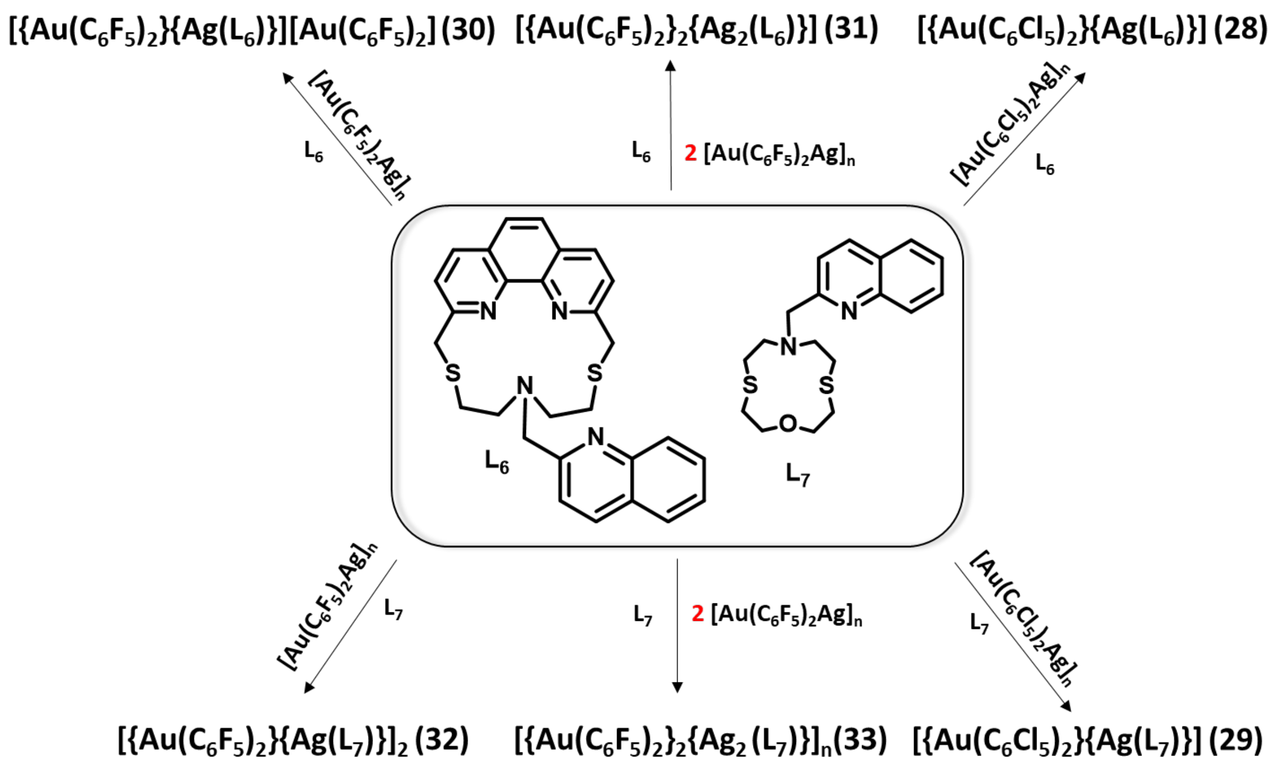

Scheme 4.

The NMR spectrum of complexes **28**, **30** and **31** show proton resonances very similar to the chemical shifts observed for the free ligand **L$_6$**. Therefore, the coordination of the macrocyclic ligand to silver affects slightly the position of the resonances observed in the ^{1}H-NMR spectra and causes a widening of the signals. The signals of the aliphatic protons of the macrocyclic ligand **L$_6$** appear as multiplets in the ranges 2.63-2.75 (4H) (**28**, **30**, **31**), 2.89-3.15(4H) (**28**, **30**, **31**) and 4.05 (**28**) or 4.42-4.44 ppm (4H) (**30**, **31**), while the signals due to the aromatic protons of the quinoline groups arise as well defined resonances between 7.40 and 8.47 (12H) (**28**,**30**,**31**) ppm. Moreover, a singlet in the range 3.76-3.95 ppm (2H) (**28**, **30**, **31**) ppm is observed corresponding to the protons of the methylene group bridging the quinoline moiety to the macrocyclic framework. A similar behaviour is observed in the ^{1}H-NMR spectra of complexes **29**, **31** and **32**. Also in these cases, it is present a singlet at around 4.0 (2H) ppm corresponding to the protons of the methylene group bridging the quinoline moiety to the macrocyclic framework. The signals of the aliphatic protons appear as multiplets in the ranges 2.74-3.02 (12H) and 3.83-3.85 ppm (4H), while the signals due to the aromatic protons of the quinoline groups arise as well defined resonances between 7.36 and 8.66 (6H) ppm. On the other hand, the ^{19}F NMR spectra of fluorinated derivatives (**30**-**33**) in [D$_8$]-tetrahydrofuran resembles that of the gold(I) precursor NBu$_4$[Au(C$_6$F$_5$)$_2$], showing signals at about -

116, -164 and -166 ppm with the characteristic pattern of pentahalophenylgold(I) derivatives (see Experimental Section).

Finally, the MALDI(-) mass spectra of the new products show the peak corresponding to the $[\{Au(C_6X_5)_2\}_2Ag]^-$ anion at *m/z* = 1497 (**28**,**29**) or 1168 (**30-33**), or a signal corresponding to $[Au(C_6X_5)_2]^-$ at *m/z* = 695 (**28**,**29**) or 531 (**30**-**33**), the latter appearing as parent peak in all the cases. In the MALDI(+) mass spectra, peaks due to the fragment $[Ag(L)]^+$ appears at *m/z* = 589 (**28,30,31**) or 445 (**29**,**32,33**). In all of them, the experimental isotopic distributions are in agreement with the calculated ones. The conductivity measurements of **28-33** in acetone solutions are in accordance with a dissociation process into $[Au(C_6F_5)_2]^-$ and $[Ag(L)]^+$ ions when dissolved, since they behave as 1:1 electrolytes.

3.4.3 X-ray structure determinations

In the process of crystallization of **29, 30, 32** by diffusion of n-hexane in a saturated solution in CH_2Cl_2 (**29**, **32**) or THF (**30**), single crystals suitable for X-ray diffraction analysis were obtained (see Figure 40-41). Unfortunately, the lack of solubility of the complexes **28**, **31** and **33** did not allow us to obtain single crystals suitable for structural resolution for these compounds. The crystal structures of **29** and **32,** with pentachlorophenyl and pentafluorophenyl ligands bonded to gold(I), respectively, show different dispositions of the metal centers. Thus, the former consists of a binuclear $[\{Au(C_6Cl_5)_2\}\{Ag(L_7)\}]$ neutral molecule showing one linear $[Au(C_6Cl_5)_2]^-$ fragment bonded to a $[Ag(\mathbf{L_1})]^+$ unit through an unsupported Au···Ag interaction of 2.9320(8) Å (see Figure 40 (left)). In the case of **32** it consists of a tetranuclear $[\{Au(C_6F_5)_2\}\{Ag(L_7)\}]_2$ neutral molecule with an alternating Ag−Au−Au−Ag sequence of metals linked through unsupported metal···metal interactions of 3.2610(4) Å (Au···Au) and 2.8784(4) Å (Au···Ag) (see Figure 40 (right)), which resembles those recently described for Au/Ag derivatives with crown-thioethers [131],[133] (Tables 28 and29).

In both crystal structures, the gold(I) centers are linearly coordinated to two perhalophenyl groups, showing typical Au−C distances of 2.055(10) and 2.043(10) Å (**29**), or 2.043(5) and 2.058(5) Å (**32**). $\mathbf{L_7}$ bind the silver(I) centers though the nitrogen and sulphur donor atoms, thus leading to a trigonal bipyramidal environment for silver (τ=0.90 (complex **29**); τ=0.80 (complex **32**))[132]. The Ag-S [2.650(3) and 2.643(3) Å for complex **29**; 2.5967(13) and 2.6026(12) Å for complex **32**] and Ag-N [2.501(8) and 2.546(8) Å for complex **29**; 2.374(4) and 2.550(4) Å for complex **32**] distances are comparable to those described for other related systems ($[\{Au(C_6Cl_5)_2\}Ag([9]aneS_3)]_2$).[131],[133]

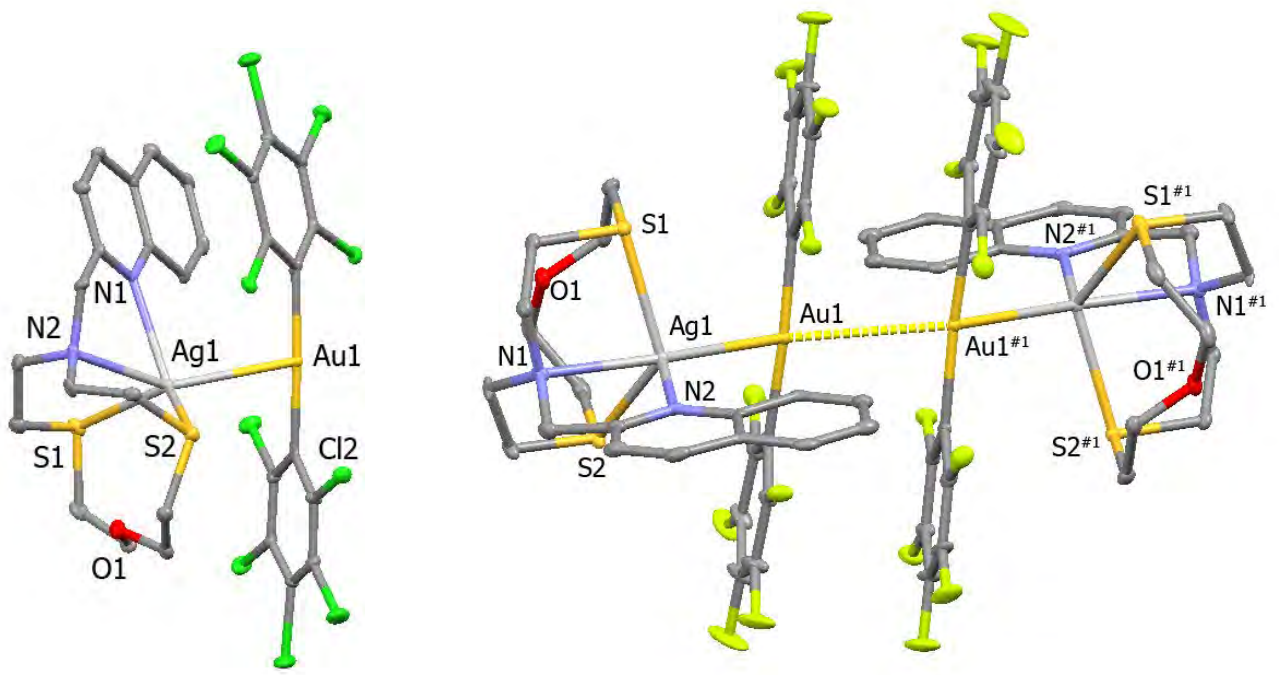

Figure 40. Crystal structures of **29** (left) and **32** (right) with the labelling scheme adopted for the atom positions. Hydrogen atoms and any solvent molecules are omitted for clarity and ellipsoids are drawn at the 30% level. #1 -x+1,-y,-z+2.

Table 28. Selected bond lengths [Å] and angles [°] for **29**.

Au(1)-Ag(1)	2.9230(8)	Ag(1)-N(1)	2.501(8)
Au(1)-C(1)	2.055(10)	Ag(1)-N(2)	2.546(8)
Au(1)-C(2)	2.043(10)	Ag(1)-S(1)	2.650(3)
		Ag(1)-S(2)	2.643(3)
C(1)-Au(1)-C(2)	175.8(3)	N(1)-Ag(1)-S(2)	87.37(19)
S(1)-Ag(1)-Au(1)	97.01(6)	N(1)-Ag(1)-N(2)	67.4(3)
S(2)-Ag(1)-Au(1)	128.09(6)	N(2)-Ag(1)-S(1)	77.88(18)
N(2)-Ag(1)-Au(1)	147.66(19)	N(2)-Ag(1)-S(2)	78.69(19)
N(1)-Ag(1)-Au(1)	93.39(17)	S(2)-Ag(1)-S(1)	122.17(8)
N(1)-Ag(1)-S(1)	128.7(2)		

Table 29. Selected bond lengths [Å] and angles [°] for **32**.

Ag(1)-Au(1)	2.8784(4)	Ag(1)-N(1)	2.550(4)
Au(1)-Au(1)#1	3.2610(4)	Ag(1)-N(2)	2.374(4)
Au(1)-C(1)	2.058(5)	Ag(1)-S(1)	2.5967(13)
Au(1)-C(7)	2.043(5)	Ag(1)-S(2)	2.6026(12)
C(7)-Au(1)-C(1)	173.26(18)	S(1)-Ag(1)-S(2)	120.90(4)
N(2)-Ag(1)-N(1)	71.27(14)	N(2)-Ag(1)-Au(1)	119.34(10)
N(2)-Ag(1)-S(1)	114.02(11)	N(1)-Ag(1)-Au(1)	168.87(9)
N(1)-Ag(1)-S(1)	76.59(9)	S(1)-Ag(1)-Au(1)	94.98(3)
N(2)-Ag(1)-S(2)	107.11(10)	S(2)-Ag(1)-Au(1)	100.01(3)
N(1)-Ag(1)-S(2)	78.70(10)		

Symmetry transformations used to generate equivalent atoms:
#1 -x+1,-y+1,-z+2

The crystal structure of compound **30** that contains pentafluorophenyl ligands bonded to gold(I), shows the same ionic structure as complex **26** containing the same phenanthroline unit. It consists of a trinuclear $[\{Au(C_6F_5)_2\}\{Ag(L)\}_2]^+$ cation with a L-Ag-Au-Ag-L trinuclear arrangement and a $[Au(C_6F_5)_2]^-$ fragment as counter-ion (see Figure 41 and Table 30); in fact, the Au-Ag distances are comparable with those described previously for the complexes **24** and **26**. Moreover, the nitrogen atoms of the quinoline and the macrocyclic units do not interact with silver showing a trinuclear L-Ag-Au-Ag-L arrangement similar to that described previously for the complex **26**. In all complexes containing the 1,10-phenantroline framework, the environment for the silver atom is distorted square-pyramidal with the gold(I) center at the vertex of the pyramid [$\tau = 0.01$ for complexes **24, 26**, **30**] [132].Finally, the Ag-N and Ag-S distances involving the aliphatic moiety of the ligand in complex **30** are 2.477(9) and 2.487(8) Å, for Ag-N distances or 2.626(3) and 2.640(3) Å, for Ag-S distances. These are similar to those found for silver(I) complexes with cyclic N- or N,S-donor ligands as [Ag(N-acylurea-[12]aneNS$_3$)][NO$_3$][64], [Ag(N-Benzyloxycarbonyl)-[12]aneNS$_3$)][NO$_3$][65], [Ag(N-pyridylmethyl)-[12]aneNS$_3$)][PF$_6$][66], [Ag(N-pyridylmethyl)-[12]aneNS$_2$O)][PF$_6$][66] and [Ag(N-CH$_2$CONH-tBu)-[12]aneNS$_3$)][NO$_3$][67], {[Ag(L1)$_{0.5}$(phen)](BF$_4$)· (H$_2$O)$_{0.5}$}$_2$ [105] [Ag$_2$(phen)$_2$(CH$_3$CN)$_2$](ClO$_4$)$_2$[106], [Ag$_2$(phen)$_2$(CH$_3$CN)$_2$](BF$_4$)$_2$[106] and [Ag(N-methyl-2,8-dithia[9],(2,9)-1,10-phenanthrolinophane)][BF$_4$][107].

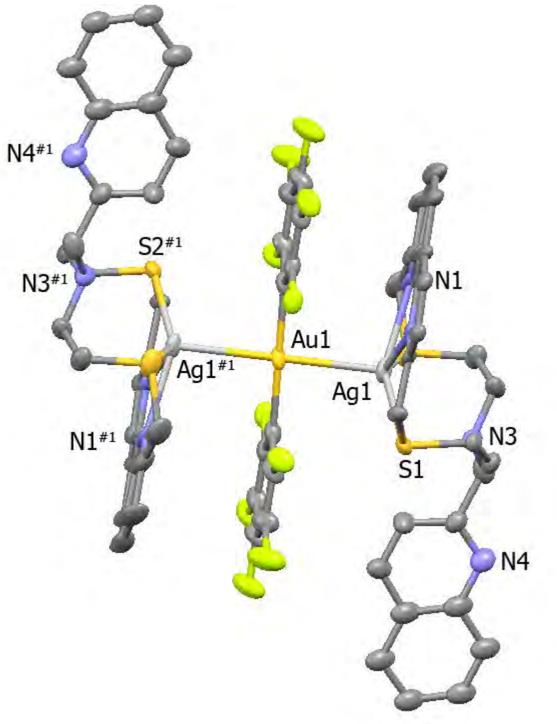

Figure 41. Trinuclear $[\{Au(C_6F_5)_2\}\{Ag(L)\}_2]^+$ unit in the crystal structure of complex **30** with the labelling scheme adopted for the atom positions. Hydrogen atoms and any solvent molecules are omitted for clarity and ellipsoids are drawn at the 30% level. 1# 1-x,1-y,-z.

Table 30. Selected bond lengths [Å] and angles [°] for **30**.

Au(1)-Ag(1)	2.8207(8)	Au(2)-C(27)	2.052(13)
Au(1)-Ag(1)#1	2.8206(8)	Ag(1)-N(1)	2.487(8)
Au(1)-C(1)#1	2.057(13)	Ag(1)-N(2)	2.477(9)
Au(1)-C(1)	2.056(13)	Ag(1)-S(1)	2.640(3)
Au(2)-C(21)	2.055(12)	Ag(1)-S(2)	2.626(3)
Ag(1)#1-Au(1)-Ag(1)	180.0	N(1)-Ag(1)-Au(1)	87.33(19)
C(1)-Au(1)-C(1)#1	180.0	N(1)-Ag(1)-S(1)	73.6(2)
C(27)-Au(3)-C(21)	172.8(5)	N(1)-Ag(1)-S(2)	137.0(2)
S(1)-Ag(1)-Au(1)	95.17(6)	N(2)-Ag(1)-Au(1)	95.43(19)
S(2)-Ag(1)-Au(1)	112.22(7)	N(2)-Ag(1)-S(1)	138.1(2)
S(2)-Ag(1)-S(1)	137.07(9)	N(2)-Ag(1)-S(2)	73.5(2)
		N(2)-Ag(1)-N(1)	66.5(3)

Symmetry transformations used to generate equivalent atoms:

1# 1-x,1-y,-z

3.4.4 Photophysical Properties

We have carried out the study of the optical properties of compounds **28**-**33**, both in the solid state and in solution. Thus, the UV-visible absorption spectra of the seven complexes, in THF solution and at a concentration of about 2.5 x 10^{-5}M, present a similar profile. The chlorinated derivatives **28** and **29** show an intense absorption band between 220 and 350 nm (Figure 42). These absorption spectra are similar to those obtained for the gold(I) precursors $NBu_4[Au(C_6Cl_5)_2]$ and $[\{Au(C_6Cl_5)_2\}Ag]_n$. Moreover, the 1,10-phenantroline and quinoline frameworks show an absorption band at 270 nm and 310 nm respectively, in the same energetic zone. For this reason, the absorption band of the complexes can be assigned to a $\pi \rightarrow \pi^*$ or $n \rightarrow \pi^*$ transitions which can overlap to the intense bands due to the aromatic moieties.

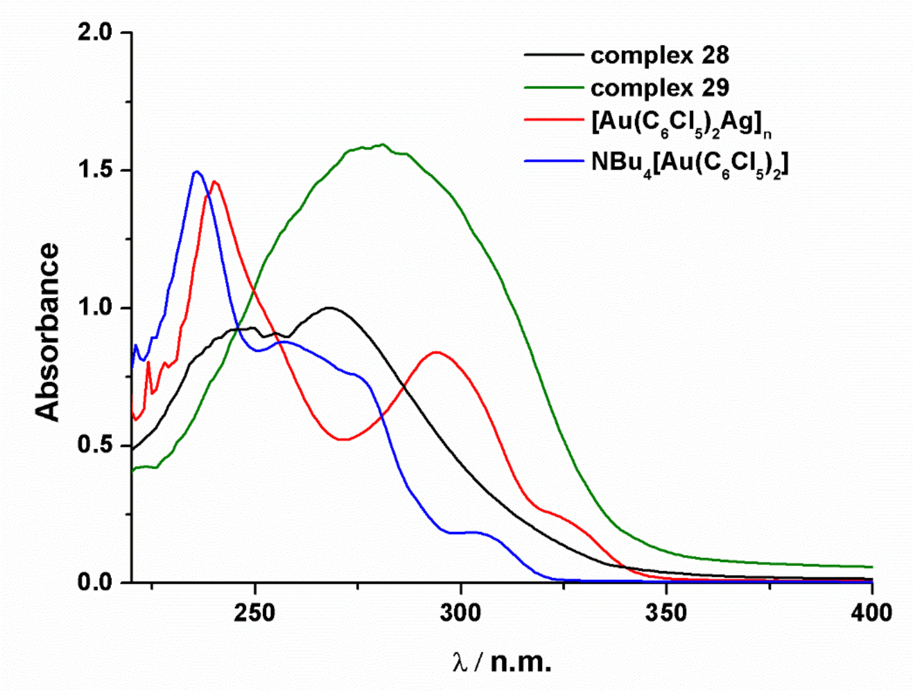

Figure 42. Absorption spectra of complexes **28** and **29** and the gold precursors $NBu_4[Au(C_6Cl_5)_2]$ and $[\{Au(C_6Cl_5)_2\}Ag]_n$ in THF solutions (C ≈ 2.5×10^{-5} M).

On the other hand, as shown in Figure 43, the fluorinated derivatives of both ligands (complexes **30**-**33**) also show features similar to those previously shown (complex **28**, **29**). Furthermore, despite the increase in the metal/ligand ratio for the formation of complexes **31** and **33**, no changes in the absorption spectrum were observed. This is probablt due to a dissociative process, which breaks down any metallophilic interactions present due to the solvation of the different ionic species by the solvent. For this reason, these systems are generally extremely soluble in coordinating solvents and insoluble in non-coordinating solvents. The same conclusion can be made by observing the absorption spectra of the complexes **32** and **33**.

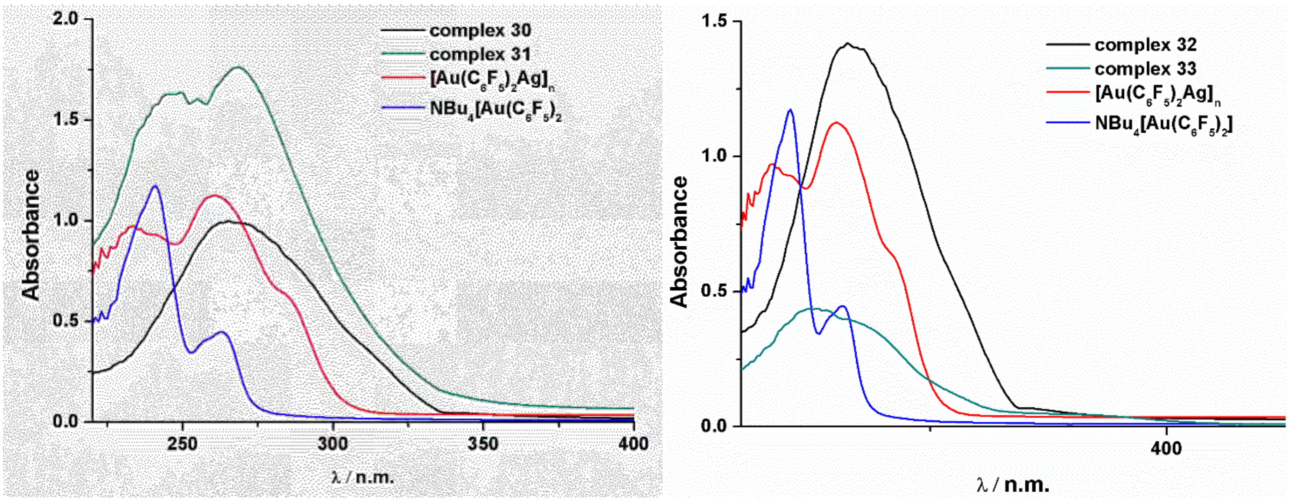

Figure 43. Absorption spectra of complexes **30** and**31** (left) and **32** and **33** (right) and the gold precursors $NBu_4[Au(C_6Cl_5)_2]$ and $[\{Au(C_6Cl_5)_2\}Ag]_n$ in THF solution (C ≈ $2.5x10^{-5}$ M).

Regarding the optical properties in solid state, similarly to the complex featuring gold(I)-thallium(I) interactions, only the 1,10-phenanthroline derivative with a metal/ligand stoichiometry of 2:1 (complex **31**) and the complexes containing $\mathbf{L_7}$ (**29**, **32**, **33**) show luminescence both at room temperature and at low temperature. In the cases of complexes **28** and **30**, the formation of the species $[Ag(\mathbf{L_6})]^+$ likely determines the quenching of the luminescent emission (see paragraph 3.3.4). Thus, complexes **29, 31-33** display emissions in the solid state between 529 and 559 nm at room temperature, and between 516 and 555 nm when the measurements are carried out at the liquid nitrogen temperature (77 K) (see Figure 44 and Table 23).

Considering the structural data, we can try to establish a relationship between the metal-metal distances or the different nuclearity of the compounds and the emission energies for complexes **29** and **32**. For instance, if we take into account that the interactions between the metal centers are the main source of luminescence frequently, we observe that the complex showing the strongest luminescence is that featuring the gold centers interacting each other (complex **32**). In addition, this system shows an Au-Ag distance shorter than that observed for the complex **29** (2.9230 Å in the complex **29** with respect to 2.8784 Å in the complex **32**). However, given the presence of a quinoline unit in these systems, we cannot exclude the influence of the ligand on the photophysical properties of the synthesized systems. Unfortunately, due to the lack of crystallographic data relative to the other complexes (**31** and **33**) we cannot comment on the optical properties of these systems in relation to their structures.

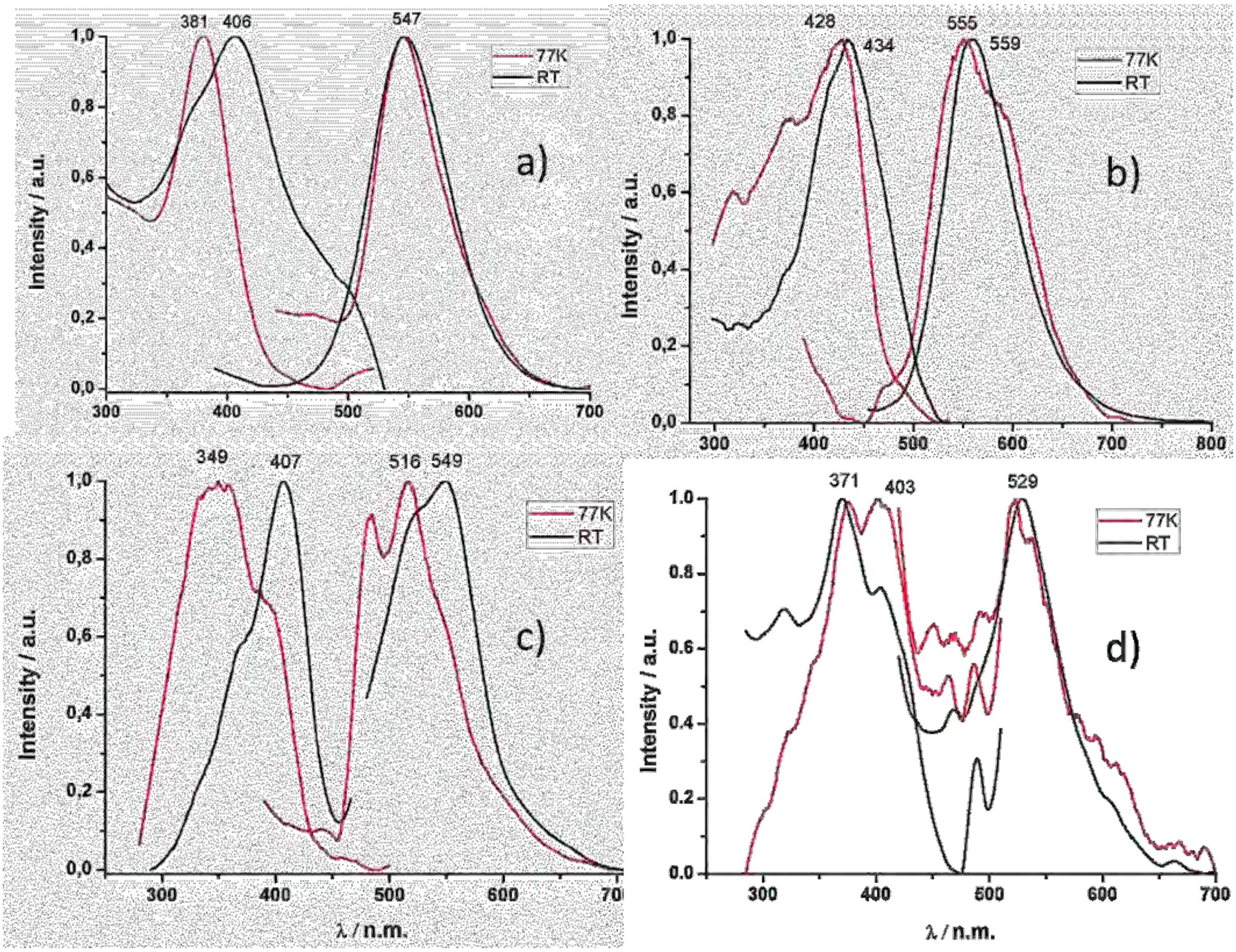

Figure. 44. Excitation and emission spectra for complexes a) **29** b) **31** c) **32** d) **33** in the solid state at RT and 77 K.

Table 23. Photophysical properties of complexes **28**-**33.**

	UV-vis in THF (nm)	Solid (RT) em (exc)	Solid (77K) em (exc)	τ (ns)	Φ (%)
Complex 28	281 (ε = 63200)	-	-	-	-
Complex 29	245 (ε = 55200)	547 (406)	547 (381)	921 ± 11	7.8
	268 (ε = 60000)				
Complex 30		-	-	-	-
Complex 31		559 (434)	555 (428)	950 ± 4	2.3
Complex 32		549 (407)	516 (349)	1025 ± 28	10.2
Complex 33		529 (371)	529 (403)	929 ± 28	7.2

3.4.5 Computational Study

To explain the optical properties of the synthesized complexes and to investigate more about the mechanism responsible for their luminescence, we performed theoretical calculations at the DFT and TD-DFT levels on the models **29a** and **31a** representative of the crystal structures of compounds **29** and **31**.

Thus, model **29a** corresponds to the binuclear neutral molecule found for complex **29**, representing the Au(I)···Ag(I) interaction between the anionic $[Au(C_6Cl_5)_2]^-$ and the cationic $[Ag(\mathbf{L_7})]^+$ fragments (see Figure 45 (left)). Meanwhile, model **32a** represents the tetranuclear L-Ag-Au-Au-Ag-L disposition observed in the complex **32** (see Figure 45 (right)). In this way, we can evaluate the contribution of any metallophilic interaction to the photophysical proprieties of each complex.

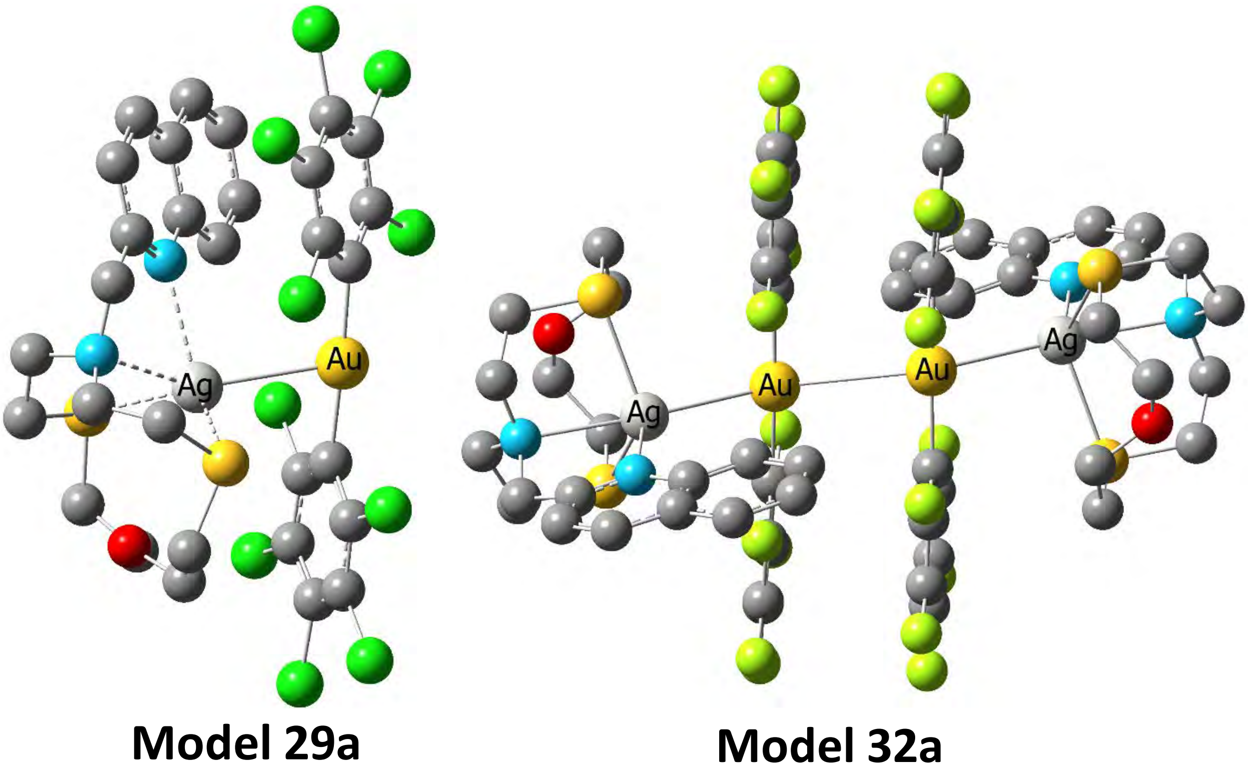

Figure 45. Theoretical model systems $[\{Au(C_6Cl_5)_2\}\{Ag(L_7)\}]$ (**29a**), $[\{Au(C_6F_5)_2\}\{Ag(L_7)\}]_2$ (**32a**).

In addition, for both complexes, a large Stokes' shift and the lifetime measurements determined by the phase-modulation technique in the solid state at room temperature indicate that the emission probably originates from an excited triplet state and, consequently, it could be tentatively assigned to a phosphorescence emission. In order to analyse the contribution of each moiety of the molecule on the different occupied/lowest molecular orbitals involved in the electronic transitions responsible for optical proprieties observed, we analysed the population of the molecular orbitals

(MOs) for both models. Figures 46-47 and Tables 24-25 display the most important frontier molecular orbitals (MOs) and the population analysis of them, respectively. From these data, we can anticipate the contribution of each part of the molecule to the frontier molecular orbitals. Thus, in the case of the binuclear molecular model [{Au(C_6Cl_5)$_2$}{Ag(**L$_7$**)}] **29a**, the population analysis of the highest occupied/lowest unoccupied MOs shows that while the HOMO orbital is mainly located on the Au and Ag metal centers (59 %) with a small contribution of the ligand (30 %), the LUMO orbital shows a strong electronic density on the quinoline framework (81 %). On the other hand, the population analysis of the other lowest empty orbitals (LUMOs) shows a main contribution of the C_6Cl_5 or [Au(C_6Cl_5)$_2$] frameworks with the exception of LUMO+4 that shows a mixed contribution of the whole molecule. The other higher occupied orbitals (HOMOs) show different features: while some orbitals (HOMO-1, HOMO-3 and from HOMO-5 to HOMO-7) show an important contribution of perchlorophenyl units, HOMO-2 and HOMO-8 are mainly localized on the [Ag (**L$_7$**)] framework. The study of the molecular orbitals (MOs) of model **32a** shows that the most important empty orbitals (LUMOs) show a stronger contribution of the ligand (>74 %) with the exception of LUMO+2 that shows a mixed contribution. As contrary, the characteristics of most important occupied orbitals (HOMOs) are very similar to those of model **29a**; while some occupied orbitals (HOMO-2, and from HOMO-5 to HOMO-8) are mainly localized on the C_6F_5 framework, HOMO-1, HOMO-3 and HOMO-4 show the main contribution of the [Ag(**L$_7$**)] unit (>81 %). Lastly, the HOMO-9 and HOMO-10 are mainly localized on the ligand unit.

Table 24. Population analysis (%) for model system **29a**

Model	Orbital	Au	Ag	L	C_6Cl_5
29a	L+4	17	22	38	24
	L+3	42	8	6	45
	L+2	1	4	2	93
	L+1	11	23	9	56
	L	9	15	81	13
	H	39	20	30	12
	H-1	16	7	13	64
	H-2	3	24	54	20
	H-3	6	5	21	70
	H-4	27	13	36	25
	H-5	1	2	4	93
	H-6	6	2	43	51
	H-7	20	7	26	48
	H-8	5	26	59	9
	H-9	2	1	80	17

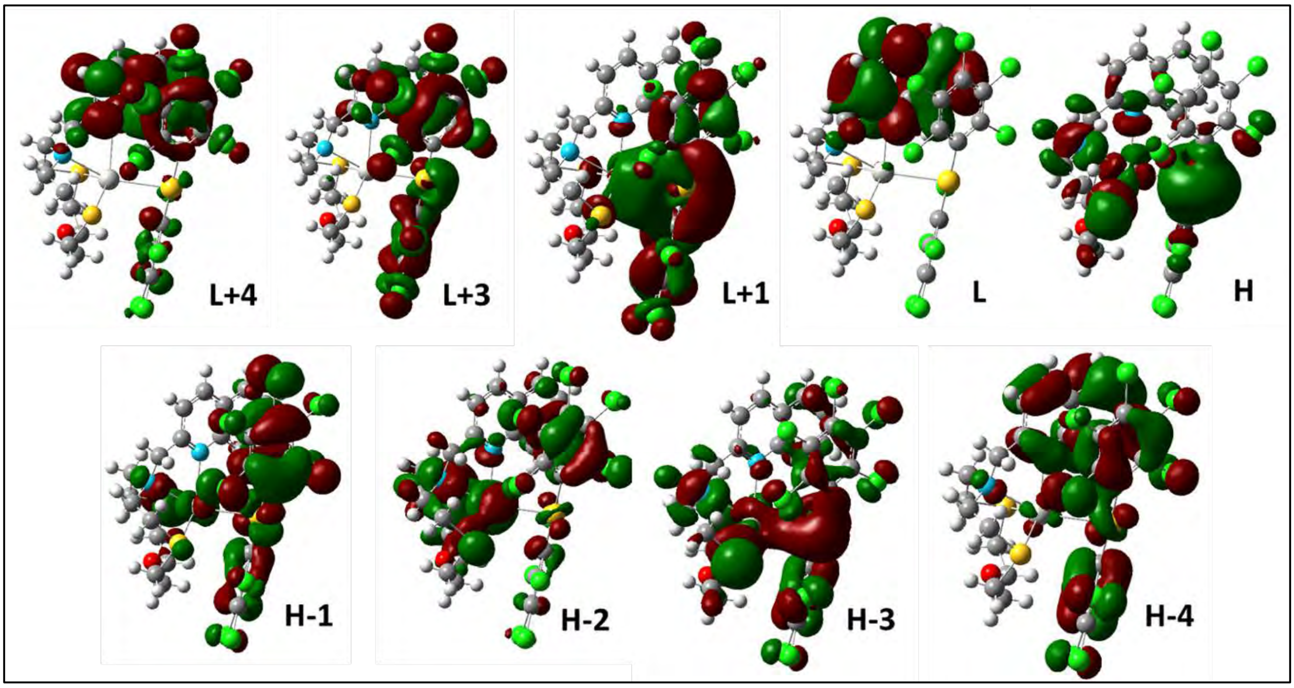

Figure 46. Most important frontier molecular orbitals (isovalue = 0.02) for model system **29a** (L=LUMO; H=HOMO).

Table 25. Population analysis (%) for model system **32a**

Model	Orbital	Au	Ag	L	C_6F_5
32a	L+3	12	12	74	2
	L+2	20	37	17	26
	L+1	9	9	82	0
	L	8	9	83	0
	H	40	20	32	8
	H-1	15	29	51	5
	H-2	19	1	2	77
	H-3	4	23	69	4
	H-4	2	23	71	3
	H-5	16	4	11	68
	H-6	24	3	11	63
	H-7	6	2	4	89
	H-8	9	4	16	72
	H-9	1	4	81	14
	H-10	1	4	77	18

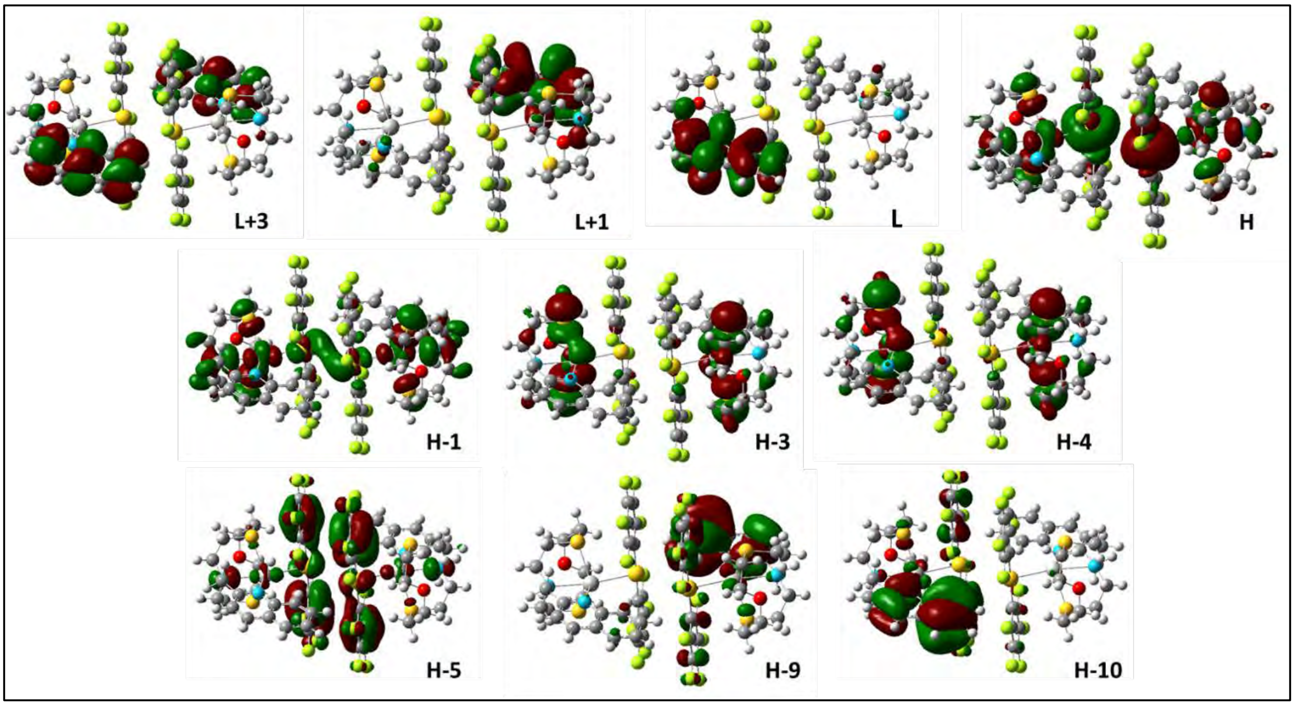

Figure 47. Most important frontier molecular orbitals (isovalue = 0.02) for model system **32a** (L=LUMO; H=HOMO).

The first 20 singlet−singlet excitation energies were computed for all model systems at the TD-DFT level of theory as described in the computational details.

We carried out the analysis of the excitation wavelengths, oscillator strengths, and orbitals involved in these electronic excitations, which can be related to the origin of the luminescent behaviour observed experimentally. The results including the most important excitations are depicted in Tables 26-27.

The TD-DFT analysis of the most important single-singlet transitions calculated for model **29a** shows that they appear between 319 and 266 nm, being the most intense singlet-singlet excitations at 319, 289 and 281 nm. These three transitions can be assigned to the transitions HOMO→LUMO+1, HOMO-1→LUMO+1 and HOMO-2→LUMO+1.

Taking into account the orbitals involved in these transitions, we could assign the first important electronic excitation (319 nm) to some transitions between the L_7/Au unit and the C_6Cl_5 ring, the second one (288 nm) to transitions involving the whole molecule and the silver center, and the third excitation to transitions between the ligand and the metal centers. The results agree well with the experimental excitation spectrum in solid state for complex **29** (See Figure 48 and Table 26).

Finally, the TD-DFT analysis of the most important single-singlet transitions calculated for model **32a** shows that they appear between 337 and 296 nm, being the most intense singlet-singlet excitation at 337, 320, and 297 nm. While, the first most intense transition consists of a single contribution, HOMO-1→LUMO+3, the other two consist of a mixture of contributions, in which the electron arises from HOMO−3/HOMO-4 (319 nm) or HOMO-9/HOMO-10 (296 nm) and arrives to LUMO/LUMO+1 (319 nm, 296 nm). Taking into account the orbitals involved in these transitions, we could assign the first two most important electronic excitations (337 and 319 nm) to transitions between the metal centers and the ligand unit; while the third important singlet-singlet excitation (296 nm) is due to a pure transition between the ligand units. The results agree quite well with the experimental excitation spectrum in solid state for complex **32** (See Figure 49 and Table 27).

Table 26. TD-DFT first Singlet-Singlet Excitation Calculations for Model system **29a**.

Model	**exc.**	**λ_{calc} (nm)**	**f (s)**	**contributions**
29a	$S_0 \rightarrow S_3$:	319	0.0714	HOMO ->LUMO+1 (46)
	$S_0 \rightarrow S_7$:	288	0.0789	HOMO-1 ->LUMO+1 (42)
	$S_0 \rightarrow S_9$:	285	0.0170	HOMO-6 ->LUMO (29)
	$S_0 \rightarrow S_{10}$:	281	0.0648	HOMO-2 ->LUMO+1 (39)
	$S_0 \rightarrow S_{13}$:	276	0.0214	HOMO-4 ->LUMO+1 (23)
	$S_0 \rightarrow S_{14}$:	275	0.0159	HOMO-9 ->LUMO (20)
	$S_0 \rightarrow S_{18}$:	269	0.0102	HOMO ->LUMO+4 (36)
	$S_0 \rightarrow S_{19}$:	266	0.0268	HOMO-1 ->LUMO+3 (13)

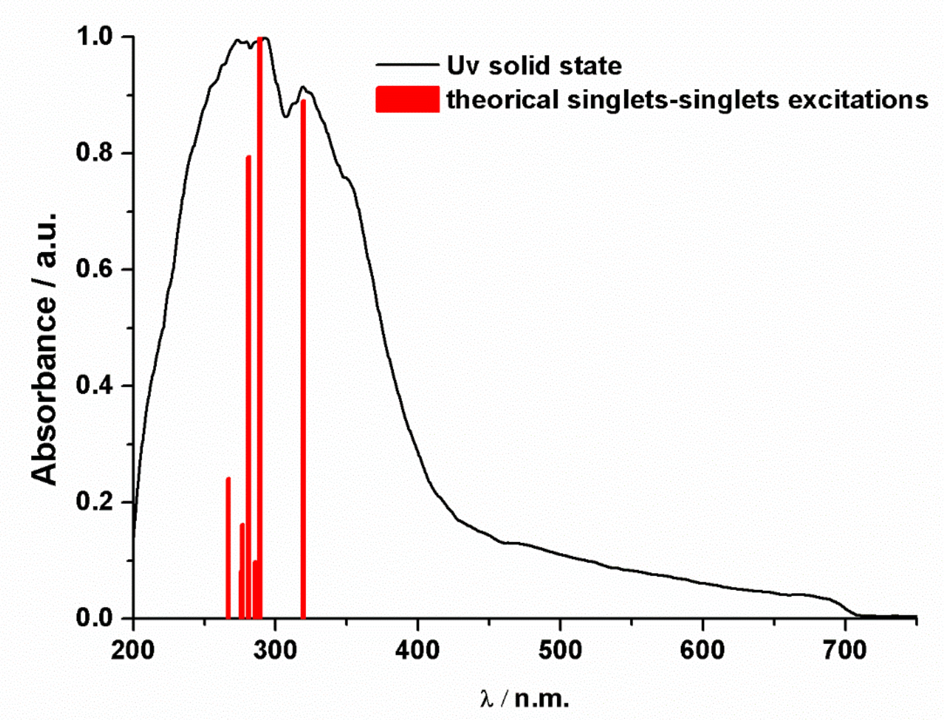

Figure 48. Experimental UV-Vis solid state absorption spectrum (black line) and TD-DFT singlet–singlet excitations (red bars) for model systems **29a**.

Table 27. TD-DFT first Singlet-Singlet Excitation Calculations for Model system **32a**.

Model	exc.	λ_{calc} (nm)	f (s)	contributions
32a	$S_0 \rightarrow S_3$:	337	0.5006	HOMO → LUMO+3 (89)
	$S_0 \rightarrow S_5$:	333	0.0175	HOMO-1 → LUMO+1 (60)
	$S_0 \rightarrow S_7$:	319	0.0719	HOMO-4 → LUMO+1 (30) HOMO-3 → LUMO (28) HOMO-3 → LUMO+1 (17)
	$S_0 \rightarrow S_{13}$:	298	0.0110	HOMO-5 → LUMO (47) HOMO-5 → LUMO+1 (28)
	$S_0 \rightarrow S_{15}$:	296	0.0537	HOMO-9 → LUMO+1 (42) HOMO-10 → LUMO (16)

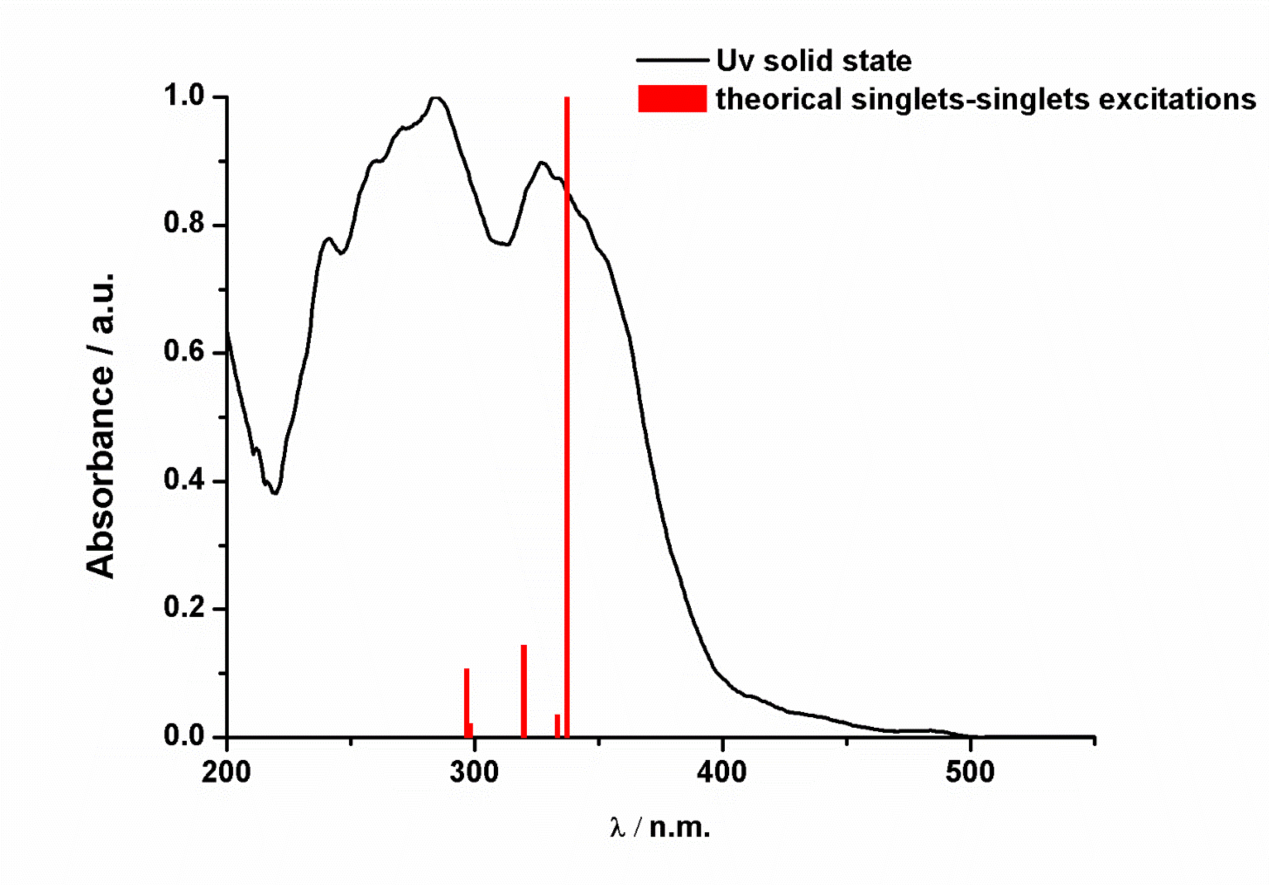

Figure 49. Experimental UV-Vis solid state absorption spectrum (black line) and TD-DFT singlet–singlet excitations (red bars) for model systems **32a**.

3.4.6 Conclusions

In this part of PhD thesis, we have reported the synthesis and study of the new six heteronuclear Au/Ag complexes **28**-**33**. Unfortunately, the lack of solubility has not allowed us to obtain structural information on three of the complexes synthesized (**28**, **31**, **33**).

The substitution of the chlorine by fluorine atoms in the aryl groups bonded to gold(I) leads to significant differences in the crystal structures of the complexes **29** and **32.** While the complex **29** consist of a binuclear neutral molecule with an Au(I)···Ag(I) interaction between the $[Au(C_6Cl_5)_2]^-$ anionic fragment and the cation $[Ag(\mathbf{L_7})]^+$, complex **33** shows a tetranuclear L-Ag-Au-Au-Ag-L disposition with Au(I)···Ag(I) and Au(I)···Au(I) interactions. In this way, we can evaluate the contribution of any metallophilic interaction on photophysical proprieties of each complex. Moreover, through DFT and TD-DFT calculations, it has been possible to highlight the importance of the quinolinic unit, which is involved in most of the molecular orbitals participating in the electronic transitions of the studied complexes.

Despite the difficulty encountered in the study of the behaviour of these complexes due to lack of structural data, the good results obtained with Au/Tl and Au/Ag heterometallic systems spurred us to exploit the structural and coordination characteristics of $\mathbf{L_7}$ to obtain the first heterotrimetallic polymeric system with an unprecedent Ag(I)-Au(I)-Tl(I) moiety. The structural and optical properties of this system will be discussed in the last paragraph of this chapter.

3.5 Heterotrimetallic complexes

3.5.1 Synthesis and characterization.

As shown by the work carried out, the synthesis of heterometallic compounds containing Au(I)/M(I) interactions (M(I) =Au(I), Tl(I), Ag(I)) has been widely developed over the years. In fact, the use of bridging ligands promotes these weak interactions strengthened by electrostatic forces and allowing the synthesis of complexes with luminescent proprieties. However, despite the countless efforts, the only known example of a compound containing an interaction between three different metals was reported by Catalano et al. in 2004 [134]. In this example, the use of a bridging ligand with different donor atoms allows the simultaneous coordination of different metal centers leading to unprecedented molecular Au(I)/Tl(I)/M(0) (M(0)=Pt, Pd) systems that displays Au(I)···Tl(I) and Au(I)···M(0) unsupported interactions.

On one hand, given the difficulty of controlling the synthetic process for the synthesis of compounds containing unsupported interactions between three different metal centers, this aim extremely complicated represents an interesting challenge for all chemists working in this field. In fact, the thermodynamic and kinetic control of the reactions that lead to formation of these weak interactions is an extremely complicated operation and consequently, there are no reports of any complex displaying unsupported interactions between more than two different metallic centers. On the other hand, computational studies conducted by Catalano et al. suggested that an increased dipole momentum in the resulting non-symmetric trimetallic core would reinforce the dispersion forces, which are largely responsible for the metallophilic interactions.

Taking into account the previous comments, a different synthetic strategy consists in the possibility of choosing two heterobimetallic precursors (Au(I)/Ag(I) and Au (I)/Tl (I)) whose reaction could lead to the formation of a new compound containing unprecedent Au(I)/Ag(I)/Tl(I) interactions thanks to the increase in the dipole moment of the whole system.

As precursor of bimetallic Au(I)-Ag(I) compound, we chose complex **32** due to the structural arrangement of the metal centers (+ - - +) that makes the resulting overall dipole moment near to zero (see Scheme 5). As precursor of the bimetallic Au(I)-Tl(I) compound, we chose the polymeric $[\{Au(C_6F_5)_2\}Tl]_n$ chain that in solution displays coordinatively unsaturated thallium centers, making the complex more reactive against ligands with higher coordinative ability.

Thus, by reacting $[AuTl(C_6F_5)_2]_n$ (**P1a**) with complex **32** in THF in different molar ratios (1:1, 2:1, or 3:1), a complex of formulation $[Au_5Ag_2Tl_3(C_6F_5)_{10}(L1)_2]_n$ (**34**) was always obtained (see Scheme 5)

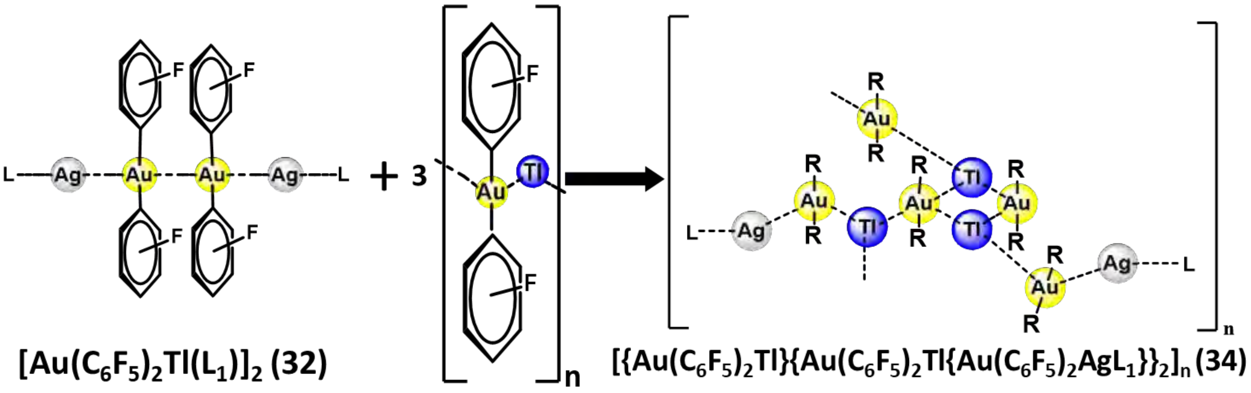

Scheme 5

Complex **34** is stable to air and moisture for long periods of time at room temperature and it is soluble in O-donor solvents such as THF or acetone, partially soluble in dichloromethane or acetonitrile, and insoluble in n-hexane or diethyl ether. The molar conductivity measurements in acetone agree with a dissociative process in solution, showing values corresponding to uni-univalent electrolytes (see experimental section). This fact is likely to be responsible for the loss of luminescence in solution due to the breakdown of the metallophilic interactions following the coordination of the solvent. About its mass spectra (MALDI(-)), the compound synthesized show a peak due to the unit $[\{Au(C_6X_5)_2\}_2M(I)]^-$ (M=Ag, Tl) at *m/z* = 1169 or 1267, or a signal corresponding to $[Au(C_6F_5)_2]^-$ at 531. In their MALDI(+) mass spectra, a peak due to the fragment $[Ag(\mathbf{L_7})]^+$ appears at *m/z* = 455, showing experimental isotopic distributions in agreement with the theoretical ones. This result could indicate a selective coordination of the ligand to the silver atom. The same conclusion can be made from the analysis of H^1-NMR spectrum; the signals due to the macrocyclic ligand are shifted with respect to those due to the free ligand and are similar to the resonances recorded for complex **32** (see experimental section), suggesting, as the MALDI(+) does, the coordination of the ligand to the silver center in solution.

In the process of crystallization by diffusion of n-hexane into a saturated solution of **34** in $C_3H_6Br_2$, suitable monocrystals for the realization of the structural resolution by X-ray diffraction were obtained. The crystal structure of **34**·$C_3H_6Br_2$ can be described as a polymeric chain formed by unprecedented decanuclear $Ag_2Au_5Tl_3$ cores made up of $[Ag(\mathbf{L_1})]^+$, $[Au(C_6F_5)_2]^-$ and Tl^+ units linked through unsupported Au···Ag and Au···Tl interactions (see Figure 50).

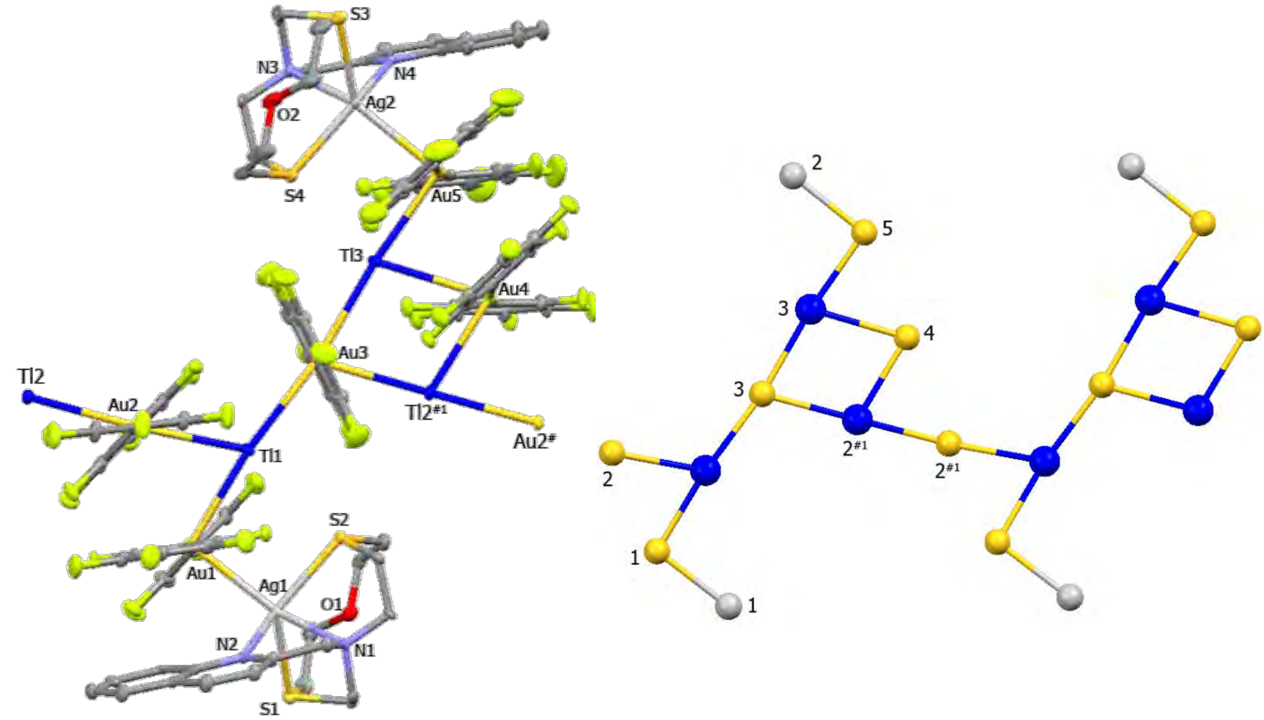

Figure 50. Asymmetric unit of the crystal structure of **34**·C3H$_6$Br$_2$ with the labeling scheme for the atom positions. Solvent and hydrogen atoms are omitted for clarity and ellipsoids are drawn at the 30% probability level. Symmetry code: #1 -x+1,-y+1,-z+2; Representation of a part of the polymeric chain of interacting metal centers in **34**·$C_3H_6Br_2$.

In the asymmetric unit, the linearly coordinated gold(I) centers undertake two Au···Tl [Au(2), Au(3) and Au(4)] or one Au···Tl and one Au···Ag contacts [Au(1) and Au(5)], with interacting Au-Tl distances ranging from 2.9661(8) to 3.2380(8) Å and Au-Ag distances of 2.8803(11) and 2.8849(12) Å. Thus, each thallium center is connected to three gold atoms, and Tl(1) and Tl(3) form an additional weak Tl···S interaction of 3.4814(3) and 3.2405(3) Å, respectively, with one of the sulphur atoms of the macrocyclic ligand. As in the case of **32**, each neutral ligand **L$_1$** binds a silver center acting as a N_2S_2 tetradentate ligand, although in **34**·$C_3H_6Br_2$ the oxygen atom keeps an additional weak Ag···O contact of 3.2103(3) or 3.2768(3) Å, which, together with the metallophilic interaction, would lead to an overall coordination number of six for each Ag(I). If the weak Ag···O contact is not considered, the coordination environment for silver can be better described as square-pyramidal (τ = 0.18 and 0.20)[132] with the S(1) and S(3) at the vertex of the pyramid. The Ag-S [2.429(10)-2.609(4) Å] and Ag-N [2.429(10)-2.538(12) Å] distances compare well with those described for **32** and for other related complexes.[131],[133] As can be seen in Figure 50 (right), the polymerization occurs via unsupported Au···Tl interactions, forming a unidimensional chain that runs parallel to the *z* axis. Finally, it is worth noting that this is the first example of a compound containing three heterometals interconnected each other through unsupported weak metal-metal interactions, since the decanuclear unit of the polymer contains two Ag···Au···Tl fragments.

Table 28. Selected bond lengths [Å] and angles [°] for **34**

Au(1)-Ag(1)	2.8803(11)	Ag(1)-N(1)	2.537(11)
Tl(1)-Au(1)	3.0087(8)	Ag(1)-N(2)	2.429(10)
Tl(1)-Au(2)	3.1581(8)	Ag(1)-S(1)	2.595(4)
Tl(1)-Au(3)	3.0220(8)	Ag(1)-S(2)	2.609(4)
Tl(2)-Au(2)	3.0083(8)	Ag(2)-N(3)	2.538(12)
Tl(2)-Au(3)#1	3.1495(8)	Ag(2)-N(4)	2.430(11)
Tl(2)-Au(4)#1	3.0348(8)	Ag(2)-S(3)	2.585(4)
Tl(3)-Au(3)	3.0833(8)	Ag(2)-S(4)	2.590(4)
Tl(3)-Au(4)	3.2380(8)		
Tl(3)-Au(5)	2.9661(8)		
Au(5)-Ag(2)	2.8849(12)		
Au(1)-Tl(1)-Au(2)	73.678(18)	N(1)-Ag(1)-S(1)	81.0(3)
Au(1)-Tl(1)-Au(3)	163.48(2)	N(1)-Ag(1)-S(2)	78.5(3)
Au(2)-Tl(2)-Au(3)#1	177.39(2)	N(2)-Ag(1)-S(1)	87.5(3)
Au(2)-Tl(2)-Au(4)#1	73.35(2)	N(2)-Ag(1)-S(2)	129.8(3)
Au(3)-Tl(1)-Au(2)	116.58(2)	N(2)-Ag(1)-N(1)	68.2(3)
Au(3)-Tl(3)-Au(4)	103.09(2)	S(1)-Ag(1)-S(2)	123.77(11)
Au(4)#1-Tl(2)-Au(3)#1	106.35(2)	S(1)-Ag(1)-Au(1)	132.42(9)
Au(5)-Tl(3)-Au(3)	173.18(2)	N(1)-Ag(1)-Au(1)	140.6(2)
Au(5)-Tl(3)-Au(4)	73.03(2)	N(2)-Ag(1)-Au(1)	90.1(2)
Tl(1)-Au(3)-Tl(3)	170.14(2)	S(2)-Ag(1)-Au(1)	93.00(8)
Tl(1)-Au(3)-Tl(2)#2	112.12(2)	N(3)-Ag(2)-S(3)	81.9(3)
Tl(2)-Au(2)-Tl(1)	160.07(2)	N(3)-Ag(2)-S(4)	77.9(3)
Tl(3)-Au(3)-Tl(2)#2	75.496(19)	N(4)-Ag(2)-S(3)	89.8(3)
Ag(1)-Au(1)-Tl(1)	97.62(3)	N(4)-Ag(2)-S(4)	127.8(3)
Ag(2)-Au(5)-Tl(3)	93.96(3)	N(4)-Ag(2)-N(3)	67.5(4)
C(1)-Au(1)-C(7)	174.2(5)	S(3)-Ag(2)-Au(5)	132.91(10)
C(19)-Au(2)-C(13)	178.2(5)	S(3)-Ag(2)-S(4)	123.34(12)
C(31)-Au(3)-C(25)	178.4(6)	N(3)-Ag(2)-Au(5)	139.9(3)
C(43)-Au(4)-C(37)	172.5(5)	N(4)-Ag(2)-Au(5)	90.1(2)
C(55)-Au(5)-C(49)	174.7(6)	S(4)-Ag(2)-Au(5)	92.50(9)

Symmetry transformations used to generate equivalent atoms:

#1 x,-y+1/2,z-1/2   #2 x,-y+1/2,z+1/2

As expected, the trimetallic complex **34** displays luminescence in the solid state at room temperature and at 77 K. It emits at 500 nm at room temperature, shifting the emission at 518 nm (λ_{exc} 385 nm) when the temperature is lowered (see Table 29 and Figure 51). In addition, the emission wavelength is intermediate to those of complex **32** (549 nm) and the polymeric unit $[Au(C_6F_5)_2Tl]_n$ (436 nm). Probably, the presence of the trimetallic system Ag(I)-Au(I)-Tl(I) and of the metallophilic interactions involved is the key to explaining the optical properties of the synthesized complex. Moreover, the bathochromic shift at lower temperature is consistent with this assignation, because the compression of the structure provoked by the cooling leads to a destabilization of the HOMO and stabilization of the LUMO reducing the energy band gap. Thus, we propose initially that the emission is likely to arise from a metal-centred transition with contributions from the three interacting metals.

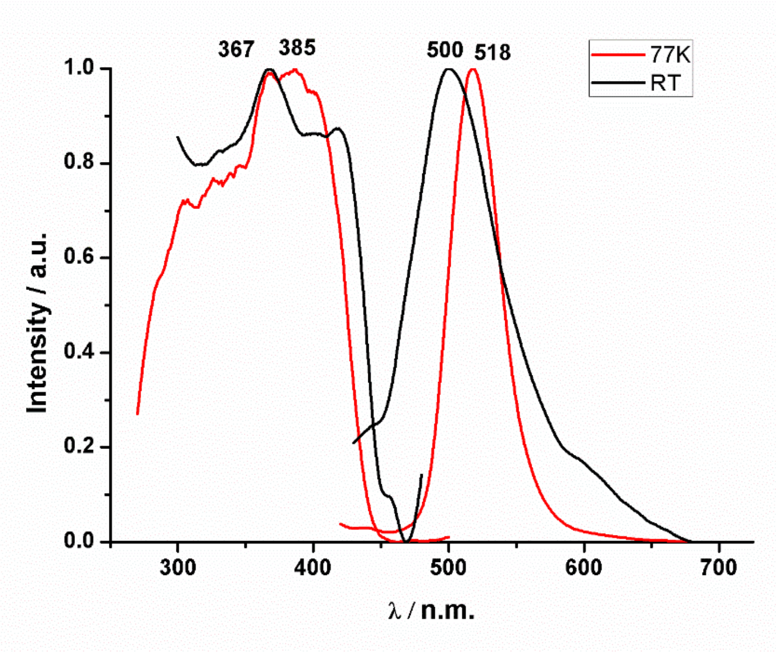

Figure 51. Excitation and emission spectra of complex **34** in the solid state at RT and 77 K.

Table 29. Photophysical properties of complex **34**

	Solid (RT) em (exc)	Solid (77K) em (exc)	τ (ns)
Complex 34	500 (367)	518 (385)	1156 ± 2

3.5.2 Computational Study and Conclusions

We have studied the nature of the metallophilic interactions and the thermodynamic stability of the heterotrimetallic arrangement found experimentally in the structure of complex **34**. We have carried out DFT calculations including dispersion corrections (DFT-D3), HF and MP2 calculations on different tetranuclear models that represent the repetition units of the structure found experimentally (see Figure 52).

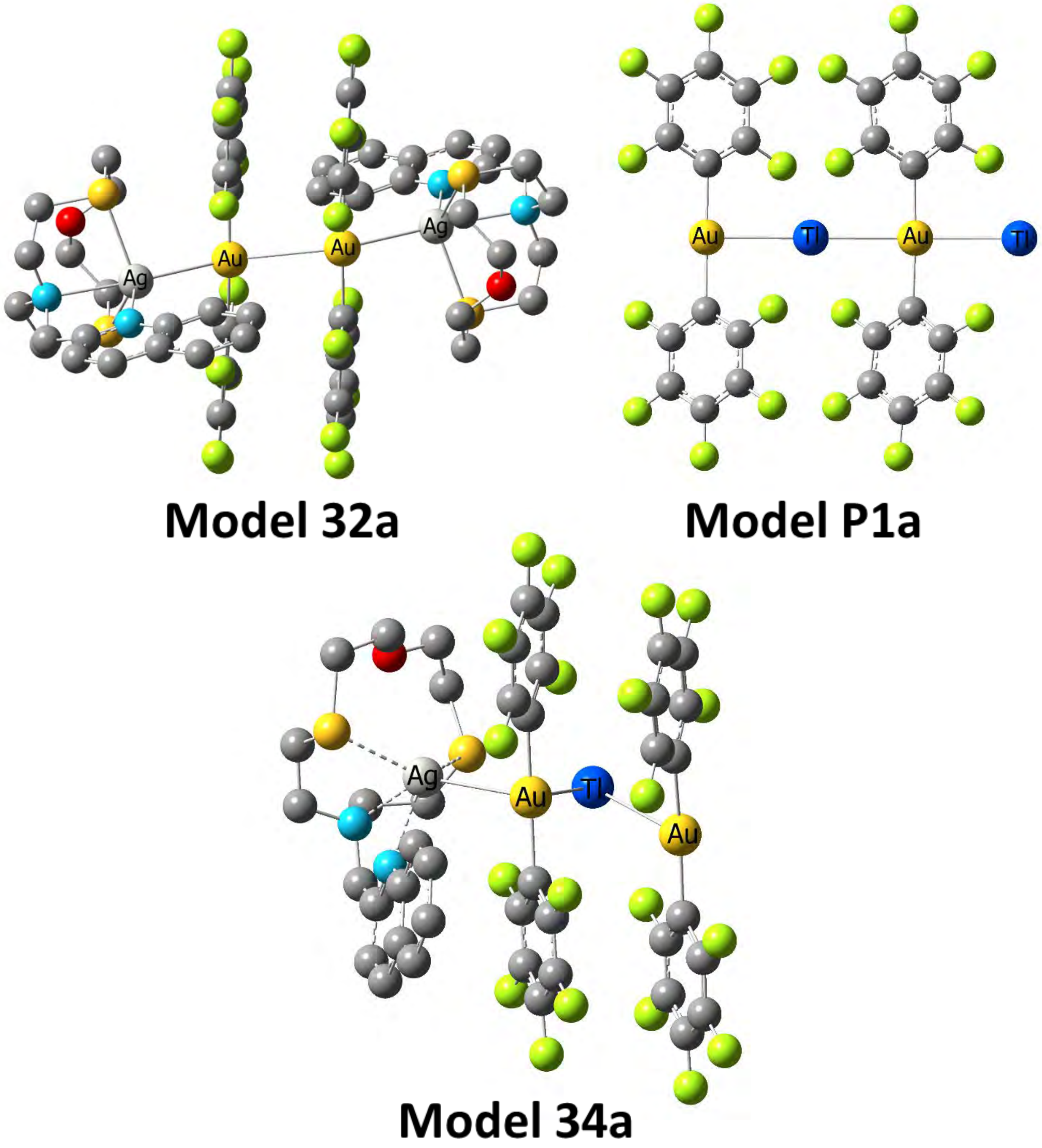

Figure 52. Theoretical model systems [{Au(C_6F_5)$_2$}{Ag(L_7)}]$_2$ (**32a**), [{Au(C_6F_5)$_2$}Tl]$_n$ (**P1a**) [{Au(C_6F_5)$_2$Tl}{Au(C_6F_5)$_2${Ag(L_7)}] (**34a**).

Moreover, to explain the optical properties of the heterotrimetallic complex and investigate more about the mechanism responsible for its luminescence, we have carried out TD-DFT calculations on model **34a**. The population analysis of a tetranuclear model system $[Au_2AgTl(C_6F_5)_4(L_7)]$, which is based on the X-ray diffraction results, together with the TD-DFT calculations, shows that the most intense computed singlet-singlet excitations arise from $[AuR_2]^-$ based molecular orbitals (HOMO-1 and HOMO-2) and arrive to an empty molecular orbital LUMO+1 mainly located on the Ag···Au···Tl moiety (see Table 30-31 and Figures 53 and 54).

Table 30. Population analysis for model systems **34a**.

	Au	Ag	Tl	L_7	C_6F_5
LUMO+2	28	20	13	16	22
LUMO+1	30	19	21	11	19
LUMO	5	9	5	79	2
HOMO	21	1	0	0	78
HOMO-1	10	1	1	1	87
HOMO-2	51	3	3	4	39
HOMO-3	40	0	8	2	51
HOMO-4	8	2	3	4	83
HOMO-5	20	20	6	38	16
HOMO-6	5	1	2	5	88
HOMO-7	19	1	3	5	72
HOMO-8	3	28	2	62	4
HOMO-9	5	11	0	82	2

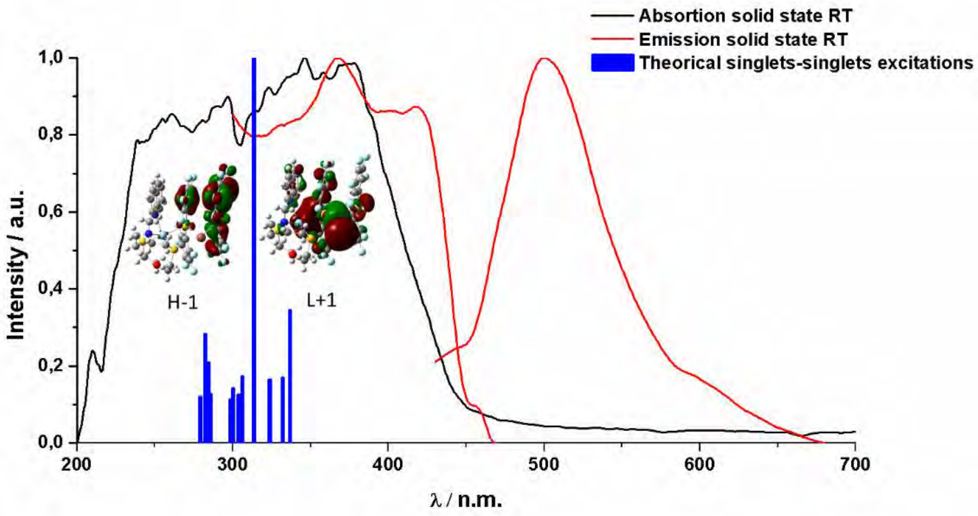

Figure 53. Experimental UV-Vis solid state absorption spectrum (black line), excitation and emission spectra at RT (red line) and TD-DFT predicted singlets-singlets excitation (blue bar) for model systems **34a** with calculated Frontier molecular orbitals H-1 and L+1 (isovalue = 0.02).

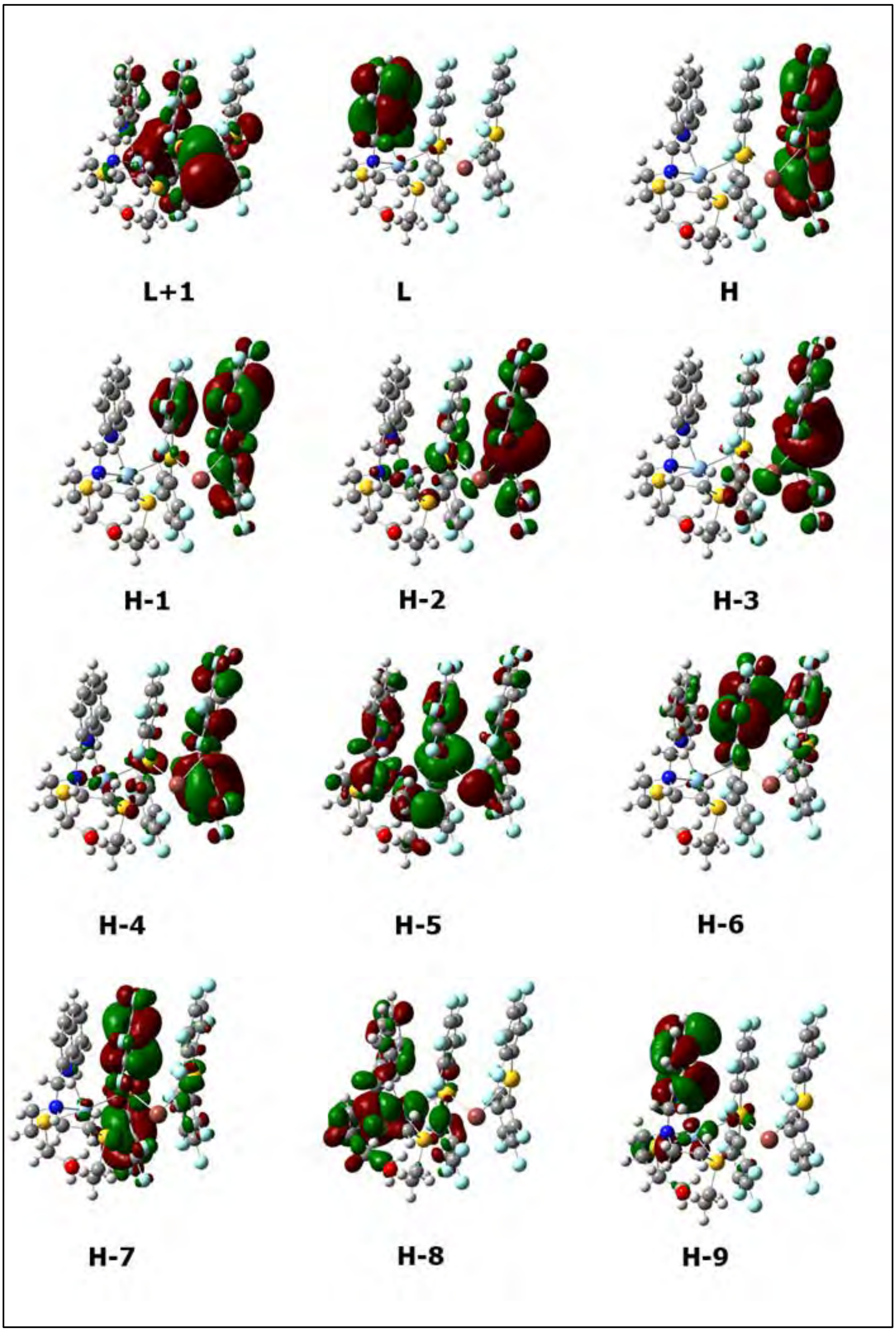

Figure 54. Frontier molecular orbitals (isovalue = 0.02) for the model system **34a** (L= LUMO; H = HOMO).

Table 31. TD-DFT first Singlet-Singlet Excitation Calculations and Lowest Singlet-Triplet Excitations for Model Systems **34a.**

Model	exc.	λ_{calc} (nm)	ƒ (s)	contributions^c
34a	$S_0 \rightarrow S_1$:	337	0.0305	HOMO -> LUMO (48) HOMO -> LUMO+1 (48)
	$S_0 \rightarrow S_2$:	332	0.0150	HOMO -> LUMO+1 (49)
	$S_0 \rightarrow S_3$:	324	0.0146	HOMO-5 -> LUMO (32) HOMO-2 -> LUMO (22) HOMO-1 -> LUMO (28)
	$S_0 \rightarrow S_5$:	314	0.0884	HOMO-2 -> LUMO+1 (40) HOMO-1 -> LUMO+1 (46)
	$S_0 \rightarrow S_6$:	306	0.0154	HOMO-3 -> LUMO+1 (23) HOMO-2 -> LUMO+1 (20) HOMO-1 -> LUMO+1 (36)
	$S_0 \rightarrow S_7$:	304	0.0111	HOMO-5 -> LUMO+1 (18) HOMO-3 -> LUMO (16) HOMO-2 -> LUMO+1 (19)
	$S_0 \rightarrow S_9$:	300	0.0126	HOMO-5 -> LUMO+1 (22) HOMO-4 -> LUMO+1 (30) HOMO-3 -> LUMO (21)
	$S_0 \rightarrow S_{11}$:	299	0.0101	HOMO-6 -> LUMO (20) HOMO-4 -> LUMO+1 (16) HOMO -> LUMO+2 (22)
	$S_0 \rightarrow S_{16}$:	286	0.0112	HOMO-9 -> LUMO (63)
	$S_0 \rightarrow S_{17}$:	285	0.0186	HOMO-9 -> LUMO (15) HOMO-7 -> LUMO (43)
	$S_0 \rightarrow S_{18}$:	282	0.0251	HOMO-2 -> LUMO+2 (30) HOMO-1 -> LUMO+2 (36)
	$S_0 \rightarrow S_{20}$:	279	0.0106	HOMO-6 -> LUMO+1 (81)

In order to gain insight into the stability of the heterometallic precursors and the final heterometallic complex, we have carried out a DFT/pbe optimization of models **32a** and **P1a** that represent the starting products in the synthesis of the complex **34,** and the model **34a** representing the heterotrimetallic unit. Model **P1a** was built up on the basis of the crystalline structure of a similar Au(I)-Tl(I) system in which the only difference is the presence of chlorine atoms in the aurate unit [137]. Subsequently, using the optimised models **32a** and **34a**, we have analysed the nature of the Au(I)···M(I) (M(I) = Au(I), Ag(I) or Tl(I)) interactions for all models. We have computed the BSSE-corrected interaction energies at different distances at HF and MP2 levels. The interaction energies (ΔE) and equilibrium distances for all models are listed in Tables 31 and 32.

The Table 31 shows the most relevant optimized distances and angles for the models. It is important to note that the computed distances are very similar to the experimental ones. In the case of the computed intermetallic Au···M(I) distances, these are slightly shorter than the experimental ones whereas the Au(I)···Au(I) distance computed for model **34a** is shorter than the experimental one by 0,35 Å, probably due to the absence of a packing effect and to the presence of a π-stacking interaction.

Table 31. Selected structural parameters (distances [Å] and angles [^{O}] for complexes **32, 34, P1** and the corresponding model systems at the DFT level of theory (distance in Å and angles in °) .

	Au-Tl	Au-Ag	Ag-E^{a}	Au-Au	C-E^{a}	Tl-Au-Tl	Ag-Au-Tl
32	-	2.877	2.356-2.557 2.598-2.596	3.257	1.413-1.455 1.478-1.423 1.829-1.836	-	-
32a	-	2.817	2.368-2.605 2.593-2.599	3.108	1.400-1.411 1.442-1.447 1.826-1.838	-	-
P1a	2.8470 2.9917	-	-	-	-	-	-
34	2.965 3.274	2.893	2.42-2.53 2.59-2.59	3.711	1.402-1.404 1.462-1.492 1.821-1.843	56.622	94.262
34a	3.045 3.234	2,734	2.485- 2.601 2.582-2.627	3.352	1.406-1.405 1.448-1.455 1.822-1.838	54.382	103.62

Table 32. Optimized Au–M(I) distance, Re, for the tetranuclear models at the MP2 and HF levels.

System	Method	Re	V(Re)	ΔE(MP2-HF)^{a}
[L$_{7}$Ag(I)-Au(I)-Au(I)]$^{-}$···[Ag(I)L$_{7}$]$^{+}$ (**32a**)	MP2	2.88	-369	-163 (43%)
	HF	3.46	-240	
[L$_{7}$Ag(I)-Au(I)]···[Au(I)-Ag(I)L$_{7}$] (**32a**)	MP2	3.15	-135	-
	HF	b	b	
[Au(I)-Tl(I)]···[Au(I)-Tl(I)] (**P1a**)	MP2	3.00	-88	-
	HF	b	b	
[L$_{7}$Ag(I)]$^{+}$···[Au(I)-Tl(I)-Au(I)]$^{-}$ (**34a**)	MP2	2.90	-339	-183 (53%)
	HF	3.46	-190	
[L$_{7}$Ag(I)-Au(I)]···[Tl(I)-Au(I)] (**34a**)	MP2	3.09	-182	.
	HF	b	b	

Equilibrium distance Re in Å; interaction energy V(Re) in kJ/mol.
[a] MP2 equilibrium distance. [b] No minimum

Taking the DFT optimized model systems as starting point we have estimated the stabilization achieved through metallophilic interactions by computing them at different metal-metal distances both at HF at MP2 levels of theory. The analysis of [L$_7$Ag(I)-Au(I)-Au(I)]$^-$···[Ag(I)L$_7$]$^+$ and [L$_7$Ag(I)-Au(I)]···[Au(I)-Ag(I)L$_7$] metallophilic interactions found in model **32a** are shown in Figure 55. The HF curve for the [L$_7$Ag(I)-Au(I)-Au(I)]$^-$···[Ag(I)L$_7$]$^+$ interaction is attractive with a minimum corresponding to the equilibrium distance of 3.46 Å and a stabilization energy of -240 kJ/mol.

Regarding the MP2 curve we can observe an attractive behaviour associated to a stabilization energy of -369 kJ/mol at an equilibrium distance of 28.8 Å, which is in excellent agreement with that found experimentally of 2.87 Å. From the calculations performed to evaluate the stabilization of the [L$_7$Ag(I)-Au(I)]···[Au(I)-Ag(I)L$_7$] interaction, it is observed that the HF curve shows a repulsive behaviour, as expected for an aurophilic interaction between two formally Au(I) centres. In contrast, the MP2 curve shows an attractive behaviour at the equilibrium distance of 3.15 Å with a value of -135 kJ/mol. In addition, in this case the equilibrium distance is in very good agreement with that experimentally determined distance (3.25 Å. If one assumes that the ionic component of the interaction energy could be estimated at the HF level, the dispersion component of the interaction is obtained as the difference between MP2 and HF. For model **32a**, the dispersion component represents 44% of the total interaction energy of the [L$_7$Ag(I)-Au(I)-Au(I)]$^-$···[Ag(I)L$_7$]$^+$ interaction.

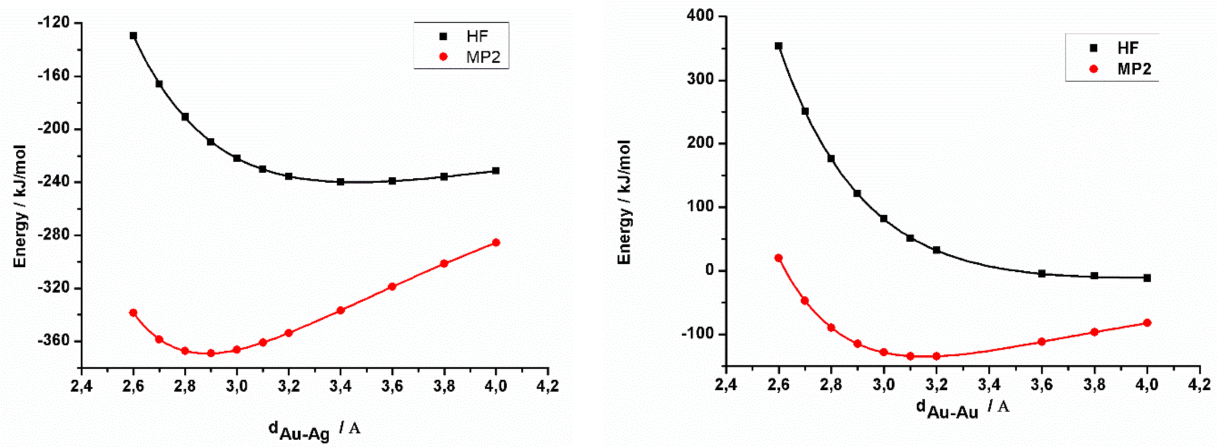

Figure 55. [L$_1$Ag(I)-Au(I)-Au(I)]$^-$···[Ag(I)L$_1$]$^+$ (left) and [L$_1$Ag(I)-Au(I)]···[Au(I)-Ag(I)L$_1$] (right) interaction distances and the corresponding interaction energy curves at HF and MP2 levels for model systems **32a**.

Figure 56 describes the interaction curves for the [Au(I)-Tl(I)]···[Au(I)-Tl(I)] interaction found in the model **P1a**. From the calculations made for the [Au(I)-Tl(I)]···[Au(I)-Tl(I)] interaction, it is observed that the HF curve shows a repulsive behaviour. It is important to underline that this behaviour is due to the neutral charge of the two [Au(I)-Tl(I)] fragments, despite the negative charge in the aurate unit and the positive charge in the thallium(I) atom. The MP2 curve shows an attractive behaviour at a equilibrium distance of 3.00 Å with a stabilization energy of -88 kJ/mol. The choice of studying the interaction strength between two units of the $[Au(C_6F_5)_2Tl]_n$ polymeric chain is due to the fact that it represents the real Au(I)-Tl(I) interaction within a polymeric system.

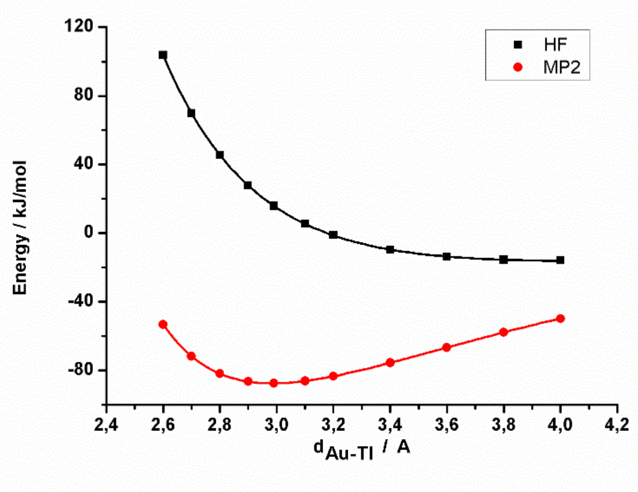

Figure 56. [Au(I)-Tl(I)]···[Au(I)-Tl(I)] interaction distances and the corresponding interaction energy curves at HF and MP2 levels for model systems **P1a**.

Finally, the results of the computed interaction energies for model **34a** are shown in Figure 57. The HF curve for the $[L_1Ag(I)]^+$···$[Au(I)\text{-}Tl(I)\text{-}Au(I)]^-$ is attractive with a minimum corresponding to the equilibrium distance of 3.46 Å with an energy of -190 kJ/ mol. Regarding the MP2 curve we can observe an attractive behaviour with an energy of -339 kJ/mol at the equilibrium distance of 2.90 Å, which is in excellent agreement with that found experimentally of 2.89 Å. From the calculations performed for the $[L_1Ag(I)\text{-}Au(I)]$···[Tl(I)-Au(I)] interaction, it is observed that the HF curve shows repulsive behaviour but that the MP2 curve shows an attractive behaviour with an equilibrium distance of 3.09 Å and a stabilization energy of -182 kJ/mol. In addition, in this case the equilibrium distance is in perfect agreement with the experimentally determined distance (3.23 Å). The contribution of dispersive effects is fundamental for the stabilization of the system: the percentage of dispersive effect is 53% for the $[L_1Ag(I)]^+$···$[Au(I)\text{-}Tl(I)\text{-}Au(I)]^-$ interaction. This value is much higher than those previously calculated on bimetallic heteronuclear systems with the same methodology [135]-[140] and higher than the ones obtained in the tetranuclear heterobimetallic metal systems **P1a** and **32a.** Therefore, the dispersive part of the interaction between the metal centres in this heterotrimetallic system plays a crucial role in the stabilization of such unprecedent supramolecular systems.

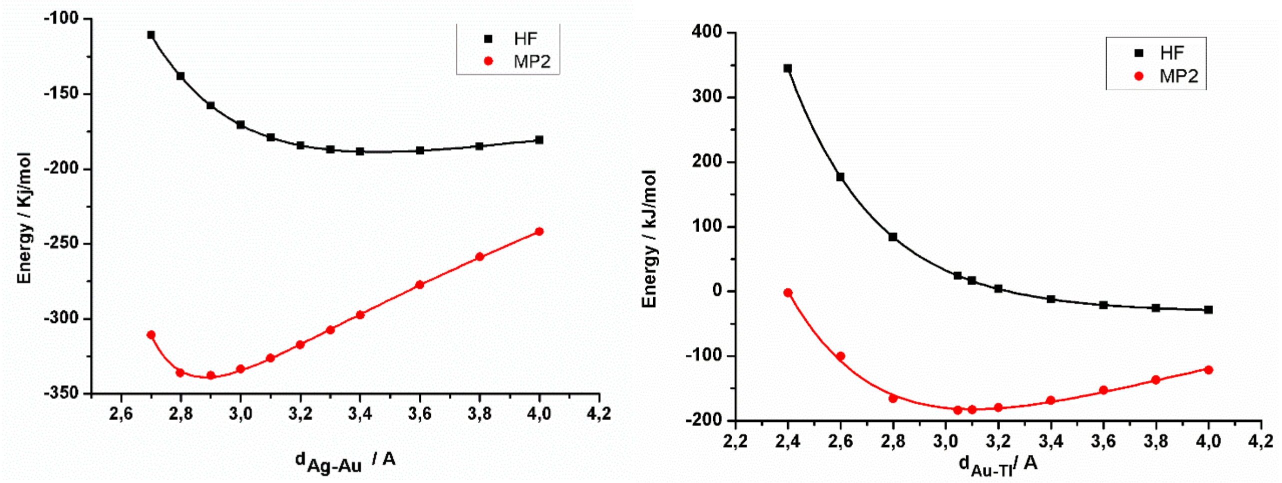

Figure 57. Ag(I)···Au(I) (left), $[L_1Ag(I)\text{-}Au(I)]\cdots[Tl(I)\text{-}Au(I)]$ (right) and $[L_1Ag(I)\text{-}Au(I)\text{-}Tl(I)]^+\cdots[Au(I)]^-$ (below) interaction distances and the corresponding interaction energy curves at HF and MP2 levels for model systems **34a**.

In addition, through the analysis of the MP2 computed strength of the Au(I)•••M(I) metallophilic interactions for **32a**, **P1a**, **34a**, it is possible to show the higher thermodynamic stability of the trimetallic system with respect to the bimetallic precursors according to the isodesmic process (see Figure. 58).

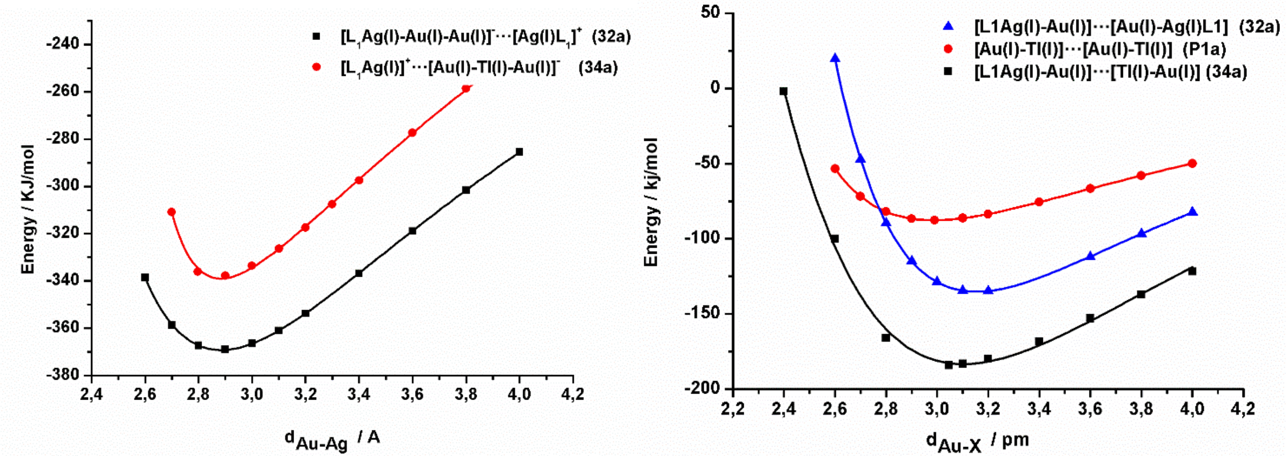

$[AuR_2\text{-}Tl\text{-}AuR_2\text{-}Tl]$ **P1a** $\quad AgL_1\text{-}AuR_2\text{-}AuR_2\text{-}AgL_1$ **32a** $\xrightleftharpoons{\Delta H = -357\ kJ/mol}$ $2\ [AgL_1\text{-}AuR_2\text{-}Tl\text{-}AuR_2]$ **34a**

$E_{int}(Au\text{-}Tl) = -88\ kJ/mol$

$E_{int}(Au\text{-}Ag) = -369\ kJ/mol$
$E_{int}(Au\text{-}Au) = -135\ kJ/mol$

$E_{int}(Au\text{-}Ag) = -339\ kJ/mol$
$E_{int}(Au\text{-}Tl) = -182\ kJ/mol$

Figure 58. Au(I)···M(I) interaction distances and the corresponding interaction energy curves MP2 levels for model systems **32a, 34a** and **P1a** (top) and isodesmic process for the formation of model **34a** (bottom).

From the reported values, it is clearly seen that the interaction Au(I)-Ag(I) loses stability in the model **34a** respect to the model **P1a** (30 kJ/mol), but it is the [L_7Ag(I)-Au(I)]···[Tl(I)-Au(I)] interaction that that plays a decisive role in the thermodynamic stability of the trimetallic system. From the MP2 curves showed in Figure 58, it is clear that the break of the Au(I)-Au(I) interaction in the model **P1a** and the Au(I)-Tl(I) interaction in the model **32a** for the formation of the new interaction Au(I)-Tl(I) in the model **34a** is thermodynamically favoured. The Au(I)-Tl(I) interaction in the presence of [Ag(I)(L_7)] unit, is about 94 kJ/mol more stable respect to the interaction Au(I)-Tl(I) in the model **P1a**, and about 47 kJ/mol more stable than the interaction Au(I)-Au(I) in model **32a**. Considering the energy of dispersive interactions in all models, model **34a** is 357 kJ/mol more stable than models **32a**, **P1a** (see Figure 58).

We have computed the dipole moment for **34a** at MP2 level of theory leading to a very large value of 17.0 D (see Figure 59). Taking into account that the expected dipole moments for the precursors **P1** and **32** are nearly zero, we can conclude that this large dipole moment gives rise to an additional stabilization to the dispersive forces in this trimetallic system, according to Catalano's hypothesis [134]. We believe that the synthetic strategy here reported for the synthesis of the first example of a multimetallic system featuring unsupported M···Au···M' moieties, might be suitable for the preparation of hetero-polymetallic assemblies with a variety of metal compositions and tuneable properties.

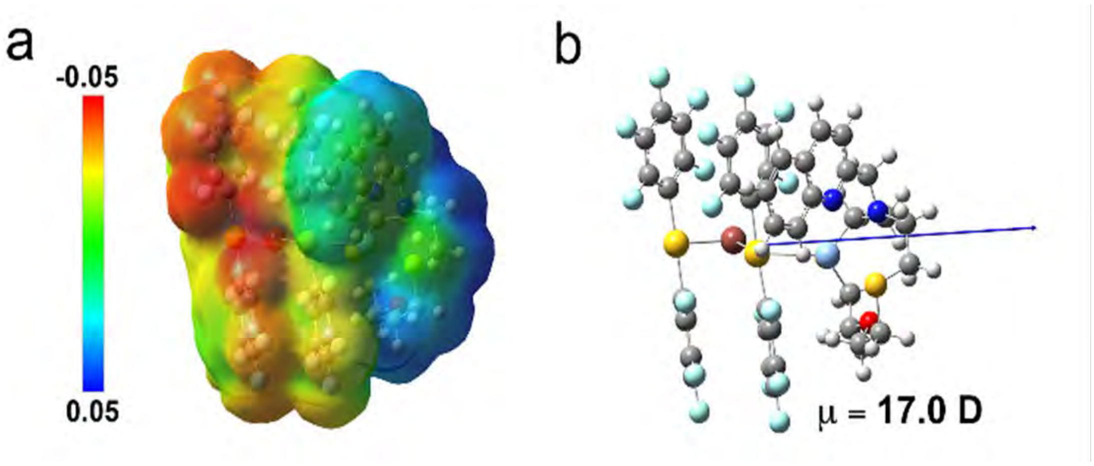

Figure 59. Electron density (MP2 density, isoval = 0.004) mapped with the electrostatic potential (ESP) for model **34a** (a) and dipole moment vector and value for **3a** (b).

3.5 References

[1] H. Schmidbaur, *Chem. Soc. Rev.*, **2008**, 37, 1931-1951.

[2] P. Pyykkö, Angew. *Chem.,* **2004**, 43, 4412-4456.

[3] H. Schmidbaur, W. Graf, G. Müller, Angew. Chem., **1991**, 30, 604-608.

[4] H. Schmidbaur, *Gold: Progress in Chemistry, Biochemistry and Technology*, John Wiley & Sons, Chichester ,**1999.**

[5] H. Schmidbaur, *Nature,* **2001**, 413, 31-33.

[6] H. Schmidbaur, *Gold Bull*., **1990**, 23, 11-21.

[7] T. F. Carlson, J. P. Fackler Jr., R. J. Staples, R. E. P. Winpenny, *Inorg. Chem.*, **1995**, 34, 426-432.

[8] O. Crespo, A. Laguna, E. J. Fernández, J. M. López De Luzuriaga, P. G. Jones, M. Teichert, M. Monge, P. Pyykkö, N. Runeberg, M. Schütz, H. J. Werner, *Inorg. Chem.,* **2000**, 39, 4786-4792.

[9] M. Bardaji, A. Laguna, *Eur. J. Chem*., **2003**, 1, 3069-3074.

[10] V. J. Catalano, B. L. Bennet, M. A. Malwitz, R. L. Yson, H. M. Kar, S. Muratidis, S. J. Horner, *Comments Inorg. Chem.*, **2003**, 24, 39-68.

[11] M. A. Rawashdeh-Omarya, M. A. OmarybJohn, J. P. Fackler Jr., *Inorg. Chim. Acta,* **2002**, 334, 376-384.

[12] O. Crespo, E. J. Fernandez, M. Gil, M. C. Gimeno, P. G. Jones, A. Laguna, J. M. López De Luzuriaga, M. E. Olmos, *J. Chem. Soc. Dalt. Trans*., **2002**, 0, 1319-1326.

[13] V. J. Catalano, S. J. Horner, *Inorg. Chem.*, **2003**, *42*, 8430-8438.

[14] V. J. Catalano, M. A. Malwitz, A. O. Etogo, *Inorg. Chem.*, **2004**, *43*, 5714-5724.

[15] P. Römbke, A. Schier, H. Schmidbaur, S. Cronje, H. Raubenheimer, *Inorg. Chim. Acta,* **2004**, 357, 235-242.

[16] E. J. Fernández, M. C. Gimeno, A. Laguna, J. M. López-de-Luzuriaga, M. Monge, P. Pyykkö, D. Sundholm, *J. Am. Chem. Soc*., **2000**, 122, 7287-7293.

[17] E. J. Fernández, A. Laguna, J. M. López-de-Luzuriaga, M. Montiel, M. E. Olmos, J. Pérez, R. C. Puelles, *Organometallics,* **2006**, 25, 4307-4315.

[18] E. J. Fernández, P. G. Jones, A. Laguna, J. M. López-de-Luzuriaga, M. Monge, M. E. Olmos, R. C. Puelles, *Organometallics,* **2007**, 26, 5931-5939.

[19] R. Usón, A. Laguna, *Coord. Chem. Rev.,* **1986**, 70, 1-50.

[20] R. Usón, *Pure Appl. Chem*., **1986**, 58, 647-652.

[21] R. Usón, *J. Organomet. Chem.,* **1989**, 372, 171-182.

[22] M. C. Gimeno, A. Laguna, *Trends Organomet. Chem.,* **1994**, 480, 231-238.

[23] E. J. Fernández, A. Laguna, M. E. Olmos, *Adv. Organomet. Chem.,* **2005**, 52, 77-141.

[24] E. J. Fernández, A. Laguna, M. E. Olmos, *Coord. Chem. Rev.,* **2008**, 252, 1630-1667.

[25] J. M. López De Luzuriaga, *Luminescence of Supramolecular Gold-Containing Materials in Modern supramolecular gold chemistry*, *gold-metal interactions and applications*, Wiley-VCH: Weinheim, Germany, **2008**.

[26] E. J. Fernández, J. M. López De Luzuriaga, M. Monge, M. E. Olmos, J. Pérez, A. Laguna, A. A. Mohammed, J. P. Fackler, *J. Am. Chem. Soc.*, **2003**, 125, 2022-2023.

[27] E. J. Fernández, A. Laguna, J. M. López De Luzuriaga, M. Monge, M. Montiel, M. E. Olmos, J. Pérez, *Organometallics*, **2004**, 23, 774-782.

[28] R. Usón, A. Laguna, M. Laguna, P. G. Jones, G. M. Sheldrick, *Chem. Commun.,* **1981**, 1097-1098.

[29] R. Usón, A. Laguna, M. Laguna, B. R. Manzano, P. G. Jones, G. M. Sheldrick, *J. Chem. Soc. Dalt. Trans.,* **1984**, 0, 285-292.

[30] E. J. Fernández, J. M. López-de-Luzuriaga, M. Monge, M. E. Olmos, R. C. Puelles, A. Laguna, A. A. Mohamed, J. P. Jr. Fackler, *Inorg. Chem.*, **2008**, 47, 8069-8076.

[31] S. R. Cooper, S. C. Rawle, *Bioinorganic Chemistry*, Vol 72, Springer-Verlag: Berlin, Heidelberg, **1990**.

[32] S. R. Cooper, *Acc. Chem. Res.,* **1988**, 21, 141-146.

[33] A. J. Blake, M. Schröder, *Adv. Inorg. Chem.,* **1990**, 35, 1-80.

[34] T. Adachi, M. D. Durrant, D. L. Hughes, C. J. Pickett, R. L. Richards, J. Talarmin, T. J. Yoshiba, *Chem. Commun.,* **1992**, 22, 1464-1467.

[35] C. Landgrafe, W. S. Sheldrick, *Dalt. Trans.,* **1996**, 0, 989-998.

[36] R. D. Adams, S. B. Fallon, J. L. Perrin, J. A. Queisser, J. H. Yamamoto, *Chem. Ber.,* **1996**, 129, 313-317.

[37] H.-J. Kim, J.-H. Lee, I.-H. Suh, Y. Do, *Inorg. Chem.,* **1995**, 34, 796-801.

[38] J. L. Shaw, J. Wolowska, D. Collison, J. A. K. Howard, E. J. L. McInnes, J. McMaster, A. J. Blake, C. Wilson, M. Schröder, *J. Am. Chem. Soc.,* **2006**, 128, 13827-13839.

[39] G. H. Robinson, H. Zhang, J. L. Atwood, *Organometallics,* **1987**, 6, 887-889.

[40] K. George, M. Jura, W. Levason, M. E. Light, L. P. Ollivere, G. Reid, *Inorg. Chem.,* **2012**, 51, 2231-2240.

[41] C. Gurnani, M. Jura, W. Levason, R. Ratnani, G. Reid, M. Webster, *Dalt. Trans.,* **2009**, 0, 1611-1619.

[42] A. J. Blake, D. Fenske, W.-S. Li, V. Lippolis, M. Schröder, *Dalt. Trans.,* **1998**, 0, 3961-3968.

[43] A. J. Blake, J. A. Greig, M. Schröder, *J. Chem. Soc. Dalt. Trans.,* **1991**, 0, 529-532.

[44] F. Cheng, A. L. Hector, W. Levason, G. Reid, M. Webster, W. Zhang, *Chem. Commun.,* **2008**, 1, 5508-5510.

[45] G. R. Willey, A. Jarvis, J. Palin, W. Errington, *Dalt. Trans.,* **1994**, 0, 255-258.

[46] H. J. Kuppers, K. Wieghardt, B. Nuber, J. Z. Weiss, *Anorg. Allg. Chem.,* **1989**, 577, 155-158.

[47] G. R. Willey, M. T. Lakin, M. Ravindra, N. W. Alcock, *Chem. Commun.,* **1991**, 0, 271-272.

[48] C. Sanaullah, K. Kano, R. S. Glass, G. S. Wilson, *J. Am. Chem. Soc.,* **1993**, 115, 592-598.

[49] E. Wyer, G. Giuccardo, V. Leigh, H.Muller- Bunz, M. J. Albrecht, *Organomet. Chem.,* **2011**, 696, 2882-2885.

[50] A. J. Blake, N. R. Champness, S. M. Howdle, P. E. Webb, *Inorg. Chem.,* **2000**, 39, 1035-1038.

[51] D. Parker, P. S. Roy, G. Ferguson, M. M. Hunt, *Inorg. Chim. Acta,* **1989**, 155, 227-230.

[52] W. N. Setzer, Q. Guo, G. J. Grant, J. L. Hubbard, R. S. Glass, D. G. VanDerveer, *Heteroat. Chem.,* **1990**, 1, 317-319.

[53] M. L. Helm, L. L. Hill, J. P. Lee, D. G. VanDerveer, G. J. Grant, *Dalt. Trans.,* **2006**, 0, 3534-3543.

[54] M. Wilhelm, S. Deeken, E. Berssen, W. Saak, A. Lutzen, R. Koch, H. Strasdeit, *Eur. J. Inorg. Chem.,* **2004**, 2301-2310.

[55] A. J. Blake, R. O. Gould, W. S. Li, V. Lippolis, S. Parson, C. Radek, M. Schröder, *Inorg. Chem.,* **1998**, 37, 5070-5077.

[56] A. J. Blake, W. S. Li, V. Lippolis, M. Schröder*, Chem. Commun.,* **1997**, 1, 1943-1944.

[57] A. J. Blake, W. S. Li, V. Lippolis, A. Taylor, M. Schröder, *Dalt. Trans.,* **1998**, 0, 2931-2938.

[58] H. J. Küppers, K. Wieghardt, Y.-H. Tsay, C. Krüger, B. Nuber, J. Weiss, *Angew. Chem.,* **1987**, 26, 575-577.

[59] A. J. Blake, R. Donamaría, V. Lippolis, J. M. López-de-Luzuriaga, E. Manso, M. Monge, and M. E. Olmos, *Inorg. Chem.,* **2014**, 53, 10471−10484.

[60] R. Usón, A. Laguna, M. Laguna, B. R. Manzano, P. G. Jones and G. M. Sheldrick, *J. Chem. Soc. Dalt. Trans.*, **1984**, 0, 285-289.

[61] R. Usón, A. Laguna, M. Laguna, B. R. Manzano and A. Tapia, *Inorg. Chim. Acta*, **1985**, 101, 151-156.

[62] A. J. Blake, R. Donamaría, E. J. Fernández, T. Lasanta, V. Lippolis, J. M. López-de-Luzuriaga, E. Manso, M. Monge, M. E. Olmos, *Dalt. Trans.,* **2013**, 42, 11559-11570.

[63] H. O. Davies, J. R. Dilworth, D. V. Griffiths, J. R. Miller, Y. Zheng, *Polyhedron*, **1999***,* 18, 459-467.

[64] J. B. Love, J. M. Vere, M. W. Glenny, A. J. Blake, M. Schroder, *Chem. Commun.*, **2001**, 22, 2678-2679.

[65] Y. Habata, K. Noto, F. Osaka, *Inorg. Chem.*, **2007**, 46, 6529-6534.

[66] Y. Habata, F. Osaka, *Dalt. Trans.*, **2006**, 1836-1841.

[67] M. W. Glenny, M. Lacombe, J. B. Love, A. J. Blake, L. F. Lindoy, R. C. Luckay, K. Gloe, B. Antonioli, C. Wilson, M. Schroder, *New J. Chem.*, **2006**, 30, 1755-1767.

[68] E. J. Fernández, A. Laguna, J. M. López De Luzuriaga, M. E. Olmos, R. C. Puelles, *Chem. Sci*., **2009**, 64, 1500-1512.

[69] A. Laguna, T. Lasanta, J. M. López De Luzuriaga, M. Monge, P. Naumov, M. E. Olmos, *J. Am. Chem. Soc.,* **2010**, 132, 456-457.

[70] E. J. Fernández, A. Laguna, J. M. López de Luzuriaga, F. Mendizábal, M. Monge, M. E. Olmos, J. Pérez, *Chem. Eur. J.,* **2003**, 9, 456.

[71] E. J. Fernández, A. Laguna, J. M. López De Luzuriaga, M. Monge, M. Montiel, M. E. Olmos, *Inorg. Chem.,* **2005**, 44, 1163-1165.

[72] Z. Chi, X. Zhang, B. Xu, X. Zhou, C. Ma, Y. Zhang, S. Liu, J. Xu, *Chem. Soc. Rev.,* **2012**, 41, 3878-3896.

[73] A. Pucci, G. Ruggeri, *J. Mater. Chem.,* **2011**, 21, 8282-8291.

[74] M. M. Caruso, D. A. Davis, Q. Shen, S. A. Odom, N. R. Sottos, S. R. White, J. S. Moore, *Chem. Rev.,* **2009**, 109, 5755-5798.

[75] K. Ariga, T. Mori, J. P. Hill, *Adv. Mater.*, **2012**, 24, 158-176.

[76] X. Zhang, Z. Chi, Y. Zhang, S. Liu, J. Xu, *J. Mater. Chem.,* **2013**, 1, 3376-3390.

[77] L. A. Summers, *Adv. Heterocycl. Chem.,* **1978**, 22, 1-69.

[78] P.G. Sammes, G. Yahioglu, *Chem. Soc. Rev.,* **1994**, 23, 327-334.

[79] C. R. Luman, F. N. Castellano in J.A. McCleverty, T.J. Meyer, *Comprehensive Coordination Chemistry*, vol. 1, Elsevier, Oxford, UK, **2004**.

[80] G. Hilt, E. Steckhan, *J. Chem. Soc. Chem. Commun.,* **1993**, 0, 1706-1707.

[81] Y. Lei, F. C. Anson, *J. Am. Chem. Soc.,* **1995**, 117, 9849-9854.

[82] X. H. Bu, H. Liu, M. Du, K. M.-C. Woung, V. W. W., Yam, M. Shionoya, *Inorg. Chem.,* **2001**, 40, 4143-4149.

[83] M. Munakata, L. P. Wu, T. Kuroda-Sowa, *Adv. Inorg. Chem.,* **1998**, 46, 173-303.

[84] M. Munakata, L. P. Wu, T. Kuroda-Sowa, *Bull. Chem. Soc. Jpn.,* **1997**, 70, 1727-1743.

[85] Y. Suenaga, T. Kuroda-Sowa, M. Maekawa, M. Munakata, *Dalt. Trans.,* **2000**, 0, 3620-3623.

[86] M. Maekawa, H. Konaka, Y. Suenaga, T. Kuroda-Sowa, M. Munakata, *Dalt. Trans.,* **2000**, 0, 4160-4166.

[87] Y. Suenaga, T. Kuroda-Sowa, M. Maekawa, M. Munakata, *Dalt. Trans.,* **1999**, 0, 2737-2741.

[88] K. A. Hirch, S. R. Wilson, J. S. Moore, *Inorg. Chem.,* **1997**, 36, 2960-2968.

[89] E. Schoffers, *Eur. J. Org. Chem.,* **2003**, 1145-1152.

[90] N. Toshima, Y. Shiraishi, T. Teranishi, M. Miyake, T. Tominaga, H. Watanabe, W. Brijoux, H. Bonnemann, G. Schmid, *Appl. Organomet. Chem.,* **2001**, 15, 178-196.

[91] Z. Ahmed, K. Iftikhar, *Inorg. Chim. Acta*, **2012**, 0, 165-172.

[92] C. Yang, J. Jianxin Luo, J. Ma, d. Zhu, L. Miao, Y. Zhang, L. Liang, M. Lua, *Synth. Met.,* **2012**, 162, 1097-1106.

[93] B. Yan, Y. J. Gu, *Inorg. Chem. Commun.,* **2013,** 34, 75-77.

[94] R. Starosta, U. K. Komarnicka, M. Sobczyk, M. J. Barys, *Lumin.,* **2012**, 132, 1842-1847.

[95] H. G. Zhang, X. T. Tao, K. S. Chen, C. X. Yuan, M. H. Jiang, *Synth. Met.,* **2011**, 161, 354-359.

[96] J.-F. Zhao, L. Chen, P.-J. Sun, X.-Y. Hou, X.-H. Zhao, W.-J. Li, L.-H. Xie, Y. Qian, N.-E. Shi, W.-Y. Lai, Q.-L. Fan, W. Huang, *Tetrahedron,* **2011**, 67, 1977-1982.

[97] I. J. Villar-Garcia, A. Abebe, Y. Chebude, *Inorg. Chem.Commun.,* **2012**, 19, 1-19.

[98] Q. Li, D. Sun, Y. Zhou, Q. D. Zhang Liu, J. Liu, *Inorg. Chem. Commun.,* **2012**, 20, 142-146.

[99] A. Kellett, O. Howeb, M. Connor, M. McCann, B. S. Creaven, S. McClean, A. Foltyn-ArfaKia, A. Casey, M. Devereux, *Free Radical Biol. Med.,* **2012**, 53, 564-576.

[100] Y.-J. Zheng, X. W. Li, Y. T. Li, Z. Y. Wu, C. W. Yan, *J. Photochem. Photobiol. B*, **2012**, 114, 27-37.

[101] N. Bridonneau, L. M. Chamoreau, G. Gontard, J. L. Cantin, J. Von Bardeleben, V. Marvaud, *Dalt. Trans.,* **2016**, *45*, 9412-9418.

[102] H. I. El-Subbagh, S. M. Abu-Zaid, M. A. Mahran, F. A. Badria, A. M. Al-Obaid, *J. Med. Chem.,* **2000**, *43*, 2915-2921.

[103] R. Usón, A. Laguna, M. Laguna, B. R. Manzano, P. G. Jones and G. M. Sheldrick, *J. Chem. Soc. Dalt. Trans.,* **1984**, 285-289.

[104] R. Usón, A. Laguna, M. Laguna, B. R. Manzano and A. Tapia, *Inorg. Chim. Acta*, **1985**, 101, 151-156.

[105] Xiu-Jian Wang, Liu-Cheng Gui, Qing-Ling Ni, Yan-Fang Liao, Xuan-Feng Jiang, Ling-Hua Tang, Zhong Zhang, Qiang Wu, *Cryst. Eng. Comm.,* **2008**, 10, 1003-1010.

[106] Peiju Yang, Fengjuan Cui, Xiao-Juan Yang, Biao Wu, *Cryst. Growth. Des.,* **2013**, 13, 186-193.

[107] G. De Filippo, F. Demartin, A. Garau, V. Lippolis, A. Yari, A. Shokrollahi, M. Shamsipur, *Inorg. Chim. Acta,* **2005**, 358, 801-810.

[108] L. Tei, V. Lippolis, A. J. Blake, P. A. Cooke, M. Schroder, *Chem. Commun*., **1998**, 0, 2633-2634.

[109] L. Tei, A. J. Blake, P. A. Cooke, C. Caltagirone, F. Demartin, V. Lippolis, F. Morale, C. Wilson, M. Schroder, *J. Chem. Soc. Dalt. Trans*., **2002**, 0, 1662-1670.

[110] Aragoni, M. C., Arca, M., Demartin, F., Devillanova, F. A., Isaia, F., Garau, A. et al., *Inorganic Chem.*, **2002**, 41, 6623-6632.

[111] J. R. Lakowicz, *Principles of Fluorescence Spectroscopy, Springer London*, Limited, **1986**.

[112] B. Valeur, *Molecular Fluorescence: Principles and Applications*, Wiley Online Library, **2001**.

[113] T. Lasanta, J. M. López-de-Luzuriaga, M. Monge, M. E. Olmos, D. Pascual, *Chem. Eur. J.,* **2013,** 19, 4754-4766.

[114] L. J. Larson, E. M. McMacauley, B. Weissbart, D. J. Tinti, *J. Phys. Chem.,* **1995**, 99, 7218-7226.

[115] E. J. Fernández, J. M. López De Luzuriaga, M. Monge, M. Montiel, M. E. Olmos, J. Pérez, A. Laguna, F. Mendizábal, A. A. Mohamed, J. P. Fackler, *Inorg. Chem.*, **2004**, 43, 3573-3581.

[116] F. Mohr, *Gold Chemistry: Applications and Future Directions in the Life Sciences*; Wiley-VCH: Weinheim, Germany, **2009**.

[117] J. C. Y. Lin, R. T. W. Huang, C. S. Lee, A. Bhattacharyya, W. S. Hwang, I. J. B. Lin, *Chem. Rev.,* **2009**, 109, 3561-3598.

[118] C. E. Strasser, V. J. Catalano, *J. Am. Chem. Soc.,* **2010**, 132, 10009-10011.

[119] J. M. Forward, J. P. Fackler, Assefa, Z. In *Optoelectronic Properties of Inorganic Compounds;* Roundhill, D. M., Fackler, J. P., Jr., Eds.; Plenum Press: New York, **1999**.

[120] V. W. Yam, E. Chung Chin Cheng, *Top. Curr. Chem.,* **2007**, 281, 269-309.

[121] A. A. Penney, V. V. Sizov, E. V. Grachova, D. V. Krupenya, V. V. Gurzhiy, L. Galina, Starova, G. L., S. P. Tunik, *Inorg. Chem.,* **2016**, 55, 4720-4732.

[122] D. C. Smith, H. B. Gray, Coord. Chem. Rev., **1990**, 100, 169-181.

[123] D. Li, C.-M. Che, H.-L. Kwong, V. W.-W. Yam, *Dalt. Trans.,* **1992**, 0, 3325-3329.

[124] W.-F. Fu, K.-C. Chan, K.-K. Cheung, C.-M Che, *Chem. Eur. J.,* **2001**, 7, 4656-4664.

[125] C. Ma, C. T.-L. Chan, W.-P. To, W.-M. Kwok, C.-M. Che, *Chem. Eur. J.,* **2015**, 21, 13888-13893.

[126] M. C.-L. Yeung,; Yam, V. W.-W. *Chem. Soc. Rev.,* **2015**, 44, 4192-4202.

[127] H. Yersin, *Highly Efficient OLEDs with Phosphorescent Materials*; Wiley-VCH Verlag GmbH & Co. KGaA: Weinheim, Germany, **2008**.

[128] V. W.-W. Yam, V. K.-M. Au, S. Y.-L. Leung, *Chem. Rev.,* **2015**, 115, 7589-7728.

[129] M. Baron, S. Bellemin-Laponnaz, C. Tubaro, M. Basato, S. Bogialli, A. Dolmella, *J. Inorg. Biochem*., **2014**, 141, 94-102.

[130] T. Zou, C. T. Lum, C.-N. Lok, J.-J. Zhang, C.-M. Che, *Chem. Soc. Rev.,* **2015**, 44, 8786-8801.

[131] A. J. Blake, R. Donamaría, V. Lippolis, , J. M. López De Luzuriaga, E. Manso, M. Monge, M. E. Olmos, *Inorg. Chem.,* **2014**, 53, 10471-10484.

[132] A. W. Addison, T. N. Rao, J. J. Reedijkvan Rijn, G. C. Verschoor, *Dalt. Trans.,* **1984**, 0, 1349-1356.

[133] R. Donamaría, M. C. Gimeno, V. Lippolis, J. M. López De Luzuriaga, M. Monge, M. E. Olmos, *Inorg. Chem.,* **2016**, *55*, 11299-11310.

[134] V. J. Catalano, M. A. Malwitz, *J. Am. Chem. Soc.,* **2004**, *126*, 6560-6561.

[135] E. J. Fernández, J. M. López De Luzuriaga, M. Monge, M. E. Olmos, J. Pérez, A. Laguna, A. A. Mohammed, J. P. Fackler Jr., *J. Am. Chem. Soc*., **2003**, 125, 2022-2023.

[136] J. M. López De Luzuriaga, M. Monge, M. E. Olmos, D. Pascual, T. Lasanta, *Chem. Commun.,* **2011**, 47, 6795-6797.

[137] J. M. López De Luzuriaga, M. Monge, M. E. Olmos, and D. Pascual, *Inorg. Chem.* **2014**, 53, 1275-1277.

[138] R. Echeverría, J. M. López De Luzuriaga, M. Monge and M. Elena Olmos, *Chem. Sci.*, **2015**, 6, 2022-2026.

[139] M. R. Castillo, M. M., J. M. López De Luzuriaga, M. E. Olmos, A. Laguna, F. Mendizabal, *Computational and Theoretical Chemistry,* **2011**, 965, 163-167.

[140] R. Donamaría, V. Lippolis, J M. López De Luzuriaga, M. Mongue, M. E. Olmos, *Computational and Theoretical Chemistry* **2014**, 1030, 53-58.

Experimental section

A Instrumental and spectroscopic technique used for the characterization of compounds.

A.1 Elemental analyses

The elemental analyses of carbon, hydrogen, nitrogen and sulfur of all the products described here have been carried out by using a Perkin-Elmer 240B microanalyzer. The presence of fluor in the samples is problematic for carrying out these analyses[1], which would justify some slight deviations between the calculated and experimental values.

A.2 Infrared spectra (FT-IR)

Infrared spectra were recorded in the 4000–200 cm^{-1} range on a PerkinElmer FT-IR Spectrum Two with an UATR (Single Reflection Diamond) accessory.

A.3 Nuclear magnetic resonance (NMR)

The NMR spectra of ^1H and ^{19}F have been carried out on Bruker ARX-300 or ARX-400 spectrometers, using $CDCl_{3,}$ DMSO-D^6 or THF-D^8 as solvent, and with external references $SiMe_4$ for ^1H , CCl_3F for ^{19}F.

A.4 Mass Spectra

The mass spectra were performed on an Bruker Microflex MALDI-TOF (MALDI: Matrix-Assisted Laser Desorption / Ionization, TOF: Time of Flight), using this ionization a nitrogen laser with an energy of 337nm. The matrices DIT or DCTB have been used.

A.5 Conductivity measurements

The conductivity measurements were made using a Jenway 4010 digital equipment with solutions in acetone 2×10^{-5} M.

A.6 X-ray diffraction

A.6.1 X-ray diffraction of single crystal.

The data collection of single crystals of the compounds presented in this report has been carried out in a Nonius Kappa CCD diffraction device or in a Bruker APEX-II CCD diffractometer with a low temperature controller Oxford Instruments. The resolution of the structures has been carried out with the program SHELX97[2] integrated in the WinGX package, while the Mercury and Olex2 programs have been used for its presentation. Monochromatic molybdenum radiation (Mo Kα) with a wavelength of 0.71073 Å was used for all the compounds. In section 4 of the experimental part there are tables containing the main distances and angles of each compound and the most important data of the structural determination of the compounds. Below are the equations for calculating the parameters that give an idea of the goodness of the models:

$$R_{int} = \sum\left|F_0^2 - \overline{F_0^2}\right| / [F_0^2] \qquad R(F) = \sum\left||F_0| - |F_c|\right| / \sum|F_0|$$

$$wR(F^2) = \{\sum w[(F_0^2 - F_c^2)^2] / \sum[w(F_0^2)^2]\}^{1/2}; \quad w^{-1} = \sigma^2(F_0^2) + (aP)^2 + bP, \text{ where}$$

$$P = [F_0^2 + 2F_c^2]/3 \;\; a\ and\ b\ are\ constants\ adjusted\ by\ the\ program$$

$$GooF = S = \{\sum[w(F_0^2 - F_c^2)^2]/(n-p)\}^{1/2};$$
$$(n = number\ of\ data, = number\ of\ parameters)$$

A.7 X ray powder diffraction.

The pattern of X-ray powder diffraction at room temperature are obtained using an X-ray powder diffractometer Bruker-AXS D8 Advanced Bragg-Bretano, equipped with a graphite single crystal monochromator and a scintillating counter or a rotating anode generator Rigaku RU 300 or D/MAX 2500, with CuK$_\alpha$ radiation operating at 40 kV and 80 mA. The pattern of X-ray powder diffraction is measured in a range of 2Ɵ from 5 ° to 60 ° with a variation of 0.03 °

A.8 UV-Vis spectra.

The UV-Vis absorption spectra were made with a Hewlett Packard 8453 Diode Array spectrophotometer. To carry out the measurements THF have been used as solvent.

A.9 Luminescence spectra. Determination of emission life times.

The steady state luminescence measurements were recorded with a Jobin-Yvon Horiba Fluorolog 3-22 Tau3 flowmeter spectrum. For measurements at 77 K, an Oxford Optistat DN cryostat with an accessory for solid samples was used. The data adjustment was made using the Jobin-Yvon software and the Origin 8.0 program. In the measurements of life times with the Single Photon Counting technique, Datastation HUB, nanoLEDs of different wavelengths and the DAS6 software were used.

B Synthesis of new compounds

B.1 Starting materials

The starting products used in this work have been acquired in Sigma-Aldrich, Fluka or Alfa-Aesar, and have been used as received. The preparation of the starting compounds has been carried out by means of the methods set out in the bibliographic references with slight modifications which are detailed in the Experimental part.

Organometallic compounds: $[Au(C_6Cl_5)_2Ag]_n$[3], $[Au(C_6F_5)_2Ag]_n$[4] $[Au(C_6Cl_5)_2Tl]_n$[5], $[Au(C_6F_5)_2Tl]_n$[6].

Organic ligands: 1-aza-4,7,10-trithiacyclododecane (L_1)[7], 1,7-dithia-4,11-diazacyclotetradecane (L_2)[8]**,** 1-aza-4,10-dithia-7-oxacyclododecane (L_3)[9], 5-aza-2,8-dithia[9](2,9)-1,10-phenanthrolinophane (L_4)[10], 1,4,7-Triazacyclononane (L_5)[11].

B.2 Synthesis of N-butoxycarbonyl-1-aza-4,7,10-trithiacyclododecane (Boc-L_1). A solution of bis(2-mercaptoethyl)thioether (2.84 g, 18.0 mol) and N-butoxycarbonyl-bis(2-chloroethyl)amine (4.47 g, 18.0 mmol) in anhydrous DMF (250 mL) was added very slowly to a vigorously stirred suspension of Cs_2CO_3 (12.01 g, 34.1 mol) in anhydrous DMF (250 mL) heated to 50 °C under N_2. After addition was completed, the solution was stirred at room temperature overnight, Cs_2CO_3 was filtered off and the solvent removed in vacuo to yield a white solid. The crude product was purified by recrystallization in hot toluene (3.54 g, 60.5 % yield). ^{1}H NMR ($CDCl_3$): δ_H 1.46 (s, 9H, $C(CH_3)_3$), 2.82 (m, 12H, CH_2-S) 3.49 (m, 4H, CH_2-N).

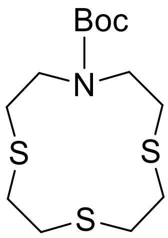

Boc-L_1

B.3 Synthesis of 1-aza-4,7,10-trithiacyclododecane (L_1). Trifluoroacetic acid (25 mL) was added to a solution of N-Boc-[12]aneNS$_3$ (2.84 g, 8.77 mmol) in CH_2Cl_2 (25 mL) and the resulting mixture stirred vigorously at room temperature under N_2 for 2 hours. The solvent was removed under reduced pressure and the residue (a pale yellow oil) taken up in water. The pH value was adjusted to 14 by adding 5 M NaOH and the product extracted into CH_2Cl_2. The organic extracts were dried over Na_2SO_4, filtered, and the solvent removed under reduced pressure to give the desired compound as a colourless solid (1.5 g, 76 % yield). ^{1}H-NMR (400 MHz, CDCl3): ^{1}H NMR (400 MHz, $CDCl_3$): δ_H 1.98 (1H, br, s, NH), 2.69-2.90 (16H, m, CH_2).

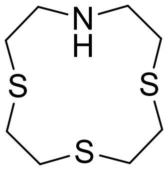

L_1

B.4 Synthesis of 4,11-Bis(tert-butoxycarbonyl)-1,7-dithia-4,11-diazacyclotetradecane (Boc-L_2). A solution of N-tert-butoxycarbonylbis(2-thioethyl)amine (1.60 g, 6.7 mmol) and N-butoxycarbonyl-bis(2-chloroethyl)amine (1.44 g, 5.9 mmol) in anhydrous DMF (250 mL) was added very slowly to a vigorously stirred suspension of Cs_2CO_3 (4.8 g, 14.6 mmol) in anhydrous DMF (250 mL) heated to 85 °C under N_2. After addition was completed, the solution was stirred at room temperature overnight, Cs_2CO_3 was filtered off and the solvent removed in vacuo to yield a white solid The crude product was purified by flash chromatography (silica) using a CH_2Cl_2:MeOH (97.5 : 2.5 V/V) mixture as eluent to give the desired compound as white solid (2.0 g, 83 % yield). ^{1}H NMR ($CDCl_3$): δ_h 1.46 (s, 9H, $C(CH_3)_3$), 3.59 (m, 8H, CH_2).

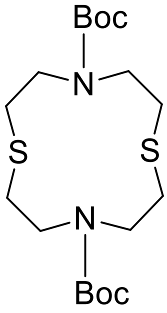

Boc-L_2

B.5 Synthesis of 1,7-dithia-4,11-diazacyclotetradecane (L_2). Trifluoroacetic acid (25 mL) was added to a solution of N-Boc-[12]aneNS$_3$ (2.84 g, 8.77 mmol) in CH_2Cl_2 (25 mL) and the resulting mixture stirred vigorously at room temperature under N_2 for 2 hours. The solvent was removed under reduced pressure and the residue (a pale yellow oil) taken up in water. The pH value was adjusted to 14 by adding 5 M NaOH and the product extracted into CH_2Cl_2. The organic extracts were dried over Na_2SO_4, filtered, and the solvent removed under reduced pressure to give the desired compound as a colourless solid (1.5 g, 76 % yield). ^{1}H-NMR (400 MHz, CDCl3): ^{1}H NMR (400 MHz, $CDCl_3$): δ_H 1.98 (1H, br, s, NH), 2.69-2.90 (16H, m, CH_2).

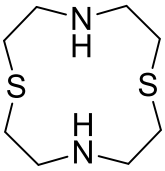

L_2

B.6 Synthesis of N-butoxycarbonyl-1-aza-4,10-dithia-7-oxacyclododecane (Boc-L_3). A solution of bis(2-mercaptoethyl)ether (2.29 g, 16.5 mmol) in anhydrous DMF (250 mL) was added very slowly to a vigorously stirred solution of N-butoxycarbonyl-bis(2-chloroethyl)amine (2 g, 16.5 mol) and Cs_2CO_3 (8.09 g, 25.0 mmol) in anhydrous DMF (500 mL) heated to 60 °C under N_2. After addition was completed, the solution was stirred at 80 C overnight, Cs_2CO_3 was filtered off and the solvent removed in vacuo to yield a yellow oil. The crude product was purified by flash chromatography (silica) using a CH_2Cl_2:MeOH (97.5 : 2.5 V/V) mixture as eluent to give the desired compound as pale yellow oil (2.67 g, 52.5% yield). ^{1}H-NMR (400 MHz, CDCl3): δ_H 1.45 (s, 9 H), 2.73–2.78 (m, 12H), 3.42–3.45 (m, 4H)

.

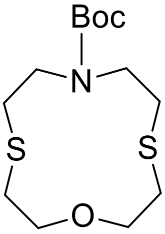

Boc-L_3

B.7 Synthesis of 1-aza-4,10-dithia-7-oxacyclododecane (L$_3$). Trifluoroacetic acid (25 mL) was added to a solution of N-Boc-[12]aneNS$_2$O (2.67 g, 8.68 mmol) in CH_2Cl_2 (25 mL) and the resulting mixture stirred vigorously at room temperature under N_2 for 2 hours. The solvent was removed under reduced pressure and the residue (a pale yellow oil) taken up in water. The pH value was adjusted to 14 by adding 5 M NaOH and the product extracted into CH_2Cl_2. The organic extracts were dried over Na_2SO_4 , filtered, and the solvent removed under reduced pressure to give the desired compound as a colourless solid (1.54 g, 86 % yield). ^{1}H-NMR (400 MHz, $CDCl_3$): δ_H 2.68–2.79 (m, 13H) 3.54 (t, J=5 Hz, 4H).

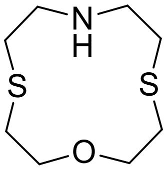

L$_3$

B.8 Synthesis of N-Boc-5-aza-2,8-dithia[9](2,9)-1,10-phenanthrolinophane (Boc-L$_4$). To a well stirred suspension of Cs_2CO_3 (1.375 g, 4.22 mmol) in DMF (50 ml) maintained at 55 °C was added under N, over 20 h a solution of 2,9-bis(chloromethyl)-1,10-phenanthroline (0.585 g, 2.11 mmol) and N-t-butoxycarbonyl-bis(3-thioethyl)amine (0.49 g, 2.11 mmol) in DMF (50 ml). The resultant mixture was stirred for 1 h at 55 °C and for 24 h at room temperature and subsequently concentrated in vacuo. The residue was extracted into CH_2Cl_2 (100 ml) and the organic extract filtered, washed with water, dried and concentrated in vacuo. The resulting deep yellow residue was purified by flash chromatography on silica gel using a mixture of CH_2Cl_2-MeOH (9.5:0.5 v/v ratio) as eluent to give the desired compound (0.52 g 55% yield) as a pale yellow product which was shown to be a single component by TLC**.** ^{1}H NMR (400 MHz, [D$_8$]tetrahydrofuran, ppm): δ 1.52 (s, 9H, CH_3), 2.67 (m, 4H, S-C*H*$_2$), 3.24 (t, 4H, N-C*H*$_2$-CH$_2$, J = 9.5 Hz), 4.08 (s, 4H, S-CH$_2$-Ar), 7.59 (d, 2H, Ar), 7.80 (s, 2H, Ar), 8.27 (d, 2H, Ar).

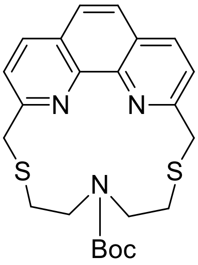

Boc-L$_4$

B.9 Synthesis of 5-aza-2,8-dithia[9](2,9)-1,10-phenanthrolinophane (L_4). N-Boc-5-aza-2,8-dithia[9](2,9)-1,10-phenanthrolinophane (0.67, 1.52 mmol) was deprotected with a mixture of TFA (60 mL) and CH_2Cl_2 (60 mL) for 2 h at room temperature. After evaporation of excess TFA and CH_2Cl_2, water was added (50 mL) and the reaction mixture was adjusted to pH 14 with NaOH. After extraction with CH_2Cl_2 (5 · 50 mL), drying over Na_2SO_4, filtering, and removal of the solvent in vacuo, [12]aneNS3 was obtained as a white solid. (0.350 g, 67 % yield). ^{1}H NMR (400 MHz, [D_8]tetrahydrofuran, ppm): δ 2.67 (m, 4H, S-C*H*$_2$), 3.24 (t, 4H, N-C*H*$_2$-CH$_2$, J = 9.5 Hz), 4.08 (s, 4H, S-CH$_2$-Ar), 7.59 (d, 2H, Ar), 7.80 (s, 2H, Ar), 8.27 (d, 2H, Ar).

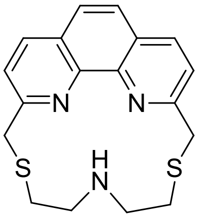

L_4

B.10 Synthesis of N-N'-N''-Tritosyl-1,4,7-triazacyclononane (Tos-L_5). To a solution of sodium N-N'-N''-tritosyl-diethylenetriamine (28 g, 45.9) in 180 mL dried DMF at 100 °C was added of ditosyl-ethylene glicol (18g 48.5 mmol) in 150 mL dried DMF for 2 hours. Then the reaction mixture was stirred for 2 hours more at 100 °C. Evaporation of the DMF at reduced pressure and recrystallization in water gave the of the compound Tos-L_5 (24.5 g, 90 % yield). ^{1}H NMR (400 MHz, $CDCl_3$) δ_H 7.65 (d, 6H, J = 8.0) 7.28 (d, 6H, J = 8.0) 3.40 (s, 12H) 2.41 (s, 9H).

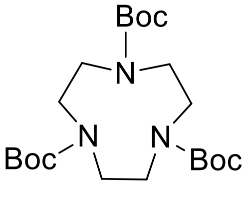

L_5

B.11 Synthesis of 1,4,7-Triazacyclononane (L_5). The solution of tritosyl-1,4,7-triazacyclononane (25.6 g 43.2 mmol) in 55 mL concentrated H_2SO_4 was heated at 95 °C for 48 hours. Then the reaction mixture was slowly poured into 300 mL of cold diethyl ether and ethanol (1 : 1) The solid was filtered and dissolved in water and pH was adjusted until 8 with 6 N KOH. Then all of the water was evaporated and the residue was dissolved in small amount of methanol. The undissolved KOH was removed by filtration. This method gave the product L_5 (3.35 g 60 %). ^{1}H NMR (200 MHz, CDCl3) 2.7 (s, 12H) 1.9 (s, 1H).

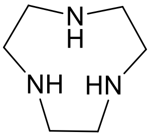

L_5

B.12 Synthesis of 5-(2-quinolinylmethyl)-5-aza-2,8-dithia[9](2,9)-1,10-phenanthrolinophane (L_6). A solution of 2-(chloromethyl)quinoline (0.104 g, 1.93 mmol) in anhydrous acetonitrile (20 mL) was added dropwise to a stirred mixture of 5-aza-2,8-dithia[9](2,9)-1,10-phenanthrolinophane (0.200 g, 0.585 mmol) and K_2CO3 (0.104 g, 1.93 mmol) in anhydrous acetonitrile (20 mL). The reaction mixture was heated at 80 °C for 24 hours under nitrogen. The solid was filtered off, and the solvent was removed under reduced pressure. The residue was dissolved in CH_2Cl_2 and washed with water. The organic phase was dried over Na_2SO_4, and the solvent removed under reduced pressure. The residue was washed with Et_2O to give a pale yellow-brown solid (0.272 g, 96% yield). ^{1}H NMR ($CDCl_3$, 400 MHz): δ_H 2.71 (4H, m, S-C*H_2*), 3.28 (4H, m, N-C*H_2*), 4.03 (2H, s, N-C*H_2*-Ar), 4.13 (4H, m, S-C*H_2*-Ar), 7.46-8.23 (12H, m, Ar).

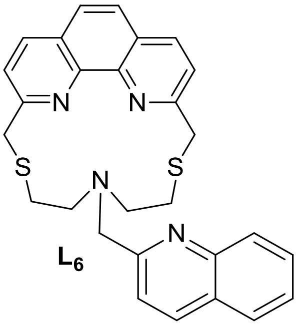

L_6

B.13 Synthesis of 1-(2-quinolinylmethyl)-1-aza-4,10-dithia-7-oxacyclododecane (L_7). A solution of 2 (chloromethyl)quinoline (0.17 g, 0.97 mmol) in anhydrous acetonitrile (20 mL) was added dropwise to a stirred mixture of 1-aza-4,10-dithia-7-oxacyclododecane ([12]aneNS2O) (0.20 g, 0.97 mmol) and K_2CO3 (0.66 g, 4.82 mmol) in anhydrous acetonitrile (20 mL). The reaction mixture was heated at 80 °C for 24 hours under nitrogen. The solid was filtered off, and the solvent was removed under reduced pressure. The residue was dissolved in CH_2Cl_2 and washed with water. The organic phase was dried over Na_2SO_4, and the solvent removed under reduced pressure. The residue was washed with Et_2O to give a pale yellow solid (0.272 g, 80% yield). ^{1}H NMR (CDCl3, 400 MHz): δ_H 2.78 (4H, m), 2.98 (8H, m), 3.82 (4H, m), 4.02 (2H, s), 7.65 (2H, m), 7.79 (1H, m), 7.88 (1H, m), 8.11 (1H, d, J = 8.4 Hz),), 8.24-8.35 (1H, m).

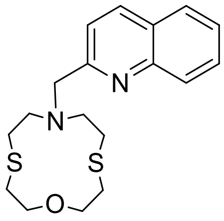

L_7

B.14 Synthesis of [{Au(C_6Cl_5)$_2$}{Tl(L_1)}$_2$][Au(C_6Cl_5)$_2$] (1). L_1 (12.2 mg, 0.055 mmol) was added to a solution of [{Au(C_6Cl_5)$_2$}Tl]$_n$ (50.0 mg, 0.055 mmol) in tetrahydrofuran. The mixture was stirred at room temperature for 3 h, and then the solvent was partially removed under reduced pressure. Finally, the addition of n-hexane led to the precipitation of product 1 as a white solid, which was filtered and washed with n-hexane (42.0 mg, 68% yield). Elemental analysis (%) calcd for $C_{20}H_{17}AuCl_{10}NS_3Tl$ (1123.43): C 21.38, H 1.53, N 1.25 S 18.19.Found: C 21.00, H 1.73, N 1.39 S 18.22. ^{1}H NMR (400 MHz, [D$_8$]tetrahydrofuran, ppm): δ 2.72 (m, 4H, N-C*H*$_2$), 2.91 (m, 12H, S-C*H*$_2$). MALDI-TOF(−) m/z (%): 695 [Au(C_6Cl_5)$_2$]$^-$ (100), 1594 [{Au(C_6Cl_5)$_2$}$_2$Tl]$^-$ (42). MALDI-TOF(+) m/z (%): 428 [Tl([12]aneNS$_3$)]$^+$ (100). ATR: ν([Au(C_6Cl_5)$_2$]$^-$) at 834 and 615 cm^{-1}. Λ_M (acetone): 110 Ω^{-1}cm^{2}mol^{-1}.

B.15 Synthesis of [{Au(C_6Cl_5)$_2$}{L_2)}$_2$][Au(C_6Cl_5)$_2$] (2). L_2 (11.4 mg, 0.055 mmol) was added to a solution of [{Au(C_6Cl_5)$_2$}Tl]$_n$ (50.0 mg, 0.055 mmol) in tetrahydrofuran. The mixture was stirred at room temperature for 3 h, and then the solvent was partially removed under reduced pressure. Finally, the addition of n-hexane led to the precipitation of product 2 as a gray solid that was filtered and washed with n-hexane (43.2 mg, 70% yield). Elemental analysis (%) calcd for $C_{20}H_{18}AuCl_{10}N_2S_2Tl$ (1106.52): C 21.71, H 1.64, N 2.53 S 5.80. Found: C 21.87, H 1.74, N 2.21 S 5.55. ^{1}H NMR (400 MHz, [D$_8$]tetrahydrofuran, ppm): δ 2.81 (m, 8H, N-C*H*$_2$), 2.98 (m, 8H, S-C*H*$_2$). MALDI-TOF(−) m/z (%): 695 [Au(C_6Cl_5)$_2$]$^-$ (100), 1594 [{Au(C_6Cl_5)$_2$}$_2$Tl]$^-$ (25). MALDI-TOF(+) m/z (%): 411 [Tl(L_2)]$^+$ (100). ATR: ν([Au(C_6Cl_5)$_2$]$^-$) at 838 and 615 cm^{-1}. Λ_M (acetone): 115 Ω^{-1}cm^{2}mol^{-1}.

B.16 Synthesis of [{Au(C_6Cl_5)$_2$}{TlL_3)}](3). L_3 (11.4 mg, 0.055 mmol) was added to a solution of [{Au(C_6Cl_5)$_2$}Tl]$_n$ (50.0 mg, 0.055 mmol) in tetrahydrofuran. The mixture was stirred at room temperature for 3 h, and then the solvent was partially removed under reduced pressure. Finally, the addition of n-hexane led to the precipitation of product 3 as a yellow solid, which was filtered and washed with n-hexane (42.0 mg, 68% yield). Elemental analysis (%) calcd for $C_{20}H_{17}AuCl_{10}NS_2OTl$ (1107.36): C 21.69, H 1.55, N 1.26 S 18.46. Found: C 21.02, H 1.53, N 1.39 S 5.79. ^{1}H-NMR (400 MHz, [D$_6$]DMSO): δ_H 2.68–2.79 (m, 12H) 3.51 (t, J=5 Hz, 4H). MALDI-TOF(−) m/z (%): 694 [Au(C_6Cl_5)$_2$]$^-$ (100), 1594 [{Au(C_6Cl_5)$_2$}$_2$Tl]$^-$ (42). MALDI-TOF(+) m/z (%): 411 [Tl(L_3)]$^+$ (10). ATR: ν([Au(C_6Cl_5)$_2$]$^-$) at 833 and 612 cm^{-1}. Λ_M (acetone): 105 Ω^{-1}cm^{2}mol^{-1}.

B.17 Synthesis of [{Au(C_6F_5)$_2$}Tl(L_1)]$_2$ (4). To a well stirred solution of [{Au(C_6F_5)$_2$}Tl]$_n$ (50 mg, 0.068 mmol) in tetrahydrofuran, L_1 (15,5 mg, 0.068 mmol) was added. After 2 h of stirring, the solution was concentrated under vacuum. Finally, the addition of n-hexane led to the precipitation of product 4 as a white solid that was filtered and washed with n-hexane (42.3 mg, 65% yield). Elemental analysis (%) calcd for $C_{20}H_{17}AuF_{10}NS_3Tl$ (958.88): C 25.05, H 1.79, N 1.46, S 10.03. Found C 25.31, H 1.88, N 1.53 S 10.33.^{1}H NMR (400 MHz, [D$_8$]tetrahydrofuran, ppm): δ 2.77 (m, 4H, N-C*H*$_2$), 2.98 (m, 12H, S-C*H*$_2$). ^{19}F NMR (400 MHz, [D$_8$]tetrahydrofuran, ppm): δ −117.1 (m, 2F, F_o), −166.0 (t, 1F, F_p, $^3J(F_p–F_m)$ = 19.3 Hz), −167.3 (m, 2F, F_m). MALDI-TOF(−) m/z (%): 531 [Au(C_6F_5)$_2$]$^-$ (100), 1267 [{Au(C_6F_5)$_2$}$_2$Tl]$^-$ (30). MALDI-TOF(+) m/z (%): 428 [Tl([12]aneNS$_3$)]$^+$ (30). ATR: ν([Au(C_6F_5)$_2$]$^-$) at 1502, 952 and 785 cm^{-1}. Λ_M (acetone): 102 Ω^{-1}cm^{2}mol^{-1}.

B.18 Synthesis of [{Au(C_6F_5)$_2$}Tl(L_2)]$_n$ (5). To a well stirred solution [{Au(C_6F_5)$_2$}Tl]$_n$ (50 mg, 0.068 mmol) in tetrahydrofuran, L_2 (14.0 mg, 0.068 mmol) was added. After 2 h of stirring, the solution was concentrated under vacuum. Finally, the addition of n-hexane led to the precipitation of product 5 as a gray solid that was filtered and washed with n-hexane (42.0 mg, 65% yield). Elemental analysis (%) calcd for $C_{20}H_{17}AuF_{10}N_2S_2Tl$ (942.01): C 25.50, H 1.93, N 2.97, S 6.81. Found C 25.35, H 2.01, N 2.90, S 6.72. ^{1}H NMR (400 MHz, [D$_8$]tetrahydrofuran, ppm): δ 2.89 (m, 8H, N-C*H*$_2$), 3.05 (m, 18H, S-C*H*$_2$). ^{19}F NMR (400 MHz, [D$_8$]tetrahydrofuran, ppm): δ −115.21 (m, 2F, F_o), −164.7 (t, 1F, F_p, $^3J(F_p–F_m)$ = 18.6 Hz), −165.3 (m, 2F, F_m). MALDI-TOF(−) m/z (%): 531 [Au(C_6F_5)$_2$]$^-$ (100), 1267 [{Au(C_6F_5)$_2$}$_2$Tl]$^-$ (10). MALDI-TOF(+) m/z (%): 411 [Tl(L_2)]$^+$ (10). ATR: ν([Au(C_6F_5)$_2$]$^-$) at 1508, 957 and 784 cm^{-1}. Λ_M (acetone): 120 Ω^{-1}cm^{2}mol^{-1}.

B.19 Synthesis of [{Au(C_6F_5)$_2$}Tl(L_3)]$_2$ (6). To a well stirred solution of [{Au(C_6F_5)$_2$}Tl]$_n$ (50 mg, 0.068 mmol) in tetrahydrofuran, L_3 (14,1 mg, 0.068 mmol) was added. After 2 h of stirring, the solution was concentrated under vacuum. Finally, the addition of n-hexane led to the precipitation of product 6 as a white solid that was filtered and washed with n-hexane (44.3 mg, 69% yield). Elemental analysis (%) calcd for $C_{20}H_{17}AuF_{10}NS_2OTl$ (942.82): C 25.48, H 1.82, N 1.49, S 6.80. Found C 25.31, H 1.88, N 1.53 S 6.12. ^{1}H NMR (400 MHz, [D$_6$]DMSO, ppm): δ_H 2.69 (m, 12H) 3.49 (t, J=5 Hz, 4H). ^{19}F NMR (400 MHz, [D$_8$]tetrahydrofuran, ppm): δ −115.1 (m, 2F, F_o), −160.8 (t, 1F, F_p, $^3J(F_p–F_m)$ = 19.3 Hz), −163.16 (m, 2F, F_m). MALDI-TOF(−) m/z (%): 531 [Au(C_6F_5)$_2$]$^-$ (100), 1267 [{Au(C_6F_5)$_2$}$_2$Tl]$^-$ (30). MALDI-TOF(+) m/z (%): 428 [Tl(L_3)]$^+$ (30). ATR: ν([Au(C_6F_5)$_2$]$^-$) at 1500, 953 and 787 cm^{-1}. Λ_M (acetone): 110 Ω^{-1}cm^{2}mol^{-1}.

B.20 Synthesis of $[\{Au(C_6Cl_5)_2\}\{TlL_4\}]$ (7). L_4 (19.0 mg, 0.055 mmol) was added to a solution of $[\{Au(C_6Cl_5)_2\}Tl]_n$ (50.0 mg, 0.055 mmol) in tetrahydrofuran. The mixture was stirred at room temperature for 2 h, and then the solvent was partially removed under reduced pressure. Finally, the addition of n-hexane led to the precipitation of product 7 as a green solid, which was filtered and washed with n-hexane (60.1 mg, 62 % yield). Elemental analysis (%) calcd for $C_{30}H_{19}AuCl_{10}N_3S_2Tl$ (1241.50): C 29.02, H 1.54, N 3.38 S 5.17. Found: C 30.02, H 1.84, N 3.68 S 5.44. ^1H NMR (400 MHz, $[D_8]$tetrahydrofuran, ppm): δ 2.43-2.74 (m, 8H, S-CH_2-CH_2-N), 4.64 (s, 4H, S-CH_2-Ar) 7.73 (d, 2H, Ar) 7.87 (s, 2H, Ar) 8.38 (d, 2H, Ar). MALDI-TOF(−) m/z (%): 695 $[Au(C_6Cl_5)_2]^-$ (100), 1594 $[\{Au(C_6Cl_5)_2\}_2Tl]^-$ (42). MALDI-TOF(+) m/z (%): 546 $[Tl(L_3)]^+$ (10). ATR: $\nu([Au(C_6Cl_5)_2]^-)$ at 830 and 615 cm^{-1}. Λ_M (acetone): 113 $\Omega^{-1}cm^2mol^{-1}$.

B.21 Synthesis of $[\{Au(C_6Cl_5)_2\}\{Tl(L_5)\}]_{2n}$ (8). [9]aneN$_3$ (7.10 mg, 0.055 mmol) was added to a solution of $[\{Au(C_6Cl_5)_2\}Tl]_n$ (50.0 mg, 0.055 mmol) in tetrahydrofuran. The mixture was stirred at room temperature for 3 h, and then the solvent was partially removed under reduced pressure. Finally, the addition of n-hexane led to the precipitation of product 8 as a grey solid, which was filtered and washed with n-hexane (35.0 mg, 61% yield). Elemental analysis (%) calcd for $C_{18}H_{15}AuCl_{10}N_3Tl$ (680.95): C 21.69, H 1.55, N 1.26 S 18.46. Found: C 21.02, H 1.53, N 1.39 S 5.79. ^1H NMR (400 MHz, $[D_8]$tetrahydrofuran, ppm): δ_H 2.80-3.03 (m, 12H, CH_2). MALDI-TOF(−) m/z (%): 694 $[Au(C_6Cl_5)_2]^-$ (100), 1594 $[\{Au(C_6Cl_5)_2\}_2Tl]^-$ (42). MALDI-TOF(+) m/z (%): 332 $[Tl(L_5)]^+$ (10). ATR: $\nu([Au(C_6Cl_5)_2]^-)$ at 837 and 617 cm^{-1}. Λ_M (acetone): 103 $\Omega^{-1}cm^2mol^{-1}$.

B.22 Synthesis of $[\{Au(C_6F_5)_2\}\{TlL_4\}]_n$ (9). L_4 (23.2 mg, 0.068 mmol) was added to a solution of $[\{Au(C_6F_5)_2\}Tl]_n$ (50.0 mg, 0.068 mmol) in tetrahydrofuran. The mixture was stirred at room temperature for 2 h, and then the solvent was partially removed under reduced pressure. Finally, the addition of n-hexane led to the precipitation of product 9 as a green solid, which was filtered and washed with n-hexane (55.1 mg, 75 % yield). Elemental analysis (%) calcd for $C_{30}H_{19}AuCl_{10}N_3S_2Tl$ (1076.95): C 33.46, H 1.78, N 3.90 S 5.95. Found: C 32.98, H 1.5, N 4.12 S 6.06. ^1H NMR (400 MHz, $[D_8]$tetrahydrofuran, ppm): δ 2.44-2.61 (m, 8H, S-CH_2-CH_2-N), 4.44 (s, 4H, S-CH_2-Ar) 7.73 (d, 2H, Ar) 7.89 (s, 2H, Ar) 8.43 (d, 2H, Ar). ^{19}F NMR (400 MHz, $[D_8]$tetrahydrofuran, ppm): δ −117.1 (m, 2F, F_o), −166.0 (t, 1F, F_p, $^3J(F_p–F_m)$ = 19.3 Hz), −167.3 (m, 2F, F_m). MALDI-TOF(−) m/z (%): 531 $[Au(C_6F_5)_2]^-$ (100). MALDI-TOF(+) m/z (%): 546 $[Tl(L_4)]^+$ (10). ATR: $\nu([Au(C_6F_5)_2]^-)$ at 1499, 950 and 780 cm^{-1}. Λ_M (acetone): 115 $\Omega^{-1}cm^2mol^{-1}$.

B.23 Synthesis of [{Au(C_6F_5)$_2$}{Tl(L_5)}] (10). To a well stirred solution of [{Au(C_6F_5)$_2$}Tl]$_n$ (50 mg, 0.068 mmol) in tetrahydrofuran, L_5 (8.78 mg, 0.068 mmol) was added. After 2 h of stirring, the solution was concentrated under vacuum. Finally, the addition of n-hexane led to the precipitation of product 10 as a white-grey solid that was filtered and washed with n-hexane (34.3 mg, 58% yield). Elemental analysis (%) calcd for $C_{18}H_{15}AuF_{10}N_3Tl$ (864.66): C 25.00, H 1.75, N 4.68. Found C 24.31, H 1.62, N 4.53. ^{1}H NMR (400 MHz, [D$_8$]tetrahydrofuran, ppm): δ_H 2.78-3.01 (m, 12H, C*H$_2$*).^{19}F NMR (400 MHz, [D$_8$]tetrahydrofuran, ppm): δ −115.36 (m, 2F, F_o), −164.1 (t, 1F, F_p, $^3J(F_p–F_m)$ = 19.3 Hz), −165.3 (m, 2F, F_m). MALDI-TOF(−) m/z (%): 531 [Au(C_6F_5)$_2$]$^-$ (100), 1267 [{Au(C_6F_5)$_2$}$_2$Tl]$^-$ (30). MALDI-TOF(+) m/z (%): 332 [Tl(L_5)]$^+$ (20). ATR: ν([Au(C_6F_5)$_2$]$^-$) at 1500, 952 and 786 cm^{-1}. Λ_M (acetone): 105 Ω^{-1}cm^{2}mol^{-1}.

B.24 Synthesis of [{Au(C_6Cl_5)$_2$}{Tl(L_6)}] (11). L_6 (20 mg, 0.041 mmol) was added to a solution of [{Au(C_6Cl_5)$_2$}Tl]$_n$ (37.2 mg, 0.041 mmol) in tetrahydrofuran. The mixture was stirred at room temperature for 2 h, and then the solvent was partially removed under reduced pressure. Finally, the addition of n-hexane led to the precipitation of product 11 as a grey solid, which was filtered and washed with n-hexane (42.0 mg, 73% yield). Elemental analysis (%) calcd for $C_{40}H_{26}AuCl_{10}N_4S_2Tl$ (1382.67): C 34.75, H 1.90, N 4.05 S 4.64. Found: C 34.02, H 1.93, N 4.39 S 4.79. ^{1}H NMR (400 MHz, [D$_6$]DMSO, ppm): δ_H 2.78 (4H, m, S-C*H$_2$*-N-C*H$_2$*), 3.16 (4H, m, N-C*H$_2$*) 3.93 (2H, s, N-C*H$_2$*-Ar), 4.06 (4H, m, S-C*H$_2$*-Ar), 7.56-8.47 (12H, m, Ar). MALDI-TOF(−) m/z (%): 694 [Au(C_6Cl_5)$_2$]$^-$ (100), 1594 [{Au(C_6Cl_5)$_2$}$_2$Tl]$^-$ (20). MALDI-TOF(+) m/z (%): 687 [Tl(L_6)]$^+$ (10). ATR: ν([Au(C_6Cl_5)$_2$]$^-$) at 832 and 621 cm^{-1}. Λ_M (acetone): 103 Ω^{-1}cm^{2}mol^{-1}.

B.25 Synthesis of [{Au(C_6Cl_5)$_2$}{Tl(L_7)}] (12). L_7 (20 mg, 0.057 mmol) was added to a solution of [{Au(C_6Cl_5)$_2$}Tl]$_n$ (51.6 mg, 0.057 mmol) in tetrahydrofuran. The mixture was stirred at room temperature for 3 h, and then the solvent was partially removed under reduced pressure. Finally, the addition of n-hexane led to the precipitation of product 12 as a yellow solid, which was filtered and washed with n-hexane (45.0 mg, 63% yield). Elemental analysis (%) calcd for $C_{30}H_{24}AuCl_{10}N_2S_2OTl$ (1248.53): C 28.86, H 1.94, N 2.24 S 5.14. Found: C 28.02, H 1.93, N 2.39 S 5.79. ^{1}H NMR (400 MHz, [D$_8$]tetrahydrofuran, ppm): δ_H 2.78 (4H, m), 2.32-3.54 (8H, m), 3.82 (4H, m), 4.02 (2H, s), 7.65 (2H, m), 7.79 (2H, m), 7.88 (2H, m), 8.11 (2H, d, J = 8.4 Hz),), 8.24-8.35 (4H, m).MALDI-TOF(−) m/z (%): 694 [Au(C_6Cl_5)$_2$]$^-$ (100), 1594 [{Au(C_6Cl_5)$_2$}$_2$Tl]$^-$ (42). MALDI-TOF(+) m/z (%): 553 [Tl(L_7)]$^+$ (10). ATR: ν([Au(C_6Cl_5)$_2$]$^-$) at 830 and 620 cm^{-1}. Λ_M (acetone): 105 Ω^{-1}cm^{2}mol^{-1}.

B.26 Synthesis of [{Au(C_6F_5)$_2$}{Tl(L_6)}] (13). To a well stirred solution of [{Au(C_6F_5)$_2$}Tl]$_n$ (30.1 mg, 0.041 mmol) in tetrahydrofuran, L_6 (20 mg, 0.041 mmol) was added. After 2 h of stirring, the solution was concentrated under vacuum. Finally, the addition of n-hexane led to the precipitation of product 13 as a brown solid that was filtered and washed with n-hexane (40.3 mg, 80% yield). Elemental analysis (%) calcd for $C_{40}H_{26}AuF_{10}N_4S_2Tl$ (1218.12): C 39.44, H 2.15, N 4.60, S 5.26. Found C 39.32, H 2.17, N 4.58, S 6.23. ^{1}H NMR (400 MHz, [D$_8$]tetrahydrofuran, ppm): δ_H 3.02 (8H, m, S-C*H$_2$*-N- C*H$_2$*), 4.03 (2H, s, N-C*H$_2$*-Ar), 4.40 (4H, m, S-C*H$_2$*-Ar), 7.52-8.42 (12H, m, Ar).^{19}F NMR (400 MHz, [D$_8$]tetrahydrofuran, ppm): δ −117.1 (m, 2F, F_o), −166.9 (t, 1F, F_p, $^3J(F_p–F_m)$ = 19.3 Hz), −167.3 (m, 2F, F_m). MALDI-TOF(−) m/z (%): 531 [Au(C_6F_5)$_2$]$^-$ (100), 1267 [{Au(C_6F_5)$_2$}$_2$Tl]$^-$ (30). MALDI-TOF(+) m/z (%): 687 [Tl(L_6)]$^+$ (100). ATR: ν([Au(C_6F_5)$_2$]$^-$) at 1501, 950 and 787 cm^{-1}. Λ_M (acetone): 103 $\Omega^{-1}cm^2mol^{-1}$.

B.27 Synthesis of [{Au(C_6F_5)$_2$Tl}{Au(C_6F_5)$_2$Tl(L_6)}]$_2$ (14). To a well stirred solution of [{Au(C_6F_5)$_2$}Tl]$_n$ (41 mg, 0.041 mmol) in tetrahydrofuran, L_7 (10 mg, 0.020 mmol) was added. After 2 h of stirring, the solution was concentrated under vacuum. Finally, the addition of n-hexane led to the precipitation of product 14 as a brown-grey solid that was filtered and washed with n-hexane (34.3 mg, 67 % yield). Elemental analysis (%) calcd for $C_{52}H_{24}Au_2F_{20}N_4S_2Tl_2$ (1952.58): C 31.99, H 1.29, N 2.87, S 3.28. Found C 31.00, H 1.62, N 2.58, S 3.23. ^{1}H NMR (400 MHz, [D$_8$]tetrahydrofuran, ppm) δ 3.00 (4H, m, S-C*H$_2$*), 3.08 (4H, m, N-C*H$_2$*), 4.06 (2H, s, N-C*H$_2$*-Ar), 4.48 (4H, m, S-C*H$_2$*-Ar), 7.55-8.45 (12H, m, Ar). ^{19}F NMR (400 MHz, [D$_8$]tetrahydrofuran, ppm): δ −117.2 (m, 2F, F_o), −165.7 (t, 1F, F_p, $^3J(F_p–F_m)$ = 19.3 Hz), −166.9 (m, 2F, F_m). MALDI-TOF(−) m/z (%): 531 [Au(C_6F_5)$_2$]$^-$ (100), 1267 [{Au(C_6F_5)$_2$}$_2$Tl]$^-$ (30). MALDI-TOF(+) m/z (%): 687 [Tl(L_6)]$^+$ (100). ATR: ν([Au(C_6F_5)$_2$]$^-$) at 1502, 942 and 787 cm^{-1}. Λ_M (acetone): 100 $\Omega^{-1}cm^2mol^{-1}$.

B.28 Synthesis of [{Au(C_6F_5)$_2$}{Tl(L_7)}] (15). To a well stirred solution of [{Au(C_6F_5)$_2$}Tl]$_n$ (41 mg, 0.057 mmol) in tetrahydrofuran, L_7 (20 mg, 0.057 mmol) was added. After 2 h of stirring, the solution was concentrated under vacuum. Finally, the addition of n-hexane led to the precipitation of product 15 as a brown solid that was filtered and washed with n-hexane (44.3 mg, 72% yield). Elemental analysis (%) calcd for $C_{30}H_{24}AuF_{10}N_2S_2OTl$ (1083.99): C 33.24, H 2.23, N 2.58, S 5.92. Found C 34.00, H 2.62, N 2.58, S 6.23. ^{1}H NMR (400 MHz, [D$_8$]tetrahydrofuran, ppm): δ_H 2.93-3.05 (12H, m, S-C*H$_2$*-N-SC*H$_2$*), 3.74 (4H, m, N-C*H$_2$*-Ar), 4.19 (2H, s, N-C*H$_2$*-Ar), 7.60 (2H, m, Ar), 7.75 (1H, m, Ar), 7.93 (1H, m, Ar), 8.16 (1H, d, J = 8.4 Hz, Ar),), 8.24-8.35 (1H, m, Ar).^{19}F NMR (400 MHz, [D$_8$]tetrahydrofuran, ppm): δ −117.1 (m, 2F, F_o), −166.9 (t, 1F, F_p, $^3J(F_p–F_m)$ = 19.3 Hz), −167.1 (m, 2F, F_m). MALDI-TOF(−)

m/z (%): 531 $[Au(C_6F_5)_2]^-$ (100), 1267 $[\{Au(C_6F_5)_2\}_2Tl]^-$ (30). MALDI-TOF(+) m/z (%): 552 $[Tl(L_7)]^+$ (100). ATR: ν($[Au(C_6F_5)_2]^-$) at 1503, 948 and 785 cm^{-1}. Λ_M (acetone): 100 Ω^{-1}cm^{2}mol^{-1}.

B.29 Synthesis of $[\{Au(C_6F_5)_2Tl\}\{Au(C_6F_5)_2Tl(L_7)\}]_n$ (16). To a well stirred solution of $[\{Au(C_6F_5)_2\}Tl]_n$ (41 mg, 0.057 mmol) in tetrahydrofuran, L_7 (10 mg, 0.028 mmol) was added. After 2 h of stirring, the solution was concentrated under vacuum. Finally, the addition of n-hexane led to the precipitation of product 16 as a brown-grey solid that was filtered and washed with n-hexane (34.3 mg, 67 % yield). Elemental analysis (%) calcd for $C_{42}H_{24}Au_2F_{20}N_2S_2OTl_2$ (1819.45): C 27.73, H 1.33, N 1.54, S 3.52. Found C 27.00, H 1.62, N 1.58, S 3.23. ^{1}H NMR (400 MHz, [D$_8$]tetrahydrofuran, ppm δ_H 2.99-3.08 (12H, m, S-CH_2-N-SCH_2), 3.75 (4H, m), 4.25 (2H, s, N-CH_2-Ar), 7.54-8.39 (6H, m, Ar). ^{19}F NMR (400 MHz, [D$_8$]tetrahydrofuran, ppm): δ −117.1 (m, 2F, F_o), −166.9 (t, 1F, F_p, $^3J(F_p–F_m)$ = 19.3 Hz), −167.1 (m, 2F, F_m). MALDI-TOF(−) m/z (%): 531 $[Au(C_6F_5)_2]^-$ (100), 1267 $[\{Au(C_6F_5)_2\}_2Tl]^-$ (30). MALDI-TOF(+) m/z (%): 552 $[Tl(L_7)]^+$ (100). ATR: ν($[Au(C_6F_5)_2]^-$) at 1503, 945 and 787 cm^{-1}. Λ_M (acetone): 100 Ω^{-1}cm^{2}mol^{-1}.

B.30 Synthesis of $[\{Au(C_6Cl_5)_2\}\{Ag(L_1)\}]$ (17). L_1 (13.8 mg, 0.062 mmol) was added to a solution of $[\{Au(C_6Cl_5)_2\}Ag]_n$ (50.0 mg, 0.062 mmol) in tetrahydrofuran. The mixture was stirred at room temperature for 2 h, and then the solvent was partially removed under reduced pressure. Finally, the addition of n-hexane led to the precipitation of product 17 as a white-grey solid, which was filtered and washed with n-hexane (48.0 mg, 75% yield). Elemental analysis (%) calcd for $C_{20}H_{17}AgAuCl_{10}NS_3$ (1026.91): C 23.39, H 1.67, N 1.36 S 9.37.Found: C 23.12, H 1.71, N 1.39 S 9.50. ^{1}H NMR (400 MHz, [D$_8$]tetrahydrofuran, ppm): δ 2.66-2.73 (m, 4H, N-CH_2), 2.80 (m, 12H, S-CH_2). MALDI-TOF(−) m/z (%): 695 $[Au(C_6Cl_5)_2]^-$ (100), 1497 $[\{Au(C_6Cl_5)_2\}_2Ag]^-$ (42). MALDI-TOF(+) m/z (%): 331 $[Ag(L_1)]^+$ (100). ATR: ν($[Au(C_6Cl_5)_2]^-$) at 836 and 614 cm^{-1}. Λ_M (acetone): 105 Ω^{-1}cm^{2}mol^{-1}.

B.31 Synthesis of $[\{Au(C_6Cl_5)_2\}\{Ag(L_2)\}]$ (18). L_2 (12,8 mg, 0.062 mmol) was added to a suspension of $[\{Au(C_6Cl_5)_2\}Ag]_n$ 50 mg, 0.062 mmol) in tetrahydrofurane. After 2 h of stirring, the solution was concentrated under vacuum. Finally, the addition of n-hexane led to the precipitation of product 18 as a pink-white solid that was filtered and washed with n-hexane (47.8 mg, 76% yield). Elemental analysis (%) calcd for $C_{20}H_{18}AgAuCl_{10}N_2S_2$ (1009.86): C 23.79, H 1.80, N 2.77, S 6.35. Found C 24.01, H 1.90, N 2.90, S 6.25. ^{1}H NMR (400 MHz, [D$_8$]tetrahydrofuran, ppm): δ 2.62-265 (m, 8H ,CH_2N,), 2.68-2.70 (m, 8H, CH_2S). MALDI-TOF(−) m/z (%): 695 $[Au(C_6Cl_5)_2]^-$ (100), 1498 $[Ag\{Au(C_6Cl_5)_2\}_2]^-$ (10). MALDI-TOF(+) m/z (%): 312 $[Ag(L_2)]^+$ (100). ATR: ν($[Au(C_6F_5)_2]^-$) at 836 and 617 cm^{-1}.

B.32 Synthesis of $[\{Au(C_6Cl_5)_2\}\{Ag(L_3)\}]$ (19). L_3 (12.1 mg, 0.062 mmol) was added to a solution of $[\{Au(C_6Cl_5)_2\}Ag]_n$ (50.0 mg, 0.062 mmol) in tetrahydrofuran. The mixture was stirred at room temperature for 2 h, and then the solvent was partially removed under reduced pressure. Finally, the addition of n-hexane led to the precipitation of product 19 as a white solid, which was filtered and washed with n-hexane (48.0 mg, 77% yield). Elemental analysis (%) calcd for $C_{20}H_{17}AgAuCl_{10}NS_2O$ (1010.84): C 23.76, H 1.70, N 1.39 S 6.34.Found: C 23.12, H 1.73, N 1.44 S 6.50. ^1H NMR (400 MHz, $[D_6]$DMF, ppm): δ 2.75-2.92 (m, 12H, N-CH_2,S-CH_2), 3.58 (m, 4H, O-CH_2). MALDI-TOF(−) m/z (%): 695 $[Au(C_6Cl_5)_2]^-$ (100), 1497 $[\{Au(C_6Cl_5)_2\}_2Ag]^-$ (42). MALDI-TOF(+) m/z (%): 313 $[Ag(L_3)]^+$ (100). ATR: ν($[Au(C_6Cl_5)_2]^-$) at 836 and 614 cm^{-1}. Λ_M (acetone): 105 $\Omega^{-1}cm^2\,mol^{-1}$.

B.33 Synthesis of $[\{Au(C_6Cl_5)_2\}\{Ag(L_3)\}]_2$ (20). L_3 (12.1 mg, 0.062 mmol) was added to a solution of $[\{Au(C_6Cl_5)_2\}Ag]_n$ (50.0 mg, 0.062 mmol) in tetrahydrofuran. The mixture was stirred at reflux for 2 h and 24h at room temperature, then the solvent was partially removed under reduced pressure. Finally, the addition of n-hexane led to the precipitation of product 20 as a grey solid, which was filtered and washed with n-hexane (38.0 mg, 61% yield). Elemental analysis (%) calcd for $C_{20}H_{17}AgAuCl_{10}NS_2O$ (1010.84): C 23.76, H 1.70, N 1.39 S 6.34.Found: C 23.12, H 1.73, N 1.44 S 6.50. ^1H NMR (400 MHz, $[D_6]$DMF, ppm): δ 2.73-2.90 (m, 12H, N-CH_2,S- CH_2), 3.58 (m, 4H, O-CH_2). MALDI-TOF(−) m/z (%): 695 $[Au(C_6Cl_5)_2]^-$ (100), 1497 $[\{Au(C_6Cl_5)_2\}_2Ag]^-$ (42). MALDI-TOF(+) m/z (%): 313 $[Ag(L_3)]^+$ (100). ATR: ν($[Au(C_6Cl_5)_2]^-$) at 837 and 615 cm^{-1}. Λ_M (acetone): 107 $\Omega^{-1}cm^2\,mol^{-1}$.

B.34 Synthesis of $[\{Au(C_6F_5)_2\}\{AgL_1\}]_2$ (21). L_1 (17,9 mg, 0.078 mmol) was added to a suspension of $[\{Au(C_6F_5)_2\}Ag]_n$ 50 mg, 0.078 mmol) in tetrahydrofurane. After 2 h of stirring, the solution was concentrated under vacuum. Finally, the addition of n-hexane led to the precipitation of product 21 as a white solid that was filtered and washed with n-hexane (42.3 mg, 62% yield). Elemental analysis (%) calcd for $C_{20}H_{17}AgAuF_{10}NS_3$ (862.37): C 27.86, H 1.99, N 1.62, S 11.15. Found C 27.79, H 2.21, N 1.42, S 11.10. ^1H NMR (400 MHz, $[D_8]$tetrahydrofuran, ppm): δ 2.69-2.73 (m, 4H ,CH_2N, $^3J_{(H-H)}$ = 5,2 Hz), 2.75-2.78 (m, 12H, S-CH_2-CH_2-S-CH_2, $^3J_{(H-H)}$ = 5,2 Hz). ^{19}F NMR (400 MHz, $[D_8]$tetrahydrofuran, ppm): δ −166.8 (m, 2F, $F_{m,}$), −163.8 (t, 1F, F_p, $^3J(F_p–F_m)$ = 20.3 Hz), −116.0 (m, 2F, F_0). MALDI-TOF(−) m/z (%): 531 $[Au(C_6F_5)_2]^-$ (80), 1168 $[Ag\{Au(C_6F_5)_2\}_2]^-$ (100). MALDI-TOF(+) m/z (%): 331 $[Ag(L_1)]^+$ (100). ATR: ν($[Au(C_6F_5)_2]^-$) at 1502, 952 and 785 cm^{-1}.

B.35 Synthesis of [{Au(C_6F_5)$_2$}{AgL_2}] (22). L_2 (16,1 mg, 0.078 mmol) was added to a suspension of [{Au(C_6F_5)$_2$}Ag]$_n$ 50 mg, 0.078 mmol) in tetrahydrofurane. After 2 h of stirring, the solution was concentrated under vacuum. Finally, the addition of n-hexane led to the precipitation of product 22 as a white solid that was filtered and washed with n-hexane (47.3 mg, 71% yield). Elemental analysis (%) calcd for $C_{20}H_{18}AgAuF_{10}N_2S_2$ (845.32): C 28.42, H 2.15, N 3.31, S 7.59. Found C 28.92, H 2.41, N 3.15, S 7.25. ^{1}H NMR (400 MHz, [D$_8$]tetrahydrofuran, ppm): δ 2.62-265 (m, 8H ,$CH_2N_,$), 2.68-2.70 (m, 8H, CH_2S). ^{19}F NMR (400 MHz, [D$_8$]tetrahydrofuran, ppm): δ −165.3 (m, 2F, F_m) −164.7 (t, 1F, F_p, $^3J(F_p–F_m)$ = 19.3 Hz) −117.1 (m, 2F, F_o). MALDI-TOF(−) m/z (%): 531 [Au(C_6F_5)$_2$]$^-$ (80), 1168 [Ag{Au(C_6F_5)$_2$}$_2$]$^-$ (100). MALDI-TOF(+) m/z (%): 312 [Ag(L_2)]$^+$ (100). ATR: ν([Au(C_6F_5)$_2$]$^-$) at 1503, 950 and 787 cm^{-1}.

B.36 Synthesis of [{Au(C_6F_5)$_2$}{Ag(L_3)}] (23). L_3 (16,1 mg, 0.078 mmol) was added to a suspension of [{Au(C_6F_5)$_2$}Ag]$_n$ 50 mg, 0.078 mmol) in tetrahydrofurane. After 2 h of stirring, the solution was concentrated under vacuum. Finally, the addition of n-hexane led to the precipitation of product 23 as a white solid that was filtered and washed with n-hexane (32.3 mg, 48% yield). Elemental analysis (%) calcd for $C_{20}H_{17}AgAuF_{10}NS_2O$ (846.30): C 28.38, H 2.02, N 1.66, S 7.58. Found C 28.32, H 2.21, N 1.52, S 7.58. ^{1}H NMR (400 MHz, [D$_8$]tetrahydrofuran, ppm^{1}H NMR (400 MHz, [D$_6$]DMF, ppm): δ 2.72-2.90 (m, 4H, N-C$H_{2,}$S-CH_2) 3.58 (m, 4H, O-CH_2). ^{19}F NMR (400 MHz, [D$_8$]tetrahydrofuran, ppm): δ −114.2 (m, 2F, $F_{m,}$), −159.8 (t, 1F, F_p, $^3J(F_p–F_m)$ = 20.3 Hz), −163.1 (m, 2F, F_0). MALDI-TOF(−) m/z (%): 531 [Au(C_6F_5)$_2$]$^-$ (100), 1168 [Ag{Au(C_6F_5)$_2$}$_2$]$^-$ (20). MALDI-TOF(+) m/z (%): 313 [Ag(L_3)]$^+$ (100). ATR: ν([Au(C_6F_5)$_2$]$^-$) at 1505, 958 and 788 cm^{-1}.

B.37 Synthesis of [{Au(C_6Cl_5)$_2$}{AgL_4}] (24). L_4 (21.3 mg, 0.062 mmol) was added to a solution of [{Au(C_6Cl_5)$_2$}Ag]$_n$ (50.0 mg, 0.062 mmol) in tetrahydrofuran. The mixture was stirred at room temperature for 2 h, and then the solvent was partially removed under reduced pressure. Finally, the addition of n-hexane led to the precipitation of product 24 as a white solid, which was filtered and washed with n-hexane (55.0 mg, 77 % yield). Elemental analysis (%) calcd for $C_{30}H_{19}AgAuCl_{10}N_3S_2$ (1123.43): C 31.47, H 1.67, N 3.67 S 5.60.Found: C 31.21, H 1.MN63, N 3.53 S 5.22. ^{1}H NMR (400 MHz, [D$_8$]tetrahydrofuran, ppm): δ 2.51-2.64 (m, 8H, S-CH_2-CH_2-N), 4.48 (s, 4H, S-CH_2-Ar) 7.64 (d, 2H, Ar) 7.90 (s, 2H, Ar) 8.36 (d, 2H, Ar). MALDI-TOF(−) m/z (%): 695 [Au(C_6Cl_5)$_2$]$^-$ (100), 1498 [{Au(C_6Cl_5)$_2$}$_2$Ag]$^-$ (10). MALDI-TOF(+) m/z (%): 448 [Ag(L_4)]$^+$ (100). ATR: ν([Au(C_6Cl_5)$_2$]$^-$) at 834 and 611 cm^{-1}. Λ_M (acetone): 110 Ω^{-1}cm^{2}mol^{-1}.

B.38 Synthesis of [{$Au(C_6Cl_5)_2$}{$Ag(L_5)$}] (25). L_5 (8.0 mg, 0.062 mmol) was added to a solution of [{$Au(C_6Cl_5)_2$}Ag]$_n$ (50.0 mg, 0.062 mmol) in tetrahydrofuran. The mixture was stirred at room temperature for 2 h, and then the solvent was partially removed under reduced pressure. Finally, the addition of n-hexane led to the precipitation of product 25 as a brown solid, which was filtered and washed with n-hexane (48.0 mg, 82% yield). Elemental analysis (%) calcd for $C_{16}H_{15}AgAuCl_{10}N_3$ (932.69): C 23.18, H 1.62, N 4.51. Found: C 24.18, H 1.72, N 4.42. ^{1}H NMR (400 MHz, [D_8]$CDCl_3$, ppm): 2.67-2.91 (m, 12H, C*H*$_2$). MALDI-TOF(−) m/z (%): 695 [$Au(C_6Cl_5)_2$]$^-$ (80), 1497 [{$Au(C_6Cl_5)_2$}$_2$Ag]$^-$ (100). MALDI-TOF(+) m/z (%): 242 [$Ag(L_5)$]$^+$ (100). ATR: ν([$Au(C_6Cl_5)_2$]$^-$) at 836 and 614 cm^{-1}. Λ_M (acetone): 105 Ω^{-1}cm^2 mol^{-1}.

B.39 Synthesis of [{$Au(C_6F_5)_2$}{AgL_4}$_2$][$Au(C_6F_5)_2$] (26). L_4 (26.8 mg, 0.068 mmol) was added to a solution of [{$Au(C_6F_5)_2$}Ag]$_n$ (50.0 mg, 0.068 mmol) in tetrahydrofuran. The mixture was stirred at room temperature for 2 h, and then the solvent was partially removed under reduced pressure. Finally, the addition of n-hexane led to the precipitation of product 26 as a yellow solid, which was filtered and washed with n-hexane (60.1 mg, 82 % yield). Elemental analysis (%) calcd for $C_{30}H_{19}AgAuF_{10}N_3S_2$ (978.95): C 36.75, H 1.95, N 4.29 S 6.54.Found: C 36,22 H 1.82, N 4.39 S 6.54. ^{1}H NMR (400 MHz, [D_8]tetrahydrofuran, ppm): δ 2.51-2.64 (m, 8H, S-C*H*$_2$-C*H*$_2$-N), 4.44 (s, 4H, S-CH_2-Ar) 7.71 (d, 2H, Ar) 7.93 (s, 2H, Ar) 8.42 (d, 2H, Ar). ^{19}F NMR (400 MHz, [D_8]tetrahydrofuran, ppm): δ −117.1 (m, 2F, F_o), −166.0 (t, 1F, F_p, $^3J(F_p{-}F_m)$ = 19.3 Hz), −167.3 (m, 2F, F_m). MALDI-TOF(−) m/z (%): 531 [$Au(C_6F_5)_2$]$^-$ (100), 1169 [{$Au(C_6F_5)_2$}$_2$Ag]$^-$ (42). MALDI-TOF(+) m/z (%): 447 [$Ag(L_4)$]$^+$(100). ATR: ν([$Au(C_6F_5)_2$]$^-$) at 1499, 950 and 780 cm^{-1}. Λ_M (acetone): 105 Ω^{-1}cm^{2}mol^{-1}.

B.40 Synthesis of [{$Au(C_6F_5)_2$}{$Ag(L_5)$}$_2$$Au(C_6F_5)_2$] (27). L_5 (10,1 mg, 0.078 mmol) was added to a suspension of [{$Au(C_6F_5)_2$}Ag]$_n$ 50 mg, 0.078 mmol) in tetrahydrofurane. After 2 h of stirring, the solution was concentrated under vacuum. Finally, the addition of n-hexane led to the precipitation of product 27 as a white solid that was filtered and washed with n-hexane (32.3 mg, 48% yield). Elemental analysis (%) calcd for $C_{18}H_{15}AgAuF_{10}N_3$ (768.15): C 28.14, H 1.97, N 5.47. Found C 28.32, H 2.21, N 5.52. ^{1}H NMR (400 MHz, [D]$CDCl_3$, ppm): δ_H 2.67-2.80 (m, 12H, C*H*$_2$). ^{19}F NMR (400 MHz, [D_8]tetrahydrofuran, ppm): δ −164.5 (m, 2F, $F_{m,}$), −159.6 (t, 1F, F_p, $^3J(F_p{-}F_m)$ = 20.3 Hz), −113.7 (m, 2F, F_0). MALDI-TOF(−) m/z (%): 531 [$Au(C_6F_5)_2$]$^-$ (100), 1168 [Ag{$Au(C_6F_5)_2$}$_2$]$^-$ (20). MALDI-TOF(+) m/z (%): 313 [$Ag(L_5)$]$^+$ (100). ATR: ν([$Au(C_6F_5)_2$]$^-$) at 1505, 958 and 788 cm^{-1}.

B.41 Synthesis of [{Au(C_6Cl_5)$_2$}{Ag(L_6)}] (28). L_2 (10.0 mg, 0.041 mmol) was added to a solution of [{Au(C_6Cl_5)$_2$}Ag]$_n$ (32.9 mg, 0.041 mmol) in tetrahydrofuran. The mixture was stirred at room temperature for 2 h, and then the solvent was partially removed under reduced pressure. Finally, the addition of n-hexane led to the precipitation of product 28 as a brown solid, which was filtered and washed with n-hexane (30.0 mg, 69 % yield). Elemental analysis (%) calcd for $C_{40}H_{26}AgAuCl_{10}N_4S_2$ (1152.52): C 37.35, H 2.04, N 4.36, S 4.98. Found: C 37.18, H 2.12, N 4.42 S 4.71. ^{1}H NMR (400 MHz, [D$_6$]DMSO, ppm): δ_H 2.75 (4H, m, S-C*H$_2$*-N-C*H$_2$*), 3.15 (4H, m, N-C*H$_2$*) 3.95 (2H, s, N-C*H$_2$*-Ar), 4.05 (4H, m, S-C*H$_2$*-Ar), 7.55-8.47 (12H, m, Ar). MALDI-TOF(−) m/z (%): 695 [Au(C_6Cl_5)$_2$]$^-$ (80), 1497 [{Au(C_6Cl_5)$_2$}$_2$Ag]$^-$ (100). MALDI-TOF(+) m/z (%): 588 [Ag(L_6)]$^+$ (100). ATR: ν([Au(C_6Cl_5)$_2$]$^-$) at 835 and 612 cm^{-1}. Λ_M (acetone): 105 Ω^{-1}cm^2 mol^{-1}.

B.42 Synthesis of [{Au(C_6Cl_5)$_2$}{Ag(L_7)}] (29). L_2 (20.0 mg, 0.057 mmol) was added to a solution of [{Au(C_6Cl_5)$_2$}Ag]$_n$ (45.8 mg, 0.057 mmol) in tetrahydrofuran. The mixture was stirred at room temperature for 2 h, and then the solvent was partially removed under reduced pressure. Finally, the addition of n-hexane led to the precipitation of product 29 as a brown solid, which was filtered and washed with n-hexane (48.0 mg, 72% yield). Elemental analysis (%) calcd for $C_{30}H_{24}AgAuCl_{10}N_2OS_2$ (1152.52): C 31.28, H 2.10, N 2.43, S 5.57. Found: C 32.18, H 2.12, N 2.42 S 5.71. ^{1}H NMR (400 MHz, [D$_8$]tetrahydrofuran, ppm):): δ 2.75-2.93 (m, 12H, C*H$_2$*) 3.39 (m, 2H, C*H$_2$*) 3.83 (m, 2H, C*H$_2$*) 4.04 (s, 2H, N- C*H$_2$*-Ar) 7.36 (d, 1H, Ar, 8.3 Hz) 7.61 (d, 1H, Ar, 7.5 Hz) 7.83 (d, 2H, Ar, 7.5 Hz) 8.31 (d, 1H, Ar, 8.5 Hz) 8.66 (d, 1H, Ar, 9.2 Hz). MALDI-TOF(−) m/z (%): 695 [Au(C_6Cl_5)$_2$]$^-$ (80), 1497 [{Au(C_6Cl_5)$_2$}$_2$Ag]$^-$ (100). MALDI-TOF(+) m/z (%): 454 [Ag(L_7)]$^+$ (100). ATR: ν([Au(C_6Cl_5)$_2$]$^-$) at 835 and 612 cm^{-1}. Λ_M (acetone): 103 Ω^{-1}cm^2 mol^{-1}.

B.43 Synthesis of [{Au(C_6F_5)$_2$}{AgL_6}$_2$][Au(C_6F_5)$_2$] (30). L_1 (20 mg, 0.041 mmol) was added to a solution of [{Au(C_6F_5)$_2$}Ag]$_n$ (26.7 mg, 0.041 mmol) in tetrahydrofuran. The mixture was stirred at room temperature for 2 h, and then the solvent was partially removed under reduced pressure. Finally, the addition of n-hexane led to the precipitation of product 30 as a brown solid, which was filtered and washed with n-hexane (33.1 mg, 71 % yield). Elemental analysis (%) calcd for $C_{40}H_{26}AgAuF_{10}N_4S_2$ (1121.61): C 42.83, H 2.34, N 5.00 S 5.72. Found: C 42,01 H 2.55, N 5.90 S 5.23. ^{1}H NMR ($CDCl_3$, 400 MHz): δ_H 2.68 (4H, m, S-C*H$_2$*), 2.89 (4H, m, N-C*H$_2$*), 3.37 (2H, s, N-C*H$_2$*-Ar), 4.44 (4H, m, S-C*H$_2$*-Ar), 7.40-8.45 (12H, m, Ar). ^{19}F NMR (400 MHz, [D$_8$]tetrahydrofuran, ppm): δ −116.9 (m, 2F, F_o), −165.7 (t, 1F, F_p, $^3J(F_p–F_m)$ = 19.3 Hz), −167.0 (m, 2F, F_m). MALDI-TOF(−) m/z (%): 530

$[Au(C_6F_5)_2]^-$ (100) 1168 $[Ag\{Au(C_6F_5)_2\}_2]^-$ (20). MALDI-TOF(+) m/z (%): 588 $[Ag(L_6)]^+$(100). ATR: ν($[Au(C_6F_5)_2]^-$) at 1505, 950 and 780 cm^{-1}**.** Λ_M (acetone): 100 Ω^{-1}cm^{2}mol^{-1}.

B.44 Synthesis of [{Au(C$_6$F$_5$)$_2$}$_2${Ag$_2$L$_6$}] (31). L_1 (20 mg, 0.041 mmol) was added to a solution of $[\{Au(C_6F_5)_2\}Ag]_n$ (73.4 mg, 0.082 mmol) in tetrahydrofuran. The mixture was stirred at room temperature for 2 h, and then the solvent was partially removed under reduced pressure. Finally, the addition of n-hexane led to the precipitation of product 31 as a yellow solid, which was filtered and washed with n-hexane (63.1 mg, 67 % yield). Elemental analysis (%) calcd for $C_{52}H_{26}Ag_2Au_2F_{20}N_4S_2$ (1760.56): C 35.47, H 1.49, N 3.18 S 3.64. Found: C 35,01 H 1.55, N 3.90 S 3.71. ^{1}H NMR (CDCl$_3$, 400 MHz): δ_H 2.63 (4H, m, S-C*H$_2$*), 2.91 (4H, m, N-C*H$_2$*), 3.34 (2H, s, N-C*H$_2$*-Ar), 4.42 (4H, m, S-C*H$_2$*-Ar), 7.41-8.47 (12H, m, Ar). ^{19}F NMR (400 MHz, [D$_8$]tetrahydrofuran, ppm): δ −115.9 (m, 2F, F_o), −165.9 (t, 1F, F_p, $^3J(F_p–F_m)$ = 19.3 Hz), −167.3 (m, 2F, F_m). MALDI-TOF(−) m/z (%): 530 $[Au(C_6F_5)_2]^-$ (100), 1168 $[Ag\{Au(C_6F_5)_2\}_2]^-$ (20). MALDI-TOF(+) m/z (%): 589 $[Ag(L_6)]^+$(100). ATR: ν($[Au(C_6F_5)_2]^-$) at 1502, 951 and 781 cm^{-1}**. .** Λ_M (acetone): 105 Ω^{-1}cm^{2}mol^{-1}.

B.45 Synthesis of [{Au(C$_6$F$_5$)$_2$}{AgL$_7$}]$_2$ (32). L_7 (20 mg, 0.057 mmol) was added to a solution of $[\{Au(C_6F_5)_2\}Ag]_n$ (36.7 mg, 0.057 mmol) in tetrahydrofuran. The mixture was stirred at room temperature for 2 h, and then the solvent was partially removed under reduced pressure. Finally, the addition of n-hexane led to the precipitation of product 32 as a brown solid, which was filtered and washed with n-hexane (43.1 mg, 76 % yield). Elemental analysis (%) calcd for $C_{30}H_{24}AgAuF_{10}N_2OS_2$ (987.47): C 36.49, H 2.45, N 2.84 S 6.49. Found: C 37,01 H 2.55, N 2.90 S 6.71. ^{1}H NMR (400 MHz, [D$_8$]tetrahydrofuran, ppm): δ 2.74-3.98 (m, 12H, C*H$_2$*) 3.36 (m, 2H, C*H$_2$*) 3.85 (m, 2H, C*H$_2$*) 4.07 (s, 2H, N- C*H$_2$-Ar*) 7.36 (d, 1H, Ar, 8.3 Hz) 7.61 (d, 1H, Ar, 7.5 Hz) 7.88 (d, 2H, Ar, 7.5 Hz) 8.31 (d, 1H, Ar, 8.5 Hz) 8.63 (d, 1H, Ar, 9.2 Hz). ^{19}F NMR (400 MHz, [D$_8$]tetrahydrofuran, ppm): δ −116.2 (m, 2F, F_o), −165.0 (t, 1F, F_p, $^3J(F_p–F_m)$ = 19.3 Hz), −167.0 (m, 2F, F_m). MALDI-TOF(−) m/z (%): 530 $[Au(C_6F_5)_2]^-$ (100). MALDI-TOF(+) m/z (%): 455 $[Ag(L_7)]^+$(100). ATR: ν($[Au(C_6F_5)_2]^-$) at 1502, 952 and 782 cm^{-1}**.**

B.46 Synthesis of [{Au(C$_6$F$_5$)$_2$}$_2${Ag$_2$L$_7$}] (33). L_7 (10 mg, 0.028 mmol) was added to a solution of $[\{Au(C_6F_5)_2\}Ag]_n$ (36.7 mg, 0.057 mmol) in tetrahydrofuran. The mixture was stirred at room temperature for 2 h, and then the solvent was partially removed under reduced pressure. Finally, the addition of n-hexane led to the precipitation of product 33 as a yellow solid, which was filtered and washed with n-hexane (33.1 mg, 71 % yield). Elemental analysis (%) calcd for $C_{42}H_{24}Ag_2Au_2F_{20}N_2OS_2$ (1626.42): C 31.02, H 1.49, N 1.72 S 3.94. Found: C 31,01 H 1.55, N 1.90 S

3.71. ^{1}H NMR (400 MHz, [D$_8$]tetrahydrofuran, ppm): δ_H 2.79-3.02 (m, 12H, C*H$_2$*) 3.43 (m, 2H, C*H$_2$*) 3.85 (m, 2H, C*H$_2$*) 4.08 (s, 2H, N- C*H$_2$-Ar*) 7.61 (d, 1H, Ar, 8.3 Hz) 7.63 (d, 1H, Ar, 7.5 Hz) 7.92 (d, 2H, Ar, 7.5 Hz) 8.32 (d, 1H, Ar, 8.5 Hz) 8.65 (d, 1H, Ar, 9.2 Hz). ^{19}F NMR (400 MHz, [D$_8$]tetrahydrofuran, ppm): δ −114.3 (m, 2F, F_o), −161.5 (t, 1F, F_p, $^3J(F_p–F_m)$ = 19.3 Hz), −164.5 (m, 2F, F_m). MALDI-TOF(−) m/z (%): 530 $[Au(C_6F_5)_2]^-$ (100), 1168 $[Ag\{Au(C_6F_5)_2\}_2]^-$ (20). MALDI-TOF(+) m/z (%): 455 $[Ag(L_7)]^+$(100). ATR: ν($[Au(C_6F_5)_2]^-$) at 1503, 952 and 780 cm^{-1}**.**

B.47 Synthesis of $[\{Au(C_6F_5)_2Tl\}\{Au(C_6F_5)_2Tl\{Au(C_6F_5)_2AgL_7\}\}_2]_n$ (34). complex 1 (20 mg, 0.057 mmol) was added to a solution of $[\{Au(C_6F_5)_2\}Ag]_n$ (36.7 mg, 0.057 mmol) in tetrahydrofuran. The mixture was stirred at room temperature for 2 h. The solution was filtered off, and the solvent was partially removed under reduced pressure. Finally, the addition of n-hexane led to the precipitation of product 34 as a yellow solid, which was filtered and washed with n-hexane (43.1 mg, 76 % yield). Elemental analysis (%) calcd for $C_{96}H_{48}Ag_2Au_5F_{50}N_4O_2S_4Tl_3$ (4181.34): C 27.58, H 1.16, N 1.34, S 3.07. Found C 27.21, H 1.25, N 1.55, S 3.14. δ 2.78-3.45 (m, 12H,), 3.85-3.92 (m, 4H) 4.07 (s, 2H,) 7.45 (d, 1H, Ar, 8.4 Hz) 7.63 (d, 1H, Ar, 7.1 Hz) 7.88 (d, 2H, Ar, 7.8 Hz) 8.31 (d, 1H, Ar, 8.3 Hz) 8.65 (d, 1H, Ar, 9.1 Hz). ^{19}F NMR (400 MHz, [D$_8$]tetrahydrofuran, ppm): δ −115.0 (m, 2F, F_o), −164.2 (t, 1F, F_p, $^3J(F_p–F_m)$ = 19.3 Hz), −165.5 (m, 2F, F_m). MALDI-TOF(−) m/z (%): 530 $[Au(C_6F_5)_2]^-$(100), 1169 $[(Au(C_6F_5)_2)_2Ag]^-$ (50), 1267 $[(Au(C_6F_5)_2)_2Tl]^-$ (10). MALDI-TOF(+) m/z (%): 455 $[Ag(L_7)]^+$(100). ATR: ν($[Au(C_6F_5)_2]^-$) at 1502, 952 and 782 cm^{-1}. ATR: ν($[Au(C_6F_5)_2]^-$) at 1502, 952 and 782 cm^{-1}.

C. Crystallographic data

Table C1. Details of data collection and refinement for complex **1**.

Compound	**1**
Empirical formula	$C_{40}H_{34}Au_2Cl_{20}N_2S_6Tl_2$
Formula weight	2246.72
Temperature/K	200(2)
Crystal system	Triclinic
Space group	P-1
a/Å	8.3501(4)
b/Å	11.4734(6)
c/Å	16.7897(5)
α/°	93.835(3)
β/°	101.573(3)
γ/°	99.077(2)
Volume/Å^3	1547.99(12)
Z	1
ρ_{calc}g/cm^3	2.410
μ/mm^{-1}	11.012
F(000)	1044
Crystal size/mm^3	0.15 x 0.075 x 0.05
Radiation	MoKα (λ = 0.71073)
2Θ range for data collection/°	3.533 to 27.431
Reflections collected	24491
Independent reflections	6993 [R_{int} = 0.0598]
Data/restraints/parameters	6993/0/332
Goodness-of-fit on F^2	0.999
Final R indexes [I>=2σ (I)]	R_1 = 0.0308, wR_2 = 0.0545
Final R indexes [all data]	R_1 = 0.0526, wR_2 = 0.0596
Largest diff. peak/hole / e Å^{-3}	0.797/-0.978

Table C2. Selected bond lengths [Å] and angles [°] for **1**.

Au(1)-Tl(1)	3.2410(2)	Tl(1)-S(1)	3.0984(13)
Au(1)-C(1)	2.058(5)	Tl(1)-S(2)	3.2018(14)
Au(2)-C(11)	2.045(5)	Tl(1)-S(3)	3.0808(14)
Tl(1)-N(1)	2.724(4)		
C(1)-Au(1)-C(1)#1	180.0	Au(1)-Tl(1)-S(2)	167.17(2)
Tl(1)#1-Au(1)-Tl(1)	180.0	S(1)-Tl(1)-S(3)	109.70(3)
C(11)-Au(2)-C(11)#2	180.0		

Symmetry transformations used to generate equivalent atoms:

#1 -x+1,-y+1,-z;#2 -x+1,-y+1,-z+1

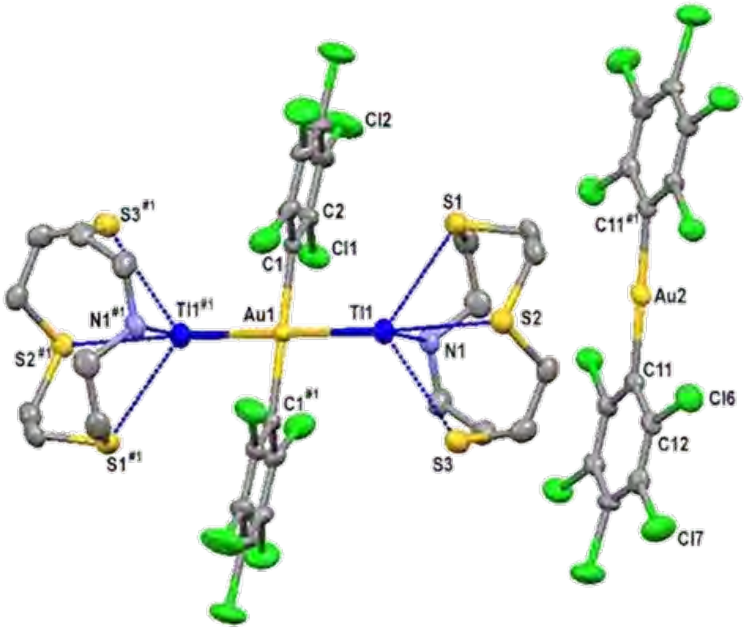

Table C3. Details of data collection and refinement for complex **2**.

Compound	**2**
Empirical formula	$C_{40}H_{52}Au_2Cl_{20}N_4S_4Tl_2 \cdot 2C_4H_8O$
Formula weight	2356.85
Temperature/K	173(2)
Crystal system	Triclinic
Space group	P -1
a/Å	9.3884(6)
b/Å	11.1159(5)
c/Å	16.9287(8)
α/°	96.203(4)
β/°	94.671(3)
γ/°	93.211(3)
Volume/Å^3	1746.76(16)
Z	1
ρ_{calc}g/cm^3	2.241
μ/mm^{-1}	9.710
F(000)	1108
Crystal size/mm^3	0.175 x 0.125 x 0.075
Radiation	MoKα (λ = 0.71073)
2Θ range for data collection/°	2.093 to 25.681
Reflections collected	25095
Independent reflections	6613 [R_{int} = 0.0677]
Data/restraints/parameters	6613/105/372
Goodness-of-fit on F^2	1.075
Final R indexes [I>=2σ (I)]	R_1 = 0.0580, wR_2 = 0.1480
Final R indexes [all data]	R_1 = 0.0827, wR_2 = 0.1610
Largest diff. peak/hole / e Å^{-3}	3.205/-2.353

Table C4. Selected bond lengths [Å] and angles [°] for **2** 2THF.

Au(1)-Tl(1)	3.3853(5)	Tl(1)-N(2)	2.710(12)
Au(1)-C(1)	2.057(10)	Tl(1)-S(1)	3.110(5)
Au(2)-C(7)	2.041(12)	Tl(1)-S(2)	3.089(5)
Tl(1)-N(1)	2.709(11)		
C(1)#1-Au(1)-C(1)	180.0	Au(1)-Tl(1)-N(2)	158.6(3)
Tl(1)#1-Au(1)-Tl(1)	180.0	S(1)-Tl(1)-S(2)	114.11(12)
C(7)#2-Au(2)-C(7)	180.0		

Symmetry transformations used to generate equivalent atoms:

#1 -x+2,-y+2,-z+1 #2 -x,-y,-z

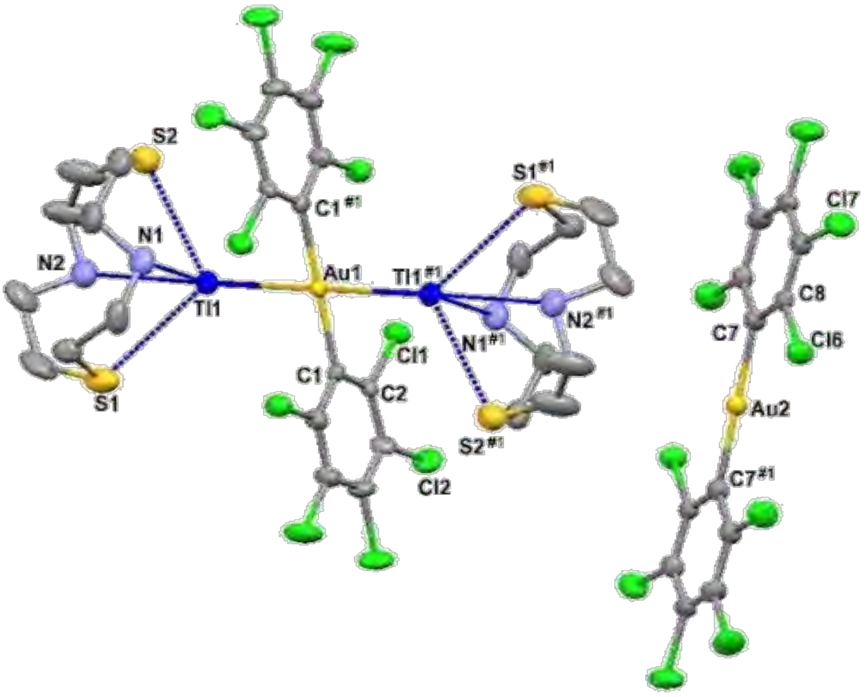

Table C5. Details of data collection and refinement for complex **3**.

Compound	**3**
Empirical formula	$C_{20}H_{17}AuCl_{10}NOS_2Tl$
Formula weight	1107.30
Temperature/K	173(2)
Crystal system	Triclinic
Space group	P -1
a/Å	10.6820(5)
b/Å	11.1902(5)
c/Å	12.6962(5)
α/°	79.002(2)
β/°	83.426(3)
γ/°	88.394(2)
Volume/Å^3	1479.93(11)
Z	2
ρ_{calc}g/cm^3	2.485
μ/mm^{-1}	11.451
F(000)	1028.0
Crystal size/mm^3	0.015 x 0.015 x 0.015
Radiation	MoKα (λ = 0.71073)
2Θ range for data collection/°	2.660 to 27.489
Reflections collected	6714
Independent reflections	6714 [R_{int} = 0.0871]
Data/restraints/parameters	6714/0/326
Goodness-of-fit on F^2	1.076
Final R indexes [I>=2σ (I)]	R_1 = 0.0408, wR_2 = 0.1110
Final R indexes [all data]	R_1 = 0.0514, wR_2 = 0.1164
Largest diff. peak/hole / e Å^{-3}	2.832/-3.197

Table C6 Selected bond lengths [Å] and angles [°] for **3**.

Au(1)-Tl(1)	3.0221(4)	Tl(1)-N(1)	2.653(6)
Au(1)-C(1)	2.056(7)	Tl(1)-S(1)	3.2128(1)
Au(1)-C(7)	2.058(7)	Tl(1)-S(2)	3.1321(19)
Tl(1)-O(1)	3.1280(1)		
C(1)-Au(1)-C(7)	176.4(3)	N(1)-Tl(1)-Au(1)	76.43(12)
C(1)-Au(1)-Tl(1)	88.79(17)	N(1)-Tl(1)-S(2)	68.44(13)
C(7)-Au(1)-Tl(1)	88.75(17)	Au(1)-Tl(1)-S(2)	102.42(4)

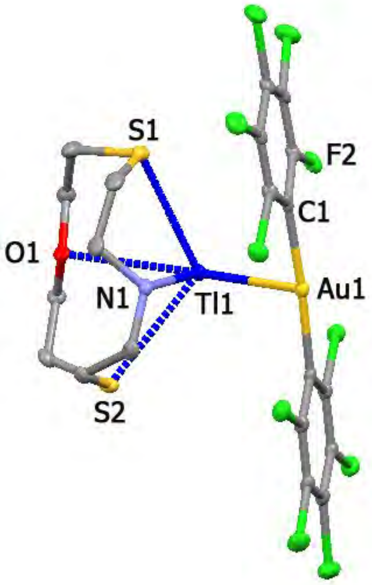

Table C7. Details of data collection and refinement for complex **4.**

Compound	**4**
Empirical formula	$C_{40}H_{34}Au_2F_{20}N_2S_6Tl_2$
Formula weight	1917.72
Temperature/K	100(2)
Crystal system	Monoclinic
Space group	C 2/c
a/Å	17.8053(14)
b/Å	17.8294(14)
c/Å	18.1323(15)
α/°	90
β/°	112.256(3)
γ/°	90
Volume/Å^3	5327.4(7)
Z	4
ρ_{calc}g/cm^3	2.391
μ/mm^{-1}	11.859
F(000)	3536
Crystal size/mm^3	0.14 x 0.13 x 0.11
Radiation	MoKα (λ = 0.71073)
2Θ range for data collection/°	3.246 to 28.047
Reflections collected	61950
Independent reflections	6434 [R_{int} = 0.0729]
Data/restraints/parameters	6434/0/328
Goodness-of-fit on F^2	1.014
Final R indexes [I>=2σ (I)]	R_1 = 0.0345, wR_2 = 0.0556
Final R indexes [all data]	R_1 = 0.0560, wR_2 = 0.0610
Largest diff. peak/hole / e Å^{-3}	1.814/-1.457

Table C8. Selected bond lengths [Å] and angles [°] for **4**.

Au(1)-Tl(1)	3.3170(4)	Tl(1)-N(1)	2.767(5)
Au(1)-Tl(1)#1	3.3815(4)	Tl(1)-S(1)	3.1644(15)
Au(1)-C(1)	2.061(5)	Tl(1)-S(2)	3.1569(16)
Au(1)-C(11)	2.055(5)	Tl(1)-S(3)	3.1686(15)
C(11)-Au(1)-C(1)	177.4(2)	S(1)-Tl(1)-S(3)	106.65(4)
Tl(1)-Au(1)-Tl(1)#1	104.27(2)	S(2)-Tl(1)-Au(1)	159.85(3)
Au(1)-Tl(1)-Au(1)#1	75.71(1)	N(1)-Tl(1)-Au(1)#1	171.25(10)

Symmetry transformations used to generate equivalent atoms:
#1 -x+1,y,-z+1/2

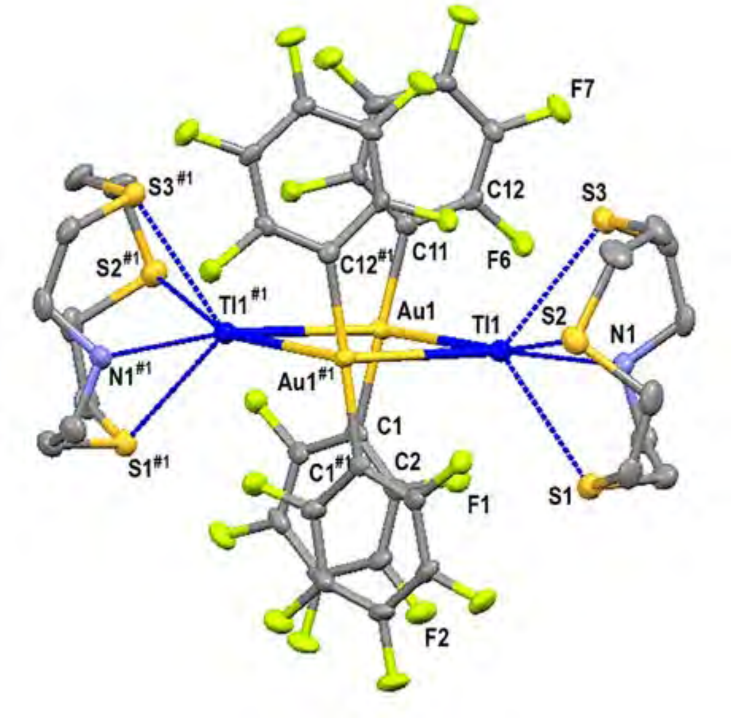

Table C9. Details of data collection and refinement for complex **5**

Compound	**5**
Empirical formula	$C_{20}H_{18}AuF_{10}N_2S_2Tl$
Formula weight	941.82
Temperature/K	173(2)
Crystal system	Orthorhombic
Space group	Cmcm
a/Å	a = 21.2568(7)
b/Å	b = 7.4264(4)
c/Å	c = 16.0389(9)
α/°	90
β/°	90
γ/°	90
Volume/Å^3	2531.9(2)
Z	4
ρ_{calc}g/cm^3	2.471
μ/mm^{-1}	12.395
F(000)	1736
Crystal size/mm^3	0.25 x 0.20 x 0.175
Radiation	MoKα (λ = 0.71073)
2Θ range for data collection/°	2.540 to 27.452
Reflections collected	1531
Independent reflections	1531 [$_{Rint}$= 0.0759]
Data/restraints/parameters	1531/ 33/89
Goodness-of-fit on F^2	1.076
Final R indexes [I>=2σ (I)]	R1 = 0.0649, wR2 = 0.1853
Final R indexes [all data]	R1 = 0.0801, wR2 = 0.1985
Largest diff. peak/hole / e Å^{-3}	3.936 and -1.735 e.Å^{-3}

Table C10. Selected bond lengths [Å] and angles [°] for **5**.

Au(1)-C(1)#1	2.02(5)	Tl(1)-N(1)	2.74(5)
Au(1)-C(1)	2.02(5)	Tl(1)-N(2)	2.76(6)
Au(2)-C(7)#2	2.02(4)	Tl(1)-S(1)	3.09(2)
Au(2)-C(7)	2.02(4)	Tl(1)-S(2)	3.11(2)
C(1)#1-Au(1)-C(1)	180(2)	N(1)-Tl(1)-N(2)	85.8(17)
C(7)#2-Au(2)-C(7)	180.000(5)	N(1)-Tl(1)-S(1)	65.8(11)
N(2)-Tl(1)-S(1)	66.2(12)	N(1)-Tl(1)-S(2)	66.9(12)
S(1)-Tl(1)-S(2)	113.4(5)	N(2)-Tl(1)-S(2)	66.1(12)

Symmetry transformations used to generate equivalent atoms:

#1 -x,-y,-z   #2 -x,-y,-z+1

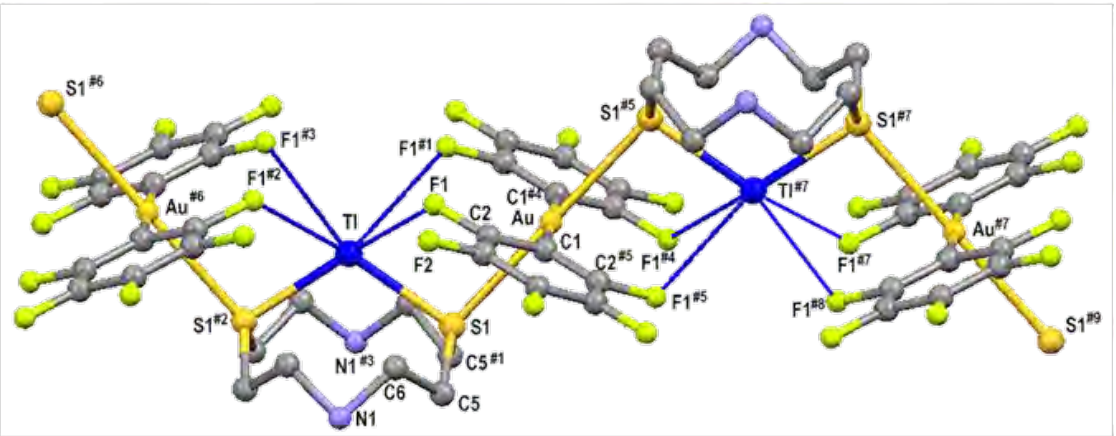

Table C11. Details of data collection and refinement for complex **6.**

Compound	**6**
Empirical formula	$C_{20}H_{17}AuF_{10}NOS_2Tl$
Formula weight	942.80
Temperature/K	173(2)
Crystal system	Monoclinic
Space group	Pnbc
a/Å	8.1975(4)
b/Å	17.7760(6)
c/Å	17.8726(7)
α/°	90
β/°	90
γ/°	90
Volume/Å^3	2604.37(19)
Z	4
ρ_{calc}g/cm^3	2.405
μ/mm^{-1}	12.052
F(000)	1736.0
Crystal size/mm^3	0.150 x 0.120 x 0.050
Radiation	MoKα (λ = 0.71073)
2Θ range for data collection/°	2.485 to 27.472
Reflections collected	2997
Independent reflections	2997 [R_{int} = 0.0586]
Data/restraints/parameters	2997/22/186
Goodness-of-fit on F^2	1.062
Final R indexes [I>=2σ (I)]	R_1 = 0.0340, wR_2 = 0. 1730
Final R indexes [all data]	R_1 = 0.0758, wR_2 = 0.0964
Largest diff. peak/hole / e Å^{-3}	4.196/-0.903

Table C12. Selected bond lengths [Å] and angles [°] for **6**.

Tl(1)-Au(1)	3.2576(6)	Tl(1)-O(1)	3.1388(4)
Tl(1)-Au(1)#2	3.2576(6)	Tl(1)-N(1)	2.780(17)
Au(1)-C(1)#3	2.077(10)	Tl(1)-N(1)#1	2.780(17)
Au(1)-C(1)	2.077(10)	Tl(1)-S(1)	3.3026(1)
C(1)#3-Au(1)-C(1)	176.8(6)	N(1)-Tl(1)-Au(1)	88.8(3)
N(1)-Tl(1)-Au(1)#2	168.5(2)	N(1)#1-Tl(1)-Au(1)	168.5(2)
N(1)#1-Tl(1)-Au(1)#2	88.8(3)		

Symmetry transformations used to generate equivalent atoms:

#1 -x+1,y,-z+1/2 #2 -x+1,-y+3/2,z #3 x,-y+3/2,-z+1/2

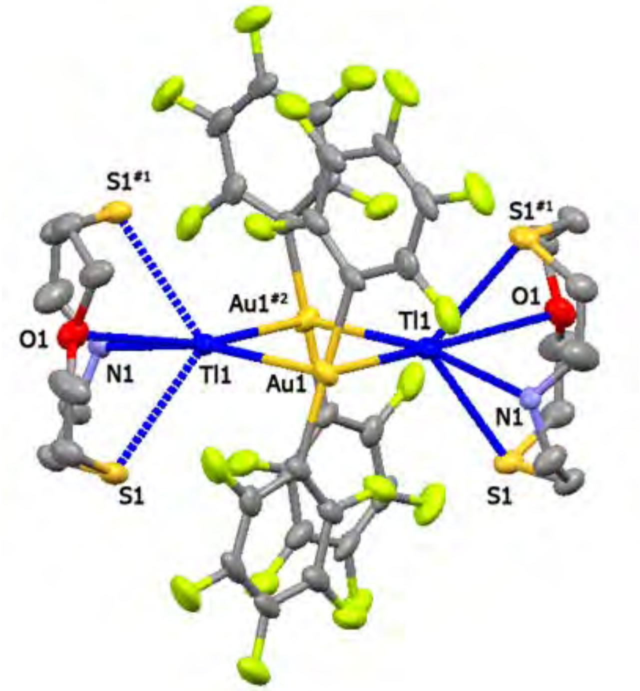

Table C13. Details of data collection and refinement for complex **7.**

Compound	**7**
Empirical formula	$C_{30}H_{18}AuCl_{10}N_3S_2Tl$
Formula weight	992.34
Temperature/K	173(2)
Crystal system	Orthorhombic
Space group	Pbn21
a/Å	10.4144(3)
b/Å	17.7013(4)
c/Å	19.1260(6)
α/°	90
β/°	90
γ/°	90
Volume/Å^3	3525.85(17)
Z	4
ρ_{calc}g/cm^3	2.337
μ/mm^{-1}	9.627
F(000)	2324
Crystal size/mm^3	0.4 x 0.25 x 0.125
Radiation	MoKα (λ = 0.71073)
2Θ range for data collection/°	2.23 to 27.49
Reflections collected	41644
Independent reflections	8056 [R_{int}=0.0642]
Data/restraints/parameters	8056/1/426
Goodness-of-fit on F^2	1.094
Final R indexes [I>=2σ (I)]	R1 = 0.0574, wR2 = 0.1419
Final R indexes [all data]	R1 = 0.0665, wR2 = 0.1489
Largest diff. peak/hole / e Å^{-3}	3.893/-2.538

Table C14. Selected bond lengths [Å] and angles [°] for **7**.

Tl(1)-Au(1)	3.2534(6)	Tl(1)-N(1)	2.703(10)
Au(1)-C(1)	2.030(11)	Tl(1)-N(2)	2.696(10)
Au(1)-C(7)	2.027(13)	Tl(1)-S(2)	3.093(3)
		Tl(1)-S(1)	3.146(3)
C(7)-Au(1)-C(1)	175.1(4)	N(2)-Tl(1)-N(1)	62.2(3)
N(1)-Tl(1)-S(2)	120.8(2)	N(2)-Tl(1)-S(2)	66.1(2)
N(1)-Tl(1)-S(1)	64.6(2)	N(2)-Tl(1)-S(1)	117.7(2)
N(1)-Tl(1)-Au(1)	104.0(2)	N(2)-Tl(1)-Au(1)	85.5(2)
S(2)-Tl(1)-S(1)	122.32(11)	S(1)-Tl(1)-Au(1)	137.83(8)
S(2)-Tl(1)-Au(1)	98.80(7)		

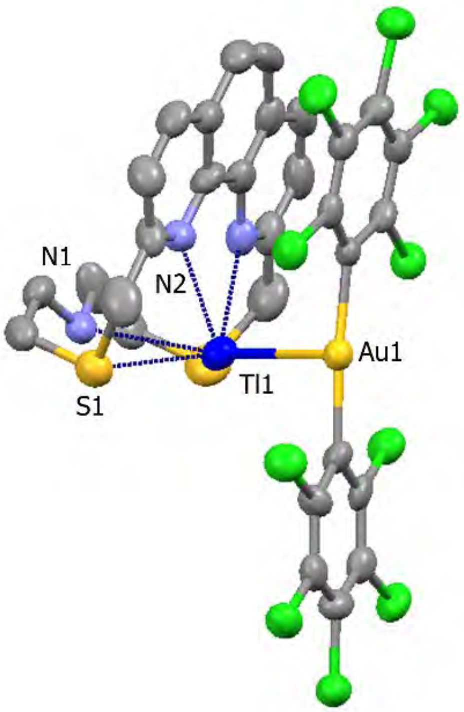

Table C15. Details of data collection and refinement for complex **8.**

Compound	**8**
Empirical formula	$C_{18}H_{14}AuCl_{10}N_3Tl$
Formula weight	1028.16
Temperature/K	105.24
Crystal system	Triclinic
Space group	P-1
a/Å	9.8906(14)
b/Å	10.6441(15)
c/Å	13.108(2)
α/°	86.361(5)
β/°	87.662(5)
γ/°	73.880(5)
Volume/Å^3	1322.7(3)
Z	2
ρ_{calc}g/cm^3	2.582
μ/mm^{-1}	12.649
F(000)	946.0
Crystal size/mm^3	0.607 × 0.143 × 0.098
Radiation	MoKα (λ = 0.71073)
2Θ range for data collection/°	6.048 to 55.788
Reflections collected	26098
Independent reflections	6265 [R_{int} = 0.1112]
Data/restraints/parameters	6265/0/307
Goodness-of-fit on F^2	1.000
Final R indexes [I>=2σ (I)]	R_1 = 0.0482, wR_2 = 0.1030
Final R indexes [all data]	R_1 = 0.0908, wR_2 = 0.1204
Largest diff. peak/hole / e Å^{-3}	3.47/-1.96

Table C16. Selected bond lengths [Å] and angles [°] for **8**.

Tl(1)-Au(1)	3.3377(6)	Tl(1)-Au(2)	3.5478(6)
Au(1)-C(1)#2	2.056(9)	Tl(1)-N(1)	2.664(8)
Au(1)-C(1)	2.056(9)	Tl(1)-N(2)	2.621(9)
Au(2)-C(7)	2.039(9)	Tl(1)-N(3)	2.671(9)
Au(2)-C(7)#2	2.039(9)		
Au(1)-Tl(1)-Au(2)	144.289(14)	N(1)-Tl(1)-Au(1)	69.97(16)
Tl(1)-Au(2)-Tl(1)#2	180	N(2)-Tl(1)-Au(1)	118.67(19)
C(7)-Au(2)-C(7)#2	180.0	N(2)-Tl(1)-Au(2)	72.49(18)
Tl(1)-Au(1)-Tl(1)#1	180.0	N(2)-Tl(1)-N(1)	65.6(2)
C(1)-Au(1)-C(1)#1	180.0	N(2)-Tl(1)-N(3)	66.5(3)
N(1)-Tl(1)-Au(1)	69.97(16)	N(3)-Tl(1)-Au(1)	126.63(17)
N(1)-Tl(1)-Au(2)	136.90(16)	N(3)-Tl(1)-Au(2)	89.08(17)
N(1)-Tl(1)-N(3)	65.7(2)		

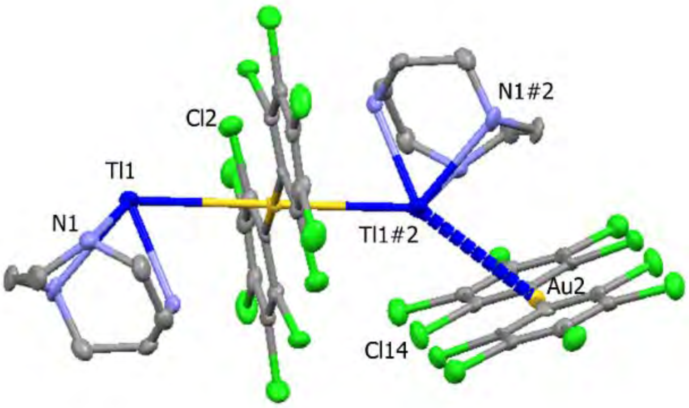

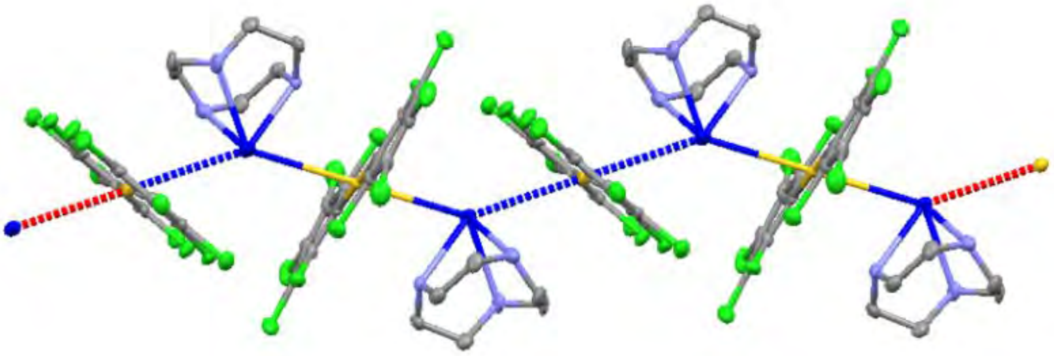

Table C17. Details of data collection and refinement for complex **9.**

Compound	**9**
Empirical formula	$C_{30}H_{18}AuF_{10}N_3S_2Tl$
Formula weight	1075.94
Temperature/K	293(2) K
Crystal system	Orthorhombic
Space group	Pbnm
a/Å	11.7204(4)
b/Å	11.9091(3)
c/Å	20.7324(6)
α/°	90
β/°	90
γ/°	90
Volume/Å^3	2893.82(15)
Z	4
ρ_{calc}g/cm^3	2.470
μ/mm^{-1}	10.864
F(000)	2004
Crystal size/mm^3	0.4 x 0.175 x 0.25
Radiation	MoKα (λ = 0.71073)
2Θ range for data collection/°	2.438 to 28.152
Reflections collected	33141
Independent reflections	3481 [R_{int}= 0.0778]
Data/restraints/parameters	3481/0/ 218
Goodness-of-fit on F^2	1.070
Final R indexes [I>=2σ (I)]	R1 = 0.0341, wR2 = 0.0847
Final R indexes [all data]	R1 = 0.0426, wR2 = 0.0889
Largest diff. peak/hole / e Å^{-3}	2.446/-1.380

Table C18. Selected bond lengths [Å] and angles [°] for **9**.

Tl(1)-Au(1)	3.3621(4)	Tl(1) -S(1)	3.2308(1)
Au-C(1)	2.050(5)	Tl(1)-N(1)	2.775(6)
Au-C(1)#1	2.050(5)	Tl(1)-N(2)	2.9726(1)
C(1)-Au-C(1)#1	171.8(3)	N(1)-Tl-Au	75.52(14)

Symmetry transformations used to generate equivalent atoms:

#1 x,y,-z+1/2

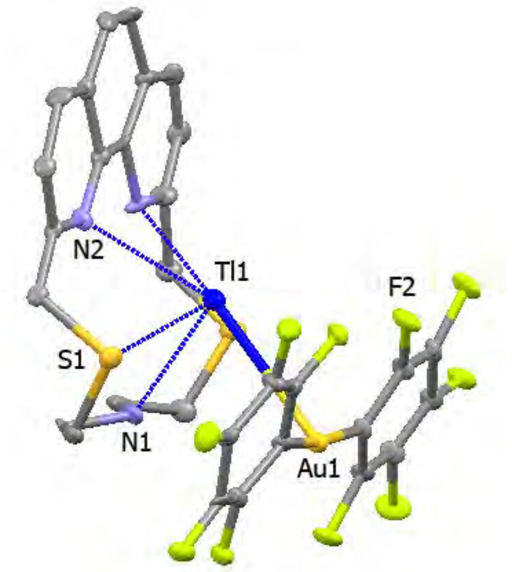

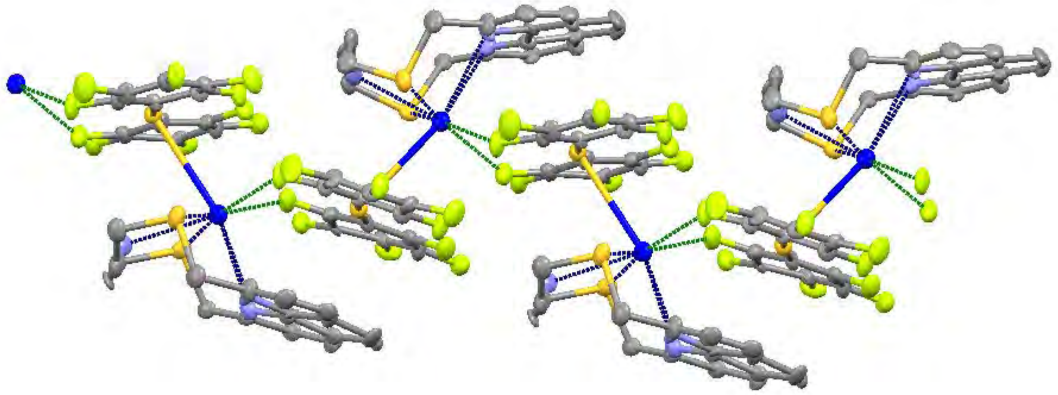

Table C19. Details of data collection and refinement for complex **13.**

Compound	**13**
Empirical formula	$C_{40}H_{26}AuF_{10}N_4S_2Tl\cdot0.5C_7H_8$
Formula weight	1263.67
Temperature/K	173
Crystal system	Triclinic
Space group	P-1
a/Å	10.2443(2)
b/Å	12.5801(4)
c/Å	16.2644(6)
α/°	95.3490(10)
β/°	90.880(2)
γ/°	102.923(2)
Volume/Å^3	2032.66(11)
Z	2
ρ_{calc}g/cm^3	2.065
μ/mm^{-1}	7.751
F(000)	1201.0
Crystal size/mm^3	0.375 × 0.15 × 0.05
Radiation	MoKα (λ = 0.71073)
2Θ range for data collection/°	4.876 to 54.984
Reflections collected	31281
Independent reflections	9163 [R_{int} = 0.0529]
Data/restraints/parameters	9163/18/555
Goodness-of-fit on F^2	1.018
Final R indexes [I>=2σ (I)]	R_1 = 0.0469, wR_2 = 0.1161
Final R indexes [all data]	R_1 = 0.0664, wR_2 = 0.1274
Largest diff. peak/hole / e Å^{-3}	2.56/-2.93

Table C20. Selected bond lengths [Å] and angles [°] for **13**.

Tl(1)-Au(1)	3.0597(4)	Tl(1)-N(1)	2.9162(58)
Au(1)-C(1)	2.043(7)	Tl(1)-N(2)	2.9019(54)
Au(1)-C(7)	2.034(7)	Tl(1)-N(3)	2.9634(53)
Tl(1)-S(2)	3.1358(17)	Tl(1)-N(4)	2.9443(55)
Au(1)-Tl(1)-S(2)	71.08(3)	C(7)-Au(1)-C(1)	175.6(3)

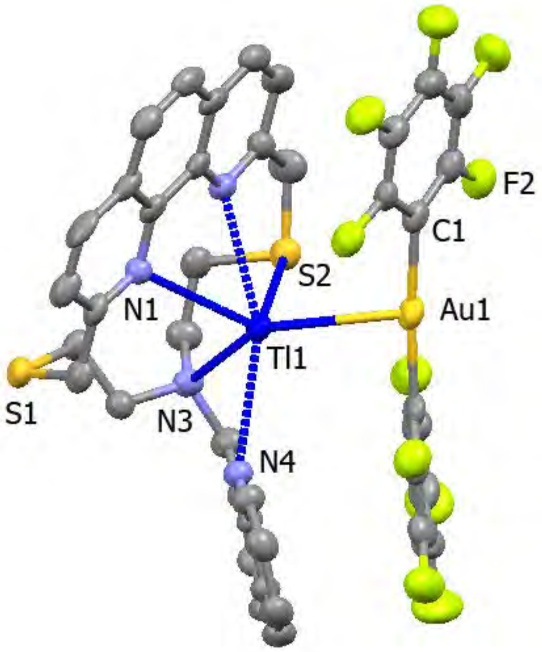

Table C21. Details of data collection and refinement for complex **14.**

Compound	**14**
Empirical formula	$C_{52}H_{26}Au_2F_{20}N_4S_2Tl_2$
Formula weight	1953.56
Temperature/K	173
Crystal system	monoclinic
Space group	$P2_1/n$
a/Å	14.6658(4)
b/Å	22.7807(6)
c/Å	17.0613(5)
α/°	90
β/°	111.4930(10)
γ/°	90
Volume/Å^3	5303.8(3)
Z	4
ρ_{calc}g/cm^3	2.447
μ/mm^{-1}	11.764
F(000)	3592.0
Crystal size/mm^3	0.2 × 0.15 × 0.075
Radiation	MoKα (λ = 0.71073)
2Θ range for data collection/°	4.402 to 54.966
Reflections collected	51383
Independent reflections	12091 [R_{int} = 0.0787]
Data/restraints/parameters	12091/337/608
Goodness-of-fit on F^2	1.072
Final R indexes [I>=2σ (I)]	R_1 = 0.0727, wR_2 = 0.1999
Final R indexes [all data]	R_1 = 0.1069, wR_2 = 0.2178
Largest diff. peak/hole / e Å^{-3}	3.28/-3.17

Table C22. Selected bond lengths [Å] and angles [°] for **14**.

Au(1)-Tl(1)	3.1996(9)	Au(2)-Tl(2)	3.0419(7)
Au(1)-Tl(2)	3.4517(8)	Au(2)-C(20)	2.052(15)
Au(1)-C(1)	2.121(9)	Au(2)-C(26)	2.034(13)
Au(1)-C(7)	2.081(9)	Tl(2)-N(3)	2.824(10)
Tl(1)-N(1)	2.667(12)	Tl(2)-N(4)	2.712(10)
Tl(1)-N(2)	2.689(11)	Tl(2)-S(1)	3.5139(29)
Tl(1)-S(1)	3.2551(36)	Tl(2)-S(2)	3.4644(34)
Tl(1)-S(2)	3.2831(30)		
Tl(1)-Au(1)Tl(2)	126.91(3)	C(20)-Au(2)-Tl(2)	87.9(4)
C(1)-Au(1)-Tl(1)	103.6(4)	C(26)-Au(2)-Tl(2)	97.0(3)
C(1)-Au(1)-Tl(2)	91.5(4)	C(26)-Au(2)-C(20)	174.9(5)
C(7)-Au(1)-Tl(1)	80.6(3)	N(1)-Tl(1)-Au(1)	86.9(2)
C(7)-Au(1)-Tl(2)	92.0(3)	N(1)-Tl(1)-N(2)	60.8(4)
C(7)-Au(1)-C(1)	171.2(5)	N(2)-Tl(1)-Au(1)	79.4(2)
N(3)-Tl(2)-Au(1)	149.57(19)	Au(2)-Tl(2)-Au(1)	116.43(2)
N(3)-Tl(2)-Au(2)	90.68(19)	N(4)-Tl(2)-N(3)	63.5(3)
N(4)-Tl(2)-Au(1)	128.3(2)		
N(4)-Tl(2)-Au(2)	85.6(2)		

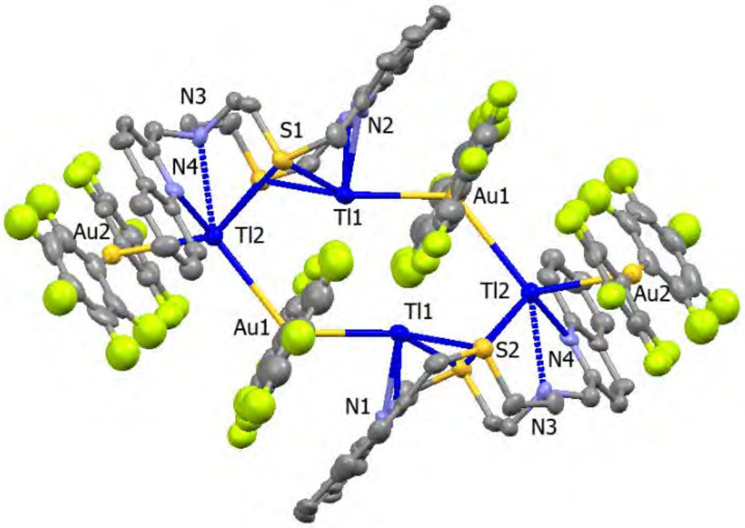

Table C23. Details of data collection and refinement for complex **15.**

Compound	**15**
Empirical formula	$C_{30}H_{24}AuF_{10}N_2OS_2Tl$
Formula weight	1083.97
Temperature/K	173
Crystal system	Monoclinic
Space group	$P2_1/c$
a/Å	12.4601(7)
b/Å	14.1891(7)
c/Å	18.1610(5)
α/°	90
β/°	100.255(3)
γ/°	90
Volume/Å^3	3159.5(3)
Z	4
ρ_{calc}g/cm^3	2.279
μ/mm^{-1}	9.952
F(000)	2032.0
Crystal size/mm^3	0.3 × 0.1 × 0.1
Radiation	MoKα (λ = 0.71073)
2Θ range for data collection/°	4.558 to 54.946
Reflections collected	36518
Independent reflections	7166 [R_{int} = 0.0877]
Data/restraints/parameters	7166/0/425
Goodness-of-fit on F^2	1.038
Final R indexes [I>=2σ (I)]	R_1 = 0.0517, wR_2 = 0.1185
Final R indexes [all data]	R_1 = 0.0730, wR_2 = 0.1289
Largest diff. peak/hole / e Å^{-3}	2.95/-2.05

Table C24. Selected bond lengths [Å] and angles [°] for **15**.

Au(1)-Tl(1)	3.2339(4)	Tl(1)-N(1)	2.778(6)
Au(1) -C(1)	2.046(7)	Tl(1)-N(2)	2.664(7)
Au(1)-C(7)	2.042(7)	Tl(1)-S(1)	3.1835(2)
Tl(1)-O(1)	3.0339(1)	Tl(1)-S(2)	3.128(2)
C(7)-Au(1)-C(1)	177.2(3)	N(2)-Tl(1)-N(1)	62.7(2)
N(1)-Tl(1)-S(2)	69.42(14)	N(2)-Tl(1)-S(2)	81.25(14)
N(2)-Tl(1)-Au(1)	97.52(14)	S(2)-Tl(1)-Au(1)	157.72(4)

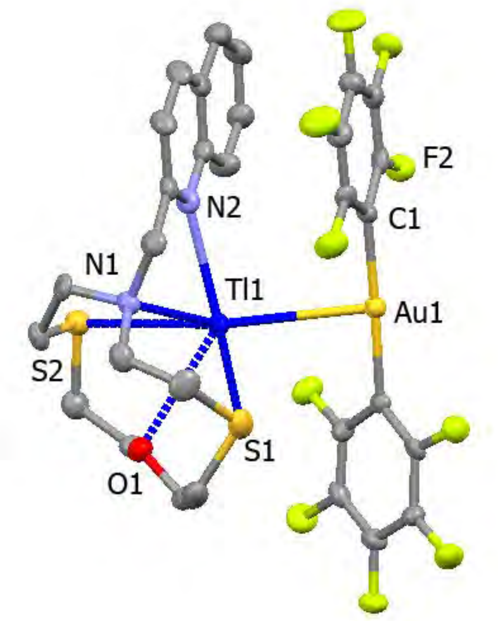

Table C25. Details of data collection and refinement for complex **16.**

Compound	**16**
Empirical formula	$C_{42}H_{24}Au_2F_{20}N_2O_1S_2Tl_2\cdot0.25CH_2Cl_2$
Formula weight	3681.31
Temperature/K	102.84
Crystal system	Monoclinic
Space group	$P2_1/c$
a/Å	30.557(4)
b/Å	11.0238(12)
c/Å	29.803(4)
α/°	90
β/°	109.107(4)
γ/°	90
Volume/Å^3	9486.2(19)
Z	8
ρ_{calc}g/cm^3	2.578
μ/mm^{-1}	13.173
F(000)	6724.0
Crystal size/mm^3	0.37 × 0.14 × 0.03
Radiation	MoKα (λ = 0.71073)
2Θ range for data collection/°	5.488 to 55.894
Reflections collected	205050
Independent reflections	22695 [R_{int} = 0.1117]
Data/restraints/parameters	22695/1332/1288
Goodness-of-fit on F^2	1.106
Final R indexes [I>=2σ (I)]	R_1 = 0.0671, wR_2 = 0.1274
Final R indexes [all data]	R_1 = 0.0976, wR_2 = 0.1389
Largest diff. peak/hole / e Å^{-3}	3.00/-3.02

Table C26. Selected bond lengths [Å] and angles [°] for **16**.

Tl(1)-Au(1)	3.3124(8)	Tl(2)-S(1)	3.4339(3)
Tl(2)-Au(1)	3.0216(8)	Tl(1)-N(1)#2	2.684(11)
Tl(2)-Au(2)	3.0852(8)	Tl(1)-N(2)#2	2.733(10)
Tl(2)-Au(2)#1	3.0808(8)	Tl(1)-S(1)	3.1940(2)
Au(1)-C(1)	2.036(15)	Tl(1)-S(2)#2	3.152(3)
Au(1)-C(7)	2.046(16)	Tl(1)-O(2)	3.0128(2)
Au(2)-C(13)	2.019(14)		
Au(2)-C(19)	2.034(15)		
Au(2)#1-Tl(2)-Au(2)	146.72(2)	N(2)#2-Tl(1)-Au(1)	118.3(2)
Au(1)-Tl(2)-Au(2)	144.38(2)	N(2)#2-Tl(1)-S(2)#2	67.4(2)
Au(1)-Tl(2)-Au(2)#1	68.593(18)	Tl(2)#3-Au(2)-Tl(2)	138.13(2)
S(2)#2-Tl(1)-Au(1)	66.37(6)	C(13)-Au(2)-C(19)	174.0(5)
N(1)#2-Tl(1)-Au(1)	98.5(3)	Tl(2)-Au(1)-Tl(1)	113.08(2)
N(1)#2 Tl(1)-S(2)#2	109.2(2)	C(1)-Au(1)-C(7)	172.8(6)
N(1)#2-Tl(1)-N(2)#2	61.9(3)		

Symmetry transformations used to generate equivalent atoms:

#1 -X,1/2+Y,1/2-Z; #2 +X,-1/2-Y,1/2+Z #3 1-X,-1/2+Y,1/2-Z.

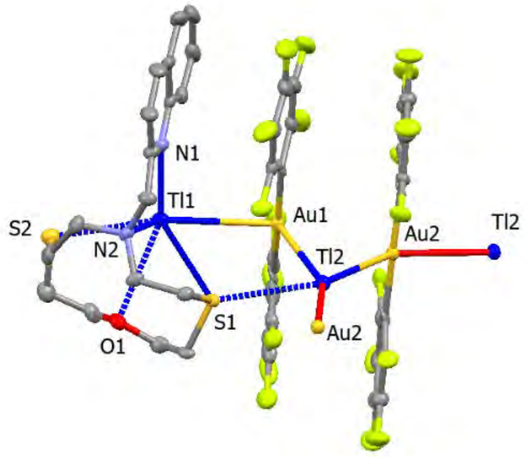

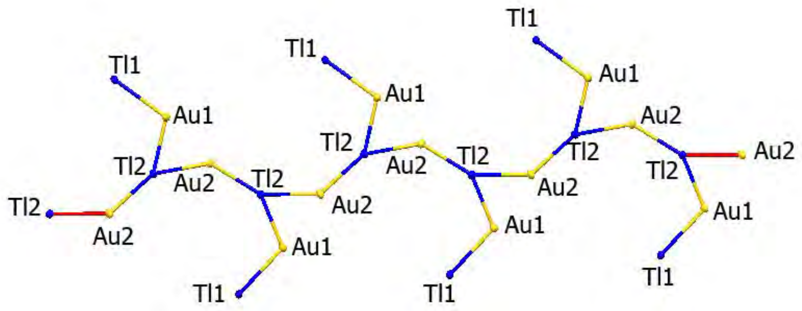

Table C27. Details of data collection and refinement for complexes **17.**

Compound	**17**
Empirical formula	$C_{20}H_{17}AgAuCl_{10}NS_3$
Formula weight	1025.86
Temperature/K	293(2)
Crystal system	Triclinic
Space group	P 1
a/Å	8.5472(8)
b/Å	8.6869(7)
c/Å	10.4422(8)
α/°	72.189(3)
β/°	89.194(3)
γ/°	88.280(4)
Volume/$Å^3$	737.82(11)
Z	1
$\rho_{calc}g/cm^3$	2.309
μ/mm^{-1}	6.763
F(000)	487.0
Crystal size/mm^3	0.150 x 0.120 x 0.050
Radiation	MoKα (λ = 0.71073)
2Θ range for data collection/°	3.136 to 25.680
Reflections collected	29662
Independent reflections	5600 [R_{int} = 0.0348]
Data/restraints/parameters	5600/436/248
Goodness-of-fit on F^2	1.074
Final R indexes [I>=2σ (I)]	R_1 = 0.0680, wR_2 = 0.1732
Final R indexes [all data]	R_1 = 0.0714, wR_2 = 0.1777
Largest diff. peak/hole / e $Å^{-3}$	12.563/-2.687

Table C28. Selected bond lengths [Å] and angles [°] for **17**.

Au(1)-Ag(1)	2.789(2)	Ag(1)-N(1)	2.45(2)
Ag(1)-C(7)	2.530(19)	Ag(1)-S(1)	2.659(8)
Au(1)-C(1)	2.04(2)	Ag(1)-S(2)	2.632(8)
Au(1)-C(7)	2.098(11)	Ag(1)-S(3)	2.654(8)
C(1)-Au(1)-C(7)	178.4(10)	N(1)-Ag(1)-S(3)	79.4(6)
S(2)-Ag(1)-S(1)	82.5(3)	N(1)-Ag(1)-S(1)	80.1(6)
S(3)-Ag(1)-S(1)	137.3(3)	N(1)-Ag(1)-S(2)	129.1(6)
S(2)-Ag(1)-S(3)	82.0(3)	S(1)-Ag(1)-Au(1)	97.27(18)
N(1)-Ag(1)-Au(1)	86.8(6)	S(2)-Ag(1)-Au(1)	142.94(19)
		S(3)-Ag(1)-Au(1)	118.46(19)

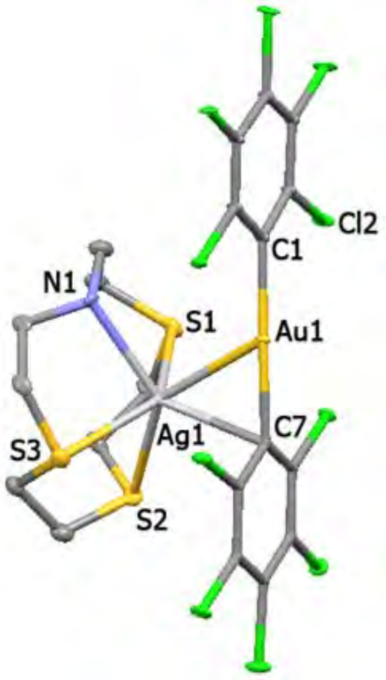

Table C29. Details of data collection and refinement for complexes **18.**

Compound	**18**
Empirical formula	$C_{20}H_{18}AgAuCl_{10}N_2S_2$
Formula weight	1009.82
Temperature/K	293(2)
Crystal system	Triclinic
Space group	P 1
a/Å	8.5552(6)
b/Å	8.6656(4)
c/Å	11.3014(8)
α/°	68.058(4)
β/°	90.052(3)
γ/°	73.914(4)
Volume/Å^3	741.58(8)
Z	1
ρ_{calc}g/cm^3	2.261
μ/mm^{-1}	6.659
F(000)	480.0
Crystal size/mm^3	0.325 x 0.200 x 0.125
Radiation	MoKα (λ = 0.71073)
2Θ range for data collection/°	2.495 to 25.680
Reflections collected	5206
Independent reflections	3563 [R_{int} = 0.0422]
Data/restraints/parameters	3563/111/224
Goodness-of-fit on F^2	1.295
Final R indexes [I>=2σ (I)]	R_1 = 0.1081, wR_2 = 0.2620
Final R indexes [all data]	R_1 = 0.1103, wR_2 = 0.2671
Largest diff. peak/hole / e Å^{-3}	8.078/ -5.880

Table C30. Selected bond lengths [Å] and angles [°] for **18**.

Au(1)-Ag(1)	2.806(3)	Ag(1)-N(1)	2.45(4)
Ag(1)-C(1)	2.67(3)	Ag(1)-N(2)	2.45(4)
Au(1)-C(1)	2.05(3)	Ag(1)-S(1)	2.649(13)
Au(1)-C(7)	2.03(4)	Ag(1)-S(2)	2.644(12)
C(7)-Au(1)-C(1)	173.9(15)	N(1)-Ag(1)-C(1)	138.7(12)
C(1)-Au(1)-Ag(1)	64.4(7)	S(2)-Ag(1)-C(1)	110.7(8)
N(2)-Ag(1)-N(1)	118.9(12)	S(1)-Ag(1)-C(1)	110.6(8)
N(2)-Ag(1)-S(2)	78.2(9)	N(2)-Ag(1)-Au(1)	140.5(9)
N(1)-Ag(1)-S(2)	78.2(8)	N(1)-Ag(1)-Au(1)	97.6(9)
N(2)-Ag(1)-S(1)	81.1(8)	S(2)-Ag(1)-Au(1)	127.0(3)
N(1)-Ag(1)-S(1)	79.3(9)	S(1)-Ag(1)-Au(1)	92.2(3)
S(2)-Ag(1)-S(1)	136.8(4)	C(1)-Ag(1)-Au(1)	43.9(7)
N(2)-Ag(1)-C(1)	102.4(10)		

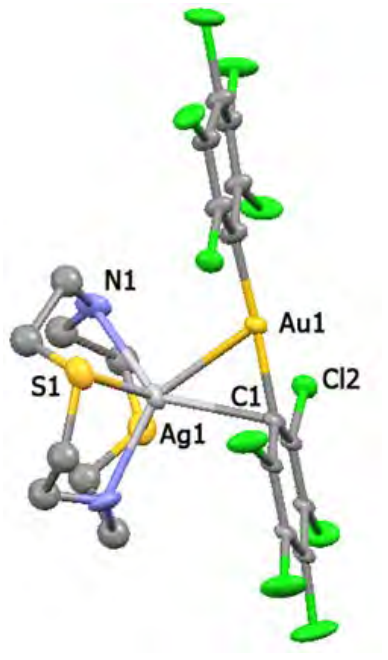

Table C31. Details of data collection and refinement for complexes **19.**

Compound	**19**
Empirical formula	$C_{20}H_{17}AgAuCl_{10}NOS_2$
Formula weight	1010.80
Temperature/K	101.56
Crystal system	Monoclinic
Space group	$P2_1/c$
a/Å	12.0304(8)
b/Å	8.8587(6)
c/Å	27.017(2)
α/°	90
β/°	102.824(2)
γ/°	90
Volume/Å^3	2807.4(3)
Z	4
ρ_{calc}g/cm^3	2.391
μ/mm^{-1}	7.038
F(000)	1920.0
Crystal size/mm^3	0.715 × 0.173 × 0.1
Radiation	MoKα (λ = 0.71073)
2Θ range for data collection/°	6.166 to 54.406
Reflections collected	56761
Independent reflections	6215 [R_{int} = 0.1093]
Data/restraints/parameters	6215/347/179
Goodness-of-fit on F^2	3.572
Final R indexes [I>=2σ (I)]	R_1 = 0.1562, wR_2 = 0.4539
Final R indexes [all data]	R_1 = 0.1676, wR_2 = 0.4559
Largest diff. peak/hole / e Å^{-3}	10.38/-4.17

Table C32. Details of data collection and refinement for complexes **19.**

Au(1)-Ag(1)	2.806(3)	Ag(1)-N(1)	2.35(2)
Ag(1)-C(7)	2.691(18)	Ag(1)-S(1)	2.566(8)
Au(1)-C(1)	2.01(3)	Ag(1)-S(2)	2.587(8)
Au(1)-C(7)	2.152(13)		

C(1)-Au(1)-Ag(1)	119.6(8)	S(1)-Ag(1)-C(7)	108.1(4)
C(1)-Au(1)-C(7)	176.2(9)	S(2)-Ag(1)-Au(1)	109.14(19)
C(1)-Au(1)-O(2)	104.9(12)	S(2)-Ag(1)-C(7)	109.2(4)
C(7)-Au(1)-Ag(1)	64.2(5)	N(1)-Ag(1)-Au(1)	138.9(5)
O(2)-Au(1)-Ag(1)	135.5(9)	N(1)-Ag(1)-S(1)	81.3(5)
O(2)-Au(1)-C(7)	71.3(11)	N(1)-Ag(1)-S(2)	81.5(5)
S(1)-Ag(1)-Au(1)	107.97(19)	N(1)-Ag(1)-C(7)	92.9(6)
S(1)-Ag(1)-S(2)	139.4(2)		

Table C33. Details of data collection and refinement for complexes **20.**

Compound	**20**
Empirical formula	$C_{20}H_{17}AgAuCl_{10}NOS_2$
Formula weight	1010.80
Temperature/K	173
Crystal system	Triclinic
Space group	P-1
a/Å	11.0652(6)
b/Å	11.2949(7)
c/Å	12.1627(9)
α/°	72.914(3)
β/°	84.006(4)
γ/°	87.884(4)
Volume/Å^3	1445.03(16)
Z	2
ρ_{calc}g/cm^3	2.323
μ/mm^{-1}	6.837
F(000)	960.0
Crystal size/mm^3	0.15 x 0.075 x 0.05
Radiation	MoKα (λ = 0.71073)
2Θ range for data collection/°	5.304 to 54.91
Reflections collected	6531
Independent reflections	6531 [R_{int} = 0.1093]
Data/restraints/parameters	6531/0/356
Goodness-of-fit on F^2	1.031
Final R indexes [I>=2σ (I)]	R_1 = 0.0340, wR_2 = 0.0804
Final R indexes [all data]	R_1 = 0.0416, wR_2 = 0.0842
Largest diff. peak/hole / e Å^{-3}	1.36/-1.36

Table C34. Details of data collection and refinement for complexes **20.**

C(1)-Au(1)	2.041(5)	S(1)-Ag(1)A	2.531(8)
C(7)-Au(1)	2.046(5)	S(2)-Ag(1)B	2.580(5)
Au(1)-Ag(1)B	2.790(4)	S(2)-Ag(1)A	2.612(8)
Au(1)-Ag(1)A	2.664(11)	Ag(1)-N(1)B	2.425(7)
S(1)-Ag(1)B	2.627(5)	N(1)A-Ag(1)A	2.57(3)
Au(1)-Au(1)	3.3852(2)		
C(1)-Au(1)-C(7)	175.32(17)	N(1)B-Ag(1)-Au(1)	156.8(3)
S(1)-Ag(1)-Au(1)	97.01(14)	N(1)B-Ag(1)-S(1)	81.07(18)
S(2)-Ag(1)-Au(1)	116.52(16)	N(1)B-Ag(1)-S(2)	80.24(18)
S(2)-Ag(1)-S(1)	131.0(2)	S(1)-Ag(1)A-S(2)	134.2(3)
S2-Ag(1)A-Au(1)	120.0(3)	S(1)-Ag(1)A-N(1)A	84.1(7)
N(1)A-Ag1A-Au1	94.8(9)	N(1)A-Ag(1)A-S(2)	77.0(6)

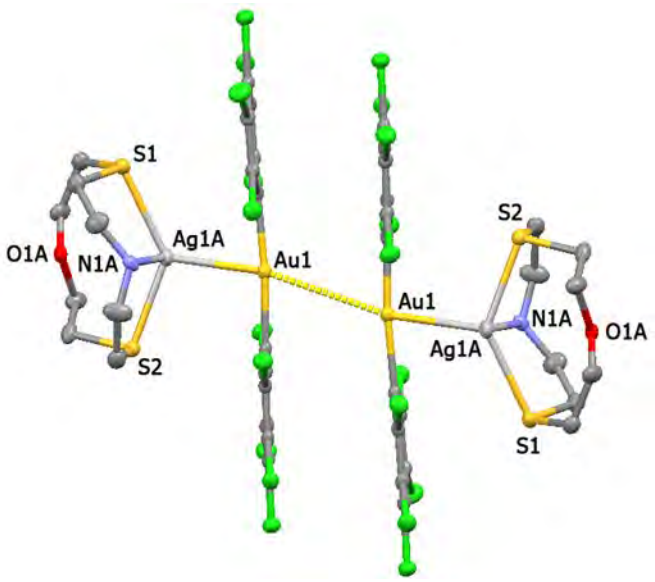

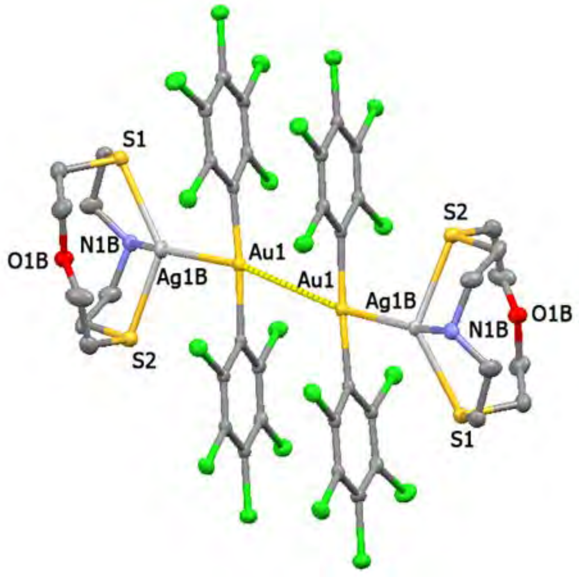

Table C35. Details of data collection and refinement for complexes **21.**

Compound	**21**
Empirical formula	$C_{40}H_{32}Ag_2Au_2F_{20}N_2S_6$
Formula weight	1722.71
Temperature/K	193(2)
Crystal system	Monoclinic
Space group	P21/n
a/Å	a = 10.9776(7)
b/Å	b = 17.4103(11)
c/Å	c = 12.9895(6)
α/°	90
β/°	96.960(4)
γ/°	90
Volume/Å^3	2464.3(2)
Z	2
ρ_{calc}g/cm^3	2.322
μ/mm^{-1}	7.082
F(000)	1628
Crystal size/mm^3	0.25 x 0.125 x 0.05
Radiation	MoKα (λ = 0.71073)
2Θ range for data collection/°	3.279 to 27.448
Reflections collected	23069
Independent reflections	5562 [R(int) = 0.0569]
Data/restraints/parameters	5562/63/325
Goodness-of-fit on F^2	1.061
Final R indexes [I>=2σ (I)]	R1 = 0.0418, wR2 = 0.1062
Final R indexes [all data]	R1 = 0.0562, wR2 = 0.1140
Largest diff. peak/hole / e Å^{-3}	1.861/-2.571

Table C36. Selected bond lengths [Å] and angles [°] for **21**.

Au(1)-Ag(1)	2.7459(5)	Ag(1)-N(1)	2.476(6)
Au(1)-Au(1)#1	3.2633(4)	Ag(1)-S(1)	2.714(2)
Ag(1)-C(1)	2.7498(58)	Ag(1)-S(2)	2.666(2)
Au-C(1)	2.057(6)	Ag(1)-S(3)	2.652(2)
Au-C(7)	2.044(6)		
Ag(1)-Au(1)-Au(1)#1	170.135(17)	S(1)-Ag(1)-S(3)	134.81(6)
C(7)-Au-C(1)	173.8(2)	S(2)-Ag-S(3)	82.75(8)
N(1)-Ag-S(1)	77.17(14)	N(1)-Ag(1)-Au(1)	95.61(13)
N(1)-Ag-S(2)	125.47(14)	S(1)-Ag(1)-Au(1)	93.51(4)
N(1)-Ag-S(3)	79.10(15)	S(2)-Ag(1)-Au(1)	135.11(5)
S(1)-Ag(1)-S(2)	80.61(7)	S(3)-Ag(1)-Au(1)	126.76(5)

Symmetry transformations used to generate equivalent atoms:

#1 -x+1,-y+1,-z+1

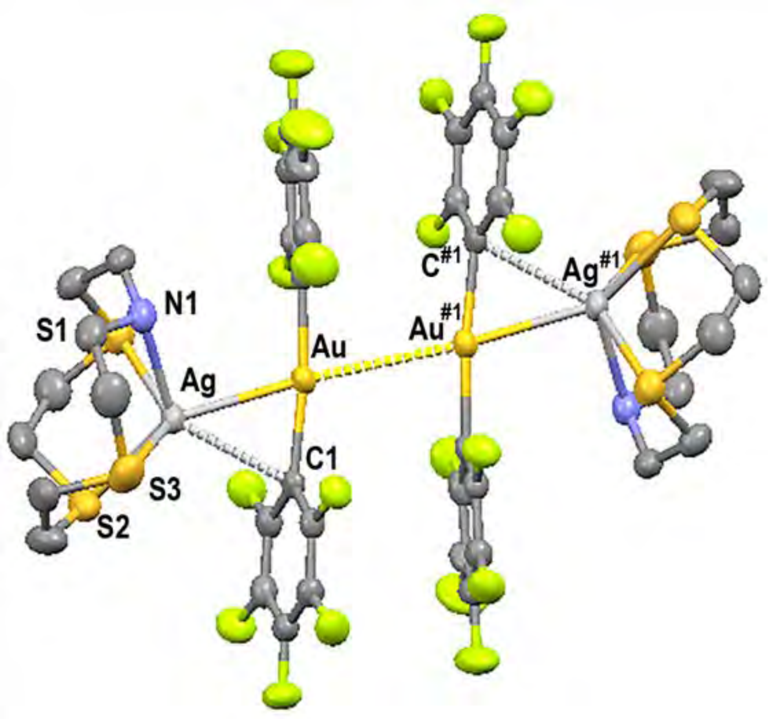

Table C37. Details of data collection and refinement for complexes **22.**

Compound	**22**
Empirical formula	$C_{20}H_{16}AgAuF_{10}N_2S_2$
Formula weight	843.30
Temperature/K	100(2)
Crystal system	Triclinic
Space group	P 1
a/Å	7.8644(8)
b/Å	8.4084(8)
c/Å	10.9345(11)
α/°	96.021(3)
β/°	105.325(3)
γ/°	115.250(3)
Volume/Å^3	610.78(11)
Z	1
ρ_{calc}g/cm^3	2.293
μ/mm^{-1}	7.060
F(000)	398
Crystal size/mm^3	0.025x0.10x0.16
Radiation	MoKα (λ = 0.71073)
2Θ range for data collection/°	2.993 to 31.475
Reflections collected	32811
Independent reflections	6938 [R_{int}= 0.0413]
Data/restraints/parameters	6938/572/266
Goodness-of-fit on F^2	1.141
Final R indexes [I>=2σ (I)]	R1 = 0.0888, wR2 = 0.2279
Final R indexes [all data]	R1 = 0.1030, wR2 = 0.2430
Largest diff. peak/hole / e Å^{-3}	9.378/-5.003

Table C38. Selected bond lengths [Å] and angles [°] for **22**.

Au(1)-Ag(1)	2.763(5)	Ag(1)-N(1)	2.49(4)
Ag(1)-C(1)	2.673(19)	Ag(1)-N(2)	2.46(4)
Au(1)-C(1)	2.068(7)	Ag(1)-S(1)	2.592(16)
Au(1)-C(7)	2.30(3)	Ag(1)-S(2)	2.622(16)
C(1)-Au(1)-C(7)	129.7(11)	N(2)-Ag(1)-S(1)	77.7(9)
C(1)-Au(1)-Ag(1)	65.4(5)	N(2)-Ag(1)-S(2)	79.8(9)
N(1)-Ag(1)-S(1)	85.8(9)	N(1)-Ag(1)-Au(1)	138.0(7)
N(1)-Ag(1)-N(2)	118.5(12)	N(2)-Ag(1)-Au(1)	92.5(9)
S(1)-Ag(1)-S(2)	136.0(5)	S(1)-Ag(1)-Au(1)	130.8(5)
N(1)-Ag(1)-S(2)	72.6(10)	S(2)-Ag(1)-Au(1)	87.3(4)

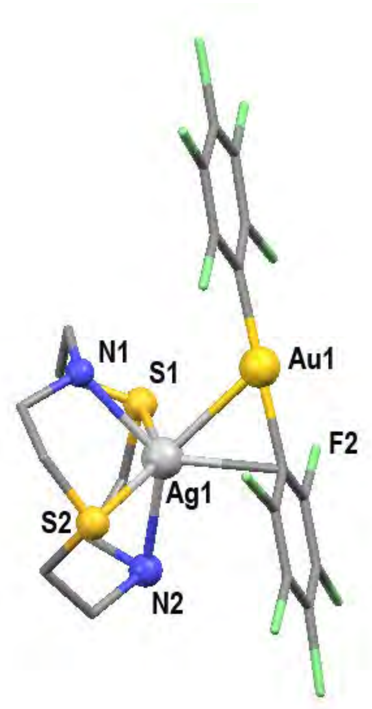

Table C39. Details of data collection and refinement for complexes **23.**

Compound	**23**
Empirical formula	$C_{20}H_{17}AgAuF_{10}NOS_2$
Formula weight	846.30
Temperature/K	101.48
Crystal system	Monoclinic
Space group	$P2_1/c$
a/Å	21.641(2)
b/Å	8.4427(8)
c/Å	28.115(3)
α/°	90
β/°	107.950(3)
γ/°	90
Volume/Å^3	4886.9(9)
Z	8
ρ_{calc}g/cm^3	2.301
μ/mm^{-1}	7.061
F(000)	3200.0
Crystal size/mm^3	0.364 × 0.347 × 0.11
Radiation	MoKα (λ = 0.71073)
2Θ range for data collection/°	5.602 to 55.938
Reflections collected	112942
Independent reflections	11675 [R_{int} = 0.1242]
Data/restraints/parameters	11675/700/660
Goodness-of-fit on F^2	1.275
Final R indexes [I>=2σ (I)]	R_1 = 0.0886, wR_2 = 0.1367
Final R indexes [all data]	R_1 = 0.1290, wR_2 = 0.1492
Largest diff. peak/hole / e Å^{-3}	3.38/-2.68

Table C40. Selected bond lengths [Å] and angles [°] for **23**.

Au(1)-Ag(1)	2.7069(11)	Au(2)-Ag(2)	2.7247(13)
Au(1)-C(1)	2.029(12)	Au(2)-C(21)	2.052(15)
Au(1)-C(7)	2.063(13)	Au(2)-C(27)	2.033(15)
Ag(1)-S(1)	2.573(4)	Ag(2)-N(2)	2.430(15)
Ag(1)-S(2)	2.501(3)	Ag(2)-S(3)	2.589(5)
Ag(1)-N(1)	2.405(12)	Ag(2)-S(4)	2.492(4)
C(1)-Au(1)-C(7)	178.6(5)	C(27)-Au(2)-C(21)	177.1(6)
S(1)-Ag(1)-Au(1)	93.79(9)	N(2)-Ag(2)-Au(2)	106.9(4)
S(2)-Ag(1)-Au(1)	121.69(8)	S(3)-Ag(2)-Au(2)	95.24(11)
S(2)-Ag(1)-S(1)	137.87(12)	S(4)-Ag(2)-Au(2)	130.34(11)
N(1)-Ag(1)-Au(1)	139.4(3)	N(2)-Ag(2)-S(3)	82.6(4)
N(1)-Ag(1)-S(1)	82.1(3)	N(2)-Ag(2)-S(4)	80.0(4)
N(1)-Ag(1)-S(2)	83.8(3)	S(4)-Ag(2)-S(3)	134.18(15)

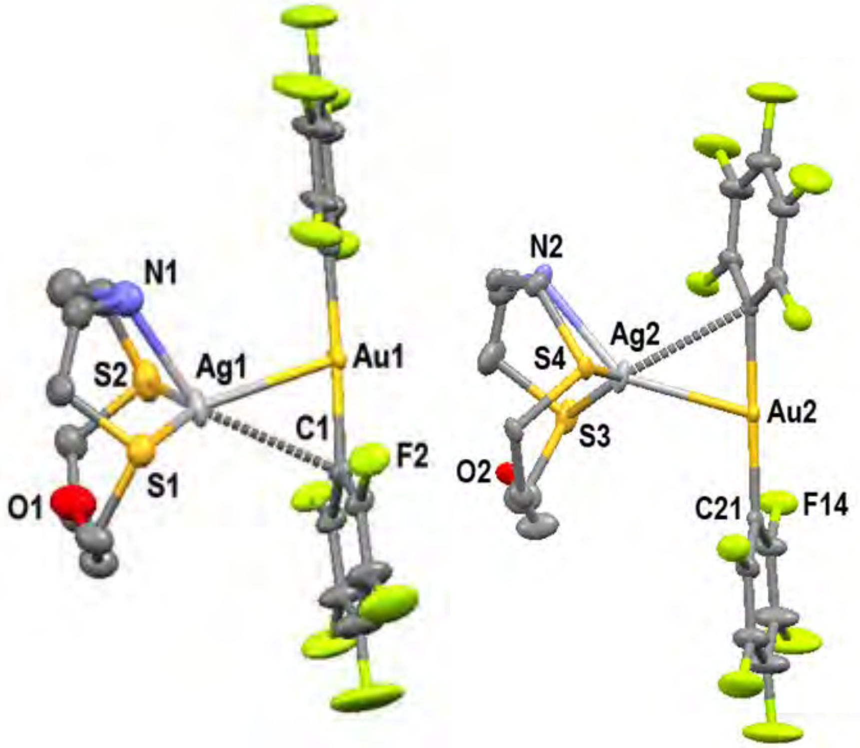

Table C41. Details of data collection and refinement for complexes **24.**

Compound	**24**
Empirical formula	$C_{30}H_{18}AgAuCl_{10}N_3S_2 \cdot C_4H_8O$
Formula weight	1161.96
Temperature/K	293(2)
Crystal system	Monoclinic
Space group	P 21/c
a/Å	7.4474(3)
b/Å	17.3673(5)
c/Å	29.8771(12)
α/°	90
β/°	91.5980(10)
γ/°	90
Volume/Å^3	3862.8(2)
Z	4
ρ_{calc}g/cm^3	1.998
μ/mm^{-1}	5.130
F(000)	2228
Crystal size/mm^3	0.625 x 0.375 x 0.25
Radiation	MoKα (λ = 0.71073)
2Θ range for data collection/°	2.970 to 27.015
Reflections collected	53910
Independent reflections	8362 [R_{int}=0.0798]
Data/restraints/parameters	8362/40/469
Goodness-of-fit on F^2	1.173
Final R indexes [I>=2σ (I)]	R1 = 0.0807, wR2 = 0.1604
Final R indexes [all data]	R1 = 0.1082, wR2 = 0.1702
Largest diff. peak/hole / e Å^{-3}	3.006/2.213

Table C42. Selected bond lengths [Å] and angles [°] for **24**.

Au(1)-Ag(1)	2.9597(12)	Ag(1)-N(1)	2.499(14)
Au(1)-C(1)	2.051(12)	Ag(1)-N(2)	2.474(12)
Au(1)-C(7)	2.008(13)	Ag(1)-N(3)	2.420(11)
Ag(1)-S(1)	2.709(4)		
Ag(1)-S(2)	2.682(4)		
C(7)-Au(1)-C(1)	176.8(5)	N(2)-Ag(1)-S(2)	73.0(3)
N(1)-Ag(1)-N(3)	118.0(4)	N(3)-Ag(1)-S(2)	138.9(3)
N(1)-Ag(1)-N(2)	127.5(5)	S(2)-Ag(1)-S(1)	146.24(14)
N(2)-Ag(1)-N(3)	67.2(4)	N(1)-Ag(1)-Au(1)	112.0(3)
N(1)-Ag(1)-S(1)	74.3(4)	N(2)-Ag(1)-Au(1)	113.3(3)
N(2)-Ag(1)-S(1)	140.4(3)	N(3)-Ag(1)-Au(1)	110.9(2)
N(3)-Ag(1)-S(1)	73.3(3)	S(1)-Ag(1)-Au(1)	77.99(8)
N(1)-Ag(1)-S(2)	79.0(3)	S(2)-Ag(1)-Au(1)	93.44(9)

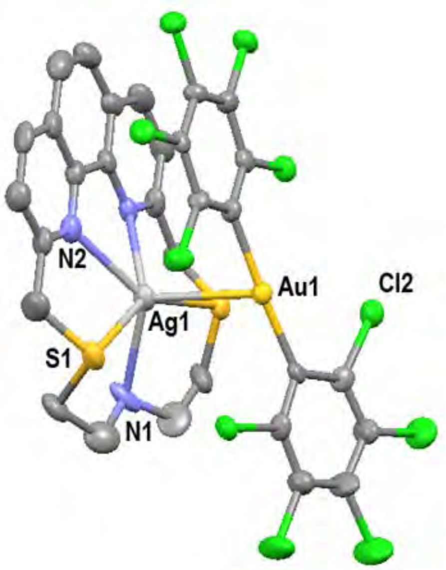

Table C43. Details of data collection and refinement for complexes **25.**

Compound	**25**
Empirical formula	$C_{18}H_{15}N_3Cl_{10}AgAu$
Formula weight	932.67
Temperature/K	109.99
Crystal system	Triclinic
Space group	P-1
a/Å	8.9202(7)
b/Å	11.8246(8)
c/Å	13.9123(11)
α/°	107.085(2)
β/°	100.045(3)
γ/°	106.406(2)
Volume/Å^3	1291.47(17)
Z	2
ρ_{calc}g/cm^3	2.398
μ/mm^{-1}	7.482
F(000)	880.0
Crystal size/mm^3	0.383 × 0.104 × 0.04
Radiation	MoKα (λ = 0.71073)
2Θ range for data collection/°	6.004 to 55.84
Reflections collected	26368
Independent reflections	6159 [R_{int} = 0.0575]
Data/restraints/parameters	6159/0/299
Goodness-of-fit on F^2	1.029
Final R indexes [I>=2σ (I)]	R_1 = 0.0308, wR_2 = 0.0632
Final R indexes [all data]	R_1 = 0.0441, wR_2 = 0.0682
Largest diff. peak/hole / e Å^{-3}	1.63/-1.77

Table C44. Selected bond lengths [Å] and angles [°] for **25**.

Au(1)-Ag(1)	2.6915(4)	Ag(1)-N(1)	2.429(4)
Ag(1)-C(1)	2.398(4)	Ag(1)-N(2)	2.365(4)
Au(1)-C(1)	2.081(4)	Ag(1)-N(3)	2.386(4)
Au(1)-C(7)	2.035(4)		
C(1)-Au(1)-C(7)	176.62(17)	N(1)-Ag(1)-N(2)	74.40(14)
C(1)-Au(1)-Ag(1)	58.68(12)	N(2)-Ag(1)-N(3)	76.05(14)
C(7)-Au(1)-Ag(1)	124.70(13)	N(3)-Ag(1)-Au(1)	133.09(10)
N(1)-Ag(1)-Au(1)	142.92(10)	N(3)-Ag(1)-N(1)	74.99(14)
N(2)-Ag(1)-Au(1)	129.07(10)		

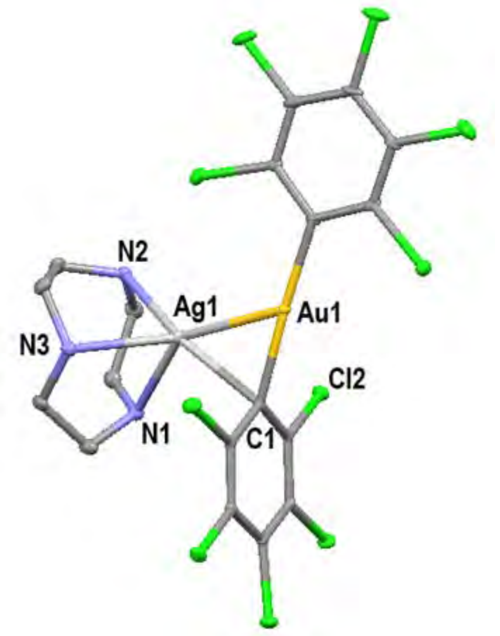

Table C45. Details of data collection and refinement for complexes **26.**

Compound	**26**
Empirical formula	$C_{30}H_{19}AgAuF_{10}N_3S_2$
Formula weight	980.44
Temperature/K	173(2) K
Crystal system	Triclinic
Space group	P-1
a/Å	9.0824(5)
b/Å	10.5300(4)
c/Å	17.4060(10)
α/°	101.793(3)
β/°	91.796(2)
γ/°	112.692(3)
Volume/Å^3	1492.16(13)
Z	2
ρ_{calc}g/cm^3	2.182
μ/mm^{-1}	5.798
F(000)	936
Crystal size/mm^3	0.2 x 0.175 x 0.1
Radiation	MoKα (λ = 0.71073)
2Θ range for data collection/°	2.21 to 27.51
Reflections collected	22073
Independent reflections	6748 [R_{int}= 0.0515]
Data/restraints/parameters	6748 / 0 / 428
Goodness-of-fit on F^2	1.038
Final R indexes [I>=2σ (I)]	R1 = 0.0414, wR2 = 0.1015
Final R indexes [all data]	R1 = 0.0522, wR2 = 0.1079
Largest diff. peak/hole / e Å^{-3}	2.791/-2.754

Table C46. Selected bond lengths [Å] and angles [°] for **26**.

Au(1)-Ag(1)	2.8432(4)	Ag(1)-N(1)	2.512(4)
Au(1)-Ag(1)#2	2.8432(4)	Ag(1)-N(2)	2.512(4)
Au(1)-C(1)	2.049(5)	Ag(1)-N(3)	2.577(4)
Au(1)-C(11)	2.049(5)	Ag(1)-S(2)	2.6576(13)
Au(2)-C(1)#1	2.049(5)	Ag(1)-S(1)	2.7155(13)
Au(2)-C(11)#2	2.049(5)		
C(1)#1-Au(1)-C(1)	180.000(1)	N(2)-Ag(1)-S(2)	73.09(10)
C(11)#2-Au(2)-C(11)	180.0(2)	N(3)-Ag(1)-S(2)	76.12(10)
C(11)#2-Au(2)-Ag(1)#2	110.52(13)	N(1)-Ag(1)-S(1)	72.45(10)
C(11)-Au(2)-Ag(1)#2	69.48(13)	N(2)-Ag(1)-S(1)	134.76(9)
C(11)#2-Au(2)-Ag(1)	69.48(13)	N(3)-Ag(1)-S(1)	72.73(10)
C(11)-Au(2)-Ag(1)	110.52(13)	S(2)-Ag(1)-S(1)	138.86(4)
Ag(1)#2-Au(2)-Ag(1)	180.0	N(1)-Ag(1)-Au(2)	107.28(9)
N(1)-Ag(1)-N(2)	65.76(13)	N(2)-Ag(1)-Au(2)	126.28(9)
N(1)-Ag(1)-N(3)	95.22(13)	N(3)-Ag(1)-Au(2)	138.86(9)
N(2)-Ag(1)-N(3)	94.15(13)	S(2)-Ag(1)-Au(2)	106.06(3)
N(1)-Ag(1)-S(2)	137.22(10)	S(1)-Ag(1)-Au(2)	81.70(3)

Symmetry transformations used to generate equivalent atoms:

#1 -x+1,-y,-z+2 #2 -x+1,-y,-z+1

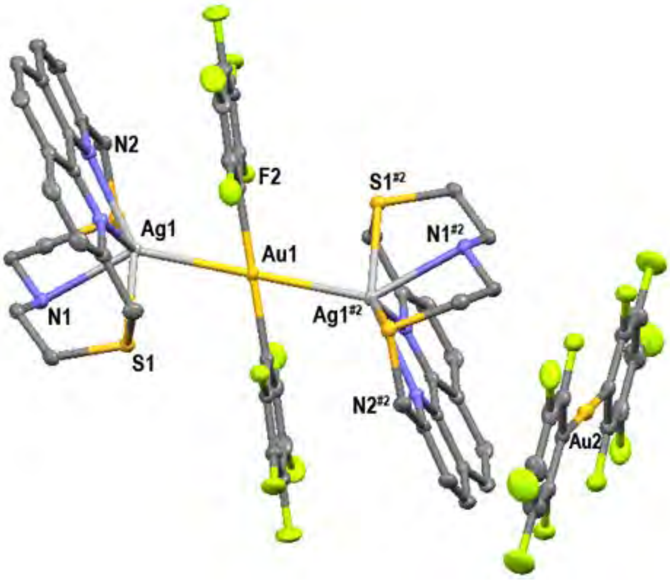

Table C47. Details of data collection and refinement for complexes **27.**

Compound	**27**
Empirical formula	$C_{18}H_{15}N_3F_{10}AgAu$
Formula weight	768.17
Temperature/K	101.05
Crystal system	Monoclinic
Space group	C2/c
a/Å	23.744(3)
b/Å	8.6609(10)
c/Å	20.843(3)
α/°	90
β/°	109.049(5)
γ/°	90
Volume/Å^3	4051.5(10)
Z	8
ρ_{calc}g/cm^3	2.519
μ/mm^{-1}	8.303
F(000)	2880.0
Crystal size/mm^3	0.709 × 0.107 × 0.061
Radiation	MoKα (λ = 0.71073)
2Θ range for data collection/°	5.67 to 53.02
Reflections collected	27708
Independent reflections	4143 [R_{int} = 0.2373]
Data/restraints/parameters	4143/301/299
Goodness-of-fit on F^2	1.025
Final R indexes [I>=2σ (I)]	R_1 = 0.0576, wR_2 = 0.0707
Final R indexes [all data]	R_1 = 0.1195, wR_2 = 0.0829
Largest diff. peak/hole / e Å^{-3}	1.18/-1.19

Table C48. Selected bond lengths [Å] and angles [°] for **27**.

Au(1)-Ag(1)	2.7331(9)	Ag(1)-N(1)	2.324(8)
Au(1)-Au(2)	3.4023(3)	Ag(1)-N(2)	2.411(8)
Au(1)-Ag(1)#1	2.7330(9)	Ag(1)-N(3)	2.464(8)
Au(1)-C(1)#1	2.087(10)	Ag(1)-C(1)#1	2.359(9)
Au(1)-C(1)	2.087(10)		
Ag(1)#1-Au(1)-Ag(1)	110.33(4)	N(1)-Ag(1)-N(2)	75.5(3)
C(1)-Au(1)-Ag(1)#1	56.7(3)	N(1)-Ag(1)-N(3)	74.8(3)
C(1)#1-Au(1)-Ag(1)	56.7(3)	N(1)-Ag(1)-C(1)#1	166.1(3)
C(1)-Au(1)-Ag(1)	124.3(3)	N(2)-Ag(1)-Au(1)	164.79(19)
C(1)#1-Au(1)-Ag(1)#1	124.3(3)	N(2)-Ag(1)-N(3)	73.2(3)
C(1)#1-Au(1)-C(1)	178.6(5)	N(3)-Ag(1)-Au(1)	106.93(19)
N(1)-Ag(1)-Au(1)	119.49(19)		

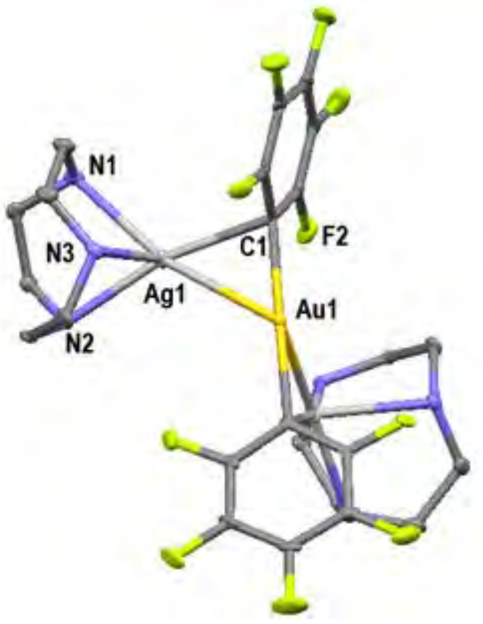

Table C49. Details of data collection and refinement for complexes **29.**

Compound	**29**
Empirical formula	$C_{30}H_{24}AgAuCl_{10}N_2OS_2$
Formula weight	1151.97
Temperature/K	130.01
Crystal system	Trigonal
Space group	$P3_121$
a/Å	18.5107(14)
b/Å	18.5107(14)
c/Å	18.7269(16)
α/°	90
β/°	90
γ/°	120
Volume/Å^3	5557.0(10)
Z	6
ρ_{calc}g/cm^3	2.065
μ/mm^{-1}	5.348
F(000)	3324.0
Crystal size/mm^3	0.348 × 0.221 × 0.064
Radiation	MoKα (λ = 0.71073)
2Θ range for data collection/°	4.4 to 55.806
Reflections collected	63765
Independent reflections	8764 [R_{int} = 0.0534]
Data/restraints/parameters	8764/143/425
Goodness-of-fit on F^2	1.269
Final R indexes [I>=2σ (I)]	R_1 = 0.0400, wR_2 = 0.0810
Final R indexes [all data]	R_1 = 0.0476, wR_2 = 0.0865
Largest diff. peak/hole / e Å^{-3}	1.88/-1.86

Table C50. Selected bond lengths [Å] and angles [°] for **29**.

Au(1)-Ag(1)	2.9230(8)	Ag(1)-N(1)	2.501(8)
Au(1)-C(1)	2.055(10)	Ag(1)-N(2)	2.546(8)
Au(1)-C(2)	2.043(10)	Ag(1)-S(1)	2.650(3)
		Ag(1)-S(2)	2.643(3)
C(1)-Au(1)-C(2)	175.8(3)	N(1)-Ag(1)-S(2)	87.37(19)
S(1)-Ag(1)-Au(1)	97.01(6)	N(1)-Ag(1)-N(2)	67.4(3)
S(2)-Ag(1)-Au(1)	128.09(6)	N(2)-Ag(1)-S(1)	77.88(18)
N(2)-Ag(1)-Au(1)	147.66(19)	N(2)-Ag(1)-S(2)	78.69(19)
N(1)-Ag(1)-Au(1)	93.39(17)	S(2)-Ag(1)-S(1)	122.17(8)
N(1)-Ag(1)-S(1)	128.7(2)		

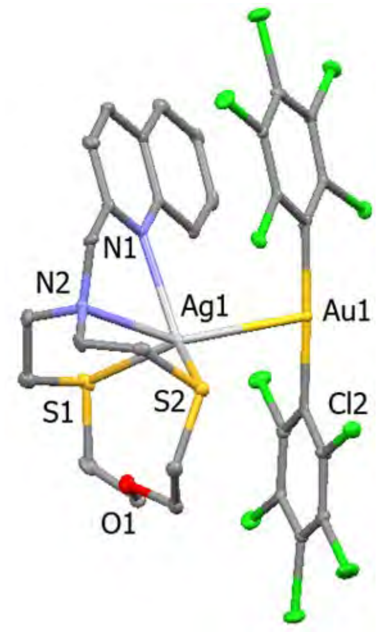

Table C51. Details of data collection and refinement for complexes **30.**

Compound	**30**
Empirical formula	$C_{40}H_{26}N_4F_{10}S_2AgAu$
Formula weight	1121.60
Temperature/K	100.15
Crystal system	Monoclinic
Space group	$P2_1/c$
a/Å	29.686(2)
b/Å	13.8957(11)
c/Å	18.6796(12)
α/°	90
β/°	106.359(2)
γ/°	90
Volume/Å^3	7393.5(9)
Z	8
ρ_{calc}g/cm^3	2.015
μ/mm^{-1}	4.695
F(000)	4336.0
Crystal size/mm^3	0.14 × 0.12 × 0.04
Radiation	MoKα (λ = 0.71073)
2Θ range for data collection/°	5.488 to 49.146
Reflections collected	84226
Independent reflections	12355 [R_{int} = 0.0756]
Data/restraints/parameters	12355/154/1019
Goodness-of-fit on F^2	1.112
Final R indexes [I>=2σ (I)]	R_1 = 0.0658, wR_2 = 0.1364
Final R indexes [all data]	R_1 = 0.0892, wR_2 = 0.1482
Largest diff. peak/hole / e Å^{-3}	4.68/-2.89

Table C52. Selected bond lengths [Å] and angles [°] for **30**.

Au(1)-Ag(1)	2.8207(8)	Au(2)-C(27)	2.052(13)
Au(1)-Ag(1)#1	2.8206(8)	Ag(1)-N(1)	2.487(8)
Au(1)-C(1)#1	2.057(13)	Ag(1)-N(2)	2.477(9)
Au(1)-C(1)	2.056(13)	Ag(1)-S(1)	2.640(3)
Au(2)-C(21)	2.055(12)	Ag(1)-S(2)	2.626(3)
Ag(1)#1-Au(1)-Ag(1)	180.0	N(1)-Ag(1)-Au(1)	87.33(19)
C(1)-Au(1)-C(1)#1	180.0	N(1)-Ag(1)-S(1)	73.6(2)
C(27)-Au(3)-C(21)	172.8(5)	N(1)-Ag(1)-S(2)	137.0(2)
S(1)-Ag(1)-Au(1)	95.17(6)	N(2)-Ag(1)-Au(1)	95.43(19)
S(2)-Ag(1)-Au(1)	112.22(7)	N(2)-Ag(1)-S(1)	138.1(2)
S(2)-Ag(1)-S(1)	137.07(9)	N(2)-Ag(1)-S(2)	73.5(2)
		N(2)-Ag(1)-N(1)	66.5(3)

Symmetry transformations used to generate equivalent atoms:

1# 1-X,1-Y,-Z; 2# 2-X,2-Y,-Z

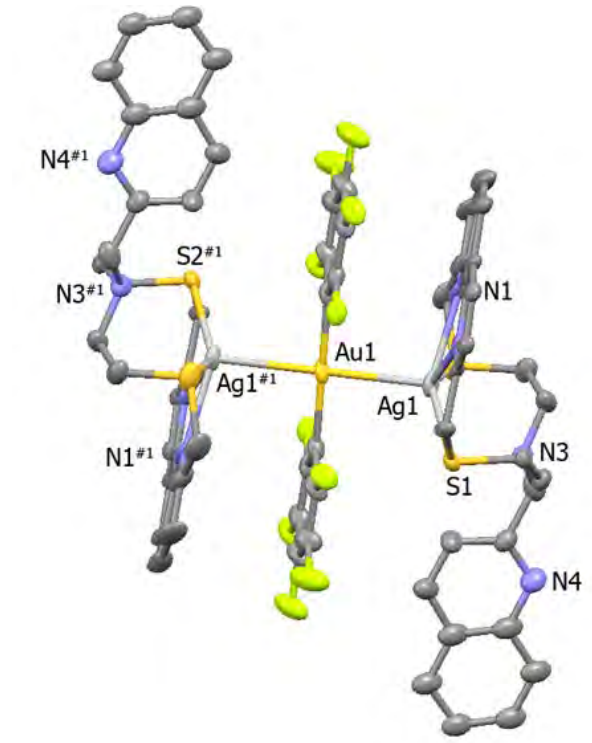

Table C53. Details of data collection and refinement for complexes **32.**

Compound	**32**
Empirical formula	$C_{30}H_{24}AgAuF_{10}N2OS2$
Formula weight	987.47
Temperature/ K	102(2)
Crystal system	Triclinic
Space group	P -1
a/Å	10.7963(9)
b/Å	12.2303(10)
c/Å	13.2956(11)
α/°	63.544(2)
β/°	76.666(3)
γ/°	79.465(3)
Volume/Å^3	1522.9(2)
Z	2
ρ_{calc}g/cm^3	2.153
μ/mm^{-1}	5.683
F(000)	948
Crystal size/mm^3	0.370 x 0.280 x 0.170
Radiation	MoKα (λ = 0.71073)
2Θ range for data collection/°	3.175 to 27.911
Reflections collected	30118
Independent reflections	7235 [R_{int} = 0.0389]
Data/restraints/parameters	7235/0/425
Goodness-of-fit on F^2	1.031
Final R indexes [I>=2σ (I)]	R_1 = 0.0316, wR_2 = 0.0692
Final R indexes [all data]	R_1 = 0.0411, wR_2 = 0.0766
Largest diff. peak/hole / e Å^{-3}	1.992/-1.561

Table C54. Selected bond lengths [Å] and angles [°] for **32**.

Ag(1)-Au(1)	2.8784(4)	Ag(1)-N(1)	2.550(4)
Au(1)-Au(1)#1	3.2610(4)	Ag(1)-N(2)	2.374(4)
Au(1)-C(1)	2.058(5)	Ag(1)-S(1)	2.5967(13)
Au(1)-C(7)	2.043(5)	Ag(1)-S(2)	2.6026(12)
C(7)-Au(1)-C(1)	173.26(18)	S(1)-Ag(1)-S(2)	120.90(4)
N(2)-Ag(1)-N(1)	71.27(14)	N(2)-Ag(1)-Au(1)	119.34(10)
N(2)-Ag(1)-S(1)	114.02(11)	N(1)-Ag(1)-Au(1)	168.87(9)
N(1)-Ag(1)-S(1)	76.59(9)	S(1)-Ag(1)-Au(1)	94.98(3)
N(2)-Ag(1)-S(2)	107.11(10)	S(2)-Ag(1)-Au(1)	100.01(3)
N(1)-Ag(1)-S(2)	78.70(10)		

Symmetry transformations used to generate equivalent atoms:

#1 -x+1,-y+1,-z+2

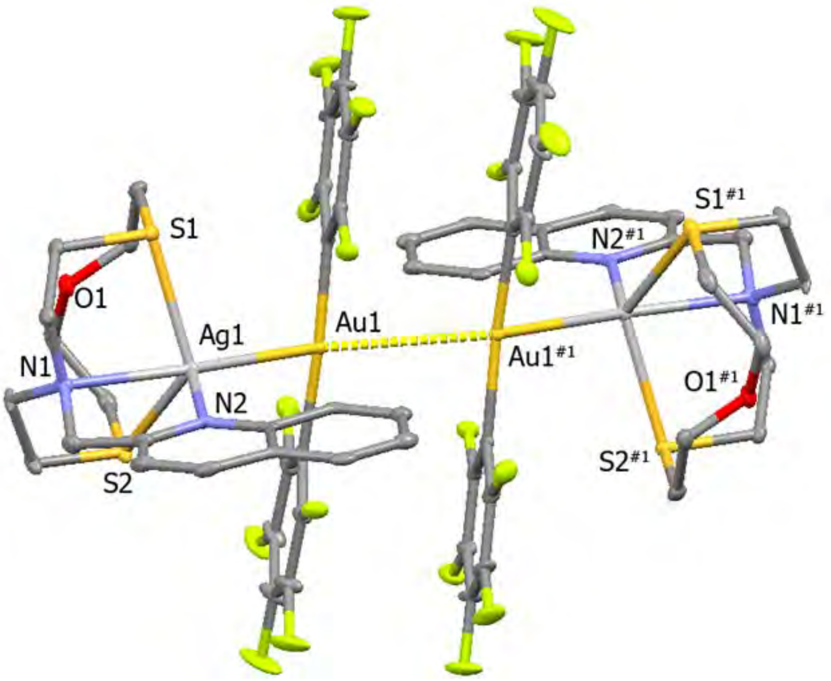

Table C55. Details of data collection and refinement for complexes **34.**

Compound	**34**
Empirical formula	$C_{99}H_{54}Ag_2Au_5Br_2F_{50}N_4O_2S_4Tl_3$
Formula weight	4383.20
Temperature/K	120(2)
Crystal system	Monoclinic
Space group	P 21/c
a/Å	21.293(3)
b/Å	24.191(3)
c/Å	21.437(3)
α/°	90
β/°	98.064(4)
γ/°	90
Volume/Å^3	10933(2)
Z	4
ρ_{calc}g/cm^3	2.663
μ/mm^{-1}	12.378
F(000)	8032
Crystal size/mm^3	0.529 x 0.194 x 0.157
Radiation	MoKα (λ = 0.71073)
2Θ range for data collection/°	0.966 to 28.010
Reflections collected	345824
Independent reflections	26115 [R_{int} = 0.1504]
Data/restraints/parameters	26115/1797/1543
Goodness-of-fit on F^2	1.185
Final R indexes [I>=2σ (I)]	R_1 = 0.0672, wR_2 = 0.1225
Final R indexes [all data]	R_1 = 0.1119, wR_2 = 0.1409
Largest diff. peak/hole / e Å^{-3}	3.423/-2.514

Table C56. Details of data collection and refinement for complexes **34.**

Tl(1)-Au(1)	3.0087(8)	Tl(2)-Au(4)#1	3.0348(8)
Tl(1)-Au(2)	3.1581(8)	Tl(2)-Au(2)	3.0083(8)
Tl(1)-Au(3)	3.0220(8)	Tl(2)-Au(3)#1	3.1495(8)
Tl(3)-Au(5)	2.9661(8)	Au(5)-Ag(2)	2.8849(12)
Tl(3)-Au(4)	3.2380(8)	Au(1)-Ag(1)	2.8803(11)
Tl(3)-Au(3)	3.0833(8)	Ag(1)-N(1)	2.537(11)
Ag(2)-N(4)	2.430(11)	Ag(1)-N(2)	2.429(10)
Ag(2)-S(3)	2.585(4)	Ag(1)-S(1)	2.595(4)
Ag(2)-N(3)	2.538(12)	Ag(1)-S(2)	2.609(4)
Ag(2)-S(4)	2.590(4)		
Au(1)-Tl(1)-Au(3)	163.48(2)	Au(1)-Tl(1)-Au(2)	73.678(18)
Au(3)-Tl(1)-Au(2)	116.58(2)	Au(2)-Tl(2)-Au(4)#1	73.35(2)
Au(2)-Tl(2)-Au(3)#1	177.39(2)	Au(4)#1-Tl(2)-Au(3)#1	106.35(2)
Au(5)-Tl(3)-Au(3)	173.18(2)	Au(5)-Tl(3)-Au(4)	73.03(2)
Au(3)-Tl(3)-Au(4)	103.09(2)	C(1)-Au(1)-C(7)	174.2(5)
C(19)-Au(2)-C(13)	178.2(5)	S(3)-Ag(2)-S(4)	123.34(12)
Tl(2)-Au(2)-Tl(1)	160.07(2)	N(4)-Ag(2)-Au(5)	90.1(2)
Ag(1)-Au(1)-Tl(1)	97.62(3)	N(3)-Ag(2)-Au(5)	139.9(3)
S(3)-Ag(2)-Au(5)	132.91(10)	C(31)-Au(3)-C(25)	178.4(6)
Tl(1)-Au(3)-Tl(3)	170.14(2)	Tl(1)-Au(3)-Tl(2)#2	112.12(2)
Tl(3)-Au(3)-Tl(2)#2	75.496(19)	C(43)-Au(4)-C(37)	172.5(5)
C(55)-Au(5)-C(49)	174.7(6)	Ag(2)-Au(5)-Tl(3)	93.96(3)
N(2)-Ag(1)-N(1)	68.2(3)	N(2)-Ag(1)-S(1)	87.5(3)
N(2)-Ag(1)-S(2)	129.8(3)	N(1)-Ag(1)-S(1)	81.0(3)
N(1)-Ag(1)-S(2)	78.5(3)	S(1)-Ag(1)-S(2)	123.77(11)
N(2)-Ag(1)-Au(1)	90.1(2)	N(1)-Ag(1)-Au(1)	140.6(2)
S(1)-Ag(1)-Au(1)	132.42(9)	S(2)-Ag(1)-Au(1)	93.00(8)
N(4)-Ag(2)-N(3)	67.5(4)	N(4)-Ag(2)-S(3)	89.8(3)
N(3)-Ag(2)-S(3)	81.9(3)	N(4)-Ag(2)-S(4)	127.8(3)
S(4)-Ag(2)-Au(5)	92.50(9)	N(3)-Ag(2)-S(4)	77.9(3)

Symmetry transformations used to generate equivalent atoms:

#1 x,-y+1/2,z-1/2 #2 x,-y+1/2,z+1/2

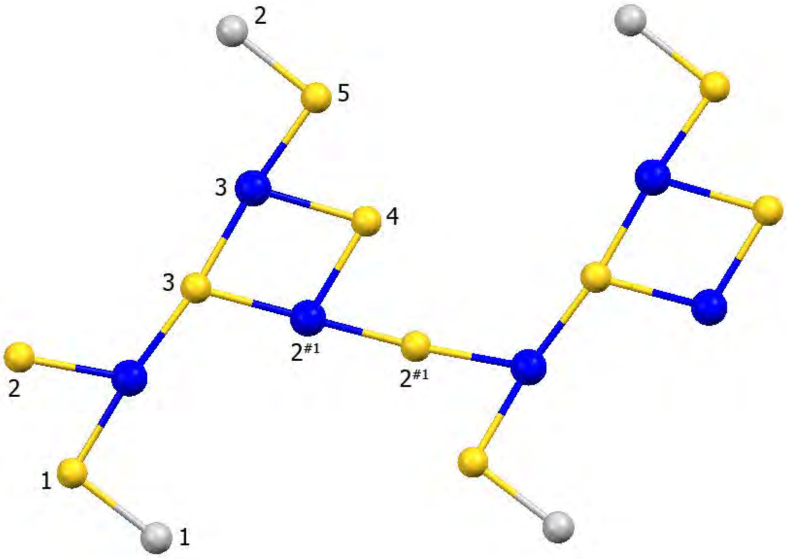
2
5
3
4
3
2#1
2#1
2
1
1

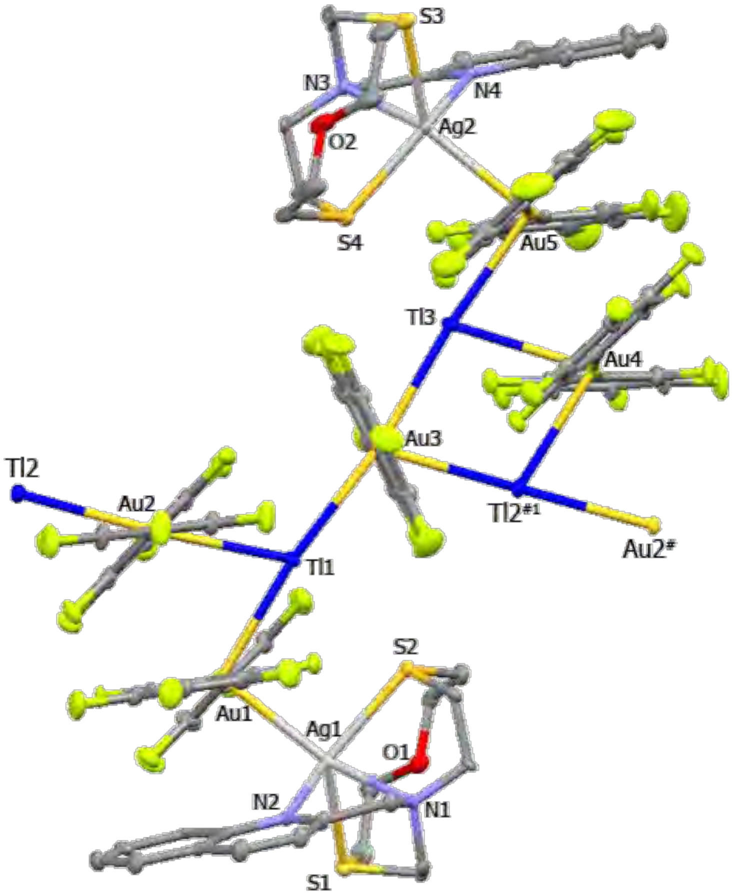
S3
N3
N4
Ag2
O2
S4
Au5
Tl3
Au4
Au3
Tl2
Au2
Tl2#1
Au2#
Tl1
S2
Au1
Ag1
O1
N2
N1
S1

D. Computational details.

The theoretical calculations DFT and MP2 have been carried out using the Gaussian 09[12] and Turbomol programs[13]. The molecular geometry of the theoretical models has been completely optimized at the theoretical level HF[14], DFT-PBE[15][16] with dispersion correction DFT-D3[17] or MP2[18] in the gas phase. The energy of interaction between fragments has been obtained, at the HartreeFock (HF) and MP2 theory level, according to the following equation:

$$\Delta E = E_{AB}{}^{(AB)} - E_A{}^{(AB)} - E_B{}^{(AB)} = V(R)$$

Correction of the counterpoise (cp) to the error of the superposition of base sets (BSSE)[19] was also carried out, adjusting the points by means of the H-Laurie expression of four parameters[20].

$$\Delta E = V(R) = Ae^{-BR} - CR^{-n}$$

For the calculations made throughout this report the following base sets have been used: in the case of gold and silver the pseudopotential has been used (PP) of Andrae[21] quasirrelativistic (QR) of 19 valence electrons (VE) and the corresponding base function increased with 2 polarization functions f; for thallium the effective core potentials employed have been 21-VE pseudo-potentials from Stuttgart and the corresponding basis sets augmented with two f polarization functions[21]. The fuzzy function of type f is required to describe the aurophylic attraction, while the compact function is used to describe the covalent bonds. The atoms of C,H, F, N, S, O and Cl were treated using the SVP basis sets[22].

E. References.

[1] W. Crutchfield Jr, *Ind. Eng. Chem. Anal. Ed.* **1942**, *14*, 57-58.

[2] G. Sheldrick, *SHELX-97 Programs Cryst. Struct. Anal.*, University of Göttingen: Göttingen, Germany, **1997**.

[3] E. J. Fernández, A. Laguna, J. M. Lopezde-Luzuriaga, M. E. Olmos, R. C. Puelles, *Zeitschrift fur Naturforsch. - Sect. B J. Chem. Sci.,* **2009**, 64, 1500-1512.

[4] R. Uson, A. Laguna, M. Laguna, B. R. Manzano, P. G. Jones, G. M. Sheldrick, *J. Chem. Soc. Dalt. Trans.,* **1984**, 0, 285-292.

[5] E. J. Fernández, J. M. López De Luzuriaga, M. Monge, M. E. Olmos, J. Pérez, A. Laguna, *J. Am. Chem. Soc.,* **2002**, 124, 5942-5943.

[6] E. J. Fernández, A. Laguna, J. M. López De Luzuriaga, M. Monge, M. Montiel, M. E. Olmos, J. Pérez, *Organometallics,* **2004**, 23, 774-782.

[7] L. G. A. van de Water, W. Buijs, W. L. Driessen, J. Reedijk, *New J. Chem.,* **2001**, *25*, 243-249.

[8] J. D. Chartres, A. M. Groth, L. F. Lindoy, M. P. Lowe, G. V. Meehan, *J. Chem. Soc. Perkin Trans.,* **2000**, 1, 3444-3450.

[9] C. Caltagirone, A. Bencini, F. Dcmartin, F. A. Devillanova, A. Garau, F. Isaia, V. Lippolis, P. Mariani, U. Papke, L. Tei, et al., *Dalt. Trans.,* **2003**, 0, 901-909.

[10] A. Casula, V. Nairi, V. Fernández-Moreira, A. Laguna, V. Lippolis, A. Garau, M. C. Gimeno, *Dalt. Trans.,* **2015**, 44, 18506-18517.

[11] J. Kang, J. H. Jo, *Bull. Korean. Chem. Soc.,* **2003**, *24*, 1403-1406.

[12] G. M. J. Frisch, W. Trucks, H. B. Schlegel, G. E. Scuseria, M. A. Robb, J. R. Cheeseman, G. Scalmani, V. Barone, B. Mennucci, G. A. Petersson, et al., *Gaussian 09, Revision A. 1; Gaussian*, **2009**.

[13] R. Ahlrichs, M. Bär, M. Häser, H. Horn, C. Kölmel, *Chem. Phys. Lett.,* **1989**, 162, 165-169.

[14] W. J. Hehre, L. Radom, P. V. R. Schleyer, J. A. Pople, *Ab Initio Molecular Orbital Theory*, **1986**.

[15] R. G. Parr, W. . T. Yang, *Density-Functional Theory of Atoms and Molecules*, **1989**.

[16] C. Lee, W. Yang, R. G. Parr, *Phys. Rev. B* ,**1988**, 37, 785-789.

[17] S. Grimme, J. Antony, S. Ehrlich, H. Krieg, *J. Chem. Phys.,* **2010**, 132, 144-146.

[18] C. Møller, M. S. Plesset, *Phys. Rev.,* **1934**, 46, 618-622.

[19] S. F. Boys, F. Bernardi, *Mol. Phys.,* **1970**, 19, 553-566.

[20] D. R. Herschbach, V. W. Laurie, *J. Chem. Phys.,* **1961**, 35, 458-460.

[21] H. T. Andrae, D. Häußermann, U. Dolg, M. Stoll, H. Preuß, *Theor. Chim. Acta,* **1990**, *77*, 123-141.

[22] A. Schäfer, H. Horn, R. Ahlrichs, *J. Chem. Phys.,* **1992**, *97*, 2571-2577.

CONCLUSIONES

La utilización de ligandos macrocílicos y derivados nos permite sintetizar diferentes complejos heterometálicos que contienen interacciones Au(I)/Ag(I) o Au(I)/Tl(I). La diferente capacidad coordinativa del ligando, así como sus características estructurales y electrónicas pueden afectar a las propiedades ópticas de los compuestos sintetizados. En particular, la luminiscencia en estado sólido en estos compuestos, aunque está basada fundamentalmente en las interacciones intermetálicas, en algún caso, está muy influenciada por la tipología del ligando. De hecho, los estudios teóricos realizados sobre el comportamiento luminiscente que muestran los compuestos 1-6, ponen de manifiesto que la emisión de estos dispositivos está relacionada con la presencia de las interacciones Au(I)/Tl(I). Por otro lado, los estudios realizados sobre los análogos complejos 17-23 que contienen interacciones Au(I)/Ag(I) muestran que la emisión de estos dispositivos está relacionada no solo con la presencia de las interacciones metalofílica sino también a la presencia de los ligandos macrocíclicos. Además, los estudios efectuados sobre el comportamiento mecanocrómico que muestra el compuesto 20, ponen de manifiesto que se trata de procesos en los que se descartan cambios de fase, tratándose de una amorfización de la fase cristalina.

Por otro lado, los estudios efectuados sobre el comportamiento de L_4,L_5 y L_6,L_7 muestran como la diferente capacidad coordinativa y características electrónicas de los ligandos pueden afectar a las propiedades ópticas de los diferente complejos. Por ejemplo, los estudios realizados sobre el comportamiento luminiscente de los derivados de fenantrolina Au(I)/Ag(I) y Au(I)/Tl(I) muestran que la formación de la especie $[L_4(M(I)]^+$ (M(I)= Ag(I) o Tl(I)) determina el quenching del sistema. Por otro lado, el aumento en la relación molar metal/ligando en el caso de los complejos 14, 16 muestra que gracias a la presencia de la unidad quinolínica, es posible obtener estructuras poliméricas debido al mayor número de átomos donadores y a la mayor libertad conformacional del ligando. Además, en la última parte del trabajo se presenta por primera vez la síntesis de un compuesto heterotrimetálico con interacciones Ag/Au/Tl, destacando cómo el aumento del momento del dipolo puede favorecer la presencia de esta novedosa disposición estructural.